Transactions of the ASME

EDITORIAL STAFF
Director, Technical Publishing,
JOS. SANSONE
Managing Editor,
CORNELIA MONAHAN
Production Editor,
JACK RUMMEL
Editorial Production Asst.
BETH DARCHI
Associate Editors
Air Pollution Control
H. E. HESKETH
Diesel and Gas Engine Power
F. PEKAR
Gas Turbine
R. A. HARMON
Power
D. T. BERUBE
Solar Energy
H. M. CURRAN
Energetics
J. B. COMLY
Fuels
R. E. BARRETT
Nuclear Engineering
M. S. OZKER

BOARD ON COMMUNICATIONS
Chairman and Vice-President
M. J. RABINS

Members-at-Large
W. BEGELL
J. CALLAHAN
M. HELMICH
D. KOENIG
M. KUTZ
F. LANDIS
J. W. LOCKE
J. E. ORTLOFF
C. PHILLIPS
K. REID

Business Staff
345 E. 47th St.
New York, N.Y. 10017
(212) 644-7789
Mng. Dir., Publ., J. J. FREY

OFFICERS OF THE ASME
President, ROBERT B. GAITHER
Exec. Dir. & Sec'y
BURKE E. NELSON
Treasurer, ROBERT A. BENNETT

Journal of Engineering for Power (ISSN 0022-0825) is edited and published quarterly at the offices of The American Society of Mechanical Engineers, United Engineering Center, 345 E. 47th St., New York, N. Y. 10017. ASME-TWX No. 710-581-5267, New York. Second Class postage paid at New York, N.Y., and at additional mailing offices.

CHANGES OF ADDRESS must be received at Society headquarters seven weeks before they are to be effective. Please send old label and new address.

PRICES: To members, $30.00, annually; to nonmembers, $60.00. Single copies, $20.00 each. Add $5.00 for postage to countries outside the United States and Canada.

STATEMENT from By-Laws. The Society shall not be responsible for statements or opinions advanced in papers or ... printed in its publications (B 7.1, para. 3).

COPYRIGHT © 1982 by the American Society of Mechanical Engineers. Reprints from this publication may be made on condition that full credit be given the TRANSACTIONS OF THE ASME – JOURNAL OF ENGINEERING FOR POWER, and the author, and date of publication be stated.

INDEXED by the Engineering Index, Inc.

Journal of Engineering for Power

Published Quarterly by The American Society of Mechanical Engineers

VOLUME 104 • NUMBER 1 • JANUARY 1982

TECHNICAL PAPERS

1 Preliminary Study on Reheat Combustors for Advanced Gas Turbines (81-GT-29)
Kenji Mori, Junichi Kitajima, Takeshi Kimura, and Sansei Miki

9 The Reheat Gas Turbine With Steam-Blade Cooling – A Means of Increasing Reheat Pressure, Output, and Combined Cycle Efficiency (81-GT-30)
I. G. Rice

23 Linear-Nonlinear Interface for Finite Element Impact Analysis (81-GT-39)
K. W. Brown and J. L. Krahula

28 Development of a Low NOx Lean Premixed Annular Combustor (81-GT-40)
P. B. Roberts, A. J. Kubasco, and N. J. Sekas

36 Premixing and Flash Vaporization in a Two-Stage Combustor (81-GT-41)
B. G. A. Sjöblom

44 Formation of SO_3 in Gas Turbines (81-GT-42)
S. C. Hunter

52 Development of a Small-Scale Catalytic Gas Turbine Combustor (81-GT-43)
S. J. Anderson, M. A. Friedman, W. V. Krill, and J. P. Kesselring

58 Use of Cascade and Small Turbine Tests to Determine Erosion of Utility Turbines (81-GT-52)
R. A. Wenglarz and M. Menguturk

64 Improved Particle Trajectory Calculations Through Turbomachinery Affected by Coal Ash Particles (81-GT-53)
B. Beacher, W. Tabakoff, and A. Hamed

69 A Theory for Fine Particle Deposition in Two-Dimensional Boundary Layer Flows and Application to Gas Turbines (81-GT-54)
M. Menguturk and E. F. Sverdrup

77 Dual Pressure Steam/Immiscible Liquid Cycles for Gas Turbine Exhaust Heat Recovery (81-GT-55)
B. M. Burnside

84 An Investigation of Axial Compressor Rotor Aerodynamics (81-GT-56)
R. P. Dring, H. D. Joslyn, and L. W. Hardin

97 Spanwise Mixing in Axial-Flow Turbomachines (81-GT-57)
G. G. Adkins, Jr. and L. H. Smith, Jr.

111 A Mean Line Prediction Method for Axial Flow Turbine Efficiency (81-GT-58)
S. C. Kacker and U. Okapuu

120 Bench Scale Testing of Low-NOx LBG Combustors (81-GT-59)
W. D. Clark, B. A. Folsom, W. R. Seeker, and C. W. Courtney

127 Comparison of the HTTT Reheat Gas-Turbine Combined Cycle With the HTTT Nonreheat Gas-Turbine Combined Cycle (81-GT-69)
I. G. Rice and P. E. Jenkins

143 Full Potential Solution of Transonic Quasi-Three-Dimensional Flow Through a Cascade Using Artificial Compressibility (81-GT-70)
C. Farrell and J. Adamczyk

154 Rotor-Tip Leakage: Part I – Basic Methodology (81-GT-71)
T. C. Booth, P. R. Dodge, and H. K. Hepworth

162 Rotor-Tip Leakage: Part II – Design Optimization Through Viscous Analysis and Experiment (81-GT-72)
A. R. Wadia and T. C. Booth

170 A Simple Model for Compressor Stall Cell Propagation (81-GT-73)
N. A. Cumpsty and E. M. Greitzer

177 A Comparison of Two Alternative Methods for Defining Fan Performance (80-WA/PTC-1)
P. M. Gerhart, R. Jorgensen and J. Kroll

184 Endwall Boundary Layer Flows and Losses in an Axial Turbine Stage
I. H. Hunter

194 A Generalized Mathematical Model to Estimate Gas Turbine Starting Characteristics (81-GT-202)
R. K. Agrawal and M. Yunis

202 Rotor Wake Mixing Effects Downstream of a Compressor Rotor (81-GT-98)
A. Ravindranath and B. Lakshminarayana

211 Calculation of the Theoretical Critical Flow Rate of Saturated Steam (80-WA/PTC-3)
J. W. Murdock

(Contents continued on p. 43)

Downloaded 03 Jun 2010 to 171.66.16.159. Redistribution subject to ASME license or copyright; see http://www.asme.org/terms/Terms_Use.cfm

(Contents Continued)

215 **Measurement of Heat Flux and Pressure in a Turbine Stage** (81-GT-88)
M. G. Dunn and A. Hause

224 **A Simplified ASME Acceptance Test Procedure for Steam Turbines**
B. Bornstein and K. C. Cotton

231 **Performance Characteristics of the Lysholm Engine as Tested for Geothermal Power Applications in the Imperial Valley**
R. F. Steidel, Jr., H. Weiss, and J. E. Flower

241 **Energy Conservation and Second Law Efficiency**
M. A. Paolino and M. D. Burghardt

TECHNICAL BRIEFS

247 **Sizing Safety Valve Vent Pipes for Saturated Steam**
H. E. Brandmaier

251 **Boundary Layer Transition and Separation on a Compressor Rotor Airfoil**
R. P. Dring

ANNOUNCEMENTS

8 **Change of address form for subscribers**

183 **Mandatory excess-page charge notice**

Inside back cover **Information for authors**

Downloaded 03 Jun 2010 to 171.66.16.159. Redistribution subject to ASME license or copyright; see http://www.asme.org/terms/Terms_Use.cfm

Kenji Mori
Assistant Manager of Combustion.

Junichi Kitajima
Research Engineer of Combustion.

Takeshi Kimura
Research Engineer of Combustion.

Research Section,
Technical Institute,
Kawasaki Heavy Industries, Ltd.,
Akashi 673, Japan

Sansei Miki
Senior Manager of Development Department,
Technology Development Group,
Kawaski Heavy Industries, Ltd.,
Tokyo 105, Japan
Mem. ASME

Preliminary Study on Reheat Combustors for Advanced Gas Turbines

Feasibility studies carried out by the Engineering Research Association for Advanced Gas Turbines under the sponsorship of the Agency of Industrial Science and Technology of Japan have indicated that the thermal efficiency of the combined cycle plant incorporating a high temperature reheat gas turbine and a steam turbine can exceed 50 percent. One of the engine components being investigated is the high temperature reheat combustor which will operate under high temperature (973 K) and heavily vitiated (12.4 percent O_2) inlet-air conditions. This paper describes the design considerations on the reheat combustor and the results of the near-atomospheric pressure tests (0.1 ~ 0.3 MPa) under vitiated conditions, using a conventional can-type combustor and a full scale model of the reheat combustor. Effects of air vitiation on inflammability limits, combustion efficiency, NOx and wall temperatures of gas turbine combustors are discussed.

Introduction

After the energy crisis, raising the thermal efficiency of power generation plants has become one of the most urgent and important subjects. Cogeneration system with the gas turbine and steam turbine plant is considered to be one of the promising methods [1]. Because of its higher level heat available in gas turbine exhaust, it will be effective to apply the cogeneration system to the high temperature gas turbines [2,3]. The reheat gas turbine cycle would be more attractive when coupled with the steam turbine cycle, and the overall efficiency of the combined cycle could exceed 50 percent [4, 5].

Feasibility studies carried out by the Engineering Research Association for Advanced Gas Turbines under the sponsorship of the Agency of Industrial Science and Technology (AIST) of Japan - Moonlight Project - have indicated that the thermal efficiency of the combined cycle plant incorporating a high temperature intercooled reheat gas turbine (AGTJ 100A) and a steam turbine can be over 5 percent higher than that of the combined cycle plant which consists of a simple gas turbine of the same temperature level [6, 7].

One of the reheat gas turbine elements of the project effort is the high temperature reheat combustor that is expected to be operated under high temperature (973K) and heavily vitiated (12.4 percent O_2) inlet-air conditions. This paper describes the studies on the reheat combustor including the preliminary combustion testing on the model reheat combustor whose objective is to obtain technical data necessary to the design and development effort for the advanced reheat combustor. Special attention is placed on the effect of the air-vitiation.

Many investigations have been undertaken into the effect of air vitiation by the addition of various diluents or by a pre-combustion upon combustion phenomena with the fundamental view to understanding the combustion mechanism or with the practical view to fire extinction and prevention. On the whole, adverse influences on combustibility such as flame propagation, inflammability and combustion efficiency have been found. But as for the gas turbine combustors, studies in the field of air vitiation seem to be limited.

Barr and Mullins [8] showed stability and combustion efficiency of their N.G.T.E. 'T scheme' combustor were deteriorated when air vitration was increased but were compensated by the elevation of the inlet-air temperature. They found an empirical relationship among the weak limit fuel-air ratio, the oxygen concentration and the inlet-air temperature in the range of $(O_2)_1$ = 21 percent ~ 14 percent and T_1 = 300K ~ 700K.

Marsland, et al. [9] studied air vitiation effects on flame tube wall temperatures of the tubo-annular combustor operating at $(O_2)_1$ = 25.6 percent ~ 17.1 percent, P_1 = 0.4 MPa, $T_1 \simeq$ 777K and $n \simeq$ 63. They reported wall temperatures of the gas turbine combustor decreased according to the increase of air vitiation mainly due to the decreased flame temperature.

Odgers and Kretschmer [10] recently showed the results of a measurement in a gas turbine combustor primary zone under the air vitiation condition of $(O_2)_1 \simeq$ 17 percent, $P_1 \simeq$ 2 MPa, $T_1 \simeq$ 800K and $n \simeq$ 60, and indicated substantial

Contributed by the Gas Turbine Division and presented at the International Gas Turbine Conference, Houston, Texas, March 8-12, 1981, of THE AMERICAN SOCIETY OF MECHANICAL ENGINEERING. Manuscript received at ASME Headquarters, December 5, 1980. Paper No. 81-GT-29.

Copyright © 1982 by ASME
Downloaded 01 Jun 2010 to 171.66.16.62. Redistribution subject to ASME license or copyright; see http://www.asme.org/terms/Terms_Use.cfm

Table 1 Operating conditions of advanced reheat combustor – feasibility study

	Full Load		Half Load	
P_1	0.9	MPa	0.6	MPa
T_1	973	K	890	K
U_f	38	m/s	36	m/s
$(O_2)_1$	12.4	Vol %	13.5	Vol %
n	60		70	

differences in temperature, air-fuel ratio distribution and composition in the primary zone between the vitiated and unvitiated conditions existed although the similarities of the combustion efficiency at the combustor exit existed.

For the design and development of the reheat combustor for the advanced high temperature gas turbine, more information about air vitiation effects seemed to be necessary. Therefore the parametric studies on the air vitiation using a conventional can-type combustor "Model M1" and also preliminary high temperature and heavily vitiated-air combustion tests using a full-scale model of the advanced reheat combustor "RCLT 1" were conducted.

Consideration on Reheat Combustor

Operating Conditions of Reheat Combustor. Table 1 shows the operating conditions of the advanced reheat combustor based on the feasibility study.

Arrangement of the reheat combustor and the other components is shown in Fig. 1.

Heavily vitiated air of the reheat combustor is caused by the higher temperature-rise combustion in the high pressure combustor and the direct water injection within the intercooler. Degree of the air vitiation is somewhat reduced by the cooling air amount used in the high pressure turbine which bypasses the high pressure combustor.

Figure 2 shows the expected tendency of the inlet air conditions of the reheat combustor of the advanced reheat gas turbine as the high temperature turbine technology advances further. In the case of no-cooling like ceramic turbine, oxygen concentration of the vitiated air at the reheat combustor inlet would become nearly 10 percent by volume, which means less than the half value of the pure air. Inlet-air temperature of the reheat combustor will go up when the high temperature combustor comes to our hands.

Hence, the most important subject for the development of the high temperature reheat combustor would be the effects of air vitiation on the combustion performance and on the heat transfer performance under the elevated inlet-air temperature.

Design Considerations. Figure 3 shows the change of the stoichiometric air-fuel ratio n_{st} and the stoichiometric adiabatic flame temperature T_{fad}, when the air vitiation is caused by the pre-combustion (a) or by the water vapour addition (b). As a typical fuel, kerosene is considered.

Remarkable increase of the chemically correct air-fuel ratio in the vitiated air combustion renders more air must be distributed to the combustion zone and as a result insufficient dilution air is available for getting the good exit-temperature profile. And, the relatively lower heat release in the reheat combustor ($T_2 - T_1 \simeq 500$K) than that, for example, in the high pressure combustor ($T_2 - T_1 \simeq 800$K) does not

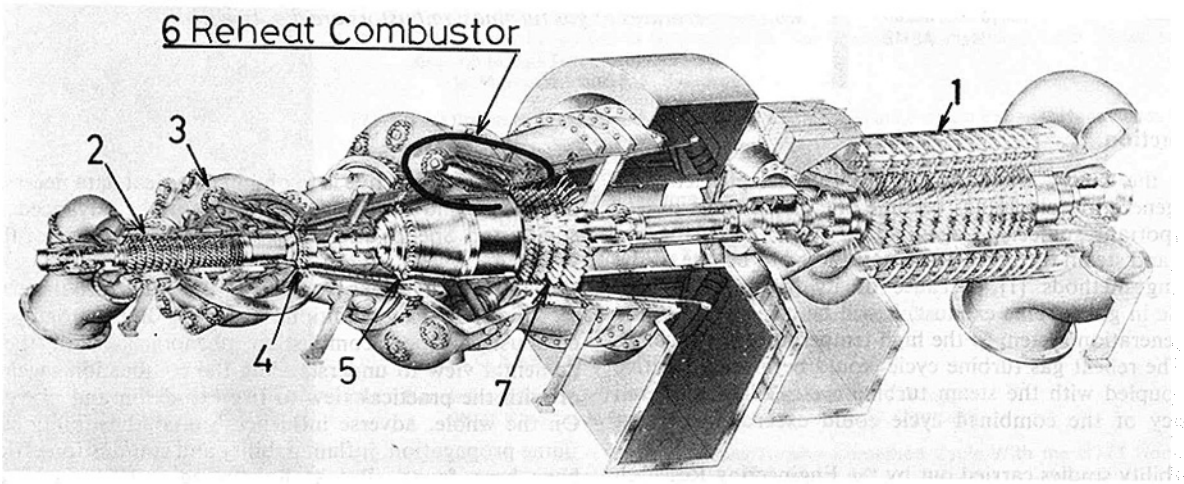


Fig. 1 Pictorial view of advanced gas turbine and reheat combustor:

1 = LP Compressor, 2 = HP Compressor, 3 = HP Combustor, 4 = HP Turbine, 5 = IP Turbine, 6 = Reheat Combustor, 7 = LP Turbine, 8 = Water Spray Intercooler (not shown)

Nomenclature

B.O. = blow out of flame
$L1$ = liner wall of primary zone
$L2$ = liner wall of secondary zone
$L3$ = liner wall of dilution zone
LH = liner head
n = air-fuel ratio
NOx = nitrogen oxides concentration, ppm
O_2 = oxygen concentration, vol. %
P = pressure, MPa
T = temperature, K
U = velocity, m/s
ΔTw = wall temperature rise, K ($\Delta Tw = Tw - T_1$)
ηb = combustion efficiency, %

Subscript

1 = upstream of combustor
2 = combustor outlet
ad = adiabatic condition
f = flame
l = liner tube
st = stoichiometric condition
std = reference standard condition
w = liner wall

Superscript

– = mean value of measured data

Downloaded 01 Jun 2010 to 171.66.16.62. Redistribution subject to ASME license or copyright; see http://www.asme.org/terms/Terms_Use.cfm

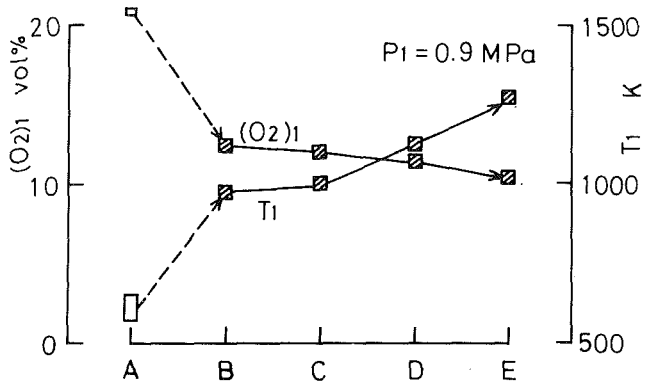


Fig. 2 Tendency of inter-air condition for high temperature reheat combustor:
A = conventional combustor, B = RC (1570K conventional air-cooled HPT), C = RC (1570K advanced air-cooled HPT), D = RC (1570K no-cooling HPT), E = RC (1770K no-cooling HPT), RC = reheat combustor, HPT = high pressure turbine

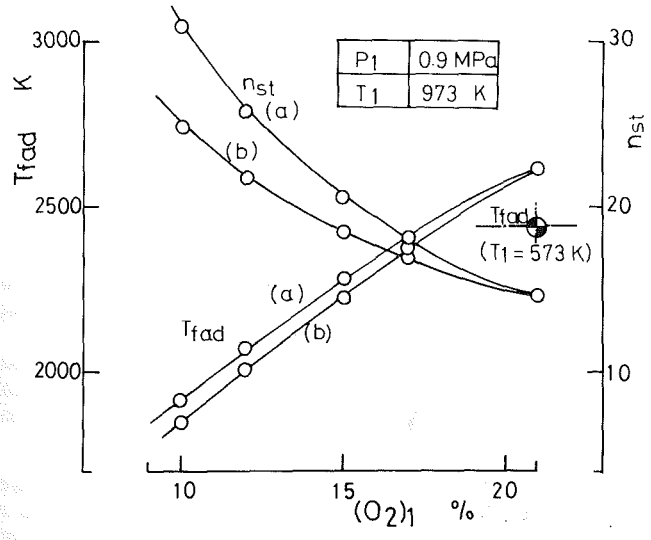


Fig. 3 Flame Temperature & Stoichiometric Air-Fuel Ratio:
(a) precombustion, *(b)* water vapour addition

necessarily mean more cooling air is available, because the increase of the chemically correct air-fuel ratio in the vitiated air combustion causes more combution air necessary.

The adiabatic flame temperature T_{fad} is supposed to play a significant role in a gas turbine combustor because diffusion flame combustion is generally dominant in a gas turbine combustor.

Accordingly thermal effects of the air vitiation upon the high temperature reheat combustor were mainly taken into account before proceeding to the design work of the model combustor. Figure 3 indicates that T_{fad} decreases by 60 to 75K as $(O_2)_1$ decreases by 1 percent by the air vitiation. Inflammability limits, NO_x formation and wall temperature rise etc. will be strongly affected by the flame temperature. As a reference, T_{fad} of a typical conventional combustor at T_1 = 573K and no air vitiation is shown in Fig. 3. 400K higher inlet-air temperature of the high temperature reheat combustor is compensated by the air vitiation of about 3.5 percent oxygen decrease so far as the flame temperature is concerned. This means that in case of the heavy air vitiation of the high temperature reheat combustor the flame temperature will be lower than that of the conventional combustor, and deteriorated combustibility, less NOx generation and less wall

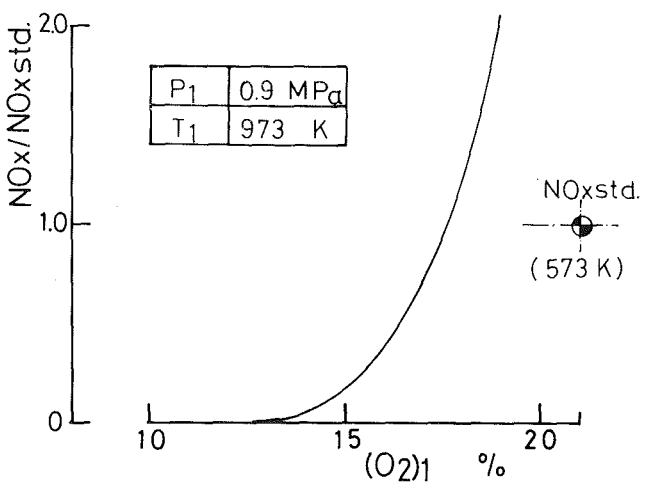


Fig. 4 NOx versus air-vitiation

temperature rise would be expected. However this does not necessarily means lower wall temperature because of the higher inlet-air temperature. In order to keep the adiabatic flame temperature constant, about 110 to 120K increase of the inlet-air temperature is necessary for each 1 percent decrease of the oxygen concentration by the air vitiation.

Figure 4 shows NOx generation tendency when the inlet-air is vitiated by the pre-combustion relative to the reference standard condition. Calculation is based on the Zel'dovich mechanism and the assumptions of the stoichiometric combustion etc. are taken into account [11].

NOx amount emitted increases exponentially as $(O_2)_1$ increases mainly because of the increase of the flame temperature. NOx emisison of the reheat combustor is considered to be at a lower level in spite of the elevated inlet-air temperature owing to the heavy air vitiation, therefore no special means for NOx reduction would be necessary.

The results of a simple calculation of the wall temperature rise ($\Delta Tw = Tw - T_1$) is shown in Fig. 5. The combustor model is the RCLT1 reheat combustor shown in Fig. 7. *L*1 denotes the primary zone and *L*3 dilution zone. The method used for calculating the film-cooled wall temperature is similar to that proposed by Ballal and Lefebvre [12], but a correction factor has been introduced for the estimation of the flame temperature and the change of the emissivity of the flame by the air vitiation is not taken into account.

The temperature rise of the combustor wall decreases linearly as the air vitiation increases. One percent decrease of the inlet-air oxygen causes 25K decrease of the wall temperature in the primary zone and 11K decrease in the dilution zone. The wall temperature rise of the high temprature reheat combustor is expected to be smaller than that of the standard nonvitiated condition, but the metal temperature itself will exceed the level of the standard condition owing to about 400K higher inlet-air temperature. Then more attention should be paid to the cooling methods for the high temperature reheat combustor.

Experimental Program and Test Facilities

Two series of combustion tests were projected to obtain the technical data necessary for the design and development of the high temperature reheat combustor.

In the first place basic parametric study was carried out to assess the air vitiation effects on the combustion performance. A conventional can-type combustor which is utilized for the Kawasaki M1 gas turbine was selected and air vitiation was produced simply by adding water vapor into the inlet-air. Secondly, in order to estimate the combustor

Downloaded 01 Jun 2010 to 171.66.16.62. Redistribution subject to ASME license or copyright; see http://www.asme.org/terms/Terms_Use.cfm

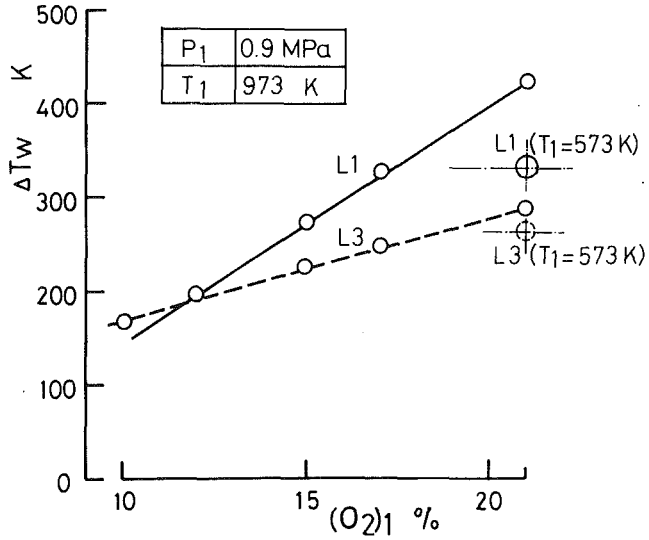


Fig. 5 Wall temperature versus air-vitiation

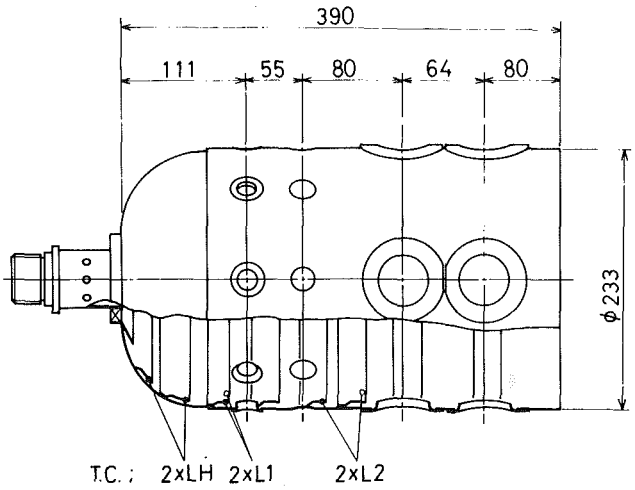


Fig. 6 Model combustor M1

performance of the high temperature reheat combustor near-atmospheric combustion tests were conducted using a full-scale reheat combustor model of the advanced gas turbine. The high temperature and heavily vitiated inlet-air conditions were attained by the pre-combustion of the slave combustor and the water addition. The inlet-air temperature and the oxygen concentration along with the gas composition of the operating conditions of the advanced reheat combustor could be simulated.

Test Combustors. Figure 6 shows the model combustor M1 used in the first parametric study. Figure 7 shows the full-scale model of the advanced reheat combustor "RCLT1."

Table 2 shows the air distribution of each model combustor.

According to the increase of the stoichiometric air-fuel ratio for the vitiated-air condition, the amount of the combustion air of the RCLT1 combustor has been increased as stated in the design consideration.

Cooling air rate of the RCLT1 combustor has been increased to cool both the combustor liner and the transition duct. In order to save the cooling-air, the length and the cooling air amount of the cooling film on the liner has been

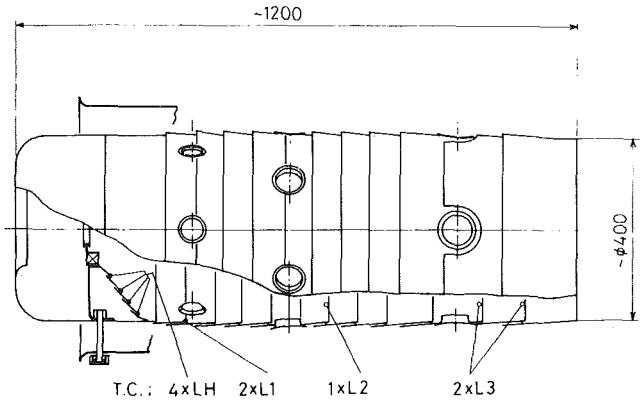


Fig. 7 Model Combustor RCLT1:
T.C. = Thermo-couple, LH = linear head, L1 = primary zone, L2 = secondary zone, L3 = dilution zone

Table 2 Air Distributions of model combustors

	M1	RCLT1
Combustion Air	23.6%	35.9%
swirler	6.9%	8.3%
comb. holes	16.7%	27.6%
Dilution Air	42.4%	15.6%
dil. holes	42.4%	15.6%
Cooling Air	34.0%	48.5%
liner tube	34.0%	38.3%
transition duct	0%	[1] 10.2%

designed in a manner that more cooling air is distributed to the primary zone and less to the dilution zone. Impingement cooling has been planned for the transition duct.

Swirl vanes of 45 deg angle have been adopted for the good flame holding performance. Swirl nozzles were used for both M1 and RCLT1 combustors, and assisted air was provided to around the swirl orifice of the RCLT1 nozzle.

Test Facilities and Test Conditions. The facilities are basically the same as stated in the author's paper [13]. As a test section for the larger RCLT1 combustor, a large plenum casing of about 2mϕ in diameter with high temperature heat insulation mounted on the inside was devised, as shown in Fig. 8. The slave combustor and the water injection nozzles were installed before the plenum casing for the purpose of getting the high temperature and heavily vitiated inlet-air. The oxygen concentration $(O_2)_1$ was calculated from the flow rate of the water and that of the fuel injected into the slave combustor using a data processing computer. Operating conditions such as P_1, T_1, U_l, and n including $(O_2)_1$ were monitored by the CRT-display of the same computer system so as to control the aimed test condition easily. The inlet-air temperature was kept in the range of ± 20K of each aimed test condition. Cond. 1, 2, and 3 in Fig. 12 to Fig. 16, respectively, indicate the aimed temperatures of 990K, 810K and 730K. T_1 of cond. 1 is nearly equal to the design temperature of the advanced reheat combustor.

Test conditions are listed in Table 3. Kerosene was used as a fuel.

Test Results and Discussions

Basic Parametric Study on M1 Combustor

Flame Appearance. Luminous yellow flames turned into

[1] Dummy transition duct.

Downloaded 01 Jun 2010 to 171.66.16.62. Redistribution subject to ASME license or copyright; see http://www.asme.org/terms/Terms_Use.cfm

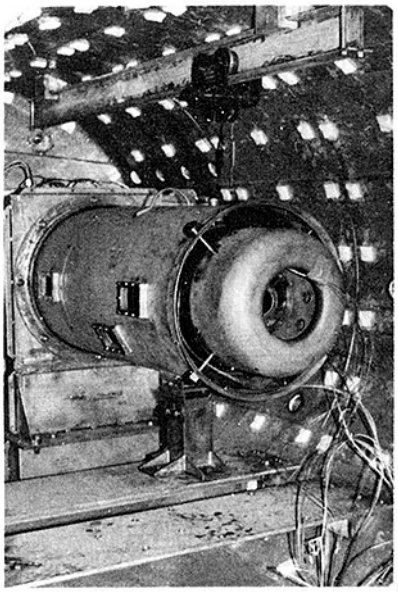


Fig. 8 Inside view of plenum casing

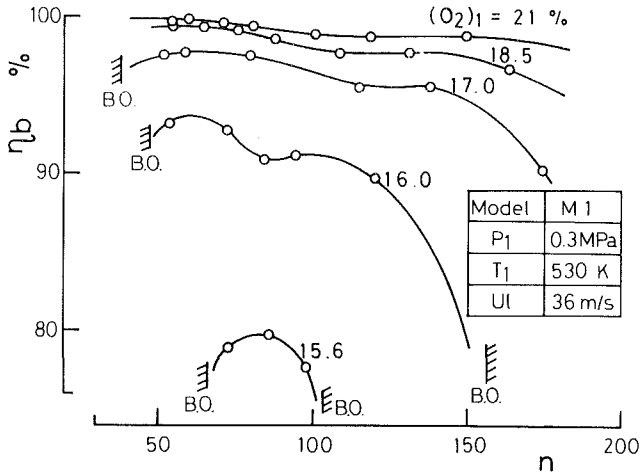


Fig. 9 Combustion efficiency - M1: B.O. = blow out

Table 3 Test conditions

	M1	RCLT 1
P_1	0.1 ~ 0.3 MPa	0.13 MPa
T_1	450 ~ 530 K	730 ~ 990 K
U_l	16 ~ 44 m/s	33 m/s
$(O_2)_1$	15.5 ~ 21.0%	8.2 ~ 12.4%
n	50 ~ 200	50 ~ 200

transparent whitish-orange or blue flames when the air vitiation in the M1 combustor was increased by water vapour addition to the inlet-air. In the larger air vitiation, blow out of the flames at both fuel-rich side and fuel-lean side occured suddenly without any unstable sign before it.

Combustion Efficiency. The combustion efficiency of the M1 combustor is shown in Fig. 9. A considerable decrease of the combustion efficiency is indicated together with the narrowing of the flammable air-fuel ratio when air vitiation is increased.

Inflammability limits. Both rich limit and weak limit appeared under the heavier air-vitiated conditions in the range of the practical air-fuel ratio in which no inflammability limits were observed under non-vitiated combustion.

Figure 10 indicates inflammability limit under vitiated-air conditions, with the various operating parameters. The upper side of each plotted line shows the respective inflammable region.

Figure 10(a) shows the effect of air-fuel ratio. It seems both rich limit and weak limit tend to approach to each other narrowing the flammable air-fuel ratio region when $(O_2)_1$ decreases due to the increase of the air-vitiation, and they eventually coinside at the critical point under which no combustion region exists. The inflammability limits are shown to be strongly affected by the inlet-air temperature. Figure 10(b) shows that an increase by about 65K in T_1 lowers the inflammability limit by as much as 1 percent of $(O_2)_1$. Figure 10(c) shows the effect of the reference velocity of the combustor liner U_l. Effect of U_l on the inflammability limit is very small in the practical U_l range of over 30 m/s. Figure 10(d) shows the effect of the pressure P_1 upon the inflammability. An increase by 0.1 MPa in P_1 causes lowering $(O_2)_1$ of the flammable limit by 0.3 to 0.4%.

NOx. NOx emission tendency by the air vitiation is shown in Fig. 11 together with the combustion efficiency ηb. NOx emission decreases in an exponential manner when the degree of the air vitiation is increased as expected in the design consideration.

Combustion Tests on Full-Scale Model of Reheat Combustor

Flame Appearance. In the high temperature and heavily vitiated combustion of RCLT1 transparent dark red flames were observed.

Flame length was not measured, but flame observation from the back-side window showed the elongating tendency of the flame according to the increase of the air vitiation. Flame shapes were always stable and no signs of unstableness were observed even at the near blow-out combustion.

Combustion Efficiency. Figure 12 shows that in the case of the high inlet-air temperature of T_1 = 900K, decreasing tendency of the combustion efficiency by the air vitiation diminishes. But when the inlet-air temperature lowers drop of the combustion efficiency will occur. Owing to the elevated inlet air temperature, the combustion efficiency of the reheat combustor at the design point will be higher than 99.9 percent.

Inflammability Limits. Figure 13 shows nearly the same tendency of the air vitiation on the inflammability limits as Fig. 10(a).

Arrow marks denote the critical point under which no combustion occurs in any air-fuel ratio. Both rich limit (left hand line of the critical point) and lean limit (right hand line of the critical point) approach to the critical point as the air vitiation is increased, narrowing the range of the flammable air-fuel ratio. Strong dependence of T_1 on the inflammability limits is also shown. The designed air vitiation level of the advanced reheat combustor (shown in Table 1) is safe enough to keep combustion owing to its higher inlet-air temperature. Figure 13 indicates that more air distribution into the primary zone (dotted line) will shift the critical point to the smaller air-fuel ratio and the heavier air-vitiation to the larger air-fuel ratio. These effects can be explained by assuming that the optium air-fuel ratio in the primary zone is obtained at the critical point.

Figure 14 shows the effect of the inlet-air temperature on the inflammability limit. Test results on both RCLT1 and M1 model combustors are shown together with the operating range of the advanced reheat combustor. A negative linear relationship between T_1 and $(O_2)_1$ at the inflammability limits can be observed. Air vitiation by 1 percent of oxygen concentration can be compensated by elevating the inlet-air

Downloaded 01 Jun 2010 to 171.66.16.62. Redistribution subject to ASME license or copyright; see http://www.asme.org/terms/Terms_Use.cfm

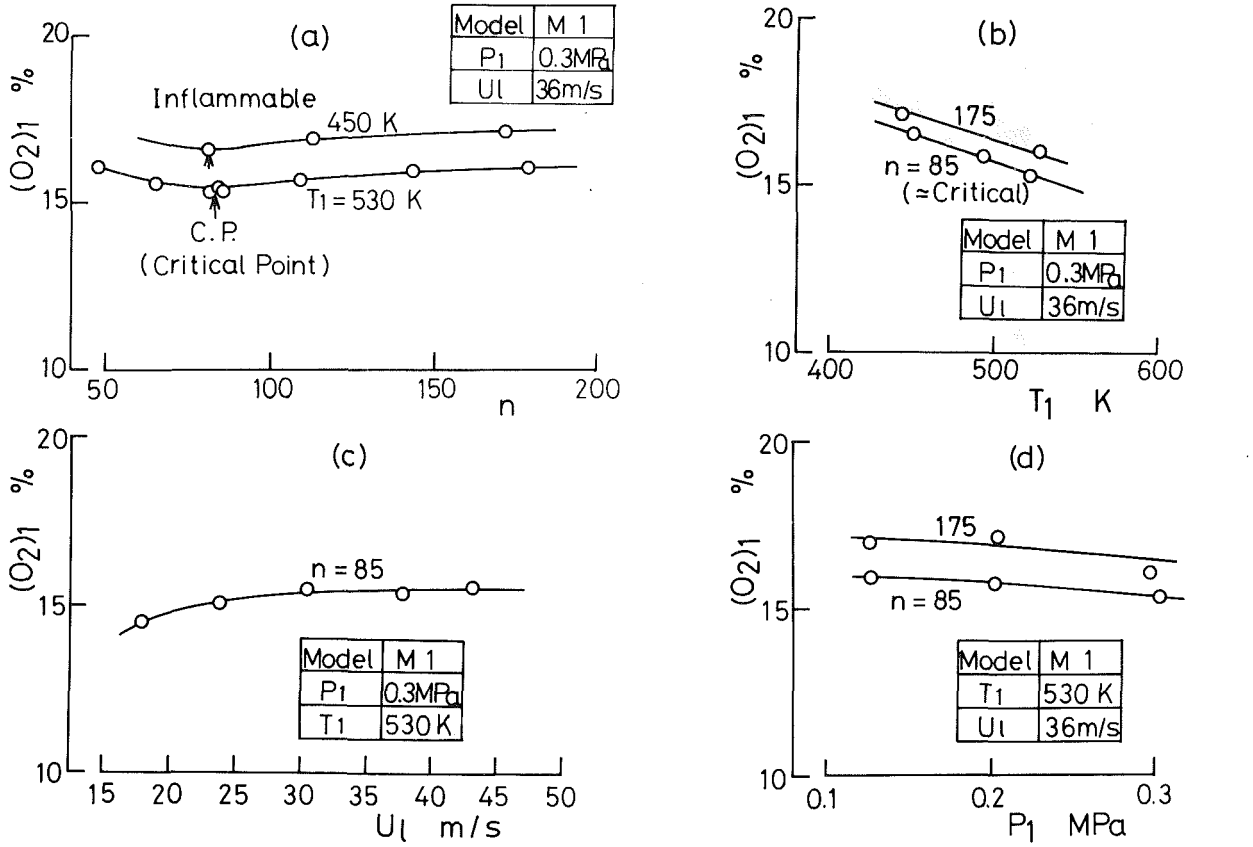


Fig. 10 Inflammability Limits - M1: *(a)* effect of air-fuel ratio, *(b)* effect of inlet-air temperature *(c)* effect of reference velocity, *(d)* effect of inlet-air pressure

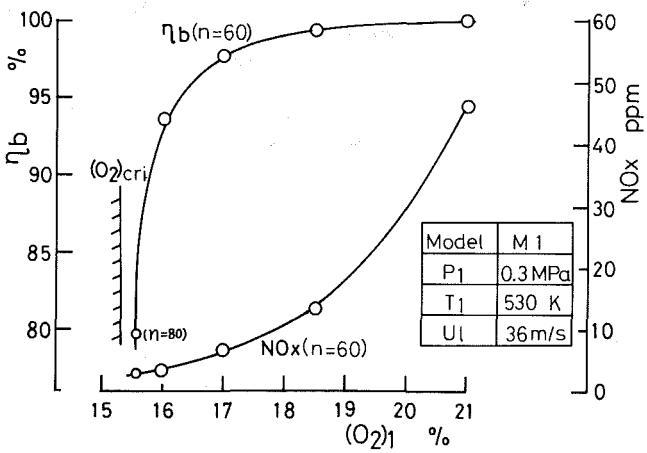


Fig. 11 Effect of air-vitiation on NOx and ηb - M1

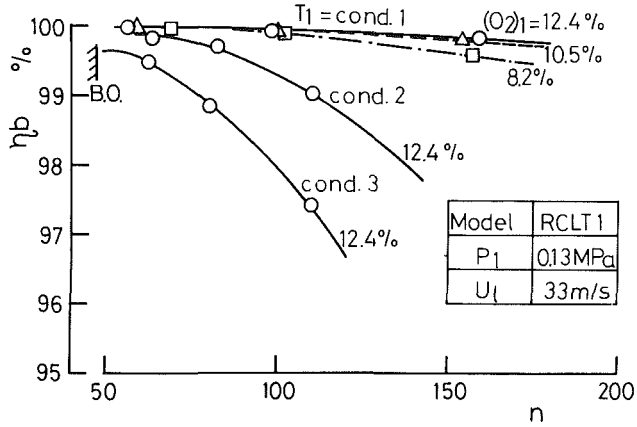


Fig. 12 Combustion Efficiency - RCLT1: B.O. = blow out

temperature by 65K to 75K, the smaller temperature rise than keeping the adiabatic flame temperature constant. In the case of the advanced reheat combustor, heavy air-vitiation could be compensated enough by the elevated inlet-air temperature so far as the inflammability is concerned.

Liner-Wall Temperature. Metal temperature of the RCLT1 model combustor were measured by the 1.6 mmϕ CA thermocouples attached to the liner wall as shown in Fig. 7.

As a typical example, Fig. 15 shows the mean wall temperature rise of the primary zone $\overline{L1}$ and that of the dilution zone $\overline{L3}$.

The tendency of LH is similar to that of $L1$, and $L2$ to that of $\overline{L3}$.

When the air vitiation is increased, wall temperatures decrease according to the decrease of the flame temperature. The increase of the air-fuel ratio tends to decrease the gas temperature especially at the combustor exit, and the wall temperature of the dilution zone decreases as the air-fuel ratio increases. The effect of the air-fuel ratio on the wall temperature in the primary zone can not be simply explained, because the wall temperature especially in the primary zone will be strongly affected by the flame shape and position.

Downloaded 01 Jun 2010 to 171.66.16.62. Redistribution subject to ASME license or copyright; see http://www.asme.org/terms/Terms_Use.cfm

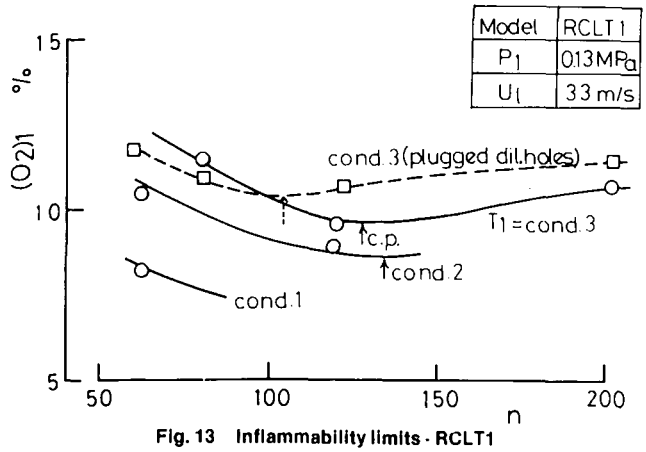


Fig. 13 Inflammability limits - RCLT1

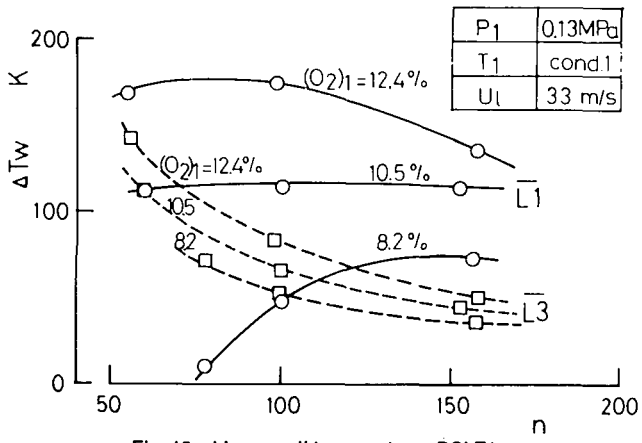


Fig. 15 Liner - wall temperature - RCLT1

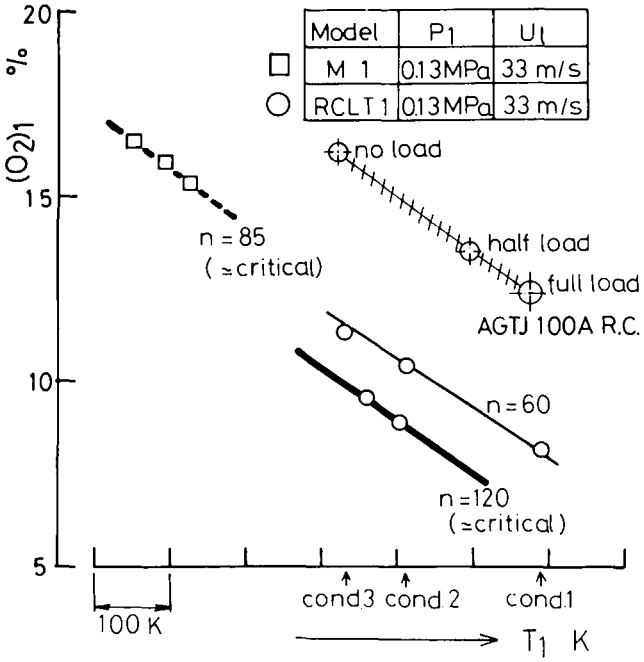


Fig. 14 Effect of air-vitiation on inflammability limits

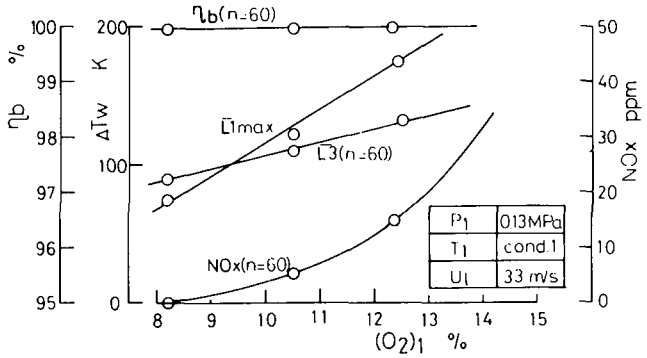


Fig. 16 Effect of air vitiation on combustor performance - RCLT1

Assuming that the maximum wall temperature would be obtained at the optimum air-fuel ratio of the primary zone, the test data in Fig. 15 indicate that the point of the optimum air-fuel ratio of the primary zone would shift to the leaner side by increasing the air-vitiation. The tendency is nearly the same as that of the critical point stated before. Attention should be paid to the fact that the maximum wall temperature rise of the primary zone does not necessarily appear at the richest air-fuel ratio.

The liner-wall temperatures of the advanced reheat combustor could be expected in the range of 1000K to 1200K which is higher than the range of the conventional combustor.

Combustor Performance. The effect of the air vitiation on the performance of the RCLT1 model combustor at the near-atmospheric pressure and at the elevated inlet-air temperature is shown in Fig. 16. The tendency of the NOx emission and the wall-temperature rise due to the change in the air vitiation is nearly the same as expected in the design considerations.

NOx decreases exponentially as $(O_2)_1$ decreases, and the temperture of L1 decreases by 25K and that of $L3$ decreases by 10K for the one percent reduction of $(O_2)_1$. Owing to the elevated inlet-air temperature, combustion efficiency is kept above 99.9 percent even in the very heavy vitiated-air conditions.

Summary and Future Development

Effects of air vitiation on the performance of the gas turbine combustors are studied from the view point of the design and development for the advanced reheat combustor.

Rich and lean combustion limits appear in the usual air-fuel ratio range and the critical oxygen concentration under which no combustion occurs in any air-fuel ratio exists under the vitiated-air conditions. These effects are compensated by elevating the inlet-air temperature, and the negative linear relationship between T_1 and $(O_2)_1$ is found to exist at the inflammability limits. Effects of air vitiation on the NOx emission and the wall temperature rise can be estimated in tendency by taking the thermal effect of air vitiation into account.

Combustion performances of the advanced reheat combustor are estimated by the near-atmospheric pressure and the elevated inlet-air temperature combustion tests.

High combustion efficiency, wide range combustibility and low NOx emission of the advanced reheat combustor are expected. The wall temperature would be higher than the conventional combustor, and much effort must be made to the cooling technology development.

Proceeding tests for the cooling performance of the transition duct, the pressure-loss performance and the outlet-temperature pattern factor are under way.

High pressure combustion tests and flow visualization tests of the model reheat combustor are projected.

Downloaded 01 Jun 2010 to 171.66.16.62. Redistribution subject to ASME license or copyright; see http://www.asme.org/terms/Terms_Use.cfm

Acknowledgments

The authors wish to thank the Agency of Industrial Science and Technology and the Engineering Research Association for Advanced Gas Turbines who sponsored the combustion test on the RCLT1 reheat combustor and to T. Miyagawa, N. Sasaki and Y. Enzaki for the contribution to the design works of the RCLT1 model combustor.

References

1 Bernstein, E., and Cashman, J., "The Energy Saver Combined Cycle," ASME Paper No. 78-GT-127.

2 Caruvana, A., Day, W. H., Manning, G. B., and Sheldon, R. C., "Evaluation of a Water-Cooled Gas Turbine Combined Cycle Plant," ASME Paper No. 78-GT-77.

3 Faize, W. and Lewis, J., "Technical and Economic Objectives for the Development of Advanced Combined Cycles for Use With Coal-Derived Fuels," ASME Paper No. 78-GT-101.

4 Rice, I.G., "The Combined Reheat Gas Turbine/Steam Turbine Cycle Part I," ASME Paper No. 79-GT-7.

5 Rice, I.G., "The Combined Reheat Gas Turbine/Steam Turbine Cycle Part II," ASME Paper No. 79-GT-8.

6 "Feasibility Study on An Advanced Gas Turbine System, 1978 Fiscal Year Report," prepared by the Engineering Research Association for Advanced Gas Turbines for the Agency of Industrial Science and Technology of Japan.

7 Takeya, K. and Hori, A., "Outline of Plan for An Advanced Reheat Gas Turbine — National Project, Japan," to be presented at the ASME twenty-sixth Annual International Gas Turbine Conference, Houston, Texas, Mar. 8-12 1981.

8 Barr, J. and Mullins, B.P., "Combustion in vitiated atomospheres 1V - Performance of a typical combustion chamber," *Fuel,* Vol. 28, 1949, pp. 225-228.

9 Marsland, J., Odgers, J., and Winter, J., "The Effects of Flame Radiation on Flame-Tube Metal Temperatures," Twelfth Symposium (International) on Combustion, Combustion Institute, 1969, pp. 1265-1276.

10 Odgers, J. and Kretschmer, D., "Considerations of the Use of Vitiated Preheat," ASME Paper No. 80-GT-61.

11 Mori, K., Kimura, T., Kitajima, J., and Kato, K., "Study of Emission Controls on Gas Turbine Combustors (Report 1)," KAWASAKI Technical Review, No. 69, Jan. 1979.

12 Ballal, D.R. and Lefebre, A.H., "A Proposed Method for Calculating Film-Cooled Wall Temperatures in Gas Turbine Combustion Chambers," ASME Paper No. 72-WA/HT-24.

13 Mori, K., Kitajima, J., Kajita, S., and Sone, H., "Development of the Can-type Gas Turbine Combustors," 1977 Tokyo Joint Gas Turbine Congress,

Downloaded 01 Jun 2010 to 171.66.16.62. Redistribution subject to ASME license or copyright; see http://www.asme.org/terms/Terms_Use.cfm

The Reheat Gas Turbine With Steam-Blade Cooling—A Means of Increasing Reheat Pressure, Output, and Combined Cycle Efficiency

I. G. Rice
Consultant,
Spring, Tex.
Fellow Mem. ASME

The reheat (RH) pressure can be appreciably increased by applying steam cooling to the gas-generator (GG) turbine blading which in turn allows a higher RH firing temperature for a fixed exhaust temperature. These factors increase gas turbine output and raise combined-cycle efficiency. The GG turbine blading will approach "uncooled expansion efficiency". Eliminating cooling air increases the gas turbine RH pressure by 10.6 percent. When steam is used (injected) as the blade coolant, additional GG work is also developed which further increases the RH pressure by another 12.0 percent to yield a total increase of approximately 22.6 percent. The 38-cycle pressure ratio 2400°F (1316°C) TIT GG studied produces a respectable 6.5 power turbine expansion ratio. The higher pressure also noticeably reduces the physical size of the RH combustor. This paper presents an analysis of the RH pressure rise when applying steam to blade cooling.

Introduction

The reheat (RH) gas turbine (GT) when combined with the steam turbine cycle offers a significant increase in overall cycle efficiency [1-2]. Besides this advantage there is a decided increase in power output per pound of airflow to reduce gas turbine machinery physical size. The concept of an axial flow arrangement of a high-cycle pressure ratio (CPR) nonintercooled compression gas generator (GG) supplying hot gas to a RH combustor and subsequently to a power turbine (PT) is thermodynamically and aerodynamically superior to the nonaxial flow RHGT configuration incorporating compression intercooling because (*a*) the heat loss due to the intercooling is saved, and (*b*) there is less parasitic pressure loss; however, intercooling does offer higher cycle pressure ratios of 50 to 60 which are compatible with the RHGT cycle.

Until recent years nonintercooled compression has been limited to CPRs of perhaps 12 for industrial gas turbines. With the advent of the second generation multispool/variable geometry aircraft gas turbine a decade ago ratios were extended to 18 and then recently to 30 without compression intercooling. An example of the latter is the GE LM5000 gas turbine with three units to date now operating – one in Japan and two in Bangladesh. The Japanese company, Ishikawajima-Harima Heavy Industries Co., Ltd. (IHI), developed the power turbine and packaged the units and General Electric Co. (GE), Evendale, supplied the gas generators.

Studies based on today's technology have shown that the 30 CPR RHGT can provide an overall combined-cycle efficiency of 50 percent lower heating value (LHV) for initial turbine inlet temperature (TIT) of 2100°F[1] and RH TIT of 1800°F [1-2]. The 30 CPR has been shown in these studies to be about optimum for these two firing temperatures. Looking into the future, the United States National Aeronautics and Space Administration (NASA) started in 1974 funding the development of the aircraft Energy-Efficient Engine (E^3) planned to supercede the RB-211, JT9D and CF6 engines.

The E^3 engine is projected to offer a substantial savings of about 15 percent fuel. The two U.S. gas turbine companies involved (Pratt and Whitney Aircraft—P & WA—and GE) both propose CPRs of about 38 whereas independently the English Rolls Royce (RR) company suggests a 42 CPR [5-9]. All three units, however, for sake of durability will fire at modest cruise temperatures of about 100°F above present levels to bring the TIT to about 2200°F for base-load operation.

History shows that aircraft technology can be successfully

Contributed by the Gas Turbine Division and presented at the International Gas Turbine Conference and Products Show, Houston, Texas, March 9-12, 1981, of THE AMERICAN SOCIETY OF MECHANICAL ENGINEERS. Manuscript received at ASME Headquarters, December 5, 1980. Paper No. 81-GT-30.

[1] See final page for all SI conversion factors.

Copyright © 1982 by ASME

Downloaded 01 Jun 2010 to 171.66.16.62. Redistribution subject to ASME license or copyright; see http://www.asme.org/terms/Terms_Use.cfm

used for industrial applications. Today there are many first-generation JT3s, JT4s, Avons, LM1500s, 501Ks and second-generation LM2500s, LM5000s, and RB-211s in operation around the world pumping natural gas, generating electrical power and propelling ships. There is every reason to believe that third-generation E^3 engines will likewise be applied industrially—especially now with the worldwide skyrocketing cost of crude, natural gas, coal and other forms of fossil fuel. Further, the E^3 technology can be used as a basis for designing a high-flow 38-42 CPR steam-cooled industrial gas generator of perhaps 450 pounds per second airflow to optimize the reheat combined cycle.

The 38 CPR is optimum for a gas generator TIT of about 2400°F which is 200°F above the proposed air-cooled E^3 base-load TIT; however, studies have shown that steam extracted from the associated steam turbine can be substituted for air as the blade coolant to achieve a 2400°F TIT base-load temperature [3-4]. The superior cooling characteristics of the lower temperature steam available at a higher working pressure can be applied to achieve better blade temperatue protection.

The present-day twin-spool 30 CPR LM5000 second-generation gas generator firing at 2100°F offers a modest 3.75 expansion ratio for the power turbine. This pressure level is lower than desired and necessitates a large RH combustor. Also, the RH temperature is limited to about 1850°F for an arbitrarily fixed exhaust temperature of about 1300°F deemed about maximum for present-day exhaust-hood materials and design.

A 38 CPR GG firing at 2400°F TIT, on the other hand, has a higher RH/PT expansion pressure ratio (EPR) of about 5.3 which is still lower than desireable. This PT EPR, however, can be appreciably increased by applying steam cooling/injection to the gas-generator blading and for the 2400°F TIT the PT EPR increases substantially to about 6.5 which in turn allows the RH temperature to be increased from 2000°F to about 2100°F. As the GG firing temperature is increased above 2400°F both the PT EPR and the RH temperature can be increased accordingly. The higher RH pressure level greatly enhances the gas turbine cycle performance and increases its practicality by reducing the physical size of the RH combustor. At the same time the combined-cycle efficiency level increases due to the higher EPR and the increased RH temperature.

The RH/PT EPR can be increased further by increasing the amount of cooling steam. A total of 4½ percent (3 percent first-stage and 1½ percent second-stage) GG cooling steam is used in this paper to equate heat absorption-wise to 12 percent cooling air. The cooling steam is lost in the stack and boiler feedwater makeup is required as replacement. Such high-grade water costs money and/or requires fuel to produce and therefore minimizing cooling steam seems desireable. Optimizing gas turbine RH EPR by increasing GG steam cooling is beyond the scope of this paper, but the continuing vitiation of the gas due to increasing amounts of steam would cause reheat combustion difficulties at some point.

This paper presents an analysis of the increase in reheat pressure and subsequent increase in reheat temperature using a 38 CPR non-intercooled gas generator with a firing temperature of 2400°F whereby steam is used as the blade coolant. The analysis is given to show what effect both compressor discharge/bleed air and extracted steam for blade cooling have on compression work required and expansion work needed to satisfy the air compression function. Also, combined-cycle efficiency and suggested methods of applying steam to the GG blading and RH combustor are mentioned.

Air-Cooled Gas Turbine Calculation Model

Accurate data are available on actual second generation gas generators—units using air cooling and firing at about 2100°F baseload. Such data can be used to develop assumptions of compressor efficiency, turbine efficiency, combustion efficiency, air leakage, etc. so that realistic calculations can be made for variations in cycle pressure ratio and firing temperature. These calculations can be used to analyze changes in cycle parameters realizing the limitations built into the mathematical model. Table 1 presents assumptions used in modeling the simple-cycle gas generator and power turbine. Cycle efficiency and output calculated using these assumptions check closely with actual gas turbines such as the LM2500 and LM5000. These general assumptions can also be applied to the analysis of steam cooling as will be shown.

When considering a 2400°F TIT it should be realized that there are no industrial gas turbines running today at baseload with this high a temperature. Therefore, using the assumptions of Table 1 for a 2400°F TIT is academic in nature and cycle data derived for TITs higher than 2100° should be treated as an analytical tool only. Nevertheless, as will be shown, such data is valuable in analyzing the effect TIT has on cycle data: reheat pressure, output, efficiency, exit temperatures, etc.

Studies have shown that the optimum CPR for the reheat gas turbine firing at 2400°F in terms of maximum efficiency and output is about 38 when applying the assumptions of Table 1 [1-4]. This optimum CPR produces the highest combined-cycle efficiency for this firing temperature. Therefore, in the analysis of this paper, a CPR of 38 has been selected to analyze the effect steam cooling/injection has on reheat pressure. Although no 38 CPR compressor without intercooling is available today, extensive R and D and component hardware tests of the E^3 engine lend credibility to the reality of such a high CPR compressor being available in a few short years.

Work of Compression

When considering a gas-generator (GG) concept for a reheat gas turbine, the work of compression must equal the

Table 1 Assumptions

1	Compressor eff (adiabatic) — %	85
2	Turbine eff (isentropic) — %	87
3	Combustor press loss — %	4
4	Combustion, radiation, and mechanical loss — %	3
5	Air leakage — %	0.5
6	Inlet pressure — psia	14.69
7	Exhaust pressure — psia	14.9
8	Fuel burned, $(CH_2)n$	
9	Fuel value — BTU/LB LHV	18,400
10	Inlet air temp — °F	59
11	1st stage GG cooling Airflow — %	8
12	2nd stage GG cooling airflow — %	4
13	Keenan and Kaye gas tables for air comp and expansion	
14	400 percent theoretical air for expansion	
15	All calculations based on one LB of air at 0 percent relative humidity	
16	KW can be calculated by multiplying BTU/lb of air net work by the airflow in lb/hr and dividing by 3413	

Downloaded 01 Jun 2010 to 171.66.16.62. Redistribution subject to ASME license or copyright; see http://www.asme.org/terms/Terms_Use.cfm

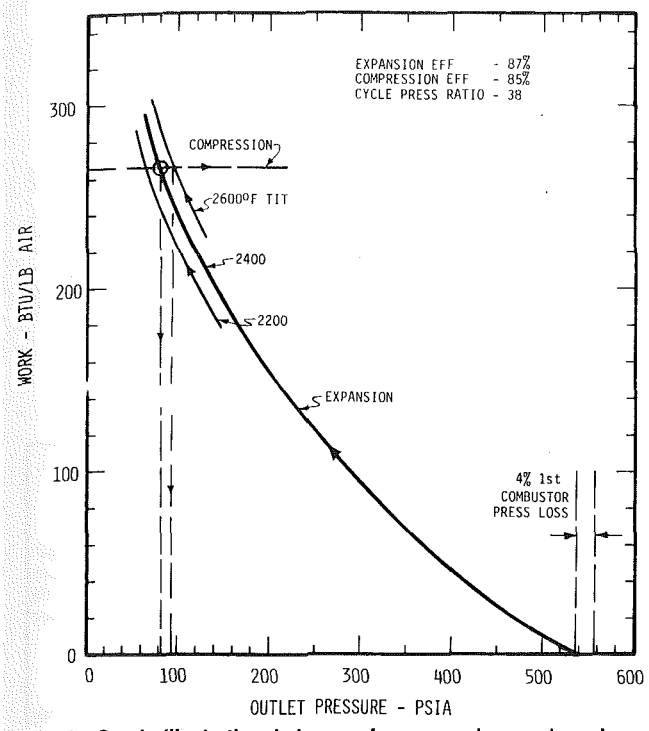


Fig. 1 Graph illustrating balance of compression work and gas-generator turbine expansion work for a 38-cycle pressure-ratio machine

expansion work of the GG turbine to establish equilibrium. The method of calculating reheat pressure and GG exit temperature depends upon this work balance. Conditions must prevail to satisfy this equation of power.

Reference is made to Fig. 1 which illustrates the work balance between compression and expansion for the 38 CPR machine. The work of compression is first plotted as a horizontal line where work of 265.68 BTU/lb of air is needed for an 85 percent adiabatic compression efficiency. Referring to the lower right side of the graph, the hot gas is expanded at 87 percent isentropic efficiency to selected pressures to form an upward sweeping curved line. At the point where the compression line and the expansion line cross, the work balance takes place to yield the GG outlet pressure. Shown on the curve of Figure 1 are conditions of 2200, 2400, and 2600°F GG inlet temperature. It can be seen that increasing the firing temperature from 2400 to 2600°F raises the GG exit pressure about fourteen psi - from 81 to 95 psia which is appreciable but comes at the expense of a 200°F higher firing temperature.

The technique of balancing compressor work and expansion work can be used to analyze the effect extraction and compressor discharge air and steam have on gas-generator exit pressure as will now be discussed.

Work of Expansion

Before examining air and steam expansion work it might be well to mention the E^3 gas-generator turbine under development. Work is underway by NASA through P & WA in the development of a high-ratio first-stage transonic nozzle/blade that yields a 91 percent uncooled efficiency at a 4-expansion ratio [6]. Such blading development could be applied to an industrial gas generator and thus make it possible to arrive at a two-stage twin-spool gas generator turbine—the first-stage ratio being about 3½ and the second about 2. A two-stage gas generator turbine would have fewer nozzle vanes and rotating blades to cool. The two independent stages—one for each spool—would give access of the cooling steam to the rotating blades—to the front for the first stage and to the rear for the second stage.

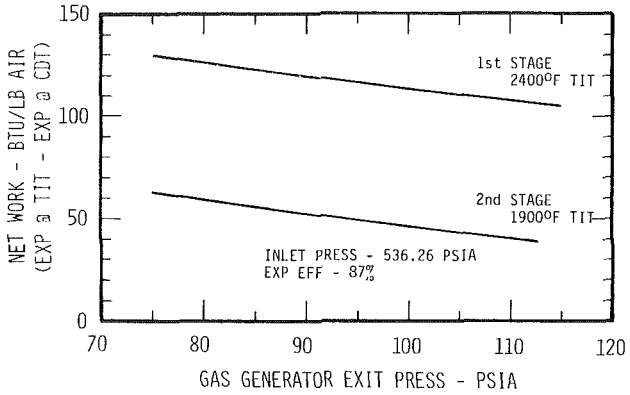


Fig. 2 Graph showing additional work of gas-generator cooling air available when heated to full inlet temperature for a 38-CPR gas generator

There are three incremental components of expansion work which must be considered when eliminating cooling air and substituting extraction steam for blade cooling. These three components are:

1 expansion work of cooling air,
2 expansion work of steam coolant,
3 expansion work of increased fuel mass flow.

The first two are significant and of equal importance and it can be said of the third that fuel is of minor importance but should be included to complete the analysis. Each of these components will be analyzed to determine the effect each has on expansion work.

Cooling Air. It will be assumed for analysis sake that all the first-stage cooling air is expanded through the GG turbine from the full firing temperature of 2400°F and the second-stage extraction cooling air will expand at an estimated 1900°F TIT at a lower inlet pressure of 200 psia - assuming a high expansion ratio first stage previously suggested.

Cooling-air pressure energy is dissipated to a certain extent by both impingement and convection cooling that takes place inside the blades, but nevertheless some recoverable expansion work is obtained from the cooling air and credit must be given for this incremental work. This credit is reflected in Figure 2 where the difference in expansion work between TIT and compressor discharge temperature of the cooling air is plotted against gas generator exit pressure.

It can be seen that the first-stage net work increase is about three times the second stage due to the lower pressure and temperature involved with the second stage. To obtain the total incremental work of the cooling air for various gas generator exit pressures, the values of Fig. 2 are multiplied by the assumed Table 1 cooling air flows of 8 percent for the first stage and 4 percent for the second stage. When these flow values are applied, the ratio of first to the second stage increases to about 5 showing the lesser work contribution of the second-stage cooling air.

Cooling Steam. When cooling steam is substituted for cooling air and different techniques of cooling are applied to take advantage of the higher pressures available [3–4], not only is blade cooling accomplished but also appreciable expansion work is obtained as the heated coolant expands through the GG turbine. Using the Keenan and Kaye gas table for water vapor, the graph of Figure 3 is persented on which steam expansion work is plotted against gas-generator exit pressure. Both the first-stage and second-stage work components are given for various inlet temperatures shown and for expansion efficiencies of 85 and 87 percent.

Downloaded 01 Jun 2010 to 171.66.16.62. Redistribution subject to ASME license or copyright; see http://www.asme.org/terms/Terms_Use.cfm

Table 2 Turbine expansion work—38 CPR—2400°F TIT

Outlet pressure—PSIA	80	90	100
Cooling Air—BTU/LB AIR			
1st stage—8 percent	10.11	9.58	9.11
2nd stage—4 percent	2.37	2.01	1.84
Cooling steam—BTU/lb air			
1st stage—3 percent	11.99	11.37	10.80
2nd stage—1½ percent	2.24	1.97	1.73
Added fuel—BTU/lb air	.47	.44	.42
Subtotal	27.28	25.37	23.90
Original expansion work @ 87 percent eff—BTU/lb air	266.38	253.14	240.99
Total	293.56	278.51	264.89
Increase—percent	10.21	10.02	9.92

It is assumed that 80 percent steam mixing with the main gas stream is accomplished and the steam is heated to an equivalent or average 2200°F TIT. The mechanism of the mixing will be explained later in this paper. Also, for the analysis the steam-expansion efficiency is assumed to be 85 percent—starting with the main gas-stream pressure but disregarding the extra internal steam pressure.

Figure 3 shows that the first-stage work is also about 3 times that of the second stage and when considering steam flows of 3 percent for the first stage and 1½ percent for the second stage, the ratio of work of the first to the second stage is about 5.5. The 3 percent and 1½ percent cooling steam flows were selected to give approximately the same heat absorption capacity of the steam at its lower temperature and higher specific heat available compared to cooling air. It should be noted that the extraction steam from the steam turbine can be de-superheated to the saturation temperature where the specific heat of steam is about 0.8 compared to 0.25 for air—giving extra heat-carrying capacity.

Fuel Mass. When compressor-discharge cooling air that normally bypasses the combustor is allowed to be heated to the full 2400°F TIT more fuel is required. Assuming this bypassed air is 8 percent, then 8 percent more fuel will be needed to heat this rerouted cooling air. The added fuel mass expands through the turbine to produce incremental work. When steam is substituted for air as the coolant and when cooling techniques incorporate film cooling with slots fed by steam nozzles contained within each vane or blade leading edge, an incrementally higher firing temperature is required to heat the steam as it passes over the vane surface; in so doing extra fuel is burned.

The work component developed by the added fuel mass helps drive the gas generator air compressor and adds to the total work available. Although the fuel component is not very large compared to the added cooling-air work and steam work, it should be included to arrive at the total expansion work produced to balance the work of compression.

Summation of Expansion Work. The various expansion work components can be added together for various outlet pressures to provide a plot of expansion work against outlet pressure. Table 2 presents data of the three components (air, steam and fuel) for outlet pressures of 80, 90, and 100 psia for the 38 CPR gas generator firing at 2400°F. Referring to Fig. 3, values for 2200°F were used for the first stage and values for 1400°F were used for the second stage - both with 85 percent expansion efficiency.

More expansion work will result for the same amount of steam in the event steam is injected directly into the combustor instead of being applied as a blade coolant. For instance, if the 4½ percent steam is in total heated to 2400°F the expansion work components for 80, 90, and 100 psia outlet

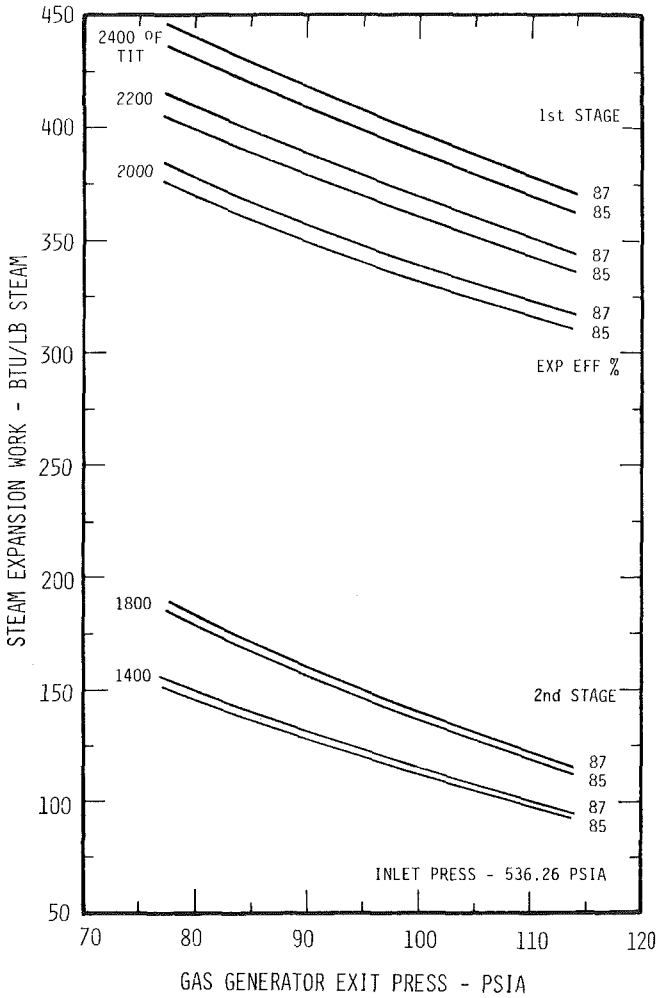


Fig. 3 Graph showing net additional work developed by the gas-generator cooling steam when heated to inlet temperatures shown for a 38 CPR gas generator

pressure are 19.86, 18.83, and 17.88 BTU/lb of air, respectively, compared to the values for steam in Table 2. These figures show that more power can be obtained by steam injection, but there would be no steam-blade cooling taking place which would be unworkable for 2400°F TIT baseload operation.

A plot of work versus gas-generator exit pressure is given in Fig. 4 showing the expansion work first with air cooling, second with steam cooling added, third if steam injection is employed with no cooling (for comparison only), fourth when giving credit for the cooling air and finally with the small fuel mass expansion added. Compression work of 265.68 BTU/lb

Downloaded 01 Jun 2010 to 171.66.16.62. Redistribution subject to ASME license or copyright; see http://www.asme.org/terms/Terms_Use.cfm

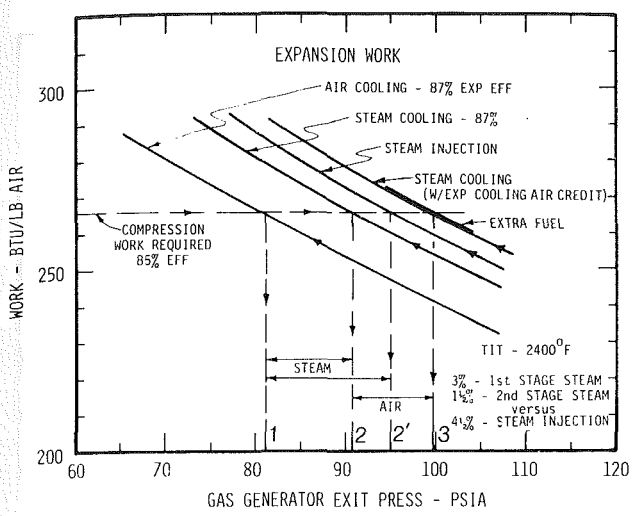


Fig. 4 Plot of compression/expansion work versus gas-generator exit pressure showing reheat pressure rise due to the elimination of cooling air, substitution of steam cooling, steam injection, and additional fuel consumed

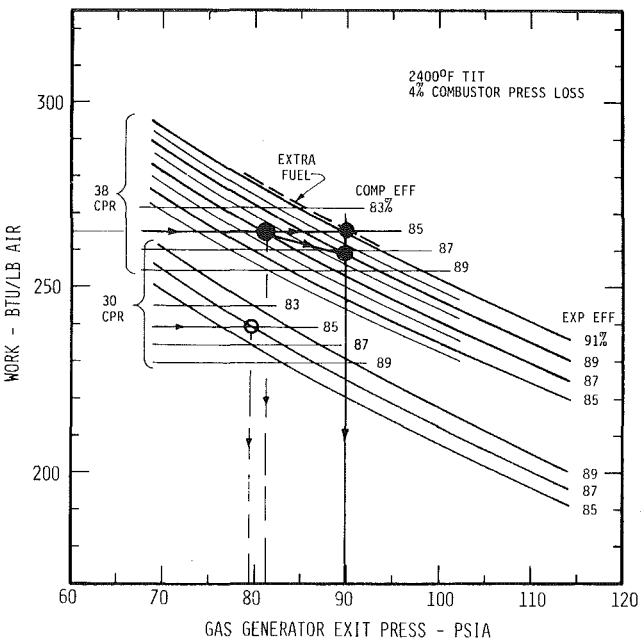


Fig. 5 Graph showing equivalent higher "uncooled" compression and expansion efficiencies to yield the same reheat pressure rise

air is drawn horizontally across the plot. The intersection points then show the increase in gas-generator exit pressure produced by steam cooling (point 1 to point 2), cooling air credit (point 2 to point 3) and then the small component of the fuel. If steam injection were incorporated, the 4½ percent steam would increase the pressure from point 1 to point 2′—but without accomplishing the cooling function.

More steam could be used for cooling and/or injection to increase the exit pressure further but it must be remembered that water make-up has a cost associated with it which must be evaluated. Secondly, too much steam could effect proper combustion in the reheat combustor due to the further vitiation of the gas stream (reduced oxygen content per unit mass flow).

Uncooled Expansion Efficiency With No Compressor Air Extraction. It is now possible to check the cooling-air flow assumptions against known values of both "uncooled expansion efficiency" and improved compression efficiency (which is not uninterrupted by extraction points and associated extraction pressure losses). Our calculation model given in Table 1 can then be modified to give realistic assumptions of upgraded expansion and compression efficiencies not penalized by the built-in factors for cooling-air losses.

Figure 5 presents lines of expansion work plotted against GG exit pressure for various expansion efficiencies shown. The upper set of curves are for a 38-CPR turbine and below are plotted expansion lines for a 30-CPR turbine for comparison. Plotted horizontally across the expansion lines are work of compression lines for several values of compressor efficiency as denoted. The expansion work available with the extra fuel added is shown as a dashed line for an uncooled gas turbine giving credit for the 8 percent cooling air per Table 2.

The intersection of the 85-percent compression line with the dashed line establishes the GG exit pressure to be just below 90 psia. Reference is made to the two top black dots - the first being the intersection of the 85 percent compression line with the 87 percent expansion line and the second the 85 percent compression line with the new expansion line including credit for both cooling air and fuel. The new gas generator pressure, now established, can also be developed by different compression and expansion efficiencies not degraded by cooling air effects. The third lower black dot shows that an 87-percent compression coupled with an 89-percent expansion will yield the same gas generator exit pressure. These values compare favorably with data on uninterrupted compression and "uncooled" expansion efficiencies and, in all probability, these values are on the conservative side. Uncooled expansion efficiencies, for instance, range from 90 to 92 percent where close blade tip clearance is maintained.

When considering a 38 CPR compressor, the high temperature and more dense flow encountered at the high end of compression requires special attention to maintain high compression efficiency. The latest techniques for high CPR compressors such as the E^3 engine is to cool the outer casing under controlled conditions, to shrink the casing and thus reduce and control compressor blade tip clearance when up to operating temperature and load. Such techniques favor the multispool aircraft generator concept with its thinner casing and smaller diameters—the latter being brought about by speed matching of the high-pressure compressor with the high-pressure turbine.

In conclusion, it is then reasonable for advanced gas generators such as the E^3 under development by NASA, when considering steam cooling and not extracting any air or using any compressor discharge air for cooling to apply 87 percent efficiency for compression and 89 percent efficiency for expansion as the basis of a new "uncooled" calculation model.

The 30-CPR plot is given in Fig. 5 to compare gas generator exit pressures with the 38 CPR. It can be seen that less pressure is developed with the 30 CPR machine and less pressure increase takes place for the newly established 87/89 percent compression/expansion efficiencies. Gas generator exit temperatures also are much higher for the 30-CPR turbine as will be reviewed later.

Using the newly established values, and including steam cooling, Fig. 6 is presented as a summary plot showing the increase in pressure created by elminating the cooling air (point 1 to point 2) and by introducing steam cooling (point 2 to point 3). The gas generator pressure is increased form 81.4 psia to 99.8 psia. Table 3 summarizes these pressures increases.

The steam acts as a pressure augmentor and steam ex-

Downloaded 01 Jun 2010 to 171.66.16.62. Redistribution subject to ASME license or copyright; see http://www.asme.org/terms/Terms_Use.cfm

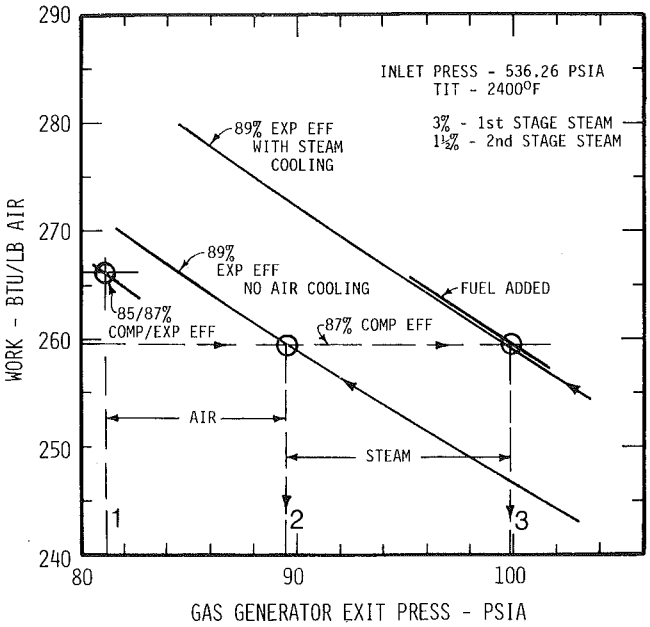


Fig. 6 Graph showing reheat pressure rise due to elimination of cooling air and the substitution of steam for cooling

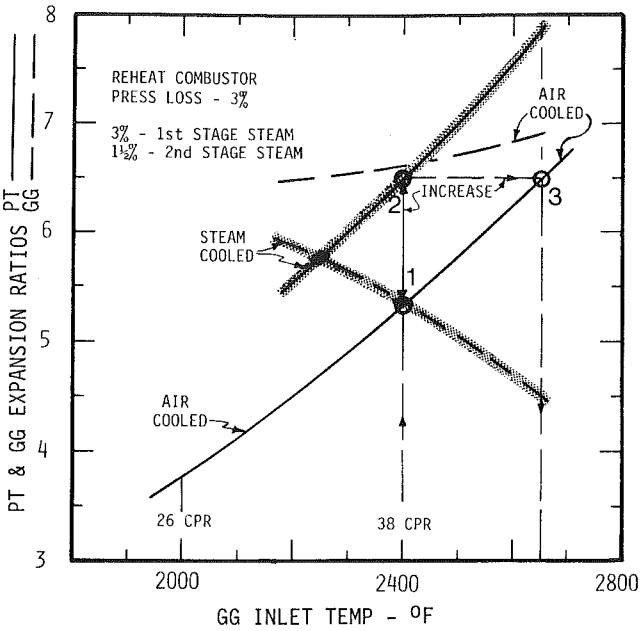


Fig. 7 Plot of power turbine and gas generator expansion ratios versus turbine inlet temperature for both air-cooled and steam-cooled gas-generator blading. The increase in PT expansion ratio for steam cooling can be noted

pansion work is in effect converted to air reheat pressure of significant proportions. This pressure not only has a decided influence on cycle performance but also reduces the physical size (cross-sectional area) of the reheat combustor by the ratio of the absolute pressures in accordance with Boyles law (PV = WRT) when considering equal velocities. The area would be reduced to 0.814 of the original dimension. With a 99.8 psia pressure, the reheat gas turbine—incorporating a more advanced aircraft derivative gas generator—becomes more workable.

Table 3 Gas generator exit pressure

	Pressure psia	Increase %
Cooling air	81.4	----
With no cooling air	89.5	10.0
With steam cooling and fuel added extra	99.8	12.6
Total		22.6

The higher reheat pressure increases the power turbine (PT) expansion ratio. Reference is made to Fig. 7 where PT expansion ratio is plotted against GG inlet temperature. The lower line shows the effect firing temperature has on expansion ratio for an air-cooled gas generator. The upper line represents the expansion ratios possible with steam-blade cooling. At the 2400°F inlet temperature, steam cooling increases the expansion ratio from 5.3 to 6.5 (point 1 to point 2). To accomplish this same PT expansion ratio with an air-cooled gas generator, the firing temperature would have to increase from 2400°F to 2650°F (point 2 to point 3). This is a large increase and of academic interest only because an air-cooled gas generator is not available today which will operate at 2400°F baseload - let alone 2650°F. If future transpiration air cooling will allow these temperatures, then the penalty would be a 250°F higher firing temperature. Note the decrease in GG expansion ratio for steam cooling shown by the shaded dashed bottom line—an important consideration for GG staging.

Figure 7 also shows that increasing the firing temperature above 2400°F for the steam-cooled gas generator increases the PT expansion ratio further. As an example, the expansion ratio for a 2600°F firing temperature can be seen to be about 7.6. At higher steam-cooling rates the ratio becomes even higher. The situation keeps improving and growth is built into the reheat cycle concept proposed in this paper.

Cycle Considerations

Gas Generator Exit Temperature. As mentioned earlier, there is the question of GG exit temperature which in turn is the reheat combustor inlet temperature. Reference is made to Fig. 8 where GG exit temperature is plotted against GG exit pressure. The upper line shows the higher temperatures associated with a 30 CPR gas generator and the lower three curves present the increase in temperature with pressure of a 38-CPR machine. It is seen that the 30 CPR 2400°F TIT GG has an exit temperature approaching 1600°F for an air-cooled turbine and this temperature increases when steam cooling is introduced to increase the pressure. The 38-CPR GG exit temperature, point 1 on the curve, for an air-cooled turbine has a reheat combustor inlet temperature of only 1514°F. When steam is applied the temperature rises to about 1574°F, point 2, for the increased pressure. The increase is tempered due to the increase in uncooled expansion efficiency from 87 percent to 89 percent as can be noted.

Even the 1574°F temperature is too high to offer the required combustor liner cooling. The radiant heat from the reheat flame would burn up the liner. Therefore, a steam-cooled combustor is suggested which will be discussed later in the paper. The practicality of the reheat combustor must be considered, and introducing the steam turbine reheat steam function offers a practical solution to the combustor cooling problem and at the same time provides other advantages such as minimum stack temperature, short piping runs to and from the steam turbine and elss heat transfer surface area required.

Reheat Temperature. A better understanding of both the GG and PT expansion is given in Fig. 9 where temperature is plotted against the natural log of the pressure ratio. In this graph, starting from the right top, gas at 2400°F is expanded to the GG exit pressure. Cooling steam, assumed to be heated to 2200°F, is also expanded to this exit pressure and, as can be noted, both the gas and the steam end up at point 2 at the same temperature—1574°F. The temperature drop of steam is

Downloaded 01 Jun 2010 to 171.66.16.62. Redistribution subject to ASME license or copyright; see http://www.asme.org/terms/Terms_Use.cfm

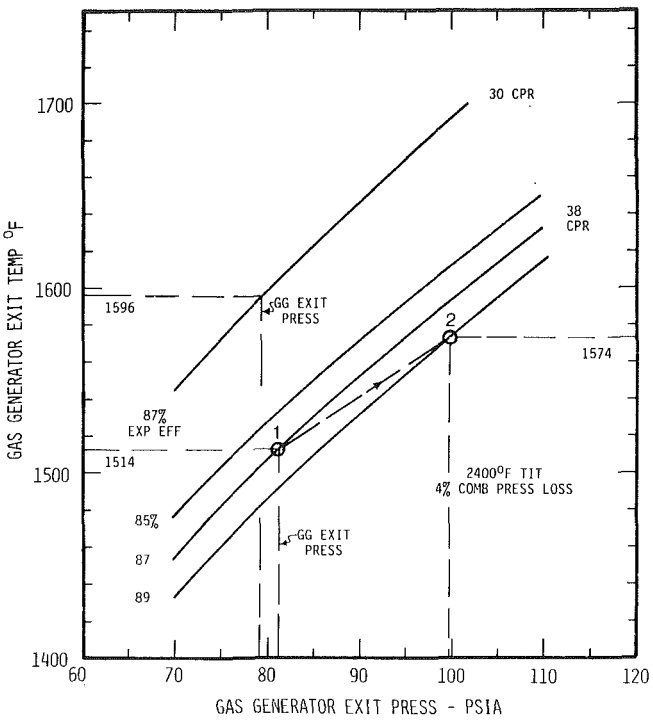


Fig. 8 Graph showing gas generator exit temperature versus gas generator exit pressure for conditions showing point (1) air cooling and point (2) steam cooling

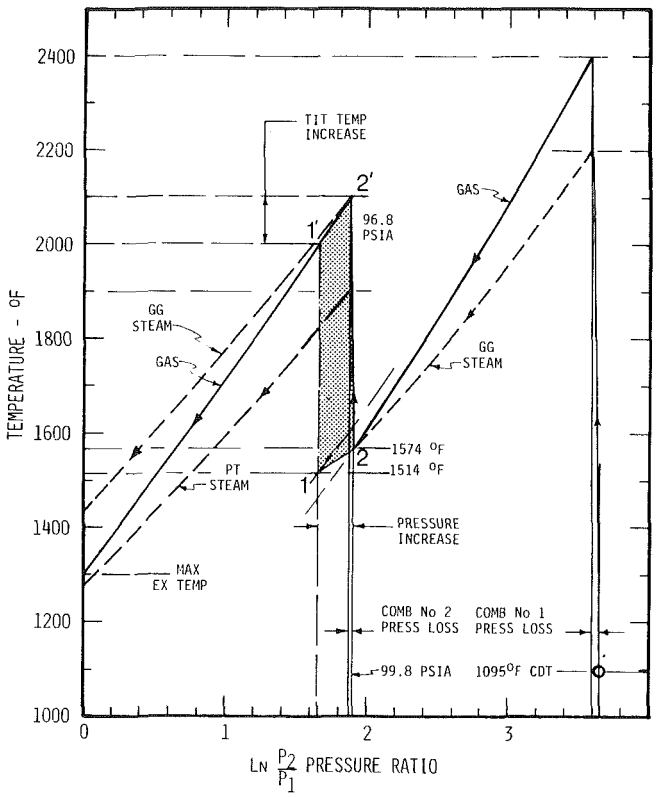


Fig. 9 Plot of temperature versus the natural log of pressure ratio showing the increase in reheat pressure and firing temperature attributed to steam cooling

less as it expands because of its different physical working fluid characteristics.

The mixture of gas and GG cooling steam is reheated to 2100°F, point 2′. The gas expands to near atmospheric pressure (14.9 psia) to yield a 1300°F predetermined maximum exhaust temperature. The 4½ percent GG steam component expands to an exhaust temperature of 1430°F. The 1½ percent PT steam, on the other hand, expands from an assumed 1900°F inlet to 1280°F. The total mixture of the gas, GG steam and PT steam—taking into consideration flow proportions, efficiencies and enthalpies—exits at about 1300°F or a few degrees above 1300°F.

When the reheat pressure is increased through GG steam-blade cooling, it becomes possible to increase the reheat firing temperature from point 1′ to point 2′ and still maintain the same maximum allowable exhaust temperature pre-selected to be 1300°F. The increase is shown to be very close to 100°F in Fig. 9. The higher pressure and reheat temperature produces more PT work. This increase is represented by the shaded area 1-1′-2-2′ which gives rise to more pure topping gas turbine power being developed per pound of air flow. The combined cycle efficiency will increase accordingly.

Air Cycle Improvement. When considering the air cycle only by separating the air from the steam, striking improvements in both cycle efficiency and output become apparent. The air must go along for the pressure ride, so to speak, with the steam, but separating the two streams for individual analysis indicates that the air side of the cycle is appreciably extended.

Reference is made to Fig. 10 which shows graphically what happens to the air portion of the cycle in terms of net cycle efficiency and net output. Plotted on the left side of the graph is the efficiency versus output curve for simple cycle CPRs increasing from 14 to 38 where air is the blade coolant (Table 1 assumptions) and 2400°F is the TIT. It is noted that the maximum cycle efficiency of 39.2 percent occurs at a CPR of 38, point 1. The GG gas is reheated from point 1 to point 2

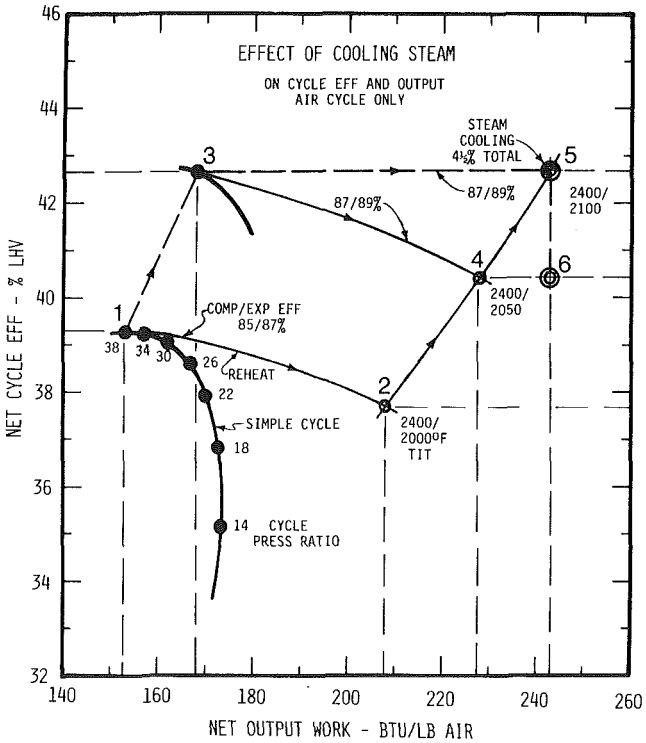


Fig. 10 Graph showing substantial overall gains in both air-cycle efficiency and net air output when substituting steam cooling for air cooling

where at 2000°F a limitation of exhaust temperature of 1300°F is imposed. Additional work output is obtained (208 BUT/lb versus 152 BUT/lb) but the cycle efficiency drops to 37.7 percent.

Downloaded 01 Jun 2010 to 171.66.16.62. Redistribution subject to ASME license or copyright; see http://www.asme.org/terms/Terms_Use.cfm

Table 4 Cycle data–2400°F TIT – 38 CPR – air only

	Air-cooled simple cycle	Air-cooled reheat cycle	Uncooled reheat cycle	Steam-cooled reheat cycle
1 Fig. 10 point no.	1	2	4	5
2 Inlet temp, t_1—°F	59	59	59	59
3 CDT temp, t_2-°F	1118	1118	1095	1095
4 TIT - 1, t_3- °F	2400	2400	2400	2400
5 GGET, t_4-°F	1514	1514	1535	1574
6 TIT - 2, t_5-°F	--	2000	2050	2100
7 PTET, t_6-°F	967	1297	1296	1299
8 INLET PRESS, P_1 - PSIA	14.69	14.69	14.69	14.69
9 CDP, P_2 - PSIA	558.60	558.60	558.60	558.60
10 TIP - 1, P_3 - PSIA	536.26	536.26	536.26	536.26
11 GGEP, P_4 - PSIA	81.44	81.44	90.56	99.80
12 TIP - 2, P_5 - PSIA	81.44	79.00	87.86	96.81
13 PTEP, P_6 - PSIA	14.90	14.90	14.90	14.90
14 COMB NO 1 PRESS LOSS - %	4	4	4	4
15 COMB NO 2 PRESS LOSS - %	-	3	3	3
16 ASSUMED THEO AIR - 1st EXP - %	400	400	400	400
17 ASSUMED THEO AIR - 2nd EXP - %	--	200	200	200
18 FUEL NO 1 (GG) - BTU/LB AIR	389.50	389.50	395.84	395.84
19 FUEL NO 2 (REHEAT) - BTU/LB AIR	--	162.47	172.28	176.57
20 FUEL TOTAL - BTU/LB AIR	389.50	551.97	568.12	572.41
21 GG EXP RATIO	6.585	6.585	5.920	5.373
22 PT EXP RATIO	5.466	5.302	5.897	6.497
23 GG EXP WORK AIR - BTU/LB AIR	265.68	265.68	259.57	246.61
24 GG EXP WORK STEAM & FUEL BTU/LB AIR	--	--	--	12.96
25 GG TOTAL EXP WORK - COMP WORK BTU/LB AIR	265.68	265.68	259.57	259.57
26 PT NET WORK - BTU/LB AIR	152.62	208.04	228.61	243.38
27 CYCLE EFF - LHV - %	39.2	37.7	40.3	42.5
28 INCREASE IN NET WORK - %	BASE	36.31	49.8	59.5
	--	BASE	9.89	17.0
29 INCREASE IN CYCLE EFF - %	--	BASE	6.90	12.7
30 INCREASE IN PT EXP RATIO - %	--	BASE	11.22	22.54

NOTE: See Final Page for SI Conversion Factors

The next step in the analysis is to assume an uncooled condition using 87 percent compression efficiency and 89% expansion efficiency. The reheat plot now moves upward to points 3 and 4. The output increases to 229 BTU/lb and the efficiency rises to 40.3 percent.

The final step is now to introduce cooling steam to the GG blading. The extra pressure created gives rise to a 2100° F reheat TIT. The greater expansion pressure and higher inlet temperature accounts for more PT work and a still higher air-cycle efficiency. Point 5 shows the output to be 245 BTU/lb and the air-cycle efficiency to be 42.5 percent. Tabulated in Table 4 are the pertinent figures associated with the simple cycle, the air-cooled reheat cycle, the uncooled reheat cycle and finally the steam-cooled reheat cycle.

It should be noted that the steam has been separated from the air flow and no fuel has been added for the cooling steam. Only the air is considered for point 5 in Fig. 10 and Table 4. No work of the expanding steam has been considered other than to show the balance in compressor work required. There is additional PT work developed by the steam which likewise is not included. If the GG steam work is subtracted from the PT air work, the cycle efficiency by substitution drops to point 6 where this steam work is taken into consideration. However, the steam should be considered as a separate loop which involves the reheat steam turbine and which will be discussed.

As can be noted in Table 4, the reheat-combustor pressure loss is assumed to be 3 percent, line 15, and the power turbine expansion theoretical air is changed to 200 percent to include the effect of the extra fuel, line 17. In the calculations air leakage of 0.5 percent is retained and a combustion efficiency of 97 percent has been included for each of the combustors to account for the latent heat of vaporization of the liquid fuel,

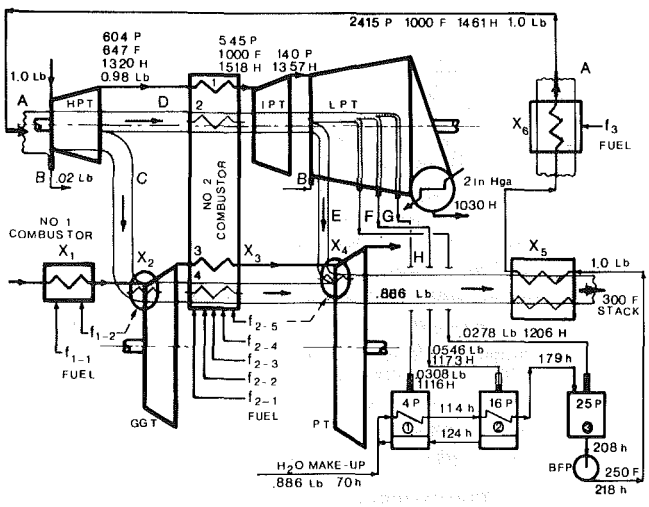


Fig. 11 Cooling steam schematic flow diagram and heat balance for reheat steam turbine and reheat gas turbine

incomplete combustion, radiation losses and mechanical losses of the system. Also note the 14.9 psia exit pressure, line 13, which takes into account the exhaust-hood loss. It is felt that these built-in constants produce realistic cycle values that approximate what a real turbine would be like.

Cooling Steam Cycle. The cooling steam takes a long and rather devious path as it expands first through the reheat steam turbine, is then extracted, heated, expanded in the gas generator, heated again in the reheat combustor and then finally expanded through the power turbine to atmospheric

Downloaded 01 Jun 2010 to 171.66.16.62. Redistribution subject to ASME license or copyright; see http://www.asme.org/terms/Terms_Use.cfm

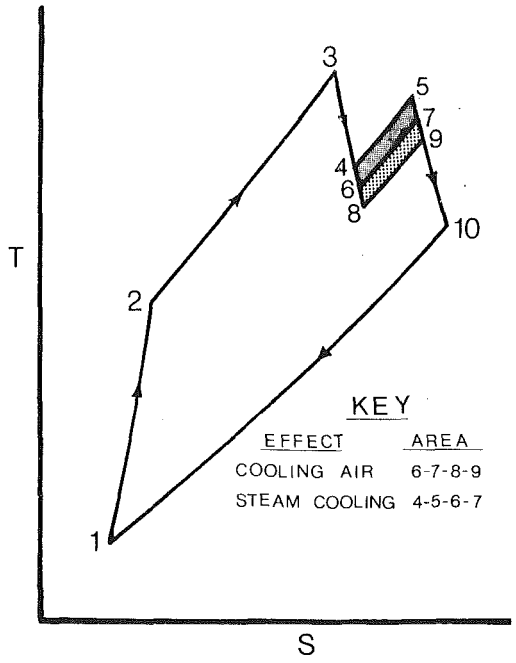


Fig. 12 Temperature-Entropy diagram of air cycle showing the effect of eliminating cooling air and then substituting steam cooling

pressure. Figure 11 presents a heat balance flow diagram for the cooling steam.

The total loop from the beginning when the condensate or make-up water is first heated, boiled and then superheated prior to entering the steam turbine until the steam passes through the gas turbine must be considered. A complicated heat balance must be applied to the cooling steam to arrive at proper fuels inputs, power outputs and losses. It should be noted that GG steam work creating the higher gas turbine RH pressure cannot be considered twice and this factor is relevant to net steam work of the loop. An overall heat balance of the entire gas-steam system must prevail.

Careful studies have been made to include all the above mentioned factors and reported to ASME [3–4]. These heat balances show that the cooling steam-cycle efficiency of the gas-generator steam can be as high as 45 percent LHV for a 38 CPR reheat gas turbine. This cycle efficiency compared favorably with the 42.5 percent HHV cycle efficiency of the air side of the cycle and the 40.43 percent LHV of the condensing steam-turbine cycle (2400 psig—1000/1000°F).

Combined Cycle Efficiency. The combined-cycle efficiency of the 38 CPR 2400/2000°F reheat gas turbine and the 2400 psig 1000/1000°F reheat steam turbine as reported to ASME was calculated to be about 55 percent LHV. These calculations did not give any credit for the extra steam pressure of the cooling steam above the gas stream nor did they give credit for the higher pressure of the reheat combustor and associated increase in reheat gas temperature. In these respects the values presented were conservative and when proper credit is given to these increases, the combined-cycle efficiency should be better perhaps by one percentage point to bring the combined-cycle efficiency level to 56 percent LHV. A more exact determination of this higher efficiency level is beyond the scope of this paper but is being mentioned as a direct effect of the increase in gas reheat pressure brought about by the steam cooling.

Temperature Entropy Diagram. A T-S diagram of the reheat gas turbine is given in Figure 12 to illustrate the effect removing the cooling air and introducing cooling steam has

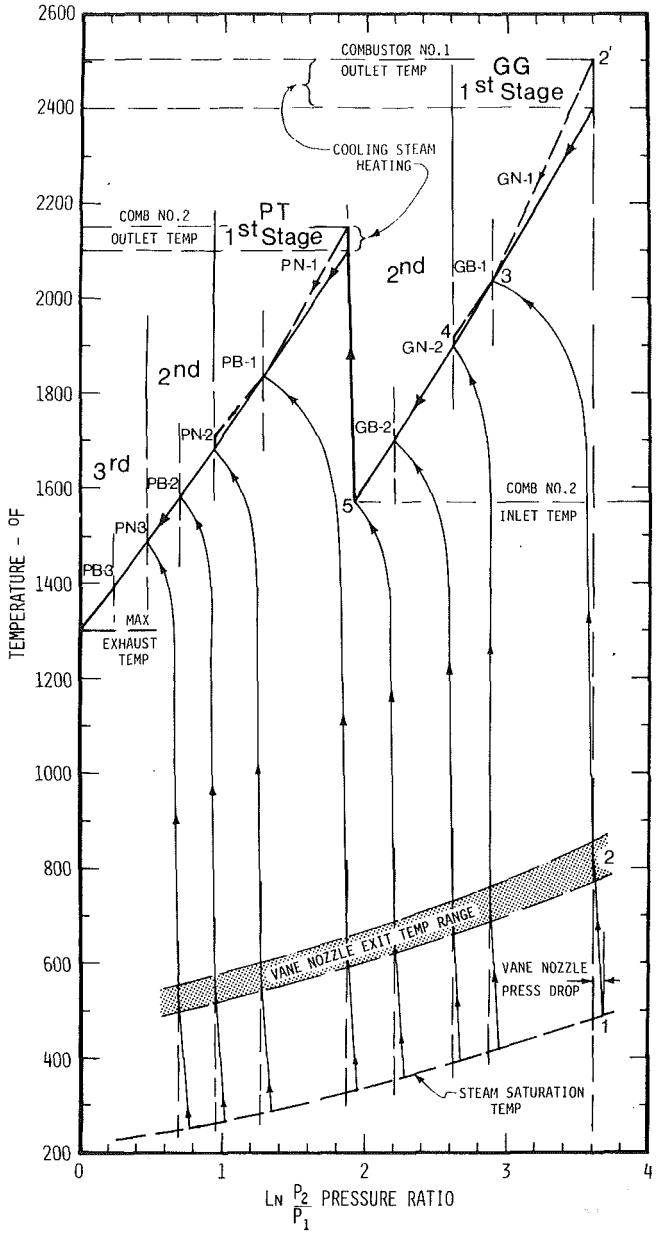


Fig. 13 Plot of temperature versus the natural log of pressure ratio showing the introduction of cooling steam near the bottom and the turbine expansion at the top

on reheat temperature and cycle output. Air is compressed from point 1 to point 2. Fuel is added from point 2 to point 3. The hot gas then expands to point 8 for the case where air-blade cooling is employed. The gas is reheated from point 8 to point 9 before it expands through the power turbine from point 9 to point 10.

When cooling air is eliminated, less compressor work is required and more GG expansion work is made available. Therefore, the GG gas expands from point 3 to point 6, is heated to point 7 (a higher temperature than before) and is finally expanded to point 10. The area 6-7-8-9 represents an additional work developed when the cooling air is cut out of the cycle. Considering steam as the blade coolant, the gas expands from point 3 to point 4, is heated to point 5 (a still higher temperature) and is then expanded to point 10. The second additional amount of work is repreented by area 4-5-6-7 made available by the steam. The total increase in work is shown as area 4-5-9-8.

Downloaded 01 Jun 2010 to 171.66.16.62. Redistribution subject to ASME license or copyright; see http://www.asme.org/terms/Terms_Use.cfm

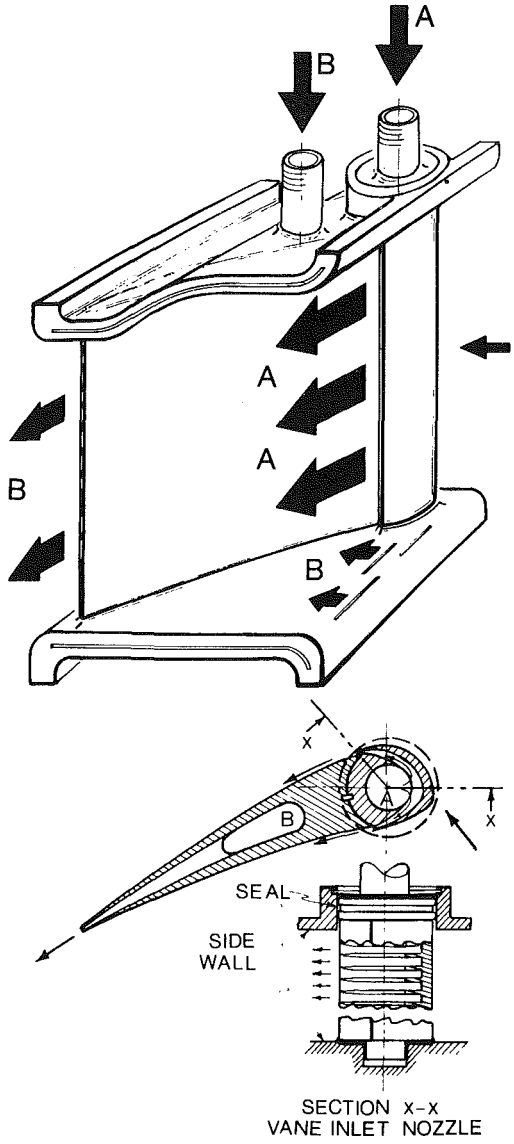


Fig. 14 Conceptual view of steam-cooled gas generator blunt-nose S wall-designed first-stage inlet nozzle vane showing internal steam nozzles and floating leading-edge nozzle cap

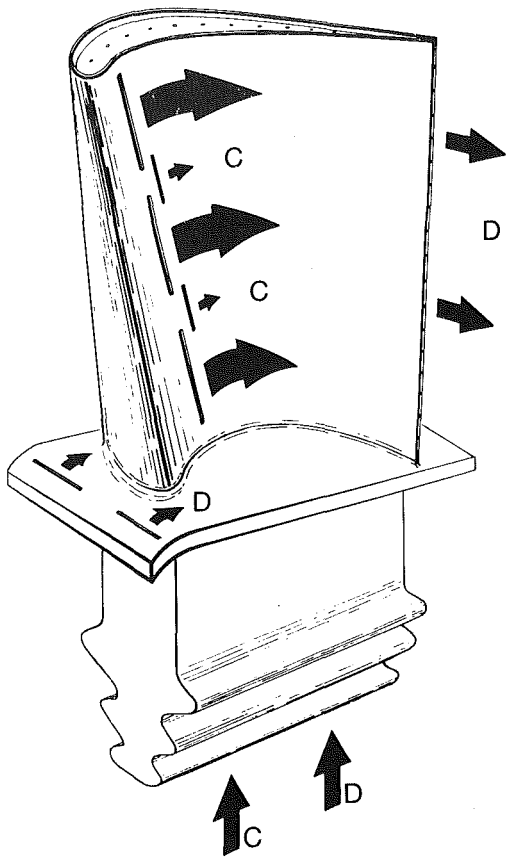


Fig. 15 Conceptual view of gas generator transonic first-stage rotating blade incorporating steam-cooling internal nozzles and exit slots

Steam Cooling Injection Process

Aside from the thermodynamics of the steam-cooled reheat cycle, there is the method and practicality of introducing steam cooling to the gas-turbine blading that must be considered. It is not a matter of simple steam injection but rather a unique system of introducing the steam which is necessary so that proper blade cooling can be accomplished and whereby the pressure energy of the steam can enhance cooling without the loss of potential expansion energy. New and different cooling techniques coupled with steam blanketing are suggested whereby cooling can be accomplished and steam-expansion energy can be conserved.

An analysis of the steam introduction process will now be reviewed. Reference is made to Fig. 13 which is a plot of temperature versus the natural log of pressure ratio. This graph shows the gas expansion on the top and the steam-cooling admission on the bottom. Referring to the bottom of the graph, extraction steam is taken at appropriate extraction points from the steam turbine. The steam pressure must be high enough to provide the required pressure drop for the vane or blade steam nozzles. Each individual extraction stream flow is de-superheated with either condensate or economizer exit feedwater. Note that de-superheating lowers the steam temperature and appreciably increases the heat-carrying capacity of the steam. At saturation temperature, for instance, the specific heat of the steam increases from about 0.6 to over 0.8 BTU/lb—°F.

The vane and blade cooling-steam paths can be traced, and as an example, starting with point 1 for the GG first-stage nozzle admission point, the steam is fed into the leading edge cap of each nozzle vane. The high-specific-heat steam at a pressure of about 50 psi above combustor discharge pressure cools the leading edge before being accelerated by the steam van nozzles to a velocity equal to or slightly higher than the leading-edge gas stream (about 700 ft/sec). The steam-nozzle pressure drop and temperature-rise conditions are shown between points 1 and 2.

The steam then passes over the surface of the vane from point 2 to point 3 where film cooling or blanketing takes place by a laminar flow Prandtl layer of steam. The majority of the steam mixes with the main gas stream at the boundary layer where there is turbulent flow. The mixture of steam and gas then expands together to point 5.

The cooling steam that enters the body of the vane (approximately 20 percent of leading-edge flow) offers interesting prospects for cooling the trailing edge where the outer steam-cooling film might break down or lose some of its effectiveness. Saturated steam is expanded to the critical nozzle pressure to obtain Mach one velocity (about 1800 ft/sec compared to about 2350 ft/sec of the main gas stream). The steam thus cools as it tries to expand at constant entropy. Some condensation will try to occur—perhaps 7 percent—as the temperature drops from 490 to 420°F. Additional cooling

Downloaded 01 Jun 2010 to 171.66.16.62. Redistribution subject to ASME license or copyright; see http://www.asme.org/terms/Terms_Use.cfm

is therefore provided and the heat transfer enhanced where anticipated need occurs.

The gas flow can also be followed as it expands through the GG turbine. Gas at point 2′ is raised above the firing temperature of 2400°F by about 100°F. This gas then mixes with the steam to exit out the first-stage nozzle at the same temperature (and velocity) as it normally would for a 2400°F TIT. The extra inlet temperature is used to heat the turbulent portion of the steam and the trailing-edge cooling steam.

The mixture of gas and steam then expands to point 5. However, the steam component having a higher specific heat and different expansion characteristics will try to expand to point 4, but the rotating first-stage blade cooling steam will cool the steam so that the total mixture will closely follow the gas expansion line from point 3 to point 5 with only slight variation depending upon the percentages of cooling steam admitted. The exact expansion pressures and temperatures encountered across each vane and blade will depend upon the specific design and the split between impluse and reaction. No attempt is made to distinguish these differences and a uniform expansion profile is shown.

Similarly, the same technique of overfiring can be used for the PT first-stage nozzle to heat the nozzle cooling steam. A three-stage power turbine is shown to extract work from the gas as it expands from about 96 psia to atmospheric pressure. A high pressure drop PT first-stage blading is shown to be consistent with the approach suggested for the gas generator. However, a three-stage turbine with maximum expansion efficiency could be justified for the lower temperature involved.

A conceptual view of the first-stage S wall gas-generator nozzle vane is shown in Fig. 14. Two steam connection points, A and B, at the top introduce steam to the leading edge (A flow) and body (B flow). A wedged shape blunt-nosed vane similar to the P & WA/E[3] engine under development or the R-R RB-211 524B is shown in cross section.

The steam cools the floating leading-edge cap by extended surface fins before it expands through the steam nozzles and then exits tangentially along the pressure and suction blade surfaces. Variations in the leading-edge design and concepts such as ceramic barriers, coatings, full ceramic, shower head and transpiration cooling have been presented to ASME (3-4) and will not be re-discussed in this paper.

A conceptual view of a first-stage high EPR rotating blade is shown in Figure 15. Considerable reaction can be observed near the tip with more impulse near the root. (NASA/P & WA suggest 40 percent reaction for their transonic blading.) The steam nozzles can be seen on the pressure side of the blade. One long slot extending the full height of the blade is desirable instead of the overlaps shown if blade strength and integrity can be maintained.

Reheat Steam Superheater/Combustor

In order that a reheat combustor inlet temperature of 1574°F can be accomodated, some type of external cooling for the combustor must be provided. The 1574°F level is too high to provide proper cooling and any combustor, other than perhaps one with a full ceramic liner not yet a reality, would burn up when subjected to the radiant heat of the reheat flame. However, fuel flow will provide cooling to prevent excessive metal temperature of the fuel lines and fuel nozzles.

A practical solution to the problem is to use the reheat steam as the reheat combustor coolant. The pressure of this steam is about 600 psia so there would be a modest pressure difference between the steam and the gas of about 500 psi. The heat transfer at 96 psia gas pressure would be greatly improved to reduce the superheat surface. At the same time the reheat-steam heat load transferred from the heat recovery boiler to the reheat combustor would make it possible to

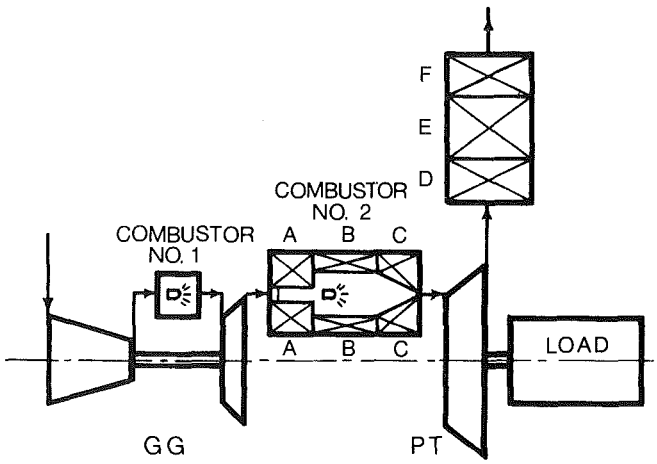


Fig. 16 Diagram of reheat gas turbine with steam-cooled reheat combustor. Reheat steam from reheat steam turbine is heated in convection surface A, radiant surface B and convection/radiant surface C. Heat recovery boiler heat exchange is shown as area D, superheater; area E, evaporator; and area F, economizer

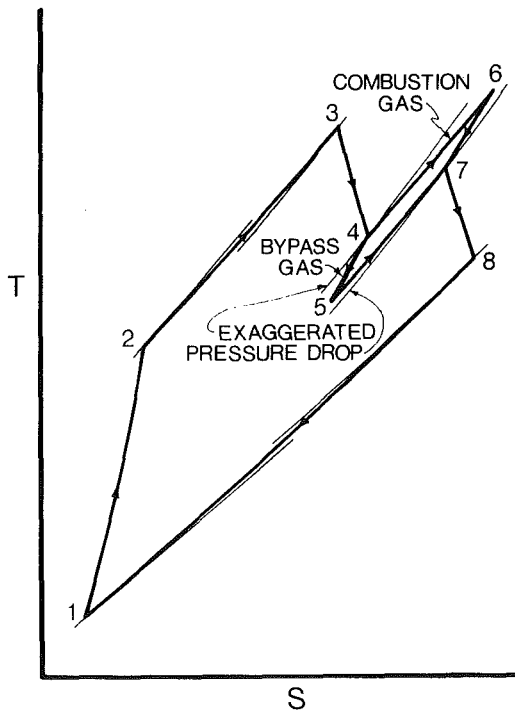


Fig. 17 Temperature-entropy diagram showing exaggerated reheat combustor pressure drop and split in flow of combustion gas and bypass gas

maintain a 300°F minimum stack temperature without resorting to economizer low-pressure steam admission to the steam turbine.

A schematic diagram of the reheat gas turbine incorporating the steam-cooled combustor is presented in Figure 16. It can be noted that steam coils are placed ahead of the burner where convection cooling takes place (heat exchange A); then there is a radiant section (heat exchange B); finally, the radiant surface gives way to another convection surface (heat exchange C). As will be shown later, the steam coils form an annular combustor to provide pressure drop and flame control.

Downloaded 01 Jun 2010 to 171.66.16.62. Redistribution subject to ASME license or copyright; see http://www.asme.org/terms/Terms_Use.cfm

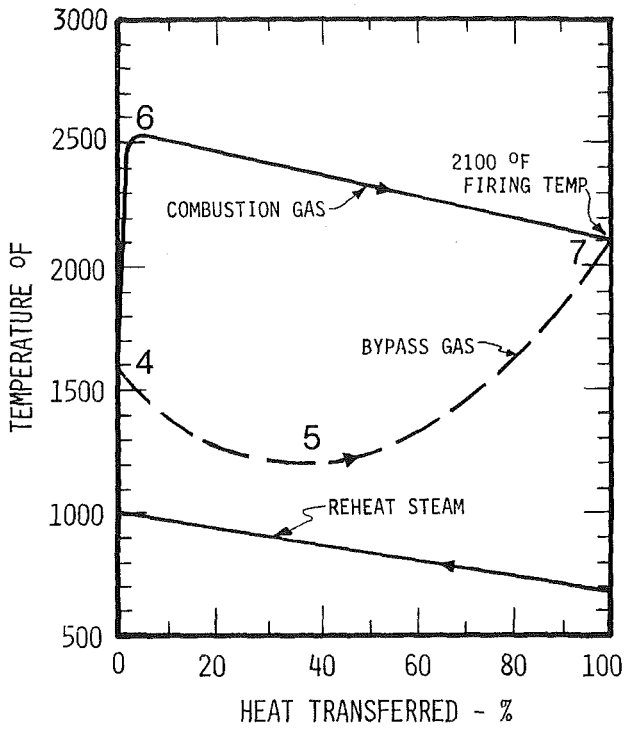


Fig. 18 Heat exchange plot of temperature versus percent heat transferred showing temperature distribution of combustion gas, bypass gas and reheat steam from steam turbine

The initial steam superheater is shown as block D. Block E represents the evaporator and F the economizer.

Referring to the T-S diagram of Fig. 17, the gas expands from point 3 to point 4 where the gas stream is divided. An exaggerated pressure drop is shown to illustrate the double flow path. Combustion gas at 1574°F goes directly to the burner for combustion to provide the proper O_2/fuel ratio and is heated to point 6. This gas is cooled by radiation and convection from point 6 to point 7 - the TIT temperature. Turning to the other stream, the bypass gas is actually cooled by the forward steam coils from point 4 to point 5 before it passes over the inside radiant exposed steam coils where heat transfer by radiation occurs. The gas is thus heated and mixed with the combustion gas to point 7—the TIT temperature. The final mixture is expanded through the power turbine from point 7 to point 8.

A temperature-heat transfer diagram is given as Figure 18. Points 4, 5, 6, and 7 represent the same numbered points of the T-S diagram of Figure 17. The combustion gas is heated from 1574°F, point 4 to point 6, by the flame and is then cooled to TIT temperature, point 7. The bypass gas is cooled from point 4 to point 5 by the reheat steam before it is heated to point 7, TIT temperature, 2100°F.

The very attractive temperature differentials between the combustion gas and the steam and the bypass gas and the steam can be noted, yet temperatures of the combustion gas and the gas mixture downstream of point 5 are not too high to present excessive levels that would burn up the steam coils—assuming they were made of proper austenitic stainless steel material.

A conceptual cross-section of an annular combustor which is cooled by reheat steam is shown in Figure 19. GG exit gas enters a steam-cooled diffuser on the far left side of the drawing. The diffuser is cooled by steam coils and shielded on the flow surface with stainless steel cladding. The diffused gas passes through distribution vanes and into a forward plenum chamber.

Part of the gas from the plenum passes through multiple-burner swirlers and openings in the steam-cooled combustion cap to the primary combustion zone to provide the proper O_2/fuel mixture. The rest of the gas (approximately 70%) passes through the forward and side steam coils before feeding the annular combustion chamber. These coils, which are exposed to the radiant heat from the flame, are cooled by bypass gas. This gas is then mixed with the primary combustion gas before exiting to the downstream plenum.

There is a built-in pressure drop produced by the steam coils to control the fuel/air ratio and to provide flame stability similar to any annular combustor. Investigations based on process heaters indicate that 25 to 30 percent of the

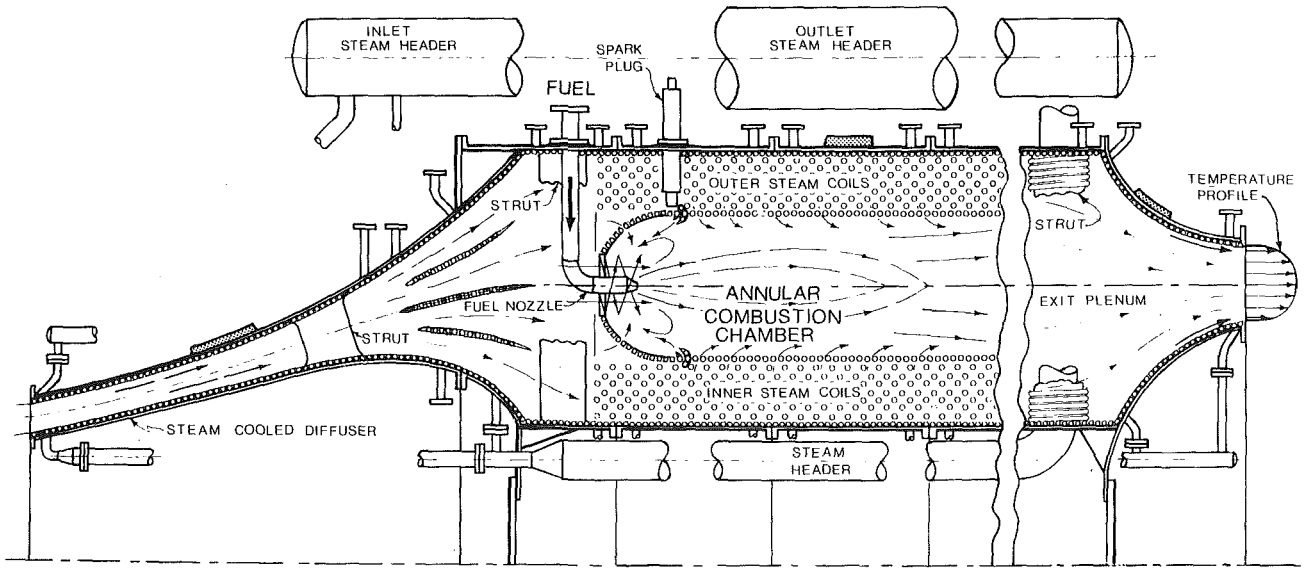


Fig. 19 Conceptual cross-section of annular reheat combustor incorporating steam reheat coils to form the reheat cavity and to provide a controlled minimum pressure drop. The gas generator exit diffuser is shown on the left and the power turbine inlet plenum on the right.

Downloaded 01 Jun 2010 to 171.66.16.62. Redistribution subject to ASME license or copyright; see http://www.asme.org/terms/Terms_Use.cfm

heat transfer will be radiant with no pressure drop - depending upon the length of the chamber.

The rest of the hot gas—after passing through the back chamber coils—then exits to an exit plenum before it flows to the PT first-stage nozzle. A steam-cooled and cladded nose-cone and bell-mouth can be seen on the far right side. the temperature profile to the first-stage PT nozzle is controlled by the cooling effect of the steam coils around this entrance area.

Forward and aft struts are required to support the internal casing and coils. The aft struts are shown wrapped with steam coils to insulate them. The internal steam-header lines pass through these struts.

Disassembly of the combustor for maintenance and access is an important factor which has to be considered. To this end, the gas generator concept lends itself to reheater maintenance. The gas generator can be removed and then the inlet diffuser assembly can be taken off followed by the inlet plenum. The outer coils can be slipped off in sections after proper support is provided for the inner casing. Manhole covers on both the inlet and exit plenums can give access to the front and back of the combustion cap without disassembly. There would be enough space in the cavity between the coils for a worker to crawl through. Other conceptual details on the steam reheater have been previously presented to ASME (3-4).

Conclusion

This paper indicates that the reheat-gas-turbine combined cycle takes on new meaning and presents realistic opportunities to develop a very high-efficiency combined cycle when consideration is given to the appreciable reheat pressure increase made possible by employing gas generator steam-blade cooling.

The following conclusions can be drawn from this paper based on the assumptions set forth and the graphs presented:

1 The latest NASA-developed E^3 technology can and should be employed to develop a nonintercooled high-cycle pressure ratio industrial gas generator using steam as the blade coolant and firing at 2400°F or higher.

2 Compression efficiency of 85 percent and expansion efficiency of 87 percent are appropriate values to assume for an air-cooled gas turbine firing at about 2100°F and using about 8 percent first stage cooling airflow and 4 percent second-stage cooling air flow.

3 Compression efficiency of 87 percent and expansion efficiency of 89 percent are representative values for an up-to-date "uncooled" gas turbine.

4 Eliminating cooling air will increase the gas-generator exit pressure from 81.4 psia to about 90 psia for a 2400°F TIT 38 CPR turbine which amounts to a 10.6 percent pressure increase.

5 Adding steam-blade cooling in the amount of 3 percent for the first stage and 1½ percent for the second-stage blading to the "uncooled" gas generator of conclusion 4 above increases the gas-generator exit pressure from 90 psia to 99.8 psia for another 12 percent increase giving a total increase of 22.6 percent. The steam work is converted to gas-generator exit pressure and thus serves as a pressure booster.

6 Correlatively to 4 and 5, the GG expansion ratio is reduced to enhance the GG staging.

7 The reheat temperature can be increased from 2000°F to 2100°F for a given preselected maximum allowable exhaust temperature of 1300°F when factoring in the effects of conclusions 4 and 5 above.

8 The output of the air-cycle side of the reheat gas turbine excluding the power turbine steam-power component will increase from 208 to 243 BTU/lb of air for a 17 percent power increase due to the effect of conclusions 4, 5, 6, and 7 above and the air-cycle efficiency rises from 37.7 percent to 42.5 percent LHV—a 12.7 percent efficiency increase.

9 The gas generator exit temperature when applying steam-blade cooling will rise moderately from 1514 to 1574°F at the higher exit pressure for the 38-CPR due to improvements in compression efficiency and expansion efficiency.

10 A combined-cycle efficiency of 56 percent LHV seems possible and within reach today for a 38 CPR 2400/2100°F reheat gas turbine employing steam-blade cooling when combined with a 2400 psig 1000/1000°F reheat steam turbine.

11 New blade cooling/steam blanketing techniques are required to obtain maximum benefit from the higher steam pressures available and superior physical characteristics of steam. Incorporating steam nozzles inside each gas-turbine nozzle vane and blade is suggested to steam-blanket the surfaces with a layer of laminar steam flow.

12 A cooled reheat combustor would be required for a 1574°F inlet gas temperature. Incorporating the reheat steam function of the steam turbine appears to be a feasible way to not only cool the reheat combustor but also to maintain a 300°F minimum stack temperature by shifting the heat load from the heat recovery boiler to the reheat combustor.

13 The increased gas-turbine reheat pressure reduces the size of the reheat combustor appreciably. The cross-sectional area for equal internal velocities would be reduced by approximately 18.4 percent.

Acknowledgments

Considerable patience, understanding and skill was required by my dear wife, business partner and manager, Carolyn Keyes Rice, in editing the script, lettering the graphs, arranging the material and typing the mats—all for which my sincere appreciation is expressed.

Also, acknowledgement is given to the authors and companies who have in the past presented and supported the many ASME papers listed following.

Conversion factors for standard international (SI) units

multiply	by	to obtain
(in)	2.54×10^{-6}	(m)
(ft)	0.3048	(m)
(lbs)	0.4535924	(Kg)
(psi)	6894.757	(N . m/m)
(psia)	6894.757	(Pa)
(fps)	.3048	(m/s)
(BTU)	1055.056	(J)
(BTU/lb)	2326.000	J/Kg
(°F)	$\frac{°F + 459.67}{1.8}$	(K)
(°F)	$\frac{°F - 32}{1.8}$	(°C)

References

1 Rice, I.G., "The Combined Reheat Gas Turbine/Steam Turbine Cycle", Part I—"A Critical Analysis of The Combined Reheat Gas Turbine/Steam Turbine Cycle," ASME JOURNAL OF ENGINEERING FOR POWER, Vol. 102, 1980, pp. 35-41.

2 Rice, I.G., "The Combined Reheat Gas Turbine/Steam Turbine Cycle", Part II—"The LM 5000 Gas Generator Applied to the Combined Reheat Gas Turbine/Steam Turbine Cycle," ASME JOURNAL OF ENGINEERING FOR POWER, Vol. 102, 1980, pp. 42-49.

3 Rice, I.G., "Steam-Cooled Blading in a Combined Reheat Gas Turbine/Reheat Steam Turbine Cycle, Part I—Performance Evaluation," ASME Paper No. 79-JPGC-GT-2.

4 Rice, I.G., "Steam-Cooled Blading in a Combined Reheat Gas Turbine/Reheat Steam Turbine Cycle, Part II—Design Considerations," ASME Paper No. 79-JPGC-GT-3.

5 Gray, D.E., and Gardner, W.B., "The Energy-Efficient Engine (E^3)—Advancing the State of The Art," ASME Paper No. 80-GT-142.

6 Crow, D.E., Vanco, M.R., Welna, H., and Singer, I., "Results from

Downloaded 01 Jun 2010 to 171.66.16.62. Redistribution subject to ASME license or copyright; see http://www.asme.org/terms/Terms_Use.cfm

Tests on a High-Work Transonic Turbine for an Energy Efficient Engine," ASME Paper No. 80-GT-146.

7 Tanrikut, S., Sokolowski, D.E., and Wagner, W.B., "Performance of Annular Prediffuser-Combustor Systems," ASME Paper No. 80-GT-15.

8 Johnston, R.P., and Ortiz, P., "Future Trends in Subsonic Transport Energy-Efficiency Turbofan Engines," ASME Paper No. 80-GT-177.

9 Kingcombe, R.C., and Dunning, S.W., "Design Study for a Fuel-Efficient Turbofan Engine," ASME Paper No. 80-GT-141.

10 Taylor, J.R., "Heat Transfer Phenomena in Gas Turbines," ASME Paper No. 80-GT-172.

11 Kobish, T.R., and Nucci, L.M., "High-Temperature Combustor Designed for Operation with Coal-Derived Low BTU Gaseous Fuels," ASME Paper No. 80-GT-187.

12 Caruvana, A., Cincotta, G.A., Alderson, E.D., and Rose, R.S., "Design and Test of a 73-MW Water-Cooled Gas Turbine," ASME Paper No. 80-GT-112.

13 Wolf, J.C., Manning, G.B., and Moskowitz, S., "Development of a High-Temperature Turbine for Operation on Coal-Derived Fuel," ASME Paper No. 80-GT-188.

14 Schilke, P.W., Blazek, W.S., and Schilling, W.G., "Water-Cooled Gas Turbine Monometallic Nozzle Development," ASME Paper No. 80-GT-97.

15 Horner, M.W., Caruvana, A., Cohn, A., and Smith, D.P., "Near-Term Application of Water Cooling," ASME Paper No. 80-GT-159.

16 Clark, J.S., "Status of the DOE/NASA Critical Gas Turbine R & T Project," ASME Paper No. 80-GT-104.

17 Lehman, S.J., Giramonti, A.J., and Meyer, R.H., "Coal Gasification/Repowering—A Means of Increasing Plant Capacity While Reducing Oil Consumption," ASME Paper No. 80-GT-161.

18 Brown, D.H., and Cohn, A., "An Evaluation of Steam-Injected Combustion Turbine Systems," ASME Paper No. 80-GT-51.

19 Keenan, J.H., and Kaye, J., *Gas Tables*, Wiley, 1956.

APPENDIX

The introduction of the paper mentions the NASA-sponsored E^3 engine program. Questions regarding the E^3 engine have been verbally presented which are answered as follows: The first technical readiness test engines are scheduled to run next year. A cross-section of the P&WA E^3 engine is presented in Fig. 20 to illustrate the general configuration. This engine technology could be used to form an industrial gas generator by removing the fan and substituting zero compressor staging. The turbine staging could be modified with the first stage driving the HP compressor and the second stage the LP compressor. Steam-cooled blading could also be incorporated to yield a high-cycle pressure-ratio gas generator suitable for the reheat-gas turbine proposed."

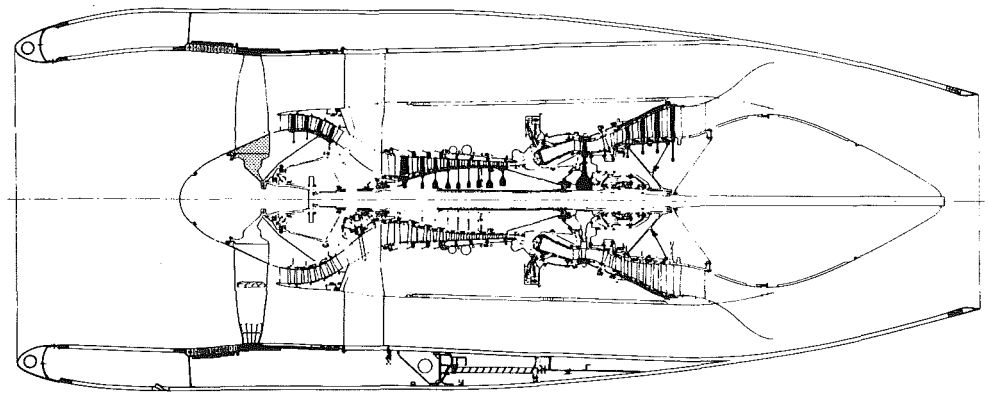


Fig. 20 Cross-section of P&WA E^3 design with a 38.6 CPR firing at 2240° F(1227°C) turbine-rotor-inlet temperature

Downloaded 01 Jun 2010 to 171.66.16.62. Redistribution subject to ASME license or copyright; see http://www.asme.org/terms/Terms_Use.cfm

K. W. Brown
Research Engineer,
Pratt & Whitney Aircraft Group,
United Technologies Corp.,
East Hartford, Conn. 06108

J. L. Krahula
Professor of Mechanics,
Hartford Graduate Center,
Hartford, Conn.

Linear-Nonlinear Interface for Finite Element Impact Analysis

A method is presented for interfacing a nonlinear, explicit finite element structural model with a linear finite element representation. The interfacing procedure allows local nonlinear modelling of a predominantly linear structural response. Conditional stability of the linear-nonlinear interface procedure is established. Very good correlations between test and analysis are shown for two test cases. Run time reductions of up to seventy percent over conventional techniques are demonstrated.

Introduction

The emphasis toward energy efficient jet engines has provided impetus for the design of compressor blades with increasingly thin leading edges. These thin-edged blades have demonstrated a susceptibility for damage in the event of a bird ingestion, exhibiting large dents, cracks, and even material break-out. The finite element method has been evolving as a most valuable tool with which to evaluate a blade's impact resistance capabilities. Due to the severity of bird impacts, dents and large deflections are experienced by fan blades during an impact. Hence, ingestion analyses must make every effort to include the effects of both geometric and material nonlinearities.

The application of the finite element method to nonlinear transient dynamic analysis has been a relatively recent development. Constantino [1] applied the method to the analysis of linear structures. Constantino later extended his capabilities [2] to include nonlinear and viscoelastic media. A stiffness matrix and explicit time integration were employed.

Wilson [3] and Farhoomand and Wilson [4] developed a finite element analysis for application to linear and nonlinear transient problems. Implicit integration and a stiffness matrix were employed. Tangential stiffness methods were employed by Dibaj [5], who used explicit time integration procedures. Geometric and material nonlinearities were treated by Haisler [6], and Stricklin, et al. [7,8], also using a tangential stiffness approach, with implicit integration procedures.

Oden [10,11] formulated the dynamic transient problem by expressing nodal forces directly. Malone and Connors [12] used a direct force approach for determining the transient dynamic response of structures containing linearly viscoelastic materials. Wu and Witmer [13] used direct nodal force calculation to analyze large deflection transient responses of structures, including elastic-plastic, strain hardening, and strain-rate dependent material behavior. Hartzman and Hutchinson [14] used a direct force calculation, and a semi-Eulerian coordinate description, including effects due to nonlinear strain-displacement relations, and nonlinear constitutive relationships.

McNamara and Marcal [15] used a tangential stiffness solution, and treated both geometric and material nonlinearities, using implicit integration procedures. Bathe, Ramm, and Wilson [16] and Bathe and Ozdemir [17] reported on a large displacement, large strain isoparametric finite element solution, which has available both Eulerian and Lagrangian formulations.

Belytschko, et al. [18–21] in several papers report on efficient finite element methods that employ an explicit time integration, lumped mass solution procedure. Belytschko includes material and geometric nonlinearities, including arbitrarily large rotations, but with the limitation of small strains.

Nickell [22] and Fujii [23] both indicated that the conditionally stable central difference operator is preferable to implicit integration procedures for nonlinear solutions. Krieg and Key [24] arrived at the same conclusion after examining several test cases, recommending explicit, central difference integration, with a diagonal mass representation. Belytschko, Chiapetta, and Bartel [21] compared implicit, explicit with tangent stiffness, and explicit with direct force calculation analysis procedures, and concluded that the explicit solution with direct force calculation is the most efficient solution technique. Therefore, it was concluded that the standard transient finite element analysis procedure that would be best suited to the blade impact problem would be the WHAM code [18,20].

The WHAM code employs a triangular plate element which is well suited to transient analysis of blade geometries. Large displacement effects are included through element coordinate system translations and rotations. Thus, while large displacements are included in the membrane forces, they are not included in the bending effects, leading to the assumption of small strains and small curvatures. Nodal forces are calculated directly from element stresses for each time step, eliminating the need for a stiffness matrix. A flow chart for the direct force, explicit analysis algorithm is available in reference [18].

Impact loadings, based upon the assumption that the projectile acts as an incompressible fluid, are applied to the blade model. When the loading model had been incorporated

Contributed by the Gas Turbine Division and presented at the International Gas Turbine Conference and Products Show, Houston, Texas, March 9–12, 1981, of THE AMERICAN SOCIETY OF MECHANICAL ENGINEERS. Manuscript received at ASME Headquarters, December 5, 1980. Paper No. 81-GT-39.

Copyright © 1982 by ASME

Downloaded 01 Jun 2010 to 171.66.16.62. Redistribution subject to ASME license or copyright; see http://www.asme.org/terms/Terms_Use.cfm

into the WHAM program, the solution technique was found through test cases to be quite feasible. However, one important drawback was noted: The analysis procedure is very high in computer run time for a blade analysis. Indeed, in a blade design application, where many configurations may require consideration, and many analyses are conducted, the analysis expense is prohibitive.

Linear-Nonlinear Interface Concept

The prohibitive expense of the WHAM nonlinear analysis, coupled with the local nature of the nonlinearities of the blade impact problem, provided the impetus for the development of the theory of reference [25], and this paper. During the impact event, projectile loads are applied along the section of the blade which is local to the impact. Large deflection effects, as well as material yielding, will all occur local to the impact area. The remaining portion of the blade - indeed, the greatest part of the blade – will remain elastic, and small deflection theory will also be appropriate. Hence, over most of the blade, a linear analysis will be adequate.

This combination of circumstances led to the development of a procedure for modelling the blade nonlinearly local to the impact zone, or any place where nonlinear effects would be important, and interfacing this nonlinear model with a linear representation of the remainder of the blade. The new procedure enhances analysis efficiency in two ways.

First, the present WHAM technique requires the reconstruction of element forces (in essence, the element stiffness) for each element, for each time step. For elements that remain linear, and have a stiffness matrix available, the element forces may be determined more efficiently through a matrix multiplication. One byproduct of the interfacing procedure is to make such a stiffness array available for linear elements.

Secondly, the interfacing procedure allows the employment of problem size reduction procedures over the linear portion of the mesh, further enhancing the analysis efficiency.

The concept of modelling the structure as an interface of linear and nonlinear zones has proven very fruitful for blade impact analysis, reducing run times by 70 to 90 percent for many applications.

Theory of the Interface

For the combined linear-nonlinear analysis, the structural model is divided into two segments; a nonlinear segment, which is local to the impact region, and a linear segment, which is remote from the impact region. The two segments share a boundary of common nodes, which are connected through an interfacing procedure.

The nonlinear zone maintains both geometric and material nonlinear capabilities. The stiffness of this region is regenerated each time step in the form of element internal forces, which act upon the nodes of the structural model. At the common boundary between regions, displacement equality is enforced, as well as force equilibrium. Therefore, the linear region will be able to exert forces on the boundary of the nonlinear zone. The forces transferred will depend on the displacements and accelerations of the structural model. The boundary forces are treated as loads acting on their respective regions. Projectile loadings are considered as external loads to the structural model. The nonlinear zone equilibrium equation may be partitioned to reflect the interior (n) and the boundary (e) of the zone, giving

$$\begin{bmatrix} M_{nn} & 0 \\ 0 & M_{ee} \end{bmatrix} \begin{Bmatrix} \ddot{u}_n(t+\Delta t) \\ \ddot{u}_e(t+\Delta t) \end{Bmatrix} = \begin{Bmatrix} F_{En}(t+\Delta t) - F_{In}(t+\Delta t) \\ F_{Ee}(t+\Delta t) - F_{Ie}(t+\Delta t) + F_{BDY}(t+\Delta t) \end{Bmatrix}. \quad (1)$$

The linear zone employs linear finite element theory. The stiffness and mass matrices for this zone are generated only once, and are saved in computer storage. The application of reduction procedures will be permitted on the linear region. As these techniques will result in mass coupling, provision must be made for non-diagonal mass matrices in the linear region. Additionally, it is assumed that the only loads acting upon the linear region are the loads generated by the nonlinear region boundary connection. The equilibrium equation for the linear zone may be partitioned for the interior (i) and for the boundary (b) of the linear zone, giving

$$\begin{bmatrix} M_{ii} & M_{ib} \\ M_{bi} & M_{bb} \end{bmatrix} \begin{Bmatrix} \ddot{u}_i(t+\Delta t) \\ \ddot{u}_b(t+\Delta t) \end{Bmatrix} + \begin{bmatrix} K_{ii} & K_{ib} \\ K_{bi} & K_{bb} \end{bmatrix} \begin{Bmatrix} u_i(t+\Delta t) \\ u_b(t+\Delta t) \end{Bmatrix} = \begin{Bmatrix} 0 \\ F_b(t+\Delta t) \end{Bmatrix}. \quad (2)$$

The linear region interior accelerations may be solved for in the first half of equation (2) as

$$\{\ddot{u}_i(t+\Delta t)\} = -[M_{ii}]^{-1}([M_{ib}]\{\ddot{u}_b(t+\Delta t)\} + [K_{ii}]\{u_i(t+\Delta t)\} + [K_{ib}]\{u_b(t+\Delta t)\}). \quad (3)$$

Putting equation (3) into the second half of equation (2), we find

$$([M_{bb}] - [M_{bi}][M_{ii}]^{-1}[M_{ib}])\{\ddot{u}_b(t+\Delta t)\} + ([K_{bi}] - [M_{bi}][M_{ii}]^{-1}[K_{ii}])\{u_i(t+\Delta t)\} + ([K_{bb}] - [M_{bi}][M_{ii}]^{-1}[K_{ib}])\{u_b(t+\Delta t)\} = \{F_b(t+\Delta t)\}. \quad (4)$$

Thus, we now have an expression for the boundary accelerations in terms of known quantities, and the boundary forces. This equation will enable the linear zone to be interfaced with the nonlinear zone.

To combine the linear and nonlinear region boundaries, let us add equation (4) to the second half of equation (1), recognizing that $u_b = u_e$, and that $F_b = -F_{BDY}$. By knowing the nodal displacements and loads for the subsequent time step, we are able to solve for the boundary accelerations,

$$\{\ddot{u}_b(t+\Delta t) = ([M_{ee}] + [M_{bb}] - [M_{bi}][M_{ii}]^{-1}[M_{ib}])^{-1} \cdot <\{F_{EXT_e}(t+\Delta t)\} - \{F_{INT_e}(t+\Delta t)\} - ([K_{bi}] - [M_{bi}][M_{ii}]^{-1}[K_{ii}])\{u_i(t+\Delta t)\} - ([K_{bb}] - [M_{bi}][M_{ii}]^{-1}[K_{ib}])\{u_b(t+\Delta t)\}>. \quad (5)$$

Equation (5) now allows the use of equation (3) to solve for accelerations over the interior of the linear region,

$$\{\ddot{u}_i(t+\Delta t)\} = -[M_{ii}]^{-1} <[M_{ib}]\{\ddot{u}_b(t+\Delta t) + [K_{ii}]\{u_i(t+\Delta t)\}\} + [K_{ib}]\{u_b(t+\Delta t)\}\}>. \quad (6)$$

Thus, equations (5), (6), and (1) allow for the solution of all nodal accelerations, and the linear and nonlinear regions have been coupled.

The procedure just described allows for the elimination of stiffness recomputation over much of the structure, hence increasing analysis efficiency. Significant additional run time reductions may be achieved through utilization of reduction procedures on the linear region. For the present analysis, the

Downloaded 01 Jun 2010 to 171.66.16.62. Redistribution subject to ASME license or copyright; see http://www.asme.org/terms/Terms_Use.cfm

Guyan reduction procedure [26] has been employed. The Guyan procedure allows for reduction of the number of degrees of freedom on the linear zone interior, hench reducing the number of integrations to be performed, with little loss of solution accuracy. Degrees of freedom on the linear-nonlinear boundary must be retained.

Selection of nonlinear region size for an analysis is largely experience based, but a guideline has been developed to aid in the choice of relative region sizes. For a soft body impact, the nonlinear region of a blade or specimen often propagates as far as a projectile diameter from the impact point. For analysis of severe impacts, the nonlinear region should be increased above this general recommendation.

Stability of the Combined Analysis

A stability criterion for the combined analysis system will be established by employing the energy method of References [23, 27, and 28]. In the energy method for stability, the system energy is studied throughout time. If boundedness of the system energy can be guaranteed, the system will remain stable.

For the purpose of establishing the stability of the region interfacing procedure, it is sufficient to linearize the nonlinear zone equilibrium equation (1), giving

$$\begin{bmatrix} M_{nn} & 0 \\ 0 & M_{ee} \end{bmatrix} \begin{Bmatrix} \ddot{u}_n(t+\Delta t) \\ \ddot{u}_e(t+\Delta t) \end{Bmatrix} + \begin{bmatrix} K_{nn} & K_{ne} \\ K_{en} & K_{ee} \end{bmatrix} \cdot \begin{Bmatrix} u_n(t+\Delta t) \\ u_e(t+\Delta t) \end{Bmatrix} = \begin{Bmatrix} F_{E_n}(t+\Delta t) \\ F_{E_e}(t+\Delta t) + F_{BDY}(t+\Delta t) \end{Bmatrix}, \tag{7}$$

where the newly defined stiffness matrices for the linearized nonlinear zone may be generated using standard linear finite element techniques.

On the linear zone, the equilibrium equation was given by equation (2). The linear and nonlinear zones may be combined by the summation of equations (7) and (2), with the recognition of the common boundary nodal displacements and the equilibrium of boundary reaction forces, giving a combined system equilibrium equation,

$$\begin{bmatrix} M_{nn} & 0 & 0 \\ 0 & M_{ee}+M_{bb} & M_{bi} \\ 0 & M_{ib} & M_{ii} \end{bmatrix} \begin{Bmatrix} \ddot{u}_n(t+\Delta t) \\ \ddot{u}_e(t+\Delta t) \\ \ddot{u}_i(t+\Delta t) \end{Bmatrix} + \begin{bmatrix} K_{nn} & K_{ne} & 0 \\ K_{en} & K_{ee}+K_{bb} & K_{bi} \\ 0 & K_{ib} & K_{ii} \end{bmatrix} \begin{Bmatrix} u_n(t+\Delta t) \\ u_e(t+\Delta t) \\ u_i(t+\Delta t) \end{Bmatrix} = \begin{Bmatrix} F_{En}(t+\Delta t) \\ F_{Ee}(t+\Delta t) \\ 0 \end{Bmatrix}. \tag{8}$$

To establish a stability condition for the combined system, we define a combined system mass matrix and a stiffness matrix, $[M_c]$ and $[K_c]$. For the case of free vibrations, the equilibrium equation for the combined system thus becomes

$$[M_c]\{\ddot{u}\} + [K_c]\{u\} = 0. \tag{9}$$

From one time step to another, the internal energy increment is

$$U(t+\Delta t) = U(t) + \frac{1}{2}\Delta u(t)^T \cdot [K_c](u(t+\Delta t) + u(t)). \tag{10}$$

The kinetic energy increment is

$$T(t+\Delta t) = \frac{1}{2}\dot{u}(t+\Delta t)^T[M_c]\dot{u}(t+\Delta t) = T(t) + \frac{\Delta t}{2}\dot{u}(t)^T[M_c](\ddot{u}(t+\Delta t)+\ddot{u}(t)) + \frac{\Delta t^2}{8}(\ddot{u}(t+\Delta t)+\ddot{u}(t))^T[M_c](\ddot{u}(t+\Delta t)+\ddot{u}(t)). \tag{11}$$

The total energy change comes from the summation of equations (10) and (11). The energy change may be simplified through application of the central difference operator, and the system equilibrium equation (9), finally giving, for symmetric mass matrices,

$$\Delta E = \frac{\Delta t^2}{8}[u(t+\Delta t)^T K_c^T (M_c^{-1})^T K_c u(t+\Delta t) - u(t)^T K_c^T (M_c^{-1})^T K_c u(t)]. \tag{12}$$

The energy increments may now be summed, yielding the energy at the n'th time step,

$$E(n\Delta t) = E(0) + \frac{\Delta t^2}{8}[u(n\Delta t)^T K_c^T (M_c^{-1})^T K_c u(n\Delta t) - u(0)^T K_c^T (M_c^{-1})^T K_c u(0)]. \tag{13}$$

By recalling the definitions of the energy terms, (13) may be expressed as

$$T(n\Delta t) + \frac{1}{2}u(n\Delta t)^T[I - \frac{\Delta t^2}{4}K_c^T(M_c^{-1})^T]K_c u(n\Delta t) = T(0) + \frac{1}{2}u(0)^t[I - \frac{\Delta t^2}{4}K_c^T(M_c^{-1})^T]K_c u(0), \tag{14}$$

where I is the identity matrix.

To determine the stability condition for the coupled system, we must assure a nonzero coefficient of the potential energy at the n'th time increment. Therefore, for system stability, it is sufficient that Δt be smaller that the smallest Δt for which there is a nontrivial solution of

$$[I - \frac{\Delta t^2}{4}K_c^T(M_c^{-1})^T]K_c u(n\Delta t) = 0. \tag{15}$$

A nontrivial solution of (15) will exist when

$$\left| K_c^T (M_c^{-1})^T - \frac{4}{\Delta t^2} I \right| = 0. \tag{16}$$

Hence, we may conclude that the analysis combination will be stable for

$$\Delta t < 2/\sqrt{\lambda_i}, \text{ for all } i, \tag{17}$$

where the λ_i are the eigenvalues for the combined, linearized system vibration problem

$$|K_c^T (M_c^{-1})^T - \lambda I| = 0. \tag{18}$$

Thus, we have established the conditional stability of the analysis coupling technique. In practice, we have a rational method for establishing an appropriate time increment for a desired analysis.

Comparisons With Test Results

Friedrich and Preston [29] impacted cantilevered flat plates with gelatin balls. The plates, which were 19.05 cm long, 5.08 cm wide, and 0.254 cm thick, were normally impacted along their center line, 7.62 cm from the base support, by a 1.27 cm diameter gelatin sphere, at a velocity of 274 m/s.

Downloaded 01 Jun 2010 to 171.66.16.62. Redistribution subject to ASME license or copyright; see http://www.asme.org/terms/Terms_Use.cfm

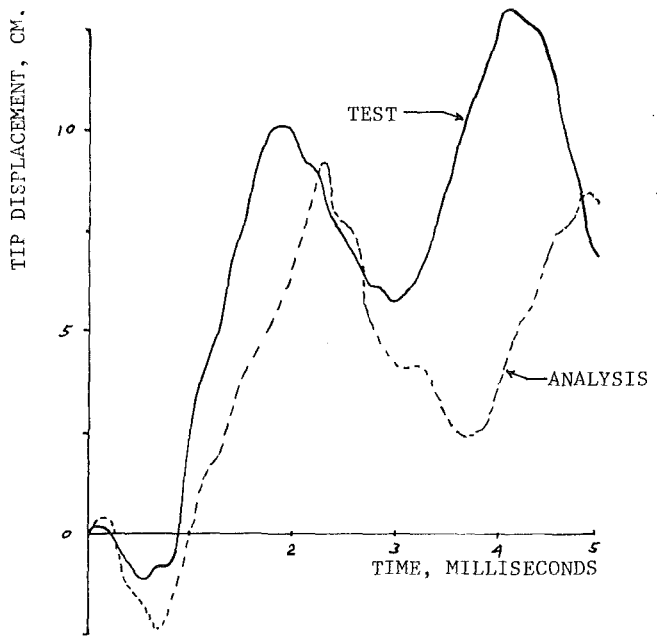


Fig. 1 Tip displacements for centrally impacted flat plate

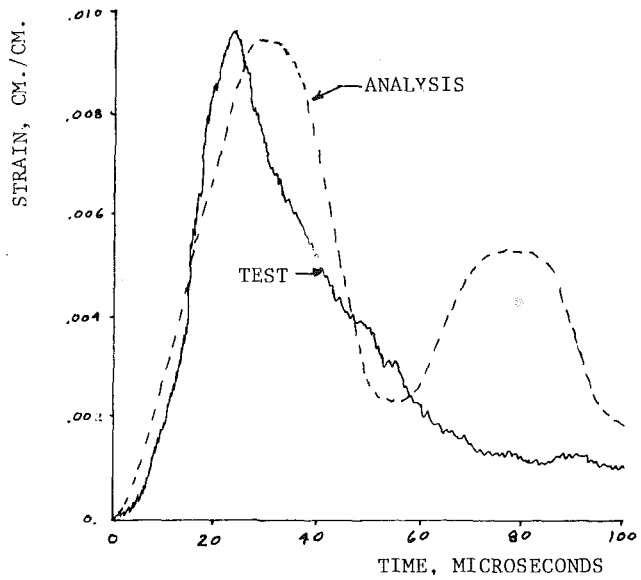


Fig. 2 Strains at impact point, flat plate impact

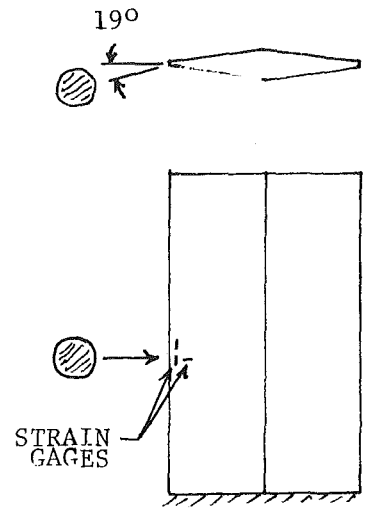


Fig. 3 Geometry of double wedge shaped impact specimen

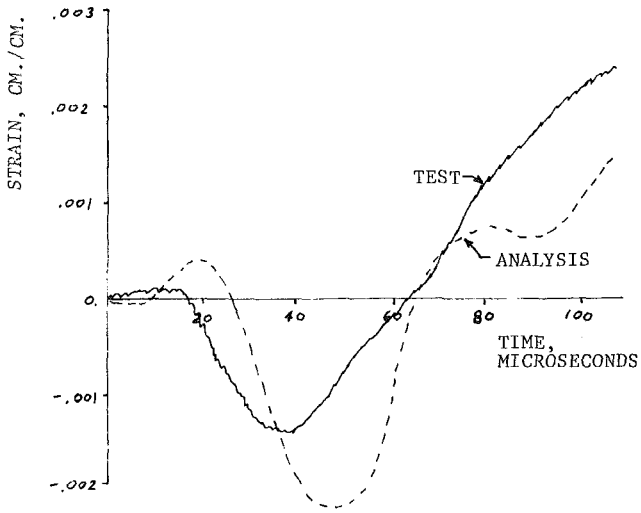


Fig. 4 Spanwise strains, 1.3 cm above load centerline, double wedge specimen

To model the impact loads, the projectile force distribution was assumed to be a half sine wave, with a load duration equal to the time for the projectile to travel its diameter. The load value was determined such that the total transmitted impulse equalled the projectile momentum.

In test, two panels were evaluated. The first panel tested was aluminum, and deflections of the panel tip were monitored. Figure 1 compares the test deflections with those predicted by analysis. Comparisons are quite good. The analytical results are somewhat attenuated, due to a low level of numerical damping employed by the WHAM code to reduce spurious oscillations caused by numerical round-off error.

Figure 2 shows strain comparisons between analysis and test for a spanwise strain gage located directly under the impact center of a titanium panel. In general, strain comparisons are quite good. The maximum predicted spanwise strain value agreed very well with test results.

Friedrich [30] tested a titanium specimen of diamond shaped cross section which was obliquely impacted at its leading edge by a gelatin sphere. Figure 3 shows the specimen, which is 14.6 cm long, 7.62 cm wide, and is cantilevered at its base. The specimen is .025 cm thick at its edge, and 0.381 cm thick at its center. Strain gages, located on the specimen back side, gave specimen strain histories.

A 2.54 cm diameter gelatin sphere impacted the leading edge 5.71 cm above the base support. The sphere had a velocity of 131 m/sec, and hit the specimen at a 19 deg relative impact angle. Approximately half of the sphere mass was involved in the impact event.

To model the gelatin ball impact, forces are calculated based upon the momentum transferred by a dynamic fluid jet which has the projectile dimensions, and is capable of interacting with the target model.

Comparisons between dynamic strain gage test results and analytically predicted strains are shown on Figs. 4 and 5. Figure 4 shows strain comparisons for a spanwise strain gage, .444 cm from the leading edge and 1.27 cm above the load center line. Figure 5 shows strain comparisons for a spanwise strain gage, 0.444 cm from the leading edge, along the load center line. In general, the strain comparisons between analysis and test are very good. Higher mode strain responses,

Downloaded 01 Jun 2010 to 171.66.16.62. Redistribution subject to ASME license or copyright; see http://www.asme.org/terms/Terms_Use.cfm

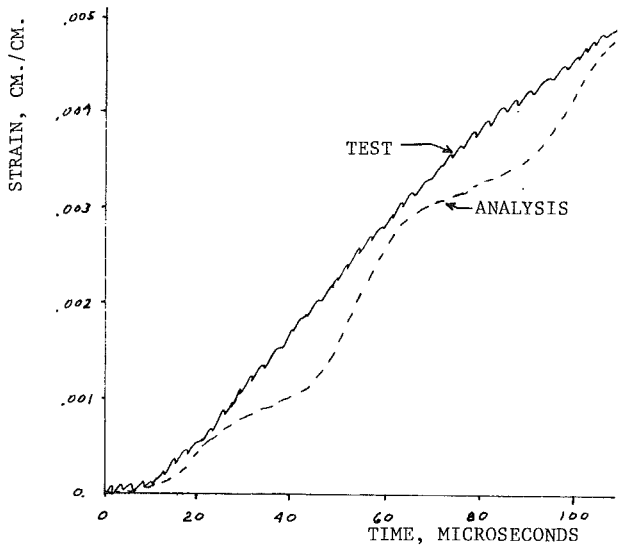


Fig. 5 Spanwise strains, along load centerline, double wedge specimen

evident in the analytical strains, are buried within the relatively large amount of noise associated with the test strain values.

It is of interest to evaluate the time savings of the present method in comparison with the conventional WHAM analysis. For the second test case, a full WHAM analysis of 1056 degrees of freedom required 18.8 min of computer run time (IBM 370/3033). Using the present method, the structure was modelled using a linear zone reduced to 157 degrees of freedom, with a nonlinear zone of 396 degrees of freedom. Virtually identical results as the first analysis were obtained, with a total elapsed run time of 5 min., for a run time savings of 73 percent.

References

1 Constantino, C. J., "Finite Element Approach to Stress Wave Problems," *J. Eng. Mech. Div., ASCE,* Vol. 93, 1967, pp. 153–166.

2 Constantino, C. J., "Stress Waves in Layered Arbitrary Media — SLAM Code Free Field Study," SAMSO Report TR-68-181, IITRI, 1968.

3 Wilson, E. L., "A Computer Program for the Dynamic Stress Analysis of Underground Structures," Report to Waterways Exp. Station, U. S. Army Corps of Eng., Rept 68-1, Univ. of Calif., Berkeley, 1968.

4 Farhoomand, I., and Wilson, E. L., "A Nonlinear Finite Element Code for Analyzing the Blast Response of Underground Structures," Rept. N-70-1 to U. S. Army Waterways Exp. Station, Univ. of Calif., Berkeley, 1970.

5 Dibaj, M., *Nonlinear Seismic Response of Earth Structures,* Ph. D. thesis, Univ. of Calif., Berkeley, 1969.

6 Haisler, W. E. Jr., *Development and Evaluation of Solution Procedures for Nonlinear Structural Analysis,* Ph. D. thesis, Texas A & M Univ, 1970.

7 Stricklin, J. A., Martinez, J. E., Tillerson, J. R., Hong, J. H., and Haisler, W. E., "Nonlinear Dynamic Analysis of Shells of Revolution by Matrix Displacement Method," *AIAA Journal,* Vol. 9, No. 4, Apr. 1971, pp. 629–636.

8 Stricklin, J. A., Haisler, W. E., and von Riesemann, W. A., "Computation and Solution Procedure for Nonlinear Analysis by Combined Finite Element — Finite Difference Methods," *Nat. Sympos. On Comp. Struct. Anal. and Design,* George Washington Univ., Mar. 1972.

9 Wempner, G. A., "Finite Elements, Finite Rotations, and Small Strains of Flexible Shells," *Int. J. Solids & Struct.,* Vol. 5, 1969, pp. 117–153.

10 Oden, J. T., "Finite Element Applications in Linear and Nonlinear Thermo-Viscoelasticity," *EMD Specialty Conf.,* ASCE, Raleigh, N. C., 1967, pp. 32–35.

11 Oden, J. T., *Finite Elements of Nonlinear Continua,* McGraw-Hill, New York, 1972.

12 Malone, D. W., and Connors, J. J., "Finite Elements and Dynamic Viscoelasticity," *J. Eng. Mech. Div., ASCE,* Vol. 97, 1971, pp. 1145–1158.

13 Wu, E. H., and Witmer, E. A., "Finite Element Analysis of Large Plastic Transient Deformations of Simple Structures," *AIAA Journal,* Vol. 9, 19791, pp. 1719–1724.

14 Hartzman, M., and Hutchinson, J. R., "Nonlinear Dynamics of Solids by the Finite Element Method," *Computers and Structures,* Vol. 2, 1972, pp. 47–77.

15 McNamara, J. F., and Marcal, P. V., "Incremental Stiffness Method for Finite Element Analysis of the Nonlinear Dynamic Problem," *Proc. Int. Symp. on Numerical and Computer Methods in Struct. Mech.,* Urbana, Illinois, Sept. 1971.

16 Bathe, K., Ramm, E., and Wilson, E. L., "Finite Element Formulations for Large Deformation Dynamic Analysis," *Int. J. for Num. Methods in Eng.,* Vol. 9, 1975, pp. 353–386.

17 Bathe, K., and Ozdemir, H., "Elastic-Plastic Large Deformation Static and Dynamic Analysis," *Computers and Structures,* Vol. 6, 1976, pp. 81–92.

18 Belytschko, T. B., and Hsieh, B. J., "Nonlinear Transient Finite Element Analysis with Convected Coordinates," *Int. J. for Num. Methods in Eng.,* Vol. 7, 1973, pp. 255–272.

19 Belytschko, T. B., and Hsieh, B. J., "Nonlinear Transient Analysis of Shells and Solids of Revolution by Convected Elements," AIAA, Paper No. 73-359.

20 Belytschko, T. B., and Marchertas, A. H., "Nonlinear Finite Element Method for Plates and its Application to Dynamic Response of Reactor Fuel Subassemblies," ASME Paper No. 74-NE-10.

21 Belytschko, T. B., Chiapetta, R. L., and Bartel, H. D., "Efficient Large Scale Non-Linear Transient Analysis by Finite Elements," *Int. J. for Num. Methods in Eng.,* Vol. 10, 1976, pp. 579–596.

22 Nickell, R. E., "On the Stability of Approximation Operators in Problems of Structural Dynamics," *Int. J. Solids & Structures,* Vol. 7, 1971, pp. 301–319.

23 Fujii, H., "Finite-Element Schemes: Stability and Convergence," *Advances in Computational Methods in Structural Mechanics and Design,* ed. Oden, J. T. et al., Huntsville, Ala.: UAH Press, 1972, pp. 201–218.

24 Krieg, R. D. and Key, S. W., "Transient Shell Response by Numerical Time Integration," *Int. J. for Num. Methods in Eng.,* Vol. 7, 1973, pp. 273–286.

25 Brown, K. W., *Linear-Nonlinear Interface for Finite Element Transient Impact Damage Analysis,* Dr. of Eng. thesis, Rensselaer Polytechnic Institute, 1980.

26 Guyan, R. J., "Reduction of Stiffness and Mass Matrices," *AIAA Journal,* Vol. 3, No. 2, 1965, p. 380.

27 Oden, J. T. and Fost, R. B., "Convergence, Accuracy, and Stability of Finite Element Approximations of a Class of Non-Linear Hyperbolic Equations," *Int. J. for Num. Methods in Eng.,* Vol. 6, 1973, pp. 357–365.

28 Belytschko, T. and Schoeberle, D. F., "On the Unconditional Stability of an Implicit Algorithm for Nonlinear Structural Dynamics," *Journal of Applied Mechanics,* Dec. 1975, pp. 865–869.

29 Friedrich, L. A., and Preston, J. L. Jr., *Impact Resistance of Fiber Composite Blades Used in Aircraft Turbine Engines,* NASA CR-134502, May 1973.

30 Friedrich, L. A., *Impact Resistance of Hybrid Composite Fan Blade Materials,* NASA CR-134712, May 1974.

Downloaded 01 Jun 2010 to 171.66.16.62. Redistribution subject to ASME license or copyright; see http://www.asme.org/terms/Terms_Use.cfm

P. B. Roberts

A. J. Kubasco

Solar Turbines Inc.
San Diego, Calif.

N. J. Sekas

National Aeronautics & Space Administration,
Lewis Research Center,
Cleveland, Ohio

Development of a Low NOx Lean Premixed Annular Combustor

An atmospheric test program was conducted to define a low NOx annular combustor concept suitable for a supersonic, high-altitude aircraft application. The lean premixed combustor, known as the Vortex Air Blast (VAB) concept, was tested as a 22.0 cm diameter model in the early development phases to arrive at basic design and performance criteria. Final demonstration testing was carried out on a full scale combustor of 0.66 m diameter. Variable geometry dilution ports were incorporated to allow operation of the combustor across the range of conditions between idle (T_{in} = 422 K, T_{out} = 917 K) and cruise (T_{in} = 833 K, T_{out} = 1778 K). Test results showed that the design could meet the program NOx goal of 1.0 g NO_2/kg fuel at a reduced atmospheric cruise condition.

Introduction

The impact of gas turbine powered aircraft on worldwide pollution can be defined within two major areas. First, the contribution of aircraft to the local air pollution of metropolitan regions and, second, the long-term effects on the chemical balance of the stratosphere of pollutants emitted from future generations of high-altitude, supersonic commercial and military aircraft. Within this second area of concern, preliminary findings have indicated that stratospheric nitrogen oxides (NOx) might need to be limited to very low levels if, for example, ozone depletion with concommitant increases in sea-level radiation are to be avoided.

A previous Solar experimental rig study investigated the low NOx potential of two distinct types of forced circulation, lean premixed combustors, namely the Jet Induced Circulation (JIC) and the Vortex Air Blast (VAB) combustors. This work defined both the basic low NOx potential of these two combustors at a simulated high-altitude, supersonic cruise condition, and their operational range limitations. This work was previously reported [1] and followed by a second program intended to define range augmentation techniques. These were to allow the JIC and VAB combustors to operate stably with acceptable emissions at a simulated engine idle without compromise to the low NOx emissions at the high-altitude, supersonic cruise condition. The range-augmentation techniques successfully demonstrated and reported [2] involved total variable geometry, variable dilution, variable dilution plus fuel switching, and axial fuel staging.

Both of these previous rig investigations were conducted on small-scale can combustors of 12.7 cm (5 in.) diameter to facilitate experimental modifications. It was recognized, however, that an evaluation of a full-size annular combustor configuration would be necessary before a realistic assessment could be made of the potential of the lean premixed combustion system. The work reported in this paper summarizes the results of an experimental atmospheric rig test program that had as its objective the confirmation of Solar's lean premixed combustor background with a full-size annular combustor of 0.66 m (26.0 in.) diameter designed to constraints typical of current aircraft systems. Some preliminary investigations, not covered in this paper, were conducted with a small-scale annular combustor of 21.6 cm (8.5 in.) diameter to define the basic configuration details and to provide a design bridge between the full-size unit and the small-scale can combustors.

The test program was restricted to atmospheric inlet conditions due to facility limitations. Future high-pressure testing of the full-size annular combustor is planned at a NASA-Lewis Research Center facility.

Combustor Concept

The combustor concept selected for the full-size experimental investigations was the Vortex Air Blast (VAB) system. The design of the unit was based on physical and operational constraints, together with background experience from Solar's previous test programs on this type of combustor.

The combustor is of the lean reaction, premixed family of well-stirred systems where NOx control is effected by minimizing the mean reaction zone equivalence ratio and the local equivalence ratio deviations that can cause high NOx levels.

As a cost-effectiveness measure, Solar's early programs were conducted with reverse-flow can combustor configurations. The full-size VAB combustor was designed as an axi-symmetric axial-flow annular system in keeping with current practice in advanced aircraft gas turbine combustion systems.

A section through the VAB combustor is shown in Fig. 1 where the key features of the design can be seen. The general

Contributed by the Gas Turbine Division and presented at the International Gas Turbine Conference, Houston, Texas, March 8-12, 1981, of THE AMERICAN SOCIETY OF MECHANICAL ENGINEERS. Manuscript received at ASME Headquarters, December 5, 1980. Paper No. 81-GT-40.

Copyright © 1982 by ASME

Downloaded 01 Jun 2010 to 171.66.16.62. Redistribution subject to ASME license or copyright; see http://www.asme.org/terms/Terms_Use.cfm

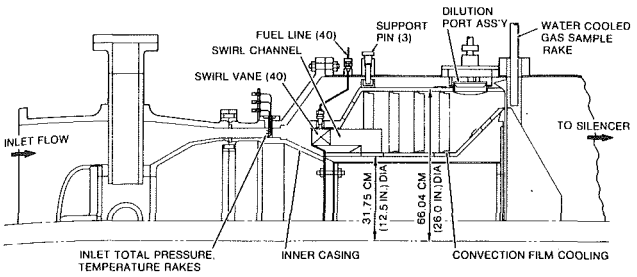


Fig. 1 Full size annular VAB combustor

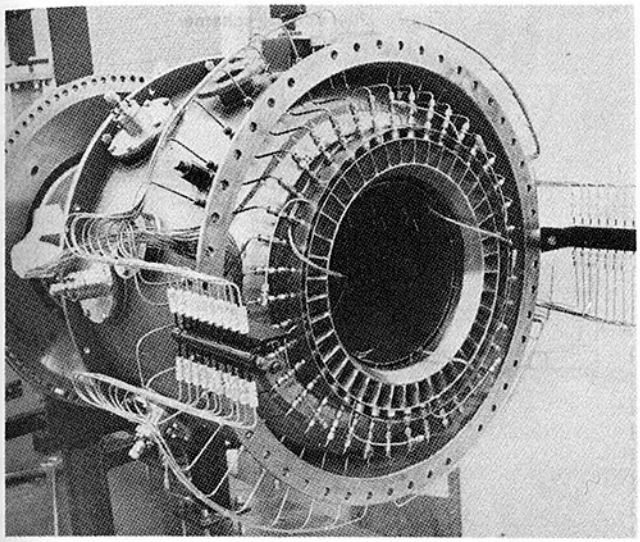


Fig. 2 VAB annular combustor - swirler inlet

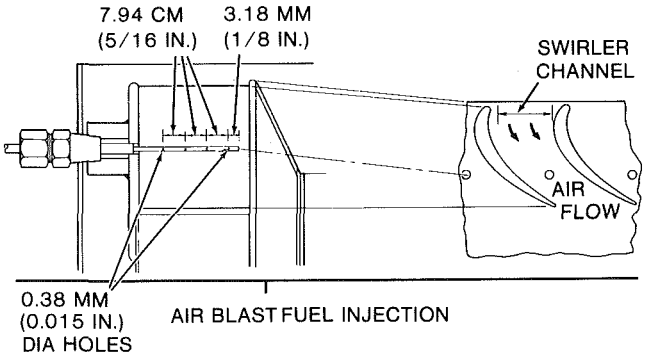


Fig. 3 Fuel injection system

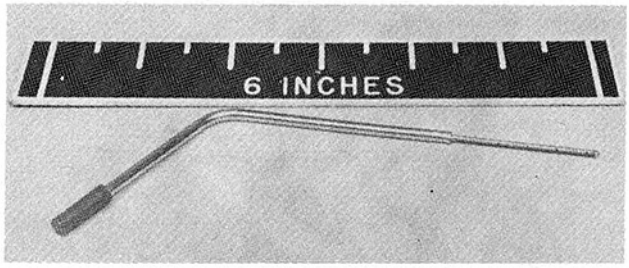


Fig. 4 Fuel Injection Rake

design strategy was to provide a combustor with a variable dilution system where at the cruise condition the dilution ports would be closed and the reaction zone equivalence ratio minimized. At the idle condition the dilution ports would be fully opened to obtain the necessary stability.

Swirl Stabilization. Solar's previous small-scale VAB can combustor designs were based on a radial inflow swirler to provide combustion stabilization. The full-size VAB unit retains the feature of swirl stabilization but an axial swirler, rather than a radial inflow design, is adopted. This feature results in a more effective integration of the combustor with the inlet flow. A front view of the combustor showing the swirler inlet is shown in Fig. 2. The swirler consists of forty vanes set at an outlet angle of 60 degrees with a pitch/chord ratio of approximately unity.

Fuel Injection. The fuel injection system was the subject of much of the experimental effort and the initial configuration is shown in Fig. 3. A radial air-blast fuel injector rake is installed in each of the forty swirl vane channels at a station slightly upstream of the channel throat. A view of a typical fuel injector rake is shown in Fig. 4. Each rake is 1.57 mm (0.062 in.) diameter with four fuel injection orifices 0.3 mm (0.012 in.) diameter positioned along the rake. Adequate injector-to-injector patternation is ensured by a system of external flow divider blocks.

Swirl Channel. The fuel is air-blast atomized slightly upstream of the vane channel throats then vaporizes and mixes with the reaction airflow in an annular swirl channel downstream of the vortex generator. The swirl channel dumps into the reaction zone of the combustor where the radial static pressure gradients of the near-homogeneous fuel/air stream serve to drive the reaction zone recirculation necessary for flame stabilization.

Dilution System. The dilution system consists of a series of eight variable-geometry ports situated around the outer annulus of the combustor. The port design is based on the translating plug and seat arrangement shown in Fig. 5. The dilution port assemblies function as the axial and radial locations for the combustor with the combustor forward end supported by three radial pins engaging slide blocks fastened to the combustor. The combustor support features are shown in Fig. 6 which is an outside view of the unit. No mechanism is provided for the dilution system area variation during a test run; instead, each of the dilution assemblies is adjusted prior to the beginning of each test. Accurate adjustment of the plug position can be guaranteed as the plug shaft is threaded into the outer casing housing.

Liner Cooling System. The inner and outer combustor liners are cooled by a combination of convective and film cooling techniques arrived at during preliminary investigations on the small-scale annular combustor. The bulk of the convective cooling air is admitted to the annulii at the forward end of the combustor. A portion is admitted through holes in the outer skins at intermediate stations along the combustor length as shown in Fig. 7.

Torch Igniter. A torch igniter is provided for light-off purposes. This is an independent unit which is isolated after ignition.

Combustor Design

The full-size design is the result of a combination of facility limitations and operational parameters selected as representative of aircraft annular combustion system practice.

The total pressure loss selected for the system is six percent with a reference velocity of 15.2 m/sec (50 ft/sec) at the cruise condition based on the outer diameter of the combustor. Combining these requirements with Solar's atmospheric

Downloaded 01 Jun 2010 to 171.66.16.62. Redistribution subject to ASME license or copyright; see http://www.asme.org/terms/Terms_Use.cfm

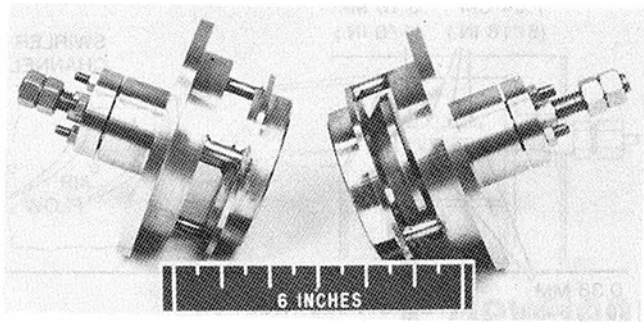


Fig. 5 Variable dilution port assembly

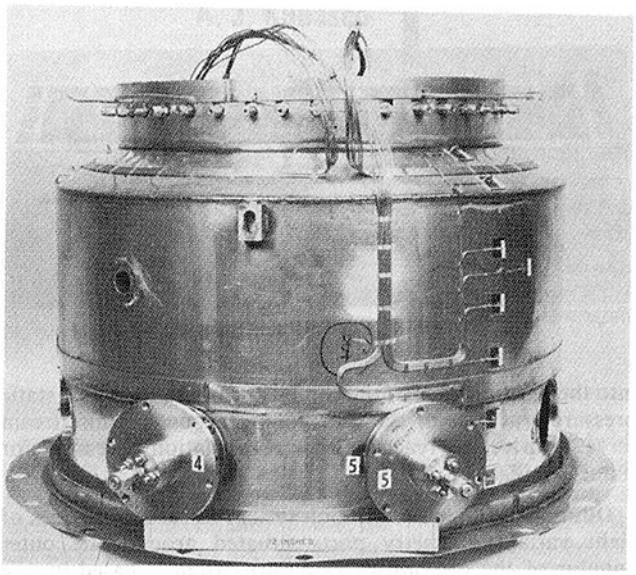


Fig. 6 VAB combustor - outside view

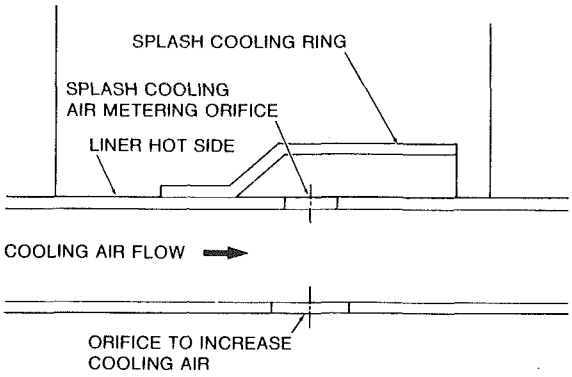


Fig. 7 Liner cooling scheme

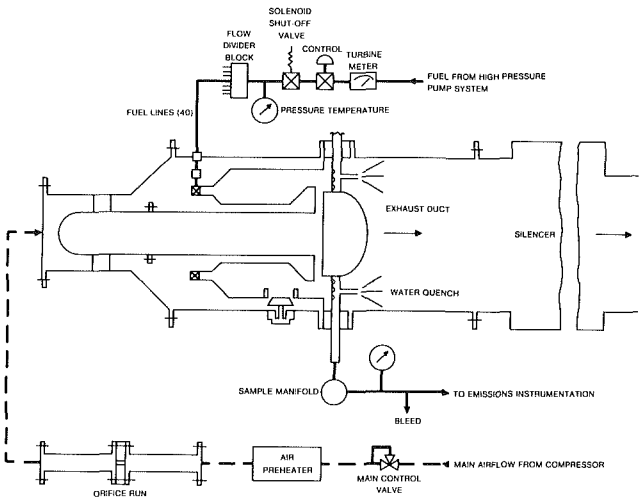


Fig. 8 Test facility schematic

facility air mass flow restrictions produces a combustor outer diameter of 0.66 m (26.0 in.).

The combustor swirler inlet is close coupled to the inlet casing annular delivery flow without the use of a conventional diffuser section. The inlet flow annulus represents the exit from a final axial compressor stage and operates with a Mach number of approximately 0.3.

The overall length of the unit is constrained to fit within an existing rig facility at NASA-Lewis Research Center where the high-pressure testing is planned.

Test Facility

A schematic of the atmospheric test rig facility is shown in Fig. 8. The main air mass flow is controlled before entering a gas-fired, indirect, air preheater that raises the temperature from ambient to the required temperature at the combustor inlet. The flow then passes through a pipe section that contains a sharp-edged orifice run for airflow metering purposes before entering the combustor inlet casing.

The exhaust from the combustor passes through an instrumentation section where, after emissions and temperature monitoring, the flow is quenched by direct water injection and exhausts to atmosphere through a silencer. The instrumentation section is shown in Fig. 9.

A photograph of the atmospheric test facility is shown in Fig. 10.

Test Procedure

The test procedure adopted during the investigations was to establish the required levels of combustor inlet temperature and air mass flow. After ignition the fuel flow to the combustor was modulated to give combustor outlet temperatures ranging from the lean stability limit of the system, where the CO and UHC readings increase rapidly to the design level. Several data points were generally obtained between these two limits.

The emissions results represented in the body of this paper are based on the exhaust gas analyses and the test fuel characteristics. The combustor outlet temperature displayed is computed from measured inlet temperatures and an ideal temperature rise, including dissociation, computed from the fuel/air ratio obtained, in turn, from the exhaust analysis carbon the design point down to a value just in excess of balance using the calculation techniques of SAE ARP 1256 [3]. The direct measurements of air and fuel flow to the combustor were utilized as a check on the gas sampling accuracy. The fuel/air ratio calculated from the exhaust analysis agreed to within ±5.0 percent with that obtained from the direct measurements.

The NOx emission indices depicted were corrected to a zero inlet-air humidity condition using a correlation developed by Marchionna [4]. The correction factors were generally less than 5 percent as a result of the normally low humidity conditions of the air supplied to the rig.

Test Conditions and Performance Goals

The combustor was characterized by testing at two discrete operating points, namely, cruise and idle.

The simulated cruise test point conditions and emissions

Downloaded 01 Jun 2010 to 171.66.16.62. Redistribution subject to ASME license or copyright; see http://www.asme.org/terms/Terms_Use.cfm

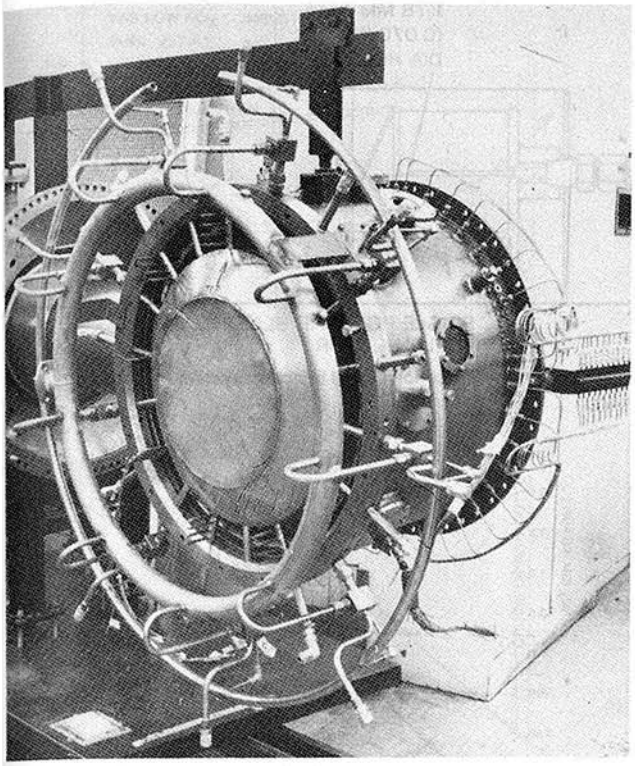


Fig. 9 Instrumentation section

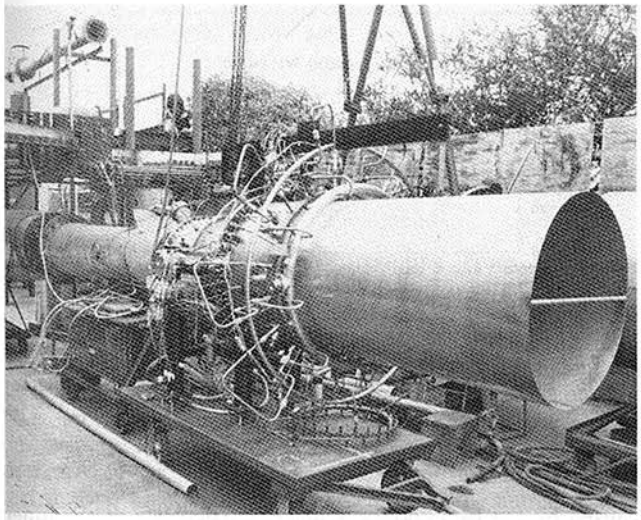


Fig. 10 Atmospheric test facility

goals for Jet-A1 fuel are shown in Table 1. The corresponding idle test point conditions and emissions goals are shown in Table 2.

Test Results and Discussion

Several previous studies and experimental programs conducted on lean premixed combustion systems [5–8] have identified the specific design features that are important in achieving minimum NOx levels. The test program strategy adopted with the full-size annular combustor was to evaluate the emissions characteristics of a baseline configuration and then to evaluate the sensitivity of the emissions signatures to variations in the key design features with the objective of defining the optimum configuration for eventual high pressure testing.

Table 1 Test conditions and emissions goals - cruise

Test conditions	Emissions goals (g/kg fuel)
P_{in} = 1 atm T_{in} = 833 K (1500 R) T_{out} = 1778 K (3200 R)	NOx – 1.0 CO – 1.0 UHC – 0.5 Smoke – 15 SAE

Table 2 Test conditions and emissions goals - idle

Test conditions	Emissions goals (g/kg fuel)
P_{in} = 1 atm T_{in} = 422 K (760 R) T_{out} = 917 K (1650 R)	CO – 20.0 UHC – 4.0

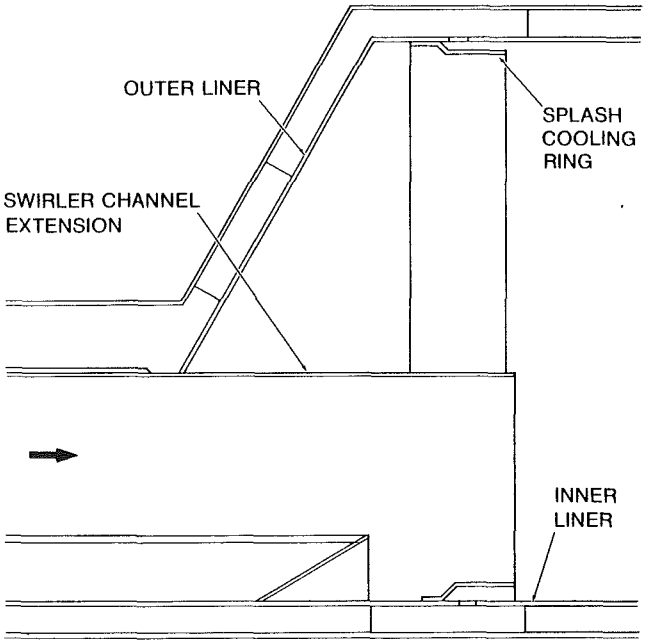


Fig. 11 Baseline swirler channel extension

The initial or baseline configuration of the full-size combustor for both cruise and idle conditions is summarized briefly below:

Fuel Injection. Fuel was injected slightly upstream of the swirler throat in each of the forty channels through the radial fuel rake shown in Figure 3. The fuel injection orifices were orientated such that the initial angle of fuel injection was along the channel mean flow line.

Swirler Channel Extension. Figure 11 shows the swirler channel extension at its original length of 8.9 cm (3.50 in.).

Inlet Casing. Figure 1 shows the initial configuration with the inlet casing in position. With this casing in place the incoming air was constrained to flow within an annulus with a sudden expansion section upstream of the swirler inlet.

Baseline Emission Characteristics.

Idle Conditions. Baseline emissions characteristics at idle conditions are presented in Fig. 12. The data indicate that both CO and UHC levels are well above the program goals noted in Table 2.

Downloaded 01 Jun 2010 to 171.66.16.62. Redistribution subject to ASME license or copyright; see http://www.asme.org/terms/Terms_Use.cfm

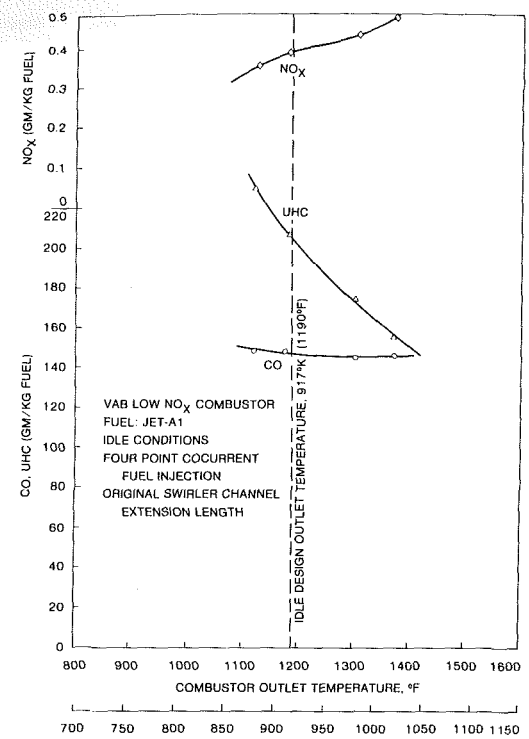


Fig. 12 Idle conditions with original combustor configuration

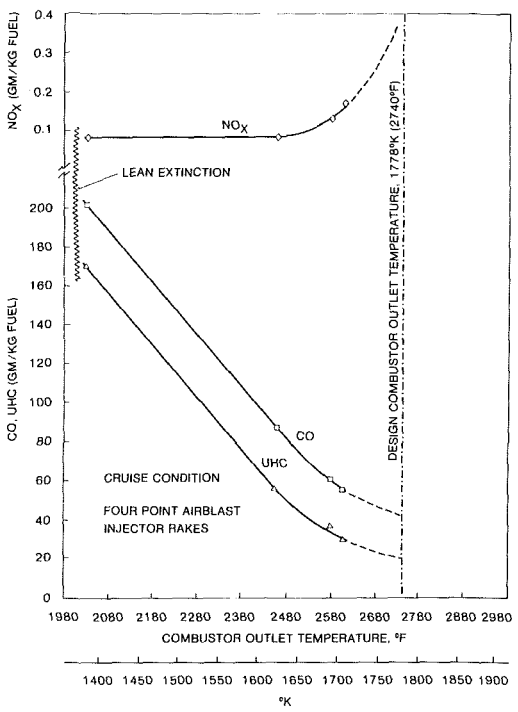


Fig. 13 Emissions characteristics - four point airblast fuel injector rakes

Cruise Conditions. The cruise baseline emissions characteristics are presented in Fig. 13. These results show that the combustor is operating with NOx levels within the 1.0 gm NO_2/kg fuel at design conditions but with CO and UHC levels much in excess of the program goals. Possible explanations for these excessive CO and UHC levels include insufficient reaction zone volume and local quenching effects

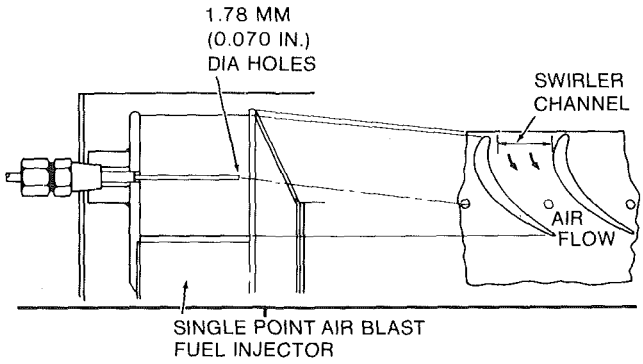


Fig. 14 Modification of fuel injection system - single point

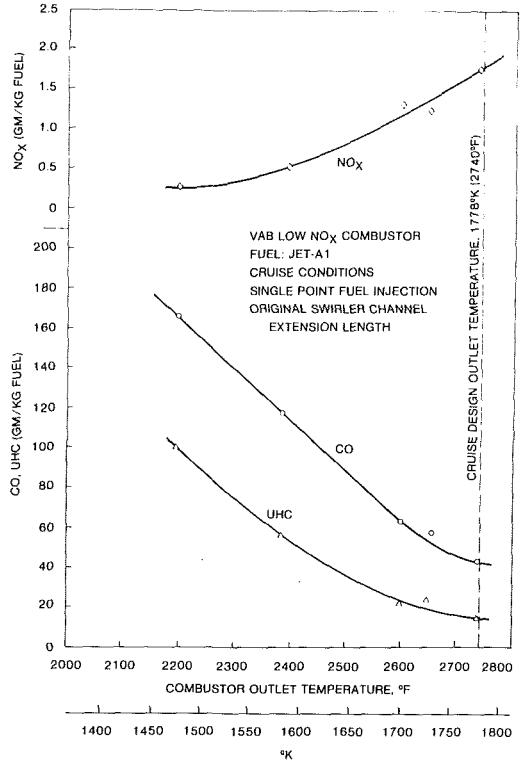


Fig. 15 Emissions characteristics - single point airblast fuel injector rakes

caused by the film cooling scheme, particularly at the inner liner where, at the forward end, the cooling air is admitted in a direction opposite to that of the local recirculation flow.

Effects of Fuel Injection Techniques. During the test program, four different fuel injection techniques were evaluated, namely:

1. Four-point concurrent injection
2. Single-point injection
3. Four-point counterflow injection
4. Eight-point counterflow injection

As a demonstration of the effect of initial fuel distribution on the combustor NOx emissions, the four-point fuel injector rakes were replaced by a simple single-point system as shown in Fig. 14. The cruise emission results from the single-point fuel injectors are shown in Fig. 15. Although no significant changes in the CO and UHC levels occurred the design point NOx increased significantly as would be expected from the

Downloaded 01 Jun 2010 to 171.66.16.62. Redistribution subject to ASME license or copyright; see http://www.asme.org/terms/Terms_Use.cfm

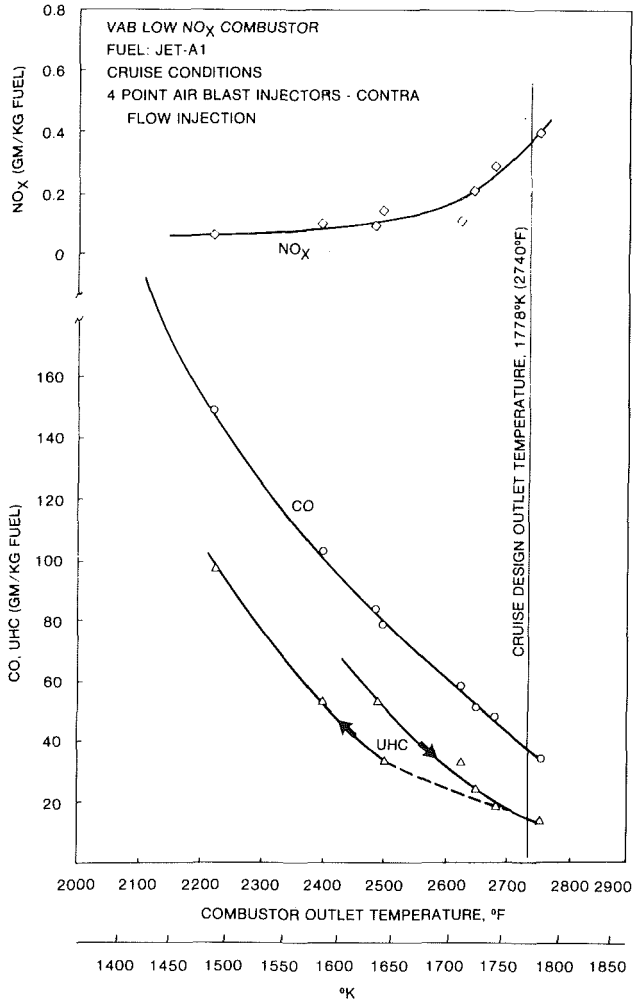


Fig. 16 Four point counterflow fuel injection

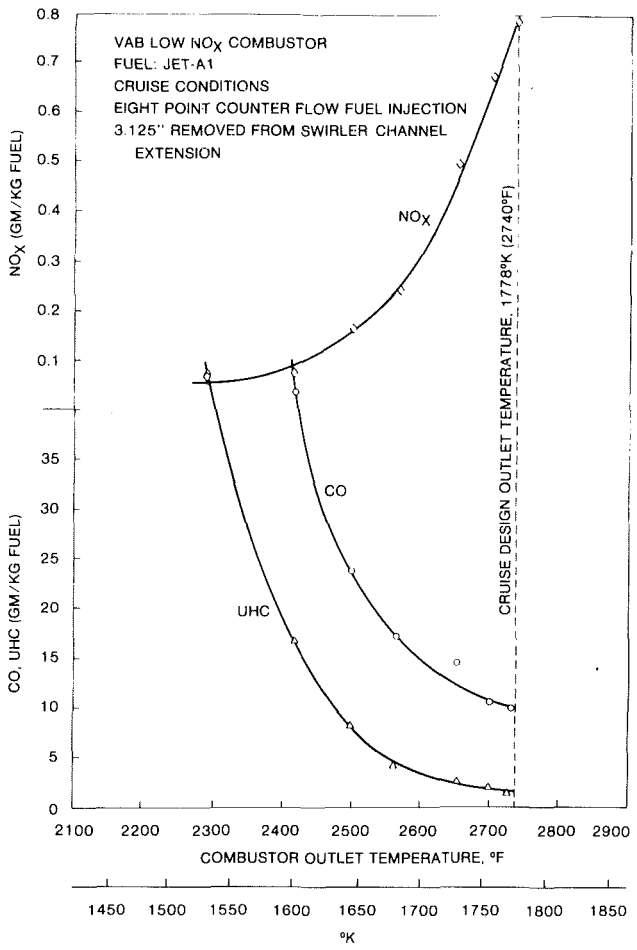


Fig. 17 Eight point counterflow fuel injection

reduced degree of premixing resulting from this configuration.

By rotating the four-point rakes 180 degrees, they were arranged to inject the fuel upstream into the reaction airflow. The emissions results are shown in Fig. 16 where, again, no significant changes occurred to the unburnt emissions but the NOx emissions dropped approximately 20 percent at the design point. Counterflow fuel injection therefore results in decreased NOx levels due to an improved initial fuel distribution which more closely resembles a line source.

The final fuel injection system modification consisted of removing the four-point counterflow rakes and replacing them with eight-point counterflow rakes. The effects of this improvement in initial fuel distribution were small and are shown in Figs. 17 and 18, representing the results of the cruise and idle test points, respectively. This final fuel injection system modification was performed with a reduced swirler channel length, the effects of which are discussed in a subsequent section.

The effects of the various fuel injection system modifications are summarized in Table 3.

Table 3 Effect of fuel injection mode: cruise test point

	Emissions at design combustor outlet temperature (grams/kg Fuel)		
	NOx	CO	UHC
Four point concurrent	0.43	41	20
Single point	1.80	43	16
Four point counterflow	0.36	39	14
Four point counterflow with reduced swirler channel length	0.67	10	2
Eight point counterflow with reduced swirler channel length	0.84	10	2

Inlet Flow Mismatch. The effects of the close-coupled compressor delivery flow and swirler inlet were evaluated by removing a portion of the casing as shown in Fig. 19. This modification was intended to reduce the jetting into the swirler inlet and obviate any swirler separation that might be occurring. The cruise emissions results are shown in Fig. 20 where it can be seen that the NOx emissions were reduced from 0.36 gm/kg fuel to 0.2 gm/kg fuel. No changes to the unburnt levels were seen.

Effect of Swirler Channel Length. As part of the original test plan it was indicated that the swirler channel extension length would be reduced to determine the effect on the combustion characteristics. This was accomplished in two stages; 5.7 cm (2.25 in.) was removed for the first test and an additional 2.2 cm (0.875 in.) was removed for the second test, as shown in Fig. 21. A summary of the emissions obtained at the cruise design point for these tests is shown in Fig. 22. The reduction in the swirler channel extension length contributed

Downloaded 01 Jun 2010 to 171.66.16.62. Redistribution subject to ASME license or copyright; see http://www.asme.org/terms/Terms_Use.cfm

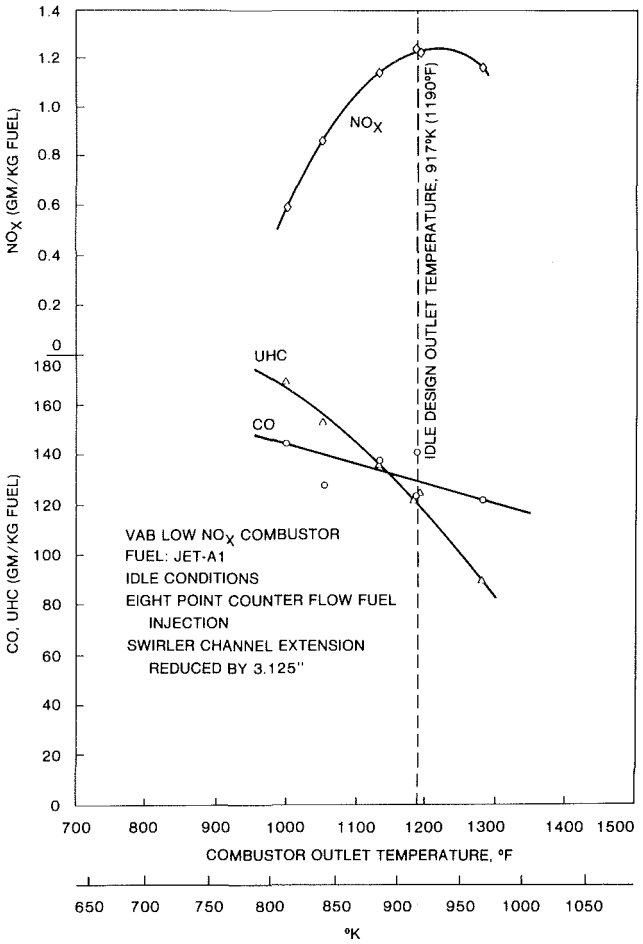


Fig. 18 Idle conditions with eight point counterflow fuel injection and short swirler channel extension

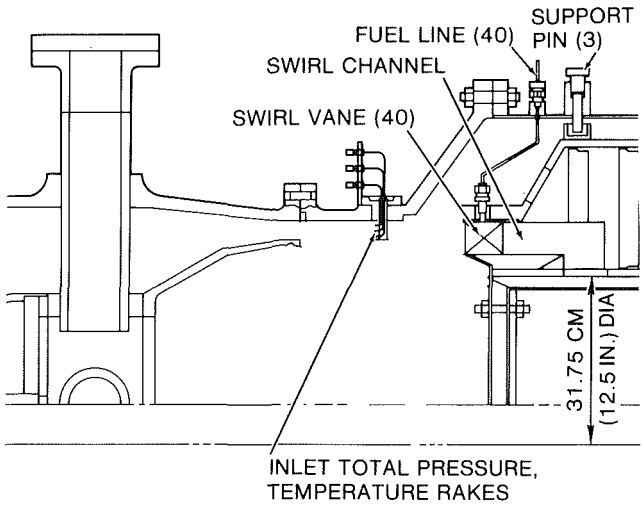


Fig. 19 Inlet casing modification

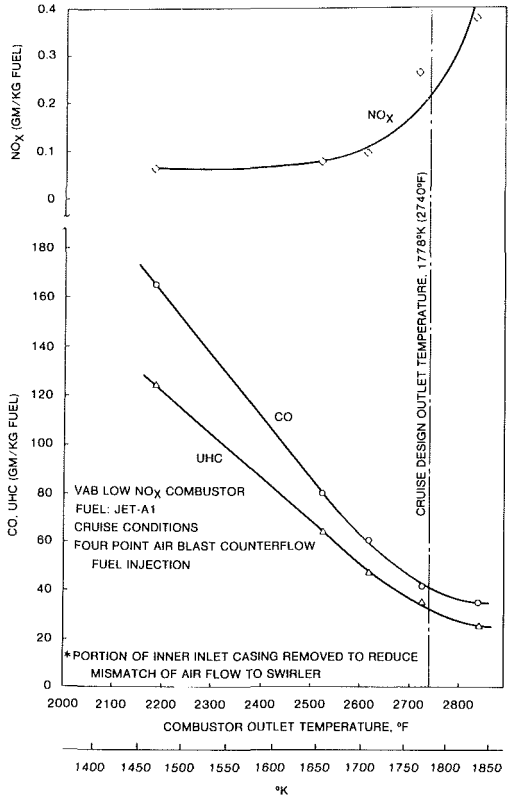


Fig. 20 Elimination of air flow mismatch

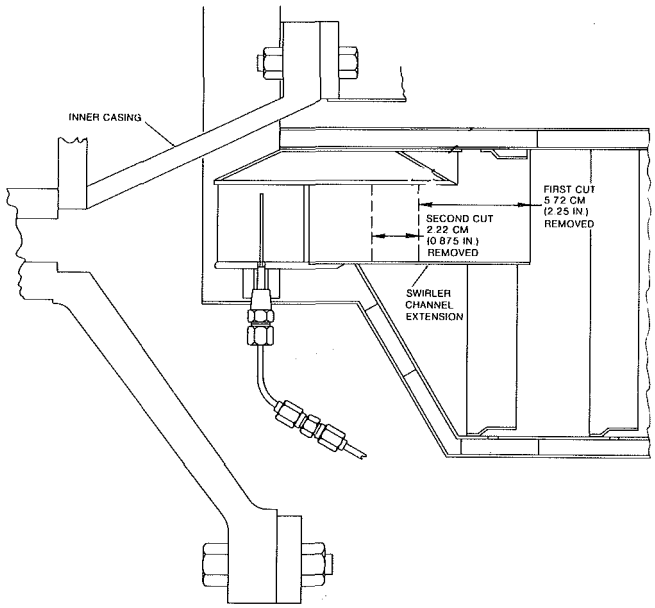


Fig. 21 Detail of swirler channel extension

significantly to a reduction in CO and UHC emissions. It had, however, the opposite effect on the NOx emissions.

These effects are probably due to the increase in effective combustor volume that occurs as the swirler channel extension is cut back. The increased residence times result in additional reaction of CO and UHC and higher NOx levels. In addition the reduced swirler channel length results in a reduced degree of premixing which also tends to increase NOx levels.

Although the overall length of the combustor was an original design constraint imposed by an existing facility, the effects on the emissions of a 30.5 cm (12 in.) reaction zone length increase were evaluated.

This residence time increase resulted in further CO and UHC decreases, to 1.8 and 0.2 gm/kg fuel respectively,

Downloaded 01 Jun 2010 to 171.66.16.62. Redistribution subject to ASME license or copyright; see http://www.asme.org/terms/Terms_Use.cfm

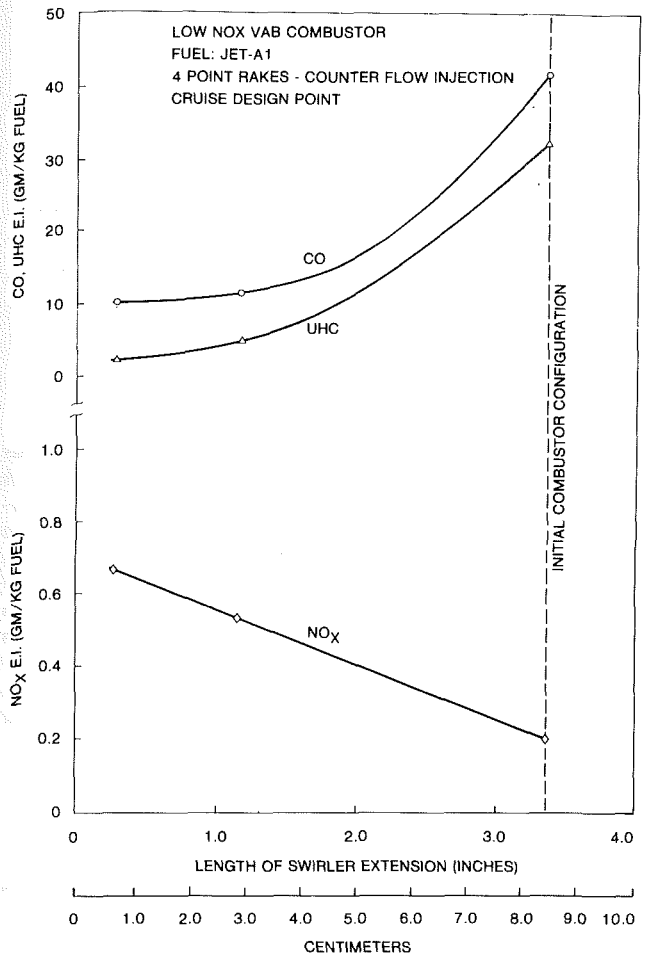


Fig. 22 Reduction of length of swirler channel extension

together with a corresponding increase in NOx to 1.4 gm NO_2/kg fuel.

Concluding Remarks

The lean premixed VAB combustor in full-size axisymmetric annular form has demonstrated the capability of operating at a reduced-pressure, simulated high-altitude, supersonic cruise condition with NOx emissions below 1.0 gm/kg fuel.

The CO and UHC emission goals were exceeded at the cruise condition but could be closely approached by increasing the reaction zone length in excess of the original design constraint.

Future high pressure testing of the combustor will reveal the effect of pressure on the NOx emissions and the sensitivity of the design to autoignition. Solar's previous investigations suggest that the effect of pressure on the NOx emissions of the VAB combustor can be expected to be minimal. Some support for this position can be found in the work of Roffe [9].

Although the idle emission goals for CO and UHC were not met, flow test results show that this was mainly due to an aerodynamic deficiency in the design of the inlet flow casing match to the combustor. This resulted in a reduced flow to the dilution port system and a leaner idle reaction zone equivalence ratio.

The testing shows that for the full range of low emissions operation, from idle to cruise, a variable dilution port system is necessary, but that fuel-switching can be avoided and a single fuel injection system used.

Acknowledgments

The research and development program described within this paper was conducted by the Research Department of Solar Turbines Inc. under a contract from NASA-Lewis Research Center. Nick J. Sekas of the Aero-Thermodynamics and Fuels Division, NASA-Lewis Research Center, was Project Manager.

References

1 Roberts, P. B., et al., "Advanced Low NOx Combustors for Supersonic High-Altitude Aircraft Gas Turbine." 1976 ASME Gas Turbine and Fluids Engineering Conference (Paper No. 76-GT-12).

2 Roberts, P. B., et al., "Wide Range Operation of Advanced Low NOx Aircraft Gas Turbine Combustors." 1978 ASME Gas Turbine Conference (Paper No. 78-GT-128).

3 "Procedure for the Continuous Sampling and Measurement of Gaseous Emissions from Aircraft Turbine Engines," SAE Aerospace Recommended Practice, ARP 1256, 1971.

4 Marchionna, N. R., "Effect of Inlet-Air Humidity on the Formation of Oxides of Nitrogen in a Gas Turbine Combustor," NASA TMX-68209, NASA Lewis Research Center, 1973.

5 Mularz, E. J., "Lean, Premixed, Prevaporized Combustion for Aircraft Gas Turbine Engines," NASA TM 79148, June 1979.

6 Roffe, G., and Ferri, A., "Effect of Premixing Quality on Oxides of Nitrogen on Gas Turbine Combustors," NASA CR-2657, Feb. 1976.

7 Cooper, L., "Effect of Degree of Vaporization Open Emissions for a Premixed, Prevaporized Combustion System," Premixed Prevaporized Combustor Technology Forum held at NASA-Lewis Research Center on Jan. 9-10, 1979, CP-2078.

8 Dickan, R. A., Dodds, W. J., and Ekstedt, E. E., "Lean, Premixed Prevaporized (LPP) Combustor Conceptual Design Study," NASA CR-159629.

9 Roffe, G., and Venkatoramani, K. S., "Emission Measurements for a Lean, Premixed Propane/Air System at Pressures up to 30 Atmospheres," NASA CR-159421.

Downloaded 01 Jun 2010 to 171.66.16.62. Redistribution subject to ASME license or copyright; see http://www.asme.org/terms/Terms_Use.cfm

Premixing and Flash Vaporization in a Two-Stage Combustor

B.G.A. Sjöblom
R&D Combustion Engineer.
Volvo Flygmotor AB,
Trollhattan, Sweden
Mem. ASME

A double recirculation zone two-stage combustor fitted with airblast atomizers has been investigated in a previous work. The present paper describes further tests with premixing tubes in the secondary combustion zone. Flash vaporization was employed to ensure complete vaporization of the secondary fuel, which was heated to 600K by the combustor inlet air. The combustor was run at conditions corresponding to four different engine power settings, and the effect of primary/secondary fuel flow split on emissions was investigated. Tests were also performed with unheated secondary fuel, and comparisons were made with flash vaporization data. The best configuration reduced the oxides of nitrogen by 54 percent, carbon monoxide by 59 percent and unburned hydrocarbons by 97 percent as compared to emission levels for the standard JT8D combustor, which was used as a reference.

Introduction

The concern about potential environmental effects caused by gas turbine exhaust emissions has led the U.S. Environmental Protection Agency (EPA) to issue emission standards for aircraft engines. These standards require quite new combustor concepts to be developed, and a number of research programs have been undertaken in the U.S. as well as in other countries to demonstrate low emission combustor technology. One major effort is the work being done by or under the sponsorship of the NASA-Lewis Research Center [1].

As a part of the combustor research activities at Volvo Flygmotor, a two-stage low emission combustor fitted with airblast atomizers has been investigated [2]. A simultaneous reduction of all emissions was achieved in comparison to a reference combustor. In this work, Pratt & Whitney's JT8D combustor was used as a reference. Information is available in the literature for this combustor, and data from [3] have been used for comparisons. The tested combustor was also manufactured by modifying a JT8D combustor.

The most difficult emission to minimize is considered to be the NO_x [1]. Uniformity of the fuel-air mixture is essential in order to avoid locally high fuel/air ratios, which burn at elevated flame temperatures and produce high NO_x emissions. Achieving uniformity of the fuel-air mixture is very difficult as long as the fuel exists as drops, which is the case when airblast atomizers are being employed. Therefore, premixing tubes were introduced to the secondary zone in an attempt to improve the uniformity. This requires not only good mixing of fuel and air but also a fully vaporized fuel. One effective approach is to use so-called flash vaporization, which has been discussed in [4, 5], and [6]. Flash vaporization as well as injection of cold secondary fuel into the premixing tubes were studied.

The present work is mainly concentrated on emissions, but it is recognized that exit temperature pattern factor, relight capability, durability, and operational safety are important factors. Although it is known that the EPA goals are subject to changes, the original 1979 goals as given in [3] have been used for comparisons in this paper.

The Double Recirculation Zone Combustor

A possible concept to meet the emission requirements is the staged combustor consisting of a primary (pilot) and a secondary (main) zone. The primary zone would be designed specifically to minimize the low-power emissions CO and HC. At the high-power operating conditions, the primary zone serves as a hot gas source to stabilize efficient combustion in the secondary stage, which would be designed to minimize NO_x and smoke emissions.

The approach for two-stage combustion presented in [2] is shown in Fig. 1. An air-cooled "zone-divider" was installed in a standard combustor. Flame tube holes were rearranged in such a way that two recirculation zones were formed – one upstream and one downstream of the "zone-divider". Fuel is fed separately to each zone through the air holes by means of airblast atomizers. Figure 1 gives the airflow distribution. About 25 percent of the total airflow is used for film-cooling and 3 percent is used to cool the "zone-divider" internally. The "zone-divider" is also cooled by the impinging jets from the primary air holes.

A flow study was performed in a water tunnel. Visualization of the flow pattern was achieved by means of water flow in a transparent model. Although such tests do not reproduce actual combustion conditions, they have proven to be very useful when studying general flow pattern, fuel distribution, and pressure losses. The general flow pattern is studied by introducing small air bubbles into the water flow. A stable flow without any undesirable flow separations is

Contributed by the Gas Turbine Division and presented at the International Gas Turbine Conference and Products Show, Houston, Texas, March 9-12, 1981, of THE AMERICAN SOCIETY OF MECHANICAL ENGINEERS. Manuscript received at ASME Headquarters, December 3, 1980. Paper No. 81-GT-41.

Copyright © 1982 by ASME

Downloaded 01 Jun 2010 to 171.66.16.62. Redistribution subject to ASME license or copyright; see http://www.asme.org/terms/Terms_Use.cfm

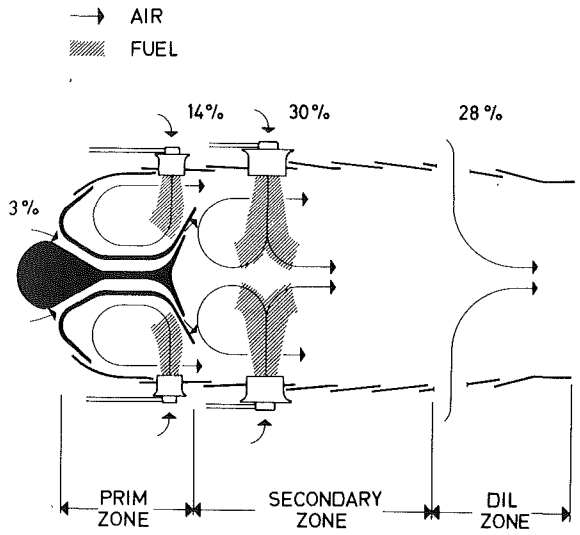


Fig. 1 Two-stage combustor concept

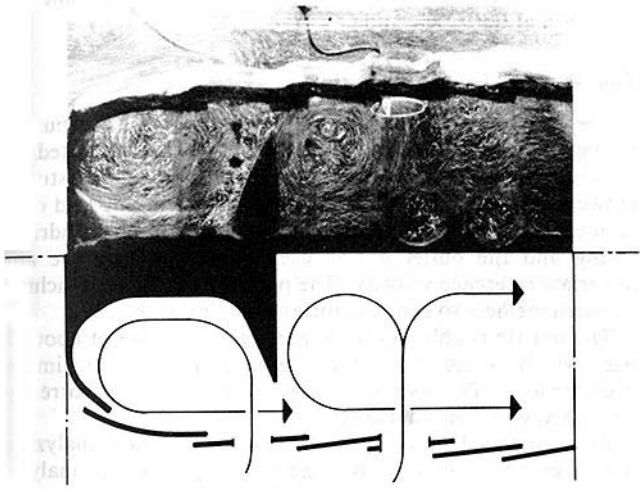


Fig. 2 General flow pattern

considered to be the basis for a successful combustor. The flow pattern of the double recirculation zone combustor is shown in Fig. 2. By proper location of air holes, it was possible to achieve two very stable recirculating zones. There are six primary air holes staggered in relation to the six secondary air holes. Each of these twelve holes are fitted with airblast atomizers. There are also six dilution air holes located downstream and in line with the secondary holes.

The airblast atomizer is shown in Fig. 3. The fuel is evenly distributed on a cylindrical surface, and the atomization is provided by air flowing on both sides of the thin fuel film. This concept gives good fuel-air mixing, which is considered to be good for reducing all emissions.

Premixing and Flash Vaporization

In order to ensure even better fuel-air mixing and hence a better degree of uniformity, the present study has been directed toward the use of premixing tubes. This was done in order to minimize the high power NO_x emissions. Since most fuel generally would be fed to the secondary zone in a two-stage combustor at high-power conditions, the use of premixing tubes was limited to this zone. However, it was found during the tests that there are cases where a large fraction of primary fuel flow can be advantageous.

The new configuration of the double recirculation zone combustor is shown in Fig. 4. The primary fuel is still fed to

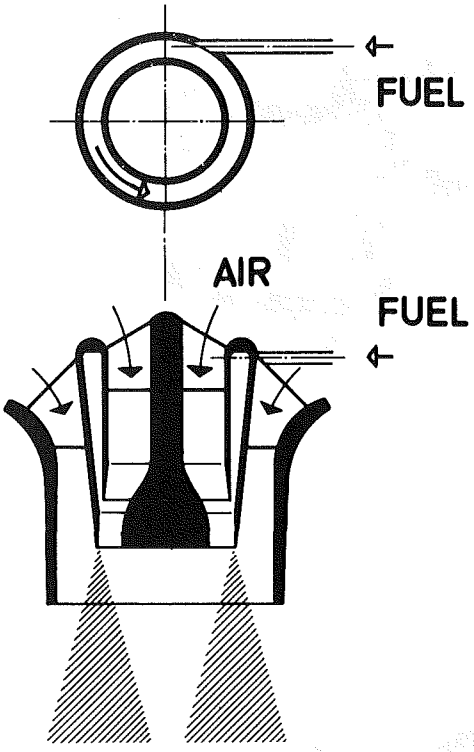


Fig. 3 Airblast atomizer

the combustor through airblast atomizers. The secondary fuel is fed to the premixing tubes through the injection arrangement shown in Fig. 5. This arrangement was designed to provide a certain predistribution prior to the mixing process by injecting the fuel at several different locations. A suitable length of the premixing tube was determined from a flow test. Colored water, simulating the vaporized fuel, was injected into a transparent model of the premixing tube where water was flowing to simulate the secondary air. The length required for complete mixing was determined subjectively, and it was found to be equivalent to a residence time of 2.2 ms.

Flash vaporization was employed since fuel-air uniformity not only requires good mixing, but also a completely vaporized fuel. By preheating the fuel under pressure and above the dewpoint temperature, vaporization can be avoided within the fuel system, but an instantaneous vaporization will be obtained as soon as the fuel leaves the nozzle [6]. The residence time of 2.2 ms would therefore be sufficient for both mixing and vaporization. The fuel was heated to 600 K which is well above the dewpoint temperature, but also below the temperature at which the fuel will start to crack. It was also decided to check whether or not cold secondary fuel would give the same results as the flash vaporization test data, since preheating of fuel results in a considerable increase in combustion system complexity. In this case, the vaporization process had to rely on the heat provided by the combustor inlet air flowing in the premixing tubes. Complete vaporization is then attainable, if the fuel droplets are small enough. It can be noted that the premixing tube is fitted with vanes in the bend upstream of the tube discharge. This is necessary in order to establish a stable secondary recirculation zone, but also advantageous for the fuel injection. The part of the fuel that has not been vaporized in the premixing tube will be distributed on the vanes, which then will act as airblast atomizers.

It is recognized that auto-ignition of the fuel might occur in the premixing tubes. The auto-ignition delay time is a strong function of the pressure level as well as the air temperature [7]. The actual combustor maximum pressure level is 17.6 bar,

Downloaded 01 Jun 2010 to 171.66.16.62. Redistribution subject to ASME license or copyright; see http://www.asme.org/terms/Terms_Use.cfm

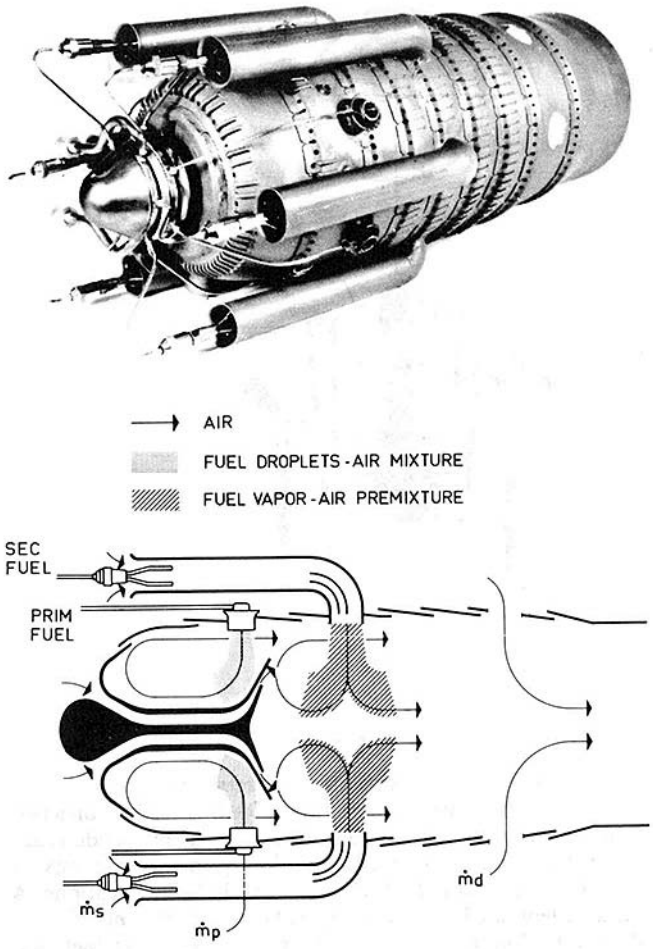


Fig. 4 Two-stage combustor with premixing tubes

which together with the corresponding inlet temperature would give a safety factor less than an order of magnitude with respect to auto-ignition. There will be a potential risk for auto-ignition. However, during the testing, the pressure level was limited to about 7 bar because of test rig limitations. In this case, an acceptable safety factor greater than an order of magnitude is obtained. Consequently, no auto-ignition was anticipated during the tests.

Combustor Configurations

Data are presented in this paper for both the original configuration of Fig. 1 (= Configuration A) as well as for the new premixed secondary configuration shown in Fig. 4 (= Configuration B).

It was found theoretically [2] that much of the NO_x produced by Configuration A was due to the situation in the primary zone, since this zone was approaching stoichiometric conditions. This was also verified experimentally in this work. In order to achieve an overall reduction of NO_x at full-power condition, the contribution of the primary zone was decreased by decreasing the primary zone air flow and fuel flow. This was done in two steps, resulting in Configuration B1 and Configuration B2. The total airflow to the combustion zone, i.e. the combined primary zone and the secondary zone, was kept the same in Configuration B1 as in Configuration A. However, the combustion zone airflow in Configuration B2 was decreased slightly in order to improve the high-power combustion efficiency. A summary of the air flows for the

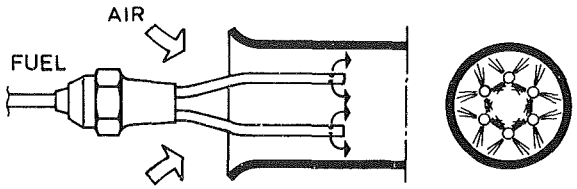


Fig. 5 Secondary fuel injector

three configurations is given in Table 1. This table also gives the primary zone equivalence ratio at idle. Since primary zone airflow has been decreased, it is obvious that the primary zone equivalence ratio at idle (as well as at other conditions) must increase. Equivalence ratios greater than unity will follow. Therefore, a certain fraction of the fuel cannot be burned in the primary zone, and there will also be an excessive CO production due to the high equivalence ratio. If this CO is not completely burned in the secondary zone, which is relatively "cool" at idle, a net increase in CO concentration at combustor outlet can be expected. In fact, this did occur to some extent showing the difficulty of achieving a simultaneous reduction of both NO_x and CO.

Test Rig and Instrumentation

The reference combustor is a can-annular combustor having nine flame tubes. Similar to the tests reported in reference [3], only one flame tube was used in this study. However, it was installed in a cylindrical casing instead of a segment of an annular casing. The diameters of the cylindrical casing and the outlet nozzle were chosen to give the appropriate reference velocity. The present tests did not include any arrangement to simulate turbine cooling air bleed.

The test rig is able to give a maximum pressure of about 7 bar, which is less than the engine combustor maximum pressure level. The combustor inlet temperature was correctly simulated with nonvitiated air.

Recommended procedures were followed when analyzing the gases and evaluating the test data [8]. The gas analysis equipment consisted of a chemiluminescence analyzer for measurement of NO_x, two nondispersive infrared instruments for CO and CO_2 and a flame ionization detector for HC. Smoke was measured by a Von Brand Smoke Meter. Combustion air humidity was measured before the start of a test. Combustor exit gas samples were withdrawn through an integrating fixed rake having six orifices and were then transported to the instruments through a heated line. Exhaust gas sample validity was checked during the tests by comparing calculated carbon balance fuel/air ratio values with metered values.

A special heating system was designed for the secondary fuel as shown in Fig. 6. The heat required to raise the fuel temperature was taken from the incoming combustion air by means of a heat exchanger in the combustor inlet section. Provisions were also made to control the secondary fuel temperature. The arrangement was designed to allow different numbers of heat exchanger tubes to be installed. Furthermore, during the tests, the fuel temperature could be controlled to some extent by varying the fuel flow through the heat exchanger. Thus, valve A was used to vary the fuel temperature. The fraction of the fuel that was not fed to the secondary combustion zone via valve B was recirculated to the pump via a cooler. The pump itself was operated against a constant pressure level controlled by a bypass valve.

Test Conditions and Data Evaluation

The present two-stage combustor was tested at the same conditions as the standard JT8D reference combustor. Test

Downloaded 01 Jun 2010 to 171.66.16.62. Redistribution subject to ASME license or copyright; see http://www.asme.org/terms/Terms_Use.cfm

Table 1 Airflow Distribution

Configuration	Primary Air (Percent)	Secondary Air (Percent)	Dilution Air (Percent)	$(\phi)_{p\ Idle}$
A	14	30	28	1.0
B1	11	33	28	1.3
B2	8	33	31	1.6

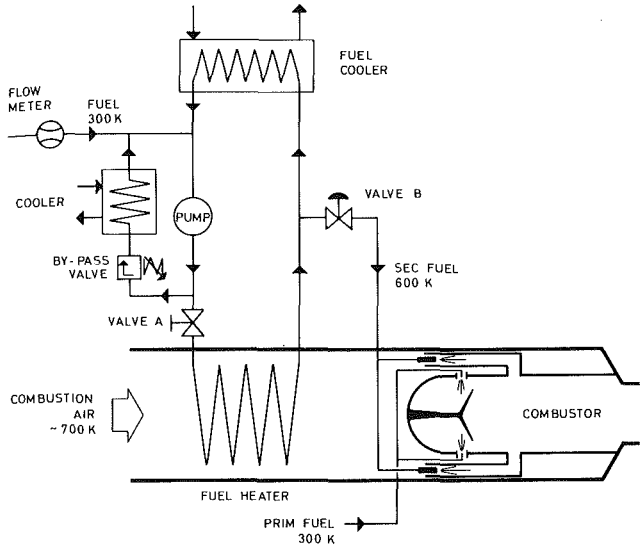


Fig. 6 Fuel heating system

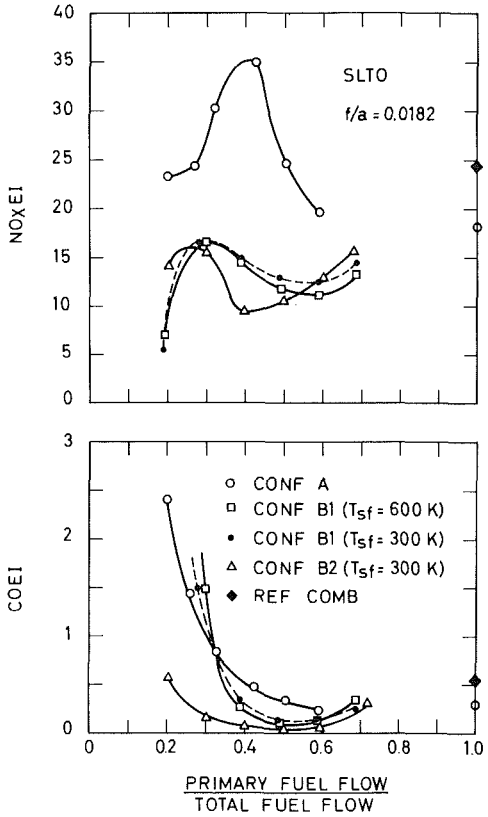


Fig. 7 Take-off emission data

conditions encountered in the actual engine are given in Table 2. Both idle and approach conditions were correctly simulated in the combustion test rig, while the rig pressure level was lower than the actual engine level at climb and take-off (SLTO) conditions. Fortunately, empirical correlation formulas are available that allow extrapolations from rig to engine conditions [9]:

$$NO_x EI \sim \frac{P_4^{0.5} T_5 \exp(T_4/288)}{U_{ref} \exp(0.0188H)} \quad (1)$$

$$COEI \sim 1/P_4 \quad (2)$$

$$HCEI \sim 1/P_4 \quad (3)$$

where:

EI = Emission index (g/kg fuel)
P_4 = Inlet total pressure (bar)
T_4 = Inlet total temperature (K)
U_{ref} = Reference velocity (m/s)
H = Inlet air humidity (g water/kg dry air)
T_5 = Combustor exit temperature (K)

All figures utilize the extrapolated engine values with H_{eng} = 6.3 g water /kg dry air. The measured air humidity that existed when the NO_x data were taken was $H_{meas} \approx 2$ g water/kg dry air.

The effect of inlet air cooling due to heat extraction was also taken into account. During the tests, the inlet air temperature was reduced in comparison to the data given in Table 2 in a degree that corresponded to the heat absorbed by the secondary fuel. The inlet air temperature correction was small – in most cases close to 10K.

The U.S. emission regulations prescribe a maximum allowable value for the EPA emission parameter. This parameter is mainly a weighting of emission indices for a prescribed landing-take-off (LTO) cycle. The following equation derived for the JT8D engine, and utilizing engine extrapolation values, was used to calculate the EPA parameter [3]:

$$EPAP_i = 0.3366\,EI_{i\text{Idle}} + 0.1256\,EI_{i\text{Approach}} + 0.1969\,EI_{i\text{Climb}} + 0.0777\,EI_{i\text{SLTO}} \quad (4)$$

where:

EPAP = EPA parameter (lb_m pollutant/1000 lb_f thrust-hr/LTO cycle)
i = Emission category (NO_x, CO, HC)

Test Results

High-Power Operation. Emission data for take-off (SLTO) condition are given in Fig. 7 versus the fraction of primary fuel at a constant overall fuel/air ratio. Configuration A is the original design with airblast atomizers. This configuration produces emission levels that are in the same region as data for the reference combustor. However, when all the fuel was fed to the primary zone, a simultaneous reduction of all emissions was achieved. Unfortunately, this mode of fuel injection was accompanied by a high primary zone fuel/air equivalence ratio that might lead to excessive smoke formation.

A substantial reduction of all emissions was achieved when the premixing tubes were introduced. Configuration B1 was tested with both a high and a low secondary fuel temperature (T_{sf}). It was found that the use of cold secondary fuel (T_{sf} = 300K) gave essentially the same results as the flash

Downloaded 01 Jun 2010 to 171.66.16.62. Redistribution subject to ASME license or copyright; see http://www.asme.org/terms/Terms_Use.cfm

Table 2 Engine combustor conditions

Engine Mode	Total Inlet Pressure (bar)	Total Inlet Temperature (K)	Fuel-Air Ratio	Comments
Idle	2.91	412	0.0100	Correct simulation in test rig
Approach 30% Power	6.92	535	0.0112	Correct simulation in test rig
Climb 85% Power	15.30	678	0.0164	Test rig pressure ≈6.5 bar
SLTO 100% Power	17.60	714	0.0182	Test rig pressure ≈6.5 bar

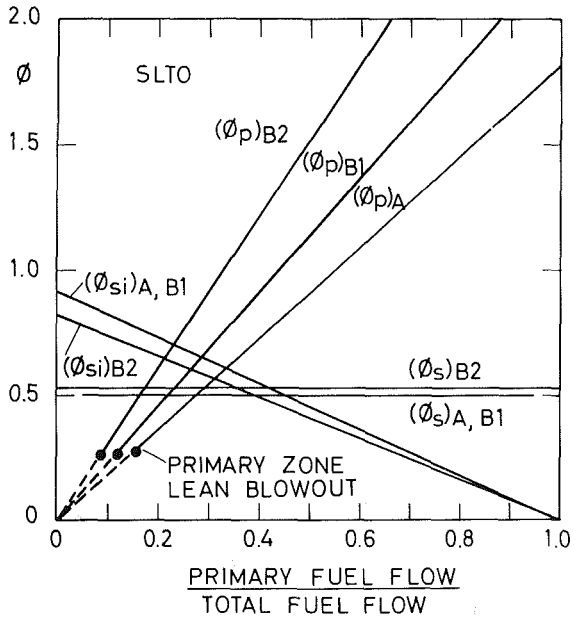


Fig. 8 Important equivalence ratios at take-off

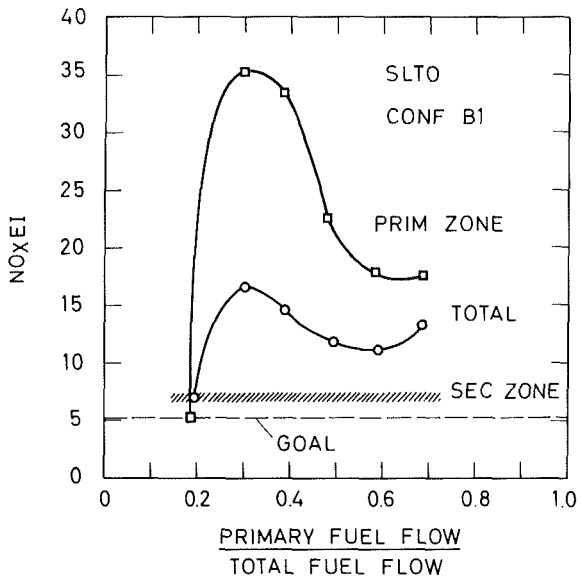


Fig. 9 NO_x formation split at take-off

vaporization data (T_{sf} = 600K). The differences are within the limits of experimental accuracy. Therefore, it can be concluded that the premixing arrangement used in this study is capable of producing the same good fuel-air preparation with cold fuel as can be expected for a more sophisticated system with flash vaporization. The results indicate that the 2.2 ms residence time in the premixing tube allows a major fraction of the fuel to be vaporized prior to injection into the secondary combustion zone. However, it is important to bear in mind that this is proved only at the tested pressure level of 7 bar. It must be recognized that auto-ignition can make it impossible to run at actual engine pressure level with a premixing tube residence time of 2.2 ms. In such a case, flash vaporization still has to be used in combination with a shorter premixing device. The final Configuration (B2) was run only with cold secondary fuel, and it gave a further slight reduction of the emission levels.

The percentage of primary fuel flow has a great impact on the emissions and there is, for example, a peak in the NO_x formation at a certain value. Figure 8 indicates how different zone equivalence ratios vary with the fraction of primary fuel flow. The primary zone equivalence ratio (ϕ_p), the overall secondary zone equivalence ratio (ϕ_s), and the equivalence ratio in the secondary premixing injection system (ϕ_{si}) are shown. By comparing Figs. 7 and 8, it is found for all three cases that the primary zone equivalence ratios are about 0.8 at the fuel flow split where maximum NO_x occurred. At primary fuel flows to the left of the peak, some very low NO_x values can be noticed. Unfortunately, there is also a tremendous increase in the CO production. The primary zone is operated even more lean at these conditions. However, if the situation to the right of the NO_x peak is considered it is found that a simultaneous reduction of all emissions is achieved. In this case the primary zone is operated slightly rich – $\phi_p \approx 1.25$. The impact of the primary zone on the total NO_x formation was demonstrated by running Configuration B1 with only primary fuel at the take-off condition. Figure 9 gives a comparison between these data and the corresponding "total" NO_x output as presented in Fig. 7 for T_{sf} = 600K. It can be seen that the NO_x production in the primary zone, as represented by an emission index, is much higher than the mean value obtained when running both zones. This confirms previous findings that the primary zone is most responsible for the total NO_x formation.

The total NO_x output is a weighting, based on the primary to secondary flow split, of primary zone emission index and secondary zone emission index. Therefore, it was also possible to back-calculate the emission index resulting from the secondary fuel combustion only. Figure 9 shows that this calculation gives a value that is quite low, and furthermore, is close to the goal value given in reference [3]. This indicates that the premixing arrangement for the secondary zone has performed well with respect to NO_x reduction. The HC concentration was virtually zero in most cases at take-off condition.

Figure 10 shows the emissions data obtained at the climb condition. Compared to the take-off condition, very similar results were obtained, although at different levels. However, in this case, the effect of decreasing the combustion zone air

Downloaded 01 Jun 2010 to 171.66.16.62. Redistribution subject to ASME license or copyright; see http://www.asme.org/terms/Terms_Use.cfm

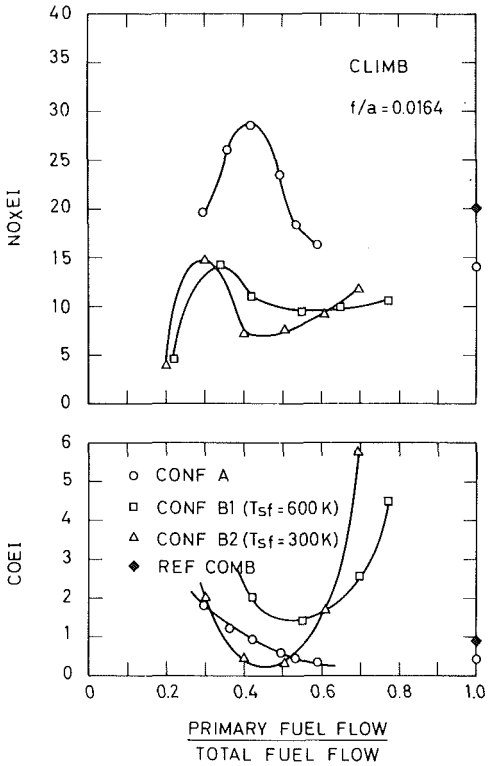


Fig. 10 Climb emission data

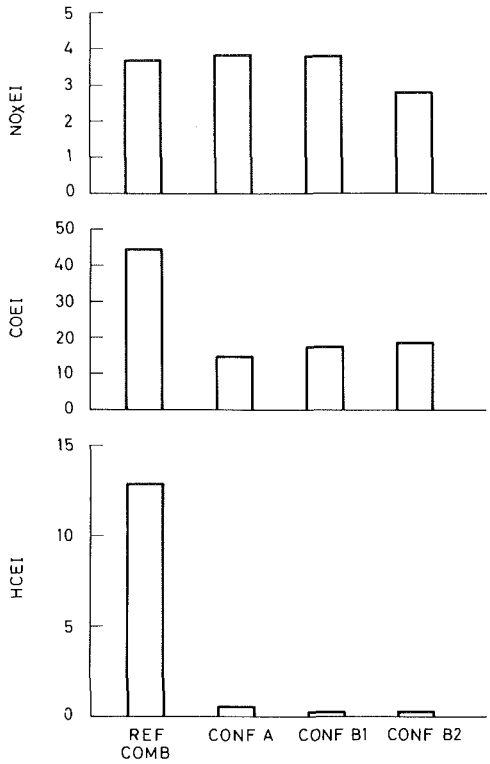


Fig. 12 Idle emission data ($f/a = 0.0100$)

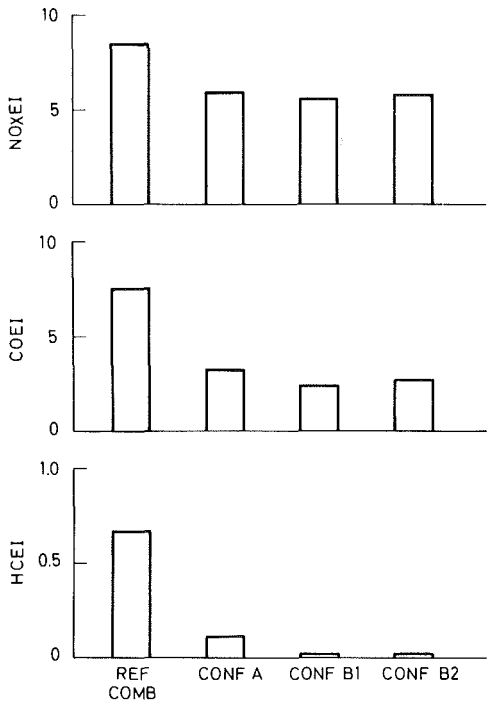


Fig. 11 Approach emission data ($f/a = 0.0112$)

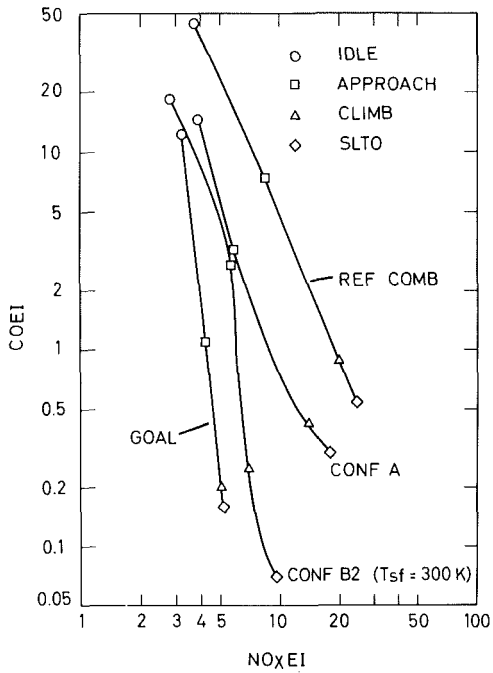


Fig. 13 CO-NO_x trade-off

flow is more obvious. There is a significant reduction in CO concentration when changing from Configuration B1 to Configuration B2. Furthermore, a simultaneous reduction in NO_x concentration was achieved. Here, too, the HC concentration was virtually zero in most cases.

Low-Power Operation. Emission data at $f/a = 0.0112$ for approach condition is given in Fig. 11. In this case, all the fuel was fed to the primary zone through the airblast atomizers. Consequently, the results for Configuration B1 and Configuration B2 are relatively similar to the results for Configuration A. The effect of increasing primary zone equivalence ratio, as shown for idle in Table 1, is reflected here to some extent by Configuration B2, since there is a slight increase in CO. However, the approach condition provides a hotter secondary zone for CO combustion than does the idle condition.

Downloaded 01 Jun 2010 to 171.66.16.62. Redistribution subject to ASME license or copyright; see http://www.asme.org/terms/Terms_Use.cfm

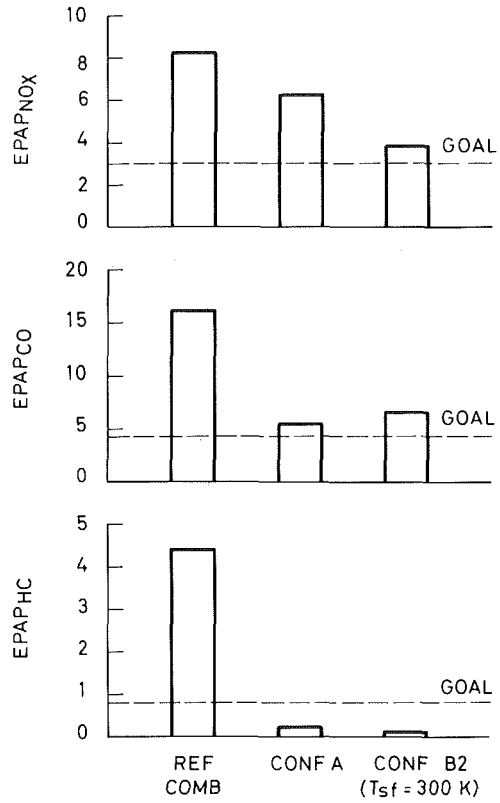


Fig. 14 LTO-cycle emission data

Idle emission data at $f/a = 0.010$ is given in Fig. 12. Similar to the approach condition, all the fuel was fed to the primary zone through the airblast atomizers. The effect of primary zone equivalence ratio according to Table 1 is more accentuated in this case. Configuration A, which operates with a stoichiometric primary zone, has decreased the CO concentration substantially in comparison to the reference combustor. As the equivalence ratio increases when changing from Configuration A to Configuration B1 and B2, the CO level is increased again, which tends to offset the gain in NO_x concentration that was demonstrated at take-off in Fig. 7 for these two latter configurations.

Technology Advancement. An indication of the technology advancement is obtained when plotting the CO-NO_x trade-off as shown in Fig. 13. Relative to the performance of the reference combustor, the emission regulations require a simultaneous decrease of both CO and NO_x, which is synonymous to a movement of the emission line towards the origin. The results for Configuration A, with all the fuel in the primary stage, as well as data for Configuration B2, with a 40- to 45-percent primary fuel flow and $T_{sf} = 300$K, shows that "true" improvements have been achieved in both cases since the CO-NO_x lines have been moved towards the goal line. This line is a combination of emissions output that would comply with the proposed EPA standard. Configuration B2 has produced a more substantial decrease in NO_x in comparison to Configuration A. This result is also reflected in Fig. 14, which gives the EPA parameters as calculated from equation (4). On the other hand, a slight increase in the CO value is obtained. Totally, it is found that NO_x has been decreased 54 percent, CO has been decreased 59 percent, and HC has been decreased 97 percent as compared to the reference combustor.

Smoke. Smoke was measured for Configuration B1 with 40 percent primary fuel and with hot secondary fuel at simulated take-off condition. The Smoke Number was found to be virtually zero. It is recognized that the measurement was performed at a reduced pressure level compared to engine conditions that might lead to dubious results. However, since the combustor is considered to be essentially free from local very fuel-rich zones, a low smoke combustion can also be anticipated at higher pressure levels.

Stability. The primary zone lean blowout limit was measured at idle condition. The overall lean limit was found to be $f/a = 0.0044$, 0.0033, and 0.0022 for Configuration A, Configuration B1, and Configuration B2, respectively. These values shall be compared with the reference combustor value of $f/a = 0.0030$. The trend in the values given above are such as would be expected from the primary zone equivalence ratios of Table 1.

Durability. The most critical part of the combustor concerning durability is the "zone-divider". It is located in the combustor in direct contact with both the primary and the secondary recirculation zones. During the major part of the test program, no problems were encountered. However, at certain high-power conditions with Configuration B2, local hot spots were obtained since this configuration provided a reduced impingement cooling due to decreased primary airflow.

Pressure Loss. The flame tube pressure loss was also measured. It was found to be equal to the pressure loss of the reference combustor.

Conclusions

A substantial reduction of all emissions was achieved when the secondary airblast atomizers were replaced with premixing tubes. Flash vaporization was employed to ensure completely vaporized fuel, and premixing tubes were used to ensure complete mixing between fuel and air prior to combustion. Tests were performed with both unheated and heated secondary fuel. It was found that the use of cold fuel gave essentially the same results as flash vaporization. This is advantageous since the heating of fuel results in a considerable increase in combustion system complexity. Furthermore, this result was obtained at a reduced pressure level as compared to the actual engine condition, which would reduce the risk for auto-ignition in the premixing tubes. At engine conditions, auto-ignition might occur due to the high pressure level and the long residence time in the premixing tubes. Therefore, these may have to be shortened, which might again make it necessary to use flash vaporization in order to achieve complete vaporization of the fuel.

The fraction of fuel used in the primary stage was found to have a great influence on the emissions. Very low NO_x values were obtained at low primary fuel flows. However, at these fuel-lean primary zone conditions, the combustor emitted large amounts of CO. At primary fuel flows in the region around 50 percent, another NO_x minima was found. The primary zone equivalence ratio was then about 1.25, and the CO concentration was at the same time very low. Thus, this mode of fuel injection gave the desired simultaneous reduction of both NO_x and CO. Furthermore the equivalence ratio was low enough to allow a smoke-free combustion.

Acknowledgment

This work has been jointly supported by the National Swedish Board for Technical Development and the Swedish Air Materiel Department. The author wishes to express his appreciation to Mr. K-A. Zetterström for his valuable comments and suggestions during the present study.

Downloaded 01 Jun 2010 to 171.66.16.62. Redistribution subject to ASME license or copyright; see http://www.asme.org/terms/Terms_Use.cfm

References

1 Jones, R. E., "Gas Turbine Engine Emissions — Problems, Progress and Future," *Progress in Energy and Combustion Science,* Vol. 4, 1978, pp. 73–113.

2 Sjöblom, B. G. A., and Zetterström, K-A., "A Double Recirculation Zone Two-Stage Combustor," *Proceedings of the Fourth International Symposium on Air Breathing Engines,* Apr. 1979, pp. 149–158.

3 Roberts, R., Fiorentino, A. J., and Greene, W., "Pollution Technology Program, Can-Annular Combustor Engines. Final Report," NASA CR-135027, PWA-5394, May, 1976.

4 Odgers, J., "Air Pollution by Gas Turbines — Is Control Possible?," *Canadian Aeronautics and Space Journal,* Oct. 1970, pp. 339–344.

5 Odgers, J., Gerardin, H., and Kretschmer, D., "A Premixed, Variable Area Combustor For a Small Gas Turbine Engine," *Paper presented at the Third International Symposium on Air Breathing Engines,* Munich, Mar., 1976.

6 Odgers, J., and Kretschmer, D., "Design Features for a Pre-Mixed Variable Area Combustor," *AGARD Conference Proceedings No. 205,* Paper No. 26, 48th PEP Meeting, Paris, Sept. 6–9, 1976.

7 Spadaccini, L. J., "Auto-ignition Characteristics of Hydrocarbon Fuels at Elevated Temperatures and Pressures," ASME Paper No. 76-GT-3, Mar. 1976.

8 "Procedure for the Continuous Sampling and Measurement of Gaseous Emissions from Aircraft Turbine Engines," SAE Aerospace Recommended Practice 1256, Oct. 1971.

9 Roberts, R., Peduzzi, A., and Niedzwiecki, R. W., "Low Pollution Combustor Designs for CTOL Engines — Results of the Experimental Clean Combustor Program," AIAA Paper No. 76-762, July 1976.

Downloaded 01 Jun 2010 to 171.66.16.62. Redistribution subject to ASME license or copyright; see http://www.asme.org/terms/Terms_Use.cfm

Formation of SO_3 in Gas Turbines

S. C. Hunter
Principal Engineer
KVB, Inc.
A Research-Cottrell Co.
Irvine, Calif.
Mem. ASME

Sulfur trioxide in gas turbine exhaust contributes to particulate emissions; reduction of this compound is a means for control of particulate emissions. The chemical kinetics of SO_3 formation were analyzed for a large stationary gas turbine. The source of SO_3 is the reaction of SO_2 with oxygen atoms in the downstream end of the combustor primary zone. The primary zone produces SO_3 levels of 1 to 2 percent of total SO_x. SO_3 increases above 1 to 2 percent during air dilution from an equivalence ratio of about 0.5 to 0.35; formation times are on the order of 1 to 10 ms. Reduction of primary zone air flow and more rapid dilution air mixing were identified as means for SO_3 reduction. Dilution air mixing in 1 ms was identified as an objective; but would be a difficult task with current combustor designs.

Introduction

The combustion of fossil fuels containing sulfur results in formation of oxides of sulfur primarily in the form of SO_2 and SO_3. The fraction of fuel sulfur that forms SO_3 is small, typically from 1 to 10 percent. However, SO_3, in contrast to SO_2, forms liquid sulfuric acid at standard ambient conditions and is therefore considered by some state emission regulations to be a particulate. Although the volumetric concentrations of SO_3 are small, the large volume of exhaust flow from stationary gas turbines can produce weight flows of SO_3 that constitute a significant fraction of total particulate weight. An understanding of the possible mechanisms for SO_3 formation is a necessary step in the effort to control total particulates.

The formation of SO_3 has been studied for many years in attempts to solve acid smut problems in the exhaust of steam boilers. Dooley and Whittingham [1] and Hedley [2] were among the first to study SO_3 formation. Two mechanisms were postulated: homogeneous gas-phase formation and heterogeneous catalytic activity on heat transfer surfaces or ash particles. A considerable amount of theoretical and experimental work has been done since then, but little has been done in analyzing the complete coupled gas-phase kinetics and fluid dynamics of SO_3 formation.

This paper presents results from a one-dimensional model that includes gas-phase kinetics and distributed mixing applied to the post-combustion and dilution zone of gas turbine combustors. The gas turbine design configurations and operating conditions were based on those of a specific current large industrial gas turbine.

Thermodynamic Equilibrium Considerations

A gas mixture in thermodynamic equilibrium represents the most probable composition that would exist if the mixture were held for a very long time at constant enthalpy and pressure. Chemical reactions will proceed in the direction of minimum free energy until a steady-state condition is reached that minimizes the free energy of the total mixture. Computation of equilibrium mixtures can be useful in defining the most probable compounds that can be expected and the directions in which kinetic reactions can be expected to proceed. Because of the strong dependence of kinetic rates on temperature, it is generally expected that mixtures will be near equilibrium at high tempertures as in a flame, but experience increasing deviation from equilibrium at lower temperatures.

Equilibrium computations were performed for hydrocarbon flames representative of oil fuels containing sulfur. The sulfur is found to combine with carbon, hydrogen, and oxygen, with predominant compounds being SO_2, SO_3, SO, CS, CH, COS, H_2S, S, and S_2. At temperatures typical of flames, nearly all the sulfur exists as SO_2. In air-rich flames, SO and SO_3 are also present. For fuel-rich flames, SO_3 is negligible and the other compounds listed above become significant. In practical combustion devices the exhaust is nearly always air rich so that the sulfur is exhausted entirely as SO_2 and SO_3. At low temperatures with moisture present, SO_3 will form sulfuric acid (H_2SO_4).

Figure 1 shows equilibrium SO_3 percentage of total SO_x as a function of temperature and oxygen content (total mixture O_2, not as dry basis). At low temperatures, equilibrium would result in virtually all of the sulfur present as SO_3. At high temperatures in a flame, the percent SO_3 is very low – less than 0.1 percent. The levels of 1 to 5 percent SO_3 typical of gas turbine stack gases occur in the range of 1370 to 1810 K (2000 to 2800°F). The figure also illustrates that the theoretical percent SO_3 is a function of the square root of the oxygen content. H_2SO_4 formation has been neglected.

Figure 2 presents the equilibrium SO_3 as a percent of total SO_x for typical gas turbine conditions as a function of equivalence ratio. At the combustor exit, SO_3 could be as high as 20 percent conversion. Test results for gas turbines tested by KVB burning distillate oil at a comparable sulfur content indicated SO_3 conversions of 2 to 14 percent. These values correspond to equilibrium values in the range of 0.3 to 0.6 equivalence ratio.

Conclusions from consideration of thermodynamic equilibrium are that at high temperatures most of the sulfur is

Contributed by the Gas Turbine Division and presented at the International Gas Turbine Conference and Products Show, Houston, Texas, March 9–12, 1981, of THE AMERICAN SOCIETY OF MECHANICAL ENGINEERS. Manuscript received at ASME Headquarters, December 3, 1980. Paper No. 81-GT-42.

Copyright © 1982 by ASME
Downloaded 01 Jun 2010 to 171.66.16.62. Redistribution subject to ASME license or copyright; see http://www.asme.org/terms/Terms_Use.cfm

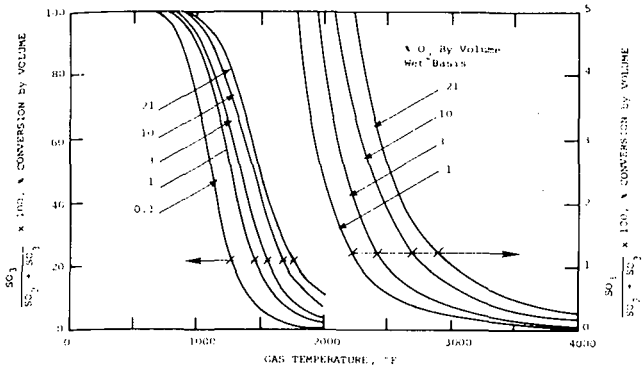


Fig. 1 Thermodynamic equilibrium SO_3 conversion

present as SO_2, and that conversion of SO_2 to SO_3 can occur at low temperature. A critical temperature zone exists between 1400 and 2000 K (2000 to 3000°F) below which nearly complete conversion to SO_3 could occur. In this critical temperature range, the percent conversion is also a function of excess oxygen content and pressure. Consideration of reaction rate kinetics is necessary to explain why very high levels of SO_3 are not observed in practice, and how lower levels might be promoted.

Gas-Phase Chemical Kinetic Mechanisms

Formation of SO_2. The predominant sulfur species in stack gas is sulfur dioxide (SO_2). Formation occurs in the flame as part of the overall combustion reactions, and SO_2 forms at rates comparable to H_2O and faster than CO_2. The fast rate ensures nearly complete conversion of fuel sulfur to SO_2 even in fuel-rich flames. Levy and Merryman [3-6] have conducted a series of probings in hydrogen sulfide (H_2S) and carbonyl sulfide (COS) flames. The composition profile data confirm the rapid formation of SO_2 within the visible flame zone.

Data for sulfur-bearing fuel oil flame profiles are limited, but rapid formation of SO_2 can be expected to occur with any type of fuel. SO_2 emission data on a wide variety of combustion devices indicate that, within measurement accuracy, all fuel sulfur is converted to SO_2 in the flame zone for solid, liquid, or gaseous fuels.

It is concluded that the only means for limiting SO_2 is through fuel sulfur content control or by stack gas treatment. Combustion controls, excess air, fuel atomization, etc. are not expected to have any significant influence.

Formation of SO_3 in Flames. Sulfur trioxide (SO_3) can be formed by several reactions. Merryman [6] and Cullis [7] present discussions of the possible and most probable formation process.

The various reactions considered include:

$$SO_2 + O + M \rightleftharpoons SO_3 + M \quad (1)$$

$$SO_3 + O \rightleftharpoons SO_2 + O_2 \quad (2)$$

$$SO_2 + O \rightleftharpoons SO_3 \quad (3)$$

$$SO_3 + H \rightleftharpoons SO_2 + OH \quad (4)$$

$$SO_2 + 1/2\,O_2 \rightleftharpoons SO_3 \quad (5)$$

$$SO + O_2 + M \rightleftharpoons SO_3 + M \quad (6)$$

$$SO_3 + H_2 \rightleftharpoons SO_2 + H_2O \quad (7)$$

$$SO_2 + NO_2 \rightleftharpoons SO_3 + NO \quad (8)$$

$$SO_2 + HO_2 \rightleftharpoons SO_3 + OH \quad (9)$$

Reactions involving direct O_2 attack on SO_2 have been shown to be very slow ([3] and [7]). Significant rates of flame-produced SO_3 are only observed in the presence of O atoms and can be attributed to reactions (1) and (3). Merryman [6] showed that SO_3 formation is strongly pressure dependent and concluded that the third body reaction (1) is the predominant reaction. This conclusion is supported by many others as discussed by Cullis. Reaction (1) is opposed by reaction (2), which acts to reconvert SO_3 back to SO_2. Sawyer [8] suggests that reaction (9) may be important in low temperature regions.

Thermodynamic equilibrium considerations indicate that at flame temperatures, the percent SO_2 converted to SO_3 is less than 0.1 percent. However, this also implies that all other species are in equilibrium and all reactions are equilibrated. This is clearly not the case in the flame zone. When one species, in particular CO, has a slower rate of reaction, the remaining much faster reactions assume a different pseudo-equilibrium. As the result of CO combustion, O atoms increase by factors of 10 to 1000 times the value established by $O\text{-}O_2$ equilibrium.

The driving force for reaction (1) then establishes a different single-reaction equilibrium for the ratio fo SO_3 to O-atom concentration, given by

$$\frac{X_{SO_3}}{X_O} = K_p\, X_{SO_2} P \quad (10)$$

where

K_p = equilibrium constant for reaction 1, kPa^{-1}
= $5.83 \times 10^{-11} \exp(83.689/RT)$.

This relation shows that the mole fraction of SO_3 can be increased over the complete equilibrium levels in proportion to the increase in O-atom concentration above complete equilibrium levels. Inclusion of reaction (2) in this consideration indicates that the SO_3-SO_2 ratio would tend to assume a steady-state value intermediate between the complete equilibrium value (lower limit) and the value given by equation (10) (upper limit) as a function of O-atom concentration. As the main combustion reactions reach completion, the O-atom concentration returns to equilibrium with O_2, and flame-produced SO_3 can be reconverted to SO_2 by

Nomenclature

A,B,N = constants in kinetic rates, k_j
F,B = constants in equation (12)
k_j = forward kinetic rate constant for the *jth* reaction, $(cc/mole)^n\ sec^{-1}$ where n = 1 for bimolecular reactions, n = 2 for 3 body reactants
k_{jb} = reverse kinetic rate constant for the *jth* reaction $(cc/mole)^n\ sec^{-1}$
K_p = equilibrium constant for reaction 1, kPa^{-1}
P = mixture total pressure, kPa
R = universal gas constant, cgs units, 1.987×10^{-3} kcal/mole•K
R' = universal gas constant, SI units = 8314.34 J/kmole•K
t = residence time, ms
T = temperature, K
X_i = mole fraction of species i, dimensionless (subscript e = equilibrium, o = time zero)
τ = relaxation time, ms
$[i]$ = concentration of species i, gram-moles/cc

Downloaded 01 Jun 2010 to 171.66.16.62. Redistribution subject to ASME license or copyright; see http://www.asme.org/terms/Terms_Use.cfm

Table 1 Reaction Set for Combustion with Sulfur

Reaction	Rate Constants A	N	B	Reference
Sulfur Reactions				
$SO_2 + HO_2 = SO_3 + OH$	5.42+8	0.0	0.0	Davis (15)
$SO_2 + NO_2 = SO_3 + NO$	6.31+12	0.0	27.0	Cullis (7)
$SO_3 + O = SO_2 + O_2$	1.20+12	0.0	9.5	Cullis (7)
Carbon Reactions				
$CO + OH = CO_2 + H$	1.51+7	−1.3	0.765	Balch (16)
$CO_2 + O = CO + O_2$	1.90+13	0.0	54.15	Balch (13)
Nitrogen Reactions				
$N + O_2 = NO + O$	6.43+9	−1.0	6.25	Balch (13)
$N + OH = NO + H$	4.20+13	0.0	0.0	Campbell (14)
$NO + N = N_2 + O$	1.63+13	0.0	0.0	Garvin (11)
$NO + NO + O_2 = NO_2 + NO_2$	2.40+9	0.0	−1.046	Balch (13)
$NO + HO_2 = NO_2 + OH$	1.81+11	0.0	0.0	Davis (15)
$NO_2 + O = NO + O_2$	1.00+13	0.0	0.6	Balch (13)
$N_2O + O = N_2 + O_2$	1.02+14	0.0	28.017	Garvin (11)
H/O Reactions				
$H + O_2 = OH + O$	2.24+14	0.0	16.8	Balch (13)
$H_2 + O = OH + H$	1.74+13	0.0	9.45	Balch (13)
$OH + H_2 = H_2O + H$	2.19+13	0.0	5.15	Balch (13)
$OH + OH = H_2O + O$	5.75+12	0.0	0.78	Balch (13)
Third Body Reactions				
$SO_2 + O + M = SO_3 + M$	3.63+14	0.0	−1.000	Garvin (11)
$CO + O + M = CO_2 + M$	5.10+15	0.0	3.580	Breen (12)
$NO + O + M = NO_2 + M$	1.05+15	0.0	−1.87	Balch (13)
$N_2 + O + M = N_2O + M$	1.00+18	1.0	0.0	Breen (12)
$N + O + M = NO + M$	6.44+16	0.5	0.0	Balch (13)
$N + N + M = N_2 + M$	3.01+14	1.0	−0.993	Garvin (11)
$OH + H + M = H_2O + M$	1.17+17	0.0	0.0	Balch (13)
$H + H + M = H_2 + M$	7.50+18	1.0	0.0	Breen (12)
$H + O_2 + M = HO_2 + M$	1.59+15	0.0	−1.0	Balch (13)
$H + O + M = OH + M$	3.60+18	1.0	0.0	Breen (12)
$O + O + M = O_2 + M$	1.90+18	0.5	0.0	Breen (12)

Rate Constant, $k = A\,T^{-N} \exp(-B/RT)$, (cc/mole)^n s^{-1} (reaction left to right)
R = 0.001987 kcal/mole^{-k}
n = 1 for bimolecular reactions
2 for third body reactions
B in kcal/mole-K
T, temperature, K

the reverse of reaction (1) and by reaction (2). The combined effects of reactions (1) and (2) are such that a peak in SO_3 is observed in flame profiles are reported by Levy and Hedley [9]. The relative rates of these reactions must be considered to determine whether there is a possibility that the high flame SO_3 levels could persist beyond the flame by quenching of the reaction rates through cooling or mixing.

Reaction rate constants have been measured by various means summarized by Cullis [7] and Bamford [10]. Reaction (1) has a very low temperature dependency consistent with third body mechanisms. The rate constant given by Cullis [7] is not temperature dependent. The recommended value for third bodies (M) of argon, nitrogen, and oxygen is

$$SO_2 + O + M \rightarrow SO_3 + M \qquad (1)$$

$$k_1 = 1 \times 10^{15} \text{ (cc/mole)}^2 \text{ s}^{-1}.$$

Bamford [10] averages a number of measurements to obtain for M = Ar, O_2, and N_2.

$$k_1 = 3.6 \pm 1 \times 10^{15} \text{ (cc/mole)}^2 \text{ s}^{-1}$$

Garvin [11] recommends the following rate constant.

$$k_1 = 3.63 \times 10^{14}\, e^{1.000/RT} \text{ (cc/mole)}^2 \text{ s}^{-1}$$

This value is most recent and is used in this reported work.

For reaction (2), Cullis [7] develops a value of

$$SO_3 + O \rightarrow SO_2 + O_2 \qquad (2)$$

$$k_2 = 1.2 \times 10^{12}\, e^{-9.500/RT} \text{(cc/mole) s}^{-1}$$

based on data by Merryman [6] and the value of k_1. Rates for the reverse reactions can be obtained from the equilibrium constants for each reaction. The rate constant for reaction (2) is not as well established as that for reaction (1), but the former reaction has been found in the current effort to be most important.

The kinetic mechanism employed for the current study, presented in Table 1, is taken from Breen [12], with addition of reactions for sulfur and updated rate constants.

As noted, the most significant reactions for SO_3 formation are reactions (1) and (2). These can be examined independently of the complete reaction set to determine the rate of change of SO_3 as a function of temperature, with all other molecular species maintained at constant concentrations.

The rate of change of SO_3 with time for reactions (1) and (2) is:

$$\frac{d[SO_3]}{dt} = k_1 [SO_2][O][M] + k_{2b} [SO_2][O_2] - k_{1b}[SO_3][M] - k_2[SO_3][O] \qquad (11)$$

Assuming that SO_3 is the only variable, equation (11) becomes a linear differential equation:

Downloaded 01 Jun 2010 to 171.66.16.62. Redistribution subject to ASME license or copyright; see http://www.asme.org/terms/Terms_Use.cfm

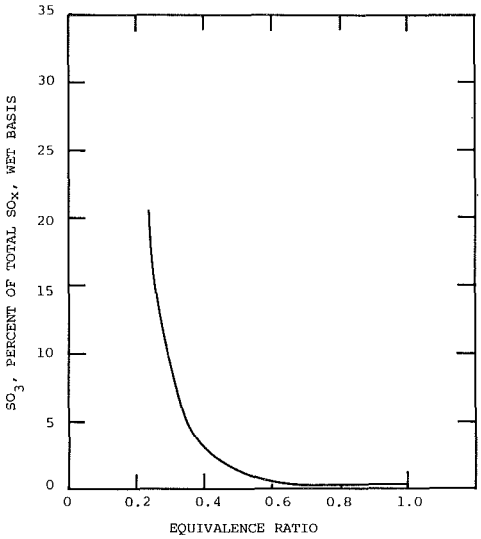


Fig. 2 Equilibrium SO_3 concentration. Pressure = 958 kPa, temperature = 594 K

$$\frac{d}{dt}[SO_3]/[SO_2] = F - B[SO_3]/[SO_2] \tag{12}$$

with boundary conditions of:

$$t = 0, [SO_3] = [SO_3]_o$$

$$t = \infty, \frac{d}{dt}[SO_3] = 0$$

The SO_3 concentration is related to mole fraction by:

$$[SO_3] = PX_{SO_3}/RT \tag{13}$$

and

$$F = \frac{P}{R'T}\left(k_1 X_O \frac{P}{R'T} + k_{2b} X_{O_2}\right) \tag{14}$$

$$B = \frac{P}{R'T}(k_{1b} + k_2 X_O) \tag{15}$$

The term F represents the production of SO_3 while B represents destruction of SO_3. Integrating (12) gives:

$$\frac{X_{SO_3}}{X_{SO_2}} = \frac{F}{B} + \left[\frac{X_{SO_{3_o}}}{X_{SO_2}} - \frac{F}{B}\right]e^{-Bt} \tag{16}$$

For

$$t \to \infty, X_{SO_3} \to X_{SO_{3_e}}$$

and

$$d[SO_3]/dt \to 0 \text{ so that}$$

$$\frac{X_{SO_{3_e}}}{X_{SO_2}} = \frac{F}{B} \tag{17}$$

Also let

$$\tau = 1/B \tag{18}$$

Using (17) and (18) in (16) and cancelling out X_{SO_2} produces the following result:

$$\frac{X_{SO_3}}{X_{SO_{3_e}}} = 1 - \left[1 - \frac{(X_{SO_3})_o}{(X_{SO_3})_e}\right]e^{-t/\tau} \tag{19}$$

The relaxation time, τ, is

$$\tau = \frac{R'T/P}{k_{1b} + k_2 X_o} \times 1000 \tag{20}$$

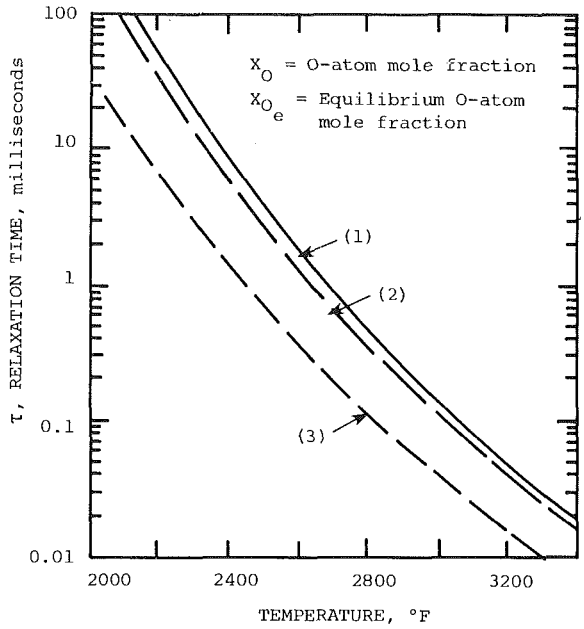


Fig. 3 SO_3 relaxation time versus temperature

(1) Equilibrium O atom conc.
(2) 10 × equilibrium O atom conc.
(3) 100 × equilibrium O atom conc.

where

k_{1b} = reverse rate constant for reaction (1)
= $7.41 \times 10^{20} T^{-1} e^{-82.689/RT}$, (cc/mole) s^{-1}

k_2 = forward rate constant for reaction (2)
= $1.2 \times 10^{12} e^{-9.500/RT}$, (cc/mole) s^{-1}

The exponential nature of equation (19) is such that an initial difference between SO_3/SO_2 ratio and the equilibrium ratio will be reduced by 63 percent in a residence time equal to one relaxation time period. For a residence time equal to three relaxation time periods, the difference will be reduced by 95 percent. Therefore, in a mixture held at constant temperature and composition, the SO_3 would nearly reach the equilibrium value in a residence time equal to about three relaxation time periods.

Figure 3 shows the SO_3 relaxation time from the above relation for adiabatic combustion with initial air temperature of 594 K (610°F) and a pressure of 958 kPa (9.46 atm) for equilibrium O-atom concentration and for 10 and 100 times the equilibrium O-atom concentration. Relaxation time is less than 0.1 ms above 1900 K (3000°F), increasing rapidly as temperature decreases to 1400 K (2000°F). The action of O-atoms in accelerating SO_3 formation by reducing relaxation time is also apparent.

Figure 4 presents the SO_3 relaxation time replotted from Figure 3 as a function of equilibrium SO_3. At high temperatures, the relaxation time is very short, but equilibrium SO_3 levels are low. With decreasing temperature, the equilibrium SO_3 increases, but the relaxation time increases very rapidly. The residence times in gas turbine combustor dilution zones cover a range of about 1 to 100 ms. Relaxation times in the range of 0.3 to 30 ms correspond to equilibrium SO_3 levels of 2 to 8 percent of SO_x. Measured SO_3 levels range from 2 to 14 percent of SO_x. Therefore, the above simplified examination of SO_3 formation by reactions (1) and (2), together with comparison of relaxation time with the residence time available for reaction, provides a fundamental

Downloaded 01 Jun 2010 to 171.66.16.62. Redistribution subject to ASME license or copyright; see http://www.asme.org/terms/Terms_Use.cfm

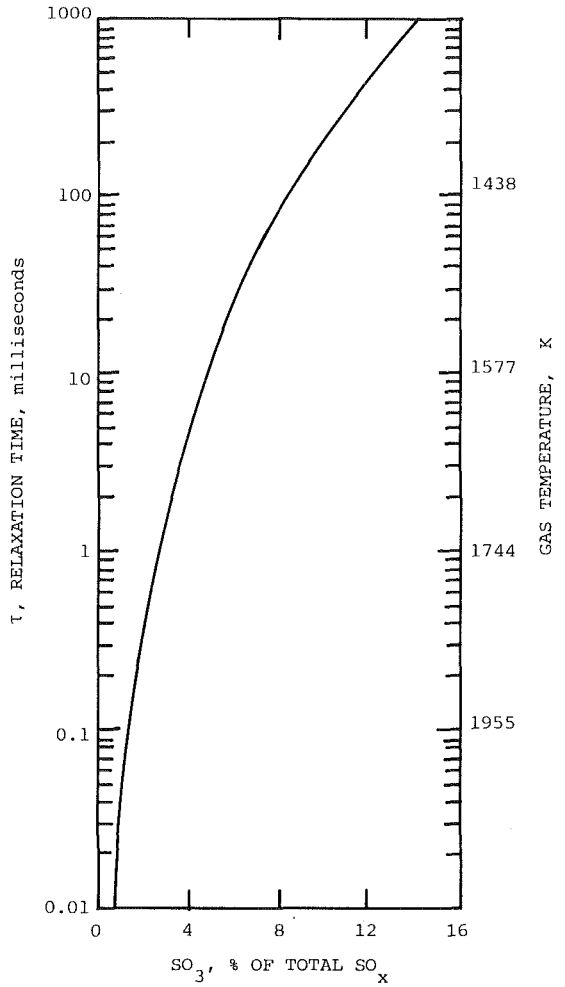


Fig. 4 SO_3 relaxation time versus equilibrium SO_3 for equilibrium O atom concentration

understanding of observed emission levels and explains why observed values are significantly less than equilibrium.

Based on the foregoing considerations of equilibrium and simplified residence time, the task of reducing SO_3 emissions would appear to involve a reduction of combustor residence time (faster mixing) in the mid-temperature region where the combination of high SO_3 equilibrium level and short relaxation time allows reaction to proceed to SO_3 levels in excess of desired limits. A complication exists in that higher mixing rates can result in O-atom concentrations in excess of equilibrium, causing a reduction in relaxation time as indicated in Fig. 3.

This simplified view of the combustion process provides some insight into the general nature of SO_3 formation and serves as a guide to more detailed analysis of the coupled chemistry and mixing as discussed below.

Coupled Gas-Phase Chemical Kinetic and Mixing Analysis

A one-dimensional solution of the mass, momentum, energy, and species kinetics equations was used to model the distributed mixing in a gas turbine combustor. The calculation procedure developed at KVB is similar to that described by Coats et al. [17]. Complete details of the procedure will be published in the near future in a final report for Air Force Contract FO4611-78-C-0011, reporting on work conducted by KVB for the Air Force Rocket Propulsion Laboratory, Edwards Air Force Base, California [18].

Geometric details, operating conditions, and air injection distribution were estimated for a large stationary gas turbine. The air injection is divided into three main flows: primary combustion air enters through swirlers at the upper end, cooling air enters through sidewall bands, and final dilution air enters through rows of ports. Actual mixing of air with fuel and combustion products does not occur instantly at the point of injection. Stratification of the gas streams results in mixture gradients that can be represented by more gradual distributed addition of air.

Modeling the complex mixing process in the combustor with a one-dimensional model required some very broad assumptions regarding the flow pattern. An initial equivalence ratio of 1.2 was assumed. The remaining primary and cooling air was assumed to mix linearly up to the point of dilution air injection. The primary zone was assumed to have a constant velocity. Flow area was set to provide constant velocity, and was increased in proportion to mass addition up to the full combustor area at the dilution injection point. Constant area was maintained in the dilution zone. Recirculation in the primary zone was neglected.

An analysis of dilution jet injection through the dilution ports was performed to estimate the axial distance of jet impingement downstream of the injection point. It was assumed that air from the first row of ports mixed in that distance; the remaining dilution air is distributed over the remainder of the dilution zone. Figure 5 is a schematic of the mixing pattern assumed.

In addition to computing SO_3 formation within the combustor, the computation was extended through the combustor-to-turbine transition duct and turbine nozzle expansion down to the turbine exit temperature.

Figure 6 presents the computed SO_3 concentration, as a function of length, from the combustor fuel injector through the turbine nozzle. Computed SO_3 is shown to increase most rapidly in the primary zone and to be lower than equilibrium levels. The formation rate is much slower in the dilution zone. A 10 percent increase occurs in the transition duct, but formation does not apear to occur in the turbine nozzle. The final SO_3 level of 6.2 percent is close to the average of SO_3 measurements obtained in gas turbine tests by KVB. The test average of 7.1 percent included several high values that could be questioned. If the highest SO_3 value at each of the three test points is excluded, the test average reduces to 5.8 percent. The agreement of computed and measured values is considered excellent in view of the relatively crude mixing assumptions and uncertainity in kinetic rate constants. However, the relaxation time considerations discussed previously show that residence time prior to dilution is of prime importance. This is clearly illustrated in the computed SO_3 profile.

Effects of Air Mixing Rate on SO_3 Formation. Reduction of SO_3 appears to be possible by designing the primary zone for a relatively higher equivalence ratio (reduced air flow) to maintain a low equilibrium SO_3 level and to increase primary zone residence time to prevent high O-atom concentrations. Dilution zone mixing must then be accomplished at a very rapid rate to quench the SO_3 reactions as rapidly as possible.

The analysis assumed a primary zone air mixing rate that was essentially linear from an equivalence ratio of 1.2 at the upstream end to 0.32 at the exit (dilution point). Three modifications to the air mixing rate schedule were evaluated for effect on SO_3 formation. Resultant SO_3 profiles are compared on Fig. 7 with that for the original rate schedule.

Rate modification 1 consisted of a lower rate of primary air addition over a greater length, and a higher primary zone exit equivalence ratio of 0.44 to maintain SO_3 below 2.4 percent. Near the end of the combustor, SO_3 begins to increase as

Downloaded 01 Jun 2010 to 171.66.16.62. Redistribution subject to ASME license or copyright; see http://www.asme.org/terms/Terms_Use.cfm

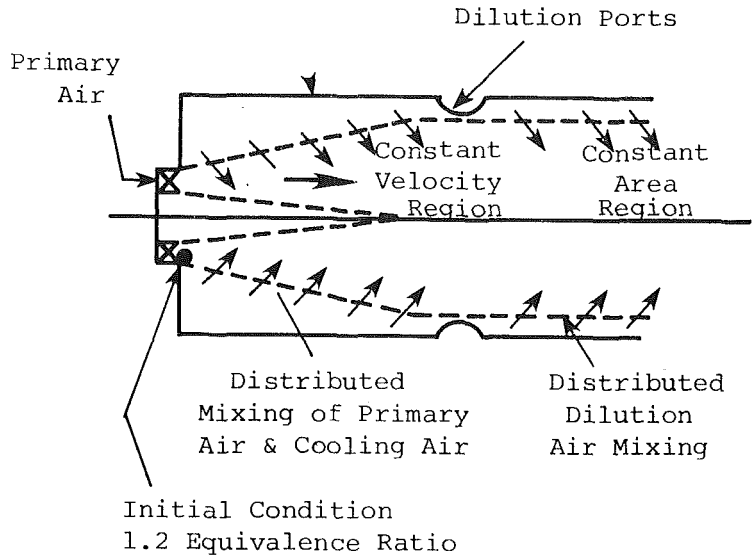


Fig. 5 Combustor flow and mixing pattern

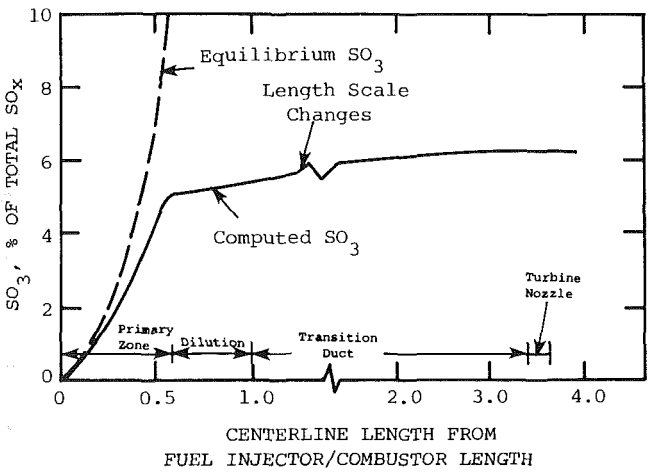


Fig. 6 SO_3 formation along combustor

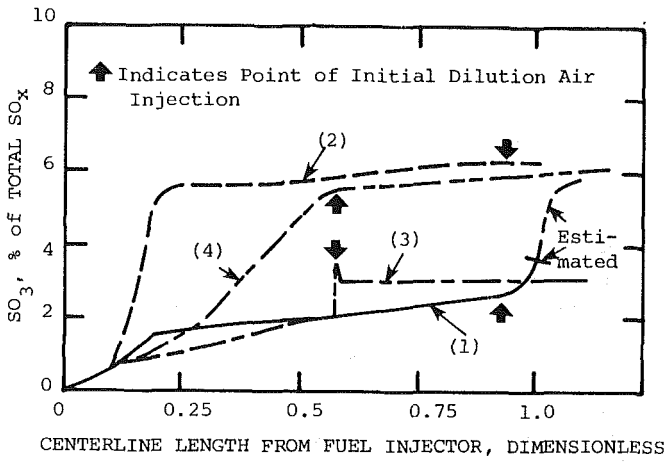


Fig. 7 SO_3 versus air mixing rates

(1) Rate modification 1
(2) Rate modification 2
(3) Rate modification 3
(4) Original rate

dilution air is added at the point indicated by the arrow. The computation was inadvertently terminated at 1.0, but the rapid increase in SO_3 from 0.9 to 1.0 indicates that SO_3 would probably increase to nearly 5 percent as shown by the dashed extension.

Rate modification 2 consisted of higher initial primary air flow to rapidly mix to 0.38 equivalence ratio followed by slow mixing up to the dilution zone with an equivalence ratio of 0.36. Compared with rate modification 1, SO_3 forms much faster at the upstream end, coinciding with the point of more rapid air addition.

Rate modification 3 was based on establishing a primary zone exit equivalence ratio of 0.55 with a corresponding 2 percent equilibrium SO_3. Full quenching of the remaining air was then performed in 1 millisecond. Even at this very rapid quenching rate, an additional 1.5 percent was formed, with subsequent dilution to a final 3 percent SO_3.

Examination of the results for the four mixing rates indicated that the SO_3 formed was almost directly proportional to the amount of air added and not sensitive to the rate of addition. The one exception was the very rapid quenching of rate modification 3. These results are consistent with the kinetic relaxation time analysis (Fig. 4). For any given equivalence ratio, if the mixing time is greater than the kinetic relaxation time, the kinetic process will maintain near-equilibrium levels of SO_3. All the mixing schedules (except 3) produced about 6 percent SO_3 at the combustor exit. Figure 4 shows that as SO_3 exceeds 6 percent, the relaxation time increases above 20 ms. SO_3 was reduced to about 3 percent by rate modification 3 because the mixing time was about 1 ms, which corresponds to the relaxation time at an equilibrium concentration of 2.8 percent shown in Fig. 4.

The nearly direct proportionality of SO_3 to the amount of air added (essentially to equivalence ratio) is shown in Fig. 8 where the SO_3 profiles are plotted as a function of air mass flow rate as percent of total air. The original air schedule and modifications 1 and 2 follow equilibrium up to about 6 percent SO_3. Only rate modification 3 shows significant deviation from the equilibrium characteristic. This figure confirms that the distribution of air along the combustor does not affect SO_3 formation unless mixing can be accomplished at a rate faster than the kinetic relaxation time.

SO_3 equilibrium concentration is directly proportional to SO_2 concentration and thereby to fuel sulfur content. Evaluation of sulfur kinetics indicates that there is no reason for percent conversion to change with fuel sulfur content.

Downloaded 01 Jun 2010 to 171.66.16.62. Redistribution subject to ASME license or copyright; see http://www.asme.org/terms/Terms_Use.cfm

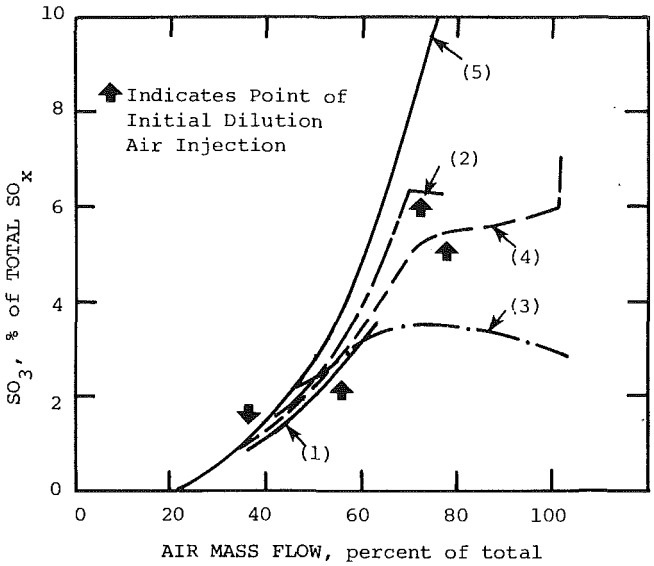


Fig. 8 SO_3 for four air mixing rate schedules

(1) Rate modification 1
(2) Rate modification 2
(3) Rate modification 3
(4) Original rate
(5) SO_3 equilibrium

Some data in the literature suggest that percent conversion increases with reduced fuel sulfur [1]. This could be attributed to catalytic reactions not accounted for in the kinetic analysis reported here or is possibly due to test measurement inaccuracies. A review of KVB data on turbines shows no specific trend of percent conversion with fuel sulfur content. It is therefore believed that the SO_3 concentrations shown in this paper can be scaled directly with fuel sulfur content.

SO_3 formation in steam boilers is frequently attributed to catalytic action on the boiler heat transfer surfaces. Various additives, primarily MgO, are employed to reduce catalytic action. However, gas-phase kinetic analysis tends to explain observed SO_3 levels as being entirely independent of any surface catalysis. The effectiveness of additives is believed to be a combination of both catalysis and gas-phase kinetics. The use of additives should therefore not be ruled out for SO_3 reduction in gas turbines. Of course, an additive may contribute to additional particulate emissions. A careful test program would be necessary to determine if a net particulate reduction could be achieved.

Conclusions

The results of this analysis indicate that SO_3 formation in turbine combustors occurs in the down-stream end of the combustor primary zone and is dependent on the rate of mixing of dilution air in a narrow equivalence ratio range. Some additional formation occurs in the combustor-to-turbine transition duct on the order of a 10 percent increase. The high rate of temperature drop that occurs in the power turbine expansion was not found to result in a noticeable SO_3 increase.

For the operating conditions evaluated, SO_3 concentration increases from 2 percent to over 6 percent at mixture equivalence ratios in the range of 0.5 to 0.35. The rate of reaction is on the order of 1 to 10 ms; mixing in a time of about 1 ms is required to limit SO_3 formation. Therefore, the detailed process of air addition and mixing within the combustor was found to be more important than physical size.

Such rapid mixing may be impossible in current combustor designs. To accomplish it, approximately 28 percent of the combustor air flow would have to be injected through a large number of small ports with sufficient diameter for adequate penetration. Reductions to SO_3 levels less than 2 percent of total SO_x appear to be practically impossible. A further conclusion is that SO_3 reduction is enhanced by a large, low-velocity primary zone and by a smaller, high-velocity dilution zone.

Further study of the relative mixing times and kinetic times may yield a more optimum mixing scheme than the single-rapid-quench approach. Also, experimental investigation on a simple laboratory-scale flame with controlled mixing would be helpful in evaluating the results of this analysis.

References

1 Dooley, A., and Whittingham, G., "The Oxidation of Sulphur Dioxide in Gas Flames," *Transactions Faraday Society,* Vol. 42, 1946, pp. 354–366.

2 Hedley, A. B., "Factors Affecting the Formation of Sulphur Trioxide in Flame Gases," *Journal of the Institute of Fuel,* April 1967, p. 142–151.

3 Levy, A., and Merryman, E. L., "The Microstructure of Hydrogen Sulfide Flames," *Combustion and Flame,* Vol. 9, 1965, p. 229.

4 Merryman, E. L., and Levy, A., "Kinetics of Sulfur-Oxide Formation in Flames," *Journal Air Pollution Control Assn.,* Vol. 17, 1967, p. 800.

5 Levy, A., and Merryman, E. L., "Sulfur-Oxide Formation in Carbonyl Sulfide Flames," *Environmental Sci. and Tech.,* Vol. 3, 1969, p. 63.

6 Merryman, E. L., and Levy, A., "Sulfur Trioxide Flame Chemistry—H_2S and COS Flames," *Thirteenth Symposium (International) on Combustion,* The Combustion Institute, 1971, p. 427.

7 Cullis, C. F., and Mulcahy, M. F. R., "The Kinetics of Gaseous Sulfur Compounds," *Combustion and Flame,* Vol. 18, 1972, p. 225.

8 Sawyer, R. F., Univ. of California at Berkeley, personal communication.

9 Hedley, A. B., "Factors Affecting the Formation of Sulfur Trioxide in Flame Gases," *Journal Inst. Fuel,* Vol. 40, 1967, p. 142.

10 Bamford, C. H., and Tipper, C. F. H., *Comprehensive Chemical Kinetics,* Vol. 6, Elsevier, 1972.

11 Garvin, D., "Chemical Kinetics Data Survey IV," NBSIR-203, National Bureau of Standards, May 1973.

12 Breen, B. P., Bell, A. W., and Bayard de Volo, N., "Combustion Control for Elimination of Nitric Oxide Emissions from Fossil-Fuel Power Plants," *Thirteenth Symposium (International) on Combustion,* The Combustion Institute, 1971, p. 391.

13 Balch, D. L., et al., *High Temperature Reaction Rate Data,* Vols. 1-5, The University, Leeds, England, Dept. of Phys. Chem., 1970.

14 Campbell, I. M., and Thrush, D. A., *Transactions Faraday Society,* Vol. 64, 1968, p. 1275.

15 Davis, D. D., "New Rate Measurements on the Reaction of $O(^3P)$, O_3, and OH," AIAA/AMS, Denver, June 1973.

16 Balch, D. L., and Drysdale, D. D., "An Evaluation of the Rate Data for the Reaction CO + OH = CO_2 + H," *Combustion and Flame,* Vol. 23, 1974, p. 215.

17 Coats, D. E., et al., *A Computer Program for the Prediction of Solid Propellant Rocket Motor Performance,* Vols. I, II, and III, AFRPL-TR-75-36, July 1975 (with specific reference to the ODK kinetics module).

18 Hunter, S. C., et al., *One-Dimensional Three-Phase Reacting Flow with Mass Transfer Between Phases,* Vols. I and II, Final Report, Contract FO4611-78-C-0011, Air Force Rocket Propulsion Laboratory, Edwards Air Force Base (to be published).

Downloaded 01 Jun 2010 to 171.66.16.62. Redistribution subject to ASME license or copyright; see http://www.asme.org/terms/Terms_Use.cfm

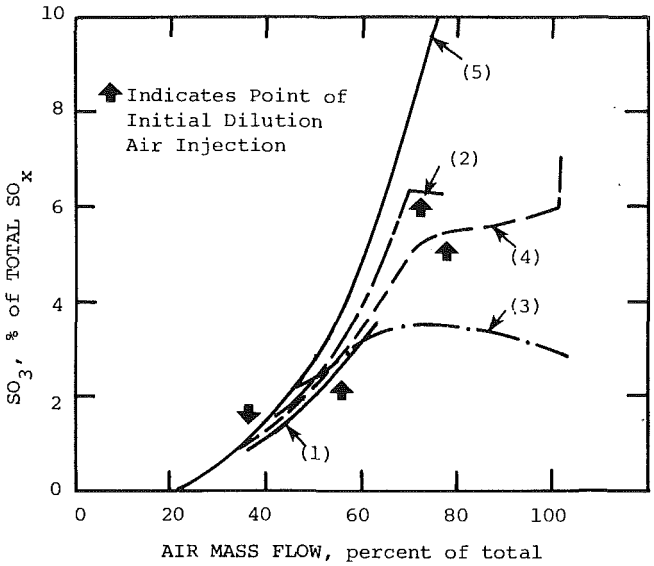


Fig. 8 SO_3 for four air mixing rate schedules

(1) Rate modification 1
(2) Rate modification 2
(3) Rate modification 3
(4) Original rate
(5) SO_3 equilibrium

Some data in the literature suggest that percent conversion increases with reduced fuel sulfur [1]. This could be attributed to catalytic reactions not accounted for in the kinetic analysis reported here or is possibly due to test measurement inaccuracies. A review of KVB data on turbines shows no specific trend of percent conversion with fuel sulfur content. It is therefore believed that the SO_3 concentrations shown in this paper can be scaled directly with fuel sulfur content.

SO_3 formation in steam boilers is frequently attributed to catalytic action on the boiler heat transfer surfaces. Various additives, primarily MgO, are employed to reduce catalytic action. However, gas-phase kinetic analysis tends to explain observed SO_3 levels as being entirely independent of any surface catalysis. The effectiveness of additives is believed to be a combination of both catalysis and gas-phase kinetics. The use of additives should therefore not be ruled out for SO_3 reduction in gas turbines. Of course, an additive may contribute to additional particulate emissions. A careful test program would be necessary to determine if a net particulate reduction could be achieved.

Conclusions

The results of this analysis indicate that SO_3 formation in turbine combustors occurs in the down-stream end of the combustor primary zone and is dependent on the rate of mixing of dilution air in a narrow equivalence ratio range. Some additional formation occurs in the combustor-to-turbine transition duct on the order of a 10 percent increase. The high rate of temperature drop that occurs in the power turbine expansion was not found to result in a noticeable SO_3 increase.

For the operating conditions evaluated, SO_3 concentration increases from 2 percent to over 6 percent at mixture equivalence ratios in the range of 0.5 to 0.35. The rate of reaction is on the order of 1 to 10 ms; mixing in a time of about 1 ms is required to limit SO_3 formation. Therefore, the detailed process of air addition and mixing within the combustor was found to be more important than physical size.

Such rapid mixing may be impossible in current combustor designs. To accomplish it, approximately 28 percent of the combustor air flow would have to be injected through a large number of small ports with sufficient diameter for adequate penetration. Reductions to SO_3 levels less than 2 percent of total SO_x appear to be practically impossible. A further conclusion is that SO_3 reduction is enhanced by a large, low-velocity primary zone and by a smaller, high-velocity dilution zone.

Further study of the relative mixing times and kinetic times may yield a more optimum mixing scheme than the single-rapid-quench approach. Also, experimental investigation on a simple laboratory-scale flame with controlled mixing would be helpful in evaluating the results of this analysis.

References

1 Dooley, A., and Whittingham, G., "The Oxidation of Sulphur Dioxide in Gas Flames," *Transactions Faraday Society,* Vol. 42, 1946, pp. 354–366.

2 Hedley, A. B., "Factors Affecting the Formation of Sulphur Trioxide in Flame Gases," *Journal of the Institute of Fuel,* April 1967, p. 142–151.

3 Levy, A., and Merryman, E. L., "The Microstructure of Hydrogen Sulfide Flames," *Combustion and Flame,* Vol. 9, 1965, p. 229.

4 Merryman, E. L., and Levy, A., "Kinetics of Sulfur-Oxide Formation in Flames," *Journal Air Pollution Control Assn.,* Vol. 17, 1967, p. 800.

5 Levy, A., and Merryman, E. L., "Sulfur-Oxide Formation in Carbonyl Sulfide Flames," *Environmental Sci. and Tech.,* Vol. 3, 1969, p. 63.

6 Merryman, E. L., and Levy, A., "Sulfur Trioxide Flame Chemistry—H_2S and COS Flames," *Thirteenth Symposium (International) on Combustion,* The Combustion Institute, 1971, p. 427.

7 Cullis, C. F., and Mulcahy, M. F. R., "The Kinetics of Gaseous Sulfur Compounds," *Combustion and Flame,* Vol. 18, 1972, p. 225.

8 Sawyer, R. F., Univ. of California at Berkeley, personal communication.

9 Hedley, A. B., "Factors Affecting the Formation of Sulfur Trioxide in Flame Gases," *Journal Inst. Fuel,* Vol. 40, 1967, p. 142.

10 Bamford, C. H., and Tipper, C. F. H., *Comprehensive Chemical Kinetics,* Vol. 6, Elsevier, 1972.

11 Garvin, D., "Chemical Kinetics Data Survey IV," NBSIR-203, National Bureau of Standards, May 1973.

12 Breen, B. P., Bell, A. W., and Bayard de Volo, N., "Combustion Control for Elimination of Nitric Oxide Emissions from Fossil-Fuel Power Plants," *Thirteenth Symposium (International) on Combustion,* The Combustion Institute, 1971, p. 391.

13 Balch, D. L., et al., *High Temperature Reaction Rate Data,* Vols. 1-5, The University, Leeds, England, Dept. of Phys. Chem., 1970.

14 Campbell, I. M., and Thrush, D. A., *Transactions Faraday Society,* Vol. 64, 1968, p. 1275.

15 Davis, D. D., "New Rate Measurements on the Reaction of $O(^3P)$, O_3, and OH," AIAA/AMS, Denver, June 1973.

16 Balch, D. L., and Drysdale, D. D., "An Evaluation of the Rate Data for the Reaction CO + OH = CO_2 + H," *Combustion and Flame,* Vol. 23, 1974, p. 215.

17 Coats, D. E., et al., *A Computer Program for the Prediction of Solid Propellant Rocket Motor Performance,* Vols. I, II, and III, AFRPL-TR-75-36, July 1975 (with specific reference to the ODK kinetics module).

18 Hunter, S. C., et al., *One-Dimensional Three-Phase Reacting Flow with Mass Transfer Between Phases,* Vols. I and II, Final Report, Contract FO4611-78-C-0011, Air Force Rocket Propulsion Laboratory, Edwards Air Force Base (to be published).

DISCUSSION

Dean C. Hammond, Jr.[1]

The author is to be commended for pointing out the potential importance of SO_3 formation during combustion in gas turbine engines. In order to improve its accuracy and extend the valid temperature range, this discussor offers a revision to the simplified analysis of SO_3 kinetics embodied in equations (12–20) of the paper. A limitation to the analysis of the paper arises from "Assuming that SO_3 is the only variable

[1] General Motors Research Laboratories, General Motors Corporation, Warren, Mich. 48090

Copyright © 1982 by ASME

Downloaded 01 Jun 2010 to 171.66.16.62. Redistribution subject to ASME license or copyright; see http://www.asme.org/terms/Terms_Use.cfm

. . . " just prior to equation (12). Note that SO_2 and SO_3 are the only sulfur-containing species (see Table 1); therefore, SO_3 can be formed only by consuming SO_2 so that conservation of mass remains satisfied.

Alternately, conservation of mass requires only that the total number of moles of sulfur-containing species remain constant, which can be approximated for isobaric, isothermal oxidation, as:

$$[SO_2] + [SO_3] = \text{const.} \tag{21}$$

Or:

$$\frac{d[SO_2]}{dt} + \frac{d[SO_3]}{dt} = 0 \tag{22}$$

Performing a change of variable in equation (11) and incorporating equation (22) yields:

$$\frac{d}{dt}\frac{[SO_3]}{[SO_2]} = \left(1 + \frac{[SO_3]}{[SO_2]}\right)\left(F - B\frac{[SO_3]}{[SO_2]}\right) \tag{23}$$

With the initial condition

$$t = 0: \frac{[SO_3]}{[SO_2]} = \frac{[SO_3]_o}{[SO_2]}$$

Note that at equilibrium:

$$t \to \infty: \frac{d}{dt}\frac{[SO_3]}{[SO_2]} = 0$$

Therefore:

$$\frac{[SO_3]_e}{[SO_2]_e} = \frac{F}{B} \tag{24}$$

Integrating equation (23) yields

$$\frac{{}^xSO_3}{{}^xSO_2} = \frac{\frac{{}^xSO_{3,e}}{{}^xSO_{2,e}}\left(1 + \frac{{}^xSO_{3,0}}{{}^xSO_{2,0}}\right) - \left(\frac{{}^xSO_{3,e}}{{}^xSO_{2,e}} - \frac{{}^xXO_{3,0}}{{}^xSO_{2,0}}\right)e^{(F+B)t}}{1 + \frac{{}^xSO_{3,0}}{{}^xSO_{2,0}} + \frac{{}^xSO_{3,e}}{{}^xSO_{2,e}} - \frac{{}^xSO_{3,0}}{{}^xSO_{2,0}}\Big)e^{(F+B)t}} \tag{25}$$

From equation (21)

$${}^xSO_3 + {}^xSO_2 = \text{const} \tag{26}$$

By definition,

$$\frac{{}^xSO_3}{{}^xSO_3 + {}^xSO_2} \equiv \frac{{}^xSO_3/{}^xSO_2}{\frac{{}^xSO_3}{{}^xSO_2} + 1} \tag{27}$$

Substituting equation (24) into (27)

$$\frac{{}^xSO_{3e}}{({}^xSO_3 + {}^xSO_2)_e} = \frac{{}^xSO_{3e}/{}^xSO_{2e}}{\frac{{}^xSO_{3e}}{{}^xSO_{2e}} + 1} = \frac{F/B}{1 + F/B} \tag{28}$$

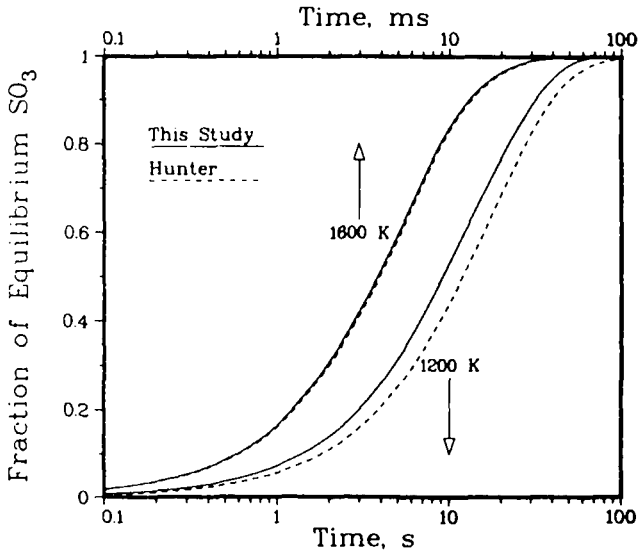


Fig. 9 Comparison of predicted SO_3 formation

From equation (26),

$${}^xSO_3 + {}^xSO_2 = ({}^xSO_3 + {}^xSO_2)_e \tag{29}$$

Therefore, dividing equation (27) by (28) and substituting (29),

$$\frac{{}^xSO_3}{{}^xSO_{3e}} = \frac{{}^xSO_3/{}^xSO_2}{1 + {}^xSO_3/{}^xSO_2}\frac{1 + F/B}{F/B} \tag{30}$$

The predictions of equation (26) are compared with those of Hunter's equation (19) in Fig. 9 for $X_{SO_3,0} = 0$. Significant differences arise at lower temperatures as a result of the inverse temperature dependence of the forward rates, which were essentially neglected in the paper, and the artificially elevated SO_2 concentration. The result is that the amount of SO_3 formed in lower temperature flow regions, where its formation rate is greatest, will be significantly under predicted (approximately 25 percent).

Author's Closure

The analysis in the paper, leading to equation 19, was a simple approximation as a prelude to the more complete gas-phase kinetic analysis presented later in the paper. Hammond is quite correct in noting that $SO_2 + SO_3$ is a constant, and his analysis is certainly an improvement of the simplified method if one wishes to use this method at very high percentage conversion of SO_2 to SO_3. However, since the SO_3 conversion in gas turbines rarely exceeds 10 percent, this improvement is of secondary practical significance. The more complete kinetic method discussed in the paper takes full account of elemental conservation, variation of SO_2, and all other species in the variable temperature and mixture environment of the combustor. Hammond's extension may be of use to those that do not have access to the more complete procedure.

Downloaded 01 Jun 2010 to 171.66.16.62. Redistribution subject to ASME license or copyright; see http://www.asme.org/terms/Terms_Use.cfm

Development of a Small-Scale Catalytic Gas Turbine Combustor

S. J. Anderson

M. A. Friedman

W. V. Krill

J. P. Kesselring

Acurex Corporation,
Energy and Environmental Division,
Mountain View, Calif. 94042

Catalytically supported thermal combustion can provide low NO_x emissions with gaseous and distillate fuels while maintaining high combustion efficiency. For stationary gas turbines, catalytic combustion may be the only emerging technology that can cost effectively meet recent federal regulations for NO_x emissions. Under EPA sponsorship, a small-scale, catalytic gas turbine combustor was developed to evaluate transient and steady state combustor performance. The combustor consisted of a multiple air-atomizing fuel injector, an opposed jet igniter, and a graded-cell monolithic reactor. System startup, including opposed jet ignition and catalyst stabilization, was achieved in 250 seconds. This time interval is comparable to conventional gas turbines. Steady state operation was performed at 0.505 MPa (5 atmospheres) pressure and 15.3 m/s (50 ft/s) reference velocities. Thermal NO_x emissions were measured below 10 ppmv, while fuel NO_x conversion ranged from 75 to 95 percent. At catalyst bed temperatures greater than 1422K (2100°F), total CO and UHC emissions were less than 50 ppmv indicating combustion efficiency greater than 99.9 percent. Compared with conventional gas turbine combustors, the catalytic reactor operates only within a relatively narrow range of fuel/air ratios. As a result, modified combustor air distribution or fuel staging will be required to achieve the wide turndown required in large stationary systems.

Introduction

Gas turbines are the fourth largest contributor of NO_x emissions from stationary anthropogenic sources in the United States [1]. Accordingly, the Environmental Protection Agency has established New Source Performance Standards (NSPS) for emissions from stationary gas turbines larger than 10.7 GJ/hr. For clean fuels, NO_x emissions are limited to 75 ppmv as corrected to 15 percent oxygen [2]. In general, NO_x emissions from uncontrolled gas turbines range from 150 to 250 ppmv. Consequently, manufacturers are actively pursuing control techniques which can achieve these standards. Currently, steam or water injection into the combustion chamber is the only available approach that can meet government regulations. Water serves as a diluent to reduce peak flame temperature and hence reduce NO_x. However, water injection has several drawbacks. To prevent alkaline corrosion of turbine hardware, purified water must be used. Since condensate-quality water is not readily available, a water purification system is required. This can increase total gas turbine capital cost by as much as 20 percent [3]. In addition, although water injection reduces NO_x emissions, it can increase both CO and UHC levels. Finally, water injection does not control NO_x emissions produced from fuel bound nitrogen. As a result, alternative pollutant control techniques are being investigated. These options include flue gas cleanup, standard gas turbine combustor modification, and the use of catalytically supported thermal combustion [4]. Because flue gas treatment is relatively expensive, advanced combustor development is being given serious consideration. Modifying fuel injection such as improved premixing of fuel and air prior to combustion can control peak flame temperature and can reduce NO_x emissions by as much as 60 to 80 percent – comparable to results obtained using water injection. In contrast, catalytically supported thermal combustion (hence referred to simply as catalytic combustion) has demonstrated NO_x reductions of 95 percent in laboratory tests while maintaining high combustion efficiency [5]. As air quality standards become more stringent, as in the South Coast Air Basin of California where standards require 90 percent reduction in NO_x by 1987 [6], catalytic combustion may be the only emerging technology available that can cost-effectively meet government regulations.

Through a series of contracts with the Environmental Protection Agency, Acurex Corporation has developed a number of prototype systems that use catalytic combustion to control NO_x emissions. Among these concepts, the gas turbine combustor appears promising for near-tearm application to full-scale machinery. Early catalytic research at Acurex introduced the graded-cell monolithic reactor. By using large cells at the catalyst inlet and small cells at the outlet, the graded configuration supports stable combustion at reference velocities comparable to those in full-scale machines. Specifically, for a given catalyst, the maximum volumetric heat release rate for a graded-cell configuration was shown to be nearly three times higher than for a single-

Contributed by the Gas Turbine Division and presented at the International Gas Turbine Conference and Exhibit, Houston, Texas, March 8–12, 1981, of THE AMERICAN SOCIETY OF MECHANICAL ENGINEERS. Manuscript received at ASME Headquarters, December 5, 1980. Paper No. 81-GT-43.

Copyright © 1982 by ASME

Downloaded 01 Jun 2010 to 171.66.16.62. Redistribution subject to ASME license or copyright; see http://www.asme.org/terms/Terms_Use.cfm

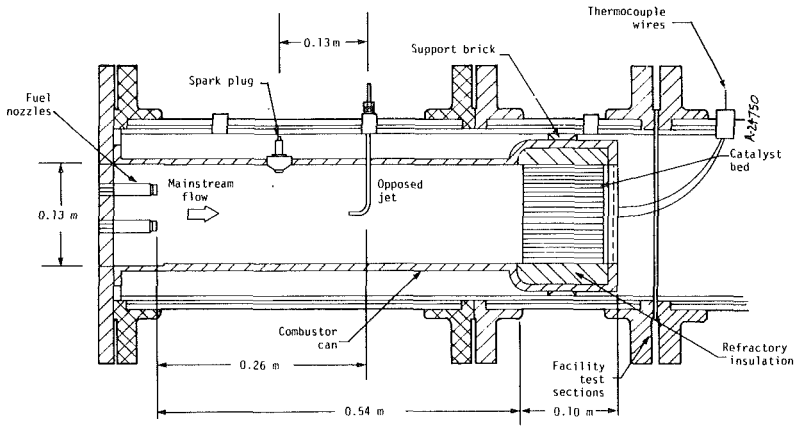


Fig. 1 Gas turbine combustor

cell system [7]. Subsequently, multiple point fuel injectors and an opposed jet igniter were added to the catalytic reactor to yield a fully integrated system. The following sections describe each of these system components and present the combustor's startup and steady state performance.

Combustor Design

The primary components of the gas turbine combustor with relevant system dimensions are shown in Fig. 1. Liquid fuel is injected into the combustor with air-atomizing nozzles. Rapid fuel/air mixing is achieved by three nozzles at the combustor inlet. Mixing is completed with 0.54 m – a mixing zone length-to-diameter ratio of 5:1. A gaseous fuel opposed jet igniter provides preheated air for light-off of the catalyst at temperatures as high as 1255K (1800°F). The catalyst is mounted in a refractory housing at the combustor outlet to insulate and protect the combustor liner from the hot catalyst surfaces. The design and performance of each of these components are discussed below.

Fuel Injector. Fuel injector design for catalytic gas turbine combustors is critical to good performance since catalytic systems require the air and fuel to be premixed. Optimum catalyst performance requires uniform reactor inlet profiles of temperature, fuel/air ratio, and velocity. This assures effective use of the entire catalyst area and prevents potential substrate damage caused by high temperatures due to locally enriched fuel/air mixtures. Therefore, the primary function of the fuel injector is to introduce the fuel to the air stream in such a manner as to provide complete mixing before entry into the catalyst. Mixing must occur rapidly to minimize the mixing length and, hence, the overall combustor length. The fuel injectors must also avoid recirculation regions which may lead to flameholding and promote vaporization of liquid fuels. Rudimentary tests at Acurex have shown that approximately 70 percent vaporization is required for stable catalyst operation [8].

The gas turbine combustor utilized three atomizing spray nozzles for fuel injection as shown in Fig. 1. Prior testing with liquid fuels was conducted with multiple conical tube, aerodynamic fuel injectors such as those shown in Fig. 2. While excellent performance with gaseous fuels was demonstrated, performance with distillate fuels resulted in poor droplet atomization. As a result, air atomizing spray nozzles were employed. These produce a mean droplet size of 60 to 100 μm which allows acceptable fuel vaporization over a fuel flow turndown ratio of 10 to 1. The three-nozzle array provided complete mixing and vaporization of fuel without autoignition difficulties.

During initial testing of the multiple injectors, the nozzles' wide spray angle caused fuel to impinge directly on the wall of the combustor can. Some thermal NO_x was produced, apparently as a result of upstream burning of the distillate fuel on the wall. This was confirmed by cold water model tests using a clear acrylic combustor can. Fuel contact with the wall was suppressed by reducing the nozzle spray angle from 77 to 15 degrees. Subsequent testing with the low spray angle revealed a uniformly delivered fuel/air mixture without upstream burning.

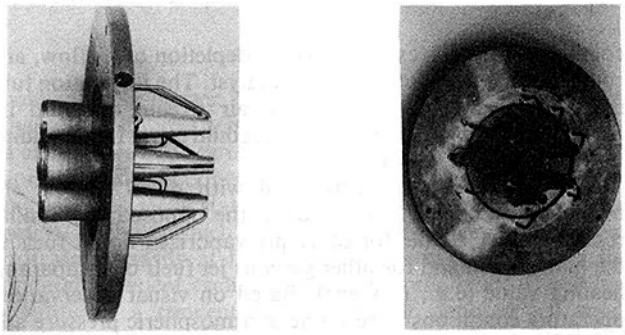


Fig. 2 Multiple venturi fuel injector assembly

Opposed Jet Igniter. Catalyst lightoff occurs when a minimum catalyst temperature is achieved. The lightoff temperature varies primarily with catalyst and fuel type and secondarily with stoichiometry and mass throughput. In general, temperatures in excess of 700K (800°F) are necessary for catalyst lightoff. For example, noble metal catalysts such as platinum and palladium require 617K to 783K (650°F to 950°F) lightoff temperatures, while metal oxide catalysts with active elements such as nickel and cobalt require 866K to 1367K (1100°F to 2000°F) temperatures. During gas turbine startup, insufficient preheat is available for catalyst lightoff. Consequently, an auxiliary heat source must be provided. A number of lightoff systems were evaluated in the development program [8], including the opposed jet igniter, packaged burners, electrical resistance preheated air, an aft-end torch, and hydrogen injection. The preferred technique is the opposed jet igniter where a jet of gaseous fuel is injected counterflow to the mainstream of reactants, producing a reacting stagnation flow condition. A spark plug ignites the jet and a bow flame front stabilizes in the jet region. By consuming the mainstream reactants, the opposed jet acts as an aerodynamic flameholder, providing a preheated fuel/air mixture to the catalyst located downstream. In application, the jet is ignited during low air flow conditions and produces energy to accelerate the machine and preheat the catalyst to its lightoff temperature. As the machine approaches a full load

Downloaded 01 Jun 2010 to 171.66.16.62. Redistribution subject to ASME license or copyright; see http://www.asme.org/terms/Terms_Use.cfm

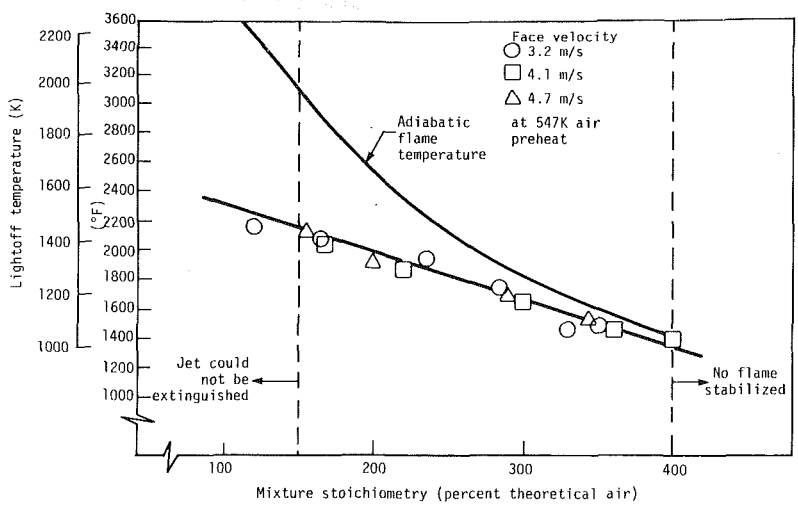


Fig. 3 Gas turbine combustor opposed jet results

condition, the jet is extinguished by depletion of its flow, and combustion occurs totally in the catalyst. The jet ignition tube is then withdrawn from the fuel/air stream to avoid interferences in the mixing region that could cause flameholding upstream of the catalyst.

Extensive tests were conducted with diesel fuel in the mainstream air and natural gas in the opposed jet. Similar results are achievable for other pre-vaporized liquid fuels in the mainstream and for other gaseous jet fuels of comparable heating value (e.g., propane). Based on visual observation, operating conditions were stable at atmospheric pressure and 547K (525°F) preheat with jet to mainstream velocity ratios between 20 and 25. Air preheat is required to vaporize liquid fuels during lightoff and to sustain catalytic combustion once the opposed jet has been extinguished. Test results are shown in Fig. 3. As the mixture stoichiometry (including jet and mainstream fuels) is decreased toward stoichiometric, the lightoff temperature increases. The increasing adiabatic flame temperature of the mixture is shown for comparison. The actual temperature achieved at a given stoichiometry is dependent on the degree of mainstream fuel consumed. Less fuel is consumed near stoichiometric conditions due to increasing difficulty burning the liquid fuel droplets in a richer environment.

At 400 percent theoretical air, the combustor is operating with only opposed jet fuel at a temperature of 1005K (1350°F). Above 400 percent, flame cannot be stabilized in the combustor. At 100 to 150 percent theoretical air, the majority of the fuel is diesel. Below 150 percent theoretical air at the preheat and velocity conditions described, the stabilized flame could not be extinguished upon depletion of the jet flow.

The advantages of an opposed jet lightoff system are simplicity in design and operation, variable temperature control, and operation over a wide range of mixture ratios and mainstream velocities. The opposed jet provides a lightoff sequence, from jet ignition to catalyst stabilization, that can be tailored to meet system requirements. However, for full-scale system applications, practical techniques must be developed to incorporate the jet into the gas turbine combustor can(s) and to control the jet position and fuel flow.

Combustor Liner. The gas turbine combustor consists of 0.13 m diameter by 0.32 cm (1/8 in.) thick stainless steel tube with a 1.27 cm (1/2 in.) thick refractory housing around the catalyst bed. Since combustion occurs entirely within the bed, combustor liner film cooling is not required. Except at the catalyst location, measured liner temperatures do not exceed 1089K (1500°F). In the vicinity of the catalyst, a refractory housing prevents liner temperatures from exceeding 1422K (2000°F). A similar refractory catalyst housing design was employed successfully by other investigators [9].

Combustor Catalyst. The 0.13 m diameter catalyst consists of four 2.54 cm (1 in.) long segments of honeycomb ceramic monolith. A large cell size is used at the catalyst entrance and successively smaller cell sizes toward the catalyst exit. This graded-cell configuration permits stable combustion at gas velocities characteristic of conventional gas turbine combustors. For these tests, chromium oxide and a UOP, Inc. noble metal catalyst were deposited on two different reactors.

System Test Results

Stationary gas turbines operate over a wide range of preheat temperatures, fuel/air ratios, and heat release rates. To employ catalytic combustion in full-scale systems, the catalytic combustor must necessarily perform over similar operating conditions. A test program was performed to investigate both transient and steady state characteristics using the catalytic combustor described above. All tests were conducted with distillate fuel at combustor inlet temperatures of 644K to 756K (700°F to 900°F). Due to facility limitations, operating pressure was limited to 0.505 MPa (5 atmospheres). Transient and steady state system performance was evaluated using a chromium oxide catalyst. A UOP, Inc. noble metal catalyst was selected for a maximum throughput test based on its demonstrated high volumetric heat release capability [5]. Under nominal operating conditions, each catalyst achieved the same combustion exhaust emissions.

Transient Characteristics. The startup and shutdown performance of the gas turbine combustor is illustrated in Fig. 4, where catalyst temperature and NO_x emissions are plotted as a function of time. After the opposed jet is ignited, approximately 160 seconds are required to establish a steady state temperature of 1255K (1800°F). Mainstream fuel is then added to increase bed temperature to the desired operating level of 1700K (2600°F). During this interval, NO_x emissions are relatively high, characteristic of gaseous combustion by the opposed jet. When the jet is extinguished, combustion occurs entirely within the catalyst resulting in an immediate drop in NO_x emissions to a level of 15 ppmv. As shown, the time period required to ignite the opposed jet and stabilize the catalyst is 250 seconds. In contrast, stationary gas turbines typically achieve stable combustion at 1 atmosphere pressure in approximately 190 seconds. The catalyst lightoff transient is dictated primarily by the thermal mass of the test facility

Downloaded 01 Jun 2010 to 171.66.16.62. Redistribution subject to ASME license or copyright; see http://www.asme.org/terms/Terms_Use.cfm

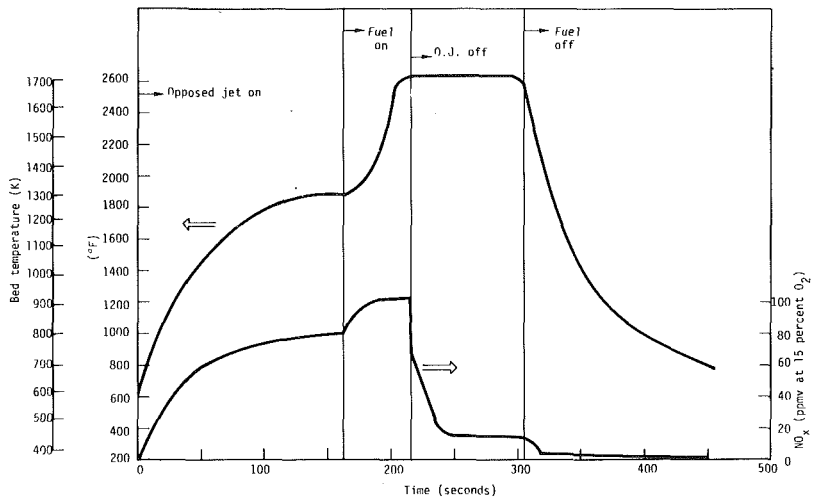


Fig. 4 Gas turbine combustor transient operation

hardware. Because the combustor can was housed within water-cooled test sections, the lightoff transient is unrealistically long and could be reduced to a time interval comparable to that found in stationary turbines. System shutdown is also displayed in Fig. 4. As expected, both temperature and NO_x emissions drop rapidly to ambient levels. Due to mechanical and thermal limitations, conventional gas turbines require an additional 150 seconds to achieve full speed, no-load combustor pressures of 0.505 to 1.01 MPa (5 to 10 atmospheres). Catalytic combustors respond rapidly to fluctuations in inlet conditions (i.e., pressure and throughput) and can match actual gas turbine requirements without impeding normal operation.

Catalytic reactors achieve high combustion efficiency only within a relatively narrow range of operating temperature (and hence stoichiometry). The lower temperature bound is set by combustion stability limits; the upper bound is set by catalyst and substrate material limitations. Depending upon the type of catalyst, stable combustion can be sustained over a 278K (500°F) range of catalyst temperature without serious loss of performance. This corresponds to typical fuel/air ratios of 0.0278 to 0.0202. In contrast, the overall stoichiometry for conventional gas turbines may vary by a factor of four to one. Typical values of fuel/air can vary from 0.006 at no load to 0.025 at peak load. Therefore, methods must be devised to sustain catalytic combustion over the broad range of conditions encountered in conventional systems. Two approaches appear promising: air distribution and fuel staging.

Although conceptually simple, air distribution may not be compatible with all gas turbine machinery. In this concept, air is distributed to the fuel mixing zone according to load. As fuel flow increases with load, proportional amounts of air are directed to the combustor head end to maintain catalyst reactor temperatures within allowable limits. Remaining air bypasses the catalyst and dilutes the combustion products downstream. The distribution of air to the catalyst is controlled by mechanically varying open area to the fuel mixing zone. At the extremes of low and high load conditions, the fraction of air passing through the catalyst varies from 30 to 85 percent. Altering the air flow pattern over this wide turndown ratio requires further design consideration.

The second technique for controlling catalytic temperature is fuel staging. This can be accomplished using either conventional and catalytic burners in combination or catalytic burners alone. For the former, combustion at low load conditions (low fuel/air ratios) can be supported using a conventional burner. Then, at full load conditions where overall stoichiometry is compatible with catalytic combustion, a catalytic reactor can be employed. An opposed jet, as in the configuration described above, could serve as a suitable pilot burner. The jet is stable over the required range of fuel/air ratios. This approach is most acceptable for machines that operate primarily at full load. However, for machines that undergo frequent cycling or run substantially at off-full load conditions, a conventional burner (or opposed jet) would generate unacceptably high NO_x emissions. To control NO_x emissions during cyclic operation, catalytic combustion must be used continuously. This can be accomplished by staging separate reactors in parallel. As fuel flow increases, additional reactors are brought on-line. For annular and coannular systems, separate combustors can be employed. For systems containing only a single combustor, a matrix of small reactors, each with separate igniters and fuel injectors, would be used. For either design, air entering inactive cans would pass directly through the catalyst and mix with combustion products. Anticipated problems include ignition and control of each reactor as well as adequate mixing of combustion products with dilution air prior to entry into the turbine.

At present, incorporating catalytic combustors into full-scale gas turbines remains a challenge to manufacturers. The ability of catalytic combustion to achieve very low NO_x emissions simultaneously with high combustion efficiency, however, provides the required incentive for further development.

Steady State Performance. Steady state testing of the gas turbine combustor was also performed to investigate thermal and fuel NO_x formation, maximum throughput capability, and combustion efficiency. Tests were conducted at preheat temperatures greater than 615K (647°F), flow velocities ranging from 6.1 to 15.3 m/s (20 to 50 ft/s), and combustor pressures from 0.101 to 0.505 MPa (1 to 5 atmospheres).

The fuel was No. 2 diesel which contained 0.035 weight percent nitrogen. Under fuel-lean conditions, greater than 80 percent conversion of fuel nitrogen to NO_x is expected (10). This would result in up to 15 ppmv of NO_x being emitted due to nitrogen contained in the fuel. During testing, total NO_x emissions averaged less than 25 ppm at combustor inlet temperatures ranging from 600K to 750K (620°F to 890°F). This indicates a value for thermal NO_x of less than 10 ppmv. These pollutant levels are substantially below the EPA's regulation of 75 ppmv NO_x for clean fuels. Test results are displayed in Fig. 5 along with conventional gas turbine

Downloaded 01 Jun 2010 to 171.66.16.62. Redistribution subject to ASME license or copyright; see http://www.asme.org/terms/Terms_Use.cfm

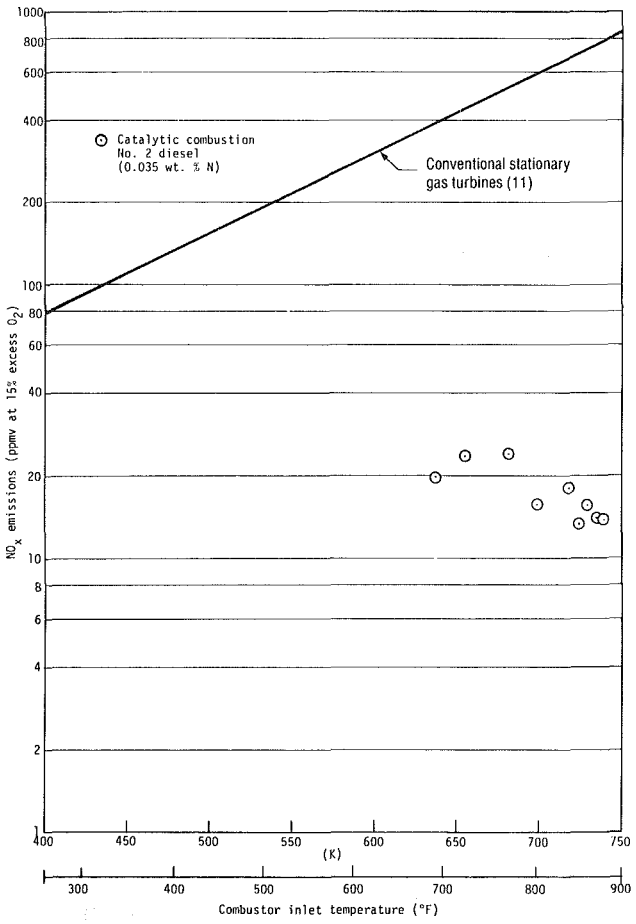


Fig. 5 Comparison of catalytic and conventional gas turbine thermal NO_x emissions

emissions obtained from reference [11]. As shown, conventional turbine emissions increase exponentially with combustor inlet temperature, whereas catalytic emissions are markedly below this level and are relatively independent of inlet temperature for catalyst temperatures up to 1700K (2600°F).

Fuel NO_x formation was investigated using diesel fuel doped with pyridine to 0.535 and 0.125 weight percent nitrogen. NO_x emissions corrected to 15% excess O_2 are presented in Fig. 6 as a function of pressure. A 2.0 weight percent chromium oxide catalyst was used for these tests. A gradual increase in fuel NO_x emissions with increasing pressure is apparent for diesel fuel with 0.535 weight percent nitrogen shown in the upper curve. The effect of pressure on NO_x is less pronounced for diesel fuel with 0.125 weight percent nitrogen. Also indicated in Fig. 6 are 1979 EPA NO_x emission regulations for both nitrogen content fuels. The 0.125 weight percent nitrogen fuel easily meets present EPA regulations over the range of pressures tested. However, for 0.535 weight percent nitrogen fuel, other control techniques such as two-stage catalytic combustion [12] are required to meet federal regulations.

The percentage conversion of fuel nitrogen to NO_x also shows a gradual increase with pressure as indicated in Fig. 7. Conversion percentages appear to be somewhat higher for the lower nitrogen concentration fuel. This result is consistent with data from Shaw [13] which shows the fractional conversion of fuel nitrogen to decrease with increasing fuel nitrogen content. The results are also supported by Carrubba [10] who reported 70 to 90 percent conversion of fuel nitrogen to NO_x based on propane doped with NH_3 and diesel fuel doped with pyridine.

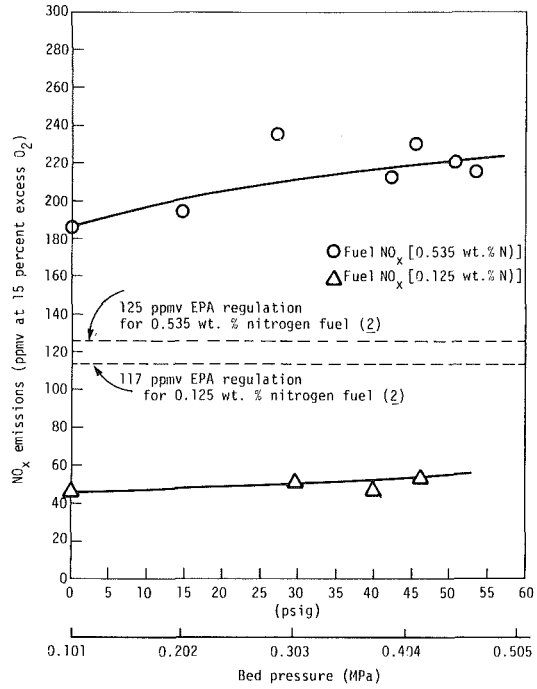


Fig. 6 Gas turbine combustor fuel NO_x emission data

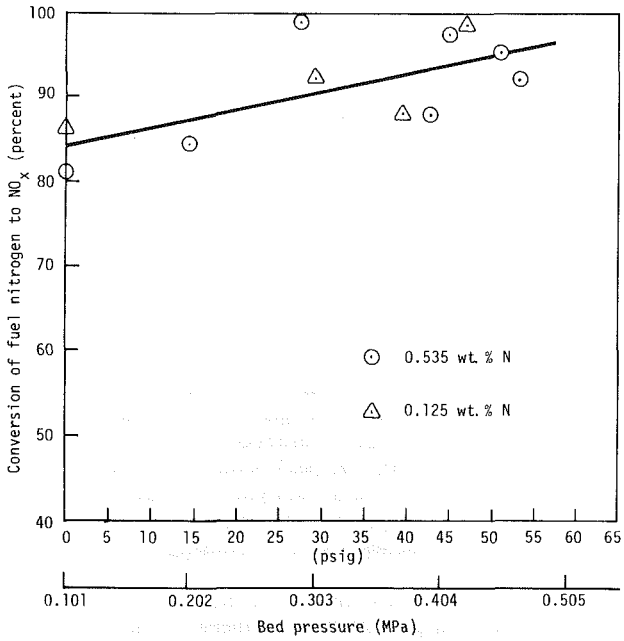


Fig. 7 Percentage fuel nitrogen conversion to NO_x

An additional fuel test was conducted in the small-scale combustor to evaluate catalyst performance at high heat release rate using a catalyst supplied by UOP, Inc. Ultimate throughput was limited by the air flow capacity of the test facility. A heat release rate of 1445 MJ/hr (28.64 MJ/hr-Pa-m^3 based on catalyst volume or 4.53 MJ/hr-Pa-m^3 based on combustor volume) was achieved at 0.505 MPa (5 atmospheres) with NO_x emissions of less than 25 ppmv (corrected to 15 percent excess O_2). The combustion efficiency was greater than 99.9 percent at bed temperatures greater than 1422K (2100°F) with total CO and UHC emissions less than 50 ppmv. This heat release rate corresponds to a reference gas velocity of 15.3 meters per

Downloaded 01 Jun 2010 to 171.66.16.62. Redistribution subject to ASME license or copyright; see http://www.asme.org/terms/Terms_Use.cfm

second (50 ft/s) and a residence time of 40 ms compared to 30.5 meters per second (100 ft/s) gas velocities and 30 ms residence times for typical stationary gas turbines at peak load.

As noted above, the maximum combustor heat release capability was not achieved due to test facility limitations. However, separate atmospheric tests using a smaller, but identical UOP, Inc. catalyst achieved a flow velocity of 39.6 meters per second (130 ft/s) while maintaining equivalent NO_x emissions and combustion efficiency. Similar flow velocities in the gas turbine combustor would result in a residence time of 18 ms which corresponds closely with stationary gas turbine performance.

Conclusions

A small-scale, distillate-fueled catalytic gas turbine combustor has been developed and shows great promise for reducing NO_x emissions to meet proposed federal standards. Air-atomized spray nozzles were used to provide rapid fuel vaporization at turndown ratios in excess of ten to one. Multiple point fuel injection enabled complete fuel vaporization and mixing to occur in a mixing zone with a length-to-diameter ratio of five. An opposed jet igniter provided controlled catalyst lightoff that can be tailored to the startup requirements of a particular gas turbine.

At steady state conditions, the small-scale combustor generated thermal NO_x below 10 ppmv at combustion efficiency greater than 99.9 percent. Fuel bound nitrogen conversion to NO_x ranged from 75 to 95 percent – typical of one-step lean combustion. For high nitrogen content fuels, staged combustion may be required to control NO_x emissions to projected standards. System startup, including catalyst lightoff, was performed in a time interval comparable to conventional gas turbines.

Compared to conventional gas turbine combustors, the catalyst operates within a relatively narrow range of fuel/air ratios. Air supply to the combustor must be distributed and/or staged combustion employed to maintain the catalyst within an acceptable temperature range. Substantial redesign of the conventional combustor may be required to implement these modifications and integrate the catalyst with full-scale machinery.

Despite the capability of catalytic combustion to control NO_x pollutants, catalyst and substrate materials have not demonstrated structural integrity and long life. The catalytic combustor performance reported here was evaluated over a relatively short 50 hour test period. However, system life times approaching 5000 hours are required for practical, full-scale applications. Aging studies have shown that, although substrate longevity can be achieved, serious catalyst degradation occurs at high pressure during 1000 hours of operation [14,15]. Current development of active substrates, with the catalyst element incorporated into the support rather than coated on the surface, appears promising for extended catalyst life.

References

1 Mason, H. B., et al., "Preliminary Environmental Assessment of Combustion Modification Techniques: Volume II, Technical Results," EPA-600/7-77-119b, NTIS-PB 276 681/AS, Oct. 1977.

2 *Federal Register,* Vol. 44, No. 176, Sept. 10, 1979.

3 Larkin, R., et al., "Environmental Assessment of Combustion Modification Controls for Stationary Gas Turbines," Acurex Final Report TR-79-18/EE, Acurex Corporation, Energy & Environmental Division, Mountain View, Calif., June 1980.

4 Pfefferle, W. C., et al., "CATATHERMAL™ Combustion: A New Process for Low-Emissions Fuel Conversion," ASME Paper 75-WA/Fu-1, Nov. 1975.

5 Kesselring, J. P., et al., "Design Criteria for Stationary Source Catalytic Combustion Systems, EPA-600/7-79-181, Aug. 1979.

6 State of California Air Resources Board, Staff Report 78-10-1, Apr. 1978.

7 Kesselring, J. P., et al., "Recent Advances in Catalytic Combustion System Development," ASME Paper 79-WA/Fu-8, Dec. 1979.

8 Anderson, S. J., et al., "Fuel Injector, Ignition, and Temperature Measurement Techniques for Catalytic Combustors," *Proceedings: Fourth Workshop on Catalytic Combustion,* EPA-600/9-80-035, Aug. 1980.

9 Lew, H. G., et al., "Experimentally Determined Catalytic Reactor Behavior and Analysis for Gas Turbine Combustors," ASME Paper 79 GT-150, Mar. 1979.

10 Carrubba, R. V., Chang, M., Pfefferle, W. C., and Polinski, L. M., "Catalytically Supported Thermal Combustion for Emission Control," presented at the EPRI NO_x Control Technology Seminar, San Francisco, Calif., Feb. 5-6, 1976.

11 Goodwin, D. R., et al., "Standard Support and Environmental Impact Statement, Vol. 1: Proposed Standards of Performance for Stationary Gas Turbines, EPA-450/2-77-017a, NTIS-PB 272 422/7BE, Sept. 1977.

12 Krill, W. V., et al., "Catalytic Combustion System Applications," ASME Paper 79-HT-54, Aug. 1979.

13 Shaw, H., "The Effects of Water, Pressure, and Equivalence Ratio on Nitric Oxide Production in Gas Turbines," ASME JOURNAL OF ENGINEERING FOR POWER, Vol. 96, No. 3, July 1974, pp. 240-246.

14 Heck, R. M., et al., "Durability Testing at One Atmosphere of Advanced Catalysts and Catalyst Supports for Automotive Gas Turbine Engine Combustors," CONS/9416-1, NASA CR-135132, June 1977.

15 Osgerby, I. T., et al., "CATCOM™ Catalyst 5 atm 1000 Hour Aging Study Using #2 Fuel Oil," *Proceedings: Fourth Workshop on Catalytic Combustion,* EPA-600/9-80-035, Aug. 1980.

Downloaded 01 Jun 2010 to 171.66.16.62. Redistribution subject to ASME license or copyright; see http://www.asme.org/terms/Terms_Use.cfm

Use of Cascade and Small Turbine Tests to Determine Erosion of Utility Turbines

R. A. Wenglarz
Westinghouse Research and Development Center, Pittsburgh, Pa.

M. Menguturk
Department of Mechanical Engineering, Bogazici University, Istanbul, Turkey

Experiments using cascades and small turbines have been conducted or are being considered to simulate large utility turbine operation with future coal-fired power plants. The purpose of these experiments is to evaluate utility turbine tolerances to particulates and to determine gas cleanup requirements for successful turbine performance. Since these tests do not fully reproduce the flow and erosion conditions in large utility turbines, this paper explores the interpretation of data from simulation experiments to assess erosion in large utility turbines. Effects of physical scale, rotation speed, and pressure differences between test cascades and small test turbines and large utility turbines are considered.

Introduction

Many of the advanced power plants being considered for utilization of coal derived fuels require large combustion turbine operation with expansion gases containing particulates. These gases must be cleaned prior to entering the turbine in order to reduce erosion, deposition, and corrosion to levels which enable acceptable turbine performance, reliability, and availability. Since large utility turbines have not previously expanded gases containing the particulates produced by advanced coal fired power plants, the degree of gas cleanup necessary for acceptable turbine operation is not yet known.

Several cascade and small turbine experiments have been conducted [1,2] or are being considered for evaluating utility turbine tolerance to coal derived fuels, especially pressurized fluidized bed combustion (PFBC) gases. Such tests are essential to determining gas cleanup requirements for successful turbine operation. However, a cascade or small test turbine cannot fully reproduce the flow and erosion environment of a large utility turbine. Consequently, the question arises as to what extent do cascade and small turbine test results indicate tolerances of large utility turbines.

This paper evaluates differences between the erosion environments produced in large utility turbines and cascades or small turbines. Some effects on erosion of physical scale, rotation speed, and test pressure are quantified. The question of the extent which cascade and small turbine test results indicate erosion tolerances of large utility turbines is explored.

Differences Between Simulators and Utility Turbines

Large utility turbines typically operate at mass flow rates of 227 kg/s (500 lb/s) to 454 kg/s (1000 lb/s). Existing advanced coal fired pilot plants and combustion simulation facilities typically provide about two orders or magnitude lower mass flow rates. Consequently, the cascades and test turbines that have been considered to evaluate turbine tolerance to coal derived fuels have typically been quite small compared to utility turbines. Their small flow passage areas provide at acceptable experimental cost the high gas velocities necessary to simulate utility turbine erosion environments. In many cases, small cascade and test turbine simulators have also been operated at lower inlet pressures than utility turbines to provide the necessary high gas velocities with yet lower mass flow rate requirements.

Turbine design practice for high efficiencies and acceptable rotor stresses results in rotor trip speeds in the vicinity of 305 m/s (1000 ft/s). Consequently, small diameter turbines (with low mass flow rates for relatively inexpensive experiments) rotate at much higher speeds than large utility turbines.

Some major differences between small cascades and small test turbines and large utility turbines are then:

i scale differences
ii rotation speed differences
iii operating pressure differences

For example, chord lengths of the vanes of a cascade tested at both the EXXON and Leatherhead PFBC pilot plants were less than 0.25 of the stator chord lengths of large utility turbines and the vane passage chord length is even smaller for the turbine that has been tested at the NASA PFBC pilot plant. Rotation speeds for large utility turbines typically range from 3000 to 4000 rpm. On one hand, the rotation speeds for small turbines (mass flow rate < 10 lb/s) typically approach order of magnitude higher values while on the other hand cascade tests simulate a nonrotating environment (0 rpm). Several PFBC pilot plant cascade tests have operated at about 5 atmospheres inlet pressure while turbine inlet pressures considered for many future PFBC power plants range up to 10 or 15 atmospheres. Some effects on erosion of operating pressure, scale, and rotation speed differences

Contributed by the Gas Turbine Division of THE AMERICAN SOCIETY OF MECHANICAL ENGINEERS and presented at the Gas Turbine Conference and Products Show, March 9-12, 1981, Houston, Texas. Manuscript received at ASME Headquarters, December 9, 1980. Paper No. 81-GT-52.

Copyright © 1982 by ASME

Downloaded 01 Jun 2010 to 171.66.16.62. Redistribution subject to ASME license or copyright; see http://www.asme.org/terms/Terms_Use.cfm

between large utility turbines and cascades or small test turbines are described in the following sections.

Pressure Effects

Erosion rate e of an object (e.g., vane or blade) in a channel of area A containing a gas flowing at velocity V with uniformly entrained particles is related to the particle arrival rate r per unit area multiplied by V to a power n which experimentally has been shown to range from 2 to 3 from most materials.

$$e \alpha \frac{r}{A} V^n \tag{1}$$

The particle mass arrival rate r is related to the gas mass flow rate $\dot{m}$ multiplied by the particle concentration. When the particle concentration c is expressed in the usual standard condition terms of grains/standard cubic feet (gr/scf) or parts per million (ppm).

$$r \alpha \dot{m}\, c \tag{2}$$

where by the continuity equation,

$$\dot{m} = \zeta\, VA \tag{3}$$

Gas density ζ is written in terms of gas pressure P, temperature T and a constant R using the gas equation of state.

$$\zeta = P/RT \tag{4}$$

Substitution of equations (2-4) into equation (1) gives

$$e \alpha c \frac{P}{T} V^{n+1} \tag{5}$$

Equation (5) suggests that erosion rates measured in a simulation which provides the same gas velocity and particle concentration (expressed in gr/scf or ppm) as a utility turbine should approximately be scaled by the ratio of P/T for the gas turbine to P/T for the simulator to be indicative of erosion rates in the turbine. For example, erosion rates measured in full scale stator cascade vane tests conducted at an inlet pressure of 5 atmospheres are about a factor of 3 lower than erosion rates for a represented first stage turbine stator which operates at 15 atmospheres inlet pressure (assuming the same cascade and turbine inlet temperatures, gas velocities, particle concentrations expressed in gr/scf or ppm and passage geometries).

Scale Effects

Primary Flows. In the following, relative erosion rates are obtained for a large utility turbine first stage stator vane passage scaled from full size down to one-fourth size while maintaining the same velocity triangles. These evaluations provide an indication of the relative rates of erosion that might be experienced in a typical large utility turbine stator compared to erosion rates for small scale cascades or small turbine stators with the same velocity triangles. This initial analysis considers only the effects on erosion of the primary flow field in the stator. Secondary flow effects will be considered later.

In Fig. 1, the nature of similitude used for stator vanes is illustrated. Passage mean radius, height, and axial chord are reduced by the scale factor, k, while the angular circumferential coordinates are kept the same.

A turbine erosion damage model [3,4] has been used to evaluate effects of varying scale factor k on stator erosion. For this model, the flow velocity field in turbine flow passages are determined with a standard computer program used by turbine designers. Aerodynamic forces on particles are calculated and particle equations of motion are integrated to obtain particle trajectories and impact angles, velocities, and

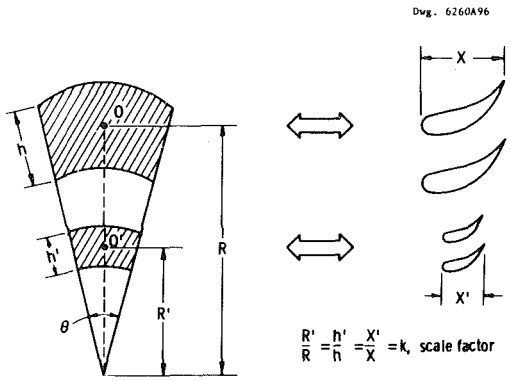


Fig. 1 Geometric similitude for stator passages. Unprimed variables refer to full size turbine, primed variables to scaled-down model

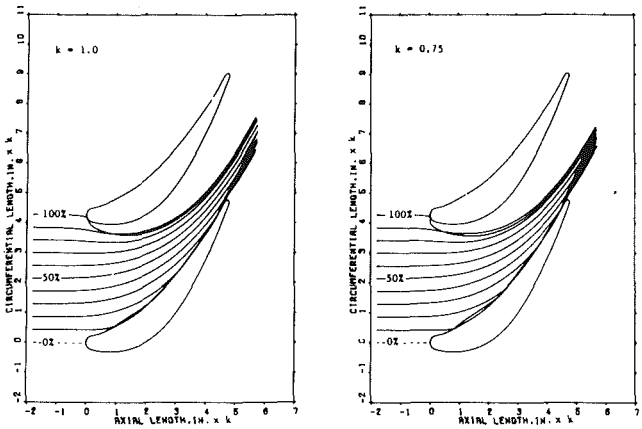


Fig. 2 9μm particle trajectories in full-scale and 3/4-scale stator passages

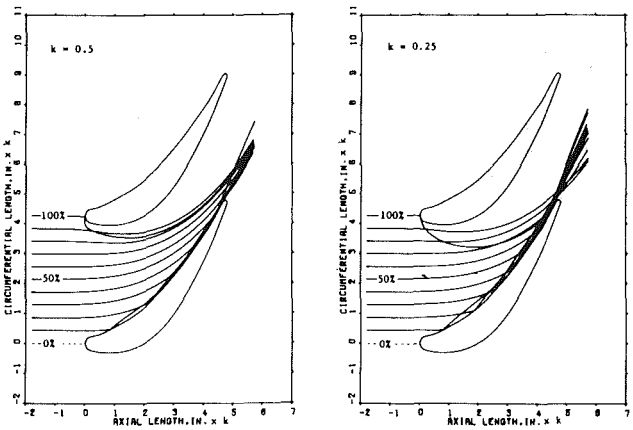


Fig. 3 9μm particle trajectories in 1/2-scale and 1/4-scale stator passages

locations in addition to rates of particle arrival. Empirical data for turbine material removed as a function of impact angle and velocity are then used to determine erosion rates versus location on the vane and blade surfaces. Results using the turbine erosion damage model will be here presented only for nine micron diameter particles. However, conclusions derived are qualitatively applicable for all sizes.

In Figs. 2 and 3, particle trajectories obtained with the erosion model are shown in the stator passages with k = 1, 3/4, 1/2, and 1/4. The axes in these figures are scaled in such a way that the stator vanes appear to be of the same size for all scale factors. In this way, it is possible to see the deviation in the trajectories. In each case, particles are given a uniform

Downloaded 01 Jun 2010 to 171.66.16.62. Redistribution subject to ASME license or copyright; see http://www.asme.org/terms/Terms_Use.cfm

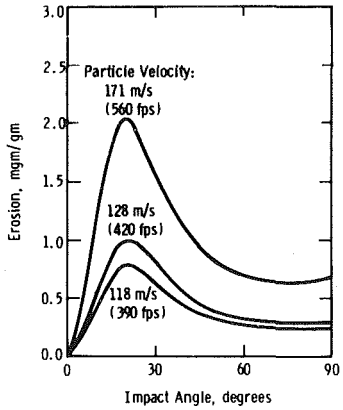


Fig. 4 Erosion results obtained for alumina particles impacting 2024 aluminum alloy

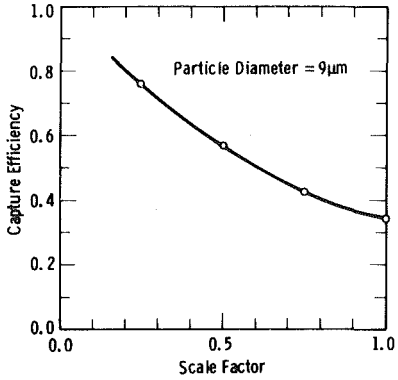


Fig. 5 Effect of scale factor on capture efficiency (capture efficiency = number of particles that hit blade surface/total number of particles at inlet)

distribution over the passage inlet and are assumed to be entering at the gas velocity. It is apparent from these figures that geometric scaling has a definite effect on the particle trajectories. The smaller the scale factor, the less able are the particles to follow the gas streamlines. This is not surprising, because, although the geometric boundaries and the flow streamlines are similar, and the velocities are equal at points of correspondence, the time and physical space available for particles to respond to flow accelerations and turning are directly reduced by the scale factor. Therefore, particles tend to deviate more and more from the gas field as the stator dimensions are decreased. This has an important bearing on the erosion damage. As will be described in greater detail, decreasing time for particles to respond to flow accelerations and turning in flow passages of decreasing scale results in (i) lower particle impact velocities, (ii) higher particle impact angles and (iii) higher particle capture efficiencies. (Capture efficiency is the fraction of particles entering the passage that impact the vanes). Lower impact velocities tend to produce lower erosion rates for smaller scales while higher capture efficiencies tend to produce higher erosion rates. Higher impact angles also tend to produce higher erosion rates for smaller scales because vane trailing edge impact angles tend to more closely approach the angle of maximum impact damage for turbine materials. Observations from materials erosivity data for a typical ductile alloy illustrates effects of particle impact angle and velocity.

Figure 4 gives erosion data collected by Grant [5] for impacts of alumina particles (of 100 μm dia.) on 2024 aluminum alloy. Although the rate of damage will be different for different materials, particle size, etc., the general shape of the curves is typical for turbine alloys and most ductile materials. Maximum erosion occurs at angles between 20 and 30 deg,[1] and the specific erosion rate (mgm of material eroded per gm of particles hitting surface) is a function of at least the square of impact velocities.

Under the light of these observations, we can now study the changes in impact parameters and determine their effect on the erosion damage. The increase in particle capture efficiency (and corresponding number of particle impacts) for decreasing scale of the vane passage described above is shown in Fig. 5. Impact velocities and angles for various scale factors are shown in Figs. 6 and 7, respectively. In accordance with the reasoning presented before, smaller scale factors imply larger deviations from the gas flow, and consequently,

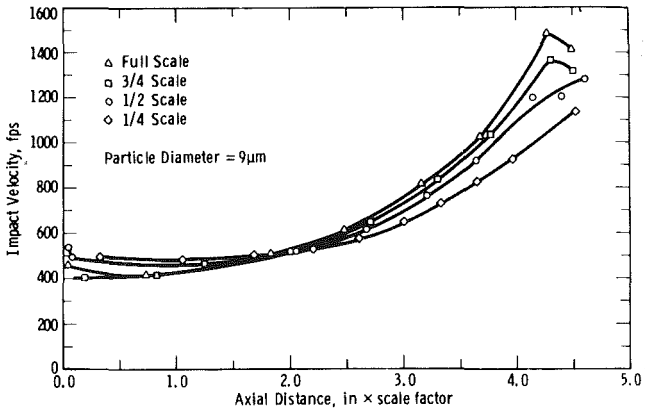


Fig. 6 Effect of scale factor on particle impact velocities

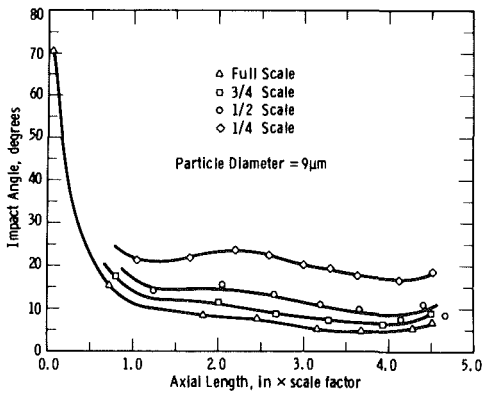


Fig. 7 Effect of scale factor on particle impact angles

corresponding particle velocity curves are flatter. Except for a small region at the leading edge, impact velocities tend to decrease as the scale is reduced. The overall effect is a considerable tendency to decrease erosion damage. The impact angles plotted in Fig. 7 tell a different story. The angles increase with a decrease in scale factor because the particle lag behind the gas flow increases, and the particles approach the vane surface with smaller curvatures. However, the effect of this phenomenon on erosion is mostly in a direction opposite to the velocity effect. With 9 μm particles, the impact angles are around 7 deg for most of the full-scale vanes. One-fourth scale factor raises the impact angles to about 20 deg where maximum erosion should occur for the material of Fig. 4. This results in a steep increase in the erosion rate.

[1] For brittle materials, maximum erosion angle shifts toward 90 deg. (The impact angle is defined as the acute angle formed by the tangent to the surface and the velocity vector).

Downloaded 01 Jun 2010 to 171.66.16.62. Redistribution subject to ASME license or copyright; see http://www.asme.org/terms/Terms_Use.cfm

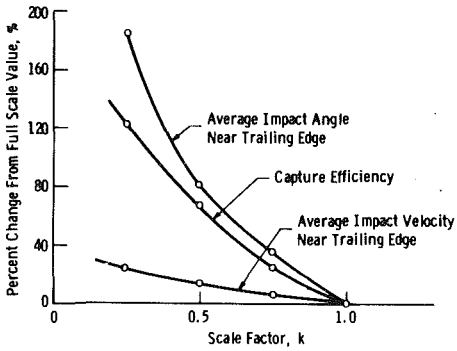


Fig. 8 Percentage change from full scale value as a function of scale factor shown for capture efficiencies and impact velocities · angles averaged near trailing edge. Particle diameter = 9μm

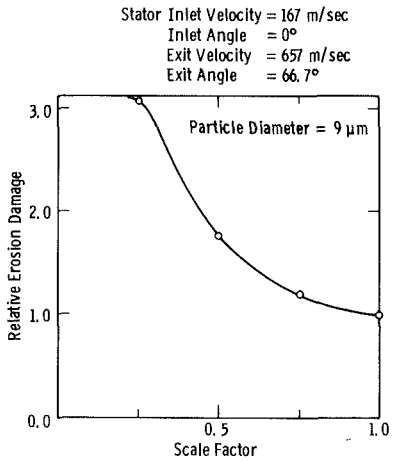


Fig. 9 Total erosion rate in first stage stator as a function of scale factor

The above results indicate the strong dependence of erosion on the scale factor. This dependence has been established through the variations in particle capture efficiencies, impact velocities, and impact angles. In order to emphasize this point, the percentage changes in capture efficiencies, impact velocities, and impact angles from their full-scale values are plotted in Fig. 8 as a function of the scale factor. Since the impact velocities and angles are also a function of the axial distance, their average values are taken near the trailing edge where the erosion damage is greatest for the 9 μm particles.

In Fig. 9 total relative erosion damage in the stator is plotted as a function of scale factor. The relative erosion damage was determined for a typical ductile alloy with an angle of maximum erosion in the vicinity of 20 deg. For this representative utility turbine vane passage, the combined effects of higher particle capture efficiencies and higher impact angles outweigh the effect of lower impact velocities for decreasing scale factors and erosion tends to increase with decreasing scale. Figure 9 indicates that the total erosion rate due to nine micron particles for the one-fourth scale vane is about three times that for the full-scale vane. Although results are shown in Fig. 9 only down to one-fourth scale, for further decreasing scales a maximum in relative erosion might be expected followed by a fairly rapid drop in erosion. This corresponds to the particle impact angles over much of the surface reaching the angle of maximum damage for the ductile material after which larger impact angles result in decreased erosion.

Secondary Flows. The above scale effects are associated with the primary flow field in turbine passages. Erosion associated with secondary flows is also expected to be influenced by scale effects. Past small turbine tests have revealed high local erosion on vanes and blades due to highly localized particle concentrations caused by secondary flows. The larger dimensions of utility turbines enable greater secondary flow development compared to small cascades and test turbines but the boundary layers tend to occupy a smaller fraction of the flow areas for large turbines resulting in lower secondary flow intensities at any particular stage of development. Consequently, it is not obvious whether the net effect results in higher or lower local erosion in large utility turbines compared to small cascades or test turbines. Although effects of secondary flows on particle trajectories have been analyzed [6], apparently no evaluations have been conducted that quantify the effect of scale on localized erosion due to secondary flows.

Rotation Effects

Fixed Cascades. Substantial uncertainties can result in attempts to extrapolate erosion results measured in fixed cascade vane experiments to turbine rotors. The erosion environments produced in fixed vane passages (such as in cascade tests) are significantly different from the erosion environments produced in rotating blade passages. For erosion of rotor blades, particle motion depends on their *absolute* velocities and directions in a fixed reference frame (Newton's equations of motion are satisfied in an inertial reference frame) while damage due to the particle impacts depends on their *relative* velocities and directions with respect to the rotating blade. A fixed cascade vane experiment does not simultaneously produce both the absolute velocities and directions of particle flight and the relative impact velocities and directions that occur in rotating blade passages.

Figures 10 and 11 show results of applying the erosion damage models to the first stage stator and rotor of a large utility turbine for a particle loading and distribution representative of the carryover from a pressurized fluidized bed combustor after three stages of cyclone cleanup. These figures give representative erosion rates (for U-710 alloy and its oxide scale erosion response) versus axial position on the vane and blade measured in fraction of axial chord distance from the leading edge. The zero value of axial chord fraction corresponds to the leading edge and positive and negative values correspond to axial distances from the leading edge on the pressure surface and suction surface, respectively.

Even though the stator and rotor are of about the same scale and the stator exit gas velocity is several hundred feet per second higher than the exit gas velocity relative to the rotor, Figs. 10 and 11 indicate that the greatest erosion rate on the rotor is about ten times the greatest erosion rate on the stator. The higher rotor erosion rates mainly result from higher particle capture efficiencies and higher trailing edge impact angles which are closer to the angles of maximum impact damage for turbine materials. For example, Table 1 compares the stator and rotor capture efficiencies versus particle size. The rotor capture efficiencies for all particle diameters from 1 to 12 μm are about three times greater than the stator capture efficiencies.

Table 1 Comparison of stator and rotor capture efficiencies

Particle Size (Microns)	Stator Capture Efficiency	Rotor Capture Efficiency	Ratio of Rotor to Stator Capture Efficiency
1	0.02	0.07	3.5
3	0.07	0.21	3.0
6	0.16	0.53	3.3
9	0.25	0.98	3.9
12	0.35	1.00	2.9

Downloaded 01 Jun 2010 to 171.66.16.62. Redistribution subject to ASME license or copyright; see http://www.asme.org/terms/Terms_Use.cfm

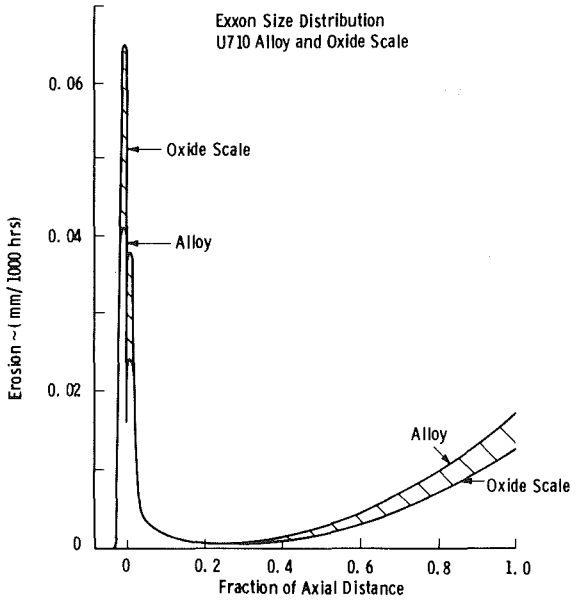


Fig. 10 10:1, 50 MW turbine stator erosion rates for 58 ppm (0.033 gr/scf) particle loading

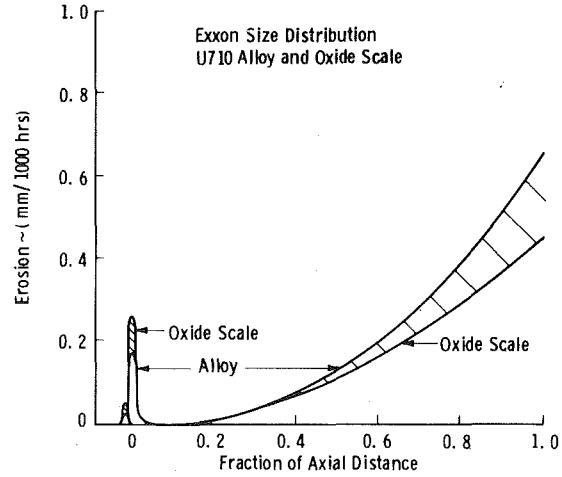


Fig. 11 10:1, 50 MW turbine rotor erosion rates for 58 ppm (0.033 gr/scf) particle loading

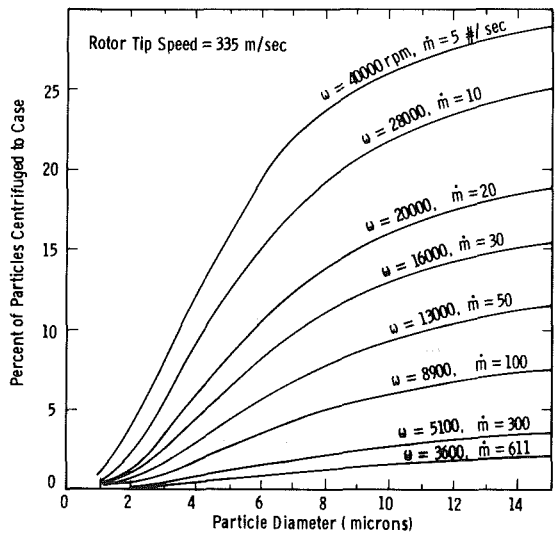


Fig. 12 Particle centrifuging in first rotor versus turbine rotation speed

Small Turbines. The following considers the use of measured rotor erosion rates in small turbine tests to assess erosion rates in large utility turbines. While cascade simulators can provide ony stationary erosion environments, small turbines rotate at speeds up to 40,000 rpm or higher compared to 3000 to 4000 rpm for large utility turbines. The much higher rotation speeds for small turbines result in higher centrifugal forces on particles to cause migration of particles to tip regions and rebounds off end walls. The result can be a substantially different erosion environment from the first rotor through all downstream stages for a small machine compared to utility machines for which centrifugal effects are relatively small.

An approximate analysis has been used to evaluate centrifugal effects. Some of the results are given in Fig. 12. In this figure, the percent of particles entering the first rotor that are centrifuged to the end wall before exiting the rotor is plotted against particle diameter for turbines of mass flow rates ranging from 611 lb/s (3600 rpm) to 5 lb/s (about 40,000 rpm). For the large utility turbine (611 lb/s mass flow rate) only a few percent of the particles less than 15 μm in diameter are centrifuged to the end wall while for the smaller turbines over 20 percent of the larger particles are centrifuged to the end wall.

These results were obtained for conceptual turbines, all having the same design variables (rotor tip speed, velocity triangles, etc.) as those for the existing large utility turbine. However, it is important to note that the degree of centrifuging is substantially affected by axial gas velocity, blade axial chord and other turbine design variables in addition to rotation speed. For example, the amount of particle centrifuging is significantly affected by the ratio of rotor blade axial chord to average axial gas velocity in the rotor passage which approximates the time that particles are subjected to rotor centrifugal forces. Consequently, an assessment of centrifugal effects for any small machine requires an evaluation using its particular design variables.

Interpretation of Cascade and Small Turbine Tests

Some bases have been provided for evaluating small cascade and turbine tests to predict erosion performance of large utility turbines. Since velocity triangle effects can be significant, the following comments refer to extrapolation of small cascade or small turbine erosion results to large utility turbines with equivalent flow velocities and flow turning angles. For dissimilar velocity triangles, the turbine erosion modeling techniques applied to the specific cascade or small turbine and the utility turbine configurations can be used to extrapolate test results.

The above discussions indicate that cascade and small turbine experiments typically do not directly yield erosion rates and erosion tolerances of large utility turbines. Erosion rates measured in simulation tests could differ from utility turbine erosion rates by factors of three up to perhaps as much as an order of magnitude. Measured erosion rates from tests conducted at equivalent gas velocities and particle loadings (expressed in gr/scf or ppm) but at lower pressures than the utility turbine simulated should be scaled by the ratio of utility turbine to test pressure (usually gas temperatures are reproduced for corrosion evaluations).

The previously described results also indicate that erosion rates for large utility turbine stators may be less than erosion rates measured on small scale cascade vanes ingesting the same particle loadings. Because fixed cascades do not produce erosion conditions in rotors, erosion rates for utility turbine rotors may be much higher than erosion rates measured on

Downloaded 01 Jun 2010 to 171.66.16.62. Redistribution subject to ASME license or copyright; see http://www.asme.org/terms/Terms_Use.cfm

small cascade vanes. The magnitude of the difference in erosion rates between a utility turbine and a cascade depends to a great extent on specific velocity triangles and scale differences.

Large utility turbine stators may experience lower erosion rates than small turbine stators due to scale effects. If centrifuging in a small turbine test is so great that a substantial percentage (perhaps above 20 percent) of the most erosive large particles entering the first rotor passage migrate to the end wall before exiting the rotor, the erosion data may be so difficult to interpret as to be inferior to fixed cascade test data in terms of extrapolation to large utility turbines. For high centrifuging, particle rebounds from the end wall and three-dimensional effects such as particle flight through regions of changing velocity triangles and blade contours due to blade twist could produce erosion environments quite unrepresentative of those in large utility turbines. Since turbines of different designs, but with similar mass flow rates and rotation speeds could produce significantly different centrifuging effects, a careful choice of test turbines can facilitate obtaining interpretable data. Although a small turbine that minimizes centrifuging may have significantly different velocity triangles from the large utility turbine being simulated, the effect of velocity triangle differences on erosion may be more readily evaluated than high centrifuging effects.

Local erosion in large utility turbines due to secondary flows may possibly be higher than secondary flow erosion measured in either small cascade or small turbine tests. Of particular concern may be possible increased local concentration of particulates due to secondary flows and resulting local erosion through successive turbine stages since most small turbine tests to date have utilized single stage turbines. Since scale effects on erosion produced by secondary flows have apparently not been quantified, these effects are a major uncertainty in establishing erosion tolerances of utility turbines to PFB combustion gases and other coal derived fuels.

Acknowledgment

This work was supported by EPRI under the direction of William W. Slaughter, Fossil Fuel and Advanced Systems Division.

References

1 Hoy, H. R., and Roberts, A. G., "Investigations on the Leatherhead Pressurized Facility," *Proceedings of the 6th International Conference on Fluidized Combustion*, Atlanta, Georgia, Apr. 9–11, 1980.

2 Moskowitz, S., "Pressurized Fluidized Bed Combined Cycle," *Turbomachinery International*, Mar. 1980, pp. 36–39.

3 Sverdrup, E. F., Archer, D. H., and Menguturk, M., "The Tolerance of Large Gas Turbines to 'Rocks', 'Dusts', and Chemical Corrodants," *Proceedings of the EPA/DOE Symposium on High Temperature Particulate Control*, EPA-600/9-78-004, CONF-770970 Sept. 1977.

4 Menguturk, M. and Sverdrup, E. F., "Calculated Tolerance of a Large Utility Gas Turbine to Erosion Damage by Coal Ash Particles," from *Erosion: Prevention and Useful Applications*, edited by W. F. Adler, American Society for Testing and Materials Special Technical Publication 664, 1979.

5 Grant, G., "Model to Predict Erosion in Turbomachinery Due to Solid Particles in Particulated Flow," University of Cincinnati, Ph.D. Thesis, 1973.

6 Ulke, A., and Rouleau, W. T., "The Effects of Secondary Flows on Turbine Blade Erosion," ASME Paper 76-GT-74, 1976.

Addendum

Subsequent evaluations have further clarified the interpretation of fixed cascade erosion experiments to determine erosion of turbine rotors. In the comparison of stator erosion rates to rotor erosion rates for a large utility turbine which were given in this paper, two major factors affect the order of magnitude higher erosion rates on the rotor compared to the stator. These two factors are (*a*) rotation effects and (*b*) the much greater flow turning angles for the rotor compared to the stator. The greater flow turning is the major contributor with the rotation effects contributing less than a factor of 1.5 to the order of magnitude higher rotor erosion rates. However, for fixed cascade erosion simulation of high rpm small turbine rotors, the rotation effects are likely much greater.

The foregoing results suggest that:

- Fixed cascade experiments should simulate relative gas velocities with respect to the turbine rotor since the highest first stage erosion rates in utility turbines occur on the rotor.
- Even then, measured erosion rates on a fixed cascade of the same scale as the rotor being simulated will be somewhat lower than for the rotor.

Downloaded 01 Jun 2010 to 171.66.16.62. Redistribution subject to ASME license or copyright; see http://www.asme.org/terms/Terms_Use.cfm

Improved Particle Trajectory Calculations Through Turbomachinery Affected by Coal Ash Particles

B. Beacher
Graduate Research Assistant,
Student Mem. ASME

W. Tabakoff
Professor.

A. Hamed
Professor,
Mems. ASME

Department of Aerospace Engineering
and Applied Mathematics,
University of Cincinnati,
Cincinnati, Ohio

Trajectories of small coal ash particles encountered in coal-fired gas turbines are calculated with an improved computer analysis currently under development. The analysis uses an improved numerical grid and mathematical spline-fitting techniques to account for three-dimensional gradients in the flow field and blade geometry. The greater accuracy thus achieved in flow field definition improves the trajectory calculations over previous two-dimensional models by allowing the small particles to react to radial variations in the flow properties. A greater accuracy thus achieved in the geometry definition permits particle rebounding in a plane perpendicular to the blade and flow path surfaces rather than in a two-dimensional plane. The improved method also accounts for radial variations in airfoil chord, stagger, and blade thickness when computing particle impact at a blade location.

Introduction

Turbine blade erosion in coal-fired gas turbines has long been recognized as a serious problem for the gas turbine industry. Particle separators and cyclones can remove a large percentage of the damaging fly ash particles, but significant amounts of small particles ranging in size between 1 and 20 μm still pass through and enter the turbine. These particles do erode the blade surfaces and result in an unacceptably short operating life. A thorough understanding of these particles' paths through the turbomachinery is required if the erosion process is to be minimized.

A study of the particle dynamic characteristics in the turbine environment was performed by Hussein and Tabakoff [1], resulting in the development of a digital computer model [2] that predicted particle trajectories and velocities. The three-dimensional equations of motion of the particles moving in a compressible gas flow were derived in a general form, assuming that the fluid drag is the only significant force acting to produce particle acceleration. Experimental data was used to develop a rebound model to predict both magnitude and direction of particle velocities after impact with the blade surface. However, the application of these equations was restricted to inviscid flow in a two dimensional blade-to-blade channel, assuming no radial gradients in either geometry or gas flow properties. Although adequate for relatively large particles, this two-dimensional representation will not predict accurate trajectories for small particles of the size found in coal ash when significant radial variations exist, such as those related to secondary flow fields and twisted blading. The three-dimensional aspects of the environment could be approximated by performing the analysis repeatedly over many sections, but the task is quite laborious. Greater accuracy and simplification are achieved when blade geometry and gas properties are continuously defined by three-dimensional array on which interpolation can be done. Further improvement is also achieved by applying the empirical rebound correlations in a plane normal to the blade surface rather than in a cylindrical plane.

Ulke and Rouleau [3] recognized the effects of secondary flows on the motion of particulates in the turbine by superimposing these flows on the primary flow field through a guide vane-rotor stage. However, the primary flows they used were characterized by fictitious streamlines passing through the geometric centers of the blade channels. These one-dimensional flow representations ignored both radial and blade-to-blade variations in the main flow that normally exist in turbomachinery. An additional restriction was imposed on the blade shapes, requiring radially constant cross-sections, based upon their profiles at mid span. The results of their study did indicate the importance of the passage vortex and of the flows in blade wakes and boundary layers upon the trajectory calculations of particles of small inertia. In fact, the motion of these particles is strongly dependent upon any velocity gradients that occur in either the main flow or in secondary flows. Ultimately, the complete three-dimensional, compressible, viscous flow field must be defined if an accurate trajectory analysis is to be obtained.

Three-Dimensional Representation of Particle Environment

During the past few years, several numerical analyses have been under development that describe the three dimensional flow field through turbomachinery, so it remains to develop a

Contributed by the Gas Turbine Division of THE AMERICAN SOCIETY OF MECHANICAL ENGINEERS and presented at the Gas Turbine Conference and Products Show, March 9-12, 1981, Houston, Texas. Manuscript received at ASME Headquarters December 9, 1980. Paper No. 81-GT-53.

Copyright © 1982 by ASME

Downloaded 01 Jun 2010 to 171.66.16.62. Redistribution subject to ASME license or copyright; see http://www.asme.org/terms/Terms_Use.cfm

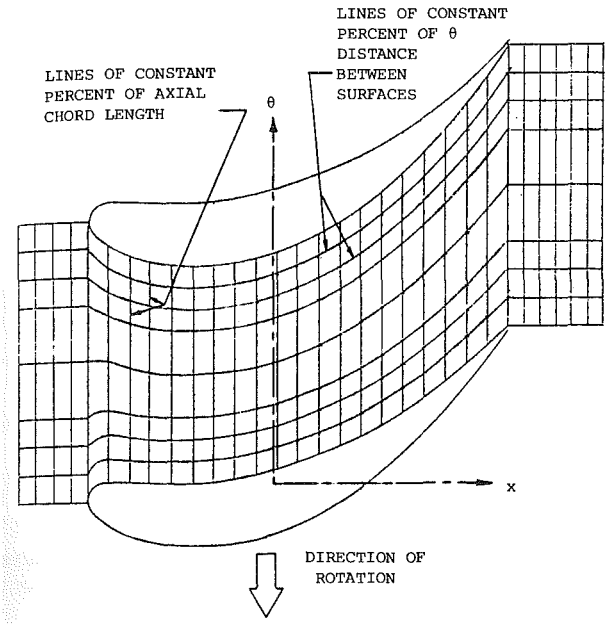


Fig. 1 Computational grid for a typical rotor cascade section

method of modeling the results of such analyses in a particle trajectory program. In general, the blade geometry and flow field properties of a given configuration are known only on discrete surfaces of revolution such as axisymmetric stream surfaces and plane manufacturing sections. Before a numerical algorithm can be used to interpolate among these known quantities, an internally consistent three-dimensional grid must be established. This grid is composed of sections of constant radius, and on each section an elastic mesh is formed. Figure 1 illustrates this mesh for a typical turbine rotor section, showing grid lines at constant percentages of axial and tangential spacing. Blade surface coordinates are defined independent of the mesh, at certain percentages of the distance measured along each surface. Within this framework, interpolation is performed to find local values of channel geometry and gas flow properties at each point along the particle trajectory.

The interpolation procedure uses a cubic spline function in preference to other higher-order polynomials. The advantage of the spline is in its smoothness, resulting from continuous piecewise first and second order derivatives of all mesh points. Severe gradients that occur near the blade edges are adequately handled by increasing the mesh fineness and treating these regions separately. The basic spline formula, described in detail in reference [4], gives the interpolated value of a variable Y or its first order derivative Y', at a spatial coordinate X, as:

$$Y(X) = \frac{M_i}{6h_i}(x_{i+1}-X)^3 + \frac{M_{i+1}}{6h_i}(X-x_i)^3 + \left(\frac{y_{i+1}}{h_i} - \frac{M_{i+1}h_i}{6}\right)(X-x_i) + \left(\frac{y_i}{h_i} - \frac{M_i h_i}{6}\right)(x_{i+1}-X)$$

and

$$Y'(X) = -\frac{M_i}{2h_i}(x_{i+1}-X)^2 + \frac{M_{i+1}}{2h_i}(X-x_i)^2 + \frac{(y_{i+1}-y_i)}{h_i} - (M_{i+1}-M_i)\frac{h_i}{6}$$

where x_i represents the axial, tangential, or radial coordinates of the i-th mesh point; y_i represents the value of a gas flow property or surface coordinate at the i-th mesh point; M_i is the second derivative of y at the i-th mesh point, and h_i is the spacing between the i-th + 1 and i-th mesh points.

The values of M_i needed in the above expressions are obtained by enforcing the continuity condition on the first derivative at each mesh point as follows:

$$\frac{h_{i-1}}{6}M_{i-1} + \frac{(h_{i-1}+h_{i-1})}{3}M_{i-1} + \frac{h_{i-1}}{6}M_{i+1} = \frac{(y_{i+1}-y_i)}{h_i} - \frac{(y_i-y_{i-1})}{h_{i-1}}$$

The two additional boundary conditions are usually specified values of slopes or curvatures of the spline at its end points. Efficient inversion algorithms rapidly solve these sets of equations on the digital computer.

Knowing the gas properties at each particle position, the equations of motion are solved in the same manner as described by Hussein and Tabakoff [2].

Particle Rebound Model

Just as important to the trajectory calculations as the three-dimensional aspects of the flow field is an accurate model describing the rebounding characteristics of the particle. Earlier correlations developed by Hussein and Tabakoff [2] and used by Ulke [3] were based upon experimental observations of nonerosive particles. Later experiments conducted by Tabakoff and Grant [5] with erosive quartz and alumina particles impacting stainless steel, titantium, and aluminum alloys at high speeds gave different results. Current experiments are in progress using the laser velocimeter to measure the rebound characteristics of coal ash particles, which in themselves represent a mixture of several different erosive compounds. Statistical analysis of the experimental data for quartz particles rebounding from stainless steel produced the following expressions for the normal and tangential restitution ratios [6]:

$$\frac{V_{n_2}}{V_{n_1}} = 1.0 - 0.4159\beta_1 - 0.4994\,\beta_1^2 + 0.292\,\beta_1^3$$

Nomenclature

h = spacing betweeen mesh points, m
M = second derivative of Y
$\mathbf{n}$ = normal vector
s = tangential spacing between blades, m
$\mathbf{V}$ = particle velocity vector, m/s
X = independent variable
x = axial direction or coordinate, m
Y = dependent variable
y = circumferential direction or coordinate, m
z = radial direction or coordinate, m
β = angle between particle velocity vector and tangent to surface at impact, degrees
θ = angle between particle velocity vector and normal to surface at impact, also circumferential direction or coordinate, radians

Subscripts

i = corresponding to the i-th mesh point
n = normal
t = tangential
0 = impact point
1 = incoming conditions
2 = rebounding conditions

Downloaded 01 Jun 2010 to 171.66.16.62. Redistribution subject to ASME license or copyright; see http://www.asme.org/terms/Terms_Use.cfm

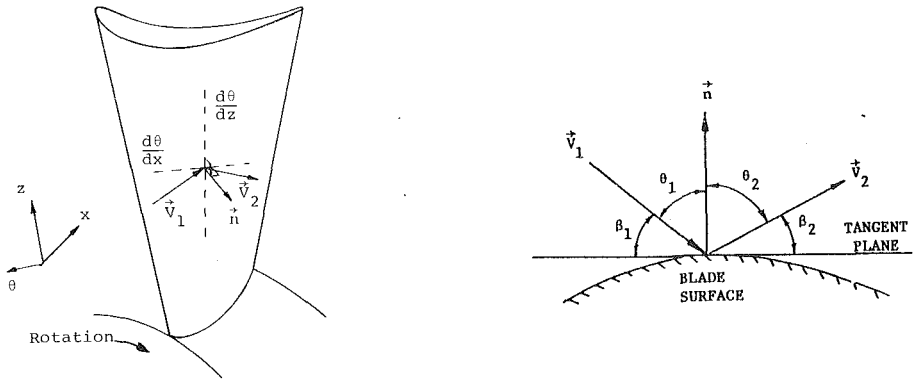


Fig. 2 Particle rebound plane

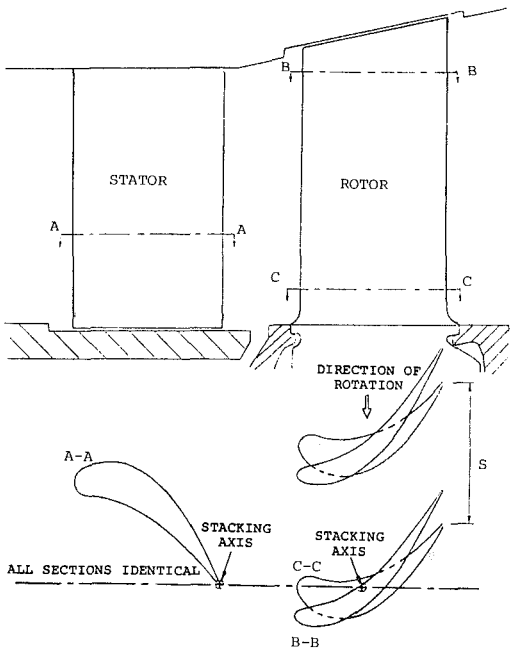


Fig. 3 First stage of a typical high-pressure axial-flow turbine

$$\frac{V_{n_2}}{V_{n_1}} = 1.0 - 2.12\beta_1 + 3.0775\,\beta_1^2 - 1.1\beta_1^3$$

Any rebound correlation that is used in the trajectory analysis must be applied in a plane that includes the normal vector to the blade or flow-path surfaces.

Figure 2 illustrates the unit vectors of interest in the particle rebound plane. The unit normal, **n**, is defined by the two surface derivatives as:

$$\mathbf{n} = z_0 \left.\frac{\partial\theta}{\partial x}\right|_{z_0} \mathbf{i} - \mathbf{j} + z_0 \left.\frac{\partial\theta}{\partial z}\right|_{x_0} \mathbf{k}$$

at impact point (x_0, y_0, z_0).

The rebounding velocity magnitude (V_2) and the rebounding angle (β_2) are calculated using the experimentally determined components of the restitution of the restitution ratio.

$$V_2 = (V_{n_2}^2 + V_{t_2}^2)^{1/2}$$

and

$$\beta_2 = \arctan\left(\frac{V_{n_2}}{V_{t_2}}\right)$$

The three components of the unit vector $\mathbf{V}_2$ needed by the trajectory analysis are determined by solving the following three simultaneous equations:

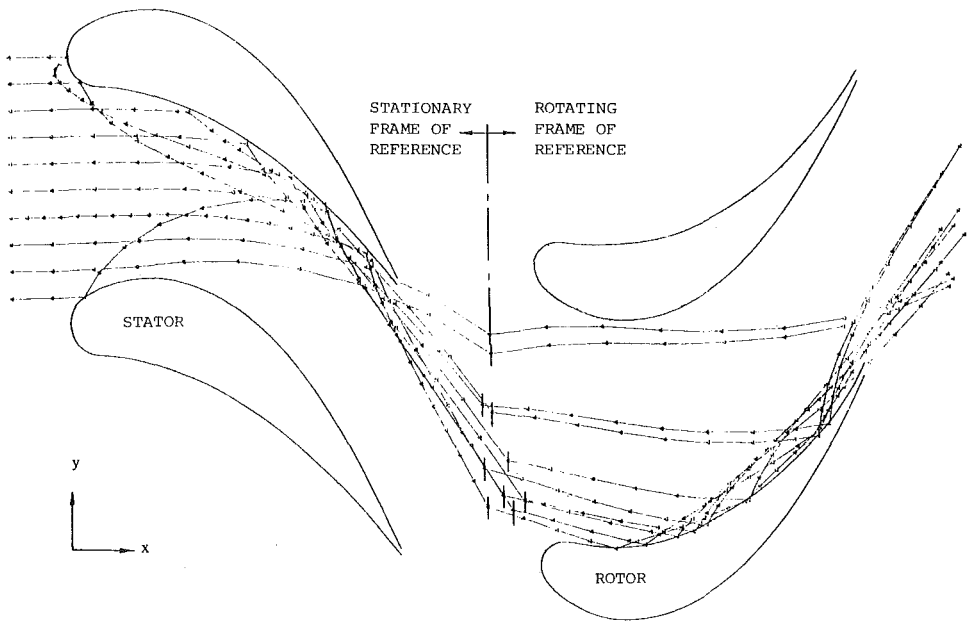


Fig. 4 Calculated trajectories in particulate flow surfaces through turbine first stage

Downloaded 01 Jun 2010 to 171.66.16.62. Redistribution subject to ASME license or copyright; see http://www.asme.org/terms/Terms_Use.cfm

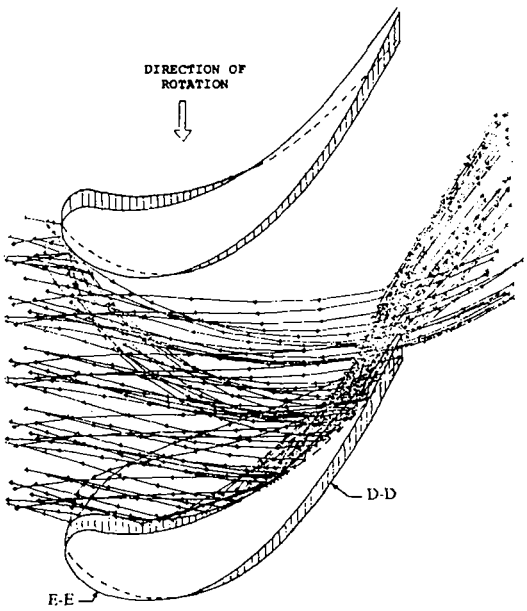


Fig 5 Calculated trajectories of ten-particle groups through rotor at five circumferential locations

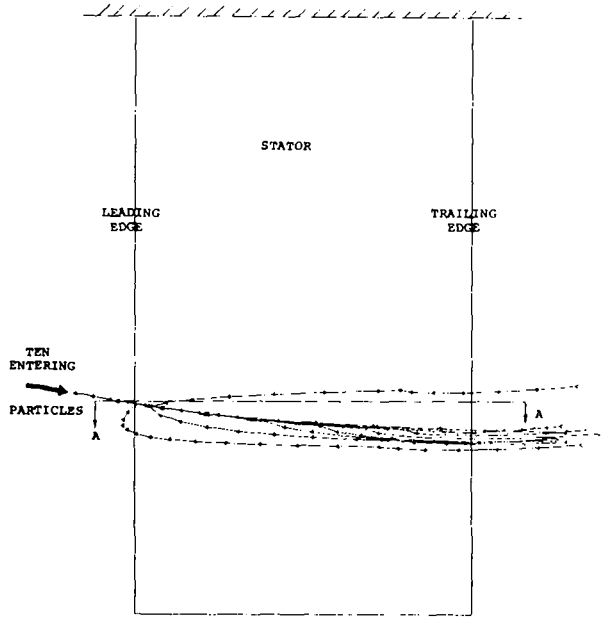


Fig. 6 Radial movement of particles through stator

$$n \cdot \mathbf{V}_2 = \cos\theta_2$$

$$\mathbf{V}_1 \cdot \mathbf{V}_2 = \cos(\beta_1 + \beta_2)$$

$$(\mathbf{n} \times \mathbf{V}_1) \cdot \mathbf{V}_2 = 0$$

In this way, the rebound data gathered in two-dimensional wind tunnels can be applied to the three-dimensional blade passages in turbomachinery.

Numerical Example

Particle trajectories through the first stage of a typical industrial gas turbine were determined using the computational improvements previously described. Figure 3 illustrates the flow path geometry and airfoil shapes for both the inlet guide vanes and the following rotor blades. Both the vane geometry and the incoming flow are radially constant, so the particle trajectories through these guide vanes did not benefit from the three-dimensional modeling. However, the swirling flow field at the nozzle discharge produced a radial pressure gradient that resulted in a significant three-dimensional particulate flow into the rotor. In addition, a significant variation in the rotor blades' cross-sections existed between the hub and tip, as shown in Fig. 3.

In determining the trajectories of particles entering at a given radial location, ten particles were evenly spaced across the inlet of one vane passage. The particles were chosen to be representative of coal ash, with a diameter of 13 μm and a density of 206 lbm/ft^3. Initial particle velocities were defined as nearly equivalent to the inlet gas velocity, with a slight radially-inward component as a result of entry from radial collectors.

Figure 4 shows trajectory projections in the $x-y$ plane through the vane passage and a subsequent rotor passage. The particles enter the nozzle cross section A-A (Fig. 3), and continue to the rotor. In this high-turning, high-solidity vane, few particles can pass through without impacting the vane pressure surface. All ten particles do not enter the same rotor passage, but their relative trajectories are shown through one passage for ease of interpretation. As in the guide vanes, most particles impact along the pressure surface of the rotor, but only ten particle paths are insufficient to give a good representation of the overall trajectory pattern.

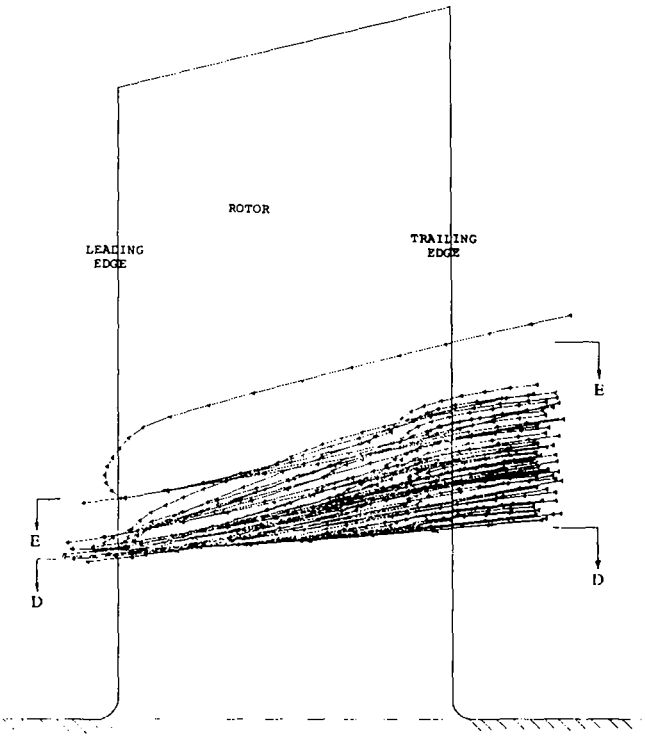


Fig. 7 Radial movement of particles through rotor

The spatial distribution of particles leaving the guide vanes would be expected to be essentially constant with time. However, this distribution continuously enters all rotor passages at many circumferential positions since the rotor position varies with time. It would be impractical to try to determine the trajectories through all rotor passages in all possible positions, so to approximate the real situation, the ten particles were processed through the rotor at five discrete circumferential positions. Figure 5 represents these five "groups" of trajectories, projected in the $x-y$ plane, again shown through one rotor passage for ease of interpretation.

Downloaded 01 Jun 2010 to 171.66.16.62. Redistribution subject to ASME license or copyright; see http://www.asme.org/terms/Terms_Use.cfm

Because the particles experience significant radial movement as a result of impacts and centripetal force effects, it is necessary to show the changing rotor passage shape in relation to the trajectories. The extent of the particles' radial movements is shown in Fig. 6 for the vane row, and in Fig. 7 for the rotor blade row. The notations D-D and E-E in Figs. 5 and 7 represent cuts through the blade along the two particle paths with trajectories at the radial extremes. Without a large swirling component of velocity, the particles experience practically no radial movement through the vane. However, there is significant radial movement through the rotor as the particles acquire tangential velocity through their impacts with the rotor blades.

Summary and Conclusions

The results of this study demonstrate the importance of recognizing the three-dimensional variations in flow field properties and blade geometry when dealing with small particles of the type found in coal ash. The strongly swirling flow fields that exist in turbomachinery produce significant radial movement of the particles, making two-dimensional representations of the gas flow and blade surfaces inadequate. Small errors induced in each blade row as a result of two-dimensional modeling would accumulate to unacceptably large values over the extent of multistage machines. The three-dimensional representation of the turbomachinery environment now permits accurate and continuous trajectory calculations not previously obtained with earlier methods.

Acknowledgment

This research work sponsored by Department of Energy Contract No. E(49-18)2465.

References

1 Hussein, M.F., and Tabakoff, W., "Dynamic Behavior of Solid Particles Suspended by Polluted Flow in a Turbine Stage," *Journal of Aircraft,* Vol. 10, No. 7, July 1973, pp. 434–440.

2 Hussein, M.F., and Tabakoff, W., "Computation and Plotting of Solid Particle Flow in Rotating Cascades," *Journal of Computers and Fluids,* Vol. 2, Pergamon Press, 1974, pp. 1–15.

3 Ulke, A. and Rouleau, W.T., "The Effects of Secondary Flows on Turbine Blade Erosion," ASME Paper 76-GT-74, 1976.

4 Ahlberg, J. B., Nilson, E. H., and Walsh, J. L., "The Theory of Splines and Their Applications," Academic Press, New York, 1967.

5 Tabakoff, W. and Grant, G., "An Experimental Investigation of Certain Aerodynamic Effects on Erosion," AIAA Paper No. 74-639, AIAA 8th Aerodynamic Testing Conference, July 1974.

6 Tabakoff, W. and Hamed, A., "Aerodynamic Effects on Erosion in Turbomachinery," JSME and ASME Paper No. 70, 1977 Joint Gas Turbine Conference, Tokyo, Japan, May 1977.

Downloaded 01 Jun 2010 to 171.66.16.62. Redistribution subject to ASME license or copyright; see http://www.asme.org/terms/Terms_Use.cfm

A Theory for Fine Particle Deposition in Two-Dimensional Boundary Layer Flows and Application to Gas Turbines

M. Mengüturk
Associate Professor,
Department of Mechanical Engineering,
Boğaziçi University,
Istanbul, Turkey

E. F. Sverdrup
Advisory Engineer,
Westinghouse Research & Development Center,
Pittsburgh, Pa.

A theory is presented to predict deposition rates of fine particles in two-dimensional compressible boundary layer flows. The mathematical model developed accounts for diffusion due to both molecular and turbulent fluctuations in the boundary layer flow. Particle inertia is taken into account in establishing the condition on particle flux near the surface. Gravitational settling and thermophoresis are not considered. The model assumes that the fraction of particles sticking upon arrival at the surface is known, and thus, treats it as a given parameter. The theory is compared with a number of pipe and cascade experiments, and a reasonable agreement is obtained. A detailed application of the model to a turbine is also presented. Various regimes of particle transport are identified, and the range of validity of the model is discussed. An order of magnitude estimate is obtained for the time the turbine stage can be operated without requiring cleaning.

Introduction

When a gas stream containing fine particles flows over a surface, particles are deposited by various mechanisms. If the flow is laminar, particles are diffused toward the surface by Brownian motion. The particle flux normal to the surface is, then, given by

$$N = -\rho D_B \frac{\partial \psi}{\partial y} \tag{1}$$

where ψ is the particle relative concentration, ρ fluid density, and y coordinate normal to the surface. The Brownian diffusion coefficient, D_B, is given by the Einstein formula [1]

$$D_B = \frac{K_B T}{3\pi\mu d_p} \tag{2}$$

where T is the fluid temperature, μ viscosity, K_B Boltzmann constant, and d_p particle diameter.

Deposition in turbulent boundary layer flows can be envisioned as a diffusion process which is highly intensified by turbulent fluctuations. Unless the particles are extremely small, the resulting particle diffusivity can be several orders of magnitude greater than in the case of molecular (Brownian) diffusion alone. The particle flux in such flows can be written as follows

$$N = -\rho (D_B + D_T) \frac{\partial \psi}{\partial y} \tag{3}$$

The additional coefficient, D_T, represents the contribution by the turbulent fluctuations and is called the eddy diffusivity of the particle.

If the diffusion coefficient and the continuity requirements on the particle flux are known in addition to the free stream concentration, the concentration profile inside the boundary layer can be calculated, and then, the particle arrival rate can be determined by evaluating equation (3) at the surface. Upon reaching the surface, some of the particles stick and some are thrown back depending on the nature of attachment and detachment forces developing near the surface. The theory presented in this paper calculates the particle arrival rates. Calculation of the net deposition rates requires additional work to account for the reentrainment due to particle removal from the surface.

The present theory has direct application in the gas turbine industry. It can be used to predict the deposition rates in turbines expanding "dirty" gas. In its present form with assumptions or experimental measurements to establish the fraction of particles which stick on arrival or when the theory is extended to calculate the particle reentrainment, it allows one to set the tolerance level on particles that can be safely directed through the turbine, and therefore, to specify the degree of gas cleaning required for reliable turbine operation.

A few investigations of particle deposition in turbines have appeared in the literature. Parker and Lee [2] studied deposition of submicron particles on turbine blades. They used a theory developed by Lin, et al. [3] for turbulent flow in pipes which neglects the streamwise variation in velocity and concentration and neglects also the effect of particle inertia on diffusion. Consequently, their calculation displayed considerable discrepancy from their experimental results. Moore

Contributed by the Gas Turbine Division of THE AMERICAN SOCIETY OF MECHANICAL ENGINEERS and presented at the Gas Turbine Conference and Products Show, March 9-12, 1981, Houston, Texas. Manuscript received at ASME Headquarters December 9, 1980. Paper No. 81-GT-54.

Copyright © 1982 by ASME
Downloaded 01 Jun 2010 to 171.66.16.62. Redistribution subject to ASME license or copyright; see http://www.asme.org/terms/Terms_Use.cfm

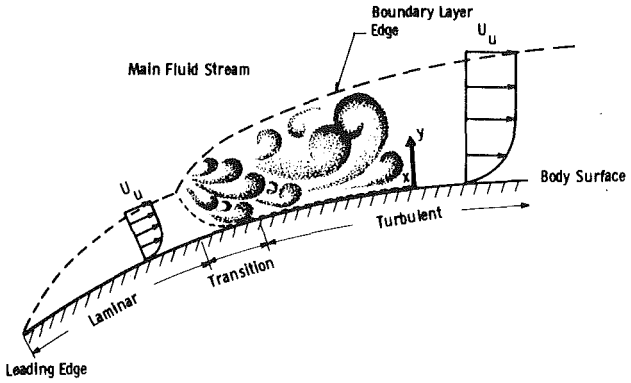


Fig. 1 The flow geometry and the coordinate system

and Crane [4] calculated diffusive deposition rates for the suction surface of a representative blade profile, again by using a pipe flow model. Crane [5] reported predictions of fog deposition on low pressure steam turbine blades. He concluded that deposition rates could not be estimated accurately unless the real compressible flow over the curved blade surfaces was considered. The theory presented here aims at closing the existing gap and at furnishing the engineer with a reliable tool to predict fine particle arrival rates in turbines.

Theory of Diffusive Particle Transport

Particle Transport Equation. A two-dimensional compressible flow is considered over a surface of arbitrary shape. The flow geometry and the coordinate system are shown in Fig. 1. The x-coordinate is the surface distance measured from the leading edge; the y-coordinate is measured normal to the surface.

The particle content of fluid is given by the particle concentration, c, which is assumed to be small enough so that the fluid properties are unaffected by the presence of particles. It is also assumed that particles are small enough so that purely inertial deposition is negligible. In other words, particle deviation from gas streamlines is small, and thus, deposition occurs mainly by diffusion. Particle inertia will be taken into account in establishing the condition on the particle flux near the surface. Gravitational effects are neglected.

The continuity requirement for steady particle flow may be expressed by the following mass transfer equation [6]

$$-\nabla\cdot(\rho D_p\nabla\psi)+\nabla\cdot(c\mathbf{V})=0 \tag{4}$$

where $\mathbf{V}$ is the velocity and D_p is the isotropic diffusion coefficient. The relative particle concentration, ψ, is defined as c/ρ.

Neglecting diffusion in x-direction and defining a stream function, G, equation (4) becomes

$$\frac{\partial}{\partial y}\left(\rho D_p\frac{\partial\psi}{\partial y}\right)=\frac{\partial G}{\partial y}\frac{\partial\psi}{\partial x}-\frac{\partial G}{\partial x}\frac{\partial\psi}{\partial y} \tag{5}$$

where $u=(1/\rho)(\partial G/\partial y)$ = x-component of velocity.

$v=(-1/\rho)(\partial G/\partial x)$ = y-component of velocity.

The diffusion coefficient may be written as

$$D_p=D_B+D_T \tag{6}$$

where D_T, the eddy diffusivity, may be expressed as the sum $\epsilon_f+\epsilon_p'$, ϵ_f being the eddy viscosity and ϵ_p' denoting the correction factor for particle size. Using the expression given by Liu and Ilori [7] for ϵ_p' and equation (1) for D_B, the diffusion coefficient takes the form

$$D_p=\frac{K_BT}{3\pi\mu d_p}+\epsilon_f+\frac{1}{18}\frac{\rho_p d_p^2y^2\tau_w^2}{\mu(y\sqrt{\rho\tau_w}+10\mu)^2} \tag{7}$$

where ρ_p is the particle density and τ_w is the shear stress at the surface.

The eddy viscosity, ϵ_f, can be represented by a two layer model. The eddy viscosity for the inner region is given by

$$\epsilon_1=K_1^2y^2\left\{1-\exp\left[-\frac{y\rho}{26\mu}\left(\frac{\tau_w}{\rho}+\frac{dp}{dx}\frac{y}{\rho}\right)^{1/2}\right]\right\}^2\cdot\left|\frac{\partial u}{\partial y}\right| \tag{8}$$

The eddy viscosity in the outer region is expressed as

$$\epsilon_2=K_2u_u\delta_d[1+5.5(y/\delta)^6]^{-1} \tag{9}$$

where u_u is the velocity at the outer edge of the boundary layer, δ boundary layer thickness, δ_d displacement thickness and τ_w shear stress at the surface.

Equations (8) and (9) include the modifications suggested by Van Driest [8], Cebeci, et al. [9], and Klebanoff [10]. Following the suggestion by Cebeci, et al. [9], the inner and outer regions are defined by the constraint of continuity in the eddy viscosity. Starting from the surface, equation (8) is used until $\epsilon_1=\epsilon_2$, and then, equation (9) applies. The choice of constants K_1 and K_2 depends on the definition of the boundary layer thickness, δ. If δ is defined as the y-distance where the velocity reaches 99.5 percent of the velocity outside the boundary layer, then $K_1=0.4$ and $K_2=0.0168$.

Transformation of Particle Transport Equation. When velocities in the boundary layer are known analytically or from a numerical computer solution, equation (5) is a linear second order partial differential equation for ψ. A direct solution impossible, because the equation contains a singularity at the origin.

The singularity in the x-y plane can be removed by a transformation into the Levy-Lees plane defined by the ξ and η coordinates. The Levy-Lees transformation [11] is written here as

$$d\xi=\rho_u\mu_uu_u\,dx \tag{10}$$

$$d\eta=\frac{\rho u_u}{(2\xi)^{1/2}}\,dy \tag{11}$$

where the subscript u denotes values at the outer edge of the boundary layer.

The partial derivative operators are transformed into the new plane according to

$$\frac{\partial}{\partial x}=\rho_u\mu_uu_u\left(\frac{\partial}{\partial\xi}+\frac{\partial\eta}{\partial\xi}\frac{\partial}{\partial\eta}\right) \tag{12}$$

$$\frac{\partial}{\partial y}=\frac{\rho u_u}{(2\xi)^{1/2}}\frac{\partial}{\partial\eta} \tag{13}$$

For convenience, a dimensionless stream function, $f(\xi,\eta)$, is related to $G(x,y)$ as follows [9]

$$f=\frac{G}{(2\xi)^{1/2}} \tag{14}$$

After substituting equations (12–14) into equation (5),

$$\frac{\partial^2\psi}{\partial\eta^2}+\left(\frac{2}{\rho}\frac{\partial\rho}{\partial\eta}+\frac{1}{D_p}\frac{\partial D_p}{\partial\eta}+\frac{A}{\rho^2D_p}\frac{\partial f}{\partial\xi}+\frac{Bf}{\rho^2D_p}\right)\frac{\partial\psi}{\partial\eta}=\frac{A}{\rho^2D_p}\frac{\partial f}{\partial\eta}\frac{\partial\psi}{\partial\xi} \tag{15}$$

where

$$A=2\xi\rho_u\mu_u \tag{16}$$

$$B=\rho_u\mu_u \tag{17}$$

Boundary Conditions. The particle transport equation in

Downloaded 01 Jun 2010 to 171.66.16.62. Redistribution subject to ASME license or copyright; see http://www.asme.org/terms/Terms_Use.cfm

the $\xi - \eta$ plane (equation (15)) can be solved when the conditions on ψ and/or its first derivative are specified at the outer edge of the boundary layer and at the surface.

The upper boundary condition requires the normal gradient of relative concentration to vanish at infinity. For numerical calculations it is appropriate to approximate this condition as

$$\frac{\partial \psi}{\partial \eta}\bigg|_{\eta=h^*} \simeq 0 \tag{18}$$

Here, h^* is a finite but sufficiently great distance in the η-direction. In many situations it is adequate to take $h^* = \delta^*$ where δ^* is the boundary layer thickness in the $\xi - \eta$ plane.

The lower boundary condition requires additional considerations. Depending on the particle size and the flow conditions, there exists a certain distance measured from the surface within which diffusion alone is insufficient to represent the transport phenomenon. Particles coming that close to the surface need only a small impetus to reach the surface. It has been proposed by Friedlander and Johnstone [12] that this impetus is provided by the particle inertia. According to their stopping distance theory, particle transport toward the surface occurs by diffusion until the stopping distance from the surface; particles are considered to complete the final phase of their travel by way of a free flight (inertial coasting) which takes place under the momentum imparted by turbulent fluctuations and molecular motions. By assuming Stokes flow and taking into account the particle radius in the manner suggested by Davies [13], the particle stopping distance may be calculated from the following equation

$$s = \frac{\rho_p d_p^2 v_s}{18\mu} + \frac{d_p}{2} \tag{19}$$

where s is the stopping distance and v_s denotes the free flight initial velocity. As Beal [14] points out, v_s may be determined by summing the Brownian velocity due to molecular motions and the rms normal fluctuating velocity at the stopping distance. The Brownian velocity is given by [14]

$$v_B = \left(\frac{3K_B T}{\pi^2 \rho_p d_p^3}\right)^{1/2} \tag{20}$$

The rms normal fluctuating velocity, v'_{rms}, can be obtained from Davies correlation [13]

$$v'_{\text{rms}} = \frac{y\tau_w}{y\sqrt{\rho\tau_w} + 10\mu} \tag{21}$$

From equations (20) and (21) the normal particle velocity at a point near the surface may be written as

$$v_p = \left(\frac{3K_B t}{\pi^2 \rho_p d_p^3}\right)^{1/2} + \frac{y\tau_w}{y\sqrt{\rho\tau_w} + 10\mu} \tag{22}$$

The stopping distance is calculated by substituting $y = s$ in equation (22) and solving the resulting expression for v_s and equation (19) by iteration. The normal particle flux at the stopping distance can be obtained from the concentration gradient at that point

$$N_s = -\rho D_p \frac{\partial \psi}{\partial y}\bigg|_{y=s} \tag{23}$$

For simplicity the particles crossing into the inertial region are assumed to be transported to the wall at an average velocity v_c which is obtained by averaging the particle velocity over the stopping distance.

$$v_c = \int_0^s v_p \frac{dy}{s} \tag{24}$$

Since some of the particles do not quite reach the surface, and some do not stick on impact, Beal [14] postulates that there will be an equilibrium concentration, ψ_s, within the stopping distance (inertial region). Thus, the flux of particles

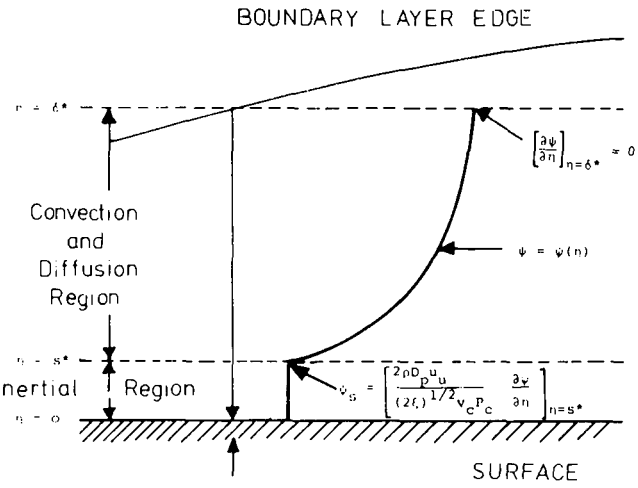


Fig. 2 Schematic illustration of the boundary conditions

reaching the surface is

$$N_w = -\frac{v_c}{2} p_c c_s \tag{25}$$

where p_c is the fraction of the particles which stick on impact. The average velocity is to be halved because there is equal probability of particles being thrown back toward the main stream.

Since $\psi = \psi_s$ in the inertial region, $N_w = N_s$. Hence, combining equations (23) and (25)

$$\psi_s = \left(\frac{2}{v_c}\frac{D_p}{p_c}\frac{\partial \psi}{\partial y}\right)_{y=s} \tag{26}$$

Equations (17) and (24) can be transformed into the $\xi - \eta$ plane as follows

$$s^* = \frac{u_u}{(2\xi)^{1/2}} \int_0^s \rho dy \tag{27}$$

$$\psi_s = \left[\frac{2\rho D_p u_u}{(2\xi)^{1/2} v_c p_c}\frac{\partial \psi}{\partial \eta}\right]_{\eta=s^*} \tag{28}$$

Equation (28) is the lower boundary condition of the particle transport equation. A schematic illustration of the boundary conditions is given in Fig. 2.

Numerical Solution of the Particle Transport Equation. Equation (15) is a second order linear partial differential equation. The fluid properties and velocities that appear in the coefficients are known as a function of position from an analytical or numerical solution of the boundary layer flow. The remaining parameters can be calculated from this flow field.

A two-dimensional five point mesh is used for the finite difference solution to equation (15). By using Lagrange's interpolation method, the ξ and η derivatives are expressed in a finite difference form. The flow surface is divided into a number of stations which constitute the streamwise mesh points. At the leading edge the flow is laminar, but it may become turbulent at the subsequent stations depending on the flow conditions. The finite difference equation is solved at each surface station by making use of the boundary conditions and the solution at the previous stations. The solution is thus marched out in the streamwise direction. The particle transport equation in the "stretched" $\xi - \eta$ plane implicity accounts for the conditions at the leading edge. Hence, when solution for the entire boundary layer is sought, there is no need to specify an initial concentration profile. However, if solution is to be started at any other location, the corresponding initial profile must be given.

Downloaded 01 Jun 2010 to 171.66.16.62. Redistribution subject to ASME license or copyright; see http://www.asme.org/terms/Terms_Use.cfm

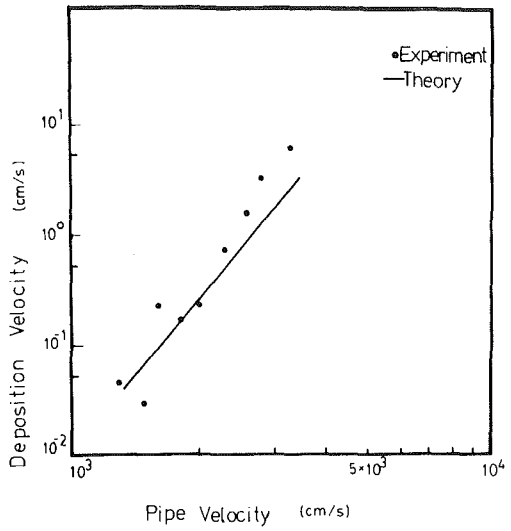


Fig. 3 Comparison with Friedlander and Johnstone's [12] experiments (1.81 μm aluminum particles in 1.38 cm pipe)

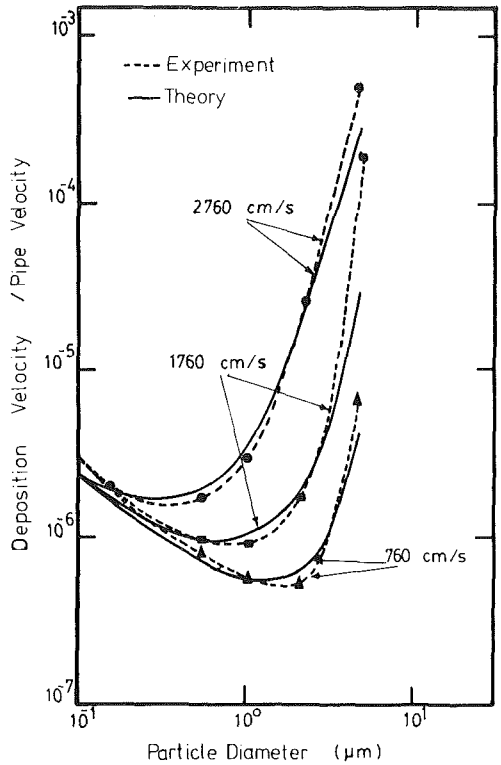


Fig. 4 Comparison with Wells and Chamberlain's [15] experiments (aitken nuclei, drops of tricresyl phosphate and polystrene spheres at three different velocities in 2.54 cm pipe)

Comparison with Experiments

Pipe Flow. In comparing the theory with pipe experiments, the particle transport equation may be greatly simplified by assuming incompressible flow and neglecting the change of the velocity and the concentration profiles in the axial direction. If it is further assumed that the diffusion thickness is much smaller than the pipe radius, equation (15) reduces to

$$\frac{d}{dy}\left(D_p \frac{dc}{dy}\right)=0 \tag{29}$$

This equation was solved by using the method described above. The upper boundary was taken at $h = 30(\mu/\rho u_*)$, where u_* is the friction velocity and the sticking fraction was assumed to be 1. The results are presented in terms of the deposition velocity, K_p, defined as

$$K_p = \frac{N_w}{c_m} \tag{30}$$

where c_m is the mean concentration in the pipe.

Comparison of the theoretical results with Friedlander and Johnstone's data [12] and Wells and Chamberlain's data [15] are shown in Figs. 3 and 4, respectively.

Cascade Flow. Comparison with pipe experiments hardly provides a rigorous verification for all aspects of the model. For a more complete test Parker and Lee's experiments [2], [16] in a two-dimensional cascade were considered. The cascade geometry and the flow data are described by Parker and Lee. The measured surface velocities were used in the computer program E7ES by Cebeci, et al. [9] to calculate the velocities in the blade boundary layer. The sticking fraction was again assumed to be 1. The calculated deposition rates per cm^2 and the experimental data for 0.13 μm, 0.19 μm and 0.24 μm mass-median diameter fluorescein particles along the suction surface are shown in Fig. 5. Here, the percentage deposition per cm^2 signifies the percentage deposition of particles passing through the blade passage in a zone 1 pitch wide by 1 cm deep. Since the flow rate was not given directly, it had to be calculated from the free stream velocities and the geometry. A consistent assessment was difficult. Therefore, the theoretical deposition rates were based on two values of the flow rate one calculated from the inlet velocity (11500 cm^3/s per cm depth) and the other from the exit velocity (17300 cm^3/s per cm depth). In view of this uncertainty, the theoretical results compare with the experiments quite well. Correlation would be improved if the size distribution had been available for each sample and had been taken into account in calculations instead of just using the mass-median diameters reported by Parker and Lee.

Application to Turbomachinery

The diffusive particle transport theory presented in this paper was applied to the first stage of an electric utility turbine rated to drive a 70 MW generator. The flow calculations were done by using the computer program of Katsanis [17] and Cebeci, et al. [9]. The location of transition was calculated by applying the following criterion due to Horlock [18].

$$(\mathrm{Re}_\theta)_{\text{transition}} = \frac{u_u \theta}{(\mu/\rho)_u} = 250 \tag{31}$$

where θ is the local momentum thickness.

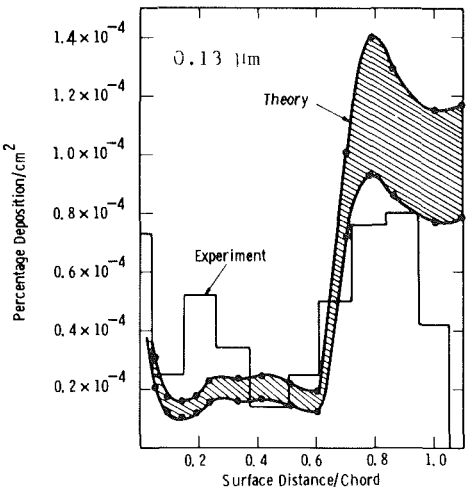
Results were obtained for particle with density of 2.5 gm/cc and diameters ranging from 0.001 μm (~ molecular size) to 3 μm. It was assumed that all particles which arrived at the surface would stick ($p_c = 1$). The removal of deposits by the lift forces acting near the surface has not been considered. In these respects, the results presented in this paper are the rates of particle arrival at the surface rather than the actual deposition rates.

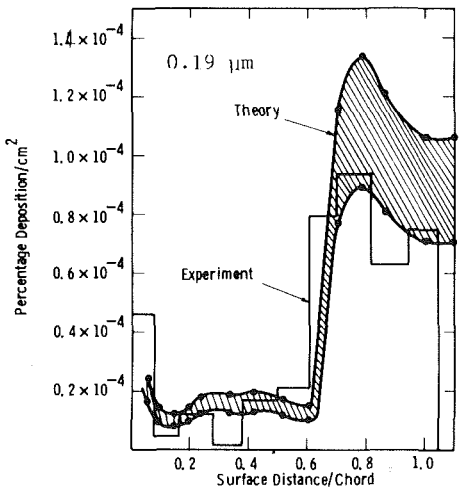
Based on the numerical results it is possible to distinguish three basic regimes of particle transport.

1 Brownian (Molecular) Diffusion Regime. This regime is characterized by extremely small particles that are transported to surface mainly by Brownian (molecular) diffusion. Since the Brownian coefficient is inversely proportional to the particle diameter, the transport rate increases as the particle size decreases.

2 Turbulent Diffusion Regime. This regime describes the transport of larger particles which diffuse under the influence of turbulent fluctuations. Since turbulent diffusion is

Downloaded 01 Jun 2010 to 171.66.16.62. Redistribution subject to ASME license or copyright; see http://www.asme.org/terms/Terms_Use.cfm





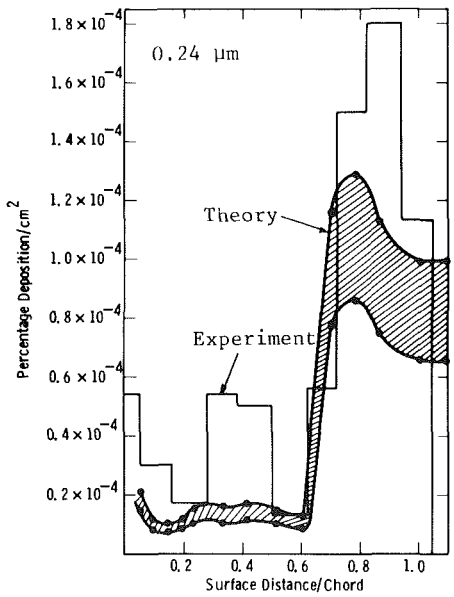


Fig. 5 Comparison with Parker and Lee's [2] Cascade experiments (0.13 μm, 0.19 μm and 0.24 μm fluorescein particles along blade suction surface)

enhanced by particle inertia, the transport rate increases as the particle diameter increases.

3 Inertial Regime. In this regime particle momentum is more important than diffusion. Particle transport to surface occurs by direct inertial impaction. The present theory neglects the deviations of the particles from the main streamlines. Account is taken of the particle inertia only in the final "inertial coasting". Therefore, the transport theory presented in this paper cannot calculate the deposition rates in this regime accurately. Instead, one needs to trace the particle trajectories inside the boundary layer and to determine the amount of particles reaching the surface. A method of doing this is presented by Mengütürk and Sverdrup [19].

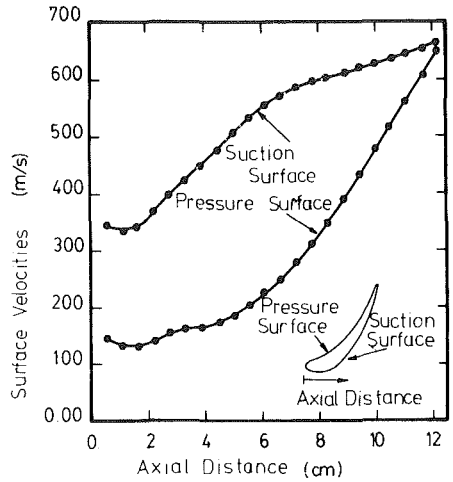


Fig. 6 Calculated surface velocities of stator blades

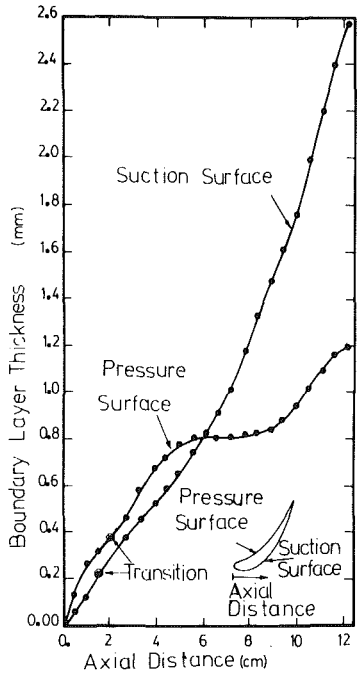


Fig. 7 Calculated boundary layer thicknesses of stator blades

There certainly exist overlapping regimes in which a combination of various mechanisms is in effect. For example, in a mixed Brownian turbulent diffusion regime where ϵ_p' is negligible (See equation (6)), the transport rate will decrease as the particle size increases, since D_p is inversely proportional to d_p but ϵ_f is independent of it.

The particle arrival rates will be presented in terms of the deposition velocity defined as

$$K_p = \frac{N_w}{c_{\text{in}}} \tag{32}$$

Downloaded 01 Jun 2010 to 171.66.16.62. Redistribution subject to ASME license or copyright; see http://www.asme.org/terms/Terms_Use.cfm

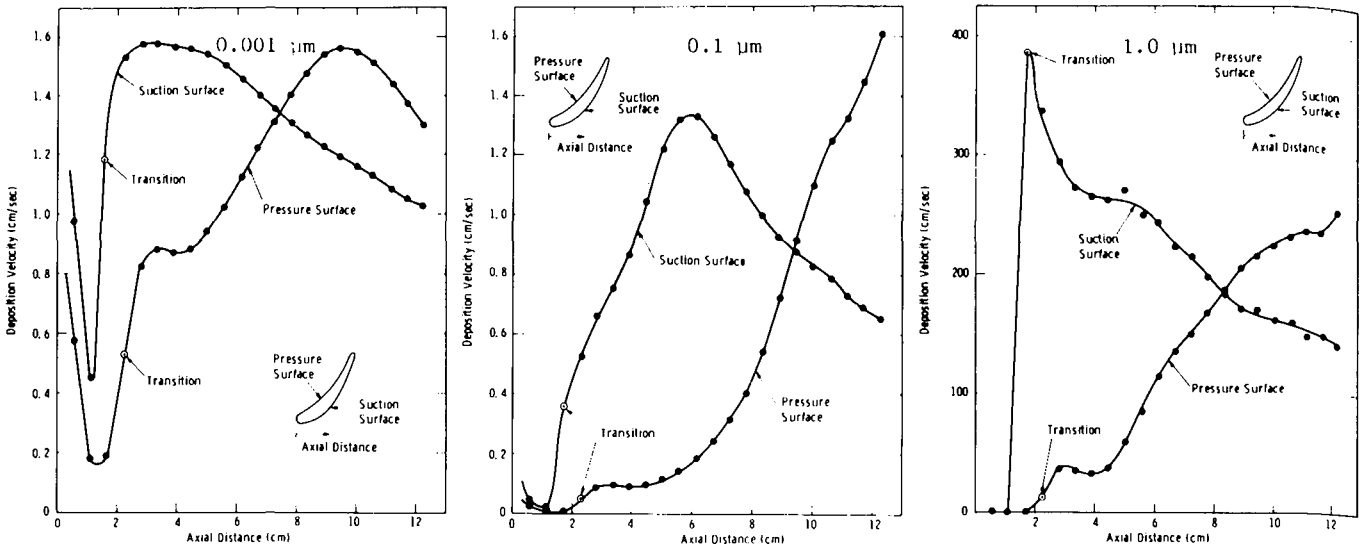


Fig. 8 Deposition velocities of 0.001 μm, 0.1 μm and 1.0 μm particles on stator blades

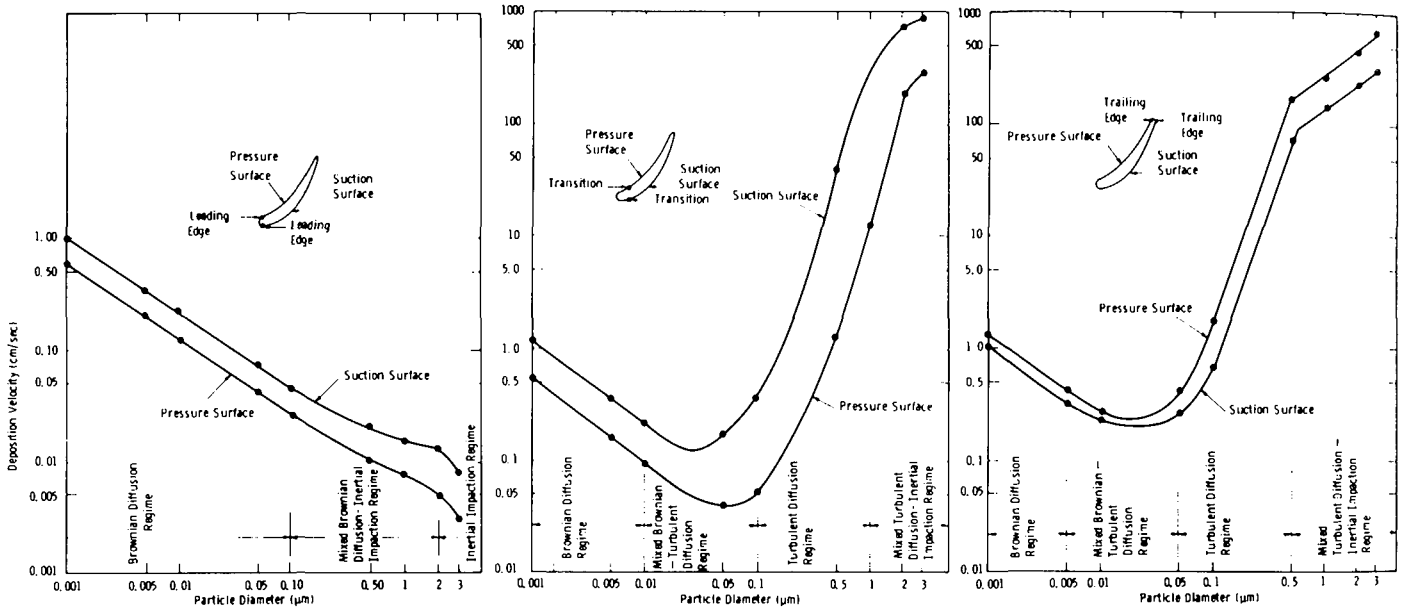


Fig. 9 Deposition velocities at stator blade leading edge, transition and trailing edge as a function of particle diameter

where c_{in} is the particle concentration at the turbine inlet. The local arrival rate can be obtained by multiplying the deposition velocity by the inlet concentration.

Figures 6 and 7 show the calculated surface velocities and the boundary layer thicknesses, respectively, for the stator blades.

The deposition velocities for 0.001 μm particles depositing on the pressure and suction surfaces of a stator blade are shown in Fig. 8. It is seen that the deposition velocity decreases between the leading edge and the locations of transition on both surfaces. This is attributed to the increase in the boundary layer thicknesses. There is a marked increase in the deposition velocity at transition indicating the significance of turbulence. After transition the deposition velocity along the suction surface decreases steadily towards the trailing edge owing to the rapidly thicknening boundary layer. On the pressure surface it continues to increase at first (since the velocity is increasing but the thickness almost remains constant), then starts decreasing (since the effect of acceleration is offset by increasing thickness). It may be concluded that the velocity effect is not strong. The transport regime is Brownian diffusion in the laminar regions and a mixed Brownian-turbulent diffusion in the turbulent regions.

The change in the trend of the deposition velocities for 0.1 μm particles is readily observed. Transition causes more than an order of magnitude increase in deposition. The prevailing effect of turbulence is also reflected in the rest of the curves. Acceleration can, now, impressively oppose the retarding effect of boundary layer thickening on the transport rate. On the suction surface deposition velocities increase approximately midway to the trailing edge and only then begin to fall down. On the pressure surface the transport rates keep increasing all the way to the trailing edge. The transport regime is again Brownian diffusion in the laminar regions but entirely turbulent diffusion in the turbulent regions.

The deposition velocities for 1 μm particles exhibit further changes in the trend. The Brownian effect is virtually zero. On the other hand, the velocity effect characterizing the turbulent

Downloaded 01 Jun 2010 to 171.66.16.62. Redistribution subject to ASME license or copyright; see http://www.asme.org/terms/Terms_Use.cfm

diffusion regime is somewhat underestimated, as evidenced by the variation of the calculated deposition velocity along the suction surface. For 1 μm particles, the stopping distance becomes comparable to the boundary layer thickness and the velocity at the stopping distance is of the order of the main stream velocity. Therefore, the model assumption of negligible deviation from streamlines is not very realistic. The transport regime should be identified as mixed turbulent diffusion-inertial impaction. The present model does not account for inertial impaction of particles. A particle trajectory model must be used to calculate the contribution from that mechanism.

It is interesting to study the variation of deposition velocity with particle diameter. Figure 9 shows the variation at the leading edge, transition points and trailing edge. The model calculates infinite deposition rate at the exact leading edge. Therefore, results for the second computation stations on both surfaces are presented in Fig. 9. For convenience these stations will be referred to as the "leading edge". On both sides of the blade nose, the deposition velocity decreases linearly (on the log-log scale) as diameter increases. The linearity starts disappearing at $d_p \approx 0.1$ μm beyond which direct inertial collection becomes important. The appropriate transport regimes are as indicated in the figure. If account were taken of direct inertial collection by means of a trajectory model, the curves would undergo a minimum (in the mixed Brownian diffusion-inertial impaction regime) and would increase with further increase in size.

The elbow shaped curves in Fig. 9 display the variation of deposition velocity with particle diameter at the transition and trailing edge points. Based on the previous discussion, the approximate ranges of transport regimes are as indicated. Suction surface deposition rate is higher at transition (higher velocity and smaller boundary layer thickness). The opposite is true at the trailing edge (same velocity, greater thickness). For the same reasons, turbulent diffusion actually breaks in earlier on suction surface than on pressure surface, but later at the trailing edge. The change in slopes at the start of the mixed turbulent diffusion-inertial impaction regime is noteworthy. At the risk of being repetitive, the authors would like to caution the reader once again that the contribution due to purely inertial mechanism is to be calculated by a separate particle trajectory model. It is important to note that this contribution may be positive or negative depending on the surface orientation. With reference to the mixed turbulent diffusion-inertial impaction regime in Fig. 9, suction surface deposition rates should be lower at the trailing edge than predicted here, but pressure surface rates should be higher.

Deposition In a Gas Turbine Stage. This calculation procedure for determining the submicron arrival rates can be used to estimate deposition in a gas turbine stage if the particle size distribution which the turbine is ingesting is known and if some assumption is made concerning the fraction of the arriving particles that will stick to the surface.

In this section, to illustrate the procedure and to provide a first estimate of the gas cleaning requirements to avoid deposition problems in a turbine expanding a gas containing large quantities of submicron particles, we estimate the growth of deposits and the effect of the deposits on turbine performance.

Figure 10 shows the particle size distribution we have selected for illustration. Fifty weight percent of the particles are larger than 1.3 μm. The distribution is an approximation of that which might be expected to leave a fabric filter. We have assumed the particle concentration at the entrance to the turbine stage to be 0.002 grains per standard cubic foot (5 mg per standard cubic meter).

The deposition rates in the turbine stage were obtained by a stepwise integration of the deposition of each particle size

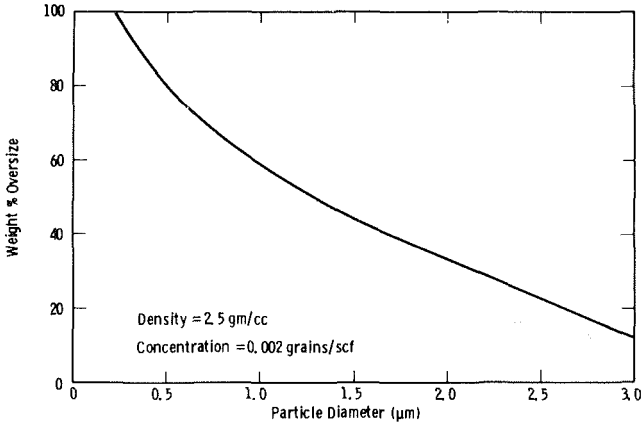


Fig. 10 Particle data used in deposition calculations

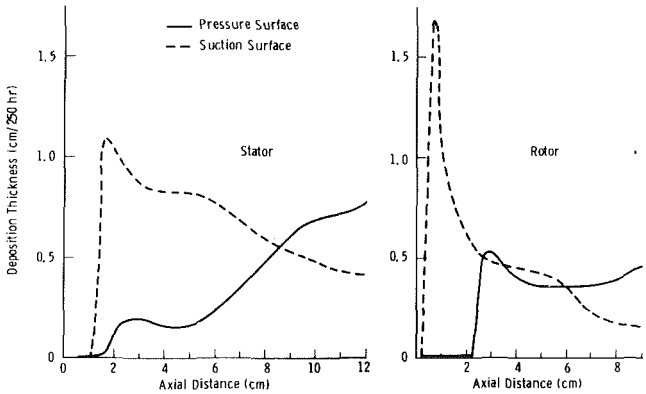


Fig. 11 Calculated deposition thicknesses on stator and rotor blades after 250 hr operation

over the range of particle sizes entering the turbine. It was assumed that all particles smaller than 3 μm dia stick to the surface and form homogeneous layers of deposit, but larger particles just impact the surface and rebound into the main stream owing to their high kinetic energy. In other words, the sticking probability was taken to be 100 percent for 3 μm and smaller particles, and 0 percent for larger particles.

Figure 11 shows the calculated thickness of deposits on the first stage stator and rotor blades after 250 hr of operation for this particle distribution entering the stage. The resulting change in the blade profiles and the blockage of the flow passage are illustrated in Fig. 12. The authors feel that the thick deposit layers predicted near the noses are not realistic. The gas flow will actually break up the deposits in these regions long before the blade profiles are distorted to the extent shown in the figure.

The effect of the deposition on the stage performance was studied by considering the flow blockage at the nozzle throat and the profile and trailing edge losses due to the deposits. It was assumed that the deposits around the blade noses would be constantly removed by the gas flow so that they would have negligible effect on the stage performance. Figure 13 shows the estimated loss in the stage output power. The stage is estimated to lose about 20 percent of its power in 150 hr of operation.

The deposition experience with a smaller 15 MW gas turbine unit reported by Nakao, et al. [20] indicates that their turbine had to be cleaned after the power output dropped by approximately 4 percent. Applying the same criterion for the 70 MW turbine under consideration, it is estimated that a turbine cleaning will be needed after every 30 hr of operation when all arriving particles smaller than 3 μm contribute to the

Downloaded 01 Jun 2010 to 171.66.16.62. Redistribution subject to ASME license or copyright; see http://www.asme.org/terms/Terms_Use.cfm

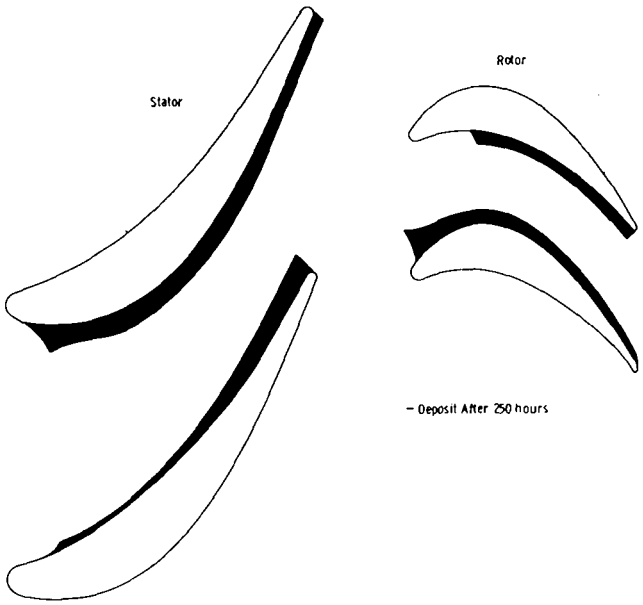


Fig. 12 Deposition in the first stage

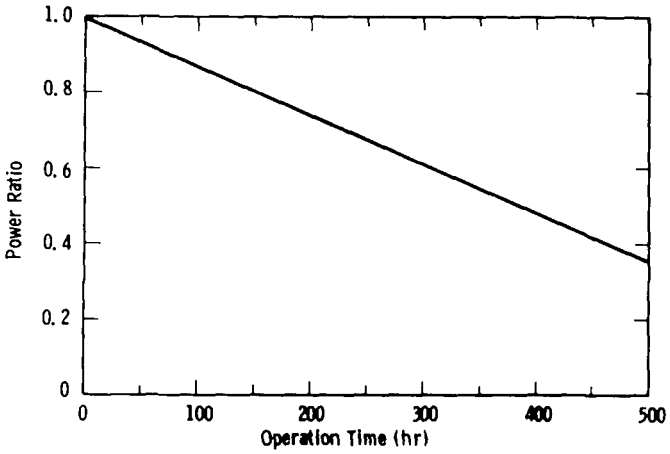


Fig. 13 Effect of deposition on power output of stage

deposit. Only about 15 percent of the deposit thickness results from the submicron particles. If 90 percent of the deposit was subsequently removed and if particles larger than 1 μm would bounce off the surface - the time before cleaning was required would be extended by a factor of roughly 50 to 100 times.

Accurate data on particle sticking fraction are required. Further research is recommended to study mechanisms of particle attachment to surfaces by theoretical and experimental means so that a reasonable estimate of sticking probability could be achieved. Observations by many investigators (e.g., See Kline, et al. [21]) revealed that the laminar sublayer in a turbulent boundary layer flow is not entirely free from turbulence. The sublayer is subjected to occasional bursts of fluid being ejected from very close to the wall well into the turbulent core. Deposits can be removed due to these eruptions in the sublayer. The net deposition rates should be obtained by extending the analysis presented in this paper by including the particle attachment-detachment mechanisms and re-entrainment.

Thermophoresis is not considered here. Vermes [22] has pointed out that when the particle size distribution which the turbine is ingesting has a considerable mass of particles in the size range, having diameters of hundredths to tenths of a micron, and if the turbine employs cooled blading, thermophoresis will increase the delivery of these fine particles to blade surfaces and should be considered. In the application considered in this work—the possible deposition problems faced by a turbine expanding a particle distribution having a mass mean diameter of 1 μm, such as might be present in gases from fluidized or entrained bed coal gasification systems with hot gas clean-up—the contribution of thermophoresis to fine particle arrival rates will be small. As pointed out by Mr. Vermes, in conventional oil or gas fueled turbines or in turbines combusting residual fuel - the particulate distributions ingested by the machines have mass mean diameters in the critical range where additional deposition by thermophoresis will occur.

References

1 Einstein, A., *Theory of Brownian Motion*, E.P. Dutton Co.

2 Parker, G.J., and Lee, P., "Studies of the Deposition of Submicron Particles on Turbine Blades," *Proc. Inst. Mechanical Engineering*, Vol. 186, No. 38, 1972.

3 Lin, C.S., Moulton, R.W., and Putnam, G.L., "Mass Transfer Between Solid Wall and Fluid Streams," *Industrial and Engineering Chemistry*, Vol. 45, No. 3, 1953.

4 Moore, M.J., and Crane, R.I., "Aerodynamic Aspects of Gas Turbine Blade Corrosion," *Deposition and Corrosion in Gas Turbines*, edited by Hart, A.B., and Cutler, A.J.B., Ch. 4, John Wiley and Sons, 1973.

5 Crane, R.I., "Deposition of Fog Drops on Low Pressure Steam Turbine Blades," *Journal Mechanical Science*, Vol. 15, 1973.

6 Welty, J.R., Wicks, C.E., and Wilson, R.E., *Fundamentals of Momentum, Heat and Mass Transfer*, John Wiley and Sons, 1969.

7 Liu, B.Y.H., and Ilori, T.A., "Aerosol Deposition in Turbulent Pipe Flow," *Environmental Science and Technology*, Vol. 8, No. 4, 1974.

8 Van Driest, E.R., "On Turbulent Flow Near a Wall," *J.A.S.*, Vol. 23, No. 11, 1956.

9 Cebeci, T., Smith, A.M.O., and Wang, L.C., "A Finite-Difference Method for Calculating Compressible Laminar and Turbulent Boundary Layers," McDonnell Douglas Aircraft Company, Report No. DAC-67131, Parts 1 and 2, 1969.

10 Klebanoff, P.S., "Characteristics of Turbulence in a Boundary Layer with Zero Pressure Gradient," NACA TN 3178, 1954.

11 Hayes, W.D., and Probstein, R.F., *Hypersonic Flow Theory*, Academic Press, New York, 1959.

12 Friedlander, S.K., and Johnstone, H.F., "Deposition of Suspended Particles from Turbulent Gas Streams," *Industrial and Engineering Chemistry*, Vol. 49, No. 7, 1957.

13 Davies, C.N., "Deposition from Moving Aerosols," *Aerosol Science*, New York, 1966.

14 Beal, S.K., "Deposition of Particles in Turbulent Flow on Channel or Pipe Walls," *Nuclear Science and Engineering*, 40, 1970.

15 Wells, A.C., and Chamberlain, A.C., *Great Britain Journal of Applied Physics*, Vol. 18, No. 12, 1967, pp. 1793-9.

16 Parker, G.J., and Ryley, D.J., "Equipment and Techniques for Studying the Deposition of Submicron Particles on Turbine Blades," *Proceedings of the Institution of Mechanical Engineers*, 184(Pt3C) 45, 1969—70.

17 Katsanis, T., "Fortran Program for Calculating Transonic Velocities on a Blade-to-Blade Stream Surface of a Turbomachine," NASA T.D. 5427, 1969.

18 Horlock, J.H., *Flow Research on Blading*, Ed. by Dzung, L.S., Amsterdam, Elsevier, 1970.

19 Mengütürk, M., and Sverdrup, E.F., "Calculated Tolerance of a Large Electric Utility Gas Turbine to Erosion Damage by Coal Gas Ash Particles," *Erosion: Prevention and Useful Applications*, ASTM STP 664, Ed. by Adler, W.F., 1979.

20 Nakao, K., Hirai, H., and Omori, T., "Two Years Experience of a Gas Turbine Firing Residual Fuel," ASME Paper No. 68-6T-11, 1968.

21 Kline, S.J., Reynolds, W.C., Schraub, F.A., and Runstadler, P.W., "The Structure of Turbulent Boundary Layers," *Journal of Fluid Mechanics*, Vol. 30, No. 4, 1967.

22 Vermes, G., "Thermophoresis - Enhanced Deposition Rates in Combustion Turbine Blade Passages," ASME Paper No. 78-WA/GT-1, 1978.

Downloaded 01 Jun 2010 to 171.66.16.62. Redistribution subject to ASME license or copyright; see http://www.asme.org/terms/Terms_Use.cfm

Dual Pressure Steam/Immiscible Liquid Cycles for Gas Turbine Exhaust Heat Recovery

B. M. Burnside
Senior Lecturer,
Department of Mechanical Engineering,
Heriot-Watt University,
Edinburgh, U.K.

A dual pressure steam/immiscible liquid cycle gas turbine bottoming plant is described. Three variants of the cycle are analysed. It is shown that under typical conditions one of these shows a 5 percent higher output than the conventional steam/steam cycle with only a 5 percent increase in heat extraction from the gas turbine exhaust. A larger LP preheater and condenser are required. Attention is drawn to the flexibility this type of cycle brings to the task of matching bottoming plant to gas turbine exhaust of combined cycles.

Introduction

Increases in fuel cost continue to present a challenge to manufacturers of gas turbine combined cycle electric utility plant to maximize efficiency. Threats, posed by current or possible legislation to the supply of premium fuels, are countered by proposals to integrate gas production plants with the power plant [1]. The use of water cooled nozzles to increase gas turbine top temperature [2] and efficiency promises a further rise in exhaust temperature to the heat recovery unit of the bottoming cycle.

In high-efficiency plant the dual pressure steam power cycle is used to extract heat from the gas turbine exhaust at temperatures over 500°C reducing it to a stack temperature just below 110°C [3]. With condensing temperatures of the order of 30°C this leaves a temperature difference of at least 50K, or about 12 percent of the enthalpy of the exhaust gas, untapped. It is true that preheater tube materials' problems arise below the gas dewpoint. However, rising fuel costs make it imperative that designs which utilise fuel more efficiently by means of relatively simple modifications of conventional plant, be kept under review.

The author has suggested [4] a modification of the conventional dual pressure cycle which replaces the LP steam section by a steam/organic LP section in which the condensed liquids are immiscible. The object of this modification is to use the benefit of the better matching of the fluid in the LP heaters to the cooling gas to increase the uptake of exhaust gas heat while, at the same time, making use of the stability of steam at the high temperature end of the cycle. It is possible by choosing suitable relative proportions of steam and organic to design for a completely dry expansion in the turbine. External shaft seals on pumps and turbine can be water or steam seals avoiding organic fluid leakage which is a problem in large plant.

Contributed by the Gas Turbine Division and presented at the International Gas Turbine Conference and Products Show, Houston, Texas, March 9-12, 1981, of THE AMERICAN SOCIETY OF MECHANICAL ENGINEERS. Manuscript received at ASME Headquarters, December 9, 1980. Paper No. 81-GT-55.

The object of this paper is to analyse this steam-organic/steam dual pressure cycle and compare it with the conventional steam/steam cycle. Three alternative cycles are presented.

Steam/Immiscible Liquid Dual Pressure Cycles

The three proposed cycles are shown in Figs. 1, 2 and 3. In the latter two figures only the LP section is shown; the rest of the cycles is the same as Fig. 1.

Fig. 1 Cycle. Only departures from the conventional dual pressure cycle will be described. After condensation and separation of the immiscible liquids the appropriate proportions of organic/water two phase liquid are pumped to the LP pressure, p_L, and circulated through the preheater, 1-2, to emerge in a separator at the eutectic temperature corresponding to p_L. Organic alone is circulated through an organic preheater, 4-5, where it is heated to the saturation temperature of the pure organic t_5, followed by boiling, 5-6, and superheating, 6-7. The superheated organic is mixed with the exhaust steam from the HP turbine before entering the LP stages. The water from the separator is pumped to the HP pressure, p_H at 8 before entering the HP heaters.

The matching diagram of this cycle is shown in Fig. 4 and the thermodynamic analysis is given in the Appendix. Given cycle pressures p_H, p_L and p_C, the top temperature t_{11}, pinch-point temperature differences Δ_1 and Δ_2, turbine and pump efficiencies, η, degrees of organic superheat Δ_3 and gas inlet temperature and mean specific heat, c_{pm} the rest of the cycle conditions including the mass fraction x, of steam expanding through the LP turbine are determined. Simplifying assumptions are detailed in the Appendix.

Examination of Fig. 2 reveals an obvious source of irreversibility – the large temperature difference across the HP preheater.

Fig. 2 Cycle. In an attempt to reduce the source of irreversibility referred to in the foregoing the HP preheater is divided into two sections. The water is heated to $t_{9'}$, 8-9′, in

Copyright © 1982 by ASME
Downloaded 01 Jun 2010 to 171.66.16.62. Redistribution subject to ASME license or copyright; see http://www.asme.org/terms/Terms_Use.cfm

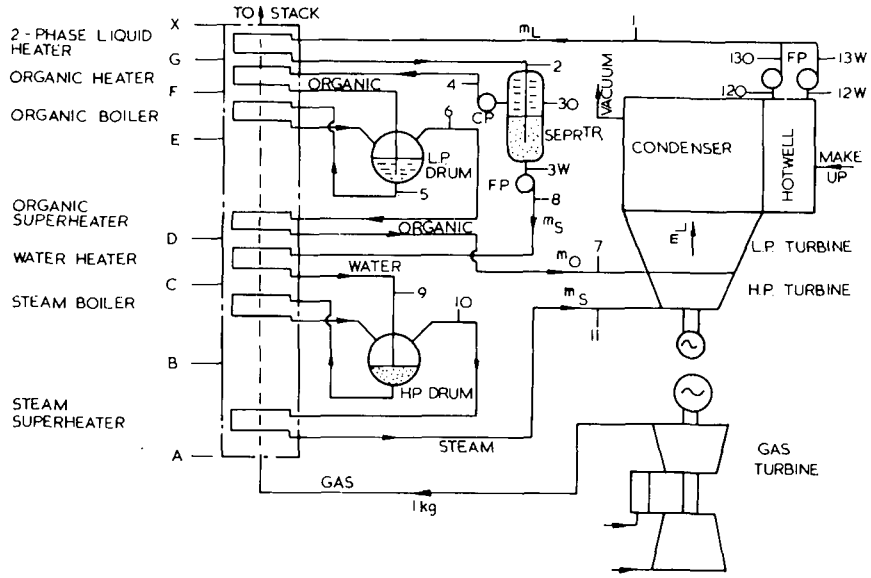


Fig. 1 Dual pressure cycle

the first section of the preheater situated in the gas stream immediately behind the LP organic preheater. The rest of the water preheat, 9′ – 9, is as in the Fig. 1 cycle. The matching diagram is shown in Fig. 5 and the cycle is analysed in the Appendix. It is convenient to obtain solutions for fixed values of stack temperature, t_X.

Fig. 3 Cycle. In this cycle water and organic are circulated through the LP evaporator and superheater. Evaporation, 5-5′, at the eutectic temperature, t_5, is followed, by circulation of organic liquid from the separator into the eutectic vapour followed by evaporation along the dew point line, 5′-6, until all the organic liquid has evaporated, and superheat 6-7. The proportion of organic vapor in the LP section is always high to avoid high mass fractions of steam in the LP turbine which result in wet expansion with wetness losses.

The matching diagram is shown in Fig. 6 and the cycle is analysed in the Appedix. Solutions are readily obtained if stack temperature, t_X, is fixed and the proportion of water, y, entering the separator which is pumped to the HP section varied until the desired LP superheater pinch point temperature difference, Δ_4 is obtained. There is a unique minimum stack temperature for which such a solution is possible.

Specific Work Output of Proposed Cycles

The specific work output/kg gas, W, was evaluated for a range of pressures p_H and p_L up to a maximum in p_H of 80 bar and a minimum p_L of 3.5 bar. Solutions were sought which resulted in completely dry expansions in the turbine and the maximum value of W. As a typical example the cycle conditions of Table 1 were held constant. No allowance was made for latent heats of condensation in the gas below the dew point. Expansion in the LP section of the turbine, unlike the conventional cycle is dry throughout, without wetness losses, which is the justification for the apparently high efficiency shown in Table 1. Other assumptions are detailed in the Appendix.

Choice of Organic Component. The alkanes *n*-octane and *n*-nonane (4) which are very stable, readily available and non-toxic are the most suitable organic fluids for the cycles proposed. They are almost completely insoluble with water and with normal boiling points of 126 and 151° C, respectively, have vapor mixtures with steam with eutectic mass fractions of 0.21 and 0.43, respectively. In this range the *T-s* dewline (4) is so shaped that expansions terminating on the dewline are possible, eliminating wetness losses in the LP

Nomenclature

c_{pm} = specific heat at constant pressure, kJ/kgK
h = specific enthalpy, kJ/kg
ILBC = immiscible liquid binary cycle
m_L = kg fluid/kg gas, LP turbine
m_O = kg fluid/kg gas, LP heaters
m_s = kg steam/kg gas, HP
p_H = high pressure, bar
p_L = intermediate pressure, bar
p_C = condenser pressure, bar
s = specific entropy, kJ/kgK
t = temperature, °C
T = temperature, K
v_f = liquid specific volume, m^3/kg
x,X = mass fractions of water in binary
y = fraction of water pumped to HP
W = specific work output of plant, kJ/kg gas
$\Delta_1,\Delta_2,\Delta_4$ = pinch point temperature difference, K
Δ_3 = degrees of superheat, K
η = isentropic efficiency

Subscripts

1-13 = vapor cycle fluid stations
$A-X$ = exhaust gas flow stations
C = condenser
eut,e = eutectic
exst = HP turbine exhaust
HP = high pressure
LP = low pressure
O = organic
P = pump
W = water

Downloaded 01 Jun 2010 to 171.66.16.62. Redistribution subject to ASME license or copyright; see http://www.asme.org/terms/Terms_Use.cfm

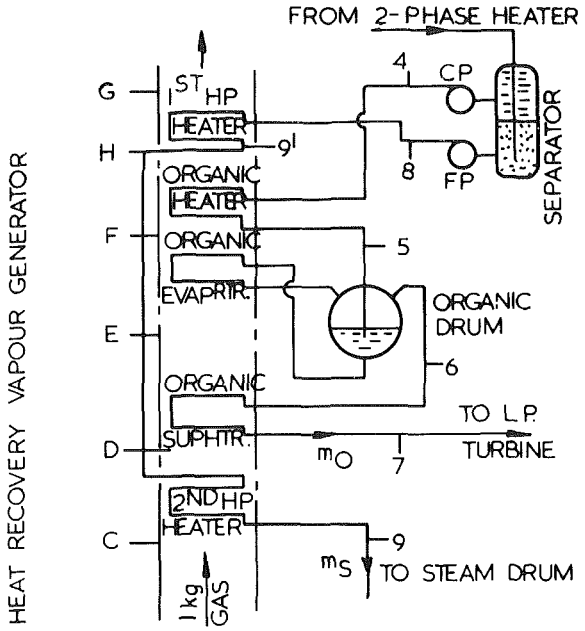


Fig. 2 dual pressure cycle

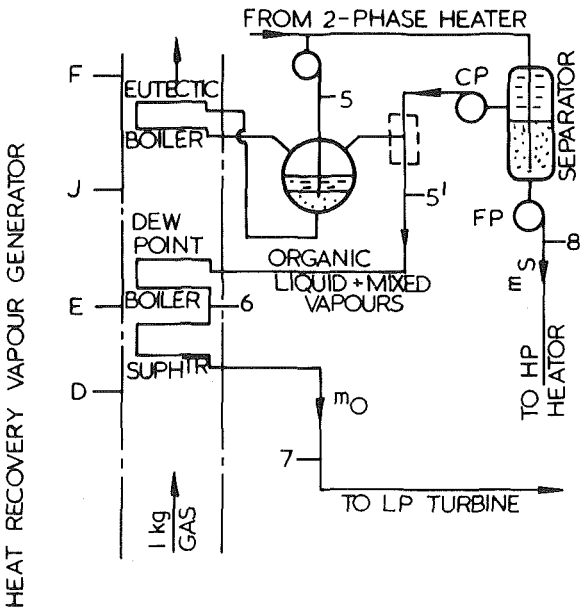


Fig. 3 Dual pressure cycle

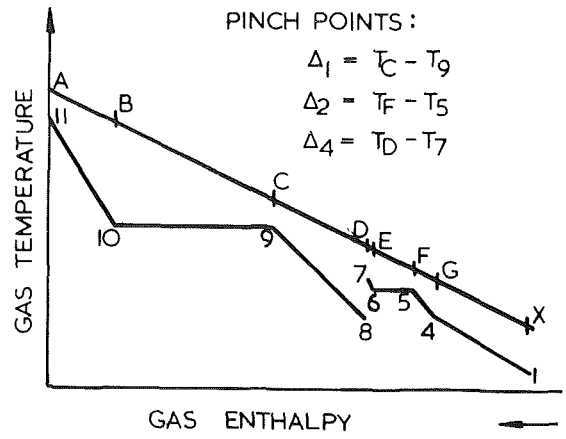


Fig. 4 Matching diagram Fig. 1 cycle

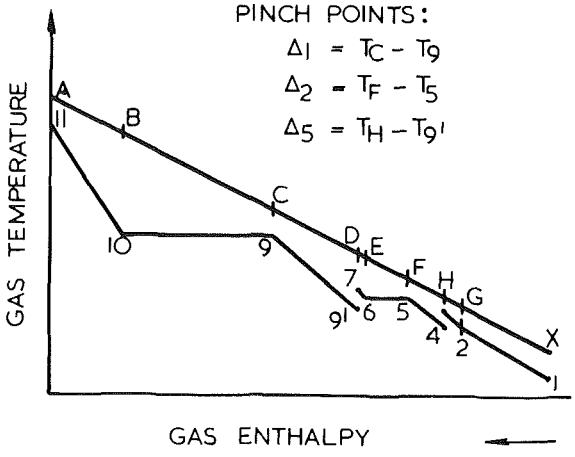


Fig. 5 Matching diagram fig. 2 cycle

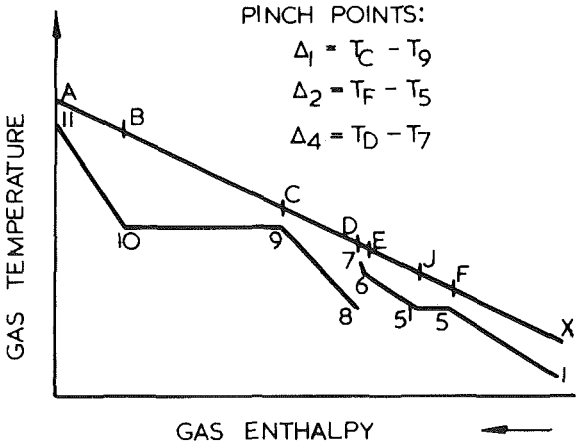


Fig. 6 Matching diagram Fig. 3 cycle

turbine and at the same time avoiding excessively superheated turbine exhaust.

For high-cycle efficiency it is equally important that the vapour mixture entering the condenser is as close to eutectic composition as possible otherwise condensation starts on the dewline at a temperature above the minimum cycle temperature – the eutectic temperature. It is this factor which usually determines which is the better organic. For the Figs. 1 and 2 configurations steam/octane is the best of the steam/alkane systems and steam/nonane optimises the Fig. 3 cycle.

Fig. 1 Cycle. Specific work output generally rises with rising p_H and falling p_L. The lower the value of p_L the more heat can be extracted from the gas and this is the dominant factor in W. Fundamentally, the LP part of this cycle is not well matched to the duty because of the high ratio of latent heat: preheat of the organic liquid from eutectic temperature to boiling point, Fig. 4. Thus it is impossible to operate with a low superheat fluid: gas temperature difference, Δ_4, and at the same time keep the stack temperature low. The maximum $W = 125$ kJ/kg gas corresponded to $p_H = 80$ bar and $p_L = 3.5$ bar with a steam/octane binary. At this condition $\Delta_4 = 71$K, stack temperature $t_x = 109°$C and cycle efficiency of the bottoming cycle is 30 percent Table 2.

Fig. 2 Cycle. Again the maximum $W = 129$ kJ/kg gas

Downloaded 01 Jun 2010 to 171.66.16.62. Redistribution subject to ASME license or copyright; see http://www.asme.org/terms/Terms_Use.cfm

Table 1 Calculation constants

Cycle temp °C/pinch pt. Δt_SK					Gas properties		Isentropic efficiencies			
t_c	t_{11}	Δ_1	Δ_2	Δ_4	t_A	h_A	c_{pm}	η_p	η_{HP}	η_{LP}
30	475	30	30	≥30	513	506	1.047	0.70	0.82	0.86

Table 2 Cycle performance details

Cycle	Performance		Pressures bar			H_2O mass fractions				Organic
	W kJ	η cycle %	p_H	p_L	p_C	$x_{LP\,turb}$	x_{ec}	X	y	
Fig. 1	125	30	80	3.5	0.067	0.381	0.212	–	–	Octane
Fig. 2	129	29	80	3.5	0.067	0.344	0.212	–	–	Octane
Fig. 3	137	31	80	7.5	0.050	0.436	0.427	0.048	0.935	Nonane
Conventional	130	31	50	3.5	0.042	–	–	–	–	–

Cycle	Temperatures °C							Δ_4K	m_L	$\eta_{LP\,turb.}$ %
	$t_{2/3}$	t_5	t_6	t_7	t_9'	t_{LPin}	t_X			
Fig. 1	125	177	177	177	–	160	109	71	0.261	0.86
Fig. 2	125	177	177	182	–	165	90	75	0.289	0.86
Fig. 3	158	158	223	231	151	216	90	30	0.244	0.86
Conventional	139	139	–	208	–	191	110	30	0.135	0.83

occurred at p_H = 80 bar, p_L = 3.5 bar with a steam/octane mixture. Corresponding stack temperature is t_X = 90°C and the cycle efficiency 29 percent, Table 2. Superheater pinch point, Δ_4, at 75K is again high for the reasons mentioned above keeping down the cycle efficiency. However, more heat is taken up from the gas due to splitting up the HP water preheat.

An important factor in the relatively low efficiency of the Figs. 1 and 2 cycles is that the LP turbine vapor mass fractions, which in effect have been determined by the matching of the cycle to the cooling gas, are between 0.35 and 0.40, Table 2, whereas the eutectic mass fraction at the condenser pressure is 0.21. As a result between 40 and 50 percent of the condensation occurs at a temperature above the minimum cycle temperature.

Fig. 3 Cycle. It is evident from figure 6 that this cycle is a good match to the exhaust gas cooling. In the LP section the important preheat: evaporation ratio can be controlled by varying the proportion of water from the separator circulated to the LP heaters. The larger this ratio the lower the stack temperature and there is a limit set by the tendency for the LP expansion to enter the wet region and the LP section flow rate to be reduced, both because of the increased water content.

The maximum W = 137 kJ/kg gas occurs at p_H = 80 bar, p_L = 7.5 bar in this case. The stack temperature is 90°C, the LP turbine steam mass fraction 0.44 and the cycle efficiency 31 percent, Table 2. If p_L is reduced to 3.5 bar the gas can be cooled to 80°C but there is a reduction in cycle efficiency and the specific work output is actually lower. This cycle has a unique combination of advantages in that it matches the heat load well at the composition which is eutectic at the condenser pressure.

Conventional Cycle. Current designs use high pressures between 50 bar and 26 bar with intermediate pressures p_L in the range 5 bar to 3.5 bar and stack temperatures of around 110°C. Based on the conditions of Table 1 specific work, W, increases only slightly with increase in p_H and decrease in p_L. Allowing a maximum turbine exhaust wetness of 12%, p_H = 50 bar, p_L = 3.5 bar gives the maximum value of W = 130 kJ/kg gas at a stack temperature of 110°C, Table 2. For comparison with the proposed cycle results, the LP turbine efficiency quoted in Table 1 was assumed to be a "dry" efficiency – the efficiency without wetness losses. A Baumann wetness correction, of 1 percent reduction in stage efficiency for each 1 percent average wetness in the stage, was made [5]. The assumption underlying this comparison of conventional and proposed cycle LP turbine efficiencies is that it is possible to design the stream/organic turbine to the same efficiency level as the steam turbine without wetness corrections.

Discussion

Clearly, in performance, the Fig. 1 cycle is much inferior to the conventional cycle and the Fig. 2 cycle slightly less so although it has the advantage of a completely dry turbine expansion. These cycles are therefore in themselves of no interest from a design point of view. However, the flexibility in positioning the preheaters in the gas stream with consequent rise in overall efficiency is interesting. A 3 percent rise in specific work results from simply switching the lower temperature part of the high pressure section water preheat from upstream of the LP boiler section to downstream. The author feels that further ingenuity in this vein can raise the output above that of the conventional cycle without the complication of binary boiling as in the Fig. 3 cycle.

Specific work output of the Fig. 3 cycle is about 5 percent greater than for the conventional dual pressure cycle for an increase in heat uptake from the gas of only 5 percent. Its cycle efficiency is no lower despite its lower overall average temperature of heat addition. This is due to a combination of better matching and lack of wetness losses in the LP turbine. The condenser cooling water requirement is increased by only 5 percent also.

Downloaded 01 Jun 2010 to 171.66.16.62. Redistribution subject to ASME license or copyright; see http://www.asme.org/terms/Terms_Use.cfm

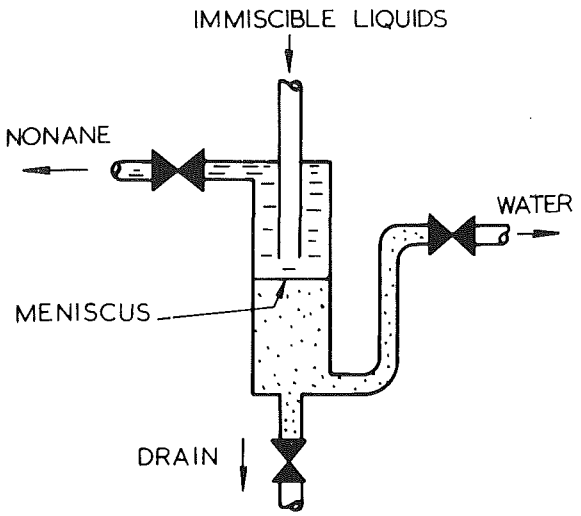


Fig. 7 Simple separator

Some comment on the choice of pinch point temperature differences and turbine efficiencies in Table 1 is necessary. These conditions were chosen merely to provide an example of the comparison with the conventional cycle which would result in a conventional cycle stack temperature similar to present designs. Lower turbine efficiencies lead to drier expansions with lower wetness corrections and less advantage to the proposed cycle. However, it is likely that the wetness corrections applied are an underestimate especially for low percentage wetness in the turbine [6].

Working Fluid Stability. The alkanes are known to be very stable compounds. In the Fig. 3 cycle proposed, Table 2, the top temperature to which the organic/steam mixture is subjected is only 231°C. The steam/nonane mixture is expected to be extremely stable at this temperature and the low pressure of 3.5 bar. Some experience of this has been gained in the author's laboratory in an experimental study of condensation of steam/nonane mixtures at atmospheric pressure. The nonane is subject to a maximum temperature of about 180°C on the surface of the boiler heaters. The mixture comes into contact with copper, brass and steel in various parts of the apparatus. Tests are run continuously for several months with no noticeable alteration in saturation temperatures. The same 2½-L sample of nonane has been used for over two years with a few changes of distilled water sample. At the end of this period samples of the nonane and samples of the original supply were analyzed by gas-liquid chromatography. No difference could be detected between them.

In these experiments complete physical separation of nonane and water was very simply achieved with the simple gravity separator shown in Fig. 7 making use of the lower density of nonane, 718 kg/m^3. This apparatus could be very simply adapted for use in the proposed cycle.

Water leaving the separator contains only a few parts in 10^5 of dissolved nonane. Raised to a temperature of around 500°C some dissociation is inevitable. The worst effect of this is a small amount of extra non-condensable gas in the condenser which can be removed in the usual way.

Nonane is inflammable with a flash point of 31°C. It is easily handled with a kinematic viscosity lower than water and is non-toxic in adequate ventillation. In the Fig. 3 configuration it is always in the presence of water or steam in oxygen-free atm. In the case of leakage into the heat recovery vapour generator a large excess of gas produces conditions in which combustion is extremely unlikely. With steam and water external shaft seals only, leakage of nonane into the ambient can be prevented entirely. In the author's opinion the risk involved is considerably less than that encountered in highway gas stations.

Design Problems. There are a number of component parts of the plant which are affected by the switch from conventional to steam/ILBC cycle. These are the LP preheater, the condenser and the LP turbine.

LP Preheater. Although the heat addition is increased by only 5 percent there is a disproportionate heat flow to the LP preheater because of the high intermediate pressure p_L, Table 3. In fact the preheater load is 65 percent higher than in the conventional cycle with a 15 percent lower log. mean temperature difference. A large increase in preheater surface area is necessary.

Condenser. Because nonane and water are immiscible liquids the pattern of flow on condensing surfaces is complex. According to Bernhardt et al. [7] the condensation heat transfer coefficient is best calculated as the liquid volume flow weighted average of the Nusselt film coefficients for water and nonane at the same film temperature difference. Based on a steam mass fraction of 0.436 – which corresponds to a water volume flow rate 35 percent of the total – the condensation heat transfer coefficient is about 46 percent of that in the steam condenser. Assuming as a rough approximation that the heat transfer resistance of the condensing film and cooling water boundary layers are about the same then the overall heat transfer coefficient of the steam/ILBC condenser is about 63 percent of the steam condenser. On this about 63 percent of the steam condenser. On this basis a 67 percent increase of condensing surface area is required allowing for the 5 percent increase in heat flow in the condenser. There is no steam-nonane intervapor diffusion resistance in the condenser since the vapour mixture entering is very close to the eutectic – the liquid condensed has the same composition as the vapour condensing.

LP Turbine. Without a complete design study it is impossible to determine all the consequences of the cycle conditions for the LP turbine performance. However, the following general remarks can be made by comparing the turbine duties, Table 4. If compressibility effects and stage loading, $\Delta h/U^2$, are to be kept to the same level then up to 40 percent more stages are required. Further the volume flow in the turbines is about the same requiring a higher blade height: mean diameter ratio and a lower mean diameter in the steam/ILBC turbine if the rotational speed is the same as the steam turbine.

Conclusion

The steam/ILBC dual pressure cycle shows some promise in extracting work from the gas turbine exhaust of combined cycles. Simple configurations like the Figs. 1 and 2 cycles, while not outperforming the conventional steam/steam cycle, indicate a flexibility brought to matching gas to fluid heat exchange which is capable of further exploitation. The Fig. 3 cycle, based on a typical set of cycle conditions, offers a 5 percent increase in output over the conventional cycle. Increased LP preheater and condenser heat transfer surface areas are the principle disadvantages of this cycle.

The author suggests that this cycle and its derivatives are worthy of consideration by designers of combined cycle plant especially at a time when increasing fuel costs is likely to permit more complication of high availability plant.

References

1 Vogt, R.L., "Low BTU Coal Gas Combustion in High Temperature

Downloaded 01 Jun 2010 to 171.66.16.62. Redistribution subject to ASME license or copyright; see http://www.asme.org/terms/Terms_Use.cfm

Table 3 LP preheater duty and temperatures

Cycle	Liquid temp. °C		Gas temp. °C		Heat flor kJ/kg gas	Percent total heat flow
	In	Out	In	Out		
Steam/steam	30	139	169	110	62	15
Steam/ILBC	30	158	188	90	102	23

Table 4 Comparison of LP turbine duties

Cycle	Enthalpy drop kJ/kg	Sonic velocity binary:steam	Volume flow ratio binary steam		Pressure ratio
			Inlet	Exhaust	
Steam/steam	553	–	–	–	118
Steam/ILBC	377	0.7	1.02	0.87	149

Turbines," ASME Gas Turbine Conference, New Orleans, Mar. 1980, Paper No. 80-GT-170.

2 Caruvana, A., Cincotta, G.A., Rose, R.S., and Alderson, E.D., "The Design Test of a 72.5 MW Water-Cooled Gas Turbine," *Ibid.*, Paper No. 80-GT-112.

3 Coats, R., "Gas Turbines in Combined Cycles, Repowering and Combined Heat and Power Production," *British Energy Exhibition,* Peking, June 1979.

4 Burnside, B.M., "Bottoming Gas Turbine-Electric Plant by Immiscible Liquid Cycle," *ASME Gas Turbine Conference,* New Orleans, Mar. 1980, Paper No. 80-GT-24.

5 Burnside, B.M., "A Professional Exercise in Applied Thermodynamics," *International Journal of Mechanical Engineering Education,* Vol. 8, No. 1, 1980, pp. 25-32.

6 Moore, M. J. and Sieverding, C. H., eds., *Two-Phase Steam Flow in Turbines and Separators*, McGraw-Hill, New York, 1976, p. 106.

7 Bernhardt, S.H., Sheridan, J.J., and Westwater, J.W., "Condensation of Immiscible Mixtures," *AIChE Symposium Series,* Vol. 68 No. 118, 1971, pp. 21-37.

8 Burnside, B.M., "The Immiscible Liquid Binary Rankine Cycle," *Journal of Mechanical Engineering Science,* Vol. 18, No. 2, 1976, pp. 79-86.

APPENDIX

In the cycle calculations the following simplifying assumptions were made in addition to those already mentioned.

(*a*) Circulating pump power, pressure losses, steam to seals, effect of alteration in heat exchanger arrangements on gas turbine back pressure and power to circulating pumps (but not to feed pumps) were ignored.

(*b*) Mixtures of steam and nonane were assumed to be ideal mixtures of real gases [8].

(*c*) Liquids were supplied to the evaporators at the saturation condition and no vapor was bled from the evaporators for deaeration.

(*d*) All flow conditions were assumed adiabatic except in the heat exchangers.

Applying the steady flow energy equation to each section of the heat exchanger, the feed pumps and turbines and solving, the following solutions were obtained. The nomenclature refers to Figs. 1-6.

Fig. 1 Cycle. Steam mass fraction in LP turbine, x, and stack gas enthalpy, h_x, are given by

$$x=\frac{(h_7-h_5)}{(h_C-h_F)\cdot(h_{11}-h_9)/(h_A-h_C)+(h_7-h_5)-(h_9-h_8)} \quad (1)$$

and

$$h_X = h_F-\frac{(h_A-h_C)}{(h_{11}-h_9)}\cdot\Big[h_{3W}-h_{13W}+h_{130}-h_5 + \frac{(h_5-h_{130})}{(h_7-h_5)}\cdot\Big\{\frac{(h_C-h_F)}{(h_A-h_C)}\cdot(h_{11}-h_9) + (h_7-h_5)-(h_9-h_8)\Big\}\Big] \quad (2)$$

Mass flows/kg gas in LP and HP turbines and in the organic heaters, m_I, m_S and m_O are

$$m_L=(h_A-h_C)/x\cdot(h_{11}-h_9) \quad (3)$$

$$m_S=m_L\cdot x \quad (4)$$

$$m_O=m_L(1-x) \quad (5)$$

Gas enthalpies h_C and h_F are determined by the pinch point temperature differences Δ_1 and Δ_2 and the enthalpy at LP turbine inlet is

$$h_{\text{inLP}}=x\,h_{\text{exst}}+(1-x)h_7 \quad (6)$$

Fig. 2 Cycle. In this case

$$x=\frac{(h_{130}-h_7)\cdot(h_A-h_C)}{\{(h_{11}-h_8-h_7-h_{13W}+h_{3W}+h_{130})\cdot(h_A-h_C) - (h_{11}-h_9)\cdot(h_A-h_x)\}} \quad (8)$$

h_C is determined by the pinch point temperature difference Δ_1. Given stack temperature, t_X, and hence h_X, x can be calculated.

LP turbine mass flow, m_L, is

$$m_L=\frac{(h_A-h_X)}{(h_2-h_1)+x\cdot(h_{11}-h_8)+(1-x)\cdot(h_7-h_4)} \quad (9)$$

Enthalpy, h_9', at outlet from the first section of HP preheat is

$$h_9'=h_9-(h_C-h_F)/m_L\cdot x+(1-x)\cdot(h_7-h_5)/x \quad (10)$$

m_s, m_O and h_{inLP} are again given by equations (4-6).

Fig. 3 Cycle. This solution is a little more complicated.

$$x=\frac{(h_A-h_B)\cdot(h_{30}-h_{130})}{\{y\cdot(h_{11}-h_{10})\cdot(h_F-h_X)+(h_A-h_B) \cdot(h_{30}-h_{130}-h_{3W}+h_{13W})\}} \quad (11)$$

and

$$h_8=h_C+(h_A-h_C)\cdot(h_{10}-h_9)/(h_{11}-h_9) \quad (12)$$

h_C and h_F are determined by Δ_1 and Δ_2. Given stack temperature, t_X, and the proportion, y, of the water entering the separator which is pumped to the HP heater, x is known.

Downloaded 01 Jun 2010 to 171.66.16.62. Redistribution subject to ASME license or copyright; see http://www.asme.org/terms/Terms_Use.cfm

The mass fraction of water in the LP heaters, X, is

$$X = x \cdot (1-y)/(1-x \cdot y) \tag{13}$$

Mass flows/kg gas are

$$m_L = (h_F - h_X)/(h_2 - h_1) \tag{14}$$

$$m_S = m_L \cdot x \cdot y \tag{15}$$

$$m_O = m_L \cdot (1 - x \cdot y) \tag{16}$$

LP turbine inlet enthalpy is

$$h_{\text{inLP}} = x \cdot y \cdot h_{\text{exst}} + (1 - x \cdot y) \cdot h_7 \tag{17}$$

The specific enthalpy, h_5', of the mixture of eutectic vapour and organic entering the LP noneutectic boiling section is [8]

$$h_5' = \{ (X - x_{eLP}) \cdot h_{fW} + (1 - X) \cdot h_{eLP} \}/(1 - x_{eLP}) \tag{18}$$

where h_{fW} is the enthalpy of water at the eutectic temperature and h_{eLP} is the enthalpy of the eutectic vapor mixture.

Downloaded 01 Jun 2010 to 171.66.16.62. Redistribution subject to ASME license or copyright; see http://www.asme.org/terms/Terms_Use.cfm

R. P. Dring
Supervisor,
Gas Turbine Technology

H. D. Joslyn
Research Engineer.

L. W. Hardin
Research Engineer.

United Technologies Research Center
East Hartford, Conn.

An Investigation of Axial Compressor Rotor Aerodynamics

The detailed nature of the three-dimensional flow over the blading, and in the wake, of an isolated compressor rotor has been studied experimentally in a large scale rotating rig. A variety of flow properties were measured including (1) blade profile and endwall surface flow visualization, (2) radial-circumferential arrays of pneumatic wake data acquired in the rotating frame and (3) full-span blade pressure distribution data. Data have been obtained over a wide range of blade loading and downstream location. These results show a hub corner stall at lower blade loadings and full-span blade separation at higher blade loadings. Under both conditions there is strong radial flow on the airfoil. The radial flow in the wake, however, increases dramatically when the blade undergoes full-span separation. The impact of these flow phenomena on the blade pressure distribution is also illustrated.

Introduction

Current trends in turbomachinery toward more highly loaded blading with lower aspect ratios are placing an increasingly severe burden on typical design systems due to the increasingly three-dimensional nature of the flows they produce. The majority of the analytical tools currently in use are severely limited in the degree to which they account for three-dimensional aspects of the flow. Through-flow calculations are fundamentally based on the assumption of strip-theory. The works by Hearsey [1] and Sehra [2], however, represent initial attempts at modeling of some of the physical mechanisms due to radial flow effects. Typical blade-to-blade calculations (e.g., Caspar, et al. [3]) account for three-dimensionality only to the degree to which they include a model of steam tube contraction. The limited capabilities of these basically two-dimensional analyses have prompted the development of a number of three-dimensional calculations. Examples of this can be seen in the works by Denton [4], Dodge [5] and Briley and McDonald [6]. The emergence of these analyses has been paralleled by the emergence of a body of high quality experimental data which is essential for comparison. The works by Langston [7] and by Graziani [8] provide a detailed description of the aerodynamics and heat transfer due to the highly three-dimensional flow near a turbine blade endwall. It was the objective of the present work to provide a similar body of benchmark aerodynamic data for an axial compressor rotor. This was achieved by acquiring experimental data describing both the flow on the airfoil, as evidenced by surface flow visualization and by pressure distributions, and the flow in the airfoil wake.

Of the existing experimental studies in the area of rotor wake flows, the most notable have been conducted by Thompkins and Kerrebrock [9], Lakshminarayana and his coworkers [10–13], Hirsch et al. [14] and by Kool et al. [15]. As a result of these and other similar studies, many of the effects that contribute to the complex three-dimensional nature of the flow in a compressor rotor have become apparent. In brief, these effects include: very large radial velocities in the wakes of transonic rotors, symmetric and asymmetric wake radial velocity profiles, similarity of wake profile shape, and local regions of large radial flows near endwalls. However, since these studies had concentrated on various specific aspects of rotor flows, there existed a need for a body of benchmark data describing all of the essential elements of the flow over, and aft of, a rotor in sufficient detail to permit careful comparison with existing analytical predictions and to provide guidance to future modeling efforts.

The present program was formulated to satisfy this need. A rotor with a clean (axial) inflow was chosen so that upstream conditions would be well defined. The airfoil and velocity triangle parameters of the rotor were representative of a blade in the middle of a multistage compressor. The rotor was relatively highly loaded and had an aspect ratio of one. The Reynolds number was typical of an engine application. The data acquired included (1) the rotor pressure rise characteristic, (2) the hub and casing inlet boundary layer velocity profiles, (3) blade surface flow visualization, (4) fullspan wake data from 10 to 110 percent of axial chord aft and over a range of incidence, and (5) fullspan blade surface pressure distributions over a range of incidence. From these data it was observed that a strong radial redistribution of fluid occurred due to three-dimensional effects (nonstrip theory effects) both in the flow over the airfoil and in its wake and that the blade pressure distribution was strongly influenced by proximity to the endwalls.

Contributed by the Gas Turbine Division and presented at the International Gas Turbine Conference and Products Show, Houston, Texas, March 9–12, 1981, of THE AMERICAN SOCIETY OF MECHANICAL ENGINEERS. Manuscript received at ASME Headquarters, December 4, 1980. Paper No. 81-GT-56.

Copyright © 1982 by ASME

Downloaded 01 Jun 2010 to 171.66.16.62. Redistribution subject to ASME license or copyright; see http://www.asme.org/terms/Terms_Use.cfm

Experimental Facility and Instrumentation

The experimental program was carried out in the United Technologies Research Center's Large Scale Rotating Rig (LSRR). This facility is 5 ft (1.52 m) in diameter. The compressor rotor model had a 0.8 hub/tip ratio and at typical running conditions the shaft speed was 510 rpm. The airfoil true chord was 6 in. (0.15 m) and was constant with span. This resulted in an airfoil aspect ratio of 1.0 and a Reynolds number range (based on relative inlet flow speed at midspan) of 4.3×10^5 to 5.0×10^5. The details of the airfoil geometry are listed in Table 1. The axial chord of the airfoil at midspan was 5 in. (0.13 m). The rotor tip clearance was 2.3 percent chord at the leading edge, 1.0 percent chord at midchord, and 3.3 percent chord at the trailing edge.

The axial locations of the planes at which traverse data were obtained were measured with respect to the airfoil midspan trailing edge locaton and normalized by the midspan axial chord. A cross-section of the flow path is shown in Fig. 1 with the traverse plane in its 10 percent aft location. The locations of the various flow path static pressure taps and the location of the hub and casing inlet boundary layer surveys are also indicated. The rig flow (C_x) was based on the static pressure at Sta. 0 and the rotor pressure rise was based on the static pressure difference between Sta. 3 and Sta. 0.

The probe was mounted in a traverse device located inside the rotor hub. The probe could be traversed circumferentially and radially from hub to casing. The probe can also be rotated in yaw until the probe yaw nulling taps are balanced. The probe used in this program was a United Sensor five hole probe (USC-F-152) which had been modified to include a cobra probe for acquiring data close to the hub. The probe diameter was small relative to the blade pitch (D = 1.5 percent τ_m). The five-hole probe was used to measure total and static pressures and flow yaw and pitch from 13 to 97 percent span. The cobra probe was used to measure total and static pressure and yaw down to 4 percent span. Pneumatic switching between the two probe tips, calibration of all the rotating frame pneumatic transducers and operation of the rotating frame Scanivalve were all carried out remotely while the rotor was turning. The accuracy of the pressure measurement system was typically ± 2 percent of reading. Since all pressure measurements were referenced to the inlet absolute total pressure (P_{T1}) the uncertainty is ± 2 percent of C_p. The details of the rig, the traverse system, the instrumentation and the flow visualization technique (ammonia gas on Ozalid paper) are discussed in greater detail in reference [16].

Table 1 Rotor airfoil geometry

Contour - NACA 65 Series
Chord (B) - 6 in. (0.1524 m)
Chamber - Circular Arc
No. of Airfoils - 28

Span (percent)	0	25	50	75	100
$-\beta_1{}^*$ (deg)	64.63	58.20	59.45	61.55	64.97
$-\beta_2{}^*$ (deg)	−14.77	4.25	11.50	15.55	15.53
t/B	0.0900	0.0825	0.0750	0.0675	0.0600
Radius (in.)	24.0	25.5	27.0	28.5	30.0

Due to the large bulk of data acquired in this program only a small fraction can be presented here. A more complete presentation and discussion of the data is available in references [17] and [18]. In addition, all of the traverse data (roughly 80,000 pieces of information) are available on magnetic tape, as described in [17] and [18].

Nomenclature

B = airfoil true chord
B_x = airfoil axial chord
C_P = flow pressure coefficient: $(P_{T1} - P)/Q_{Um}$
C_P = blade pressure coefficient: $(P-P_1)/Q_1$
$C_{PT(rel)}$ = relative total pressure drop: $(P_{T1}(r) - P_{T2}(r))/Q_{Um}$
C_x = axial component of flow velocity
C_θ = tangential component of absolute flow velocity
D_{loc} = local diffusion factor: $(V_{max} - V_2)/V_{max}$
F = pressure force per unit span on the airfoil
H = boundary layer shape parameter: (δ^*/θ)
h = stream tube height
P = pressure
P_s = static pressure
P_T = total pressure
P_{T1} = inlet absolute total pressure
Q_1 = inlet relative dynamic pressure
Q_{Um} = dynamic pressure based on midspan wheel speed: $1/2\ \rho U_m{}^2$
r = radius
r_m = radius at midspan
t = airfoil thicknes
U_m = wheel speed at midspan: $(\Omega \cdot r_m)$
V = flow velocity in the rotating frame
V_c = ideal (inviscid) flow speed at wake center (where $V = V_m$)
V_i = inviscid flow speed
V_m = minimum flow speed in the wake
V_{max} = maximum suction surface flow speed
V_2 = downstream flow speed
W = wall static pressure
X = axial distance
y = tangential distance
β^* = airfoil metal angle (from axial direction, positive in direction of rotation)
δ = wake half width
δ^* = displacement thickness
θ = momentum thickness
θ = circumferential angular position
Θ = yaw (from axial direction, positive in direction of rotation)
ϕ = pitch (positive away from rig axis)
ρ = fluid density
Ω = rotational lspeed
ζ = relative vorticity
τ_m = airfoil pitch at midspan

Subscripts

R = radial component (positive away from rig axis)
T = tangential component (positive in direction of rotation)
X = axial component

Downloaded 01 Jun 2010 to 171.66.16.62. Redistribution subject to ASME license or copyright; see http://www.asme.org/terms/Terms_Use.cfm

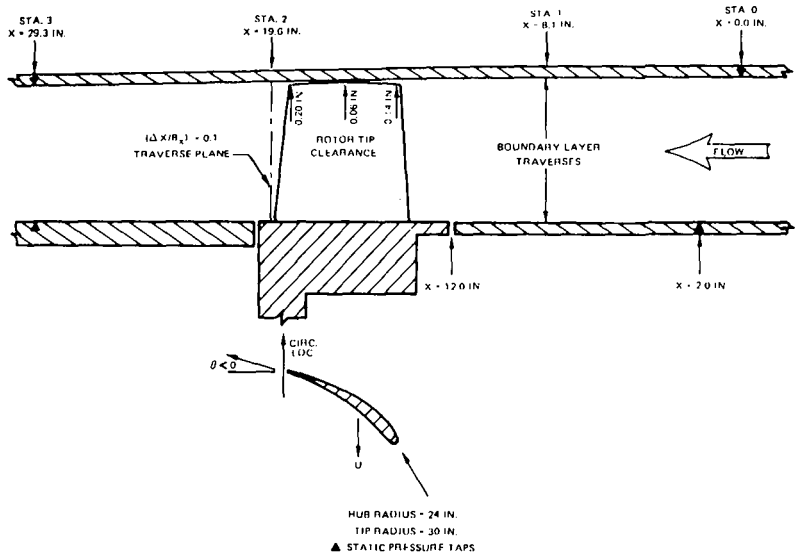


Fig. 1 Flow path schematic

Table 2 Inlet boundary layer integral properties

	Hub	Tip
δ^* (in.)	0.053	0.087
θ (in.)	0.041	0.060
H	1.30	1.32

Background Data

Two types of stationary frame data were acquired in order to document the overall rotor performance: the hub and tip inlet boundary layer velocity profiles and the rotor static pressure rise characteristic. The inlet velocity profiles were measured at Sta. 1 (Fig. 1). Integral properties of the inlet boundary layers are listed in Table 2. Variation of C_x over the test range was seen to have no significant effect on the profiles. The displacement and momentum thicknesses were 1 to 2 percent of the blade chord (or span) and the boundary layer thickness was 5 to 10 percent of the blade chord. The hub boundary layer was somewhat thinner than that at the tip because the length of the hub centerbody was less than that of the flow path casing.

The rotor static pressure rise characteristic is shown in Fig. 2. The static pressure rise data from the hub and tip pressure taps (at Sta. 3, Fig. 1) are shown along with the interpolated midspan static pressure rise. The midspan static pressure rise was interpolated assuming a free-vortex flow variation between the measured hub and tip values.

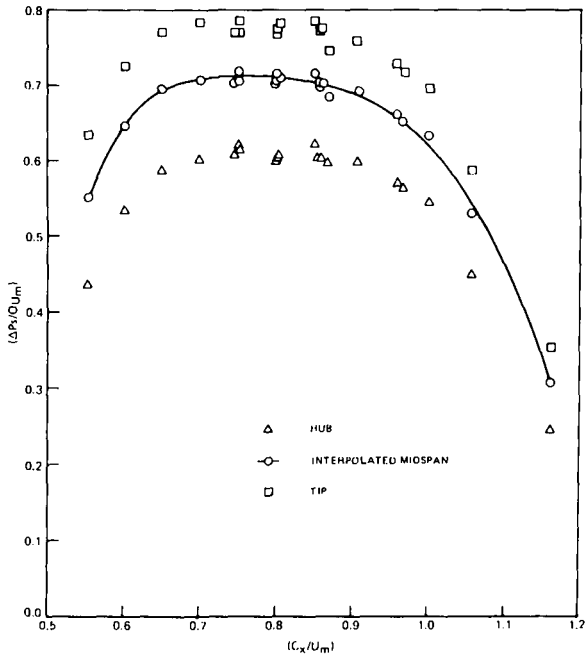


Fig. 2 Rotor static pressure rise

Flow Visualization

The results of the airfoil surface flow visualization will be discussed in some detail in order to clarify at the outset many of the phenomena that will be seen in the traverse data and in the airfoil pressure distributions.

The nature of the blade surface flow at a (C_x/U_m) of 0.85 is shown in Fig. 3. At this condition it was clear that there was a hub corner stall on the suction surface and that there was considerable back-flow. The back-flow persisted out to about 25 percent span and there was a strong spanwise displacement of the boundary layer out to 50 percent span. Ahead of this region and near the tip, the boundary layer flow was essentially streamwise and attached.

At this same condition the pressure surface was found to have only a weak spanwise velocity component toward the tip (see [18]). At the tip the radial component was slightly stronger due to flow leaking over the unshrouded tip of the blade. There was no direct evidence of a scraping vortex as described by Hansen et al. ([19], Chapter XV). Direct evidence would consist of radial flow toward the hub in the immediate vicinity of the tip on the pressure surface. The scraping vortex, however, may have been present and simply limited to reducing the amount of radial out-flow due to tip leakage.

The hub flow visualization started approximately 25 percent B_x ahead of the airfoil leading edge (Fig. 3) and indicated a skew of approximately 10 deg, relative to the main stream flow direction, toward the pressure surface. This was due to the skewing of the hub boundary layer as it passed from the stationary upstream hub to the moving rotor hub. By the time the hub boundary layer entered the blade channel the skewing was reduced and the surface stream lines were

Downloaded 01 Jun 2010 to 171.66.16.62. Redistribution subject to ASME license or copyright; see http://www.asme.org/terms/Terms_Use.cfm

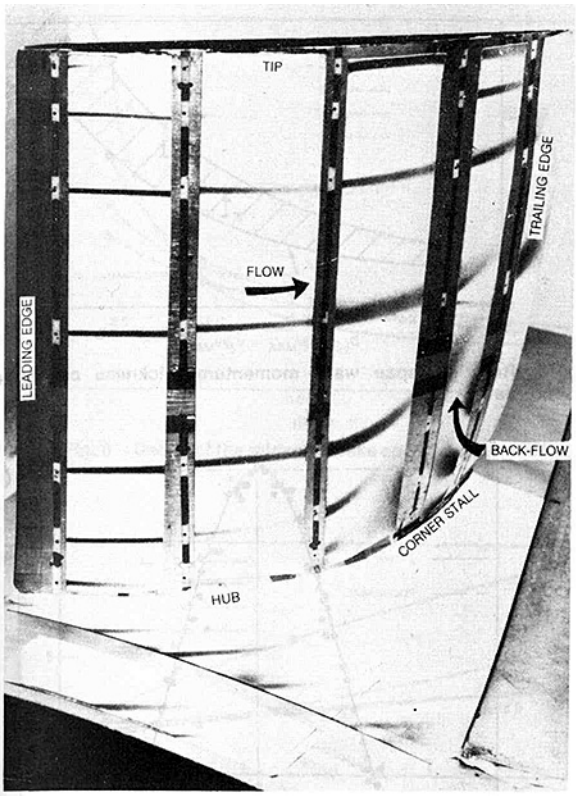


Fig. 3 Suction surface flow visualization at $(C_x/U_m) = 0.85$

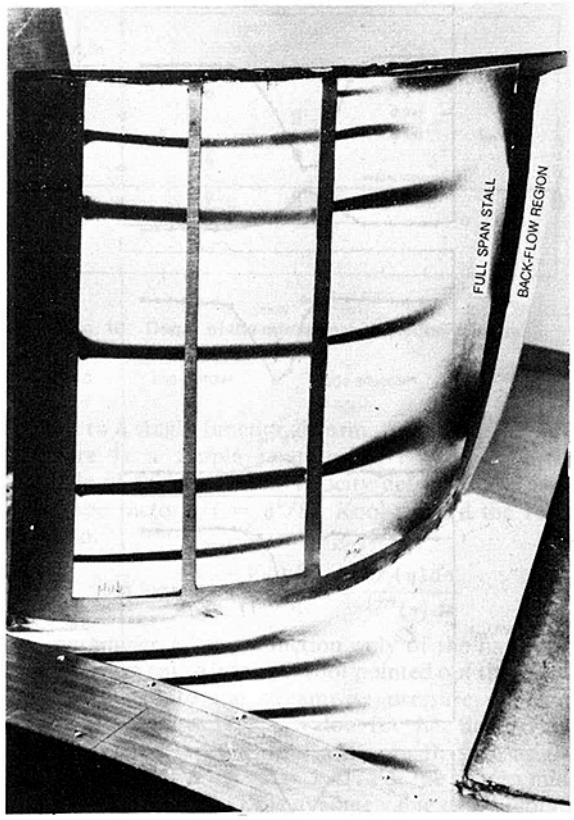


Fig. 4 Suction surface flow visualization at $(C_x/U_m) = 0.65$

nearly parallel to the main flow stream lines. There was little evidence of secondary flow this far forward in the hub endwall boundary layer.

As the loading was increased and the rotor was driven toward stall there was a dramatic change in the nature of the suction surface flow. This could be seen in the flow visualization at a (C_x/U_m) of 0.65 (Fig. 4). The airfoil suction surface boundary layer had separated over its entire span and there was back-flow near the trailing edge extending from hub to tip. The suction surface flow had no significant radial component until it reached the separated region, at which point it abruptly developed a strong component toward the tip. The endwall boundary layer fluid that had been accumulating at the hub at higher values of (C_x/U_m) due to a relatively healthy blade boundary layer was found to be flowing out to the tip through the back-flow region.

As a result of the flow visualization one can begin to appreciate the complexity of the flow in the rotor passage. At higher values of (C_x/U_m), greater than 0.65, it can be anticipated that the hub corner stall will have an impact on the pressure distribution over the inner half span. In addition, it should show up as a region of high loss concentration in the wake. At values of (C_x/U_m) at and below 0.65, it can be anticipated that the suction surface boundary layer separation will have an impact on the pressure distributions across the entire span and that as a result of the radial flow in the separated region there will be strong radial flow in the wake and a strong spanwise redistribution of high loss fluid.

Midspan Wake Traverse Data

Wake traverse data were acquired at axial locations 10 percent, 30 percent, 50 percent, and 110 percent of axial chord aft of the blade trailing edge at midspan. At each axial plane, full span data were acquired for values of (C_x/U_m) of 0.65, 0.75, 0.85, and 0.95. By way of introduction to the fullspan data, attention in the present section will be limited to the midspan data.

The behavior of the blade wake at midspan and 10 percent aft of the blade trailing edge is shown in Fig. 5 for (C_x/U_m) decreasing from 0.95 to 0.65. This corresponds to the midspan inlet flow angle (yaw) increasing from 46.5 to 57.0 deg, or the incidence going from -13.0 to -2.5 deg. Figure 5 illustrates the normalized flow speed and the radial component of velocity over the portion (25 percent) of the pitch which contains the blade wake. At a (C_x/U_m) of 0.95 the maximum wake speed defect was about 30 percent and the radial velocity variation was small and asymmetric across the wake. As the flow (C_x/U_m) was reduced and the rotor loading was increased, the maximum wake speed defect increased to about 70 percent at a (C_x/U_m) of 0.65. The magnitude of the radial velocity in the wake increased and the distribution became nearly symmetric. As the rotor loading was increased the wake progressed from having weak in and out flow ($\pm$ 2 percent of U_m at 0.95) to having a very strong radial out flow (+ 18 percent of U_m at 0.65). Clearly, airfoil loading had a strong impact on the magnitude of the nonstrip theory effects as a result of such flows.

These conclusions are consistent with the observations made earlier based on the flow visualization. Note that for a (C_x/U_m) of 0.65, by 10 percent aft of the blade trailing edge the separation bubble had closed, i.e., the back-flow region did not penetrate this far aft at midspan. In addition, the pitch angle which was locally 90 deg on the blade surface (Fig. 4) had dropped considerably by 10 percent aft (to 30 deg in the center of the wake). Centrifugal effects appear to have been strong on the blade surface and in the wake when the airfoil boundary layer was separated. However, when the boundary layer was attached the radial flow on the airfoil (Fig. 3) and in the wake (Fig. 5) was relatively weak.

For reasons that will be discussed below it is believed that the asymmetric nature of the wake pitch angle distributions at 0.85 and 0.95 were due to the shed vorticity arising from a spanwise gradient in blade circulation, i.e., increasing cir-

Downloaded 01 Jun 2010 to 171.66.16.62. Redistribution subject to ASME license or copyright; see http://www.asme.org/terms/Terms_Use.cfm

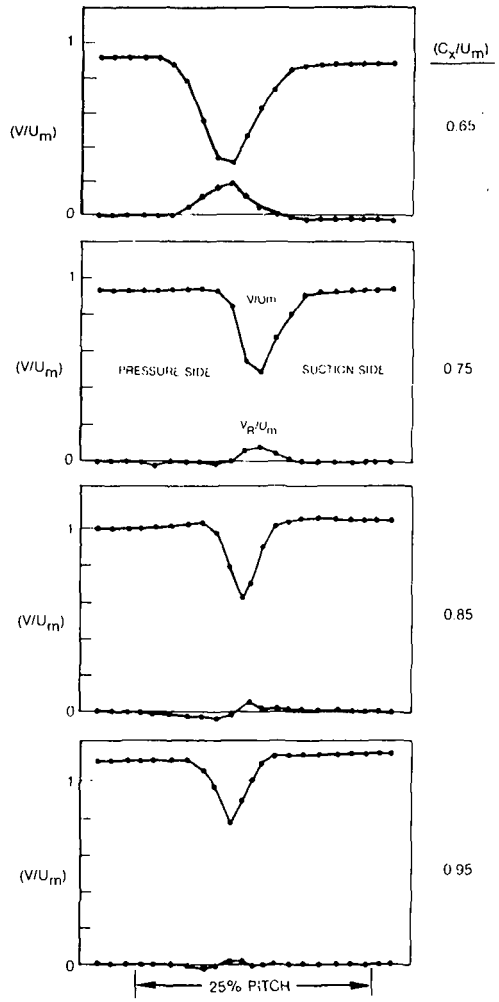


Fig. 5 Rotor midspan wake, 10 percent aft

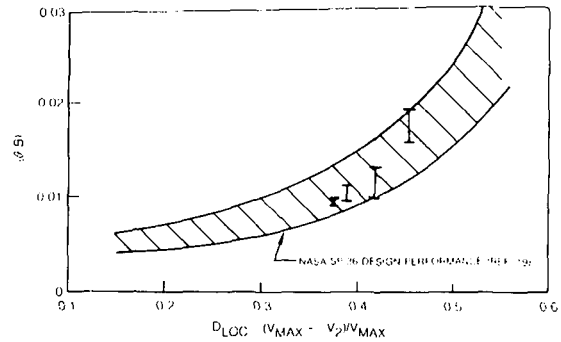


Fig. 6 Rotor midspan wake momentum thickness compared to cascade data

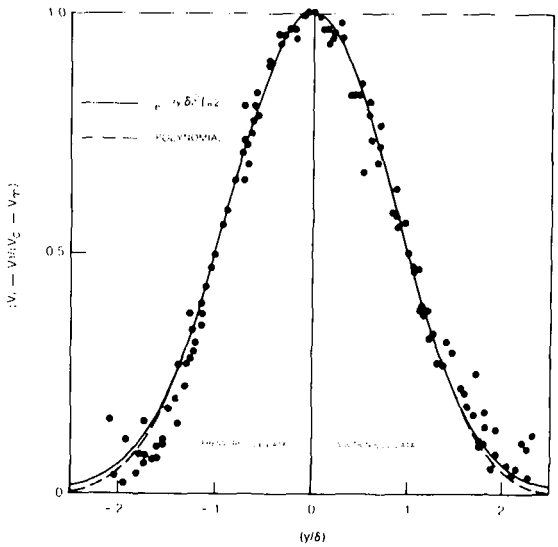


Fig. 7 Normalized midspan wake profile

culation with radius. These inviscid effects become apparent when the blade boundary layer and wake were sufficiently weak (thin and shallow) so as to be only weakly influenced by centrifugal effects.

The rotor midspan wake momentum thickness (normalized by airfoil chord) was compared with the design point cascade data of reference [19] (Fig. 146) as a function of the measured local D factor in Fig. 6. The D factor ([19], equation 265) was computed directly from the measured pressure distributions. Although the rotor data represents several incidences, it was seen to be in excellent agreement with the cascade data.

The rotor midspan wake has been analyzed from the points of view of a universal defect function, defect decay, and wake width growth. These are important considerations in the area of rotor/stator interaction. Both the acoustic and structural response of a stator to gust fluctuations will depend on the nature of the defect profile and the way in which it decays as it is convected downstream. In addition, the nature of the wake migration within downstream rows (see Kerrebrock and Mikolajczak [20]) depends on the wake profile shape and defect strength.

Since the free-stream velocity at the pressure and suction side edges of the wake may be different due to potential flow effects, the wake edges were defined by examining the total pressure. The "inviscid" flow speed (V_i) was assumed to vary linearly between the measured values of the flow speed at the wake edges. The inviscid reference velocity (V_c) was chosen as the value of the inviscid speed (V_i) at the location corresponding to the center of the wake at its mid-depth, $(V_c + V_m)/2$. Distances (y) were measured relative to the wake center at the mid-depth. The local wake depth ($V_i - V$) was normalized by the maximum wake depth ($V_c - V_m$) and the distance from the mid-depth wake center (y) was normalized by the mid-depth semi-width (δ). The result is illustrated in Fig. 7. This figure includes all sixteen midspan wake traverses (for four values of (C_x/U_m) and four values of $(\Delta X/B_x)$). The data are seen to correlate very well on this basis. Included in the figure is the Gaussian distribution (exp $(-\eta^2 \ln 2)$) proposed by Reynolds et al. [11]. The fact that this function agrees so well with the data is not surprising when one considers that they must agree exactly at $\pm\infty$, ± 0.5 and near 0. There is a slight difference between the correlation in reference [11] and that shown in Fig. 7. Reynolds et al. [11] suggest using V_m to define wake suction and pressure side mid-depth widths which are not necessarily equal (i.e., $\delta_s \neq \delta_p$). This added degree of complexity of the correlation results in the wake minimum speed being located precisely at $y = 0$. In the present work the wake semi-width was taken as the same for both sides of the wake and the wake minimum speed was not necessarily precisely at $y = 0$. The data of the present program were examined using both approaches and the differences were negligible. The advantage of the present approach over that of Reynolds et al. is that whereas they need three parameters to describe the wake ($V_c - V_m$, δ_s and δ_p), the present approach requires only two ($V_c - V_m$ and δ). For both approaches, agreement with the Gaussian is worst near ± 2. On the average the Gaussian overpredicts the local

Downloaded 01 Jun 2010 to 171.66.16.62. Redistribution subject to ASME license or copyright; see http://www.asme.org/terms/Terms_Use.cfm

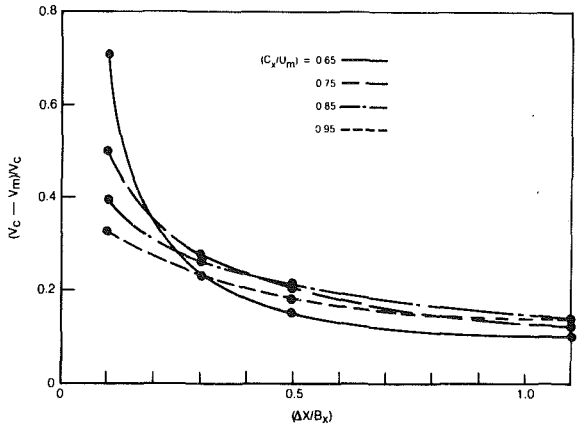


Fig. 8 Decay of the midspan wake speed defect

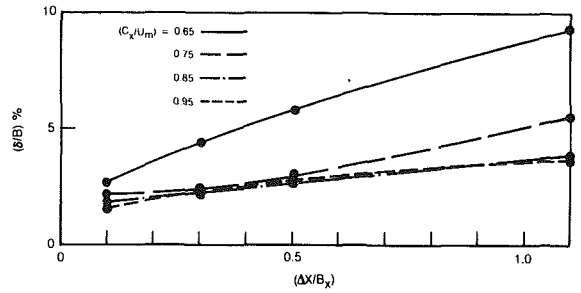


Fig. 9 Growth of the midspan wake semi-width

wake depth on the pressure side (near $(y/\delta) = -2$) and underpredicts it on the suction side (near $(y/\delta) = +2$).

The universal nature of the speed defect profile is useful only insofar as its depth and width vary in a systemmatic manner with distance downstream and with blade loading (C_x/U_m). The decay of the wake defect and the growth of the wake semi-width with axial distance, and as a function of blade loading, are illustrated in Fig. 8 and 9. The decay of the normalized wake speed defect (Fig. 8) had a number of interesting features. The defect at 10 percent aft varied monotonically with blade loading, i.e., from the maximum defect (70 percent) at 0.65 to the minimum defect (33 percent) at 0.95. However, by 30 percent aft the defect at 0.65 had mixed out to the extent that it was less than those at 0.75, 0.85, and 0.95. This condition persisted for as far downstream as data were obtained (to 110 percent aft). The reason for the rapid decay was probably related to the fact that the airfoil was separated at this condition. The resultant back-flow region and the strong radial flows (Figs. 4 and 5) resulted in a more rapid mixing process in the wake. Note that any analytical correlation of wake defect decay which scales monotonically with the airfoil drag (or loss), such as reference [12] (equation 3), will never collapse this data onto a single curve. However, in the far downstream region, $(\Delta X/B_x) > 0.5$, the wake defect decay began to match the power law behavior of a two-dimensional wake, i.e., $\propto X^{-1/2}$ ([21], equation 24.16).

The growth of the wake mid-depth semi-width (δ) is shown in Fig. 9. The wake semi-width not only grew smoothly with distance, but it was also, for the most part, a monotonic function of blade loading. In the downstream region, $(\Delta X/B_x) > 0.3$, the wake semi-width growth began to match the power law behavior of a two-dimensional wake, i.e., $\propto X^{1/2}$ ([21], equation 24.15).

It had been shown by Kool [15] that when the velocity profiles at various streamwise locations in a wake can be

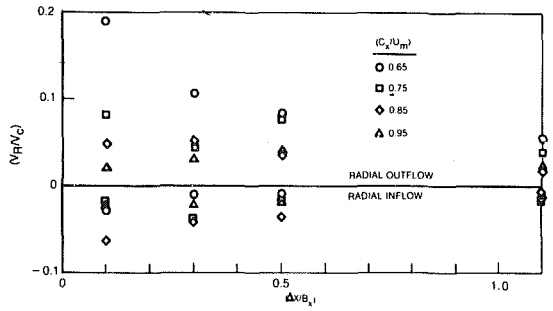


Fig. 10 Decay of the midspan wake radial velocity

collapsed to a single functional form, $F(\eta)$, such as in Fig. 7, then there is a simple relationship between the relative magnitude of the maximum velocity defect (Fig. 8) and the wake shape factor ($H = \delta^*/\theta$). Kool derived the following expression.

$$K' = \frac{(V_c - V_m)/V_c}{1 - (1/H)} = \frac{\int F(\eta)\, dn}{\int F^2(\eta)\, dn}$$

The parameter K' is a function only of the nature of the profile shape, $F(\eta)$. Although Kool pointed out that the value of K' is related to the streamwise pressure gradient, he suggested 1.45 as a typical value for his data. For any Gaussian distribution ($F(\eta) = \exp(-a\eta^2)$), such as that in Fig. 7, the value of K' is $\sqrt{2} = 1.41$. For the sixteen midspan wakes correlated in Fig. 7 the average value of K' (computed from the velocity defect and the wake shape factor) was 1.39, with a standard deviation of 0.06. A polynomial representation of this universal wake shape was derived which, for all intents and purposes, is identical with the Gaussian except that it goes to zero with a slope of zero at values of (y/δ) of $\pm$ 2.5 (see Fig. 7). The polynomial is as follows:

$$F(\eta) = 1 - (0.8911)\,\eta^2 + (0.4569)\eta^3 - (0.0658)\eta^4$$

This profile has a K' of 1.40. Both the Gaussian and the polynomial accurately describe the wake profile and the relationship between the velocity defect and the wake-shape factor (δ^*/θ).

The decay of the radial velocity in the wake is illustrated in Fig. 10. Both the maximum radial outflow ($V_r > 0$) and inflow ($V_r < 0$) are shown. Except for the case at highest blade loading (0.65) the radial velocities in the wake were relatively small. Generally speaking, midspan radial transport (nonstrip theory effects) were weak both in the airfoil boundary layer and in the wake, so long as the boundary layer was attached. When separation occured, the radial transport of low total pressure fluid became very strong in the separated region and in the wake. Under these conditions the radial transport on the airfoil surface appeared to be stronger than that in the wake.

Fullspan Traverse Data

The radial-circumferential distribution of the relative total pressure coefficient, $(P_{T1} - P_{T2,\ rel})/Q_{U_m}$ is presented in Fig. 11 for $(C_x/U_m) = 0.65$, 10 percent aft. The tip, in sharp contrast to the hub, had a large accumulation of low total pressure fluid. The nature of the flow field at the plane 10 percent aft was significantly different at values of (C_x/U_m) higher than 0.65 (e.g., see Fig. 12). For these cases (0.75, 0.85, and 0.95) the region near the intersection of the airfoil and the hub had very low velocities and very large pitch angles. The data indicated that the blade was experiencing corner stall at the hub and that the region of backflow extended to the traverse plane 10 percent aft of the rotor. Because of the very low velocities and high pitches, data could not be obtained

Downloaded 01 Jun 2010 to 171.66.16.62. Redistribution subject to ASME license or copyright; see http://www.asme.org/terms/Terms_Use.cfm

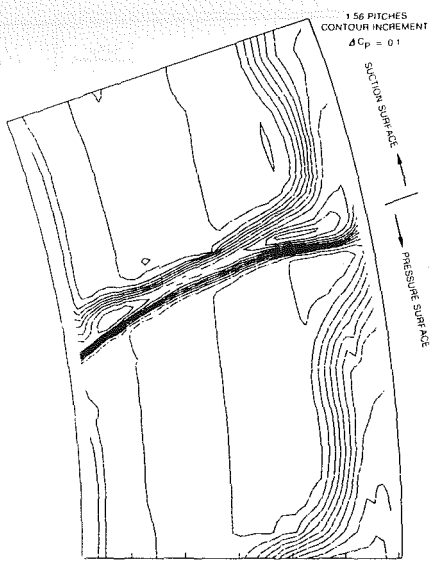


Fig. 11 Relative total pressure contours, 10 percent aft, (C_x/U_m) = 0.65

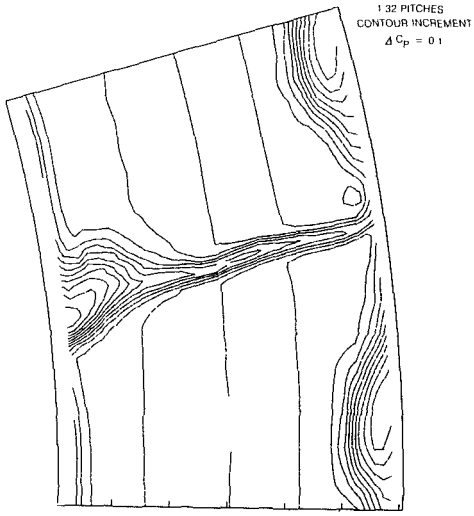


Fig. 13 Relative total pressure contours, 30 percent aft, (C_x/U_m) = 0.85

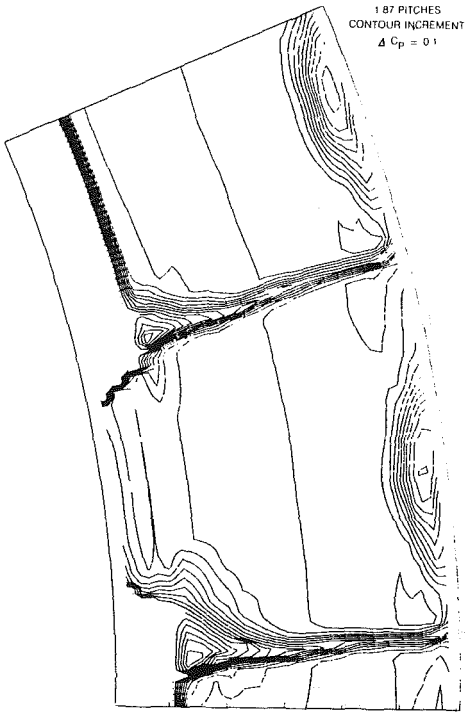


Fig. 12 Relative total pressure contours, 10 percent aft, (C_x/U_m) = 0.85

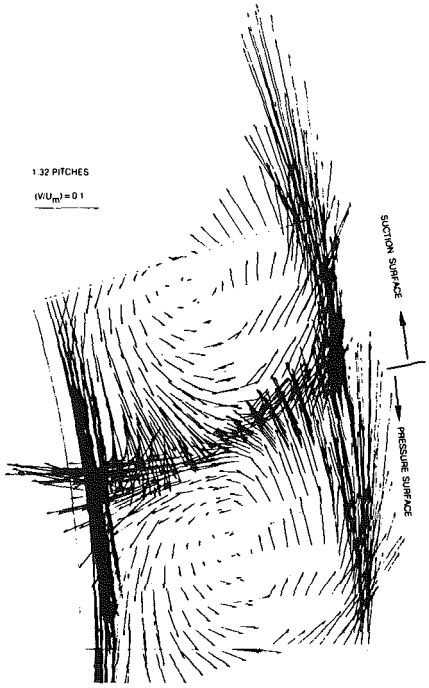


Fig. 14 Rotor exit flow vectors, 30 percent aft, (C_x/U_m) = 0.85

from either the Cobra probe or the 5-hole probe when they were in this region. In order to learn as much as possible, however, data were acquired outside these stalled regions. The total pressure field is shown in Fig. 12 for the traverse plane 10 percent aft, at a (C_x/U_m) of 0.85. The flow field was considerably different from that at the more highly loaded condition at a (C_x/U_m) of 0.65 (Fig. 11). At 0.85 the wake near midspan was much thinner, as could also be seen in Figs. 5 and 9. At the higher (C_x/U_m) there was a considerably smaller region of high loss fluid at the tip but there was a much larger region of high loss fluid at the hub. The reason for the breakdown in flow at the hub at higher values of (C_x/U_m) could be explained by the surface flow visualization (Figs. 3 and 4) and by the wake radial velocity profiles (Fig. 5). At the higher values of (C_x/U_m) the endwall boundary layer fluid tended to accumulate on the airfoil suction surface near the hub. The radial flows in the wake and on the airfoil surface were relatively weak so the low total pressure fluid accumulated there and caused the corner flow to break down. As the rotor was loaded up by going down in (C_x/U_m) to 0.65 the airfoil boundary layer thickness, the wake defect and the wake width all increased. This permitted the low total pressure fluid on the airfoil surface and in the wake to be centrifuged radially outward (due to its higher absolute swirl velocity). The effect was to remove the low total pressure fluid from the hub and to move it out toward the tip, thus inhibiting the hub corner stall, i.e., reducing the streamwise extent of the back-flow region. The final result was that, due

Downloaded 01 Jun 2010 to 171.66.16.62. Redistribution subject to ASME license or copyright; see http://www.asme.org/terms/Terms_Use.cfm

to nonstrip theory effects, corner stall had been inhibited (contracted axially) by increasing the loading on the rotor.

The nature of the fullspan wake decay process is illustrated in Figs. 12 and 13. These figures show the total pressure fields at a (C_x/U_m) of 0.85 and at axial distances 10 and 30 percent aft, respectively. At 10 percent aft (Fig. 12) contours were shown near the hub between wakes but not in the wakes themselves. This was due to the inability of the probe to null in this stalled region. By the traverse plane 30 percent aft (Fig. 13) it was possible to acquire data in all parts of the wake. Upon examining the flow as it proceeded further downstream it was clear that both in the airfoil wake and in the endwall regions, the total pressure defects were decreasing and that these regions of high loss fluid were increasing in extent. The process (at this C_x/U_m) appeared to be primarily a diffusion process due to gradients rather than strong radial redistribution. The radial flow in most of the flow field was relatively weak (as mentioned above). The region of consistently highest pitch angle was near the airfoil wake in the vicinity of the hub. These same observations as to the nature of the fullspan wake decay were true even at 0.65. In summary, most of the major spanwise redistribution of the fluid appeared to occur either near the airfoil surface (in the fullspan and corner stall regions) or in the near wake, i.e., upstream of a $(\Delta X/B_x)$ of 0.1.

The nature of the flow downstream of the rotor is shown in terms of its flow pattern in Fig. 14. The arrows represent vectors corresponding to the radial and tangential components of relative velocity at each measurement location for this data plane, $(C_x/U_m) = 0.85$ and $(\Delta X/B_x) = 0.3$. The radial and tangential components of the flow velocity vectors were calculated as follows:

$$(V_r/U_m) = (V/U_m)\ \mathrm{Sin}\phi$$

$$\bar{\theta}_m = 1/\tau_m \int_0^{\tau_m} \theta(r_m)\, dy$$

$$(\Delta V_T/U_m) = (V/U_m)\ \mathrm{Cos}\,\phi\ \mathrm{Cos}\,\theta\,(\mathrm{Tan}\theta - \mathrm{Tan}\bar{\theta}_m)$$

Note that the tangential component was the difference between the actual tangential speed and the tangential speed corresponding to the actual axial speed and the gap-averaged yaw angle at midspan. Viewing the flow in this way is equivalent to looking upstream in the direction of $\bar{\theta}_m$ while moving with the rotor. The magnitude of the flow velocity could be estimated from the vector corresponding to (V/U_m) of 0.1. For this value of (C_x/U_m) this corresponds to a pitch angle of typically 6 deg. Thus, most of the vectors in Fig. 14 correspond to angle differences from the main stream direction of several degrees.

Viewing the data in this manner revealed a number of interesting features of the flow. There was a large scale counter-clockwise vortical pattern filling the entire field. This was consistent with the radial flow toward the hub on the pressure-surface side of the wake and toward the tip of the suction-surface side of the wake seen in Fig. 5. This flow pattern occurred due to (1) the imposition of the nonfree vortex radial distribution of rotor exit relative flow (yaw) angle by the blading and (2) the irrotational nature (in the absolute frame of reference) of the flow entering the rotor. Since inlet absolute flow is irrotational, the relative inlet and exit flows (outside of the regions influenced by viscosity) must have relative vorticity vector (ζ) of -2Ω in the axial direction.

$$\zeta_x = \frac{1}{r}\left\{\frac{\partial(rV_T)}{\partial r} - \frac{\partial(V_R)}{\partial\theta}\right\}$$

This condition would be satisfied without the presence of radial velocities if the absolute rotor exit tangential velocity component varied inversely with radius, i.e., free-vortex flow.

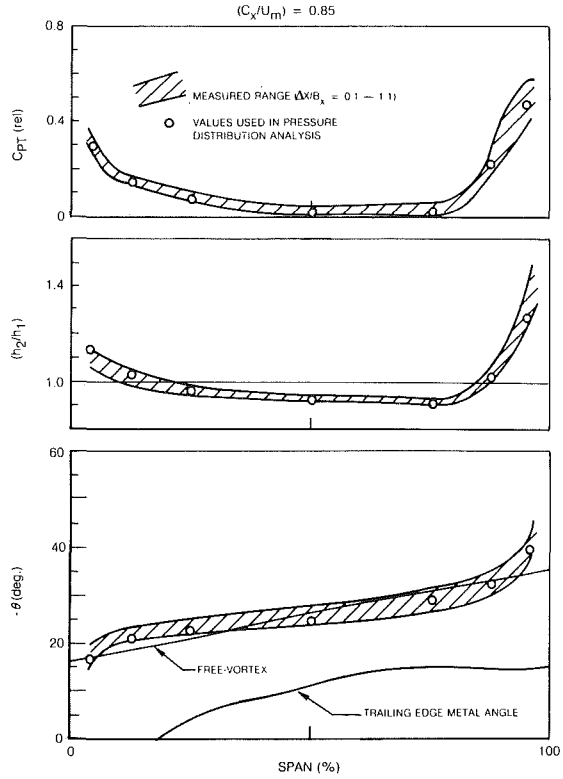


Fig. 15 Spanwise distributions of loss, stream tube contraction, and rotor exit flow angle, $(C_x/U_m) = 0.85$

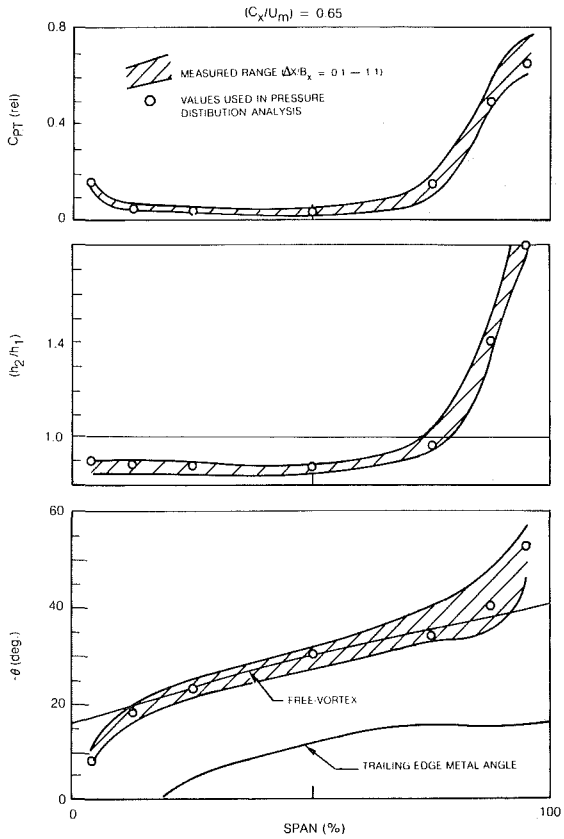


Fig. 16 Spanwise distributions of loss, stream tube contraction, and rotor exit flow angle, $(C_x/U_m) = 0.65$

Downloaded 01 Jun 2010 to 171.66.16.62. Redistribution subject to ASME license or copyright; see http://www.asme.org/terms/Terms_Use.cfm

The rotor blading, however, overturns the flow relative to free-vortex at the tip and underturns at the hub (Fig. 15). The result is a radial derivative of relative tangential velocity which is less than the free-vortex value. This gives rise to a circumferential derivative of radial velocity to make up the difference. The near linear difference between the radial distributions of free-vortex and actual relative tangential velocity gives rise to the near linear gapwise variation of the radial velocity. This variation of radial velocity was particularly evident near midspan (Fig. 14). The radial component at midspan is positive (toward the tip) of the suction surface side of the channel. It decreases across the channel until it is negative (toward the hub) on the pressure surface side. The axial component of relative vorticity was computed from the data at midspan and at a gapwise position midway between wakes. At a (C_x/U_m) of 0.85 the vorticity was typically within $\pm$ 10 percent of -2Ω and the gapwise gradient of radial velocity contributed typically 25 percent of the total. These observations are consistent with the observation (discussed below) that the rotor had a spanwise gradient in circulation (generally increasing toward the tip). The presence of this radial flow is a direct consequence of the nonfree vortex nature of the spanwise rotor lift (circulation) distribution.

As the rotor loading was increased (by decreasing (C_x/U_m) to 0.65) it was observed that there was a gradual change toward (and slightly beyond) a free-vortex radial distribution of rotor exit tangential velocity and exit yaw angle (Fig. 16). At 0.65 the radial gradient of relative tangential velocity exceeded the free vortex value and hence the gapwise gradient of radial velocity was of opposite sign (from that at 0.85) in order to have a relative vorticity in the rotor exit flow of -2Ω. Although the magnitude was relatively small, the data clearly indicated this change in direction of the radial flow and a total vorticity typically within $\pm$ 10 percent of -2Ω. This raises some questions about the spanwise gradient of blade circulation at this condition which will be discussed below.

The fullspan traverse data have been analyzed from the point of view of providing gap averaged performance input to a through-flow analysis and to a blade-to-blade flow analysis. The key input for both is the spanwise distributions of relative total pressure loss, stream tube contraction ratio and turning across the rotor. The distributions of each for values of (C_x/U_m) of 0.85 and 0.65 are shown in Figs. 15 and 16, respectively. The data were shown as bands, each band including the results of the four traverses from 10 to 110 percent aft. Also included on the figures are symbols indicating the values of each parameter that were used in the blade-to-blade flow analysis at seven spanwise locations. Finally, the blade trailing edge metal angle (Table 1) was included for comparison with the exit flow angle.

At 0.85 (Fig. 15) the spanwise distributions of total pressure loss and stream tube contraction were roughly symmetric about midspan. At 0.65 (Fig. 16), however, there had been a shift in the high loss fluid and the blockage from the hub to the tip. This was not surprising in the light of what has already been seen in the contour plots (Figs. 11 and 12). It might be reasonable to expect a typical design system to predict the hub and tip distributions at 0.85. In this case there were two relatively distinct endwall regions separated by a wide region of core flow (from 30 to 80 percent span). Such endwall flow behavior might have been simulated reasonably well in a plane cascade test (even the hub corner stall). At 0.65, however, the large radial redistribution of loss (and with it, blockage) was peculiar to a rotating frame compressor environment. It was this type of nonstrip theory effect that was of particular interest. For example, if the only evidence one had was the loss distribution at 0.65 (Fig. 16), one might conclude that the blade tip was generating high loss; however, as has been shown, this is not the case. The origin of much of the high loss fluid is at the hub.

The spanwise distribution of the exit flow angle had a relatively wide band. At 0.65 in the region from 80 to 100 percent span, there was an increase in yaw (of typically -6 deg) due to the mixing that occurred between 10 and 30 percent aft. From 30 percent aft there was little further change in the yaw in this region. As the rotor was loaded upon going from 0.85 to 0.65 the deviation increased (turning dropped) in the region from approximately 25 percent span out to the tip. This trend was not unexpected, at least qualitatively. The interesting feature was that there was an increase in turning in the region from 25 percent span in to the hub. This was contrary to normal (cascade) experience and was doubtless related to the radial transport of high loss fluid out of the hub region. The reduction of the axial extent of the back-flow region of the corner stall (present from $(C_x/U_m) = 0.75$ to 0.95), relative to that of the fullspan stall (present at 0.65) had apparently caused a local reduction in deviation, i.e., locally increased turning near the hub. The result was that the spanwise distribution of the exit flow angle was much closer to free vortex at 0.65 then at 0.85. This trend is consistent with the change in the nature of the radial velocity distribution mentioned above.

Airfoil Pressure Distributions

Rotor airfoil surface static pressure distributions were acquired in order to complement the wake traverse data described above. Two airfoils were provided with static pressure taps at alternating chordwise locations around their perimeters. Taps were installed at a total of twenty-four chordwise locations. At each location data were obtained at seven spanwise locations: 4, 12.5, 25, 50, 75, 87.5, and 95 percent span. As a result, the spanwise variation of the pressure force on the airfoil was determined. It was also reduced to its axial and tangential components. Fullspan data were acquired at each of the four values of (C_x/U_m) at which traverse data were acquired, i.e., 0.65, 0.75, 0.85, and 0.95. In addition, midspan static pressure data were acquired along the speed line from 0.55 to 1.16.

The static pressure data have been compared to the results computed using the inviscid analysis of Caspar et al. [3]. The analysis required specification of the airfoil geometry and solidity (Table 1) as well as aerodynamic inlet and exit conditions. For incompressible flow, such as in the present work ($M < 0.15$) the aerodynamic conditions included the inlet and exit flow angles, the stream tube contraction ratio and the total pressure loss. The inlet flow angle was calculated directly from (C_x/U_m) and the radius ratio (r/r_m). The exit conditions were computed directly from the traverse data, as discussed in the previous section and as illustrated in Figs. 15 and 16. For the cases at midspan where (C_x/U_m) was either less than 0.65 or greater than 0.95 the exit conditions had to be extrapolated based on the available data. Over the last 15 percent of axial chord the computed results were faired to smoothly meet the downstream static pressure at the trailing edge. For typical turbomachinery airfoils, with relatively blunt trailing edges, this is a more physically representative result than the theoretical stagnation point it replaces.

The rotor midspan pressure distribution is shown in Fig. 17 for (C_x/U_m) varying from near stall (possibly in rotating stall at 0.55 (see Fig. 2) to 1.16. Measured pressure distributions in increments of 0.1 in (C_x/U_m) are shown which correspond to the data points shown on the pressure rise characteristic (Fig. 2). The computed pressure distributions were based on measured input data (e.g., Figs. 15 and 16) and on an extrapolation of these data where necessary.

Downloaded 01 Jun 2010 to 171.66.16.62. Redistribution subject to ASME license or copyright; see http://www.asme.org/terms/Terms_Use.cfm

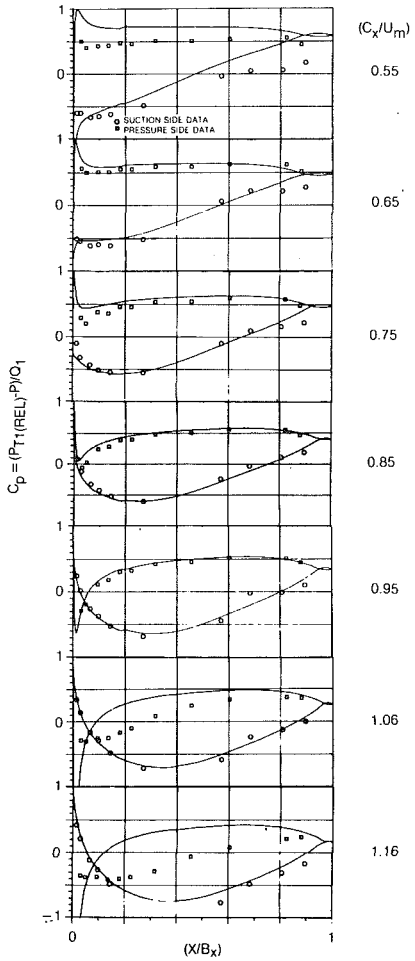


Fig. 17 Pressure distributions at midspan

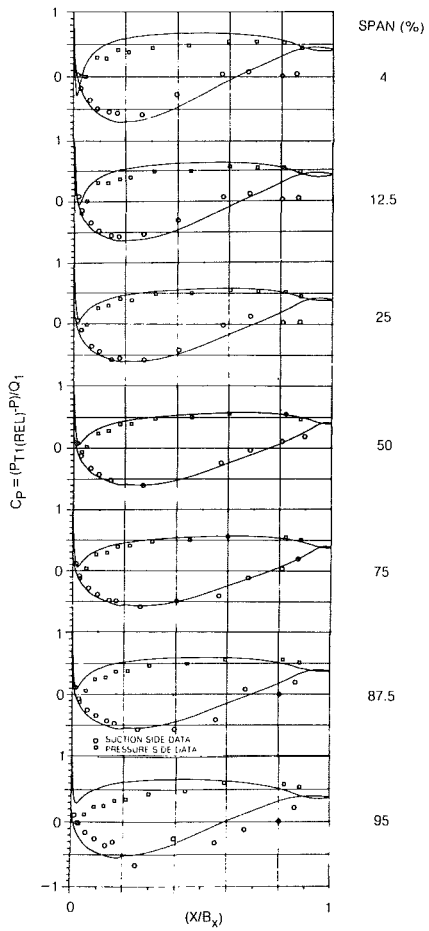


Fig. 18 Fullspan pressure distributions at $(C_x/U_m) = 0.85$

At the highest flow, (C_x/U_m) of 1.16, a strong pressure surface over speed was predicted due to the large negative incidence. The measured data, however, indicated that there was a pressure surface separation at the leading edge which caused most of the pressure surface to have a flow speed much higher than predicted. The pressure surface separation had apparently caused sufficient blockage in the channel to produce suction surface speeds which were somewhat higher than predicted. In general, however, the suction surface was in reasonably good agreement considering what was occurring on the pressure surface.

At a (C_x/U_m) of 1.06 the pressure surface was still separated. The impact of the bubble, however, was considerably weaker and the pressure surface data were in closer agreement with the computed values, especially toward the trailing edge. This trend continued to 0.95 where agreement between the measured and computed results was excellent, particularly in the leading edge region which had been stalled. Similar excellent agreement existed at 0.85. At 0.75 suction surface agreement was still excellent but the velocities on the pressure surface were somewhat higher than predicted, especially near the leading edge. The saw-tooth pattern in the pressure surface data over the first 20 percent of chord was related to alternating pressure taps being on two different airfoils.

At a (C_x/U_m) of 0.65 the agreement between the measured and computed results was surprisingly good, especially in light of the fullspan separation that was known to be present on the suction surface (Fig. 4). The flattening of the last three suction-surface data points with the reduction in (C_x/U_m) was probably an indication of this separation. A similar type of behavior can be seen in the cascade data presented by Starken et al. [22].

At the lowest flow tested, $(C_x/U_m) = 0.55$, the airfoil was stalled and the entire aft half of the suction surface showed little pressure rise. The flow speed on both the suction and pressure surfaces was considerably higher than predicted. This was probably due to severe boundary layer displacement effects at this flow condition. The possibility also exists that the actual turning may be far different from the extrapolated value used in the calculation.

The nature of the spanwise variation of the rotor blade pressure distribution from near the hub (at 4 percent span) to near the tip (at 95 percent span) is illustrated in Fig. 18 for a value of (C_x/U_m) of 0.85. Recall that at 0.85 there was a corner stall (with back-flow) on the suction surface near the hub (Fig. 3). The back-flow region extended out to approximately 25 percent span and the radial flow around the stalled region extended out to approximately 50 percent span. The impact of the hub corner stall could be seen in the airfoil pressure distribution (Fig. 18) as the constant pressure region on the suction surface from 60 percent chord aft at 4 percent span and from 70 percent chord aft at 25 percent span. There was considerable suction surface trailing edge recompression from 50 percent span to 95 percent span. This was consistent with the nature of the attached boundary layer in this region (Fig. 3). On the pressure surface the measured flow speed was considerably higher than predicted near the hub (at 4 and 12.5 percent span) and near the tip (at 87.5 and 95 percent span). At the hub this was probably related to blockage caused by the corner stall. At the tip it was probably caused by the leakage of flow over the unshrouded tip of the airfoil. Finally, the

Downloaded 01 Jun 2010 to 171.66.16.62. Redistribution subject to ASME license or copyright; see http://www.asme.org/terms/Terms_Use.cfm

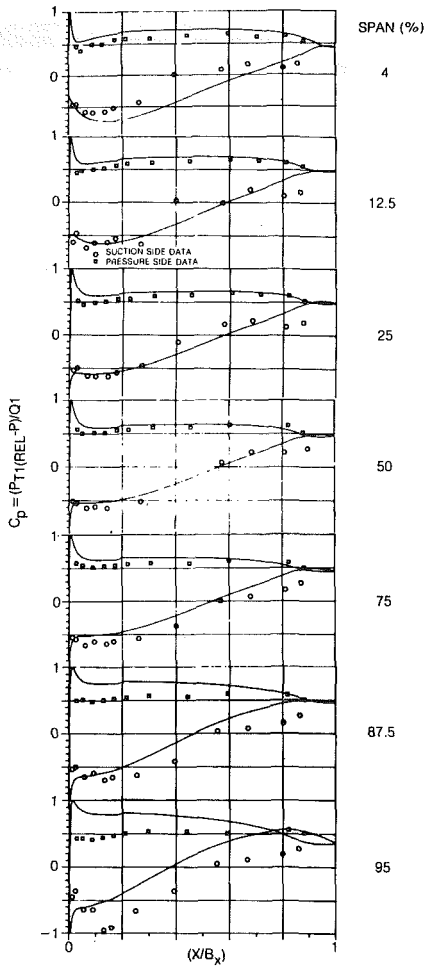


Fig. 19 Fullspan pressure distributions at $(C_x/U_m) = 0.65$

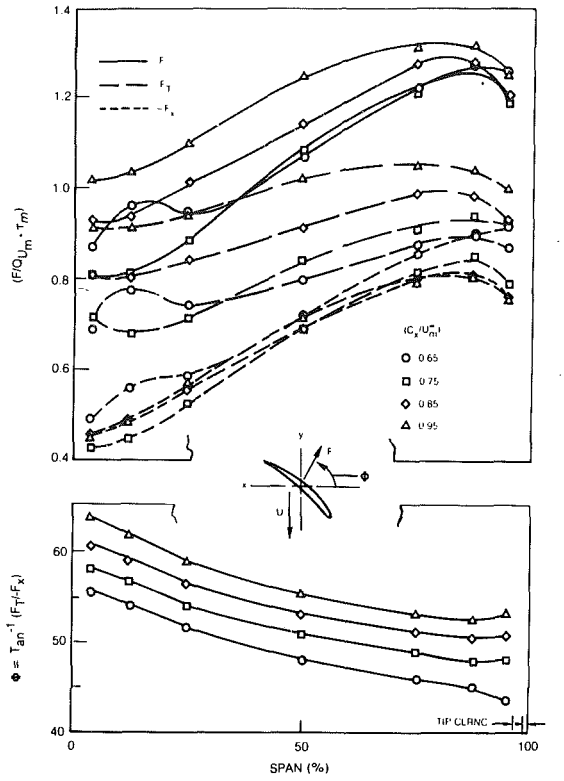


Fig. 20 Rotor pressure force variations with span

flow over the center portion of the airfoil (between roughly 25 and 75 percent span) was in good agreement with the computed pressure distributions.

When the flow was reduced to a (C_x/U_m) of 0.65, there was a considerable change in the nature of the fullspan pressure distribution (Fig. 19). At this condition there was a fullspan stall on the suction surface (Fig. 4). The boundary layer separation occurred at typically the 60 to 70 percent chord location. Evidence of this separation could be seen in the pressure distributions in that the suction surface pressures were nearly constant from the separation location aft. Near the tip (from 87.5 percent span outward) there was some suction surface recompression but the local flow speeds were considerably higher than predicted. The pressure surface flow speed was higher than predicted from 75 percent span outward. This may be related to the added blockage in the channel due to the strong spanwise migration of high loss fluid (Fig. 11) at this flow rate $(C_x/U_m = 0.65)$. Clearly, as stall was approached the analytical tools currently available for predicting the blade pressure distribution had been stretched beyond their limits.

The force exerted by the air on the blade as a result of the fullspan pressure distributions (e.g., Figs. 18 and 19) is illustrated in Fig. 20. The data are shown in terms of the axial and tangential components of force per unit span (F_X and F_T), the total force per unit span (F) and the angle from axial (Φ). The forces were calculated from the measured pressure distributions by interpolating linearly with surface arc length between measurement locations. The skin friction force was estimated to be approximately 2 to 4 percent of the pressure force. Thus, in discussing the pressure force one is accounting for the vast majority of the total force on the airfoil.

Of the two components of force on the airfoil, axial and tangential, it was the axial which was least sensitive to (C_x/U_m). Over the entire span, but especially from 25 to 75 percent span, F_X varied only slightly over the range of (C_x/U_m) from 0.65 to 0.95. The reason for this was that the axial component of blade force was closely related to the rotor static pressure rise, and as could be seen in Fig. 2, the rotor static pressure rise (when normalized by Q_{Um}) was relatively flat over this range of (C_x/U_m).

Near the blade tip there was a drop-off in both the axial and tangential force components. The impact of this reduction was felt over the outermost 20 percent of span. The source of this reduction in blade force was most probably the tip annulus boundary layer and the leakage flow over the unshrouded blade tip. It has already been pointed out that the pressure distributions near the tip are quite different from those one would expect based on potential flow considerations. Furthermore, near the hub the force was somewhat higher than one would have expected from extrapolating the forces over the center half span. Even with the rather complicated variations of the force components, the variation of the force direction (Φ) was very smooth and regular.

The measured spanwise force variations were compared with a free vortex variation. The free vortex was based on C_x and $r \cdot C_\theta$ being constant with span. The free vortex variation had spanwise constant blade circulation and hence had no shed vorticity in the wake. Constant circulation resulted in a constant normalized tangential force per unit span. In the midspan region, however, it could be seen that the measured tangential force per unit span was increasing with radius. From this, one would expect the shed vorticity in the blade wake to produce radial inflow on the pressure surface side of the wake and radial outflow on the suction surface side of the

Downloaded 01 Jun 2010 to 171.66.16.62. Redistribution subject to ASME license or copyright; see http://www.asme.org/terms/Terms_Use.cfm

wake. This was observed in the data at the higher values of (C_x/U_m), 0.85, and 0.95 (Figs. 5 and 14).

As discussed above, the spanwise gradient in circulation produced a radial gradient in relative tangential velocity which was less than that of free vortex flow at a (C_x/U_m) of 0.85. This required a gapwise gradient of radial velocity in order to preserve the relative vorticity of the exit flow at a value of -2Ω. The shed vorticity was in the blade wakes and could be seen as the rapid adjustment from radially inward to outward flow while going from the pressure to the suction surface sides of the wake near midspan (Figs. 5 and 14). The shed vorticity was modeled analytically as an array of semi-infinite vortex sheets of finite span. The span and strength of the sheets were based on the data of Fig. 20. At a (C_x/U_m) of 0.85 the span was taken as 80 percent of the blade span. At midspan and at the leading edge plane of the vortex sheets, this model predicted a nearly linear gapwise variation in radial velocity, which was in agreement with the data of Fig. 14 (and also the data of Smith, [23], Fig. 11), and a magnitude for the change in radial velocity across the sheet which was also in reasonably good agreement with the data. The conclusion was that at a (C_x/U_m) of 0.85 the shed vorticity in the wake was the mechanism which produced the radial velocity necessary to satisfy the conditions on vorticity in the rotor exit flow.

At the value of (C_x/U_m) of 0.65 the midspan wake was dominated by radial outflow due to centrifugal effects (Fig. 5) and the impact of any shed vorticity was unclear. As mentioned earlier, however, the region between the wakes at this condition had a gapwise gradient of radial velocity which was opposite to that at a (C_x/U_m) of 0.85 (Fig. 14). At 0.65 there was a variation from weak radial outflow on the pressure surface side of the wake to weak radial inflow on the suction surface side. This implied a shed vorticity (at midspan) of opposite sign to that at 0.85. Also, as mentioned earlier, the radial gradient of relative tangential velocity and yaw angle at 0.65 was slightly greater than the free vortex value (Fig. 16). All this would lead one to expect a tangential blade force which was decreasing (slightly) with span. This, however, was not the case (Fig. 20). The reason for this apparent contradiction was probably tied to the strong radially outward flow in the separated region on the blade suction surface and in its wake (Figs. 4 and 5). The simple model of a trailing vortex sheet which explained the flow at 0.85 (where the radial flows were relatively weak) no longer applied. With boundary layer separation and the resultant strong radial flows a more complex model was required to redistribute the shed vorticity.

Conclusions

An extensive body of experimental results has been presented which provides detailed information as to the nature of the flow over an isolated compressor rotor and in its wake. The data will serve as a benchmark for comparisons with a wide variety of two- and three-dimensional inviscid and viscous computational methods. Specific conclusions are as follows.

A hub corner stall on the blade suction surface at lower blade loadings developed into a fullspan stall as blade loading was increased. A large spanwise redistribution of fluid occurred with this change in the nature of the stalled region. Generally speaking, radial flow near the airfoil surface was more significant than that in its wake. Radial flow in the wake was dominated by shed vorticity at lower blade loadings and by centrifugal effects at higher blade loadings. Midspan performance compared closely with stationary cascade performance. The wake velocity defect profile could be accurately characterized with a "universal" profile. The depth of the wake velocity defect was not a monotonic function of blade loading. The fullspan wake decayed in a self-similar manner with little indication of radial redistribution. The blade pressure distribution was strongly influenced by proximity to the hub endwall and to the unshrouded blade tip. The nonfree vortex nature of the spanwise blade loading and of the rotor exit flow resulted in radial velocities in the region between wakes.

In summary, considerable effort will be required before many of the physical mechanisms observed in the flow over this rotor are made available to the designer in the form of practical analytical tools.

Acknowledgments

The wake traverse data reported on here were acquired under Air Force contract under the direction of C. Herbert Law (AFWAL/POTX), project engineer, Contract Number F33615-77-C-2083. The principal investigator was Robert P. Dring of the United Technologies Research Center. The remainder of the data (the flow visualization and the pressure distribution measurements) were acquired under UTRC corporate funding.

The authors are indebted to many people for the successful completion of this program and in particular to Mr. Hugh Hall and Mr. John Kostic for helping in acquiring the data, to Miss Diane Rodimon for reducing the data, and to the grace of God.

References

1 Hearsey, R. M., "A Revised Computer Program for Axial Compressor Design," Aerospace Research Laboratories, ARL 75-0001, Vol. I, ARL (AFSC), Wright-Patterson AFB, OH 45433, Jan. 1975.

2 Sehra, A. K., and Kerrebrock, J. L., "The Effect of Blade-to-Blade Flow Variations on the Mean Flow-Field of a Transonic Compressor," AIAA Paper No. 79-1515, July 1979.

3 Caspar, J. R., Hobbs, D. E., and Davis, R. L., "Calculation of Two-Dimensional Potential Cascade Flow Using Finite Area Methods," *AIAA Journal,* Vol. 18, No. 1, Jan. 1980, pp. 103-109.

4 Denton, J. D., "A Time-Marching Method for Two- and Three-Dimensional Blade to Blade Flows," Aeronautical Research Council, R&M No. 3775, London, Oct. 1974.

5 Dodge, P. R., "A Numerical Method for Two- and Three-Dimensional Viscous Flows," AIAA Paper No. 76-425, *AIAA 9th Fluid and Plasma Dynamics Conference,* San Diego, 1976.

6 Briley, N. R., and McDonald, H., "Analysis and Computation of Viscous Subsonic Primary and Secondary Flows," *4th AIAA Computational Fluid Dynamics Conference,* 1979, Williamsburg, Va.

7 Langston, L. S., Nice., M. S., and Hooper, R. M., "Three-Dimensional Flow Within a Turbine Cascade Passage," ASME JOURNAL OF ENGINEERING FOR POWER, Vol. 99, Jan. 1977.

8 Graziani, R. A., Blair, M. F., Taylor, J. R., and Mayle, R. M., "An Experimental Study of Endwall and Airfoil Surface Heat Transfer in a Large Scale Turbine Blade Cascade," ASME Paper No. 79-GT-99, Mar. 1979.

9 Thompkins, W. T., and Kerrebrock, J. L., "Exit Flow From A Transonic Compressor Rotor," Mass Inst. of Tech., Gas Turbine Lab., Report No. 123, Sept. 1975.

10 Raj, R. and Lakshminarayana, B., "Three-Dimensional Characteristics of Turbulent Wakes Behind Rotors of Axial Flow Turbomachinery," ASME JOURNAL OF ENGINEERING FOR POWER, Apr. 1976, pp. 218-228.

11 Reynolds, B., Lakshminarayana, B., and Ravindranath, A., "Characteristics of the Near Wake of a Compressor or Fan Rotor Blade," *AIAA Journal,* Vol. 17, No. 9, Sept. 1979, pp. 959-967.

12 Reynolds, B., and Lakshminarayana, B., "Blade Loading and Spanwise Effects on the Near- and Far-Wake Characteristics of a Compressor Rotor Blade," AIAA Paper No. AIAA-80-0201, *18th Aerospace Sciences Meeting,* Jan. 14-16, 1980, Pasadena, Calif.

13 Ravindranath, A. and Lakshminarayana, B., "Mean Velocity and Decay Characteristics of the Near- and Far-Wake of a Compressor Rotor Blade of Moderate Loading," ASME Paper No. 79-GT-202, Mar. 1979.

14 Hirsch, C. and Kool, P., "Measurement of the Three-Dimensional Flow Field Behind an Axial Compressor Stage," ASME JOURNAL OF ENGINEERING FOR POWER, Apr. 1977, pp. 168-180.

15 Kool, P., DeRuyck, J., and Hirsch, C., "The Three-Dimensional Flow and Blade Wake in an Axial Plane Downstream of an Axial Flow Compressor Rotor," ASME Paper No. 78-GT-66, Mar. 1978.

16 Dring, R. P., and Joslyn, H. D., "Measurements of Turbine Rotor Blade Flows," ASME *Gas Turbine Conference,* New Orleans, La., *Measurement Methods in Rotating Components of Turbomachinery,* pp. 51-58.

Downloaded 01 Jun 2010 to 171.66.16.62. Redistribution subject to ASME license or copyright; see http://www.asme.org/terms/Terms_Use.cfm

17 Dring, R. P., Joslyn, H. D., and Hardin, L. W., "Experimental Investigation of Compressor Rotor Wakes," AFAPL-TR-79-2107, Air Force Aero Propulsion Laboratory, Technology Branch, Turbine Engine Division (TBX), Wright-Patterson Air Force Base, Ohio.

18 Dring, R. P., Joslyn, H. D., and Hardin, L. W., "Compressor Rotor Aerodynamics: An Analytical and Experimental Investigation," United Technologies Research Center, UTRC80-15, Mar. 1980.

19 Johnson, I. A., and Bullock, R. O., (ed.), *Aerodynamic Design of Axial-Flow Compressors* (revised), NASA SP-36, 1965.

20 Kerrebrock, J. L., and Mikolajczak, A. A., "Intra-Stator Transport of Rotor Wakes and its Effects on Compressor Performance," ASME JOURNAL OF ENGINEERING FOR POWER, Oct. 1970, p. 359.

21 Schlichting, H., *Boundary Layer Theory*, 6th ed., McGraw-Hill, 1968.

22 Starken, H., Breugelmans, F. A. E., and Schimming, P., "Investigation of the Axial Velocity Density Ratio in a High Turning Cascade," ASME Paper No. 75-GT-25, Mar. 1975.

23 Smith, L. H., Jr., "Secondary Flow in Axial-Flow Turbomachinery," *Trans.* ASME, Vol. 77, No. 7, Oct. 1955, pp. 1065-1076.

Downloaded 01 Jun 2010 to 171.66.16.62. Redistribution subject to ASME license or copyright; see http://www.asme.org/terms/Terms_Use.cfm

Spanwise Mixing in Axial-Flow Turbomachines

G. G. Adkins, Jr.

L. H. Smith, Jr.

Aircraft Engine Engineering Division
General Electric Company
Cincinnati, Ohio 45215

Flow measurements taken in multistage axial-flow turbomachines suggest that substantial spanwise mixing of flow properties often occurs. In addition, measured blade row turnings often show considerable deviation from two-dimensional cascade theory, particularly in the end-wall regions. An approximate method is presented with which both of these effects can be included in design through-flow calculations. The method is based on inviscid, small-perturbation secondary flow theory. Frictional effects are not directly included but secondary flows caused by annulus wall and blade boundary layers are included in an approximate way. The secondary flow model includes effects of 1) main-stream nonfree-vortex flow, 2) end-wall boundary layers, 3) blade end clearances, 4) blade end shrouding, and 5) blade boundary layer and wake centrifugation. The spanwise mixing phenomenon is modeled as a diffusion process, where the mixing coefficient is related to the calculated spanwise secondary velocities. Empirical adjustments are employed to account for the dissipation of the secondary velocities and interactions with downstream blade rows. The induced blade row overturnings are related to the calculated cross-passage secondary velocities. The nature of the assumptions employed restricts the method to design-point-type applications for which losses are relatively small and significant regions of separated flow are not present.

1 Introduction

Virtually all analytical methods used today in the design of compressors and turbines contain the assumption that the flow remains on axisymmetric stream surfaces as it passes through the machine, even though designers are aware that this assumption is not really valid. Secondary flows generate spanwise as well as cross-passage velocities, which convect fluid from hub to tip or vice versa, and these can be expected to persist for some distance downstream of the blade row that generates them. Also, there is a tendency for blade boundary layer fluids to be centrifuged outward on rotor blades and moved inward on stator vanes by the prevailing static pressure field. The sweeping of blades can also cause boundary layer cross flows.

The magnitude of the role that spanwise flows play in the overall flow process depends upon the configuration of the machine being considered. It is generally known that secondary flows increase in strength when aerodynamic loading, expressed most simply as turning angle, is increased. It is also known that the depth of penetraton into the main stream of end-wall secondary flows is more or less proportional to blade circumferential spacing, although other variables also play a role in this. Thus, machines with low passage aspect ratios tend to have their end-wall flows affect a larger fraction of the total flow. Tip clearance and leakage flows also tend to be three-dimensional in nature, and their magnitudes are proportional to the size of the clearances involved. Spanwise boundary layer flow depends on blade boundary layer thickness and form as well as the prevailing free-stream pressure field, and hence these are also highly configuration-dependent.

An indication of the potential importance of mixing in multistage axial flow compressors was observed at General Electric in the mid 1960s. At that time tests were being conducted on compressors with higher stage loadings and lower aspect ratios than had previously been common. When flow synthesis calculations were made that employed measured distributions of stagnation temperature and stagnation pressure, the deduced spanwise distributions of loss coefficient appeared to be unreasonable in the stages aft of stage 3 or stage 4; higher losses near mid-passage than near the end-walls were often implied. Since there was nothing in the blading design or operation that would cause losses to originate in that way, this strongly suggests that some of the higher temperature fluid near the end-walls was being convected to mid-passage by secondary flows.

The continuing trend, at least in aircraft engine turbomachines, toward higher stage loadings and lower aspect ratios, has caused secondary flow and mixing effects to have increased importance. This paper provides an approximate method for including these effects in design calculations.

Contributed by the Gas Turbine Division and presented at the International Gas Turbine Conference and Products Show, Houston, Texas, March 9–12, 1981, of THE AMERICAN SOCIETY OF MECHANICAL ENGINEERS. Manuscript received at ASME Headquarters, December 4, 1980. Paper No. 81-GT-57.

Copyright © 1982 by ASME

Downloaded 01 Jun 2010 to 171.66.16.62. Redistribution subject to ASME license or copyright; see http://www.asme.org/terms/Terms_Use.cfm

2 Scope and Assumptions

It should be appreciated that the real flow in a multistage turbomachine is highly complex and that a rigorous treatment of it is not possible at this time. The general approach taken here is to try to account for the secondary flow mechanisms that are believed to initiate spanwise fluid movements in a more or less rational way, but to rely upon empirical data and engineering judgment to specify how rapidly these movements die out downstream of their points of initiation.

The secondary flow models that are employed are inviscid, so there is no hope that they can adequately model cases for which significant regions of flow separation are present. This alone restricts application to design-point or near-peak-efficiency operation of machines that have good performance. A rather over-simplified model for blade boundary layer and wake centrifugation is employed. A considerable amount of research on this subject is currently going on around the world, as witnessed by the several papers being presented at this Conference that deal with this subject, and it is our intention to incorporate the results of this research into a more precise model in the future.

The spanwise distributions of the losses that originate in each blade row have an important influence on the secondary flows that are generated and hence on the mixing process. The basic philosophy of loss assignment employed here is that developed by Smith [1] and Koch and Smith [2]. Losses, specified at each blade row trailing edge, are made up of a profile loss that depends upon the usual cascade parameters and an end-wall loss that depends upon clearances, passage aspect ratios, and proximity to stall. The profile loss is taken directly from [2]; it is usually relatively small and varies only slightly along the span, at least for subsonic cases. The end-wall loss is concentrated in the end-wall boundary layers, whose penetrations into the main stream are related to the blading staggered spacings as described in [1]. The method employed for determining the distributions of loss coefficient through each end-wall boundary layer from the boundary layer thickness parameters given in [1] is described in the Appendix. The loss determination and distribution methods employed do not incorporate consideration of all blading and end-wall details that are known to affect losses, but more elegant treatments are beyond the scope of this paper.

There are two methods that have been used by various workers to account for the blockage effect of annulus wall boundary layers in turbomachinery through-flow calculations. In the first method, the calculation domain extends across the full annulus from metal casing to metal hub, and an effective-area coefficient (blockage coefficient) is employed in the continuity equation. In the second method the calculations are carried out between the annulus wall boundary layer displacement thickness streamlines. We have elected to use the first method in the present paper. The velocity perturbations associated with the secondary flows that are calculated often contribute some end-wall boundary layer features to the calculated flow pattern that imply a displacement thickness; these might have caused confusion if the other method had been elected. The numerical magnitudes of the blockages that have been employed in the examples given in Section 5 have been specified to give stagewise loading distributions that are in general agreement with test data by means that are outside the scope of this paper. Test data have been used when they exist to provide the inlet flow profile for the first blade in each machine considered.

The large majority of the work done so far by the authors in developing the present method has been associated with compressors. However, it is believed that the basic approach should also be applicable to axial-flow turbines, although the

Nomenclature

a = passage width at blade exit, $a = \frac{2\pi r}{N}\cos\beta_{2D}$
b = axial chord projection
C = absolute velocity
c = chord
c_p = specific heat at constant pressure
g = blade staggered spacing, $g = \frac{2\pi r}{N}$ cos (chord angle)
H = stagnation enthalpy
h = enthalpy
h = annulus height
$\mathbf{i}$ = unit vector
k_1 = end-wall boundary layer velocity deficit at wall, expressed as fraction of main flowfield wall velocity
k^* = factor controlling rate at which end-wall boundary layers approach a repeating-stage condition
k_ℓ = fraction of blade circulation remaining at tip after clearance is opened
k_w = ratio of representative velocity in boundary layer to free-stream velocity; single value chosen to best match wake spanwise velocity test data
ℓ = tip clearance
N = number of blades in a blade row
n = distance normal to axisymmetric stream surfaces of the main flowfield
n = blade row number; see Appendix
P = a fluid property subject to mixing
P_T = stagnation pressure
p = static pressure
Q = parameter affecting achievement of repeating-stage condition; see Appendix
Q_L = volume flow rate of leakage
r = radius
s = entropy
T = temperature
U = blade speed, $U = \omega r$
V = velocity, either absolute or relative
V_s = spanwise secondary velocity on ($-\theta$)-side of a blade
V_w = maximum spanwise velocity in wake caused by wake
W = velocity relative to rotor
$W_\infty^2 = \frac{1}{2}(W_1^2 + W_2^2)$
w = velocity in blade boundary layer or wake, relative to rotor
w_r' = maximum radial velocity in wake caused by wake
x = distance normal to primary flow streamlines and normal to n-direction

Downloaded 01 Jun 2010 to 171.66.16.62. Redistribution subject to ASME license or copyright; see http://www.asme.org/terms/Terms_Use.cfm

larger turning angles characteristic of turbines make some of the approximations employed much less suitable.

3 Calculation of Spanwise Velocities at a Blade Row Trailing Edge

3.1 Secondary Flow from the Main Flowfield. The basic approach employed to calculate this contribution to mixing is that developed by L. H. Smith [3,4]. A condensation of that work is presented in [5] but as part of the condensation, consideration was restricted to the treatment of barotropic fluids which, for present applications, means homentropic flows. Since spanwise entropy variations can sometimes significantly influence secondary velocities, particularly in turbines, their consideration has been included in the present analysis.

The equation that gives the spanwise component of secondary velocity that creates the trailing vortex sheet, for any stator blade row or for a rotor blade row of the axial-flow type, is [3]

$$V_s = \frac{1}{2}\left[W_1 \zeta_{\perp_1} \frac{\Gamma_A}{W_\infty{}^2} - \frac{1}{2}\left(1 + \frac{W_1{}^2}{W_\infty{}^2}\right)\frac{\Gamma_A}{c_p}\frac{ds}{dn_1} + \frac{d\Gamma_A}{dn_1}\right]\frac{dn_1}{dn_2}. \tag{1}$$

Although V_s is indeed the quantity being sought because it is the secondary flow component that causes mixing, equation (1) is not directly usable because Γ_A is the actual blade circulation, including secondary flow effects that are unknown at this point. This difficulty is serious only for the last term in equation (1), but it can affect that term in a dominant fashion. It is therefore necessary to approach the problem differently, to calculate secondary vorticity and to integrate it over a Trefftz-type surface to deduce secondary velocities. As has been shown [3,5], Stokes law can be employed to relate secondary vorticity and secondary velocities on a Trefftz surface, and its application in the present context gives, using equation (1),

$$\zeta_s a = \left[W_1 \zeta_{\perp_1} \frac{\Gamma_A}{W_\infty{}^2} - \frac{1}{2}\left(1 + \frac{W_1{}^2}{W_\infty{}^2}\right)\frac{\Gamma_A}{c_p}\frac{ds}{dn_1} + \frac{d\Gamma}{dn_1}\right]\frac{dn_1}{dn_2}, \tag{2}$$

the right-hand side of which is identical to that of equation (1) except that the blade circulation in the last term now is that of the primary flow only. The secondary vorticity, ζ_s, as defined and employed in references [3-5], is an average value across a passage from blade to blade but varies along the span from hub to tip.

The primary flow to which the secondary flow is added to get the total flow is obtained as follows. We start with a circumferential-average (axisymmetric) flow solution that has been updated through an iteration procedure to include all sources of secondary flow cross-flow and mixing effects. This solution is used to give us the inlet conditions to the blade row being considered and the distribution of meridional stream-tube lamina thickness at its exit. Then, from a cascade analysis of the flow in each stream-tube, using the actual blade geometry and accounting for changes in lamina thickness and changes in radius as appropriate, a "two-dimensional" circumferential-average exit flow angle is deduced. (This cascade analysis may be a very simple one, such as the application of Carter's rule.) Taking that exit flow angle, the exit static pressure from the circumferential-average flow solution, and the entropy of that streamline at cascade inlet, the primary flow exit tangential velocity component is deduced. This is then used to compute the

Nomenclature (cont.)

y = distance in n-direction
z = axial coordinate
z', z'', z''' = distances in z-direction having various origins, see equation (43)
α = angle between absolute velocity and meridional direction
β = angle between relative velocity and meridional direction
β_z = arc tan (W_θ / W_z)
Γ = blade absolute circulation of primary flow
Γ_A = blade absolute circulation of primary flow plus secondary flow
$\gamma_W{}^\circ$ = arc sin (W_r / W)
δ = end-wall boundary layer full thickness
δ_w = blade wake full thickness
δ^* = end-wall boundary layer displacement thickness
ϵ = mixing coefficient, equation (42)
ζ = absolute vorticity
ζ_s = secondary vorticity
η = stage polytropic efficiency
θ = circumferential angular coordinate
ρ = fluid density
υ = tangential-force thickness, reference [1]
ψ = secondary flow streamfunction
ω = rotor angular velocity
$\bar{\omega}$ = total-pressure loss coefficient based on inlet dynamic head

Subscripts

$\perp$ = component perpendicular to relative velocity
i = at inlet to the turbomachine
L = related to leakage flow
m = meridional component
o = at trailing edge plane
R = rotor
r = radial component or in radial direction
r-s = repeating-stage condition
S = stator
T = stagnation condition
t = at outer casing
x = cross-passage component
y = spanwise component
z = axial component
θ = circumferential component
1,2 = before and after a blade row
2D = primary flow

Sign Conventions

$+\theta$ = direction of rotation $(+\omega)$
$+\zeta_s$ = $-\omega$ sense
$+x$ = $+\theta$ sense
$+\Gamma$ = increase in C_θ across a blade row
$+n, +y, +V_y, +V_s$ = radial sense

Note: These sign conventions are different in some cases from those of references [3–5].

Downloaded 01 Jun 2010 to 171.66.16.62. Redistribution subject to ASME license or copyright; see http://www.asme.org/terms/Terms_Use.cfm

primary flow blade circulation,

$$\Gamma = \frac{2\pi}{N}(r_2 C_{\theta_2} - r_1 C_{\theta_1}). \tag{3}$$

This can then be used in equation (2) for both Γ and Γ_A, and ζ_s can be calculated.

It is worth mentioning that the secondary vorticity ζ_s employed here is generally not the same as the streamwise component of the actual absolute passage vorticity because the primary flow employed here generally contains streamwise vorticity. Sir William Hawthorne's primary flows generally do not contain streamwise passage vorticity, and his secondary vorticity therefore sometimes differs from that employed here. Horlock [6,7] has pointed out this difference in definition and has shown that the two approaches are not in conflict.

Another form of equation (2) that contains variables with more physical significance (does not contain $\zeta_{\perp_1}$) can be obtained by substituting a form of the radial equilibrium equation,

$$W\zeta_\perp = \frac{d}{dn}\left(h + \frac{W^2}{2} - \frac{U^2}{2}\right) - T\frac{ds}{dn} \tag{4}$$

into equation (2) and by employing the thermodynamic relationships

$$\frac{1}{\rho_T}\frac{dP_T}{dn} = \frac{d}{dn}\left(h + \frac{C^2}{2}\right) - T_T\frac{ds}{dn} \tag{5}$$

$$c_p(T_T - T) = \frac{C^2}{2} \tag{6}$$

and a velocity triangle relationship

$$\frac{C^2}{2} - \frac{W^2}{2} = UC_\theta - \frac{U^2}{2}. \tag{7}$$

Equation (2) then becomes

$$\zeta_s a = \left\{\left[\frac{1}{\rho_{T_1}}\frac{dP_{T_1}}{dn_1} - \frac{d(UC_\theta)_1}{dn_1} + \left(U_1 C_{\theta_1} - \frac{U_1^2}{2}\right)\frac{ds}{c_p dn_1}\right]\frac{\Gamma_A}{W_\infty{}^2} - \frac{\Gamma_A}{2c_p}\frac{ds}{dn_1} + \frac{d\Gamma}{dn_1}\right\}\frac{dn_1}{dn_2}. \tag{8}$$

The expression contained in the brackets in equation (8) can be shown to be consistent with Hawthorne's equation (38) of reference [8]. Equation (8) also satisfies the requirement pointed out by Hawthorne [8,9] that there be no secondary flow generated in a two-dimensional stationary cascade with an axial inflow having constant stagnation pressure even though there is a (spanwise) stagnation temperature gradient. In that case each term in the brackets in equation (8) is zero and the last two terms in the braces can be shown to cancel.

In this paper the secondary flow velocities are obtained from the secondary vorticity as follows. The solution surface for the secondary flow calculation is a Trefftz-type plane. The plane is approximated as a rectangle whose height (in the y-direction) is the blade span and whose x-direction width, $\bar{a}$, is the average of the blade cross-passage staggered spacings at casing and hub. The secondary-flow is considered to be a perturbation on the primary flow. The perturbation streamfunction satisfies the Poisson equation

$$\nabla^2\psi = \zeta_s \tag{9}$$

with ψ constant on the boundaries. When calculating ζ_s, which is a function of y only, from equation (8), $\bar{a}$ is used for a.

Equation (9) is solved using a standard separation-of-variables approach which yields a product of two Fourier sine series.

Secondary velocities are found using

$$V_x = -\frac{\partial\psi}{\partial y} \text{ and } V_y = \frac{\partial\psi}{\partial x}. \tag{10}$$

For the purposes of this paper we are primarily interested in the maximum values of V_y, which occur along the spanwise boundaries of the rectangle, but we are also equally interested in the cross-passage-average values of V_x because these influence our mainstream flow solution through their effect on blade row exit angles.

3.2 Endwall Boundary Layer Secondary Flow. The degree to which the actual velocity distributions that occur in an endwall boundary layer should be modeled in turbomachinery through-flow calculations has historically been decided arbitrarily by each individual worker. The most prevalent current trend seems to be to avoid inclusion of the very strong meridional velocity gradients that occur adjacent to an endwall but to recognize them to some degree by employing increased losses and, perhaps, increased deviation angles there. And there is the feeling among designers that, since the blade geometry cannot or should not incorporate extreme spanwise angle gradients, there is no point in employing a design flow model that has them.

In the present case we are faced with the need for recognizing all flow phenomena that might contribute substantially to spanwise fluid movements, so a fuller inclusion of end-wall boundary layer velocity gradients than is contained in the main flowfield solution is desired. This is accomplished by postulating that the velocity vector on an endwall at entrance to a blade row *in the frame of reference of the upstream blade row* is reduced in magnitude with unchanged direction by a fraction k_1 from that of the main flowfield solution. Hence k_1, which was subsequently chosen to be 0.25, establishes the strength of the endwall boundary layer. As with other constants in the model, this numerical value was chosen so that the total model would give reasonable agreement with the test data that were being employed, much of which are present in Section 5. The fact that the upstream blade row frame of reference is used recognizes that the boundary layer has most recently been influenced by viscous effects in that blade row. When the upstream blade row is moving relative to the blade row being considered, as it usually is, a skewing of the boundary layer is thereby produced. It is well known that skewing is of dominant importance in many applications (see, for instance, Horlock [10]).

Since any inviscid steady-flow modeling of end-wall boundary layer flows is going to be crude anyway, further simplifying assumptions beyond those used in the main flowfield modeling are employed here. The geometry is assumed to be a semi-infinite-span cascade whose blade shape models that of the end-wall blade section. Since the boundary layer thickness is small compared to the radius, the vorticity in it will be large compared to 2ω and the latter is ignored when deducing the vorticity entering a stator from the upstream rotor end-wall velocity defect. Inlet velocities are assumed to vary linearly with distance from the wall, so the inlet boundary layer has constant vorticity everywhere in it and the free-stream vorticity is zero. The free-stream velocity vector is taken to be the end-wall vector from the main flowfield solution. Entropy gradient effects are omitted. With these assumptions, for the case of a rotor hub section, the inlet vorticity component perpendicular to the inlet relative velocity is

$$\zeta_{\perp_1} = \frac{k_1 C_1}{\delta_1}\cos(\alpha_1 - \beta_1). \tag{11}$$

When this is substituted into equation (2) together with

Downloaded 01 Jun 2010 to 171.66.16.62. Redistribution subject to ASME license or copyright; see http://www.asme.org/terms/Terms_Use.cfm

$$\frac{d\Gamma}{dn_1} = \frac{2\pi}{N}\left(r_2 \zeta_{m_2} \frac{dn_2}{dn_1} - r_1 \zeta_{m_1}\right) \tag{12}$$

from reference [5] and

$$\zeta_{m_2} = \zeta_{\perp 2} \sin \beta_2, \tag{13}$$

because there is no streamwise exit vorticity in the primary flow with the cascade approximation employed here, and

$$W_2 \zeta_{\perp 2} = W_1 \zeta_{\perp 1} \frac{dn_1}{dn_2}, \tag{14}$$

which is an application of equation (4) across a blade row, we obtain

$$\zeta_s a = \frac{k_1 C_1}{\delta_1}\left\{W_1 \cos(\alpha_1 - \beta_1)\frac{\Gamma_A}{W_\infty{}^2} + \frac{2\pi}{N}\left[r_2 \frac{W_1}{W_2}\cos(\alpha_1 - \beta_1)\sin\beta_2 - r_1 \sin\alpha_1\right]\right\}\frac{dn_1}{dn_2} \tag{15}$$

giving the secondary vorticity associated with an end-wall boundary layer passing through a rotor hub. Similar expressions can be written for the other three end-wall elements. All quantities in equation (15) apply to the primary flow, obtained as a described in Section 3.1. The inlet boundary layer thickness, δ_1, is taken to be five times the displacement thickness adapted from the correlations of Smith [1] as described in the Appendix.

For end-wall boundary layer secondary flows the solution plane is considered to be a semi-infinite strip whose width, a, is the blade cross-passage staggered spacing at the end wall. The secondary vorticity is assumed to be contained within the boundary layer thickness δ_2 where $\delta_2 = \delta_1 (dn_2/dn_1)$. The vorticity is constant within this slab and zero elsewhere. As with the analysis of the main flowfield secondary flow, a secondary flow stream function is defined and a Poisson equation results. For its solution a separation-of-variables approach is again used. For the semi-infinite strip boundary geometry, this gives a Fourier sine series in the cross-passage x-direction and a semi-infinite Fourier sine integral in the spanwise y-direction. $V_y(y)$ on the spanwise boundaries and $V_x(y)$ are again calculated.

3.3 Tip Clearance Secondary Flow. An approximate method for the calculation of tip clearance secondary flow proposed by Lakshminarayana and Horlock [11] has been adopted for use here. In this method the strength of the secondary flow is proportional to the shed vortex strength given by

$$\Gamma_{SV} = (1 - k_\ell)\,\Gamma_{2D}, \tag{16}$$

where Γ_{2D} is the circulation a blade would have in two-dimensional flow (taken by us to be Γ_V of the primary flow defined in Section 3.1) and k_ℓ is an empirically determined function of clearance/chord ratio (Fig. 16(a) of [11]):

ℓ/c	0	0.01	0.02	0.04	0.06	0.08
k_ℓ	1.0	0.73	0.58	0.41	0.32	0.27

Although Γ_{SV} is in reality largely concentrated in a vortex core that lies roughly midway between the wakes of adjacent blades, it was found [11] that a rather good representation of the induced pitchwise-average cross-passage secondary-flow angle distribution could be obtained by treating the vortex core as if its vorticity were uniform in the pitchwise direction and varied as the first half-cycle of a sine wave in the spanwise direction, and then using this vorticity distribution like secondary vorticity in a Trefftz plane integration to obtain secondary flow velocities. The sine wave half-cycle extends from the wall to a distance δ_ℓ. Cascade test data in [11] indicate that the spanwise penetration of tip clearance effects is roughly proportional to the clearance itself, and we have selected

$$\delta_\ell/\ell = 6.5 \tag{17}$$

after trying several values and comparing the resulting pitchwise average secondary flow angles with those measured and presented in [11].

In these cascade calibrations it was found to be necessary to allow for some loss in pitchwise average cascade turning in addition to that induced by the shed vortex. This has been done by reducing $|\tan\beta_1 - \tan\beta_2|$ of the primary flow at the tip by an amount related to the shed vortex strength as follows. Let $|\beta_2^* - \beta_2|$ be this additional turning angle loss. Then

$$|\tan\beta_1 - \tan\beta_2^*| = k_\ell^* |\tan\beta_1 - \tan\beta_2|, \tag{18}$$

with

$$1 - k_\ell^* = \frac{1}{4}(1 - k_\ell). \tag{19}$$

The fraction 1/4 was empirically determined. This additional turning angle loss varies linearly from its full value at the wall to zero at a distance of one staggered spacing away from the wall.

It is recognized that satisfactory agreement with data for pitchwise average velocities does not necessarily mean that spanwise velocity distributions are correct. In fact, because the tip vortex core is actually located roughly at mid-passage, it is to be expected that the actual spanwise velocities induced at the spanwise boundaries are less than those given by our model which has the secondary vorticity uniformly distributed in the pitchwise direction. We account for this in an approximate way by assuming that the actual values are only two-thirds of those calculated, and these reduced values are summed with the other secondary flow contributions, as described in Section 4.2, when calculating mixing coefficients.

3.4 Shrouded Blade End Leakage Secondary Flow. Leakage flows enter the annulus with zero or very small meridional velocity, and they become entrained by the main flow. This entrainment process removes momentum from the main flow and tends to create an additional boundary layer on it that is more or less colateral in the frame of reference of the following annulus surface and blade row. We assume that it is colateral, and treat it in a fashion similar to that done in Section 3.2 for end-wall boundary layer secondary flow. For the case of a stator at the hub we then have

$$\zeta_{\perp 1} = \frac{k_1 C_1}{\delta_1}. \tag{20}$$

This is substituted into equation (2) together with equations like (12)-(14), except β_2 is replaced with α_2 and W is replaced with C because our example is a stator, to obtain

$$\zeta_s a = \frac{k_1 C_1}{\delta_1}\left\{C_1 \frac{\Gamma_A}{C_\infty{}^2} + \frac{2\pi}{N}\left[r_2 \frac{C_1}{C_2}\sin\alpha_2 - r_1 \sin\alpha_1\right]\right\}\frac{dn_1}{dn_2} \tag{21}$$

giving the secondary vorticity associated with leakage flow passing through a shrouded stator at the hub. The inlet boundary layer thickness δ_1 is taken to be six times δ_L^*, where δ_L^* is the leakage flow displacement thickness as defined in the Appendix. As with end-wall boundary layer secondary flow, 0.25 is used for k_1. All quantities in equation (21) apply to the primary flow, obtained as described in Section 3.1.

Secondary flow velocities are calculated from the secondary vorticity with the method described in Section 3.2.

Experience, some of which is given in Section 5, has indicated that leakage causes a loss in turning angle in the blade row following its entry into the main stream. This probably results from a weakening of the blade suction surface boundary layer, perhaps caused by entrainment of the leakage

Downloaded 01 Jun 2010 to 171.66.16.62. Redistribution subject to ASME license or copyright; see http://www.asme.org/terms/Terms_Use.cfm

flow. This loss in turning is accommodated by reducing $|\tan \alpha_1 - \tan \alpha_2|$ of the primary flow at the wall by an amount related to the leakage as follows. Let $|\alpha_2^* - \alpha_2|$ be this turning angle loss. Then

$$|\tan \alpha_1 - \tan \alpha_2^*| = (1 - \Delta\Gamma/\Gamma)\ |\tan \alpha_1 - \tan \alpha_2| \tag{22}$$

where $\Delta\Gamma/\Gamma$ is an empirically determined function of the ratio of the leakage flow displacement thickness to the staggered spacing:

δ_L^*/g	0	.02	.04	.08	.16	.32	∞
$\Delta\Gamma/\Gamma$	0	.031	.115	.341	.675	.892	1.0

This turning angle loss was assumed to vary linearly from its full value at the wall to zero at a distance of one staggered spacing away from the wall.

3.5 Blade Boundary Layer Crossflow. The simplified approach employed in this paper for treatment of this complex phenomenon is as follows. Neglecting viscous stresses, the spanwise acceleration of a representative small mass of fluid in the blade boundary layer is calculated at a representative point along the chord and assumed to act over the time it takes for the small mass to travel a representative distance. The resulting spanwise velocity is then compared with some available test data, which leads to the selection of the value of a constant in the model.

The velocity of the representative small mass in the boundary layer is denoted by **w**. The equation of motion for flow in rotating coordinates is

$$\frac{D\mathbf{w}}{Dt} + 2\boldsymbol{\omega} \times \mathbf{w} = \omega^2 \mathbf{r} - \frac{\nabla p}{\rho}. \tag{23}$$

If we assume that the pressure in the boundary layer is the same as that in the adjacent free stream and that the position vector, **r**, is nearly the same, we can combine equation (23) with a similar one written for free-stream fluid and obtain

$$\frac{D\mathbf{w}}{Dt} = \frac{D\mathbf{W}}{Dt} + 2\boldsymbol{\omega} \times (\mathbf{W} - \mathbf{w}), \tag{24}$$

which can also be written

$$w_z \frac{D\mathbf{w}}{Dz} = W_z \frac{D\mathbf{W}}{Dz} + 2\boldsymbol{\omega} \times (\mathbf{W} - \mathbf{w}). \tag{25}$$

In cylindrical coordinates,

$$\mathbf{w} = w_r\, \mathbf{i}_r + w_\theta\, \mathbf{i}_\theta + w_z\, \mathbf{i}_z. \tag{26}$$

This is differentiated following the fluid, and the unit vector relationships

$$D\mathbf{i}_r = \mathbf{i}_\theta D\theta, \quad D\mathbf{i}_\theta = -\mathbf{i}_r D\theta, \quad D\mathbf{i}_z = 0 \tag{27}$$

are used to obtain

$$D\mathbf{w} = Dw_r\, \mathbf{i}_r + Dw_\theta\, \mathbf{i}_\theta + Dw_z\, \mathbf{i}_z + (w_r\, \mathbf{i}_\theta - w_\theta\, \mathbf{i}_r) D\theta. \tag{28}$$

A similar equation, (28*a*), can be written for $D\mathbf{W}$. For axial-flow machines the spanwise direction is radial, so we take the scalar product of equation (25) with $\mathbf{i}_r$ after substituting equations (28) and (28(*a*)) into it to obtain

$$w_z \left(\frac{Dw_r}{Dz} - w_\theta \frac{D\theta}{Dz} \right) = W_z \left(\frac{DW_r}{Dz} - W_\theta \frac{D\theta}{Dz} \right) + \mathbf{i}_r \cdot [2\omega\, \mathbf{i}_z \times (\mathbf{W} - \mathbf{w})]. \tag{29}$$

Application of vector algebra yields

$$-2\omega(W_\theta - w_\theta)$$

for the last term in equation (29), and using

$$r \frac{D\theta}{Dz} = \frac{w_\theta}{w_z} = \frac{W_\theta}{W_z} = \tan\beta_z, \tag{30}$$

and defining

$$k_w = \frac{w_z}{W_z}, \tag{31}$$

equation (29) becomes, after rearrangement,

$$\frac{Dw_r}{W_z} = \frac{1}{k_w} \left\{ \frac{DW_r}{W_z} - \frac{Dz}{r} \left[\tan^2\beta_z (1 - k^2{}_w) + 2 \tan\beta_z \frac{\omega r}{W_z} (1 - k_w) \right] \right\}. \tag{32}$$

This equation gives an inviscid approximation for the development of spanwise velocity in the boundary layer on an axial-flow turbomachine blade in terms of mainstream properties and the depth in the boundary layer as measured by k_w. Our general scheme is to employ a representative single value for k_w selected such that equation (32) gives a spanwise velocity that is in reasonable agreement with selected available measurements of the peak spanwise velocity in the wake.

Further assumptions are made when applying equation (32): 1) The first term on the right-hand side is neglected; this is analogous to neglecting the meridional streamline curvature term when calculating the mainstream radial static pressure gradient from a radial-equilibrium equation. 2) Trailing edge values are employed for β_z and W_z, since logic and experience have shown that, except in some cases of shock-induced separation, most of the spanwise flow occurs near the trailing edge. 3) The axial distance over which the spanwise acceleration is assumed to act, Dz, is taken to be 50 percent of the axial chord projection. This can be thought of as covering the aft 30 percent of the blade plus 20 percent downstream of the trailing edge. Equation (32) then becomes

$$\frac{w_r'}{W_{z_2}} = -\frac{z_2 - z_1}{2r_2} \cdot \frac{1 - k_w}{k_w} \left[(1 + k_w) \tan^2\beta_{z_2} + 2 \frac{\omega r_2}{W_{z_2}} \tan\beta_{z_2} \right], \tag{33}$$

where w_r' is the spanwise velocity at the center of the wake measured a short distance (typically 20 percent axial chord projection) downstream of the trailing edge. For a reaction compressor rotor blade row β_2 is usually negative, and the second term in the brackets is usually dominant, leading to radially outward flow in the wake (centrifugation). Radially inward flow occurs in stator vane wakes.

Although some end-wall boundary layer fluid could become entrained in a blade boundary layer or wake and be moved radially with it, we do not include such fluid in the present analysis. This choice is made because it is argued that, in most cases, the end-wall fluid is already given a sufficient spanwise motion through the mechanism of its own secondary flow.

Wake measurement data from references [4] and [12-16] near the mean diameter have been examined, and a value of 0.5 has been selected for k_w. Comparisons with data are given in Table 1. For the rotors, agreement is poorest for Cases 2 and 4. Case 2 is a transonic rotor operating at 70 percent speed, so it is possible that the blade boundary layer may thicken near the leading edge and the spanwise acceleration may therefore occur over a longer length and with a higher β_z than assumed. Reference [15] indicates that the rotor of Case 4 is operating with the rather low efficiency of 82 percent which violates our condition of good efficiency, although this same rotor was previously found to have an efficiency of 95 percent at the same flow rate [4]. Cases 5 and 6 represent measurements on the same stator vanes, although the vanes had been moved further downstream from the rotor for Case 5. The inlet guide vanes of Case 7 produced no turning at the

Downloaded 01 Jun 2010 to 171.66.16.62. Redistribution subject to ASME license or copyright; see http://www.asme.org/terms/Terms_Use.cfm

Table 1 Maximum spanwise velocity of wake

Case	Type	Reference	Calculated w_r'/W_{z_2} ($k_w = 0.5$)	Test w_r'/W_{z_2}	Test $\frac{z-z_2}{z_2-z_1}$
1	Rotor	Dring, et al [12] ($W_z/\omega r = 0.85$)	0.07	0.06	0.10
2	Rotor	Strazisar & Powell [13]	0.16	0.28	0.65
3	Rotor	Larguier [14]	0.15	0.07-0.14	0.30
4	Rotor	Ravindranath & [15] Lakshminarayana	0.12	0.3	0.2
5	Stator	Lakshminarayana [16] & Davino	0.05	0.08	0.16
6	Stator	Smith [4]	0.05	0.04	0.16
7	IGV	Smith [4]	0.02	0	0.16

hub but turned the flow 35 deg at the casing. They therefore produced a strong mainstream secondary flow, but no spanwise wake flow superposed on the shed vortex sheet could be discerned.

4 Mixing Analysis

4.1 Mixing Equation. The mixing analysis described here is an inviscid phenomenon resulting from the convection of fluid properties by the secondary velocity field as calculated in Section 3. At locations downstream of a blade row trailing edge, the distribution of a fluid property is determined by its original distribution at the blade row exit and by its movement under the action of the secondary flow field. For simplicity, let us assume that the flow between two adjacent blades moves downstream in a straight channel of rectangular cross-section having width, a, and spanwise height, h. Let P be a fluid property, e.g. stagnation enthalpy. Then

$$P(x,y,z) = P(x_o, y_o) \tag{34}$$

where

y_o = spanwise coordiniate at the blade trailing edge
x_o = cross-passage coordinate at the blade trailing edge

The relation between the coordinates x_o, y_o (blade trailing edge) and the local coordinates, x, y is given by

$$y_o = y - \frac{V_y}{V_z} z \tag{35a}$$

$$x_o = x - \frac{V_x}{V_z} z \tag{35b}$$

where

V_y = spanwise secondary velocity
V_x = cross-passage secondary velocity
V_z = main stream axial velocity
z = axial distance from trailing edge plane

For each location x_o, the function $P(x_o, y_o)$ is represented by a Taylor series as follows:

$$P(x_o,y_c) = P(x_o)_{y_o=o} + y_o \frac{\partial P(x_o)}{\partial y}\bigg|_{y_o=o} + \frac{1}{2} y_o{}^2 \frac{\partial^2 P(x_o)}{\partial y^2}\bigg|_{y_o=o} + \ldots . \tag{36}$$

Combining equations (34), (35a) and (36) gives:

$$P(x,y,z) = P(x_o)_{y_o=o} + \left(y - \frac{V_y}{V_z} z\right) \frac{\partial P(x_o)}{\partial y}\bigg|_{y_o=o} + \frac{1}{2}\left(y - \frac{V_y}{V_z} z\right)^2 \frac{\partial^2 P(x_o)}{\partial y^2}\bigg|_{y_o=o} + \ldots . \tag{37}$$

The context within which the mixing is applied is a circumferential-average (meridional-plane) calculation. In this sense, the cross-passage (x-direction) distribution of properties is not known. The pertinent variable is the cross-passage averaged value,

$$\bar{P}(y,z) = \frac{1}{a}\int_o^a P(x,y,z)\, dx \quad . \tag{38}$$

The effect of mixing is to cause the property $\bar{P}$ to change with z. From equation (38),

$$\frac{\partial \bar{P}(y,z)}{\partial z} = \frac{1}{a}\int_o^a \frac{\partial P(x,y,z)}{\partial z}\, dx \tag{39}$$

where it is assumed that there is no variation of passage spacing with z. Combining equations (37) and (39) and evaluating at the reference spanwise coordinate, $y = o$, gives

$$\frac{\partial \bar{P}(y,z)}{\partial z} = -\frac{1}{a}\int_o^a \frac{V_y}{V_z}\frac{\partial P(x_o)}{\partial y}\bigg|_{y_o=o} dx + \frac{z}{a}\int_o^a \frac{V_y{}^2}{V_z{}^2}\frac{\partial^2 P(x_o)}{\partial y^2}\bigg|_{y_o=o} dx + \ldots . \tag{40}$$

Finally, if the first and second spanwise derivatives of P are assumed constant in x at the trailing edge and if the trailing edge second spanwise derivative is represented by its local value, an equation of the following form results:

$$\frac{\partial \bar{P}}{\partial z} = \epsilon \frac{\partial^2 \bar{P}}{\partial y^2} \quad , \tag{41}$$

where

$$\epsilon = \frac{z}{a}\int_o^a \frac{V_y{}^2}{V_z{}^2}\, dx \quad . \tag{42}$$

The first term in equation (40) has disappeared because the cross-passage average of the spanwise velocity must be zero to satisfy continuity. It is recognized that the fluid properties in a general turbomachinery environment do have cross-passage variations so that equation (41) should be considered a simplification of the actual physical process. Furthermore, as the mixing process proceeds downstream there are generally interactions with end walls and with succeeding blade rows as well as effects due to viscosity. These complexities are beyond the scope of this analysis. Therefore, the approach taken is to use equation (41) but to allow empirical modification of the mixing coefficient, ϵ, to account for downstream interactions, as described in the following section.

Downloaded 01 Jun 2010 to 171.66.16.62. Redistribution subject to ASME license or copyright; see http://www.asme.org/terms/Terms_Use.cfm

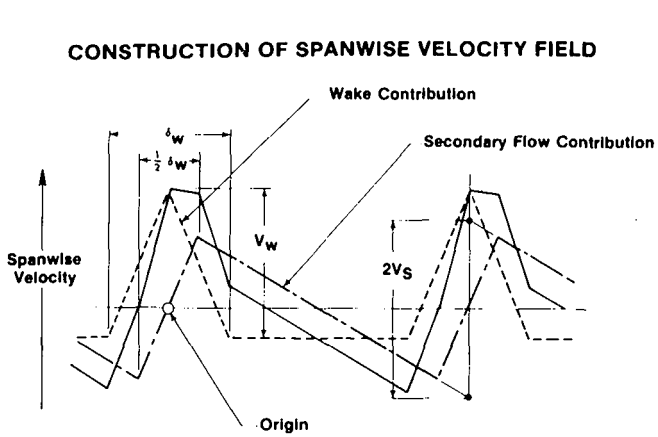


Fig. 1 Construction of spanwise velocity field from secondary flow and wake contributions

4.2 Mixing Coefficient Evaluation. The total spanwise secondary velocity V_y to be used in equation (42) is taken as the sum of the passage secondary velocities (Sections 3.1 - 3.4) and the blade boundary layer crossflow velocity (Section 3.5). All of these are assumed to occur at the trailing edge plane even though the blade boundary layer crossflow velocity was calibrated using data measured some distance downstream of the trailing edge. The spanwise passage secondary velocities (Sections 3.1 - 3.4) are symmetric about the passage centerline with the maximum velocities occurring at the edges of the passage and with zero velocity at the center. For purposes of this analysis, a linear distribution of V_y with x we has been assumed using the sum of the maximum velocities, V_s, which come from the several Trefftz-plane integrations, at the spanwise boundaries. In some cases these velocities tend to cancel and in others they add. At the edges of adjacent Trefftz-planes a velocity discontinuity of magnitude $|2V_s|$ is produced. To provide a continuous distribution in x we have assumed that this velocity jump occurs over a distance equal to one-half the blade wake thickness, which is described two paragraphs hence.

The spanwise velocity due to blade-boundary-layer crossflow (Section 3.5) is assumed to be contained in the blade wake. The maximum value V_w comes from equation (33) and is assumed to occur at the wake centerline, which is placed at the edges of the Trefftz planes. A linear distribution is assumed with zero velocity at the edge of the wake. Finally, the whole level of this velocity is shifted so that the average velocity is zero (to satisfy continuity). The final resulting velocity distribution has a shape like that shown in Fig. 1. The total velocity, V_y, is then normalized by the main flowfield axial velocity, squared, and integrated as required by equation (42). The only additional parameter needed is the blade wake thickness, δ_w.

The wake thickness is related to the profile loss which, as mentioned in Section 2, is taken from [2], including shock losses. A corresponding wake momentum thickness is found using Lieblein's equation (264) of reference [17] with a wake form factor of 1.08. The wake full thickness δ_w is taken to be 6.3 times this wake momentum thickness.

The description above allows the calculation of $\epsilon(y)$ from equation (42). This formulation shows that ϵ increases linearly in the downstream direction. Furthermore, the nature of the secondary flow field generally results in high values of ϵ being concentrated near the end-walls with rather low values of ϵ at mid-span locations. The analysis which led to equation (42), however, did not allow for viscous dissipation of the secondary flow field, nor did it allow for interactions with end-walls and succeeding blade rows. In order to account for these phenomena and to provide a better match with test data, empirical adjustments have been made to the mixing coefficient formulation, and these are described below.

The linear increase of ϵ with downstream distance has itself been decreased by a linear function of downstream distance. The resulting term is a parabolic function which initially increases at the proper rate but later peaks out and then decreases to zero at a downstream distance (in the flow direction) taken to be five times the annulus height. The origin for z in equation (42) is not placed at the trailing edge but is located at mid-axial chord to recognize the fact that the mixing effectively starts ahead of the trailing edge.

The integral part of ϵ is usually a strong function of spanwise position. This has been modified to linearly approach a constant value, the constant value being the spanwise average. Again, the downstream distance required to reach full flattening has been taken to be five times the annulus height.

The chopping action of succeeding blade rows has been represented by an exponential decay of ϵ which starts at the leading edge of the second downstream blade row and which proceeds at a rate that produces a 50 percent reduction by the trailing edge of that same second downstream blade row.

Finally, the effect of changes in axial velocity has been accounted for by including the square of the ratio of the trailing edge axial velocity to the local axial velocity.

Combining all these factors leads to the following expression for the mixing coefficient

$$\epsilon(z,y) = \begin{cases} \left[z'\left(1-\frac{z'}{\Delta z}\right)\right]\left[\left(1-\frac{z''}{\Delta z}\right)\frac{1}{a}\int_o^a \frac{V_{y_o}^2}{V_{z_o}^2}\,dx + \frac{z''}{\Delta z}\overline{\frac{1}{a}\int_o^a \frac{V_{y_o}^2}{V_{z_o}^2}\,dx}\right] \\ \quad \cdot \left[e^{\frac{-0.693 z'''}{b}}\right]\left[\frac{V_{z_o}^2}{V_z^2}\right] & 0 < z' < \Delta z \\ = 0 & z' > \Delta z \end{cases} \tag{43}$$

where

z' = axial distance downstream from mid-axial-chord location

Δz = axial distance corresponding to five trailing edge annulus heights in the flow direction

z'' = axial distance downstream from the trailing edge

z''' = axial distance downstream from leading edge of second downstream blade row
$z''' = 0$ for points upstream of leading edge of second downstream blade row

b = axial chord projection of next blade row

and the bar over the integral indicates the spanwise mass average value.

The mixing coefficient at any location is then taken to be the sum of the contributions of all the upstream blade rows, obtained by applying equation (43) to each of them.

The mixing equation (41) together with the mixing coefficients of equation (43) is applied between calculation stations during the main flowfield meridional plane solution. The quantities that are mixed are stagnation temperature,

Downloaded 01 Jun 2010 to 171.66.16.62. Redistribution subject to ASME license or copyright; see http://www.asme.org/terms/Terms_Use.cfm

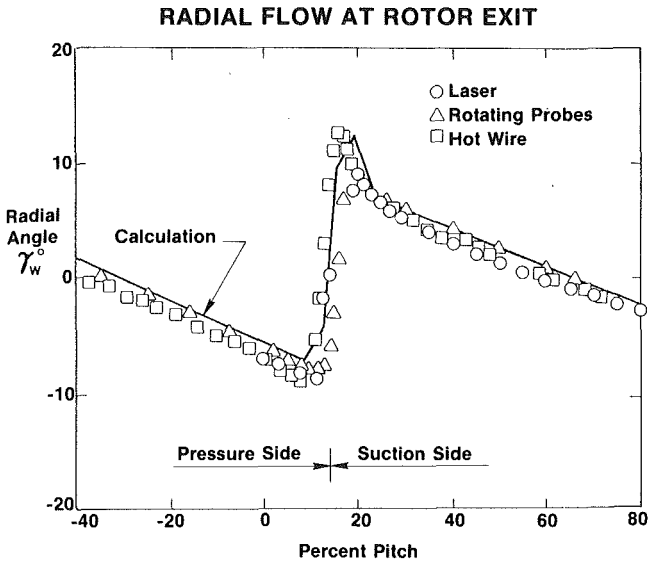


Fig. 2 Radial flow angles downstream of an untwisted rotor near the mean diameter; measurements by Laguier [14]

stagnation pressure, and angular momentum (rC_θ). End-wall boundary conditions applied to the mixing equation allow no flux of the mixed properties out of the flow, thus providing a conservative system. The meridional plane solution and the secondary flow solutions are mutually dependent, thus requiring an iterative loop. Typically, convergence of this process takes three to four iterations.

5 Applications

5.1 ONERA Rotor. This rotor has been used for research at the Office National d'Etudes et de Recherches Aerospatiales (ONERA) in Chatillon, France. Larguier [14] reports measurements of spanwise velocity taken near the mean diameter at 30 percent axial chord projection downstream of an isolated low-speed compressor rotor having 20 blades and a hub/tip radius ratio of 0.67. This research rotor is of particular interest because its blades have radially constant solidity and no twist, and therefore tend to have a rather nonuniform circulation distribution along their span. This leads to a rather substantial main flowfield secondary flow contribution and, since the exit relative flow angle is around -35 deg, the potential for substantial blade boundary layer cross-flow is also present. The tip clearance is relatively small (0.6 percent tip chord) and inlet end-wall boundary layers are thin (full thicknesses about 4 percent span).

The spanwise velocities calculated from our flow model have been expressed as the angle

$$\gamma_w^\circ = \arcsin(W_r/W) \tag{44}$$

and plotted in Fig. 2 together with data from [14]. When constructing the lines in Fig. 2 it was assumed that W was circumferentially constant between wakes[1] and 20 percent lower at the center of the (assumed) triangular-shaped wake. Agreement with test data is very good, but it should be remembered that the flow is unusually smooth in this example.

5.2 LSRC Configuration 9. This is a configuration tested in the General Electric Low Speed Research Compressor (LSRC) for which data were previously given by Smith [1] and which has been analyzed by DeRuyck & Hirsch [18]. It is comprised of four identical stages that employ unshrouded rotor and stator blading of 2.8 aspect ratio and about 1.05 pitchline solidity. The hub/tip radius ratio is 0.7. The vector diagram type can be described as rotational, but the main flowfield secondary flow is not very large because the passage aspect ratios are relatively high. Our main interest here is with tip clearance effects; both rotors and stators have a tip clearance/chord ratio of 0.040.

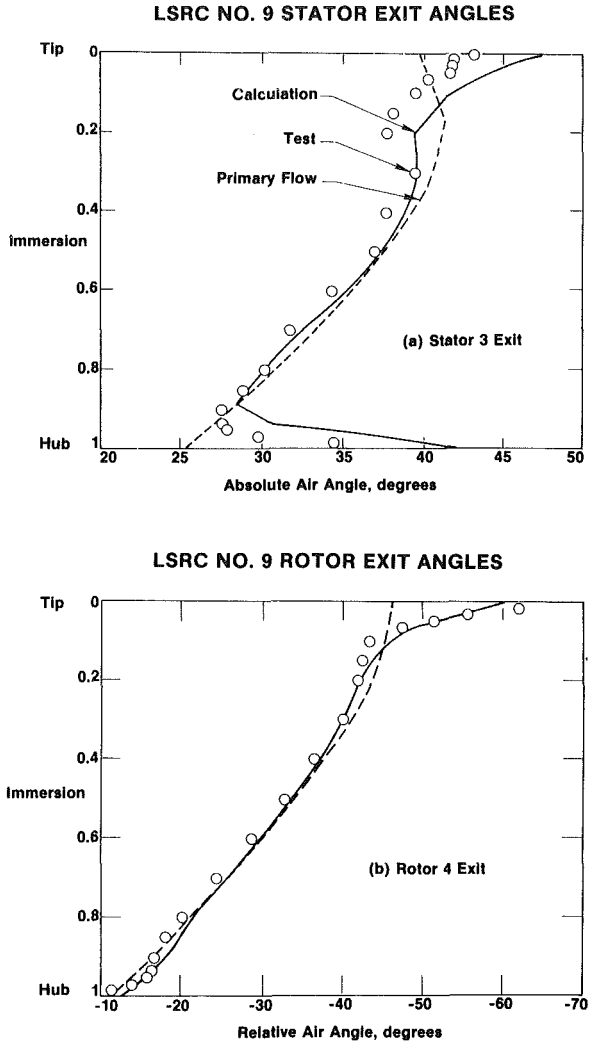


Fig. 3 Stator 3 and rotor 4 exit air angles for LSRC configuration 9

Figure 3 gives comparisons of calculated and measured exit flow angles from stator 3 and rotor 4. Carter's rule was used in these calculations to obtain the primary flow exit flow angles. Agreement with test data is not perfect, but it appears that the essential features of the clearance flow have been modeled.

Figure 4 gives the axial velocity distribution at rotor 4 exit and agreement is rather good. The fall-off at the outer wall is not calculated to be quite as large as was measured, but this is not surprising because wall shear stresses are only included in the model through their influence on loss coefficients. The reduction of end-wall velocity through k_1, described in Sections 3.2 and 3.4, is only employed for the purpose of calculating secondary vorticity; it does not appear directly in the velocities of the flow solution.

[1] This assumption is in error by several percent for this example because the Coriolis term in the equation of motion in the circumferential direction tends to cause the static pressure to be low at the shed vortex sheet and high at mid-passage.

Downloaded 01 Jun 2010 to 171.66.16.62. Redistribution subject to ASME license or copyright; see http://www.asme.org/terms/Terms_Use.cfm

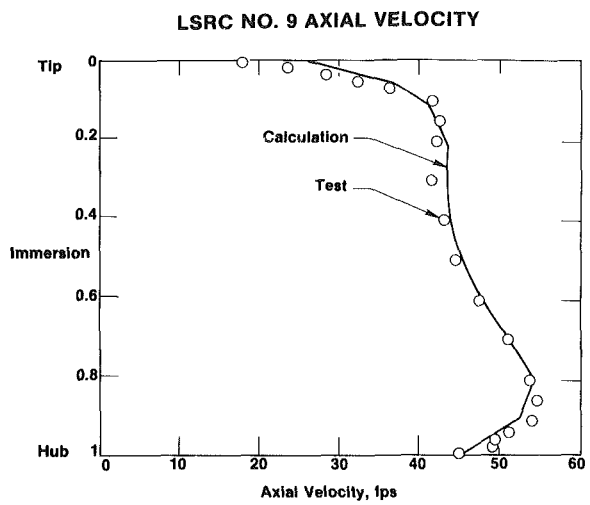


Fig. 4 Axial velocity distribution at rotor 4 exit for LSRC configuration 9

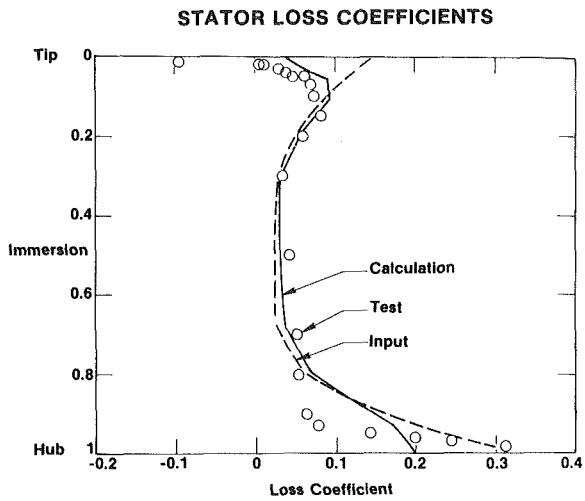


Fig. 6 Loss coefficient distributions for stator 3 of LSRC configuration 64

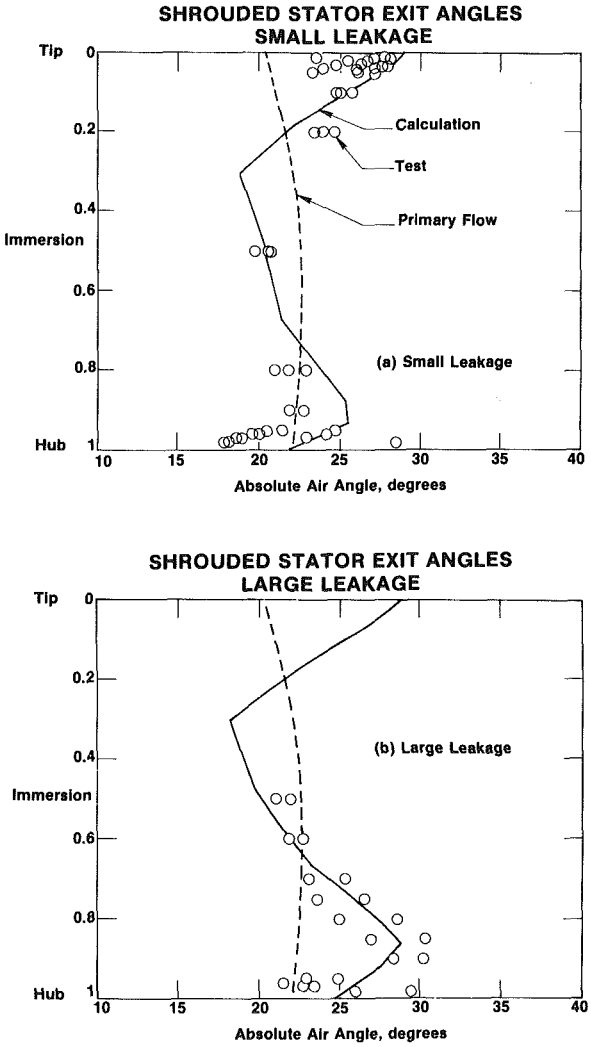


Fig. 5 Effect of stator shroud leakage on stator 3 exit air angles for LSRC configuration 64. Some of the test data were measured at stator 2 exit.

5.3 LSRC Configuration 64. This configuration, designed at General Electric under NASA sponsorship, employs Type B rotors and Type A stators whose designs are described by Wisler [19]. It is comprised of four identical stages; the rotor blades have an aspect ratio of 1.20, a pitchline solidity of 1.16 and are unshrouded; the stator vanes have an aspect ratio of 1.34, a pitchlilne solidity of 1.43 and are shrouded. The hub/tip radius ratio is 0.85. The vector diagram type can be described as mildly rotational, and the pitchline reaction is about 63 percent. Aerodynamic loading levels are fairly high.

Tests were conducted with small and large stator shroud seal clearances that gave leakage rates of 0.5 percent and 1.0 percent of the main airflow, respectively. The rotor tip clearance/chord ratio was 0.017 for both cases. Figure 5 shows calculated flow angles at stator 3 exit and measurements at both stator 3 exit and stator 2 exit; the calculated angles were nearly the same for stator 2 and stator 3. Some of the data shown came from tests of configuration 62, which employed Type A rotors (these have a different airfoil shape in the tip region only) [19], to boraden the data base. Agreement between calculation and test is seen to be fair; the model does not yield as large an increase in angle with increased leakage as the data show, but the trend is there. The primary flow angles for this case were obtained from two-dimensional cascade potential flow calculations. In general, the departure of the real flow angles from the two-dimensional values is modeled reasonably well.

Measured stator loss coefficients were obtained from circumferential surveys of stagnation pressure taken before and after a stator with miniature Kiel probes. Simple circumferential averages across one pitch were employed. The resulting loss coefficients were found to be negative very near the outer wall as shown in Fig. 6 for stator 3 (small shroud leakage case). Loss coefficients deducted from stagnation pressures calculated by our model at the axial locations where the measurements were taken are also shown in Fig. 6 and a similar tendency is observed. The input loss distribution, obtained as described in the Appendix, is also shown. Mixing has clearly played a dominant role in redistributing apparent losses near the outer wall. Near the inner wall agreement is not as good, and there is the suggestion that the method employed may have overestimated the loss magnitude.

5.4 P&WA Compressor Exit Stages. Two three-stage compressors, differing primarily in aspect ratio, were designed and tested at Pratt & Whitney Aircraft under NASA sponsorship [20, 21]. Both employed a cylindrical annulus with a hub/tip radius ratio of 0.915 and were operated at relatively low speed (rotor inlet relative Mach numbers were

Downloaded 01 Jun 2010 to 171.66.16.62. Redistribution subject to ASME license or copyright; see http://www.asme.org/terms/Terms_Use.cfm

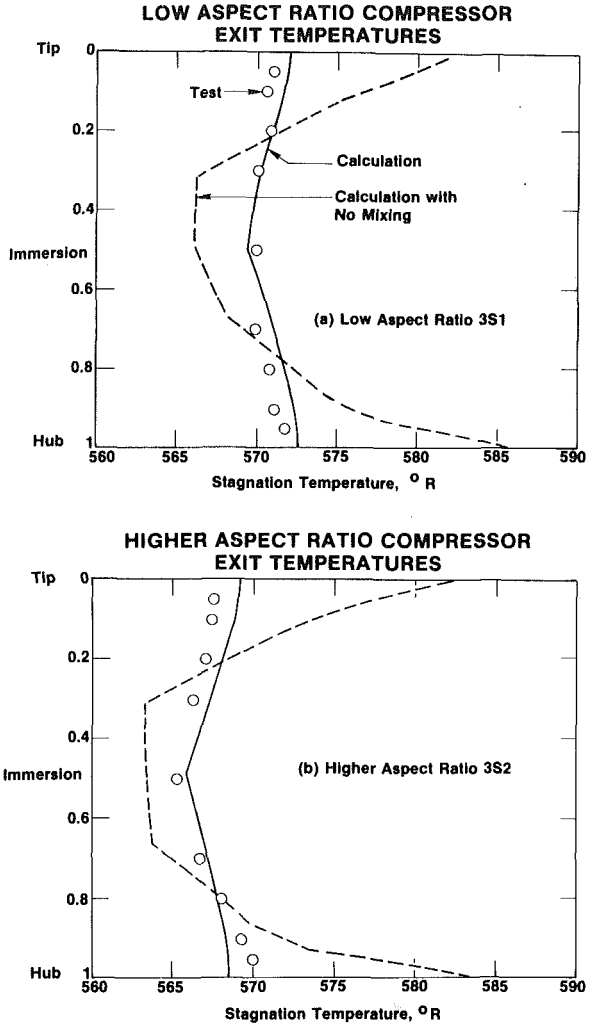


Fig. 7 Exit temperature distributions from 3-stage compressors having different aspect ratios

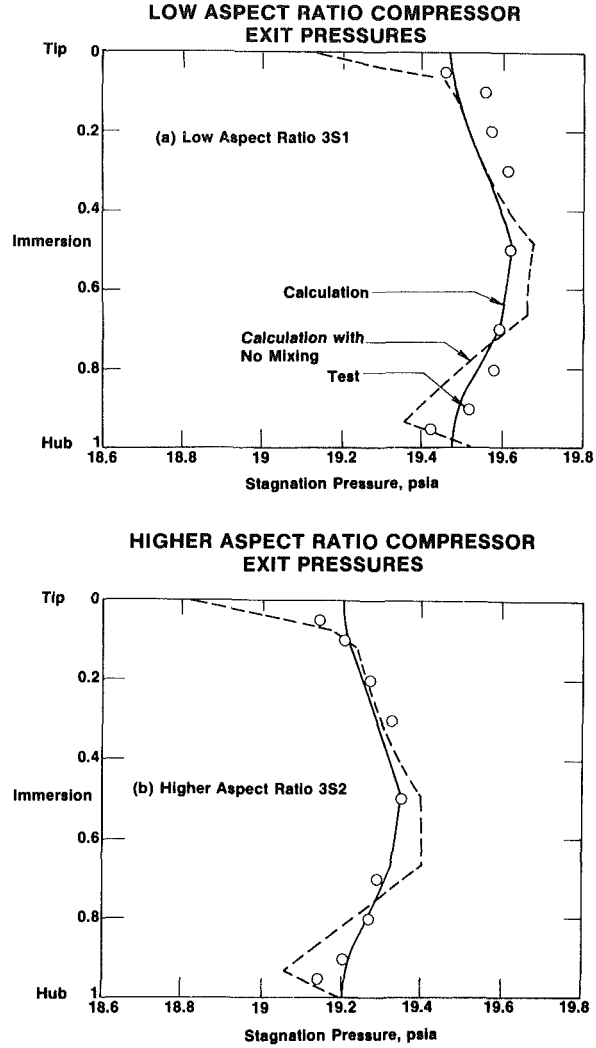


Fig. 8 Exit pressure distributions from 3-stage compressors having different aspect ratios

about 0.4). Configuration 3S1 had an average aspect ratio of 0.81, and the average aspect ratio of configuration 3S2 was 1.22. Average solidities were 1.10 in both cases, and pitchline reaction was 52 percent. Rotors and stators were both of cantilever construction, and the average tip clearance was 1.4 percent span for 3S1 and 1.6 percent for 3S2. Aerodynamic loading levels were fairly high. The low passage aspect ratios of these compressors gave them a substantial potential for secondary flow.

In the analysis, Carter's rule was employed to obtain the primary flow exit angles. Figure 7 compares calculated and measured stagnation temperatures at the exit survey plane, which was located several annulus heights downstream of the last stator trailing edge. Also shown are temperatures obtained from calculations for which the cross-passage secondary flow angle perturbations were maintained as previously calculated but for which mixing was not allowed to occur ($\epsilon = 0$). The effects of mixing are seen to be very strong for both configurations, and make it difficult to identify the locations where losses really do initiate.

Figure 8 shows calculated and measured stagnation pressures. Agreement is reasonable, except near the walls where our lack of wall shear stress acting over the substantial distance from the last blade row to the measurement plane has caused the discrepancy.

5.5 9-Stage Compressor. The analysis techniques have been applied to a high-speed compressor for which some interstage traverse data were available. This compressor had an average aspect ratio of 1.5 and an average pitchline solidity of 1.3. All stators were shrouded; rotors were unshrouded. An annular diffuser was in place just aft of the last row of stator vanes; it had a length/inlet-width ratio of about 2.5 and an area ratio of about 1.4. Carter's rule was used in our analysis to obtain primary flow angles.

Stagnation temperature profiles from the last few stages are compared in Fig. 9. Although traverse measurements were not taken at rotor 9 exit, it is believed that the temperature profile there was similar to that measured in the earlier stages. The substantial flattening of the profile that ocurs through stator 9 and the following diffuser must be caused primarily by mixing. The analysis models most, but not all, of this flattening.

As in the previous example, the analysis without mixing yields temperature profiles that are much too severe.

6 Conclusions

1 The current trend in aircraft engine axial-flow turbomachinery design is toward bladings with lower aspect ratios and higher aerodynamic loadings. This significantly increases the potential for secondary flows from all sources. The conclusion stated twenty-five years

Downloaded 01 Jun 2010 to 171.66.16.62. Redistribution subject to ASME license or copyright; see http://www.asme.org/terms/Terms_Use.cfm

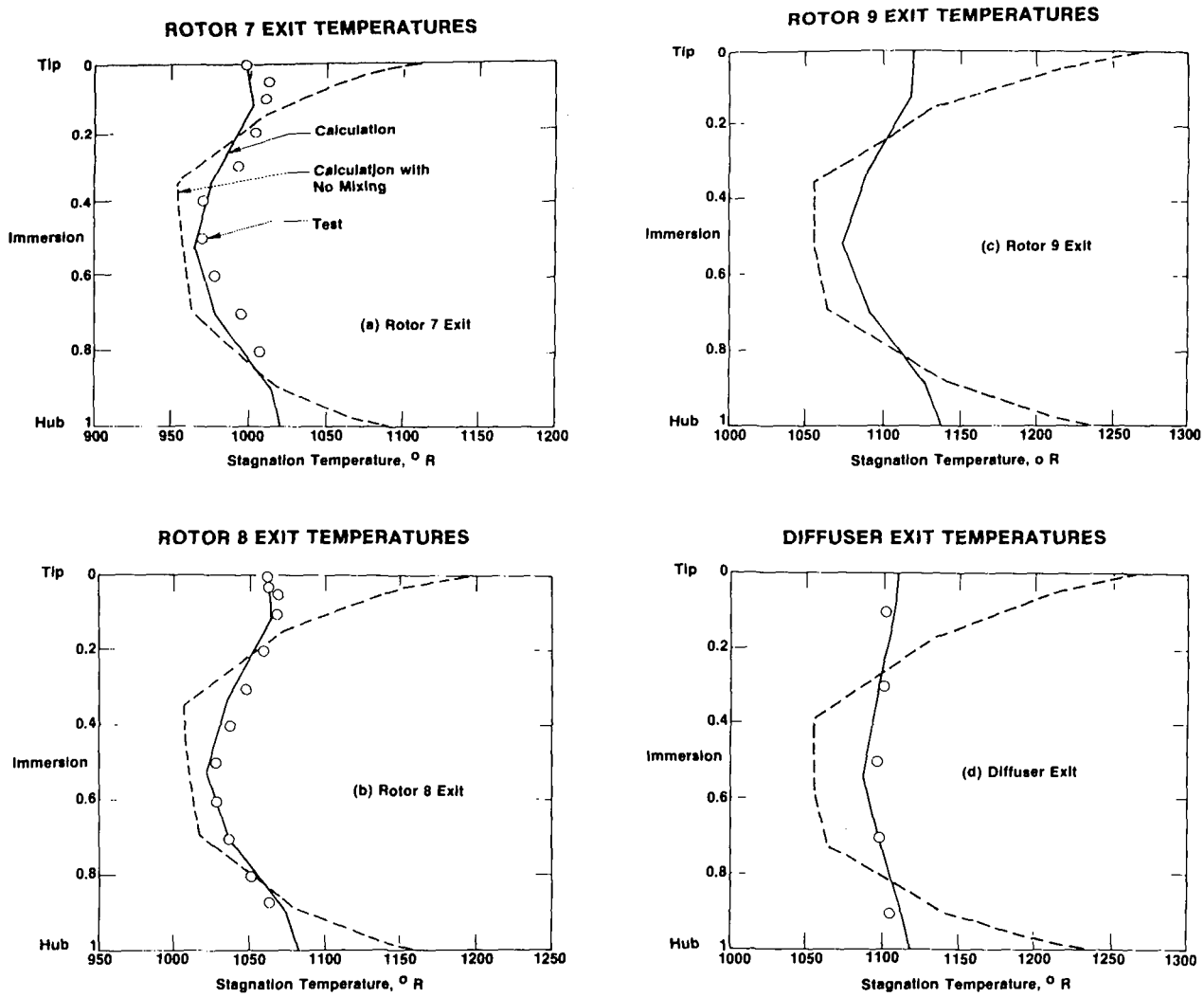


Fig. 9 Temperature distributions in the rear stages of a 9-stage compressor

ago [5] that secondary flow is usually small enough to be neglected no longer seems valid.

2 Much of the observed difference between measured blade row exit angles and those given by two-dimensional cascade rules or analyses can be attributed to secondary flows that can be calculated by inviscid methods, at least for the class of machines studied here (compressors operating near design point).

3 In the rear stages of multistaging machines, mixing can substantially influence the spanwise distributions of thermodynamic properties. This makes it difficult to pinpoint loss sources when measured data are being studied.

4 The mixing process downstream of a blade row trailing edge is quite complex and our modeling of it is rather crude and empirical. We hope to develop somewhat more rational models in the future.

References

1 Smith, L. H., Jr., "Casing Boundary Layers in Multistage Axial-Flow Compressors," *Flow Research on Blading*, L. S. Dzung, ed., Elsevier, Amsterdam, 1970, p. 275

2 Koch, C. C., and Smith, L. H., Jr., "Loss Sources and Magnitudes in Axial-Flow Compressors," ASME Paper No. 75-WA/GT-6, ASME JOURNAL OF ENGINEERING FOR POWER, Vol. 98, No. 3, July 1976, p. 411.

3 Smith, L. H., Jr., "Three-Dimensional Flow in Axial-Flow Turbomachinery, Part I, Theoretical Determination of Secondary Flow," Report I-14, Inst. for Coop. Res., Mechanical Engineering Department, The Johns Hopkins University, Baltimore, Md., Nov., 1953.

4 Smith, L. H., Jr., "Three-Dimensional Flow in Axial-Flow Turbomachinery, Part II, Experimental Investigations," Report I-16, Inst. for Coop. Res., Mechanical Engineering Department, The Johns Hopkins University, Baltimore, Md., May, 1954[2].

5 Smith, L. H., Jr., "Secondary Flow in Axial-Flow Turbomachinery," *Trans. ASME*, Vol. 77, No. 7, Oct. 1955, p. 1065.

6 Horlock, J. H., Discussion of "Secondary Vorticity in Axial Compressor Blade Rows," by S. L. Dixon, *Fluid Mechanics, Acoustics, and Design of Turbomachinery, Part I*, NASA SP-304, 1974, p. 196.

7 Horlock, J. H., and Lakshminarayana, B., "Secondary Flows: Theory, Experiment, and Application in Turbomachinery Aerodynamics," *Annual Review of Fluid Mechanics*, Vol. 5, 1973, p. 247.

8 Hawthorne, W. R., Discussion of "Effects of Inlet Temperature Gradients on Turbomachinery Performance," by B. Lakshminarayana, ASME *Journal of Engineering for Power*, Jan. 1975, p. 72.

9 Hawthorne, W. R., "The Growth of Secondary Circulation in Frictionless Flow," *Proc. Camb. Phil. Soc.*, Vol. 51, No. 4, 1955, p. 737.

10 Horlock, J. H., "Annulus Wall Boundary Layers in Axial Compressor Stages," ASME *Journal of Basic Engineering*, Vol. 85, D, 1, 1963, p. 55-61.

11 Lakshminarayana, B., and Horlock, J. H., "Leakage and Secondary Flows in Compressor Cascades," ARC, R&M No. 3483, Mar. 1965.

12 Dring, R. P., Joslyn, H. D., and Hardin, L. W., "Experimental Investigation of Compressor Rotor Wakes," Air Force Systems Command Technical Report AFAPL-TR-79-2107, Jan. 1980.

[2]Note: References [3] and [4] have been combined and published under the title "Three-Dimensional Flow in Axial-Flow Turbomachinery" as Wright Air Development Center Technical Report 55-348, Aug. 1955.

Downloaded 01 Jun 2010 to 171.66.16.62. Redistribution subject to ASME license or copyright; see http://www.asme.org/terms/Terms_Use.cfm

13 Strazisar, A. J., and Powell, J. A., "Laser Anemometer Measurements in a Transonic Axial Flow Compressor Rotor," *Measurement Methods in Rotating Components of Turbomachinery*, p. 165, presented at ASME Joint Fluids Engineering, Gas Turbine Conference and Products Show, New Orleans, Louisiana, Mar. 10–13, 1980.

14 Larguier, R., "Experimental Analysis Methods for Unsteady Flows in Turbomachinery," *Measurement Methods in Rotating Components of Turbomachinery*, p. 71, presented at ASME Joint Fluids Engineering, Gas Turbine Conference and Products Show, New Orleans, Louisiana, Mar. 10–13, 1980.

15 Ravindranath, A., and Lakshminarayana, B., "Three-Dimensional Mean Flow and Turbulence Characteristics of the Near Wake of a Compressor Rotor Blade," NASA Contractor Report 159518, PSU TURBO R 80-4, June 1980.

16 Lakshminarayana, B., and Davino, R., "Mean Velocity and Decay Characteristics of the Guidevane and Stator Blade Wake of an Axial Flow Compressor," ASME Paper No. 79-GT-9, Mar. 1979.

17 Lieblein, S., "Experimental Flow in Two-Dimensional Cascades," *Aerodynamic Design of Axial-Flow Compressors (Revised)*, NASA SP-36, Chapter VI, 1965, p. 183.

18 De Ruyck, J., and Hirsch, C., "Investigations of an Axial Compressor End-Wall Boundary Layer Prediction Method," ASME Paper No. 80-GT-53, Mar. 1980.

19 Wisler, D. C., "Core Compressor Exit Stage Study, Volume 1 — Blading Design," NASA CR-135391, GE R77AEG400, Dec. 1977.

20 Burdsall, E. A., Canal, E., Jr., and Lyons, K. A., "Core Compressor Exit Stage Study — I. Aerodynamic amd Mechanical Design," NASA CR-159714, PWA-5561-55, Sept. 1979.

21 Behlke, R. F., Burdsall, E. A., Canal, E., Jr. and Korn, N. D., "Core Compressor Exit Stage Study — II. Final Report," NASA CR-159812, PWA-5561-66, Oct. 1979.

APPENDIX

Loss Distribution Method

The endwall loss model of Smith [1] is structured in such a way that a stage efficiency multiplier for endwall effects is identified directly from end-wall boundary layer thickness parameters in the multistage environment without employing loss coefficients in the analysis. For the present paper it is necessary to deal with spanwise distributions of loss through an end-wall boundary layer, and the purpose of this section of the Appendix is to provide such distributions. Further assumptions are introduced as necessary or for simplicity.

In order to isolate the loss in an end-wall boundary layer let us consider a fictitious compressor repeating stage that has no profile loss, a frictionless hub, and whose span is δ_t, the thickness of the casing boundary layer. Then equation (5(a)) from [1], which is strictly applicable only for low Mach number flow but is used for all cases, becomes

$$\eta = \frac{1 - \dfrac{\delta_t^*}{\delta_t}}{1 - \dfrac{\upsilon}{\delta_t}} \quad , \tag{45}$$

where δ_t^* is the displacement thickness of the casing axial velocity boundary layer and υ is its tangential-force thickness, both defined in [1]. Another expression for stage efficiency employing rotor and stator loss coefficients, also strictly applicable only for low Mach number flow, is

$$\eta = 1 - \bar{\omega}_R \frac{W_1^2}{2\Delta H} - \bar{\omega}_S \frac{C_1^2}{2\Delta H} \quad , \tag{46}$$

where ΔH is the stagnation enthalpy change across the stage and the loss coefficients are average values. Equations (45) and (46) can be combined to eliminate η:

$$\bar{\omega}_R \frac{W_1^2}{2\Delta H} + \bar{\omega}_S \frac{C_1^2}{2\Delta H} = 1 - \frac{1 - \dfrac{\delta_t^*}{\delta_t}}{1 - \dfrac{\upsilon}{\delta_t}} \quad . \tag{47}$$

The span, δ_t, is taken to be two-thirds g_t, where g_t is the staggered spacing of the rotor blades. This value is representative of end-wall boundary layer full thicknesses for operation near peak efficiency as measured in the multistage environment in the General Electric Low Speed Research Compressor.

More information is needed to split the losses between the rotor and stator, and this is provided as follows. In the casing boundary layer the rotor has clearance and the stator does not. The assumption is made that if the rotor also had no clearance, the rotor and stator loss coefficients would be equal and have the value $\bar{\omega}_{\ell=0}$, which can then be determined from equation (47) using the zero clearance line in Fig. 6(a) of [1] to obtain $\delta^*_{t,\ell=0}$ and the assumption $\upsilon/\delta^*_{t,\ell=0} = 0.5$. This loss coefficient value is kept for the stator, and equation (47) can then be solved for the rotor average loss coefficient using the line in Fig. 6(a) of [1] corresponding to the proper clearance and again assuming $\upsilon/\delta^*_t = 0.5$. The appropriate value of loading for determining the abscissa in Fig. 6(a) of [1] is determined from test data when available or from correlations beyond the scope of this paper. For representative studies an abscissa value of 0.9 is employed.

The spanwise distribution of loss coefficient across an end-wall boundary layer is obtained from the end-wall average value as follows. It is assumed that the loss coefficient varies parabolically, with the vertex of the parabola located a distance (2/3)g_t from the casing (g_t now applies to the blade row being considered). It is a property of a parabola that its maximum value (which occurs at the casing) is three times its average value. For cases in which this loss spike would exceed 0.4 it is limited to 0.4 and a loss slab of 0.4 magnitude is added at the casing having the thickness required to achieve the required average loss, and the parabola vertex is moved away from the casing a distance equal to the slab thickness.

For the hub boundary layer in a machine employing cantilever stator vanes a similar procedure is followed except the roles of rotor and stator are interchanged, and Fig. 6(b) of [1] would be employed. For simplicity, however, we average the curves from Figs. 6(a) and 6(b) and use the average values for both casing and hub boundary layers.

For stator or rotor blades with shrouds attached to their tips a loss is employed that is related to the leakage flow around the shroud. A leakage flow displacement thickness on the main through-flow is defined as

$$\delta^*_L = \frac{Q_L}{2\pi r C_m} \quad , \tag{48}$$

where Q_L is the volume flow rate of the leakage and C_m is the main flowfield meridional velocity, both taken where the leakage re-enters the annulus. An equivalent cantilever blade tip clearance is then related to this displacement thickness by

$$\ell_L = K_L \delta^*_L \quad , \tag{49}$$

and losses are determined as if the blade were of cantilever construction. A value of 3.0 is employed for K_L for compressors.

Endwall Boundary Layer Displacement Thickness Selection for Secondary Flow Calculations

The boundary layer thicknesses of [1] apply to compressor flows in which the repeating-stage condition has been achieved. Investigators who have studied the growth of δ^* through compressors having similar geometries in all stages have found that the repeating-stage flow condition is usually reached around stage 3 or 4. DeRuyck & Hirsch [18] present a formulation for this behavior. For our purposes we employ the following approximation for all cases. The δ^*_1 to be used in the endwall boundary layer secondary flow calculations is given by

$$\frac{\delta^*_1}{h} = \left(\frac{\delta^*}{h}\bigg|_{r-s} - \frac{\delta^*}{h}\bigg|_i \right) k^* + \frac{\delta^*}{h}\bigg|_i \tag{50}$$

Downloaded 01 Jun 2010 to 171.66.16.62. Redistribution subject to ASME license or copyright; see http://www.asme.org/terms/Terms_Use.cfm

where h is annulus height, δ^*_i is the known or assumed inlet value, δ^*_{r-s} is the repeating-stage value obtained from [1] as previously described in this Appendix, and k^* is given by a simplified adaption of the formulation of DeRuyck & Hirsch [18]:

$$k^* = 1 - e^{-Q} \tag{51}$$

with

$$Q = (n-1)/2 \text{ (Compressors without IGV)} \tag{52a}$$
$$Q = (n-0.5)/2 \text{ (Compressors with IGV)} \tag{52b}$$

where n is blade row number and $n = 1$ for the first rotor, $n = 2$ for the following stator, etc. This gives $k^* = 0.86$ at third rotor inlet without IGV and $k^* = 0.89$ at third rotor inlet with IGV.

It is important to understand that the displacement thicknesses obtained from equation (50) are used only for secondary flow calculation purposes; they are not used in equation (47) for loss determination purposes. Although it is fundamentally incorrect to do so, equation (47) with repeating-stage values for boundary layer thicknesses is used for inlet stages because our experience suggests that, when profile losses, loading levels, aspect ratios, and clearance levels are comparable, inlet stages are no more efficient than stages operating in the repeating-stage environment.

For cases in which the thicknesses calculated from equation (50) are very small, their use in inviscid secondary flow calculations is of questionable value because the neglected viscous effects must strongly influence the secondary flow development. We have therefore adopted the following procedure. When an inlet boundary layer full thickness is less than $0.15\,a$, where a is the passage exit width, the value of k_1, which gives the boundary layer velocit defect, is decreased so as to keep the boundary layer vorticity at the value it would have if δ_1 were $0.15\,a$. With this procedure, secondary flow velocities approach zero as the inlet boundary layer thickness approaches zero. This procedure is also applied for shrouded blade end secondary flow but not for tip clearance secondary flow.

Acknowledgments

The authors wish to thank J. S. Keith and C. E. Whitfield for their consultations on parts of the paper and General Electric Company for permission to publish the paper.

Downloaded 01 Jun 2010 to 171.66.16.62. Redistribution subject to ASME license or copyright; see http://www.asme.org/terms/Terms_Use.cfm

S. C. Kacker
Staff Aerodynamicist.
Pratt & Whitney Aircraft of Canada Ltd.,

U. Okapuu
Chief, Turbine Aerodynamics.
Pratt & Whitney Aircraft of Canada Ltd.,
Longueuil, Quebec, Canada

A Mean Line Prediction Method for Axial Flow Turbine Efficiency

A mean line loss system is described, capable of predicting the design point efficiencies of current axial turbines of gas turbine engines. This loss system is a development of the Ainley/Mathieson technique of 1951. The prediction method is tested against the "Smith's chart" and against the known efficiencies of 33 turbines of recent design. It is shown to be able to predict the efficiencies of a wide range of axial turbines of conventional stage loadings to within ± 1½ percent.

Introduction

In choosing the gas path for a new turbine the designer has to carry out an optimization study which involves the calculation of velocity triangles. Blade lengths and radii are thereby determined early in the design cycle, before blade shapes are known. This is done by means of a "mean line" velocity triangle calculation, which is based on the assumption that the thermodynamic processes undergone by the working fluid can be represented by velocity triangles at midspan. To produce an optimum gas path such a calculation must incorporate a system of aerodynamic losses expressed as a function of blade row inlet and exit velocity triangles. Its excellence is ultimately judged by its ability to predict the aerodynamic efficiencies of known turbines of "competent" design.

Over the past 30 yr, a number of such turbine mean line loss systems have been described in the open literature, Traupel [1], Craig and Cox [2], and Stewart [3]. Perhaps the best known and most completely documented of these is that due to Ainley and Mathieson [4], published in 1951. Due to the improvement in our analytical capability and the accumulation of test results on a variety of turbines, it is fitting that such a loss system be critically reviewed and updated at least once every decade. It is a tribute to the durability of the Ainley/Mathieson system that it has become a foundation worthy of subsequent refinement, the most notable of which was published in 1970 by Dunham and Came [5]. Now, a decade later, may be an appropriate time to take a fresk look at the subject.

The present paper describes modifications to the Ainley/Mathieson/Dunham/Came (AMDC) loss system. These modifications are tested against experimental results where possible. The complete loss system is finally tested against design point efficiencies of 33 recent turbines.

Overall Description of Loss System

The loss of total pressure in a cascade of blades, expressed in terms of cascade exit dynamic pressure, is assumed to be the sum of profile, secondary, trailing edge and tip leakage losses, where the profile losses are corrected for Reynolds' number effects

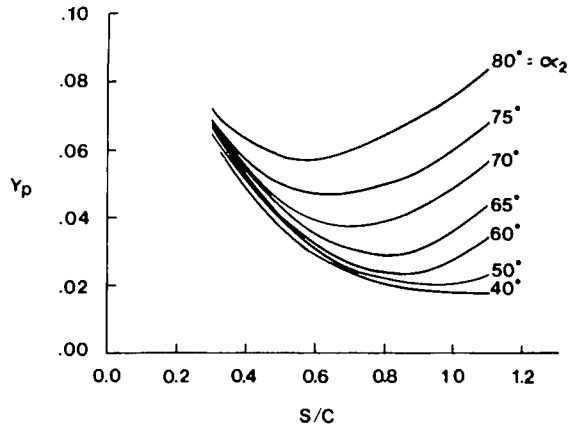


Fig. 1 Profile loss coefficient for $\beta_1 = 0$, $t_{MAX}/c = 0.2$ after Ainley and Mathieson [4]

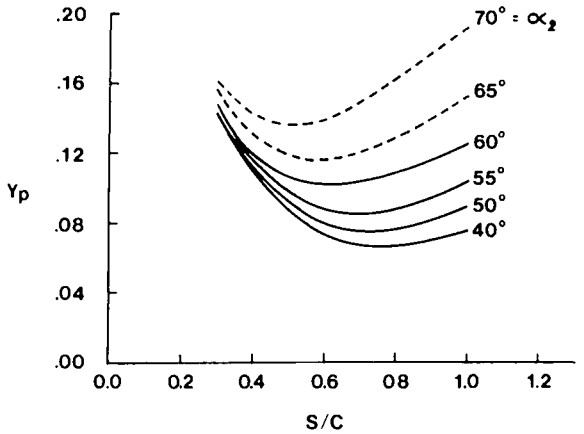


Fig. 2 Profile loss coefficient for $\beta_1 = \alpha_2$, $t_{MA}/c = 0.2$ after Ainley and Mathieson [4]

Contributed by the Gas Turbine Division and presented at the International Gas Turbine Conference and Products Show, Houston, Texas, March 9-12, 1981, of THE AMERICAN SOCIETY OF MECHANICAL ENGINEERS. Manuscript received at ASME Headquarters, December 9, 1980. Paper No. 81-GT-58.

Copyright © 1982 by ASME
Downloaded 01 Jun 2010 to 171.66.16.62. Redistribution subject to ASME license or copyright; see http://www.asme.org/terms/Terms_Use.cfm

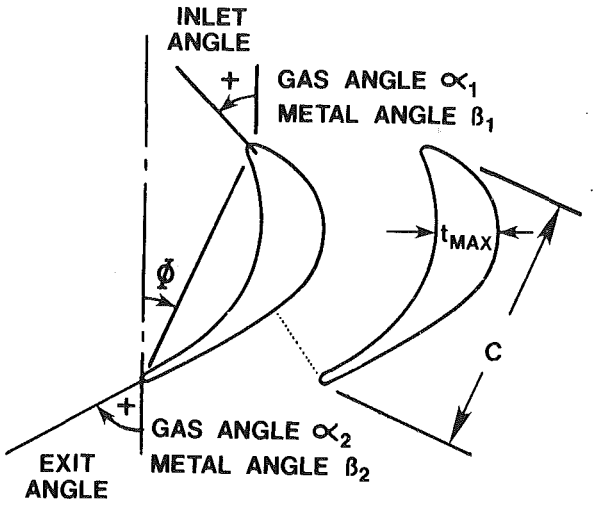


Fig. 3 Blade section terminology

$$Y_T = Y_P f_{(\mathrm{Re})} + Y_S + Y'_{TET} + Y_{TC} \quad (1)$$

This formulation is seen to differ from that of the AMDC system [4, 5], which is

$$Y_T = [(Y_P + Y_S)\mathrm{REFAC} + Y_{TC}]Y_{TET} \quad (2)$$

where Y_{TET} in Equ. (2) is a multiplier, not a loss coefficient.

In equation (1), blade Reynolds' number is taken to affect only the profile loss coefficient, and the trailing edge loss coefficient is separated from the other loss terms. This would appear a more logical arrangement, since it is difficult to justify a connection between trailing edge losses and tip clearance losses, for example.

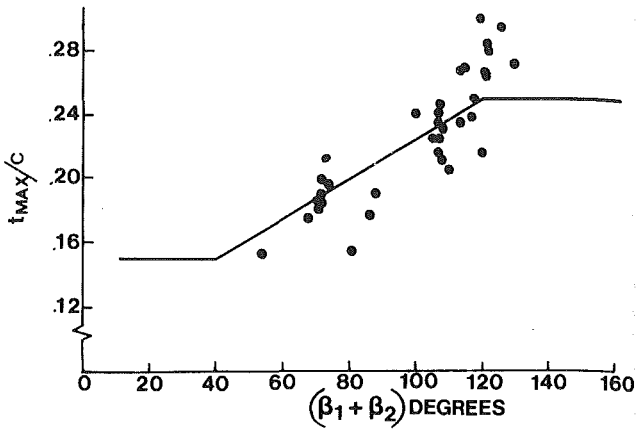


Fig. 4 Thickness/chord ratio for typical turbine blade sections

The Profile Loss Coefficient Y_P

The basis for the profile loss coefficient is a set of cascade test results incorporated in the AMDC loss system [4]. These results are expressed in terms of pitch/chord ratio and cascade exit gas angle α_2 for two special cases of $\beta_1 = 0$ (Fig. 1) and $\beta_1 = \alpha_2$ (Fig. 2). For any other combination of angles, these graphs are interpolated by means of the following equation:

$$Y_{P,\mathrm{AMDC}} = \left\{ Y_{P(\beta_1=0)} + \left| \frac{\beta_1}{\alpha_2} \right| \left(\frac{\beta_1}{\alpha_2} \right) \left[Y_{P(\beta_1=\alpha_2)} - Y_{P(\beta_1=0)} \right] \right\} \left(\frac{t_{\mathrm{MAX}}/c}{0.2} \right) \frac{\beta_1}{\alpha_2} \quad (3)$$

The foregoing equation is similar to the interpolation

Nomenclature

b_x = axial chord
C = true chord
C_L = airfoil lift coefficient
C_x = axial velocity component
CFM = supersonic drag rise multiplying factor to profile loss coefficient Y_P
$f_{(AR)}$ = aspect ratio function
$f_{(\mathrm{Re})}$ = Reynolds number correction factor
h = blade or vane height
ΔH = enthalpy drop
k = tip clearance
k' = equivalent tip clearance for shrouded blade
K_1, K_2, K_3, K_p, K_s = correction factors defined in text
M = Mach number
o = throat opening
P = total pressure
p = static pressure
q = dynamic head (P-p)
REFAC = Reynolds number correction factor for AMDC loss system
Rec = Reynolds number based on true chord and exit gas conditions
R = radius
s = pitch
U = blade velocity at mid height
t = trailing edge thickness (TET)
t_{MAX} = blade maximum thickness
Y = loss coefficient $\Delta P/q$ where q is (generally) taken at blade exit
Y_T = total loss coefficient for a blade row
Y_P = profile loss coefficient
Y_S = secondary loss coefficient
Y_{SHOCK} = component of profile loss coefficient due to leading edge shock
Y_{TET} = trailing edge loss multiplier, in AMDC loss system
Y'_{TET} = trailing edge loss coefficient
Y_{TC} = tip clearance loss coefficient
α = absolute/relative gas angles for vane/blade
α_m = mean gas angle defined in equation (13)
β = metal angle for vane or blade
γ = ratio of specific heats
$\Delta\phi^2_{\mathrm{TET}}$ = trailing edge K.E. loss coefficient
$\eta_{t\text{-}t}$ = turbine efficiency (total-to-total)
η_o = $\eta_{t\text{-}t}$ at zero tip clearance
Φ = stagger angle
ϕ^2 = kinetic energy coefficient = (actual gas exit velocity/ideal gas exit velocity)^2

Subscripts

H = hub
T = tip
1,2 = inlet and exit conditions
Sub = subsonic
AMDC = as per Ainley, Mathieson, Dunham and Came

Downloaded 01 Jun 2010 to 171.66.16.62. Redistribution subject to ASME license or copyright; see http://www.asme.org/terms/Terms_Use.cfm

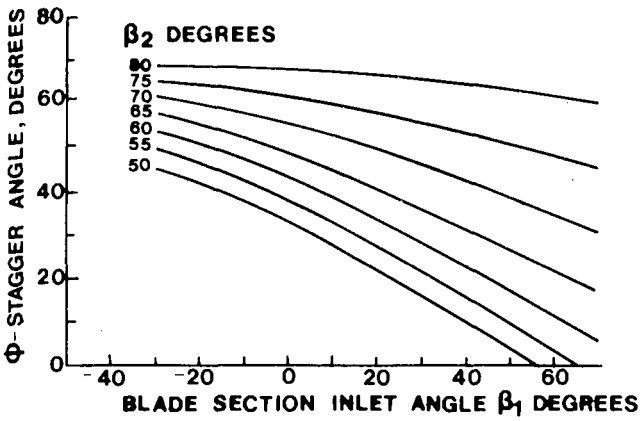


Fig. 5 Stagger angle for typical turbine blade sections

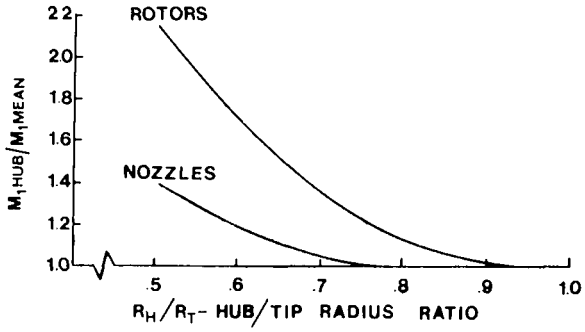


Fig. 6 Inlet Mach number ratio for nonfree-vortex turbine blades

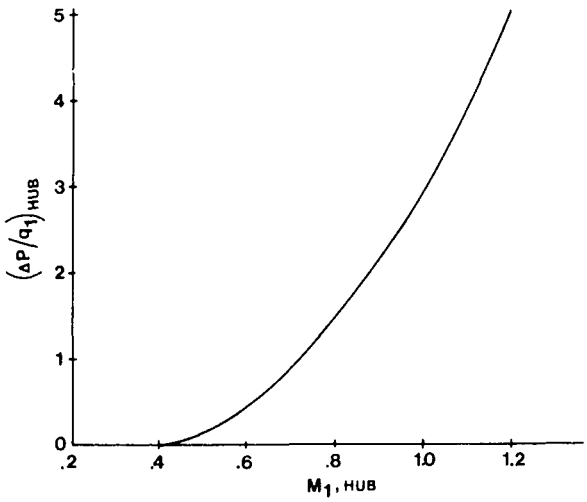


Fig. 7 Combined effect of leading edge shock on inner end wall flow and the blade channel next to it

equation given by the AMDC method except for the term $|\beta_1/\alpha_2|$, which was introduced to allow for negative inlet angle.

Figure 3 clarifies the terminology. Figure 4, a plot of thickness/chord ratios of a number of recent blade designs, proposes a general curve for this ratio, to be used when blade sections are not yet designed. Figure 5, similarly of statistical derivation, proposes values of stagger angle which can be used to estimate true chords, c, from axial chords which are generally established early in the design.

The cascade results of Figs. 1 and 2 are valid for vanes and blades having a trailing edge thickness to pitch ratio (t/s) of 0.02. In the AMDC loss system Y_p is multiplied by Y_{TET} to obtain the combined profile and trailing edge loss at any other t/s ratio. In the present loss system, since Y'_{TET} is a separate additive loss, Y_p from Figs. 1 and 2 is multiplied by 0.914, which is the value of Y_{TET} at $t/s = 0$ according to AMDC loss system, to obtain Y_p at zero trailing edge thickness.

The AMDC profile loss correlations, Figs. 1 and 2, were perfectly valid at the time of publication of the original AMDC loss system, and efficiencies of turbines of that era should be predictable by these data. However, advances in aerodynamic analysis, made over the last three decades, suggest that a factor of 2/3 should be applied to these loss coefficients for the efficiency prediction of present-day turbines.

The Subsonic Mach Number Correction. Cascade tests in the decades following the publication of the AMDC loss system have revealed that the profile loss coefficient Y_p is in general not independent of Mach number, even in the subsonic flow regime. Compressibility can affect Y_p in two ways, by causing shocks at blade leading edges and by affecting the flow acceleration within blade channels.

Shock Loss. Shocks at blade leading edges can set in at relatively low average inlet Mach number levels, due to the local flow acceleration adjacent to the highly curved leading edges. Evidence of the possible detrimental effects of this can be deduced from design rules of bygone days, which warn us about designing for relative inlet Mach numbers greater than approximately 0.6, and admonish us to design thinner leading edges when inlet Mach numbers are high.

Due to the radial variation in gas conditions, necessary for the flow to be in equilibrium, incident Mach numbers are always higher at the hub than at midspan. A sampling of known turbines resulted in the curve shown in Fig. 6, which estimates the incident Mach number at the hub of nonfree-vortex turbine blades when midspan Mach number and hub/tip radius ratio are known. The "shock loss" next to the inner endwall of a blade can then be found from Fig. 7, which states

$$\left(\frac{\Delta P}{q_1}\right)_{\text{HUB}} = 0.75(M_{1,\text{HUB}} - 0.4)^{1.75} \tag{4}$$

However, since this loss is only local, it would be unfair to penalize the whole blade by this amount: a long blade would be less affected, overall, by a loss here than would a short blade. Therefore, the contribution to the mean line loss of blade inlet shock losses is taken to be

$$\left(\frac{\Delta P}{q_1}\right)_{\text{SHOCK}} = \left(\frac{R_H}{R_T}\right)\left(\frac{\Delta P}{q_1}\right)_{\text{HUB}} \tag{5}$$

Finally, the subsonic shock loss coefficient, until now expressed in terms of blade inlet mean line dynamic head, can be expressed in terms of blade exit dynamic head by

$$\left(\frac{\Delta P}{q_2}\right)_{\text{SHOCK}} \equiv Y_{\text{SHOCK}} = \left(\frac{\Delta P}{q_1}\right)_{\text{SHOCK}} \left(\frac{p_1}{p_2}\right) \frac{1-\left(1+\frac{\gamma-1}{2}M_1^2\right)^{\frac{\gamma}{\gamma-1}}}{1-\left(1+\frac{\gamma-1}{2}M_2^2\right)^{\frac{\gamma}{\gamma-1}}} \tag{6}$$

Channel Flow Acceleration. Flow in the passage formed by two adjacent blades will undergo a larger velocity change when operated at a higher (subsonic) Mach number level. This is a consequence of the compressibility of the working

Downloaded 01 Jun 2010 to 171.66.16.62. Redistribution subject to ASME license or copyright; see http://www.asme.org/terms/Terms_Use.cfm

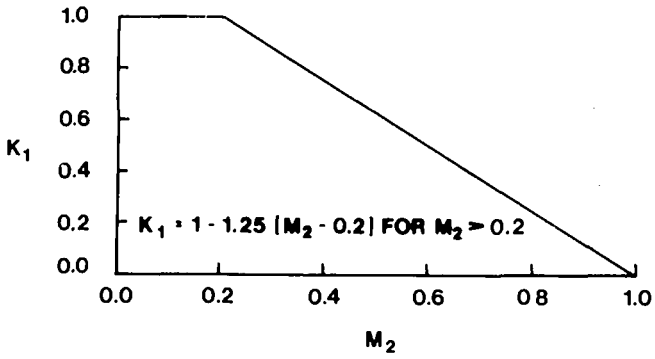


Fig. 8 Mach number correction factor K_1 for the profile loss coefficient, for accelerating cascades of $M_1 - M_2$

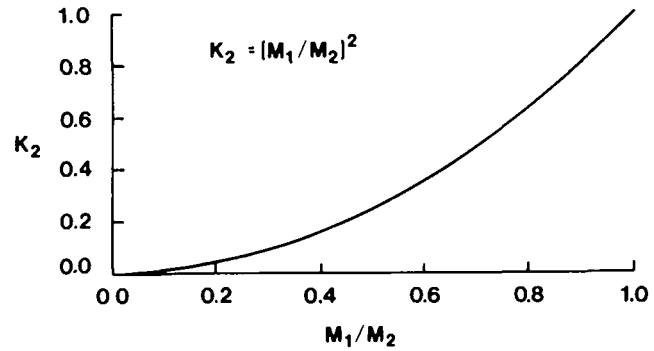


Fig. 9 Mach number correction factor K_2 for the profile loss coefficient

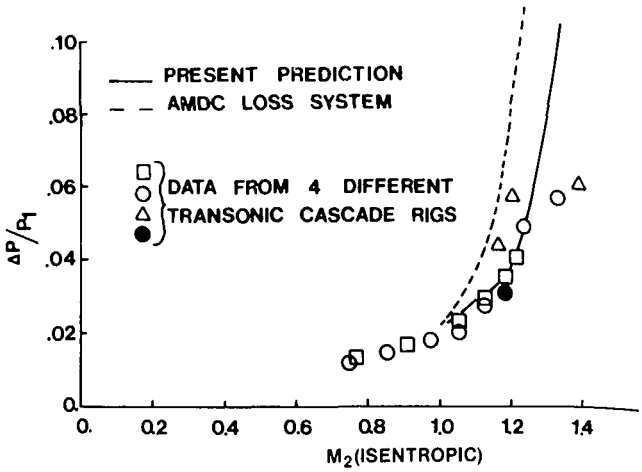


Fig. 10 Comparison of transonic cascade test results with prediction, blade profile 23

medium. In an accelerating flow passage, therefore, operation closer to sonic exit velocities will tend to cause suppression of local separations and the thinning of boundary layers. This effect is most pronounced where inlet Mach numbers are only slightly lower than exit Mach numbers.

Profile loss coefficients shown in Figs. 1 and 2 are derived from cascade tests carried out at low subsonic velocities and are therefore pessimistic when applied to turbines operating at higher Mach number levels. Figures 8 and 9 correct for the effects of exit Mach number and channel acceleration, respectively. The combined effect of these corrections is

$$K_P = 1 - K_2(1 - K_1) \tag{7}$$

In the subsonic regime of operation of a cascade of blades, therefore, the profile loss coefficient Y_P becomes:

$$Y_P = 0.914\left(\frac{2}{3} Y_{P,\mathrm{AMDC}} K_P + Y_{\mathrm{SHOCK}}\right) \tag{8}$$

As discussed in the forthcoming section, "Verification of Loss System," these compressibility corrections were necessary to make the AMDC loss system predict the correct shapes of the efficiency islands on "Smith's chart."

Supersonic Drag Rise. In the regime of supersonic exit velocities additional pressure losses occur as a result of shocks originating in the trailing edge wake. Due to the lack of cascade test results of adequate quality, a reliable loss model is not yet available.

The AMDC loss system assumes a supersonic drag rise according to

$$\mathrm{CFM} = 1 + 60(M_2 - 1)^2 \tag{9}$$

where CFM is applied as a multiplier to Y_P, when the exit Mach number exceeds unity. This factor is taken to be independent of blade (metal) exit angle. This assumption appears to be the major shortcoming of this correction in that it ignores limit loading of airfoils.

Limit load is the condition at which a given cascade of airfoils operating at a constant inlet pressure develops maximum tangential force. When blade trailing edges are more tangential, this condition occurs at a higher Mach number, and therefore different cascades will have different limit load exit Mach numbers. Limit load Mach number can be estimated from blade geometry [6,7], but it can also be predicted from supersonic drag rise, if that is known [8]. Alternatively, the supersonic drag rise may be deduced from known limit load Mach number calculated from blade geometry. Work on this approach is currently in progress. Early results look promising as shown in Fig. 10. This regime is as yet primarily of interest for efficiency prediction at off-design operating conditions, however. Design point exit Mach numbers of turbines in current gas turbine engines rarely assume magnitudes where supersonic drag rise plays a significant part in the loss system.

Reynolds' Number Correction. It is assumed that the profile loss coefficient Y_P is calculated at a reference Reynolds' number of 2×10^5, based on true chord, and cascade exit gas conditions. At any other Reynolds' number, the correction $f_{(\mathrm{Re})}$ in equation (1) is

$$\left.\begin{aligned} f_{(\mathrm{Re})} &= \left(\frac{\mathrm{Rec}}{2\times 10^5}\right)^{-0.4} \quad \text{for } \mathrm{Rec} \le 2\times 10^5 \\ &= 1.0 \quad \text{for } 2\times 10^5 < \mathrm{Rec} < 10^6 \\ &= \left(\frac{\mathrm{Rec}}{10^6}\right)^{-0.2} \quad \text{for } \mathrm{Rec} > 10^6 \end{aligned}\right\} \tag{10}$$

This formulation is similar but not identical to Denton's [9]. It is applied to the profile loss coefficient only as there is little evidence in the literature that other loss terms are affected. The Reynolds' number independence in the 2×10^5 to 10^6 range is an approximation to the complex loss coefficient variation in the transitional regime. The true variation of loss coefficient with Reynolds' number cannot be estimated without a detailed knowledge of blade shapes.

The Secondary Loss Coefficient Y_S

The secondary loss coefficient calculation is the same as given by Dunham and Came [5], except for its dependence on blade aspect ratio. In [5] it is assumed that Y_S varies as the

Downloaded 01 Jun 2010 to 171.66.16.62. Redistribution subject to ASME license or copyright; see http://www.asme.org/terms/Terms_Use.cfm

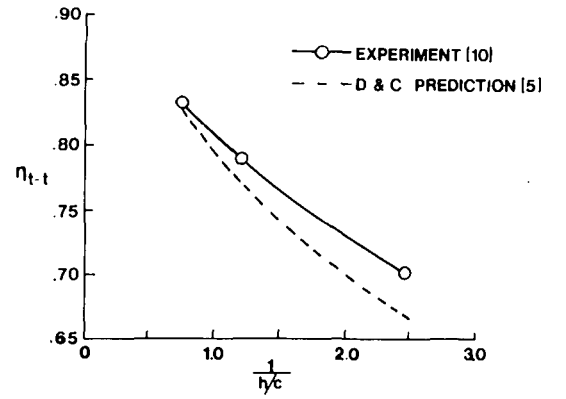


Fig. 11 Comparison of the effect of blade aspect ratio as predicted by the Dunham and Came method [5] with the test results of Rogo [10]

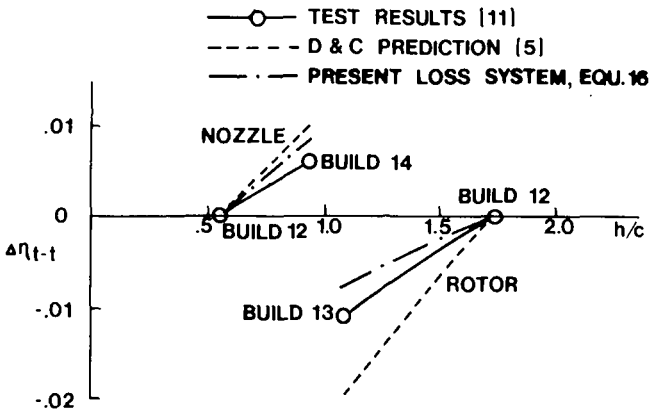


Fig. 12 Comparison of the effect of blade aspect ratio as predicted by Dunham and Came [5] and the present method, with the test results of Okapuu [11]

reciprocal of blade aspect ratio, over the complete range of aspect ratios. Its authors noted that their method predicted a more rapid increase in losses, as aspect ratio was reduced, than shown by the experimental data of Rogo [10], Fig. 11. The same trend has been confirmed by the data of Okapuu [11]. In the present loss system this rise in Y_S (with a reduction in aspect ratio) is less rapid for aspect ratios less than two. The following equations are employed:

$$Y_{S,\mathrm{AMDC}} = 0.0334 f_{(AR)} \left(\frac{\cos\alpha_2}{\cos\beta_1}\right) \left(\frac{C_L}{s/c}\right)^2 \frac{\cos^2\alpha_2}{\cos^3\alpha_m} \tag{11}$$

where

$$\frac{C_L}{s/c} = 2(\tan\alpha_1 + \tan\alpha_2)\cos\alpha_m \tag{12}$$

$$\alpha_m = \tan^{-1}\left[\frac{1}{2}(\tan\alpha_1 - \tan\alpha_2)\right] \tag{13}$$

$$\left.\begin{aligned} f_{(AR)} &= \frac{1 - 0.25\sqrt{2 - h/c}}{h/c} \quad \text{for } h/c \le 2 \\ &= \frac{1}{h/c} \quad \text{for } h/c > 2 \end{aligned}\right\} \tag{14}$$

Figure 12 shows the effect of aspect ratio on predicted turbine efficiency. The modification introduced here is seen to provide a better prediction of test results.

In the AMDC loss system, Y_S given by equation (11) is multipled by Y_{TET}. However, in the present loss system the secondary losses and the trailing edge losses are not linked. Therefore, it is required that Y_S, as given by equation (11), should be suitably modified before it can be used in the present loss system. This is done by multiplying Y_S (equation (11)) by a factor of 1.2. An initial estimate for the multiplying factor was based on the assumption that Dunham and Came [5] developed their loss system for turbines having a typical value of $t/o \simeq .1$ and an airfoil gas exit angle of 60 deg. This implied that their turbines had $t/s \simeq .05$. In the AMDC loss system, for $t/s \simeq 0.05$, the value of Y_{TET} is not much different from 1.2. The value of the multiplying factor was further confirmed by optimisation of the present loss system performance (to be discussed later).

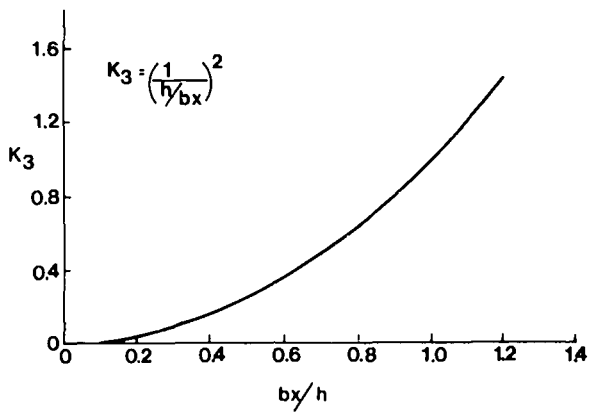


Fig. 13 Mach number correction factor K_3 for the secondary loss coefficient

The Subsonic Mach number Correction. As with profile losses, compressibility also has an effect on the acceleration of flow next to endwalls, and hence endwall losses. To account for this the subsonic Mach number correction factor for secondary losses is defined in terms of the factor for profile loss and aspect ratio as

$$K_s = 1 - K_3(1 - K_P) \tag{15}$$

where K_3 is defined in Fig. 13 and K_p as defined in equation (7). Leading edge shocks at high subsonic incident Mach numbers are also likely to have some effect on secondary losses. These effects are here assumed to be included in the term Y_{SHOCK}, equation (6), and not separately accounted for here. In the supersonic exit regime no additional Mach number correction is applied to Y_S, which is kept fixed at its value corresponding to exit Mach number of unity. Therefore:

$$Y_s = 1.2\, Y_{S,\mathrm{AMDC}} K_s \tag{16}$$

The Trailing Edge Loss Coefficient Y'_{TET}

The physically most meaningful expression of pressure losses due to trailing edge blockage is in terms of trailing edge blockage itself, i.e., in terms of the trailing edge thickness/throat opening ratio of a cascade.

An extensive survey of published and in-house cascade results produced the relationship shown in Fig. 14. Trailing edge losses are here expressed in terms of an energy coefficient $\Delta\phi^2_{TET}$. Two distinct curves exist for axial entry nozzles and impulse blades. The difference lies in the thicknesses of profile boundary layers at the trailing edges of blades: impulse blades, with their thick boundary layers have lower (less negative) base pressure coefficients and thus have lower trailing edge losses, while the trailing edge thickness contributes significantly to the drag of highly accelerating cascades. For blades other than the two basic types shown,

Downloaded 01 Jun 2010 to 171.66.16.62. Redistribution subject to ASME license or copyright; see http://www.asme.org/terms/Terms_Use.cfm

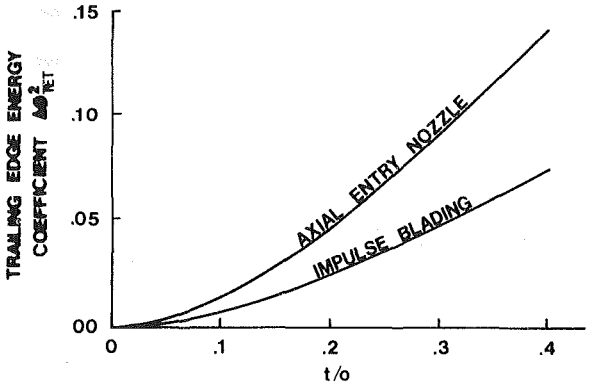


Fig. 14 Trailing edge loss [energy] coefficient correlated against the ratio of trailing edge thickness to throat opening

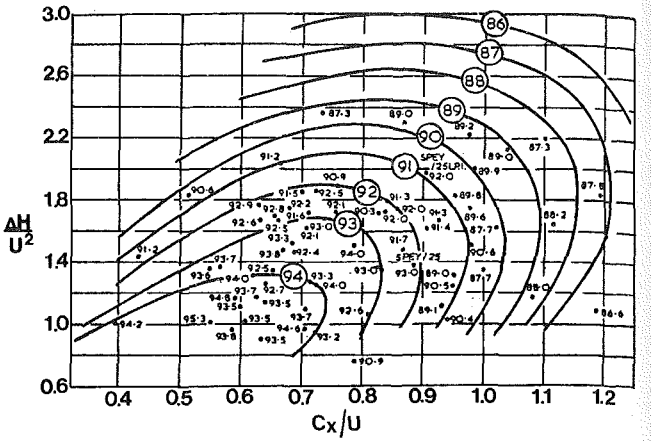


Fig. 15 Turbine stage efficiency at zero tip leakage, after Smith [12]

trailing edge losses are interpolated in a manner similar to equation (3), i.e.,

$$\Delta\phi^2_{TET} = \Delta\phi^2_{TET\,(\beta_1=0)} + \left|\frac{\beta_1}{\alpha_2}\right| \left|\left(\frac{\beta_1}{\alpha_2}\right)\left[\Delta\phi^2_{TET\,(\beta_1=\alpha_2)} - \Delta\phi^2_{\mathrm{TET}(\beta_1=0)}\right]\right| \quad (17)$$

The conversion from kinetic energy loss coefficient to the pressure loss coefficient is given by

$$Y'_{TET} = \frac{\left[1-\frac{\gamma-1}{2}M_2^2\left(\frac{1}{1-\Delta\phi^2_{TET}}-1\right)\right]^{-\frac{\gamma}{\gamma-1}}-1}{1-\left(1+\frac{\gamma-1}{2}M_2^2\right)^{-\frac{\gamma}{\gamma-1}}} \quad (18)$$

The variation of Y'_{TET} with Mach number is not well documented at present. For supersonic exit velocities the supersonic drag rise, as discussed under profile losses, is assumed to include trailing edge losses.

The Tip Clearance Loss Coefficient Y_{TC}

Overtip leakage losses on unshrouded rotor blades constitute a major source of turbine inefficiency. A large body of experimental data exists on this subject, relating changes in turbine efficiency to changes in rotor tip clearance. Most of the available results correlated within ± 15 percent with the following expression:

$$\frac{\frac{\Delta\eta}{\eta_o}}{\frac{\Delta k}{h\,\cos\alpha_2}\times\frac{R_{\mathrm{TIP}}}{R_{\mathrm{MEAN}}}} = 0.93 \quad (19)$$

When the loss system is structured as equation (1) $\Delta\eta$ has to be converted to an equivalent loss coefficient Y_{TC}. This may be done iteratively (by first calculating turbine efficiency with zero tip clearance, assessing the efficiency penalty due to clearance and increasing the rotor loss coefficient until the process converges on efficiency, all the while recalculating the velocity triangles and other loss coefficients) or directly, by making certain simplifying assumptions. The exact process is beyond the scope of this paper.

In the case of shrouded turbine blades the loss system incorporates the relationship proposed in [5], i.e.

$$Y_{TC} = 0.37\frac{c}{h}\left(\frac{k'}{c}\right)^{0.78}\left(\frac{C_L}{s/c}\right)^2\frac{\cos^2\alpha_2}{\cos^3\alpha_m} \quad (20)$$

where

$$k' = \frac{k}{(\text{number of seals})^{0.42}} \quad (21)$$

The reason for deviating from the AMDC loss system in the case of unshrouded blades was that tip leakage losses were found to be overpredicted by that system on recent turbines.

Verification of Loss System

The loss system outlined in the foregoing evolved to its final formulation largely thanks to a 1965 paper by Smith [12], which proposes a correlation of turbine efficiency on a "loading diagram" having stage loading factor $\Delta H/U^2$ as one axis and stage flow factor Cx/U as the other (Fig.15). Design point efficiencies (corrected to zero tip clearance) of some 69 turbines, plotted on this diagram, strongly suggest concentric locii of constant efficiency. This correlation is so convincing that it must be accepted as one of the tests which any mean line loss system must satisfy.

These 69 turbines were, clearly, all designed before 1965. In addition they all share certain common design features described in [12], features which are a reflection of the consistent design philosophy in the organization whence they originated. Considering the probable sizes of these turbines, the state of the (design) art at the time and the manner of testing, one arrives at the conclusion that the efficiency contours shown in Fig. 15 are caused mainly by profile losses and somewhat more weakly (due to the prevailing moderate to large aspect ratios) by secondary losses. Therefore, if a candidate loss system fails to duplicate the Smith's chart, the fault is likely to lie with its profile and/or secondary loss components.

To test these loss system components, the equivalent of 103 turbine stages were designed, using design rules and mechanical limitations current in the 1950's. As a guide, multistage turbine gas paths and approximate cycle design points of three engines of this period were used as a framework for these stages. The design point efficiency of each was then calculated by a candidate loss system and a plot similar to the Smith's chart was constructed.

The Ainley/Mathieson loss system, while predicting quite well the variation of efficiency with $\Delta H/U^2$, failed to adequately predict its variation with Cx/U at Cx/U values in excess of 0.6. In this respect our results were quite similar to those of Amann and Sheridan [13]. After examining various alternatives we were forced to conclude that only the compressibility and shock loss corrections to profile and secondary loss coefficiencts, described in the foregoing, can produce an adequate simulation of Smith's chart. It was found that the shock loss correction (Y_{SHOCK}) mainly affected the high Cx/U regime of the chart, while the acceleration correction (K_p) affected the general level of the efficiency contours. Figures 6, 7, 8, 9 and 13 were evolved by trial and error until a simulation of Smith's curves was obtained. The

Downloaded 01 Jun 2010 to 171.66.16.62. Redistribution subject to ASME license or copyright; see http://www.asme.org/terms/Terms_Use.cfm

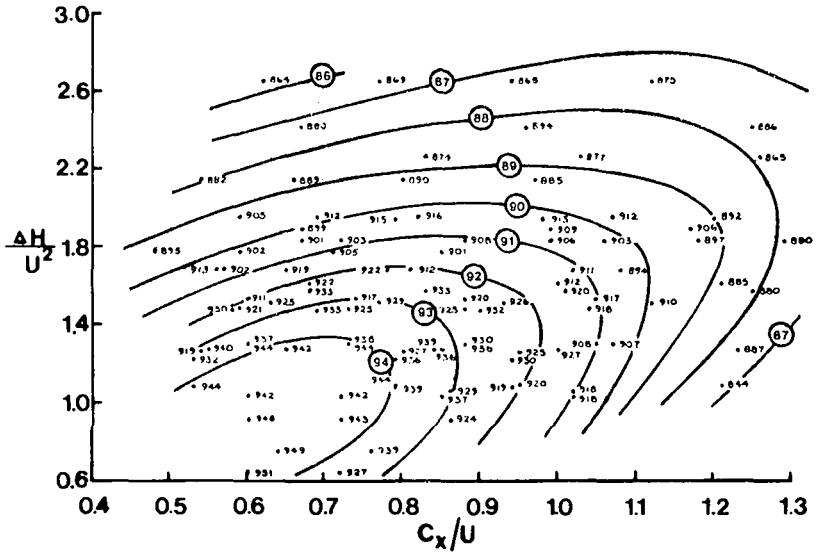


Fig. 16 Turbine stage efficiency at zero tip leakage calculated by the present method

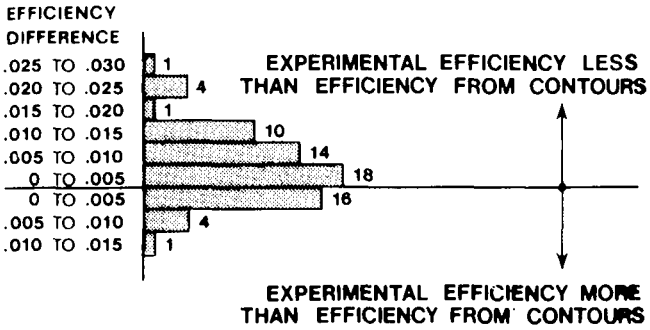


Fig. 17 Histogram for experimental data used to define contours in Fig. 15, after Amann and Sheridan [13]

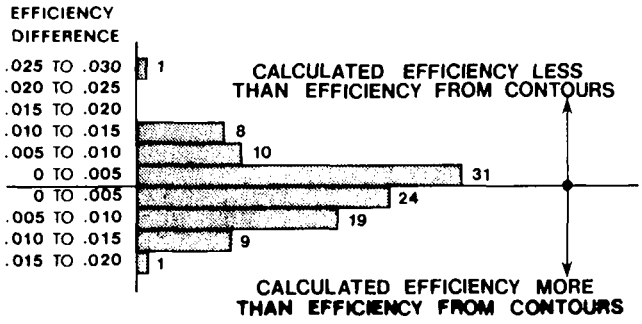


Fig. 18 Histogram for calculated data used to define contours in Fig. 16

result is shown in Fig. 16. Calculations were carried out with the whole AMDC value of Y_P (rather than 2/3) in equation (8) to simulate the state of blade design art of the time.

A qualitative comparison of Figs. 15 and 16 indicates that a satisfactory duplication of the shapes of efficiency contours has been achieved. At low values of $\Delta H/U^2$ there is unquestionably an initial increase in efficiency with $\Delta H/U^2$, at constant Cx/U. The lack of this feature has been the major shortcoming of the AMDC loss system as demonstrated in Fig. 9 of [13].

Quantitatively, Fig. 16 differs from Fig. 15 in that a given efficiency curve of Fig. 16 attains a lower peak $\Delta H/U^2$ value but extends to a higher peak Cx/U value. At 90 percent efficiency, for example, the maximum discrepancy amounts to 1½ efficiency points in each regime, while at 94 percent the discrepancy is ½ efficiency point. This is partly explained by an examination of the data from which efficiency contours were derived. Figure 17 describes the differences between data points and contours of Fig. 15, as reported in [13]. It is clear that a considerable uncertainty exists in the positioning of efficiency contours. It is also evident that a bias exists in the contours, which are predicting efficiencies approximately ½ point higher than supported by data points. This would tend to reduce the discrepancy between Figs. 15 and 16, at peak $\Delta H/U^2$. As to the region of peak Cx/U, Fig. 15 has too few data points at $Cx/U > 1.0$ to substantiate the curves drawn. Unpublished test data from other sources suggest that these curves may in fact extend to higher Cx/U, as in Fig. 16. These speculations aside, the quantitative agreement may nevertheless be considered satisfactory in the light of the inevitable data scatter inherent in both figures. Figure 18 shows the corresponding differences between data points and contours of Fig. 16, for completeness.

The second test of a loss system is the demonstration of its ability to predict the design point efficiencies of existing turbines of more recent vintage. Design point data were collected for 33 turbines ranging from the gas generator turbine of a small automobile engine to the low pressure turbine of a 45,000-lb thrust turbofan. In view of the advances made in blade profile design over the last 25 yr, the loss system was operated with only 2/3 of the AMDC profile loss coefficient. Since none of these turbines had bladerow exit Mach numbers in excess of 1.17 the supersonic drag rise correction (by the present prediction, Fig. 10) had only a small effect on the efficiencies of transonic stages. Figure 19 shows the comparison. The closed symbols describe P&WA turbines. The open symbols describe turbines from other sources. Table 1 lists the more important design parameters of these turbines.

The agreement is generally very good, the majority of predictions falling within an error band of 1½ efficiency points. Of the few turbines which fall significantly outside this error band two can readily be shown to be "incompetent" designs, and the experimental techniques used in the case of two more are open to criticism.

Figure 20 shows an identical comparison of the same 33

Downloaded 01 Jun 2010 to 171.66.16.62. Redistribution subject to ASME license or copyright; see http://www.asme.org/terms/Terms_Use.cfm

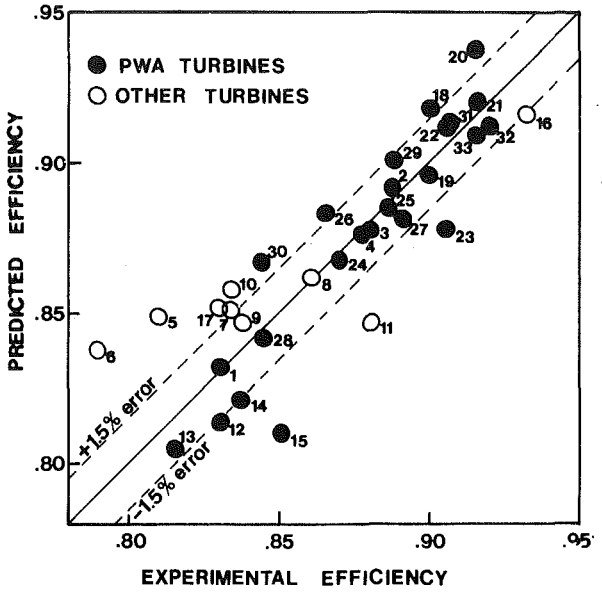


Fig. 19 Comparison of predicted efficency with experimental efficiency of 33 turbines (new loss system)

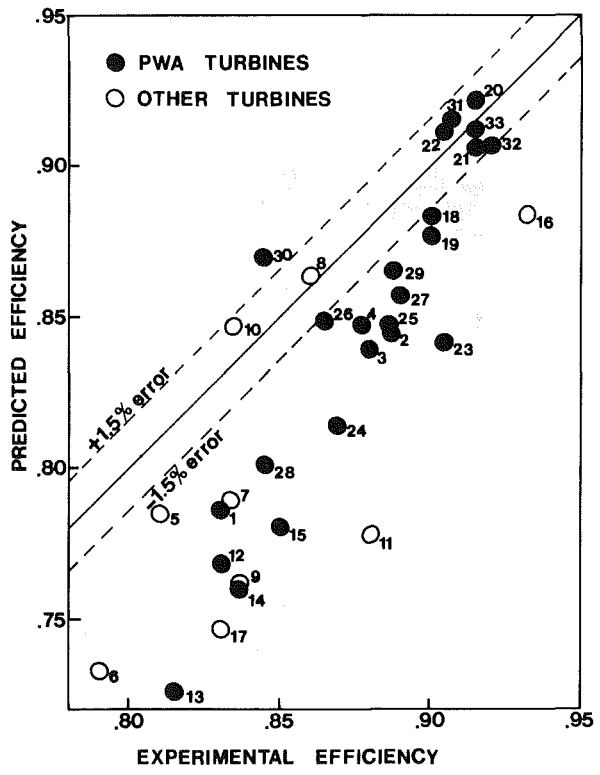


Fig. 20 Comparison of predicted efficency with experimental efficency of 33 turbines (AMDC loss system)

turbines carried out with the AMDC loss system. The agreement is not satisfactory.

The design point efficiencies under discussion here are those obtainable on rotating aerodynamic rigs. In the engine environment these turbines will generally show a lower efficiency for a variety of reasons such as effects of secondary air injection, leakages, nonuniformities in the turbine inlet flow, etc. These features are not accounted for the in the loss system described in the foregoing. Also not accounted for are the inevitable future advances in the art of turbine design:

NO.	SOURCE	# STAGES	STAGE	$\Delta H/U^2$	Cx/U	PRESS. RATIO	$\overline{h/c}$ NOZZLE	$\overline{h/c}$ ROTOR
1	P&WA	1	1	1.88	.54	2.67	.366	1.75
2	P&WA	1	1	1.51	.533	4.00	.612	1.98
3	P&WA	1	1	1.45	.565	3.89	.571	1.72
4	P&WA	1	1	1.55	.570	2.95	.437	2.188
5	OTHER	1	1	1.25	.613	2.98	.520	.671
6	OTHER	1	1	1.55	.675	2.90	.55	.825
7	OTHER	1	1	1.59	.642	2.90	.725	1.26
8	OTHER	1	1	1.11	.383	1.48	1.50	1.50
9	OTHER	1	1	1.656	.595	2.77	1.0	1.0
10	OTHER	2	1	.989	.309	1.11	1.44	1.456
			2	.987	.318	1.11	1.32	1.489
11	OTHER	1	1	1.672	.696	1.82	.71	1.01
12	P&WA	1	1	1.19	.397	2.00	.317	.739
13	P&WA	1	1	1.19	.531	2.00	.247	.777
14	P&WA	1	1	1.19	.497	2.00	.253	.670
15	P&WA	1	1	1.139	.322	3.40	.24	.486
16	OTHER	2	1	1.65	.690	1.71	1.47	1.87
			2	1.65	.813	1.87	1.54	2.16
17	OTHER	1	1	2.00	.721	1.99	.468	.847
18	P&WA	1	1	1.44	.566	2.76	.637	1.9
19	P&WA	2	1	1.50	.924	1.45	1.27	2.09
			2	1.77	.990	1.65	1.95	2.47
20	P&WA	2	1	.9	.622	1.44	1.102	2.23
			2	.83	.502	1.53	1.81	3.02
21	P&WA	2	2	1.28	.758	1.70	1.102	2.23
			1	1.02	.698	1.73	1.81	3.02
22	P&WA	1	1	1.94	.529	2.24	1.23	2.67
23	P&WA	1	1	2.388	.712	2.68	1.23	2.67
24	P&WA	1	1	1.45	.565	3.89	.571	1.08
25	P&WA	1	1	1.45	.561	3.89	.984	1.72
26	P&WA	1	1	1.516	.583	2.81	.421	1.95
27	P&WA	1	1	1.463	.492	3.23	.527	2.155
28	P&WA	1	1	1.38	.485	1.99	.710	.921
29	P&WA	1	1	1.58	.545	1.94	1.328	1.111
30	P&WA	4	1	2.44	1.50	1.33	2.61	3.94
31	"		2	2.32	1.28	1.35	4.07	4.98
32	"		3	2.38	1.25	1.45	5.01	5.76
33	"		4	2.71	1.50	1.68	5.68	5.80

novel techniques to minimize overtip leakage losses and fully three-dimensional flow analysis methods are already showing promise of a bright future.

A mean line efficiency prediction method is the sum of a large number of loss components. While some of them may prove to be quantitatively imperfect, the manner in which they are combined may cause errors to cancel. The final proof of a loss system must be its ability to correctly predict the efficiencies of well documented turbines.

Conclusion

Regardless of the degree of sophistication of analytical tools available for the detail design of turbine blading, a mean line design technique will always be needed for the optimization of the turbine gas path and the prediction of attainable turbine efficiency of a new engine.

The mean line loss system described, a development of the Ainley/Mathieson/Dunham/Came system, appears to be capable of predicting design point efficiencies of current turbines of conventional stage loadings and "competent" design to within ± 1½ efficiency points. A major departure from AMDC is the restructuring of the loss system and the introduction of compressibility effects and shock losses into the calculation of profile and secondary loss coefficients.

Acknowledgments

The work reported herein has been partially funded by the

Downloaded 01 Jun 2010 to 171.66.16.62. Redistribution subject to ASME license or copyright; see http://www.asme.org/terms/Terms_Use.cfm

Research and Development Centre of Transport Canada, Contract No. 107380 under the program management of W. H. D. Hanchet. Technical contributions by V. Ozarapoglu, K. K. Lam and M. Mueller are hereby also acknowledged.

References

1 Traupel, W., "Thermische Turbomaschinen," Springer-Verlag, Berlin, 1966.

2 Craig, H.R.M., and Cox, H.J.A., "Performance Estimate of Axial Flow Turbines," *Proceedings of the Institution of Mechanical Engineers*, Vol. 185, No. 32, 1971, pp. 407-424.

3 Stewart, W.L., "A Study of Axial Flow Turbine Efficiency Characteristics in Terms of Velocity Diagram Parameters," ASME Paper No. 61-WA-37, 1961.

4 Ainley, D.G., and Mathieson, G.C.R., "A Method of Performance Estimation for Axial Flow Turbines," British ARC, R&M 2974, 1951.

5 Dunham, J., and Came, P.M., "Improvements to the Ainley/Mathieson Method of Turbine Performance Prediction," ASME JOURNAL OF ENGINEERING FOR POWER, July 1970, pp. 252-256.

6 Hauser, C., and Plohr, H.W., "Two-Dimensional Cascade Investigation of the Maximum Exit Tangential Velocity Component and Other Flow Conditions at the Exit of Several Turbine Blade Designs at Supercritical Pressure Ratios," NACA RME51F12, Aug. 1951.

7 Fruchtman, I., "The Limit Load of Transonic Turbine Blading," ASME Paper No. 74-GT-80, Apr. 1974.

8 Okapuu, U., "Limit Load and Supersonic Drag Rise of Transonic Turbine Cascades," Pratt & Whitney Aircraft of Canada, Internal Memo, July 1974.

9 Denton, J.D., "A Survey and Comparison of Methods for Predicting the Profile Loss of Turbine Blades," Institute of Mechanical Engineers Conference Publication 3, Paper C76/73, 1973, pp. 204-212.

10 Rogo, C., "Experimental Aspect Ratio and Tip Clearance Investigation on Small Turbines," SAE Paper 680448, Mid Year Meeting Detroit, Mich., May 20-24, 1968.

11 Okapuu, U., "Some Results from Tests on a High Work Axial Gas Generator Turbine," ASME Paper No. 74-GT-81, Apr. 1974.

12 Smith, S.F., "A Simple Correlation of Turbine Efficiency," *Journal of Royal Aeronautical Society*, Vol. 69, July 1965, pp. 467-470.

13 Amann, C.A., and Sheridan, D.C., "A Comparison of Some Analytical and Experimental Correlations of Axial Flow Turbine Efficiency," ASME Paper No. 67-WA/GT-6, Nov. 1967.

Downloaded 01 Jun 2010 to 171.66.16.62. Redistribution subject to ASME license or copyright; see http://www.asme.org/terms/Terms_Use.cfm

W.D. Clark

B.A. Folsom

W.R. Seeker

C.W. Courtney

Energy and Environmental Research Corporation, Santa Ana, Calif. 92705

Bench Scale Testing of Low-NO_x LBG Combustors

The high efficiencies obtained in a combined gas-turbine/steam-turbine power cycle burning low Btu gas (LBG) make it a potentially attractive alternative to the high sulfur emitting direct coal-fired steam cycle. In the gasification process, much of the bound nitrogen in coal is converted to ammonia in the LBG. This ammonia is largely converted to nitrogen oxides (NO_x) in conventional combustors. This paper examines the pressurized bench scale performance of reactors previously demonstrated to produce low NO_x emissions in atmospheric laboratory scale experiments. LBG was synthesized in a catalytic reformer and fired in three reactors: a catalytic reactor, a diffusion flame, and a stirred reactor. Effects of scale, pressure, stoichiometry, residence time, and preheat were examined. Lowest NO_x emissions were produced in a rich/lean series staged catalytic reactor.

Introduction

The limited availability and the increasing cost of petroleum-based fuels have generated an increased interest in coal as a primary power source. The potential for low sulfur emissions makes combustion of gasified coal an environmentally attractive alternative to direct-fired coal combustion. High efficiencies can be obtained burning low Btu coal gas in a gas-turbine/steam-turbine combined cycle. However, LBG can contain ammonia concentrations as high as 0.38 percent [1]. In a conventional combustor, much of this ammonia may be converted to nitrogen oxide resulting in significant pollutant emission: up to 1370 ng/J (3.2 lbm/10^6 Btu) for full conversion of NH_3 to NO_2.

The current New Source Performance Standard (NSPS) for steam generators firing coal-derived gaseous fuels with greater than 73.3 MW (250 × 10^6 Btu/hr) heat input is 210 ng/J (0.5 lbm $NO_2/10^6$ Btu) [2]. For a combined cycle firing LBG with 3800 ppm NH_3 to meet this standard, conversion of NH_3 to NO would have to be less than 15.7 percent. With the anticipated decline in ambient air quality and the advent of new gas-cleaning technology, it is reasonable to expect that future NSPS will be more stringent; therefore, in the development of energy-efficient LBG combustion systems it is important to achieve the lowest NO_x emissions possible.

Equilibrium and kinetic calculations have been carried out to predict trends in fuel nitrogen processing in idealized LBG combustion. Testing of these predicted trends in laboratory scale experiments at atmospheric pressure has resulted in the development of several low NO_x combustor concepts [3]. This paper describes experiments performed on scaled-up LBG combustors, utilizing these low-NO_x concepts, operated at pressures more nearly approximating gas turbine combustors. Sections are included to discuss background, experimental systems, results, and conclusions.

Background

Previous work performed under this program has included investigation of the properties of LBG, thermodynamic optimization of combined-cycle performance, kinetic optimization of fuel nitrogen reduction in conceptual low-NO_x combustors, and experimental examination of the practical effects of fuel/air contacting on fuel nitrogen processing in laboratory scale reactors.

Low Btu Gas. Coal-derived low Btu gas comprises a family of fuels of varying composition, ranging in heating value from 3.0 × 10^6 to 7.5 × 10^6 J/m^3 (80 to 200 Btu/ft^3), produced by reforming coal with air and steam. Its principle components are C0, H_2, and light hydrocarbons (HC) as combustibles; and N_2, H_20, and $C0_2$ as inerts. Significant amounts of ammonia, sulfur compounds, and particulate matter may also be present. These impurities may be partially removed in several alternative gas cleaning systems prior to combustion [4]. The most energy-efficient cleanup systems operate hot, removing a majority of sulfur products and particulates; but it is difficult to remove ammonia from LBG in a hot system.

Combined-Cycle Power Plant. A simplified schematic of a combined-cycle power plant firing gasified coal is shown in Fig. 1. In the high-pressure gas turbine topping cycle, LBG is produced in a gasifier and burned in an adiabatic gas generator to produce the hot pressurized gas that turns the gas turbine. Heat in the exhaust gas is recovered in a waste heat boiler and utilized to drive a steam turbine bottoming cycle. Utilizing high temperature sulfur removal, the optimized combined cycle can achieve efficiencies up to 40 percent. Variations of the combined cycle which can improve the performance of the bottoming cycle and increase the overall efficiency include utilizing the gas generator as a supercharged boiler or reheating the gas turbine exhaust to produce higher

Contributed by the Gas Turbine Division and presented at the International Gas Turbine Conference and Products Show, Houston, Texas, March 9-12, 1981, of THE AMERICAN SOCIETY OF MECHANICAL ENGINEERS. Manuscript received at ASME Headquarters, December 9, 1980. Paper No. 81-GT-59.

Copyright © 1982 by ASME

Downloaded 01 Jun 2010 to 171.66.16.62. Redistribution subject to ASME license or copyright; see http://www.asme.org/terms/Terms_Use.cfm

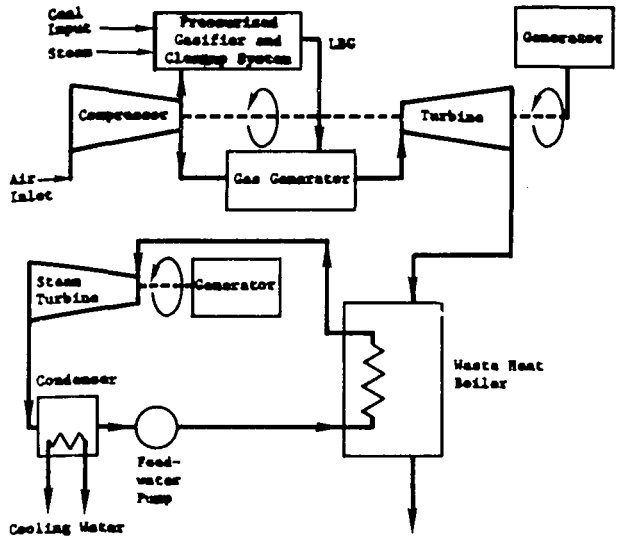


Fig. 1 Combined cycle power plant

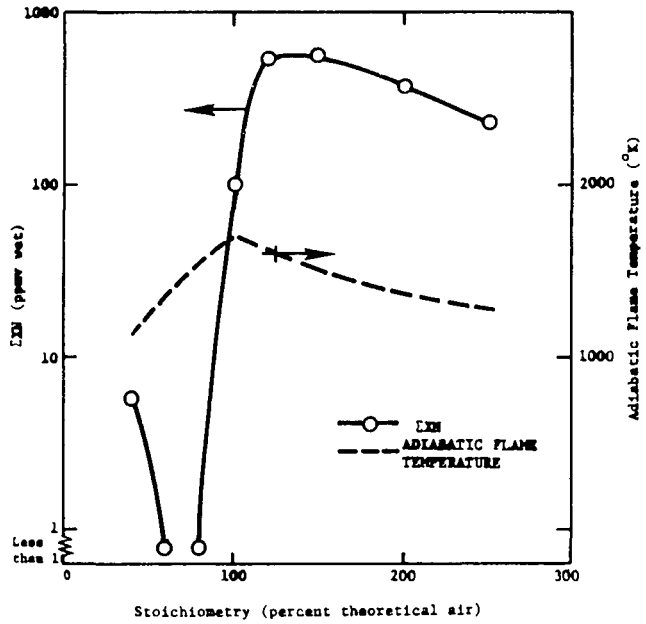


Fig. 2 Equilibrium ΣXN and adiabatic flame temperature for LBG

temperature steam. A more detailed discussion of combined-cycle optimization is included in reference [5].

Ideal Low-NO_x Combustor. The ideal low-NO_x LBG combustor would function as the high-pressure gas generator of the optimized combined cycle, operating overall fuel-lean for maximum gas turbine efficiency, and emitting low concentrations of pollutants such as carbon monoxide, hydrocarbons, and nitrogen oxides. Figure 2 shows that minimum equilibrium fixed nitrogen concentrations of less than 1 ppm occur in the adiabatic combustion of a 3.35×10^6 J/m^3 (90 Btu/ft^3) LBG at stoichiometries between 60 and 80 percent theoretical air. This corresponds to less than 0.9 ng/J LBG (0.002 lbm $NO_2/10^6$ Btu). The stoichiometry and value of this minimum change with adiabatic flame temperature, depending upon the composition and preheat temperature of the LBG. Lower temperatures push the minimum to leaner stoichiometries. An ideal low-NO_x combustor, shown in Fig. 3, would operate in two stages. In the fuel-rich primary stage, sufficient holdup time would allow total bound nitrogen ($\Sigma XN = NH_3 + HCN + NO + NO_2$) to approach an equilibrium favoring N_2. In the fuel-lean secondary stage, the remnants of the fuel would be burned out, meeting the low CO and HC requirements.

Kinetic calculations, based on combinations of idealized well-stirred and plug-flow reactors, indicate that conditions which tend to minimize nitrogeneous emissions from LBG combustors include [6]:

- Optimum fuel-rich stoichiometry
  - — Rich enough to keep NO low
  - — Lean enough to avoid excessive NH_3 and HCN
- Long primary residence time
- Optimum temperature
  - — High enough for fast XN processing
  - — Low enough to avoid thermal NO_x production
- High pressure

Practical Fuel/Air Contacting Effects. In a practical combustor, the mechanics of primary fuel/air contacting influences the fuel nitrogen processing. In the limits, fuel and air can be introduced to the combustors either separately or together. When fuel and air are introduced separately, combustion is dominated by the mixing process which is controlled by molecular or turbulent diffusion. When fuel and air are premixed, combustion can be back-mixed, in which case a continuous distribution of residence times exists within the products, or it can be plug-flow, in which case the products share a single common residence time. Laboratory scale flame reactor experiments to investigate fuel/air contacting effects under approximately limit case conditions were performed in a previous part of this program discussed in detail in references [7 and 8]. Promising results were achieved utilizing either a catalytic reactor or a diffusion flame reactor, while relatively higher XN emissions were produced in a premixed flat flame reactor. A well-stirred backmixed reactor, although not studied on the laboratory scale, was included in the bench scale experiments to represent a fourth important reactor type.

Catalytic Reactor. In a catalytic reactor, ignition is a heterogeneous process, controlled by diffusion of premixed reactants to active surface sites. As heat and combustion products are released to the mainstream, homogeneous reactions begin to dominate the combustion. In the final "cleanup" stage of catalytic combustion, after heat release is complete, many reactions are again diffusion controlled [9]. Use of a catalyst in the rich stage of a combustor could shorten the holdup time required to reach low ΣXN levels, reducing the size of the combustor necessary to achieve a given NO_x concentration. Studies of NO reduction in automotive exhaust have shown that platinum effectively promotes the reduction of NO to NH_3 and in combination with an NH_3 to N_2 catalyst, such as nickel, can speed the complete reduction of NO to N_2 [10]. Catalytic combustion studies have indicated the potential of several catalysts for XN reduction in rich combustion [11,12]. For gas turbine combustion applications, pressure drop must be kept to a minimum. The graded cell catalyst concept, discussed in detail in reference [13], has been developed to maximize throughout while keeping emissions and pressure drop low. Ceramic honeycomb monoliths are coated with the catalyst and stacked in the order of decreasing cell size. The coarse upstream cells tend to hold the flame while the fine downstream cells tend to complete the reaction.

Diffusion Flame Reactor. In a lean diffusion flame, the fuel passes through the entire range of stoichiometries: from an initially very rich zone, through the stoichiometric flame front, into the lean post-flame zone. Thus, a lean diffusion flame is, in effect, a multi-stage combustor. Low conversions

Downloaded 01 Jun 2010 to 171.66.16.62. Redistribution subject to ASME license or copyright; see http://www.asme.org/terms/Terms_Use.cfm

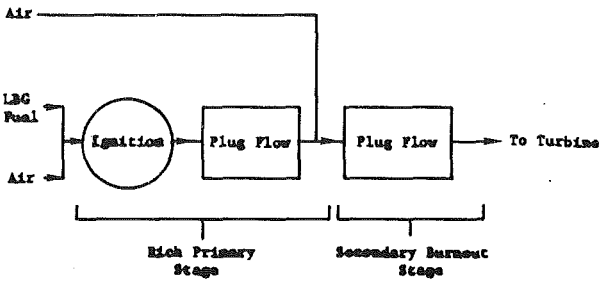


Fig. 3 Rich/lean series staged combustor

of fuel nitrogen to NO_x have been observed in fuel-lean laminar diffusion flames, especially in the combustion of hydrocarbon-free fuels. Turbulence tends to increase NO_x emissions [14].

In a fuel-rich laminar diffusion flame, part of the fuel never passes through the flame front; thus, depending on downstream temperatures and mixing conditions, it is possible for some of the fuel nitrogen to pass through unprocessed. In the laboratory scale experiments, high NH_3 concentrations were measured in the products of an NH_3-doped fuel-rich laminar diffusion flame. Turbulence in a rich diffusion flame would be expected to enhance mixing in the hot region within the flame and immediately downstream, increasing the reduction of fuel nitrogen.

Flat Flame Reactor. In laboratory scale premixed flat flame experiments, equilibrium and measured ΣXN minimums occurred at stoichiometries around 65 percent theoretical air. In a staged, premixed, simulated gas turbine LBG combustor, NO_x minimums have been measured at primary stoichiometries around 77 percent theoretical air [15].

Stirred Reactor. With the diminished importance of mass transfer, a premixed backmixed reactor is easily modeled. A computer model, described in detail in reference [16], is used to predict stirred reactor results and to optimize low-NO_x combustor design utilizing three elements: a kinetic reaction mechanism, idealized combustion modules, and a suitable computer code. The kinetic mechanism, employing reaction rates within published error bounds, describes the formation and destruction of 13 nitrogenous species and 17 species involved in the oxidation of the fuel, utilizing 140 reactions. The idealized combustor modules include combinations of a zero-dimensional premixed backmixed perfectly stirred reactor and a one-dimensional premixed plug flow reactor. Species distributions for specified input conditions (fuel composition, stoichiometry, stirred reactor and plug flow residence times, heat loss, pressure, and reactant temperatures) are calculated utilizing Energy and Environmental Research Corporation's GKAP computer code.

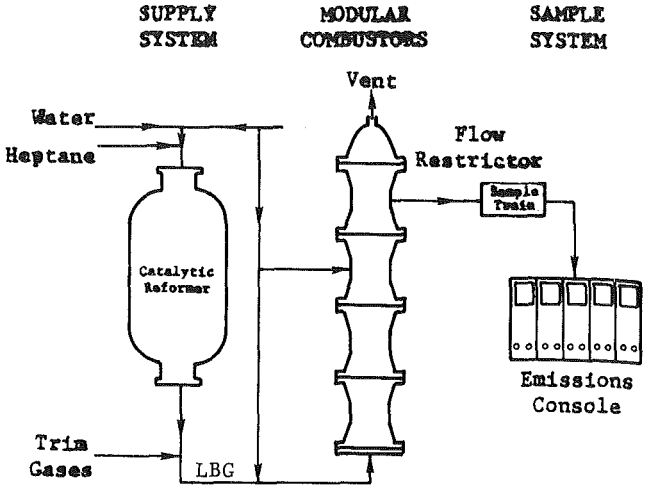


Fig. 4 Bench scale pressurized test facility

Experimental Systems

The pressurized bench scale facility includes the supply system, the modular combustors, and the sample system, as well as ancillary control systems. Figure 4 is a simplified schematic of the facility.

Supply System. Hot air, heptane, and water are premixed and passed through a catalytic reformer to produce a synthetic LBG. The reformer is operated at pressures between 6.4 and 11.9 atms at a stoichiometry of 45 percent theoretical air, the richest stoichiometry attainable without excessive sooting. Sufficient water is added to hold the maximum temperature of the catalyst bed to around 1370 K. Measured and equilibrium LBG compositions for this standard operating point are listed in Table 1. The reformer product gas passes through a variable heat exchanger, cooling it to the desired preheat temperature. Ammonia and methane can be added to trim the gas to the desired fuel nitrogen and hydrocarbon content. The LBG passes through a soot filter and into a valve system which controls the fraction of the LBG which goes to the combustors and the fraction which is bypassed. If none of the gas is bypassed, maximum combustor capacity is 60,000 J/s (200,000 Btu/hr).

Table 1 Reformer-produced low Btu gas composition

Product	Measured	Equilibrium
Pressure (atm)	9.2	11.9
NO (ppm)	1	0
NH_3 (ppm)	50	65
HCN (ppm)	1	0
O_2 (%)	0.0	0.0
CO (%)	7.1	7.8
CO_2 (%)	8.7	7.0
CH_4 (%)	0.2–0.8	0.0
H_2O (%)	27.1	28.4
H_2 (%)	19.5 [a]	17.7
C(S) (%)	0.0 [a]	0
N_2 (%)	37.3 [a]	39.2
Heating value (10^6 J/m^3)	3.25	3.0

[a] By difference between measured output and input

Downloaded 01 Jun 2010 to 171.66.16.62. Redistribution subject to ASME license or copyright; see http://www.asme.org/terms/Terms_Use.cfm

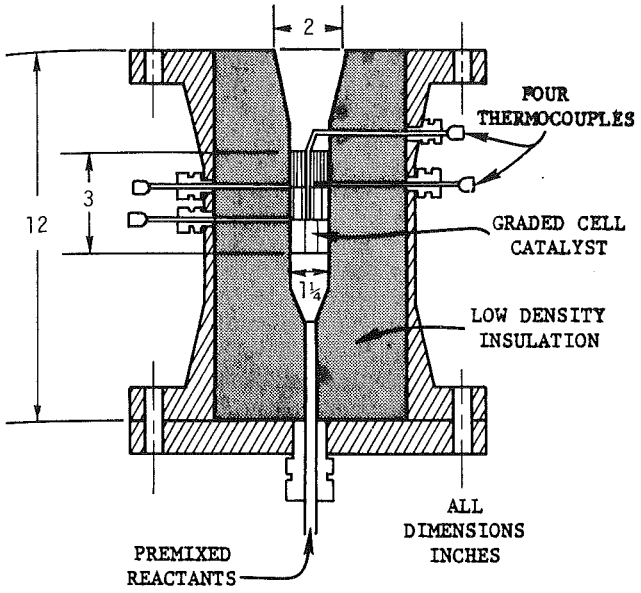


Fig. 5 Catalyst module

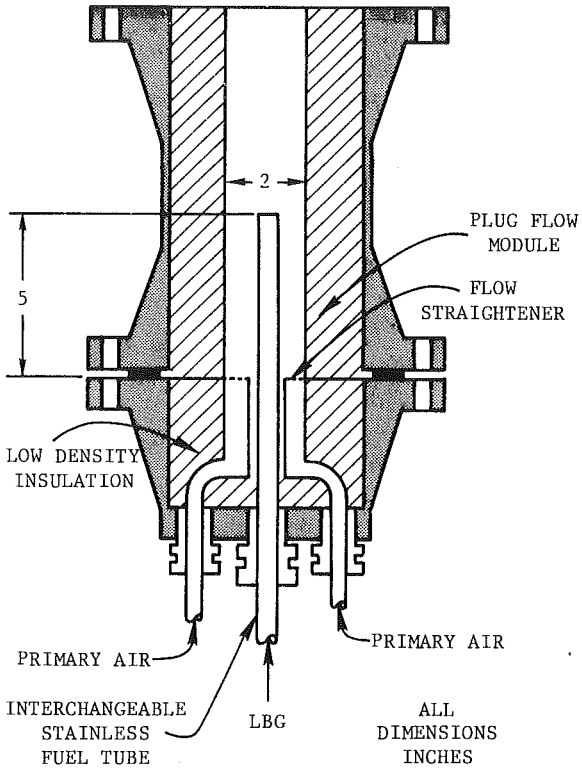


Fig. 6 Diffusion flame module

Modular Combustors. The combustors consist of a series of modules with 5 cm (2 in.) ID reaction/flow chambers enclosed in 15 cm (6 in.) OD low-density insulation and housed in flanged steel pipe. Ignition modules include the catalyst, the diffusion flame, and the stirred reactor as primary combustors and the jet-stirred secondary air injector as the single burnout module. Primary and secondary residence times can be controlled utilizing combinstions of plug flow modules of various lengths. Platinum/rhodium thermocouples in each module allow primary and secondary temperature measurements. A variety of low-NO_x combustor concepts can be modeled utilizing combinations of the interchangeable modules.

In the catalyst module, shown in Fig. 5, premixed LBG and primary air are injected from a small tube flashback arrestor into a tapered chamber below the graded cell catalyst. The catalyst, supplied by Acurex, consists of three zirconia honeycomb monoliths of decreasing cell size coated with nickel oxide. Platinum has been added to the coating of the upstream monolith to promote ignition. Thermocouples detect flashback and measure catalyst bed and wall temperatures.

The concentric diffusion flame module, shown in Fig. 6, is simple in design and operation. LBG is introduced through a removeable fuel tube of variable diameter while straightened primary air passes annularly around the fuel tube in the direction of the fuel flow. If a swirled flame is desired, vanes can be added to the air annulus to supply the necessary tangential momentun.

In the stirred reactor, shown in Fig. 7, equal streams of premixed reactants are injected at sonic velocity at 24 points along a 30-cm (12-in.) long, 5-cm (2-in.) ID combustion chamber which is open on the exit end. This reactor can be viewed as a series of stirred reactors, the products of one being combined with fresh reactants in the next. Assuming perfect mixing within the segments, a sample taken from any segment would contain the same distribution of products/reactants with residence times stretching from very short to very long.

Sample System. Samples are taken from the secondary region, through a water-cooled stainless steel probe situated on the centerline of the flow chamber. The cooling water is preheated and the stainless steel sample lines are wrapped with

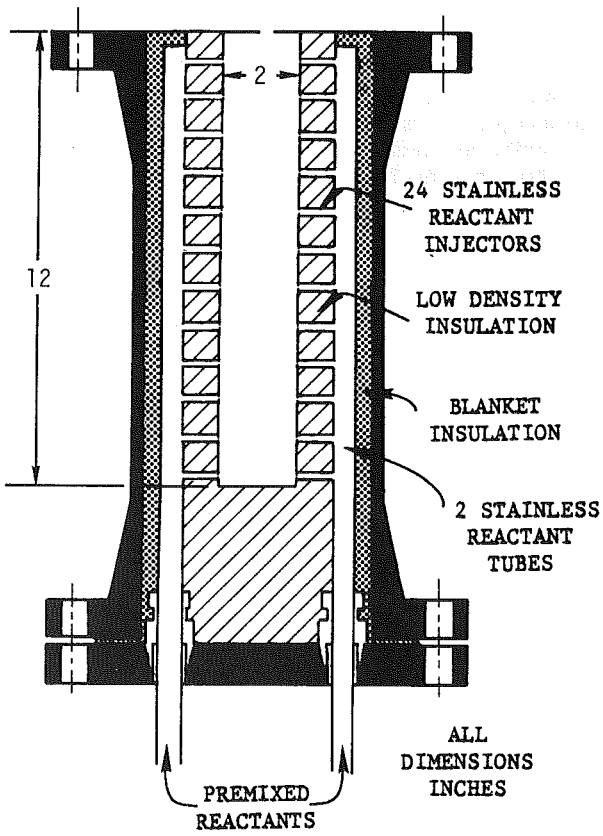


Fig. 7 Stirred reactor module

Downloaded 01 Jun 2010 to 171.66.16.62. Redistribution subject to ASME license or copyright; see http://www.asme.org/terms/Terms_Use.cfm

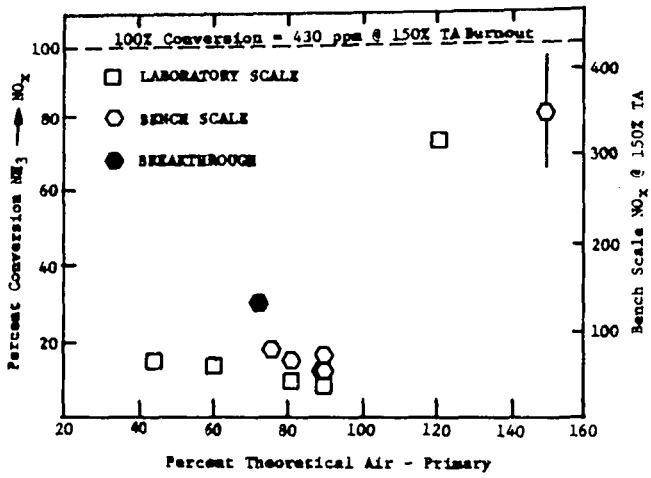


Fig. 8 Pt/NiO catalyst: scale-up

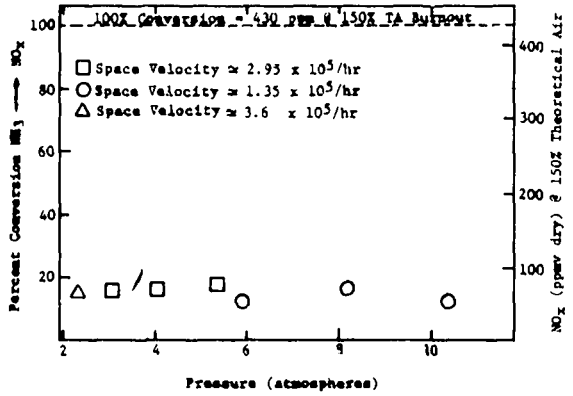


Fig. 9 Pt/NiO catalyst: effects of pressure and space velocity

heat tape to maintain the sample system above the dewpoint of the exhaust gases. The sample stream is throttled to nearly atmospheric pressure; and continuous gas samples are passed through a water trap maintained at 0 C, through a teflon-lined sample pump and into the emissions console which measures CO and CO_2 by infrared analysis, NO and NO_x by chemiluminescence, O_2 by paramagnetic analysis, and hydrocarbons by flame ionization. LBG samples are taken downstream of the soot filter in a similar system. NH_3 and HCN concentrations in the LBG or the combustor products are measured by specific ion analysis of batch bubbler samples. Low NH_3 and HCN concentrations have been measured (less than 10 percent of ΣXN) in the secondary products, indicating that the secondary zone is long enough for nearly complete processing to NO_x.

Ancillary Control Systems. Air, water, heptane, methane, and ammonia streams are measured by rotameter. LBG flow to the combustors and primary and overall stoichiometry are calculated by oxygen balance, utilizing the secondary O_2 concentration and the primary and secondary air flows. Reformer pressure is controlled by a valve on the LBG bypass line. Combustor pressure is maintained by passing the exhaust gases through a small orifice downstream of the combustors. The pressure upstream of the orifice is a function of the mass flow rate and the temperature of the exhaust gases. Constant pressure tests are performed by keeping the LBG flow and the total air flow constant. The primary stoichiometry can be changed by varying the ratio of primary to secondary air; but the overall stoichiometry is maintained constant, generally at 150 percent theoretical air. The exhaust gas temperature in the nearly adiabatic system is a function primarily of the overall stoichiometry. Variable pressure tests at constant flow (variable residence time) can be performed by changing the size of the flow restricting orifice.

Results

Bench scale pressurized tests were performed on variations of a catalytic reactor, a diffusion flame reactor, and a stirred reactor; their performances were compared; and several additional low-NO_x combustor concepts were evaluated.

Catalyst. On the basis of encouraging laboratory scale results, a rich/lean series staged platinum/nickel oxide primary catalytic reactor was selected as a potential low-NO_x concept for bench scale testing. Effects of scale, stoichiometry, pressure, and space velocity were examined.

The bench scale results were in general agreement with the laboratory scale results. Figure 8 compares NO_x emissions from staged combustion of a 500 ppm NH_3, doped LBG at two scales: 1200 and 20,000 J/s (4000 and 70,000 Btu/hr). Each had high conversions of NH_3 to NO_x in fuel-lean combustion, sharply dropping to low conversions in fuel-rich combustion. There were fluctuations in the NO_x concentrations emitted from the fuel-lean bench scale flame, but emissions from the staged bench scale flame were quite steady. Minimum conversions occurred in rich/lean staged combustion when the primary was operated close to a stoichiometry of 90 percent theoretical air, the laboratory scale catalytic reactor converted 8 percent of the input NH_3 to NO_x while the bench scale combustor had an average conversion of 14 percent. Conversions in the bench scale combustor remained low (less than 18 percent) over all rich primary stoichiometries under normal operation; but breakthrough (incomplete fuel processing) occurred if the primary was operated richer than 75 percent theoretical air: the temperatures on the walls of the catalyst monoliths dropped and the conversion rose sharply. Breakthrough was not observed in the laboratory scale experiment where the adiabatic flame temperature was maintained at a constant 1473 K by varying the amount of nitrogen diluent in the reactants. The undiluted flame reactor LBG had a higher heating value (HHV) of 6.7×10^6 J/m^3 (180 Btu/ft^3) while the HHV of the bench scale LBG was only 3.0×10^6 J/m^3 (80 Btu/ft^3). This indicates that raising the heating value of the gas could extend the operating range of the Pt/NiO catalyst, and that catalyst effectiveness is limited by a threshold flame temperature below which breakthrough occurs.

Effects of pressure and space velocity on the staged bench scale Pt/NiO catalyst are shown in Fig. 9. For a 553 ppm-doped LBG, NH_3 conversion to NO_x remained between 12 and 18 percent over pressures ranging from 2 to 11 atmospheres and space velocities ranging from 1.35×10^5 to 3.6×10^5/hr. This indicates that the catalyst was sufficiently long for nearly complete XN processing and that low pressure experimental results can be applied to high pressure gas turbine operation.

Diffusion Flame. In order to study fuel nitrogen processing in a diffusion flame, a number of interrelated parameters had to be considered: flame structure, stoichiometry, residence time, Reynolds number, pressure, fuel tube size, hydrocarbon content, and swirling.

Flame Structure. The bench scale flame was visually inaccessible, and there was no reliable indicator of flame length or as to whether the flame was attached or lifted. Rapid fluctuations in NO_x emissions, as shown by the bars in the following figures, indicated that the diffusion flame was not totally stable under many operating conditions. Throughput

Downloaded 01 Jun 2010 to 171.66.16.62. Redistribution subject to ASME license or copyright; see http://www.asme.org/terms/Terms_Use.cfm

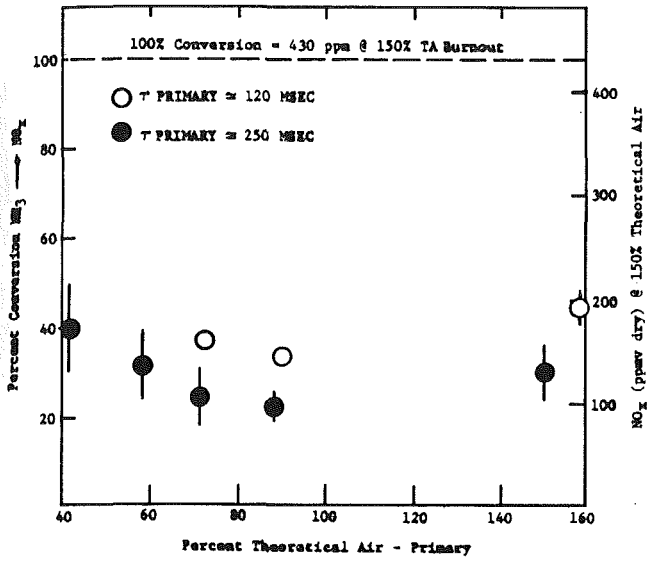


Fig. 10 Diffusion flame: effect of residence time

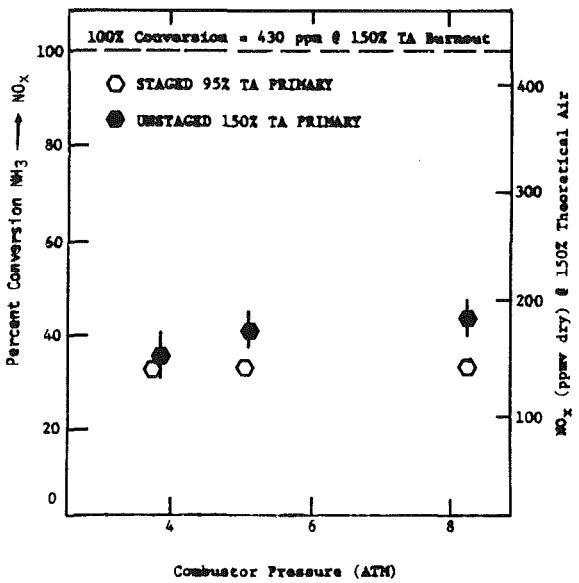


Fig. 11 Diffusion flame: variable pressure/Reynolds number

and tube size ranged from conditions where the flame should definitely be attached to conditions where the flame should definitely be lifted. Changes in the magnitude of NO_x fluctuation occurred; but no sharp changes were observed in NO_x emission levels or in other measured parameters, indicating that the attached/lifted transition was not an important factor. This agreed with previous variable throughput laboratory scale tests of a hydrocarbon containing diffusion flame, where a smooth NO_x transition was observed as the flame became detached.

Stoichiometry. Figure 10 shows the effects of primary stoichiometry at two residence times on a 17-mm ID fuel tube diffusion flame burning 553 ppm NH_3-doped LBG at a pressure of 8 atmospheres. Due to the low heating value of the LBG, thermal NO_x occurred at nearly stoichiometric conditions. However, effects of stoichiometry on fuel nitrogen processing in the turbulent bench scale diffusion flame were not nearly so pronounced as had been previously observed in an unstaged laboratory scale laminar diffusion flame which emitted high NH_3 concentrations in fuel-rich combustion.

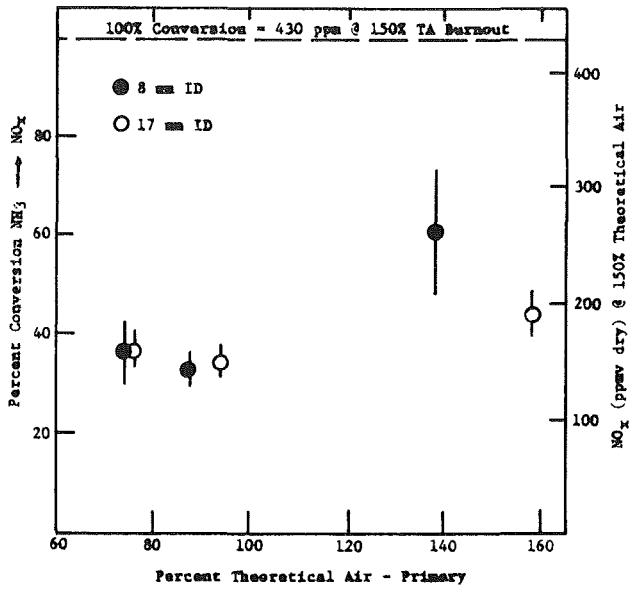


Fig. 12 Bench scale diffusion flame: effect of fuel tube size

Residence Time. Figure 10 also shows that NO_x emissions from a diffusion flame decrease with increasing primary residence time. Residence time was varied at constant pressure by changing the pressure control orifice size. In constant pressure operation at a fixed stoichiometry, fuel flow and Reynolds number were inversely proportional to primary residence time. Using a large pressure control orifice, a pressure of 8 atm was achieved at fuel tube Reynolds numbers around 40,000 and primary residence times around 120 ms; and a minimum XN conversion of 34 percent was observed at a primary stoichiometry around 90 percent theoretical air. Using a smaller pressure control orifice, half the flow was necessary to achieve the same pressure, doubling the primary residence time at Reynolds numbers around 20,000. Under these long residence time conditions, a minimum XN conversion of about 22 percent was observed at a primary stoichiometry around 90 percent theoretical air. This was the lowest XN conversion level achieved on the bench scale diffusion flame burning a 553 ppm NH_3-doped LBG.

Reynolds Number and Pressure. In order to isolate Reynolds number from residence time, a variable throughput experiment was performed. Utilizing a single pressure control orifice, Reynolds number and fuel flow at fixed stoichiometries were proportional to pressure, but residence time was constant. Figure 11 shows the effects of Reynolds number/pressure on NO_x emissions from staged and lean combustion of a 553 ppm NH_3-doped LBG utilizing a 17 mm ID fuel tube diffusion flame. In the staged test, performed at a primary stoichiometry of 95 percent theoretical air and a primary residence time of 120 ms, NH_3 conversion to NO_x remained constant at 33 percent over pressures ranging from 3.7 to 8.5 atm (Reynolds numbers from 16,000 to 40,000). Thus, pressure and Reynolds number had minimal effects on NO_x emissions in staged combustion. However, in the lean test, performed at a stoichiometry of 150 percent theoretical air and a residence time of 90 msec, conversion increased slightly with increasing pressure/Reynolds number.

Fuel Tube Size. Variable tube size tests were performed to isolate Reynolds number from pressure and residence time. Figure 12 shows the effect of fuel tube size on fuel nitrogen conversion in a 553 ppm NH_3-doped LBG diffusion flame operated at 8 atm, utilizing 17 and 8 mm fuel tubes. Fuel tube

Downloaded 01 Jun 2010 to 171.66.16.62. Redistribution subject to ASME license or copyright; see http://www.asme.org/terms/Terms_Use.cfm

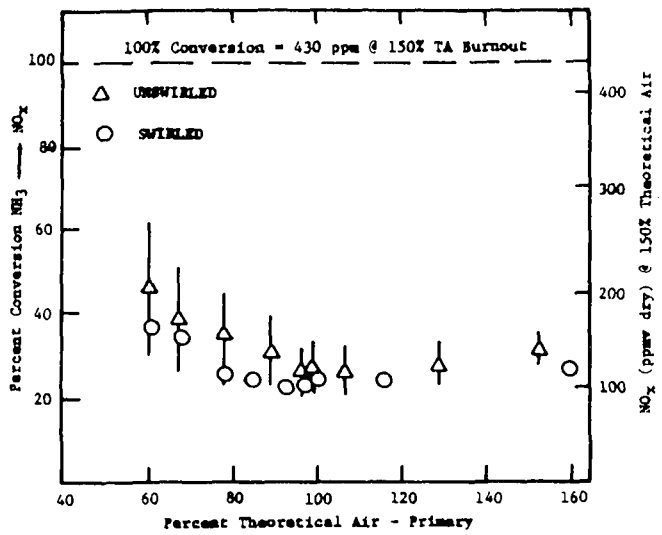


Fig. 13 Swirled/unswirled diffusion flame comparison

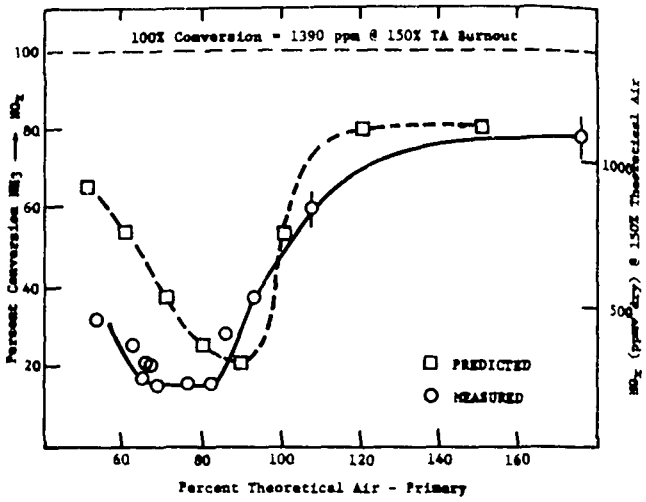


Fig. 14 Stirred reactor: predicted/measured

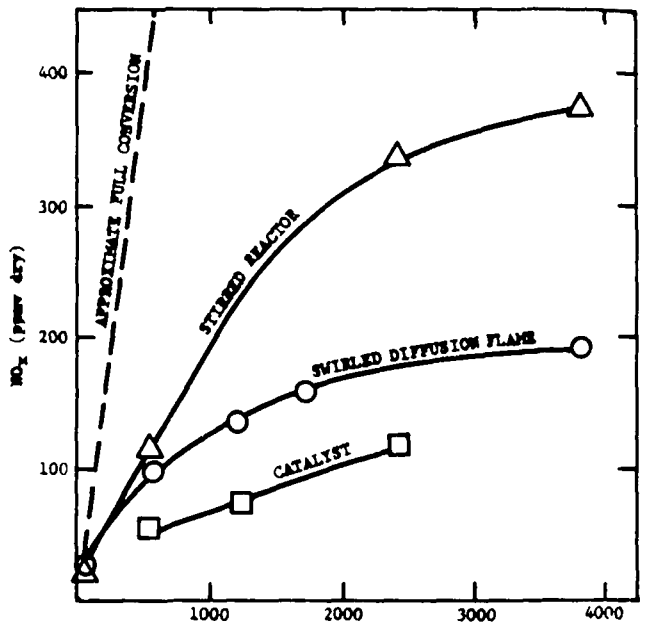


Fig. 15 Reactor comparison: fuel nitrogen content

size had litte effect on XN conversion in fuel-rich combustion. However, in lean combustion, increasing tube size (decreasing Reynolds number) decreased NH_3 conversion to NO_x. Increased tube size also decreased the NO_x noise level (high frequency concentration fluctuation shown by the error bars in the figure), perhaps an indication of flame stability. These trends did not hold true when fuel tube size was further increased to 30 mm: noise increased and conversions increased for both lean and staged combustion, perhaps due to instability and an effective shortening of primary residence time caused by increasing flame length.

Hydrocarbon Content. Hydrocarbon content of the LBG was not as important as previous laboratory scale diffusion flame results had indicated. Addition of 2 percent CH_4 to the untrimmed bench scale LBG caused only a slight increase in NO_x emissions. However, the reformer product gas always contained at least 0.2 percent hydrocarbon, and the most significant effects of hydrocarbons in the laboratory scale experiments were observed at very low HC concentrations.

Swirling. Swirling a diffusion flame decreases flame length and increases flame stability. Swirl vanes at a 45 deg angle were added to the air annulus of a 30-mm ID fuel tube diffusion flame. Figure 13 shows swirled and unswirled combustion of a 553 ppm NH_3-doped LBG at 8 atmospheres over a 250-ms primary residence time. Swirling eliminated the noise and reduced NO_x levels to the lower end of the unswirled fluctuation range. The 100 ppm NO_x emitted from a 90 percent theoretical air primary staged swirled 30-mm diffusion flame was comparable to the lowest NO_x levels achieved in an unswirled 17-mm diffusion flame under similar conditions; however, the apparent stability (lack of noise) of the swirled flame, made it the most promising diffusion flame configuration tested on the pressurized bench scale facility.

Stirred Reactor. The stirred reactor results provide the most direct comparison of experimetnal results with theoretical predictions. This is an important phase of the program as kinetic calculations will be used to optimize future low-NO_x prototype combustor design.

Figure 14 shows predicted and measured NO_x emissions from a 50-ms stirred reactor followed by a 90-ms plug flow reactor prior to 150 percent theoretical air burnout. For combustion of a 1794-ppm NH_3-doped LBG at 5 atm, predicted and measured NO_x were in substantial agreement at primary stoichiometries leaner than 80 percent theoretical air. However, in richer combustion, increased NH_3 production in the primary raised the predicted secondary NO_x concentrations well above the measured ones. Possible explanations for the predicted/measured disagreement under very rich conditions include:

- Problems with NH_i kinetics;
- Inadequate modeling of secondary burnout—the fast (3.5 m) secondary air addition used in the model essentially converted all XN to NO; whereas, even in a lean combustor, much of the NH_3 can be reduced to N_2 if mixing is slow.
- Inadequate estimation of reactor heat loss—kinetic analyses indicated that ΣXN Decreased significantly with increasing flame temperature in rich combustion.
- Imperfect mixing in the bench scale stirred reactor.

However, the model accurately predicted the level of the NO_x minimum, and the trends, even in very rich primary com-

Downloaded 01 Jun 2010 to 171.66.16.62. Redistribution subject to ASME license or copyright; see http://www.asme.org/terms/Terms_Use.cfm

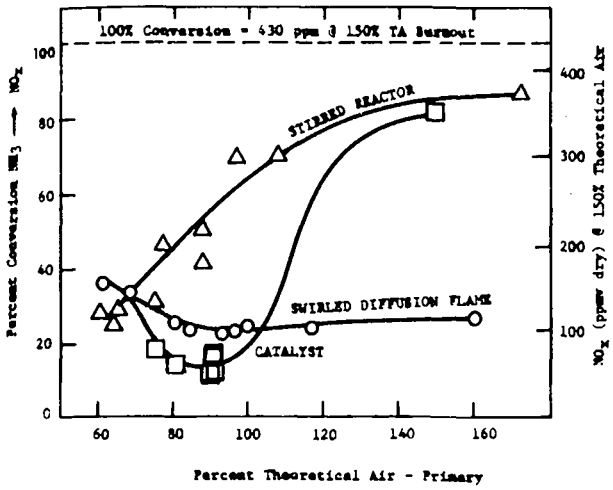


Fig. 16 Reactor comparison: fuel nitrogen content

bustion, were in general agreement with the measurements; thus, similar calculations are expected to be useful in the design of prototype low-NO_x combustors.

Reactor Comparison. Effects of fuel nitrogen content of the LBG and of primary stoichiometry were evaluated for all reactor types. Figure 15 shows the effects of NH_3 concentration in the fuel for rich/lean staged combustion under nearly optimum conditions utilizing a PT/NiO catalytic primary, a swirled diffusion flame, and a stirred reactor. In each case, conversion of NH_3 to NO_x decreased, but the actual NO_x emissions increased with increasing NH_3 in the LBG. NO_x emissions were lower from the catalyst than from the swirled diffusion flame, and lower from the swirled diffusion flame than from the stirred reactor. Effects of primary stoichiometry for the three reactors are compared in Figure 16. The Pt/NiO catalyst and the stirred reactor were sharply dependent on primary stoichiometry, each having much higher conversions in fuel-lean combustion than in rich combustion. Lowest emissions from a 553 NH_3-doped LBG burned out to 150 percent theoretical air were achieved in the staged catalyst operating at rich stoichiometries above the breakthrough threshold (75 percent T.A.) producing about 60 ppm NO_x. The swirled diffusion flame, less dependent on stoichiometry, produced a minimum of 100 ppm NO_x with a nearly stoichiometric primary, and only 120 ppm in quite lean combustion.

Additional Low-NO_x Concepts. Several additional low-NO_x combustor concepts were tested on the bench scale facility:

- Heat feedback
- Rich Pt/NiO cleanup catalyst
- Lean/lean staged diffusion flame.

Heat feedback invloves utilizing hot primary combustion gases to preheat the reactants, operating the rich primary hotter and increasing the fuel nitorgen reducing reaction rates. An increase of 150 K in the preheat temperature of diffusion flame reactants had no measureable effect on NO_x emissions at maximum flame temperatures around 1620 K.

Rich catalytic cleanup is achieved by passing rich combustion products, already low in ΣXN, through a catalyst prior to secondary burnout. NO_x emissions from a rich/rich/lean, diffusion flame/Pt:NiO catalyst/secondary burnout reactor were lower than from a staged diffusion flame but higher than from a staged catalyst. This suggests that the catalyst is most effective when 1) fuel nitrogen is in the form of NH_3, or 2) combustion is occurring.

Lean/lean staging is an attempt to bring NH_3, NO, and O_2 together at the optimum temperature range for homogeneous reduction of NO by NH_3 to form N_2 (around 1250 K in the absence of hydrogen). The primary stage was a lean diffusion flame which emitted O_2 and intermediate NO concentrations, while the secondary stage was a jet-stirred injector of NH_3-laden LBG. Wide variations in NH_3/NO ratio and in primary temperature failed to produce low NO_x emissions. In every case, even at primary temperatrues as low as 920 K, combustion occurred in the secondary. This suggests that homogeneous reduction of NO by NH_3 will not occur in a combustion environment.

Although these additional low-NO_x concepts appeared attractive in theory, in practice none of them achieved lower NO_x emissions than a staged Pt/NiO catalyst.

Conclusions

A rich/lean series staged combustor with a platinum/nickel oxide primary was the most promising low-NO_x combustor investigated. It had low conversion of fuel nitrogen to NO_x over a wide range of fuel-rich primary stoichiometries. Thus, it could be operated rich enough to maintain the adiabatic flame temperature relatively cool, prolonging the life of the catalyst. However, catalyst-coated ceramics are often short-lived due to loss of activity of the coating and structural problems of the support caused by thermal shock. During the course of the bench scale experiments, there was a great change in the appearance of the Pt/NiO catalyst. A green coating, which had no apparent effect on NO_x emissions, formed on the surface. Also, the zirconia honeycombs became quite fragile after repeated thermal cycling, especially the fine cell downstream monolith which was almost completely destroyed in the final experiments. Further investigation is necessary of catalyst aging under optimized combustor conditions before such a catalyst could be utilized in a practical gas turbine combustor.

A rich/lean series staged combustor with a diffusion flame primary also had low conversions of fuel nitrogen to NO_x. Primary stoichiometry and residence time had the most significant effects on fuel nitrogen conversion, while swirling tended to increase the apparent flame stability. Minimum NO_x emissions were achieved at nearly stoichiometric primary conditions for long primary residence times (250 ms or longer). Due to the low heating value of the LBG, thermal NO_x emissions were low. Pressure and Reynolds number had little effect on NO_x in a staged diffusion flame, while an increase in the hydrocarbon content of the LBG caused a slight increase in NO_x emissions. Combustion of a hydrocarbon-free LBG was not tested on the bench scale, but laboratory scale tests indicated that the absence of hydrocarbons in the fuel could cause a significant reduction in NO_x emissions.

A lean unstaged swirled diffusion flame produced higher NO_x emissions than the rich/lean staged swirled diffusion flame. However, because of its simplicity, it remains an attractive low-NO_x combustor concept. The influence of Reynolds number on NO_x levels in the lean flame suggests that NO_x emissions could be lowered by utilizing larger fuel tubes, perhaps approaching the levels achieved by the staged diffusion flame.

A stirred reactor produced higher NO_x emissions than either the diffusion flame or the catalytic reactor. However, it reproduced kinetic predictions fairly well, especially in fuel-lean and slightly fuel-rich combustion. This lends confidence in the future use of the kinetic code for optimization of low NO_x combustor design.

Downloaded 01 Jun 2010 to 171.66.16.62. Redistribution subject to ASME license or copyright; see http://www.asme.org/terms/Terms_Use.cfm

Acknowledgment

The investigations described in this paper were carried out under EPA contract 68-02-2196. The authors wish to express their appreciation to Mr. G. B. Martin, the EPA Project Officer, to Dr. J. Kesselring of the Acurex Corporation for his help in obtaining the catalysts, to Mr. M. Maser of Energy and Environmental Research Corporation for his assistance in conducting the experiments, and to Dr. J. Kramlich of Energy and Environmental Research Corporation for his assistance in the kinetic analysis.

References

1 Robson, F.L., Blecher, W.A., and Giramonti, A.J., *Combined-Cycle Power Systems*, EPA-600/2-76-149, U.S. Environmental Protection Agency, Washington, D.C., 1976, p. 359.

2 Environmental Protection Agency Title 40, Chapter 1, Subcharter C, Part 60—Standards of Performance for New Stationary Sources, *Federal Register*, Vol. 44, No. 113, June 11, 1979.

3 Folsom, B.A., Courtney, C.W., Corley, T.L., and Clark, W.D., "Advanced Combustion Concepts for Low Btu Gas Combustion," *Proceedings of the Third Stationary Source Combustion Symposium*, Vol. 2, Advanced Processes and Special Topics, EPA-600/7-79-050b, Feb. 1979.

4 Dravo Corporation, *Handbook of Gasifiers and Gas Treatment Systems*, NTIS Report No. FE-1772-11, Feb. 1976.

5 Folsom, B.A., Corley, T.L., Lobell, M.H., Kau, C.J., Heap, M.P., and Tyson, T.J., "Evaluation of Combustor Design Concepts for Advanced Energy Conversion Systems," *Proceedings of the Second Stationary Source Combustion Symposium*, Vol. 5 Addendum, EPA-600/7-77-073, July 1977.

6 Tyson, T.J., Heap, M.P., Kau, C.J., Folsom, B.A., and Brown, N.D., *Low NO_x Combustion Concepts for Advanced Power Generation Systems Firing Low-Btu Gas*, EPA-600/2-77-235, U.S. Environmental Protection Agency, Washington, D.C., Nov. 1977.

7 Folsom, B.A., Courtney, C.W., and Heap, M.P., "The Effects of LBG Composition and Combustor Characteristics on Fuel NO_x Formation," ASME JOURNAL OF ENGINEERING FOR POWER, Vol. 102, Apr. 1980, p. 459.

8 Folsom, B.A., Clark, W.D., Courtney, C.W., Heap, M.P., and Seeker, W.R., "Fuel Nitrogen Conversion—The Impact of Catalyst Type," EPA-600/9-80-035, US Environmental Protection Agency, Washington D.C., Aug. 1980.

9 Kendall, R.M., Kelly, J.T., Chu, E.K., and Kesselring, J.P., "An Analysis of Catalytic Combustion in Monolithic Honeycomb Beds," *Proceedings of the Third Workshop on Catalytic Combustion*, EPA-600/7-79-038, Feb. 1979.

10 Klimisch, R.L., and Taylor, K.C., "Ammonia Intermediacy as a Basis for Catalyst Selection for Nitric Oxide Reduction," *Environmental Science & Technology*, Vol. 7, No. 2, Feb. 1973, pp. 127–131.

11 Chu, E.K., and Kesselring, J.P., "Fuel NO_x Control by Catalytic Combustion," *Proceedings of the Third Workshop on Catalytic Combustion*, EPA-600/7-79-038, Feb. 1979.

12 Folsom, B.A., Courtney, C., and Heap, M.P., "Environmental Aspects of Low-Btu Gas-Fired Catalytic Combustion," *Proceedings of the Third Workshop on Catalytic Combustion*, EPA-600/7-79-038, Feb. 1979.

13 Krill, W.V., and Kesselring, J.P., "The Development of Catalytic Combustors for Stationary Source Applications," *Proceedings of the Third Workshop on Catalytic Combustion*, EPA-600/7-79-038, Feb. 1979.

14 Fenimore, C.P., "Effects of Diluents and Mixing on Nitric Oxide from Fuel-Nitrogen Species in Diffussion Flames," *Proceedings of the Sixteenth Symposium (International) on Combustion*, The Combustion Institute, Pittsburgh, Pa., 1976.

15 Pierce, R.M., Smith, C.E., and Hinton, B.S., "Low NO_x Combustor Development for Stationary Gas Turbine Engines," *Proceedings of the Third Stationary Source Combustion Symposium*, Vol. 3, Stationary Engine and Industrial Process Combustion Systems, EPA-600/7-79-050c, Feb. 1979.

16 Corley, T.L., Kramlich, J.C., and Seeker, W.R., "Development of a Kinetic Mechanism to Describe the Fate of Fuel Nitrogen in Gaseous Systems," *Proceedings of the Contractors Workshop on Fundamental Combustion Research Applied to Pollution Control*, EPA/IERL Report, to be published.

Downloaded 01 Jun 2010 to 171.66.16.62. Redistribution subject to ASME license or copyright; see http://www.asme.org/terms/Terms_Use.cfm

Comparison of the HTTT[1] Reheat-Gas-Turbine Combined Cycle With the HTTT Nonreheat Gas-Turbine Combined Cycle

I. G. Rice
Consultant,
Spring, Texas
Fellow Mem. ASME

P. E. Jenkins
Texas A & M University
College Station, Texas
Mem. ASME

High-temperature turbine technology (HTTT) when applied to the reheat-gas-turbine combined cycle (RHGT/CC) offers distinct advantages over the presently contemplated United States Department of Energy (DOE) HTTT simple-cycle gas-turbine combined cycle (SCGT/CC) being developed for gaseous fuel derived from coal. Specific improvements are: 1) higher combined-cycle efficiency, 2) higher specific output per unit of air flow, 3) less critical high-temperature nozzle-vane and rotating-blade surface area to be cooled, 4) less strategic high temperature metal material to be used, and 5) less overall cycle-cooling degradation allowing growth potential. New cooling techniques employing steam are required to accomplish these projections which necessitates advanced research and development and presently unavailable mathematical analytical approaches.

Introduction

There is a compelling world-wide need for higher electric-power-generation efficiency in view of the crude-oil crunch and the present atomic-fission and breeder-reactor development and installation slowdown. Fossil-fuel-fired power-plant efficiency increase is a necessity because fuels for such plants must fill the gap until and if fussion power becomes a reality after the turn to the Twenty-first Century.

The U.S. has issued a mandate to shift to coal for domestic electric-power generation, and to this end the U.S. Department of Energy (DOE) is pursuing various projects. One such project involves a High-Temperature-Turbine Technology (HTTT) twelve-cycle pressure-ratio water-cooled simple-cycle gas turbine combined with a more or less conventional 2400 psig - 1000/1000°F[2] reheat steam turbine whereby low BTU fuel-gas derived from a low-pressure coal gasifier is burned by the gas turbine [1]. Water cooling presents real challenges because of the well-known implementation problems such as deposits, corrosion, thermal stresses, instabilities of rotating liquids, and the requirement of leak tightness under rotational-developed presures of 4000 to 7000 psi.

There are technical and scientific reasons to believe that a high-cycle pressure-ratio reheat-gas turbine employing steam-barrier thermal protection can be developed to avoid the above problems and then obtain its fuel from a high-pressure coal-gasification process to obtain considerably higher coal-pile to bus-bar efficiency. Proposed coal-gasifier processes such as Ruhr-100, Hygas, Synthane, Texaco, Bi-gas, and Rockwell International all operate at pressure levels of about 1000 psig [2]. Gas produced at these pressures can be burned in a 40 to 42 cycle-pressure ratio (CPR) reheat-gas turbine (RHGT) to take triple advantage of the much greater than normal fuel-mass flow available at the higher pressure: first, because fuel-pressure let-down power loss is saved, second because the fuel-gas mass is heated to the full gas-turbine inlet temperature, and third, because the gas-turbine reheat function further increases the fuel-mass power output. These three advantages are not possible with the proposed 12 CPR Technology-Readiness-Vehicle (TRV) gas turbine.

Previous studies on the reheat-gas turbine combined cycle indicate appreciable cycle-efficiency gains [3-6]. A companion paper presented at this Conference by Ivan G. Rice reveals how steam-blade cooling can be applied to increase the reheat-pressure level of the proposed axial-flow nonintercooled reheat-gas turbine which in turn increases cycle efficiency and output and decreases the physical size of the reheat combustor to make the RHGT more practical [7].

The reheat-gas turbine proposed makes use of a readily removable high-cycle pressure-ratio gas generator of a type presently being developed by NASA through General Electric Co. (GE) and Pratt and Whitney Division of United Technologies (P & WA) [8-9]. The so-called Energy-Efficient Engine (E^3) will have a 38 CPR; however, for cruise it will fire at a modest 2200°F—not much higher than present-day units—but the aim is to increase durability. This emerging high-CPR technology can be applied to the development of a

[1] High-Temperature Turbine Technology
[2] See p. 140 for all SI conversion factors

Contributed by the Gas Turbine Division and presented at the International Gas Turbine Conference and Products Show, Houston, Texas, March 9-12, 1981, of THE AMERICAN SOCIETY OF MECHANICAL ENGINEERS. Manuscript received at ASME Headquarters, December 8, 1980. Paper No. 81-GT-69.

Copyright © 1982 by ASME
Downloaded 01 Jun 2010 to 171.66.16.62. Redistribution subject to ASME license or copyright; see http://www.asme.org/terms/Terms_Use.cfm

higher CPR steam-cooled gas generator to fire at HTTT temperatures of 2600 - 2800°F to obtain a very high-efficiency combined cycle. While steam cooling is not possible for aircraft because of weight and size of steam-generation equipment and weight of the water consumed, land-based power plants do not face these limitations. Yet no meaningful R & D has been done on steam-blade cooling and no precise mathematical models are presently available to adequately analyze the proposed method of steam-blade temperature-barrier protection; moreover, the projected theory of steam blanketing needs test-rig verification and empirical input.

This paper compares a 40 CPR nonintercooled axial-flow reheat-gas turbine utilizing steam-cooling RH -pressure boost to the proposed DOE TRV 12-CPR simple-cycle gas turbine both in combined cycle operation and burning distillate fuel for comparative purposes. The cycle-firing temperature is set at 2600°F and the exhaust temperature is limited to a nominal 1300°F for structural integrity and materials of construction. The steam turbine of both cycles has steam conditions of 2400 psig 1000/1000°F reheat.

This paper also touches on the basic heat transfer considerations encountered, the mathematical approaches available, and the R & D requirements needed for steam blanketing/cooling with reheat-pressure augmentation. A more complete status of these considerations is presented by the authors in an accompanying paper entitled "Blading Heat Transfer Considerations in a Reheat-Gas-Turbine Combined Cycle", being presented at this same conference [10].

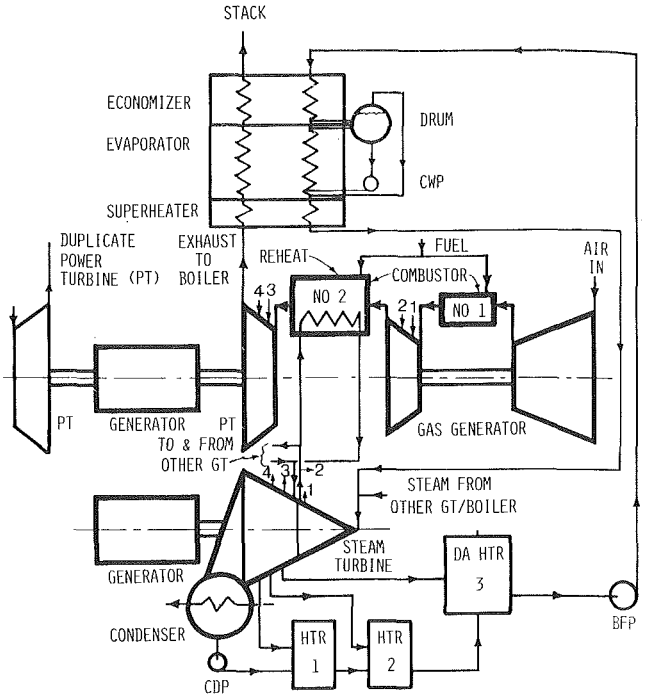


Fig. 1 Schematic-flow diagram of reheat-gas-turbine combined cycle showing extraction-steam points numbered 1-4 for gas-turbine vane and blade cooling

Assumptions

A comparison of the two different cycles relies on certain assumptions and predictions since neither cycle is in operation. More test-rig data are in hand on the water-cooled simple-cycle gas turbine and very little actual lab work has been accomplished on steam cooling—only that study work which has been reported [3-7] and investigations NASA has presented [11]. Therefore, assumptions are required, in the first case with some more certainty. Mathematical modeling for steam cooling likewise is not available, and the latter part of this paper deals with this subject.

In the interest of continuity and correlation of cycle data the same general assumptions and steam-heat balances have been retained in this paper as used in previous papers [3-7]. In comparing the steam-cooled reheat-multi-spool gas turbine with the water-cooled simple-cycle single-shaft unit, data were taken from the published flow diagram accompanying the ASME DOE/GE updata report presented last year [1]. Because of the increased mass flow of the low BTU coal gas, corrections have been made to equate gas-path flow to an equivalent inlet air flow to arrive at comparable blade-heat loads, cooling-water consumption and output.

Gas-turbine and steam-turbine data are reduced to the basis of one pound of inlet-air flow for comparison. Air being the dominant working fluid in terms of total flow and power developed is of primary concern and is where the higher cycle efficiency originates. Steam-turbine heat balances have used one pound of steam as the basis of heat balances for years and it is just one step further to relate these values to one pound of air flow. Both cycles incorporate steam conditions of 2415 psia 1000/1000°F to be compatible with present-day power plants with the thought of repowering existing plants.

A limitation of 1300°F maximum exhaust temperature has been imposed for structural and material reasons for both cycles; however, the reheat-cycle exhaust temperature calculates to be 1316°F, a slightly higher temperature but of no significant difference.

Firing Temperature. The firing temperature for both gas turbines reflects, in our comparison, the equivalent total temperature to the first-stage rotating blade, the temperature that would occur if no first-stage nozzle cooling were used and the firing temperature were 2600°F and 2200°F RH. Incremental fuel is added to accomplish this end; whereby overfiring, so to speak is introduced to balance the cooling of the first-stage nozzle vanes and blades and second-stage vanes.

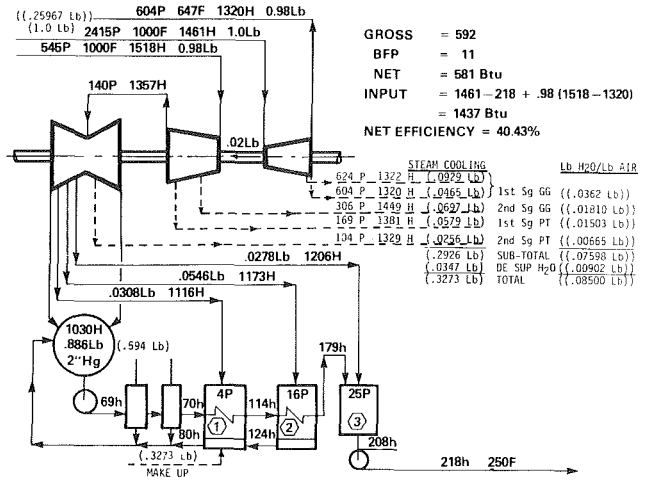


Fig. 2 Heat balance of a conventional 2400 psig 1000/1000°F steam turbine with three stages of feed-water heating showing steam-extraction rates for vane and blade cooling

Reheat-Gas-Turbine Cycle. A schematic diagram of the reheat-gas turbine combined cycle is given in Fig. 1. As can be noted, there is no compression intercooling. The gas generator, reheat combustor/steam reheater and power turbine are also arranged in an axial-flow fashion as shown. Cooling-steam extraction/admission points are numbered 1-4.

Downloaded 01 Jun 2010 to 171.66.16.62. Redistribution subject to ASME license or copyright; see http://www.asme.org/terms/Terms_Use.cfm

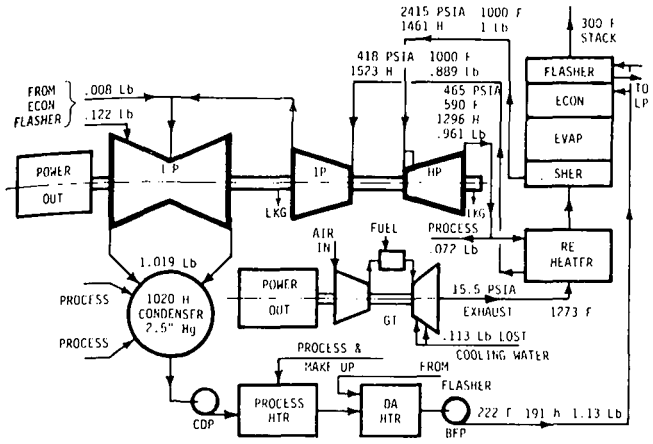


Fig. 3 Simplified schematic-flow diagram of simple-cycle DOE/TRV coal-gasification combined cycle

The steam-turbine-reheat steam is reheated in the gas-turbine combustor instead of the boiler. This steam provides the coolant necessary for the combustor and makes possible a 300°F stack temperature and at the same time retains conventional feed-water heating. Three stages of such feed-water heating is employed with heating steam being extracted from the steam turbine.

The gas turbine operates at a 40 CPR and the reheat-inlet pressure calculates to be 8.13 atmospheres; and the turbine is assumed to incorporate the latest features being developed by NASA for the E^3 engine.

The reheat-steam-turbine heat balance used is presented in Fig. 2. The solid lines and bold numbers present data on a standard-study turbine. Super-imposed on the diagram are dashed steam-extraction lines and smaller numbers giving data on the extraction cooling-steam flows assumed, with the actual injection flows being reduced through de-superheating. It is believed that the cooling-steam rates are adequate to accomplish blanketing cooling and at the same time allow steam heating to produce the assumed gas-generator-expansion power to augment reheat pressure.

Simple-Cycle Gas-Turbine Cycle. A simplified-flow diagram of the DOE/TRV cycle is given in Fig. 3 and all the numbers were taken from reference [1]. The gas turbine exhausts axially into a separate steam reheater before entering the heat-recovery boiler. Because the temperature exiting the economizer is on the order of 420°F, it is necessary to add a flasher or second low-pressure boiler to generate steam at two levels for admission to the low-pressure (LP) turbine section as shown.

No extraction steam is used for feed-water heating. This arrangement necessitates a high gas-turbine back pressure of 15.5 psia (22" H_2O) and a high-flow LP turbine (1.019 lb versus 0.594 lb for the reheat cycle). The reheat-gas-turbine back pressure is estimated to be about 14" H_2O due to the elmination of the reheat surface and the much better temperature differentials (less evaporator surface). These differences along with additional differences will be discussed later.

Gas-Turbine Reheat Pressure and PT-Exit Temperature

The effect steam cooling/injection has on reheat-combustor pressure is presented in Fig. 4. The extra GG work developed by the steam raises the pressure from 106.5 psia to 119.5 psia for reasons as explained in detail in reference [7].

The assumed amounts of saturated steam injection related to air flow are as follows:

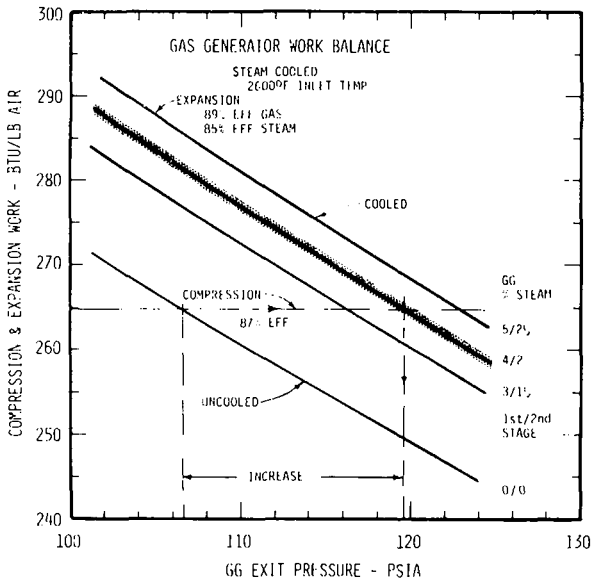


Fig. 4 Graphical solution of balancing compressor work and GG-expansion work when steam cooling is introduced

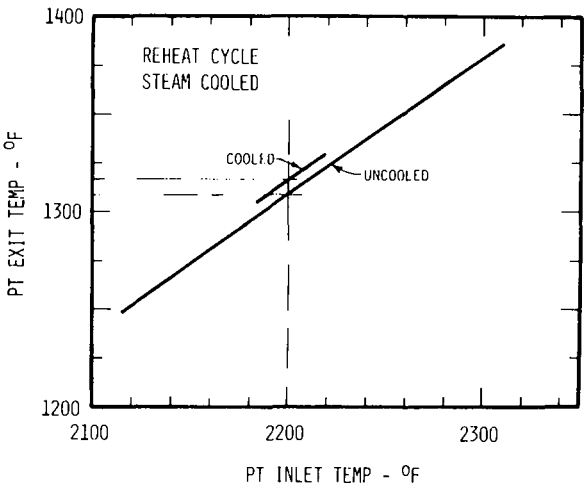


Fig. 5 Reheat-gas turbine-exhaust temperature to boiler plotted against PT inlet temperature showing effect of cooling steam

	weight flow
First-stage gas generator	= 4 percent
Second-stage gas generator	= 2 percent
First-stage power turbine	= 1.75 percent
Second-stage power turbine	= 0.75 percent
Total	8.5 percent.

Figure 5 is a plot of the power-turbine-exit temperature versus the reheat-combustor-outlet temperature. The bottom line indicates that a 2200°F inlet temperature produces a 1308°F exit temperature without steam cooling. When steam cooling is introduced both in the GG and PT, the PT-exit temperature rises slightly to 1316°F due to the flatter expansion of the steam, in particular through the PT, as will be shown later.

Simple-Cycle-Exhaust Temperature

Unlike the reheat-gas turbine, the simple-cycle gas-turbine exhaust temperature falls considerably when nozzle cooling takes place and cooling water is lost at the rotating blade tips. Reference is made to Fig. 6 which is a plot of gas-turbine-exit temperature against cycle-pressure ratio. The top line gives

Downloaded 01 Jun 2010 to 171.66.16.62. Redistribution subject to ASME license or copyright; see http://www.asme.org/terms/Terms_Use.cfm

the exhaust temperatures for uncooled expansion at 88 percent and shows that for a 12 CPR the exit temperature will be 1435°F. However, with the addition of nozzle cooling and lost water at a latent heat of evaporation of about 1000 BTU/lb, the exit temperature drops to 1273°F as given in reference [1]. The shaded area represents a projection of exhaust temperatures as a function of CPR.

If the CPR is raised to 18, shown by the right dashed line, the uncooled exit temperature is 1300°F, the target value, but when cooling is introduced, the temperature drops to less than 1200°F. This lower temperature seriously effects the steam-turbine cycle when considering steam conditions of 2400 psig 1000/1000°F. Therefore, the 12 CPR is perhaps a better selection relevant to the steam-bottoming cycle.

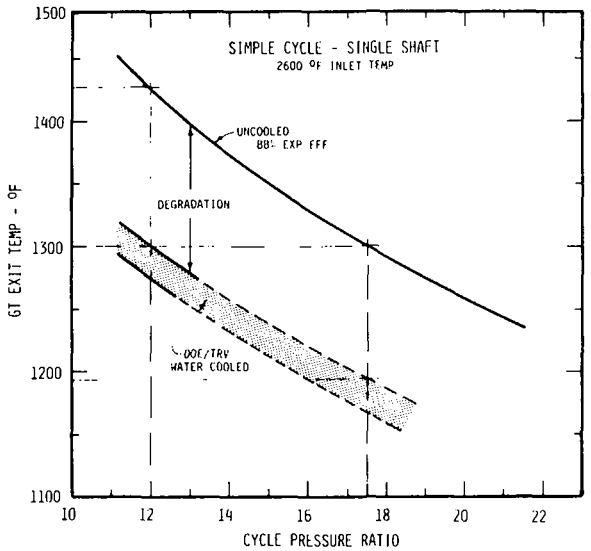


Fig. 6 Simple-cycle gas-turbine-exhaust temperature for 2600°F inlet temperature showing effect of vane and blade-water cooling

Simple-Cycle Gas-Turbine Data

Pertinent data on the simple-cycle gas turbine taken from reference [1] are tabulated in Table 1 in the left-hand column. The second column, going to the right, tabulates corrections that have been made to equate the data to distillate fuel without the greater mass flow of the low BTU gas. The two right-hand columns list data that have been calculated from the assumptions made.

It can be noted that the DOE/TRV compressor discharge temperature is given as 657°F whereas the calculated value is 669°F which indicates that the DOE/TRV compression efficiency is higher than the 87 percent assumed for the calculations. In this regard, the calculated values are conservative which is reflected in the output, line 14, where the calculated value of 194.4 BTU/lb air is lower than the 202.18 DOE/TRV value.

In considering uncooled compression and expansion of a single-shaft versus a multi-spool aero-derivative configuration, it has been assumed that the compression efficiency of the latter is one percentage point higher (87 versus 86 percent). Justification of this is based on multi-speeds being available on the GG to better match the turbine stages and specific speeds involved for optimum compression. Secondly, the latest E^3 compression-casing shrinking by cooling when up to load is considered to control blade-tip clearance better. Finally, the blading of an aero-derivative is more precise with thinner trailing edges to improve the aerodynamics.

Similarly, the uncooled expansion efficiency of the single shaft is assumed to be one percentage point less than the reheat turbine (88 versus 89 percent) for the same basic reasons.

Referring back to Table 1 again, it can be seen that the exhaust flows (line 20) check very closely (1.0522 versus 1.0513) showing that the fuel consumption is comparable. In each case the cooling-water loss is the same (0.02041 lb/lb air).

Line 21 indicates that the calculated air-cycle efficiency - excluding the cooling water - is reduced from 0.3516 to 0.3244 due to the lost power brought about by the quenching effect

Table 1 DOE/TRV Data For 12-CPR SC-IS GT

	PUBLISHED* DOE/TRV LOW BTU FUEL	CORRECTED DOE/TRV $(CH_2)_n$ FUEL	UNCOOLED CALCULATED DATA BTU/LB AIR	COOLED CALCULATED DATA BTU/LB AIR
1. INLET AIR FLOW - LB/SEC	301	301	---	---
2. INLET TEMP, t_1 - °F	59	59	59	59
3. CDT TEMP, t_2 - °F	657	657	669	669
4. CYCLE TIT, t_3 - °F	2600	2600	2600	2600
5. EX TEMP, t_6 °F	1273	1285	1435	1275
6. INLET PRESS, P_1 - PSIA	14.70	14.70	14.69	14.69
7. CYCLE PRESS RATIO (CPR)	12.11	12.11	12.0	12.0
8. CDP PRESS, P_2 - PSIA	178	178	176.28	176.28
9. TIP PRESS, P_3 - PSIA	---	---	169.23	169.23
10. TEP PRESS, P_6 - PSIA	15.5	15.5	14.9	14.9
11. FUEL - BTU/LB AIR	---	---	575.55	598.64
12. OUTPUT (NET) MW	72.84	---	---	---
13. OUTPUT (GROSS) MW (ADD 2%)	74.297	---	---	---
14. OUTPUT (GROSS) BTU/LB AIR	234.01	202.18	202.4	194.4
15. OUTPUT (GROSS) WITHOUT H_2O BTU/LB AIR	---	194.50	202.4	186.72
16. COOLING WATER EX FLOW - LB/SEC	6.7	6.7	---	---
17. NET FUEL FLOW - LB/SEC	36.3	9.02	---	---
18. EQUIVALENT AIR FLOW FOR BLADE COOLING - LB/SEC	328.27	---	---	---
19. EX FLOW - LB/SEC	343.6	316.72	---	---
20. EX FLOW - LB/LB AIR	---	1.0522	1.02971	1.0513
21. AIR CYCLE EFF - LHV	---	---	0.3516	.3244

NOTES: *Reference (1) for Date
See Final Page for SI Conversion Factors

Downloaded 01 Jun 2010 to 171.66.16.62. Redistribution subject to ASME license or copyright; see http://www.asme.org/terms/Terms_Use.cfm

Table 2 Cycle Data - 2600°F Inlet Temp

	UNCOOLED SC-IS 12 CPR	WATER-COOLED SC-IS 12 CPR	UNCOOLED RH-MULTI-SPOOL 40 CPR	STEAM-COOLED RH-MULTI-SPOOL 40 CPR
1. INLET TEMP, t_1 - °F	59	59	59	59
2. CDT TEMP, t_2 - °F	669	669	1114	1114
3. TIT - 1, t_3 - °F	2600	2689	2600	2749
4. GGET, t_4 - °F	---	---	1781	1749
5. TIT - 2, t_5 - °F	---	---	2100	2328
6. PTET, t_6 - °F	1435	1275	1308	1316
7. INLET PRESS, P_1 - PSIA	14.69	14.69	14.69	14.69
8. CDP, P_2 - PSIA	176.28	176.28	587.60	587.60
9. TIP, P_3 - PSIA (4% LOSS)	169.23	169.23	564.10	564.10
10. GGEP, P_4 - PSIA	---	---	106.46	119.50
11. TIP-2, P_5 - PSIA (3% LOSS)	---	---	103.27	115.92
12. PTEP, P_6 - PSIA	14.90	14.90	14.90	14.90
13. FUEL NO. 1 - BTU/LB AIR (400% TA)	575.55	598.64	454.71	500.82
14. FUEL NO 2 (NO STEAM HEAT) BTU/LB AIR	---	---	---	146.56
15. FUEL NO 2 (NO ST TURB REHEAT) BTU/LB AIR	---	---	---	199.36
16. FUEL NO 2 - BTU/LB AIR (200% TA)	---	---	129.71	239.21
17. TOTAL FUEL (NO STEAM HEAT) BTU/LB AIR	---	---	---	601.27
18. TOTAL FUEL (NO ST TURB REHEAT) BTU/LB AIR	---	---	---	700.18
19. TOTAL FUEL - BTU/LB AIR (WITH COOLANT)	575.55	598.64	584.42	740.03
FUEL/AIR RATIO - LB/LB AIR*				
20. NO 1 COMBUSTOR	0.02971	0.03091	0.02347	0.02586
21. NO 2 COMBUSTOR	---	---	0.006696	0.01235
22. TOTAL	---	---	0.030166	0.03821
THEORETICAL AIR - %*				
23. NO 1 COMBUSTOR	227.3	218.4	287.7	251.15
24. NO 2 COMBUSTOR	---	---	223.8	176.80
25. EXHAUST FLOW LB/LB AIR	---	1.0513	---	1.1232
26. GG EXP RATIO	---	---	5.299	4.721
27. PT EXP RATIO	---	---	6.931	7.780
28. EXP WORK AIR BTU/LB AIR	---	---	264.82	272.73
29. EXP WORK (STEAM & FUEL) BTU/LB AIR	---	---	---	309.55
30. GG TOTAL EXP WORK - BTU/LB AIR	149.31	149.31	264.82	264.82
31. PT WORK (AIR CYCLE) BTU/LB AIR	202.44	186.72	250.28	272.73
32. PT WORK (WITH STEAM) BTU/LB AIR	---	194.40	---	309.55
33. GT AIR CYCLE EFF - % LHV	35.16	32.44	42.83	45.36

NOTES: *Based on 19,370 BTU/LB Fuel and 14.81 lb Air/Lb for 100% Theoretical Air
See Final Page for SI conversion Factors

of the gas stream by the cooling and the heat removed by the nozzle-cooling water.

Reheat-Gas-Turbine Data

Pertinent-calculated data on the reheat-gas turbine are given in Table 2. The two right-hand columns list the important numbers and compare them to the simple-cycle numbers - left-hand columns. Both uncooled and cooled calculations are presented for comparison.

There are many differences - some of which have already been mentioned. Five significant and basic differences are emphasized as follows:

1 The reheat-gas turbine compressor-discharge temperature (CDT) is higher (line 2 - 1114 versus 669°F) which reduces the amount of fuel in the first combustor relative to the simple cycle.

2 The reheat-gas-turbine output is much higher (line 32 - 194.4 versus 309.55 BTU/lb air) which gives rise to much more topping power produced by the reheat-gas turbine.

3 The reheat-gas-turbine air-cycle efficiency is much higher (line 33 - 32.44 versus 45.36 percent) which is a reflection of the improved topping capability.

4 The exhaust temperature is not deteriorated by the coolant (line 6) which indicates less deterioration of the reheat-gas-turbine cycle by the steam coolant.

5 The steam-reheat function is accomplished by the reheat combustor which enhances the steam cycle (lines 13 to 19); incremental power is obtained by the increased fuel burned at a topping-efficiency level.

Referring to Item 1 just mentioned, although fuel consumption is reduced, the increase in CDT imposes a more stringent requirement for GG combustion-liner cooling, but not to an extent that makes cooling impractical considering the latest liner cooling techniques, the reduced primary flame zone (reduced radiation length) and some 23 percent more cooling air made available.

Other differences can be observed from Table 2 such as fuel flow, theoretical air, cycle-pressure levels, etc., but these observations will be left to the reader to analyze.

Reference is now made to Fig. 7 which plots cycle efficiency against cycle-work output. The effect of simple-cycle CPR is shown on the center curve where CPR increases from 12 to 42. It can be noted that the SC CPR is about 18 for maximum output. Selecting a CPR of 12 is a compromise for the DOE/TRV turbine and is assumed to be done because of the exhaust temperature deterioration and the effect a lower temperature would have on the steam cycle.

Downloaded 01 Jun 2010 to 171.66.16.62. Redistribution subject to ASME license or copyright; see http://www.asme.org/terms/Terms_Use.cfm

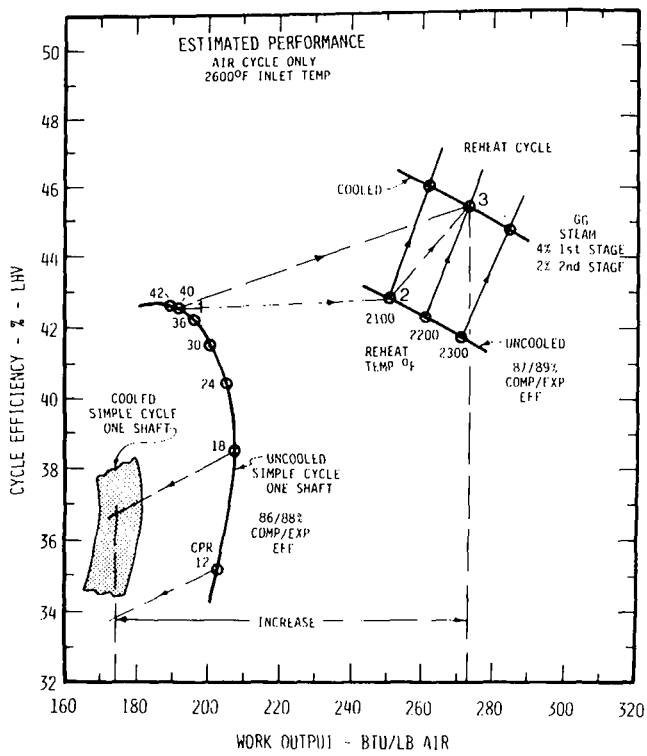


Fig. 7 Plot of cycle efficiency versus work output showing effect of reheat and steam cooling opposed to simple-cycle water cooling for a 2600°F turbine inlet temperature

To the left is shown a shaded area which represents the deterioration in air-cycle efficiency and output due to cooling.

The right-hand portion of the graph shows what happens when steam cooling/injection is applied to the 40 CPR near optimum efficiency gas trubine. When reheat is introduced the output and efficiency moves from point 1 to point 2. Then when steam is injected the efficiency and output moves to point 3. Note that the firing temperature is allowed to increase 100°F for a given nominal exhaust temperature of 1300°F.

This graph presents the striking difference between the two cycles where the gas-turbine output is increased from about 180 BTU/lb to about 270 BTU/lb. No steam or cooling-water power are included in these numbers. The increase is right at 50 percent a significant number. This increase accounts for the greater overall combined-cycle efficiency brought about by the 50 percent greater gas-turbine topping power being made available.

T-S and P-V Diagrams

Figure 8 is given to show the comparison of the two cycles in terms of their respective T-S and P-V diagrams. Figure 8(*a*) shows the lower compressor-discharge temperature and lower pressure of the simple cycle whereas Fig. 8(*b*) shows the decided difference in overall CPR.

Both graphs show clearly that the reheat-gas-turbine power-turbine expansion very closely matches the simple cycle's last three stages, and for all practical purposes the last three stages are the same. They see the same flows, temperatures and pressures; therefore, only the two GG stages and the first simple-cycle stage need full comparison as will be done.

Temperatures of Expansion

There is a considerable difference in the expansion temperatures encountered in the two cycles as shown in Fig. 9.

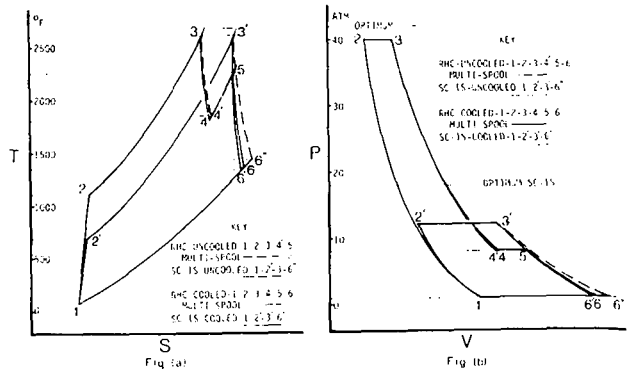


Fig. 8 T-S and P-V diagram HTTT comparison of a 12-CPR simple-cycle gas turbine to a 40-CPR reheat-gas turbine

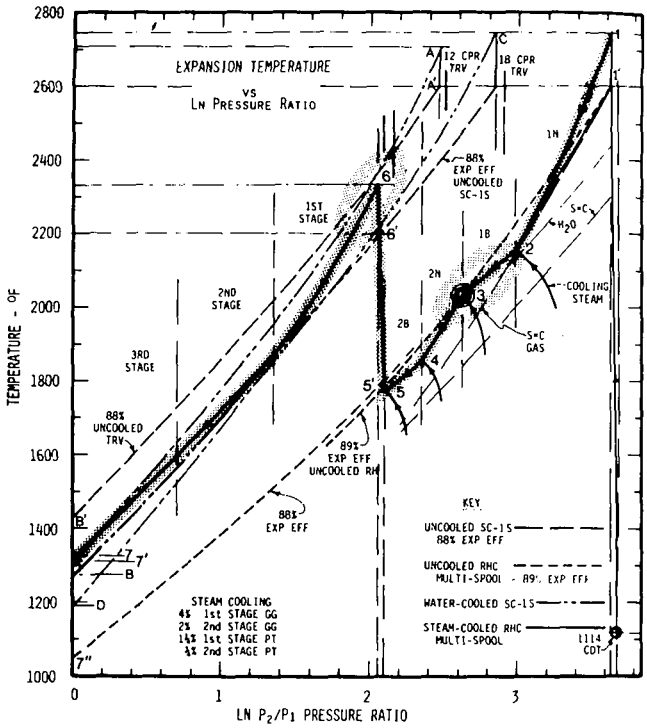


Fig. 9 HTTT expansion-temperature comparison of reheat-gas turbine and simple-cycle gas turbine

Temperature, in this graph, is plotted against the natural log of pressure ratio for the two cycles.

Reheat Cycle Expansion. First, the reheat-air cycle without cooling can be traced. Air at 1114°F CDT is heated to 2600°F, point 1′. The air and products of combustion are then expanded to point 5′ as shown by the dashed line. Reheat fuel is then added to arrive at point 6′ (2200°F) after which the gas is expanded to point 7′ (1308°F).

Now retracing the cycle and considering steam injection and the added fuel for the steam heating, the inlet temperature is raised to 2748°F, point 1. Over-firing takes place to balance the steam heat required. The hot gas mixes with the first-stage nozzle-cooling steam to arrive at point 2 considering the critical pressure ratio to be about 0.53 for sonic velocity. The nozzle-expansion efficiency is known to be high, about 96 percent, and expansion approaches constant entropy ($S = C$) conditions. Point 2 contains full sonic $V^2/2g$ energy for the gas and steam mixture assuming 80 percent steam mixing in the turbulent flow encountered. The gas then passes over the first-stage blades to develop work before arriving at point 3.

Downloaded 01 Jun 2010 to 171.66.16.62. Redistribution subject to ASME license or copyright; see http://www.asme.org/terms/Terms_Use.cfm

Both impulse and reaction work components are developed with perhaps 35 percent reaction. Point 3 represents the targeted temperature to match the air-cycle temperature without cooling.

The gas then expands from point 3 to point 4 and on to point 5. No additional fuel can be added and the temperature starts to sag as can be noted (point 5 is lower than point 5′).

Reheat takes place from point 5 to point 6 where again overfiring is applied to pick up the sagging temperature and to satisfy the steam-cooling heat load (a portion of the GG second-stage blade and the PT first and second-stage blading).

Because of the increased steam coming from the GG (assumed 6 percent) the gas expansion does not sag as badly after reheat as the steam expansion is flatter with less temperature drop. The steam helps hold up the rest of the gas temperature.

Careful heat balances using total enthalpy calculations indicate that the final temperature of the mixture rises slightly at point 7 from 1308 to 1316°F.

It can be noted that all the heat is left inside the cycle to do work and not extracted as in the case of the water-cooled simple cycle.

Table 3 Comparison of Blading-Heat Loads

	BTU/LB AIR		
	STATIONARY VANES		ROTATING BLADES
12 CPR - SC-IS			
FIRST STAGE	23.09		20.69
SECOND STAGE	6.60		12.41
THIRD STAGE	3.30		8.27
SUB TOTAL	32.99*		41.37*
TOTAL		74.36*	
40 CPR-RHC-MULTI SPOOL			
GG 1st STAGE	32.58		21.72
GG 2nd STAGE	12.13		9.92
PT 1st STAGE	8.05		6.58
PT 2nd STAGE	2.53		2.07
SUB TOTAL	55.29		40.29
TOTAL		95.58	

NOTES: *Total Calculated from Reference (1) with Assumed Distribution
See Final Page for SI Conversion Factors

Simple-Cycle Expansion. The 12-CPR simple-cycle gas-turbine expansion can now be traced in the same manner. First, starting with the compressor-discharge air being heated from 669°F to 2600°F, considering no blade cooling, the gas is expanded from A′ to point B′ where the exhaust temperature is 1435°F. This temperature is noted to be appreciably above the limit of 1300°F.

Retracing the expansion, but with water cooling, the air is heated to point A (approximately 2690°F) to balance the heat absorbed by the first-stage-nozzle vanes. The gas expands through the assumed four-stage turbine and in so doing is continually being cooled by the water circulating through the vanes and the water passing through and out the blades; however, the blade water that is lost, 67 percent, is the most detrimental and accounts for most of the drooping temperature and lost power-development potential. Further, the heat from the nozzle vanes is taken out of the cycle, and this energy is recovered for power conversion at a very low efficiency level.

The exit temperature at point B calculates to be 1275°F based on the blading-heat loads given in reference [1] which is very close to the 1273°F referenced value.

If the simple-cycle CPR is raised to 18, then the exhaust temperature falls off to Point D which is below 1200°F. The reheat steam-turbine cycle starts to deteriorate and the stack temperature out the boiler rises perhaps to 375°F. Therefore, going to a 18 CPR does not improve the overall water-cooled cycle to any great, if any extent.

The critical high-temperature area of real concern is the first-stage rotating blades, both of the GG and the simple-cycle turbine. The oval-shaped shaded areas show that the 12-CPR first-stage blades see a higher temperature than the 40-CPR reheat GG. As can be noted, the simple-cycle blade-temperature environment ranges from 2200 to 2400°F whereas the RH-GG blade has a lower temperature by some 200°F. The second stage RH-GG blade temperature falls off to an even lower temperature, whereas the second-stage simple-cycle blade sees about the same temperature as the first-stage RH power turbine. These temperature environments favor the RH gas-turbine cycle, and in terms of initial firing temperature, the RH GG could be fired some 200°F hotter and yet the first-stage rotating blades would not encounter any higher temperature.

Table 4 Comparison for cooling water/steam make-up/condenser flow

	12 CPR SIMPLE CYCLE		40 CPR REHEAT CYCLE
STEAM THROTTLE FLOW LB STEAM/LB AIR	.18087		.25967
TOTAL COOLING STEAM EXTRACTION LB H_2O/LB AIR AIR	--		.07596
H_2O TO DE-SUPERHEATERS LB H_2O/LB AIR	--		.00904
H_2O LOST TO STACK			
LB H_2O/LB AIR	.02041		.085
LB H_2O/LB THROTTLE STEAM	.1128		.3273
MAKE-UP-%	11.28		32.73
RATIO 40 CPR H_2O/12 CPR H_2O		2.902	
STEAM TO CONDENSER			
LB/LB THROTTLE STEAM			
TURB GEN SET	1.019		.594
AIR BOOST COMP	.072		---
TOTAL	1.091		.594
DECREASE - %		45.6	

NOTE: See Final Page for SI Conversion Factors

Downloaded 01 Jun 2010 to 171.66.16.62. Redistribution subject to ASME license or copyright; see http://www.asme.org/terms/Terms_Use.cfm

Blading-Heat Loads

The two-cycle blading-heat loads of the two cycles for which incremental fuel must be added is given in Table 3. The simple-cycle total-heat load of the water-cooled turbine was calculated from the data of reference [1]; however, the distribution shown is assumed for this study. The total calculations are straightforward and easy to obtain for the nozzle vanes and the rotating blades. Figure 10 presents the referenced data.

The heat loads for the 40 CPR reheat-gas turbine are based on the assumed steam flows and mixing presented earlier. These assumptions are best estimates until rig tests can be performed. More accurate estimates can then be assigned; however, as can be noted, the steam-cooling heat loads given in Table 3 run about 28 percent higher than for the water-cooled loads. Incremental fuel, in both cases, must be added to balance these loads.

Cooling Water Versus Steam Flows

A comparison can now be made of the flow rates of cooling water lost to the gas stream with the steam injected. Reference is made to Table 4.

Here the total steam flow is shown for the two cycles. The throttle flow of the reheat cycle is about 44 percent greater primarily due to the reheat-steam-heat load being shifted to the reheat combustor and, secondly, because of the greater amount of steam at a higher temperature in the exhaust.

The extracted steam is desuperheated to obtain the maximum film cooling and lowest possible viscosity. The total of extraction steam plus desuperheating water is 8.5 percent versus 2.041 percent for the water-cooled cycle. A breakdown of the reheat-steam flows is given in the flow diagram of Fig. 2. The steam-cooled RHGT CC, in terms of make-up water required relative to air flow, would necessitate approximately four times as much water make-up as the water-cooled cycle and the total make-up would be about 34 percent of the throttle flow. However, because the total RHGT-CC work output per pound of air is approximately 45 percent greater and because of the increase in the ratio of gas-turbine power to steam-turbine power of the RHGT CC, the make-up in terms of cycle output is reduced to approximately 2.75 times that of the SC-GT CC.

Although this is a disadvantage for the reheat-gas turbine steam-cooled cycle as make-up water is costly, it can be noted that the condenser flow for the water-cooled cycle actually exceeds the throttle flow because of the added steam admission from the economizer flasher. There is a large difference in condenser flows of the two with the reheat-gas-turbine cycle being 45.6 percent less when the condensing flow of the air-boost compressor is added to that of the turbine generator set. This lower flow would appreciably reduce the physical size of the low-pressure steam-turbine section. At the same time the condenser and cooling towers would be reduced by this same amount. Cooling-tower evaporation and blow-down would about be cut in half.

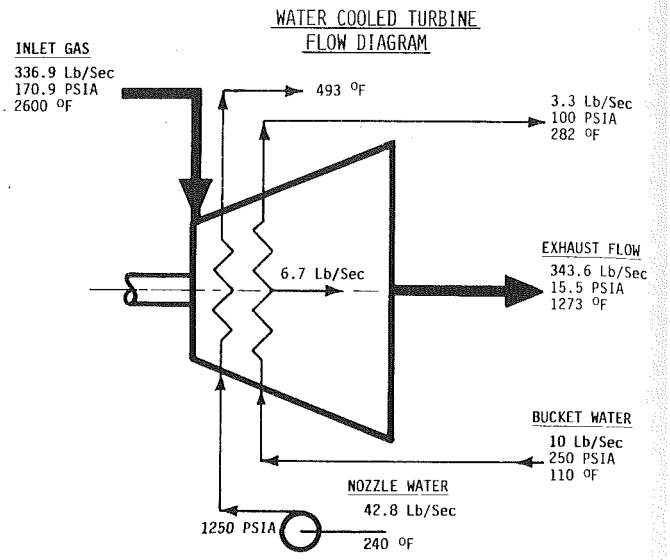


Fig. 10 Flow diagram of DOE/TRV water-cooled turbine giving flow rates, pressures and temperatures

Blade Size, Surface and Volume Comparison

The last-stage rotating blade is assumed to be the limiting item in terms of mass flow and temperature similar to a steam turbine. This being the case, the maximum size and output of the turbine is thus limited for 3600 rpm by the last-stage blade.

A comparison of blade and vane size of the two machines can be made by working backwards from the exhaust to the reheat combustor and then onto the 40-CPR inlet. The law of $PV = WRT$ can be applied to calculate the various sizes asssuming that the exit velocity is equal to the inlet velocity. Corrections can be made for water vapor by assuming that super-heated steam has an R value of 85.5. A size comparison is presented in Table 5. It can be noted that the RH-cycle-inlet vanes are only 0.0422 times as long as the last-stage blade. Also it can be noted that the simple-cycle inlet vane is three times the length of the RH-gas-turbine inlet vane.

Figure 11 gives a graphical view of the change in blading size of the two turbines. The top half above the pitch-center line represents the simple-cycle gas turbines and the bottom half represents the reheat-turbine cycle. The radius can be considered infinite in length to make both upper and lower portions the same. All blades are considered to rotate the same RPM and aerodynamics are not considered for the size analysis so that the pitch diameter of each blade and vane can be the same. The blade-path diagram is in effect a plot of volume versus a diminishing scale of blade-path distance

Table 5 Comparison of vane and blade size relative to last stage blade

	12 CPR SIMPLE CYCLE	40 CPR REHEAT CYCLE
GT LAST STAGE BLADE LENGTH - L	1	1
REHEAT PT 1st STAGE VANE @ 7.89 ATM - L	---	.1842*
SIMPLE-CYCLE VANE @ RH PRESS OF 7.89 ATM - L	.1870*	---
INLET TO RH COMBUSTOR @ 8.13 ATM - L	---	.1485*
INLET TO SIMPLE CYCLE @ 11.52 ATM - L	.1461*	---
INLET TO GG @ 38.4 ATM - L	---	.0422*

NOTES: *Corrected for H_2O Volume
See Final Page for SI Conversion Factors

Downloaded 01 Jun 2010 to 171.66.16.62. Redistribution subject to ASME license or copyright; see http://www.asme.org/terms/Terms_Use.cfm

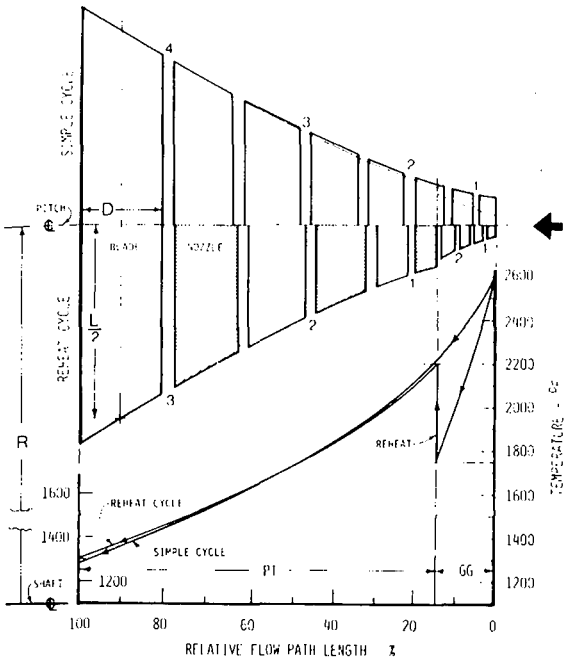


Fig. 11 Diagrams showing size and temperature relationships of vanes and blades of the simple-cycle and reheat-cycle HTTT gas turbines

whereby the aspect ratio L/D stays constant and L is directly proportional to volume. The inlet velocity to each nozzle vane, in this approach, is constant and equal to the last-stage blade-exit velocity.

The temperature plot below the blade diagram shows quite clearly the rapid fall of the GG-blading-temperature environment which leads to a better opportunity to steam-cool the critical rotating blades.

An isometric/perspective view of the front end of the blade plot of Fig. 11 is presented in Fig. 12. A portion of the pitch-line of circumference of length C is laid out flat to simplify the analysis of comparing both machines.

Using the simple relationship of PV = WRT, a comparison of blade lengths L, blade cords D and the distances between blades D can be determined for the different positions. Table 6 presents these values to correspond with Fig. 12.

The first-stage length of the blades, the total surface area and the side-wall area of the 40-CPR-RH turbine are only 30 percent of the values for the 12-CPR simple cycle. The volume of the first-stage RH-nozzle ring drops to less than 10 percent of the volume of the simple cycle due to the cube law coming into play. These striking differences lead to the possibility of easier cooling even though the heat transfer factors increase due to the greater density. The velocities remain about the same to somewhat offset the effect of the greater density. Aside from cooling considerations, less strategic material would be required for the critical GG hot-gas parts because of the much greater density.

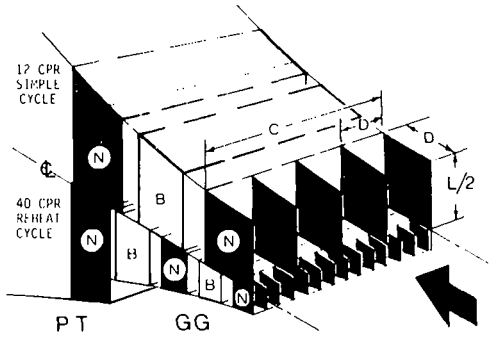


Fig. 12 Isometric/perspective view of simple and reheat gas-turbine-inlet vanes and blades showing relative sizes

RH GT/ST Combined-Cycle Efficiency

The combined-cycle efficiency-heat balance, breakdown in fuel input and power components will now be discussed.

Combined-Cycle Efficiency and Heat Balance. The RH GT/ST combined-cycle efficiency has been carefully calculated taking into consideration the incremental work and fuel components of the steam and fuel. Cycle losses such as generator, boiler, and boiler-feed pump have all been dealt with. Figure 13 presents an overall heat balance of the reheat-gas-turbine/reheat-steam-turbine cycle. The net cycle efficiency calculates to be 57.4 percent LHV. All the losses are shown on the diagram.

It can be noted that the cooling steam accounts for a sizeable stack loss of 94.56 BTU/lb air and is about 13 percent of the input and 65 percent of the condenser heat rejection. The high cooling-steam stack loss is due to the latent heat of evaporization which is not recovered. Any attempt to recover any of this heat is beyond the scope of this paper. The water volume of the cooling steam (13.6 percent), however, added to the water-volume of combustion (8.0 percent) gives a partial pressure of 3.17 psia. This pressure indicates from the steam tables that condensation will take place at a temperature of 144°F, but the acid-condensation temperature could be higher to be a limiting factor.

The heat balance closes very closely (0.1 percent), but care was taken to balance each step in the calculations to ensure a tight overall final heat balance.

Cycle-Fuel-Input Breakdown. Table 7 presents a breakdown of the various components of the fuel input starting with the air cycle and then listing the blading-steam-heat loads. The extra feedwater steam passing through the steam reheater (1.41 BTU/lb) is added to the steam-turbine flow-reheat fuel to arrive at the total steam-reheat input. The total fuel input calculates to be 740.03 BTU/lb of air. This amount of fuel then yields a value of 176.76 percent theoretical air at the RH combustor exit which is a safe value for efficient combustion allowing for bypass air around the primary zone.

Table 6 Comparison of first stage gas path size surface and volume

	12 CPR SIMPLE CYCLE	40 CPR REHEAT CYCLE
1st STAGE INLET VANE HEIGHT - L	1	.300
RATIO OF NUMBER OF VANES	1	3.333
SURFACE AREA OF EACH VANE	1	.090
SURFACE AREA OF TOTAL VANES	1	.300
VOLUME OF VANES	1	.090
SIDEWALL SURFACE AREA	1	.300

NOTES: L/D Ratio Can Be Any Value
No H_2O Included
See Final Page for SI Conversion Factors

Downloaded 01 Jun 2010 to 171.66.16.62. Redistribution subject to ASME license or copyright; see http://www.asme.org/terms/Terms_Use.cfm

Table 7 Cycle fuel input breakdown

	FUEL INPUT - BTU/LB AIR			
	GG NO 1 COMBUSTOR		RH/PT NO 2 COMBUSTOR	TOTAL
AIR CYCLE	454.71		146.56	601.27
EXTRA FUEL FOR EXTRA POWER	.49		1.43	1.92
BLADING - STEAM HEATING				
GG 1st STAGE	42.82		11.48	54.30
GG 2nd STAGE	3.29	9.70*	+9.06	22.05
PT 1st STAGE	---		14.63	14.63
PT 2nd STAGE	---		4.60	4.60
STEAM TURBINE REHEAT				
ST/PT FW FOR STEAM	---		1.41	1.41
ST STEAM	---		39.85	39.85
TOTAL	501.31		238.72	740.03
% FUEL	67.74		32.26	100
LBS FUEL/LB AIR**	0.025881		0.012324	0.03820
TA** - %	260.89		176.76	176.76

NOTES: *Assuming Breakdown of Heating Between Combustors for Mixing
**Based on 19,370 BTU/LB and 14.81 LB Air/LB Fuel for 100% TA
See Final Page for SI Conversion Factors

Table 8 Cycle power output breakdown

	BTU/LB AIR			
	GAS TURBINE			STEAM TURBINE
STEAM TURBINE				
BASIC OUTPUT (NO COOLING STEAM)				108.76
COOLING STEAM (TOPPING)				18.17
GAS TURBINE		272.73		
AIR CYCLE				
COOLING STEAM (GG ONLY)				
1st STAGE (GG - 4%)	13.98			
2nd STAGE (GG - 2%)	1.89	(16.36)*		
EXTRA FUEL	.49			
COOLING STEAM (PT ONLY)				
1st STAGE (GG - 4%)	17.81			
2nd STAGE (GG - 2%)	8.90			
1st STAGE (PT - 1¼%)	6.55	36.82		
2nd STAGE (PT - ¾%)	1.64			
EXTRA FUEL	1.92			
TOTAL GROSS		309.55		126.93
2% LOSS		−6.19		−2.54
BOILER FEED PUMP		---		−2.90
TOTAL NET OUTPUT		303.36		121.49
% OF TOTAL		71.40		28.60
TOTAL NET OUTPUT GT & ST			424.85	

NOTES: *Work for Compression - Not to be Included for Output
See Final Page for SI Conversion Factors

Cycle-Power-Output Breakdown. In calculating the power output of the cycle, like calculating the fuel input, many steps are necessary and care has been taken with each step. Now that a logical approach has been formulated, a sophisticated computer program can be written to obtain faster and very accurate answers for any preselected value of cooling-steam flow, compressor efficiency or expansion efficienty. There would be very little advantage to writing such a program, however, until lab-rig tests are run on the steam cooling; empirical input is needed.

Table 8 presents a breakdown of the power components of both the gas turbine and steam turbine. It can be noted that the work developed by the steam in the GG (16.36 BTU/lb) to help drive the air compresor and thus raise the RH pressure has not been included in the output.

The power developed by each stage of steam cooling/injection is listed to arrive at a total PT component of 36.82 BTU/lb air. The total output is shown to be 309.55 BTU/lb air.

Looking at the steam turbine, 108.76 BTU/lb air is developed by the main steam flow through the steam turbine with extraction for feed-water heating and flow to the condenser of 0.886 lb/lb steam. The work developed by the GT-cooling steam as it passes through the steam turbine prior to extraction plus that which is required for feed-water heating is calculated to be 18.17 BTU/lb air. This is pure noncondensing topping power as far as the steam turbine is concerned. This, however, assumes that the stack loss is charged to the gas turbine.

The net output calculates to be 424.85 BTU/lb air when appropriate losses are subtracted. All the losses and output summations are shown on the heat-balance diagram of Fig. 13.

Cooling-Steam Heat Balance. A sample heat balance of the GG first-stage-nozzle cooling steam is given in Table 9. The gas turbine/steam turbine flow diagram (including steam values) is given in references [5] and [7]. It can be seen that the cycle efficiency calculates to be 46.58 percent LHV which is notably above that of the reheat-steam-turbine efficiency (40.43 percent LHV, Fig. 2). The various work components and fuel inputs are all listed. The only cycle loss associated with the balance is the stack loss which includes the latent heat down to an enthalpy of 70 BTU/lb, the starting point.

Downloaded 01 Jun 2010 to 171.66.16.62. Redistribution subject to ASME license or copyright; see http://www.asme.org/terms/Terms_Use.cfm

Table 9 Cooling steam heat balance GG first stage nozzle steam

	BTU/LB THROTTLE STEAM INPUT	OUTPUT
1. NO. 1 COMBUSTOR FUEL, $f_{1\text{-}2}$	1024.24	---
2. NO. 2 COMBUSTOR FUEL, $f_{2\text{-}4}$	274.68	---
3. FW REHEAT FUEL, $f_{2\text{-}2}$	22.40	---
4. PSEUDO HEAT EX FUEL, f_3	675.73	---
5. BOILER FEED PUMP	10.00	---
6. GG WORK DEVELOPED	---	334.46
7. PT WORK DEVELOPED	---	425.96
8. STEAM TURB WORK DEV		
HP TURB	---	136.22
IP TURB	---	18.23
LP TURB (FW)		
FW HTR NO. 3	---	4.20
FW HTR NO. 2	---	10.05
FW HTR NO. 1	---	7.42
9. STACK LOSS - 300°F to 70h	---	1074.07
10. CLOSURE - LEAKAGE, ETC.	3.56	---
TOTAL	2010.61	2010.61

11. CYCLE EFF (LHV) = $\frac{936.54}{2010.61}$ = .4658

NOTE: See Final Page for SI Conversion Factors

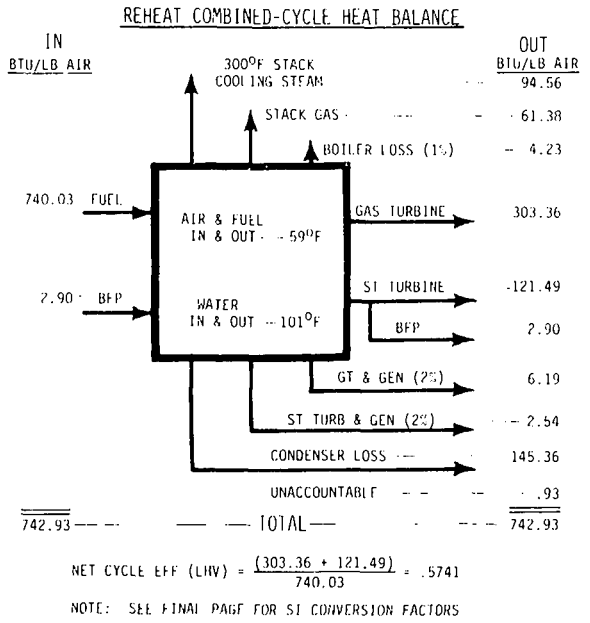


Fig. 13 HTTT reheat-gas-turbine combined-cycle heat balance

Combined-Cycle Efficiency Comparison

The final comparison step can now be taken: to compare the overall combined-cycle efficiency of the reheat-gas-turbine cycle to that of the simple cycle.

Reference is made to Fig. 14 which is a plot of combined-cycle efficiency versus cycle-inlet temperature. The top solid line represents calculated values for the reheat-gas turbine for increasing inlet temperatures. The very top black dot pinpoints the 57.4 percent efficiency calculated for the nominal 2600°F inlet temperature.

The curve is extended by dashed lines as a projection. It appears that the cycle efficiency will peak out at about 2725°F for steam cooling.

The lower dashed line represents comparable estimates of cycle efficiencies when employing water cooling with a simple-cycle gas turbine. It appears that the cycle will peak out at about 2600°F, about 100°F lower than for the reheat cycle. The overall combined-cycle efficiency, however, is much lower by about 12.5 percent (6.4 percentage points).

The top dashed line represents reheat-gas-turbine combined-cycle efficiency improvements possible by going to higher steam-turbine temperatures, for instance 1050/1100°F reheat. The gas-turbine-reheat cycle proposed lends itself to increasing these steam temperatures better than the simple cycle because of the latter's degradation caused by the steam reheater and need for greater low-pressure-steam flow from the flasher to the LP section fo the steam turbine.

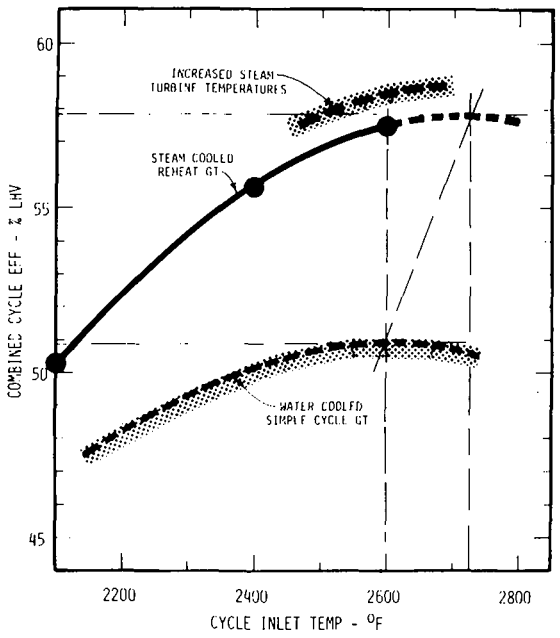


Fig. 14 Combined-cycle efficiency versus cycle-inlet temperature for both simple-cycle and reheat-cycle gas turbines

Heat Transfer Considerations

Advanced-turbine technology requiring higher compressor pressure ratios and turbine-inlet temperatures for increased performance has led to the necessity of providing some form of equipment cooling. Air or steam-cooling schemes must be developed in order to preserve the integrity of the turbine components in the hot combustor-gas environment.

A complete energy balance on the blade must be made in any turbine-cooling design to arrive at a cooling configuration which meets the given blade-metal-temperature limit. The analysis can be broken up into three parts in order to provide this energy balance which encompasses all aspects of blade cooling: 1) the formulation of the complex internal coolant-flow paths for the convection-heat-transfer calculations, 2) a heat-conduction analysis in order to detail the blade-metal temperatures for mechanical considerations, and 3) a scheme to predict the heat flux to the turbine blades from the hot-gas stream.

Several areas of flow interaction must be obtained or predicted in order to develop a blade-heat-flux scheme. These areas are: an understanding of the boundary-layer development over the airfoil, the potential flow-velocity distribution, the temperature profile of the gas leaving the combustor-transition section and the location of the transition of the boundary-layer transition region. The complete heat-transfer process (convection from hot gas to the first-stage blades, conduction through the blade wall and convection from the blade to the coolant) must be treated

Downloaded 01 Jun 2010 to 171.66.16.62. Redistribution subject to ASME license or copyright; see http://www.asme.org/terms/Terms_Use.cfm

simultaneously in order to provide a closed-form solution of the energy-balance problem.

A limit to the capabilities of plain-convection cooling is evident due to limited internal-passage size and the restriction on the quantity of cooling fluid available. The limit in the applications of advanced cooling is about 1644°F (2500°F) hot-spot turbine-inlet temperatures and about 20 atmospheres pressure. Cooling designs must incorporate some form/combination of film or transpiration cooling to exceed these gas conditions while maintaining reasonable operating blade-metal temperatures.

Film cooling is an effective way to protect the surface from the hot-gas stream by directing cooling air into the boundary layer to provide a protective cool film along the blade surface. The injection of film air into the boundary layer, however, causes turbine aerodynamic losses which tend to reduce some of the advantages of using higher pressures and temperatures. The aerodynamic and heat-transfer designs must be integrated to achieve an optimum configuration that ensures blade-metal temperatures compatible with long blade life and yet minimizes the turbine-efficiency losses.

Transpiration cooling used with porous-blade wall is the most efficient air-cooling scheme available; however, it has several weaknesses which limit its use to advanced turbine designs operating under extreme temperature conditions. The inlet pores should be small for efficient transpiration, which leads to problems of blockage due to contaminates and possible blade oxidation. Also, the aerodynamic losses can be severe because of the perpendicular injections of cooling air into the boundary layer. It should be noted, however, that transpiration cooling requires less cooling air than other identified schemes.

Much R & D work is needed in order to utilize steam as a coolant in the reheat-combined-cycle configuration. The basic theoretical concepts associated with using steam as a coolant in the turbine cycle must be developed. Experimental data also is needed to validate this analysis; however, with continued efforts, the state-of-the-art of blade cooling will be extended to the point where the higher-level technology can then be used to solve our energy problems.

Summary

In summary, the reheat-gas-turbine combined cycle studied has been shown to have many advantages and is worthy of in-depth pursuit with test-rig R & D. The only notable disadvantage found, other than mechanical and control complication, is the extra feedwater make-up required which is counter-balanced by far less cooling-tower evaporation and blow down.

Conclusion

The following conclusions are drawn from this paper based on the assumptions made and the graphs and tables presented:

1 The RHCC, due to its higher CPR and reheat function would produce a higher coal pile to bus-bar efficiency when burning low-BTU gas from a high-pressure gassifying process.

2 The steam-cooled RHGT-combined cycle is projected to have approximately 12.5 percent higher cycle efficiency than the water-cooled simple-cycle DOW/TRV cycle for a nominal 2600°F inlet temperature; the RHGT combined-cycle lefficiency calculates to be 57.4 percent - LHV.

3 The steam-cooled RHGT will produce 50 percent more power per pound of air flow than the water-cooled simple-cycle GT.

4 The first-stage blade surface to be cooled on the RHGT is calculated to be 70 percent less than that of the simple-cycle GT.

5 The first-stage side-wall area to be cooled on the RHGT is calculated to be 70 percent less than that of the simple-cycle GT.

6 The first-stage nozzle-ring volume is calculated to be 90 percent less for the RHGT compared to the simple cycle; the first-stage strategic material required would be less by a corresponding amount.

7 The RHGT-CC steam-turbine low-pressure section would be 45.6 percent smaller.

8 The RHGT-CC condenser and cooling tower physical sizes would each be 45.6 percent smaller; the cooling-tower water make-up would be 45.6 percent less.

9 The ratio of gas-turbine power to steam-turbine power would be higher for the RHGT CC—2.50 versus 1.63 for the SCGT CC—giving credit for the SCGT CC air-boost compressor.

10 The RH gas-turbine back pressure to the heat-recovery boiler would be less—14″ versus 22″ H_2O—due to less steam-generation heat-transfer surface being required.

11 There would be less steam-generation heat-transfer surface required for the RHGT CC; the superheater and economizer would encounter higher differential temperatures to reduce the surface required. The steam reheater would likewise encounter higher temperature differentials and would also have better heat-transfer coefficients at the elevated eight atmospheres of the RH combustor.

12 There would be more growth in the RHGT CC before peaking out, perhaps 200°F delta TIT.

13 The RHGT lends itself better to increasing the steam-turbine inlet temperatures to further increase cycle efficiency.

14 The RHGT CC would require approximately 2.75 times more boiler-water make-up in terms of cycle output.

15 The RHGT CC would require extensive Research and Development; steam-cooling rig tests would be required to verify and optimize the design and flow rates; the steam-cooled gas generator would require development along the lines of the NASA E^3 engine. Mathematical heat-transfer equations based on empirical data not yet available would be needed.

Conversion factors for standard international (SI) units

	Multiply	By	To Obtain	
(in)	inch	2.54×10^{-6}	meter	(m)
(ft)	feet	.3048	meter	(m)
(lbs)	pounds (mass)	.4535924	kilograms	(Kg)
(psi)	pounds per square inch	6894.757	Newtons per square meter	(N.m/m)
(psia)	pounds per square inch absolute	6894.757	Pascal	(Pa)
(fps)	feet per second	.3048	meters per second	(m/s)
(BTU)	British thermal units	1055.056	Joules	(J)
(BTU/lb)	British thermal units per pound	2326.000	Joules per kilogram	J/Kg
(°F)	degrees Farenheit	$\frac{°F + 459.67}{1.8}$	Kelvin	(K)
(°F)	degrees Farenheit	$\frac{°F-32}{1.8}$	Celsius	(°C)

Downloaded 01 Jun 2010 to 171.66.16.62. Redistribution subject to ASME license or copyright; see http://www.asme.org/terms/Terms_Use.cfm

16 The DOE/TRV SCGT CC may be father along in U.S. development than the RHGT CC with possibly fewer unknowns and with problem areas more specifically defined; however, the greater number of advantages of the RHGT CC, particularly those relating to cycle efficiency, are so compelling that the RHGT CC deserves meaningful parallel U.S. Research and Development.

Acknowledgments

Appreciation is expressed to Carolyn Keyes Rice for editing the script, lettering the graphs, arranging the material, and typing the mats. Also acknowledgment is given to the Texas A & M University Gas Turbine Laboratories for interest expressed in the reheat-combined cycle and the R and D work underway there in studying the heat transfer parameters of steam-film cooling.

References

1 Caruvana, A., Rose, R.S., Alderson, E.D., and Cincotta, G.A., "Design and Test of a 73-MW Water-Cooled Gas Turbine," ASME Paper No. 80-GT-112.

2 "Alternate Fuels," *Oil and Gas Journal*, June 16, 1980, pp. 55-68.

3 Rice, I.G., "The Combined Reheat Gas Turbine/Steam Turbine Cycle," Part I - "A Critical Analysis of the Combined Reheat Gas Turbine/Steam Turbine Cycle," ASME Paper No. 79-GT-7, ASME JOURNAL OF ENGINEERING FOR POWER, Jan. 1980.

4 Rice, I.G., "The Combined Reheat Gas Turbine/Steam Turbine Cycle," Part II - "The I.M 5000 Gas Generator Applied to The Combined Reheat Gas Turbine/Steam Turbine Cycle," ASME Paper No. 79-GT-8, ASME JOURNAL OF ENGINEERING FOR POWER, Jan. 1980

5 Rice, I.G., "Steam-Cooled Blading in a Combined Reheat Gas Turbine/Reheat Steam Turbine Cycle," Part I - "Performance Evaluation," ASME Paper No. 79-JPGC-GT-2.

6 Rice, I.G., "Steam-Cooled Blading in a Combined Reheat Gas Turbine/Reheat Steam Turbine Cycle," Part II - "Design Considerations," ASME Paper No. 79-JPGC-GT-3.

7 Rice, I.G., "The Reheat Gas Turbine with Steam-Blade Cooling - A Means of Increasing Reheat Pressure, Output and Combined-Cycle Efficiency," ASME Paper No. 81-GT-30.

8 Johnston, R.P., and Ortiz, P., "Future Trends in Subsonic Transport Energy-Efficient Turbo-fan Engines," ASME Paper No. 80-GT-177.

9 Gray, D.E., and Gardner, W.B., "The Energy-Efficient Engine (E^3) - Advancing the State-of-the Art," ASME Paper No. 80-GT-142.

10 Jenkins, P.E., and Rice, I.G., "Blading Heat Transfer Considerations in a Reheat-Gas Turbine Combined Cycle," ASME Paper No. 81-GT-155.

11 Clark, J.S., "Status of the DOE/NASA Critical Gas Turbine R & T Project," ASME Paper No. 80-GT-104.

12 Larson, J.W., "Survey of Integrated-Gasification Combined-Cycle Power-Plant-Performance Estimates," ASME Paper No. 80-GT-113.

13 Horner, M.W., Day, W.H., Smith, D.P., and Cohn, A., "Development of A Water-Cooled Gas Turbine," ASME Paper No. 78-GT-72.

14 Fraize, W., and Lewis, J., "Technical and Economic Objectives for the Development of Advanced Combined Cycles for Use With Coal-Derived Fuels," ASME Paper No. 78-GT-101.

15 Mogul, J.M., Cole, R.W., and Manning, G.B., "Design of A High-Efficiency Combined-Cycle Electric Power Plant for Low BTU Coal-Gas," ASME Paper No. 78-GT-125.

16 Rieke, K.L., and Wander, S.M., "Program to Establish Ceramic Technology Readiness for Large Combustion Turbine Utility Application," ASME Paper No. 78-WA-GT-8.

Addendum

The authors have received a number of favorable verbally-expressed comments on the paper following the presentation at the Houston Conference and during the ensuing months. However, there seems to be a reluctance to put these comments in writing to appear in the *Transactions*. The following points, thus, are presented as addendum.

Steam-blade cooling has not been explored in depth and, as pointed out in the paper, when steam cooling/injection is applied to the reheat-gas-turbine gas generator an entirely different combined-cycle efficiency emerges than when applied to a simple-cycle gas turbine. The combined-cycle efficiency is increased instead of being decreased. Studies of steam cooling in the past have centered around the simple-cycle gas turbine.

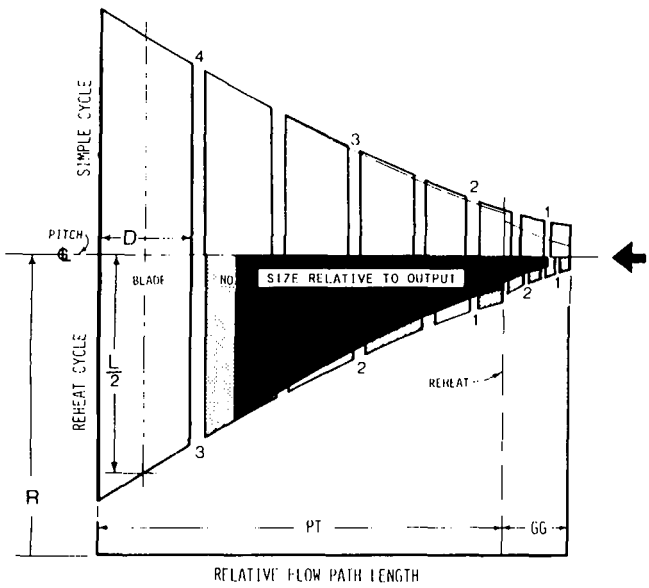


Fig. 15 Diagram showing relative size of simple-cycle and reheat-cycle gas turbine blading with respect to gas turbine output

Efficiency numbers for compression and expansion used in the paper were conservative for values being realized with the emerging E^3 technology for variable geometry twin-spool aero-derivative gas generators. An adiabatic compression of 89 percent for the low-pressure spool and 88 percent for the high-pressure spool would be more appropriate for compression instead of 88 percent used in the paper. Also an "uncooled" isentropic-expansion efficiency of 91 percent would be more realistic instead of 89 percent. These improved component efficiencies would appreciably raise the combined-cycle efficiency of the reheat-gas turbine. However, appropriate inlet and exhaust pressure losses should be applied.

The section in the paper on blade size, surface, and volume comparison relates to equal gas-path mass flow. A more meaningful comparison can be made relative to gas-turbine output. The data of Table 1 and as plotted in Fig. 7 indicate that the air portion of the water-cooled simple-cycle gas turbine will produce 186.72 BTU/lb of air whereas the air of the steam-cooled reheat-gas turbine will develop 272.73

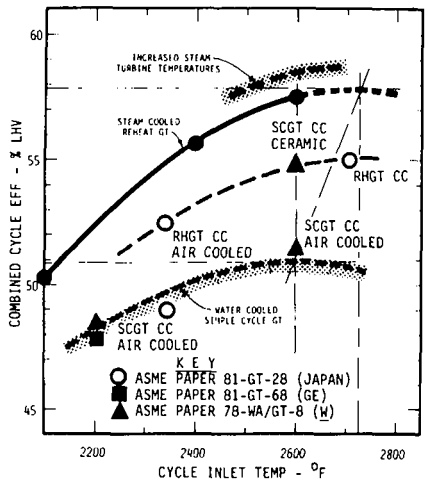


Fig. 16 Combined-cycle efficiency versus cycle-inlet temperature for both simple-cycle and reheat-cycle gas turbines with superimposed data points taken from recent ASME publications

Downloaded 01 Jun 2010 to 171.66.16.62. Redistribution subject to ASME license or copyright; see http://www.asme.org/terms/Terms_Use.cfm

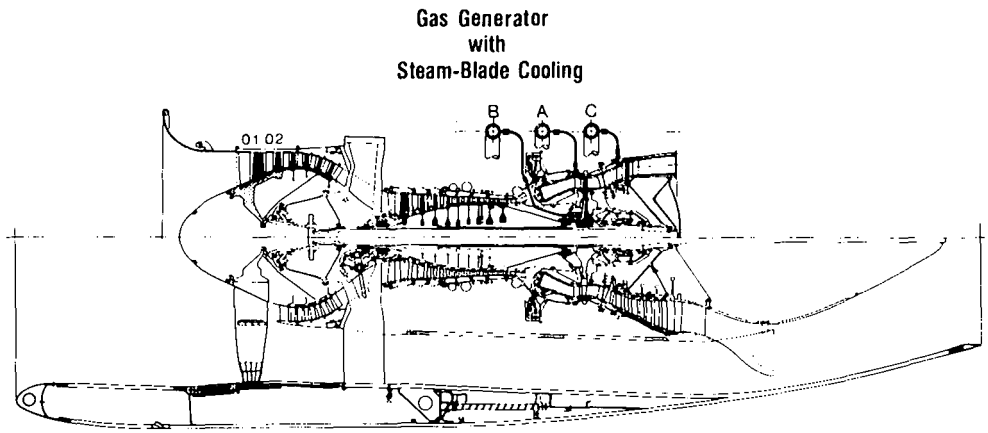


Fig. 17 Cross section of the E^3 aircraft-gas turbine shown on the bottom half with the top half showing conceptual modifications to form a steam-cooled gas generator

BTU/lb of air. Therefore, the ratio of these two numbers shows that it will take only 0.685 times as much air for the reheat cycle to yield the same output. The hot-gas length and blading size of the reheat-gas turbine are reduced by this ratio when comparing equal output. Fig. 15 clearly shows this reduction not only for the gas generator but also for the power turbine. The reduction in surface area and volume is appreciable when considering the cube law being involved.

The combined-cycle efficiency graph, Fig. 14, for the simple-cycle gas turbine can be substantiated by transposing in terms of LHV data points taken from recent ASME technical papers, two of which were presented at the Mar. 1981 ASME Gas Turbine Conference [17, 18]. Also, data from an earlier paper [16] correlate very well with the simple-cycle curve of Fig. 14 as can be noted in Fig. 16 of this addendum.

An all ceramic simple-cycle gas-turbine point is given in Fig. 16 for a 2600°F TIT. Although no such gas turbine is available today or expected in the near future, this point does show the simple-cycle degradation in combined-cycle efficiency due to blade cooling – either by air or water. If an all ceramic gas turbine were possible, then such a turbine when applied to the reheat cycle is projected to yield a combined-cycle efficiency well over 60 percent LHV.

The Japanese intercooled RHGT-CC data points taken from the aforementioned paper [17] indicate that the dashed trend curve of efficiency correlates very well with the non-intercooled RHGT-CC. The lower efficiency of the Japanese cycle is due to degradation brought about by the additional intercooling loss that is rejected out the stack. Nevertheless, the Japanese RHGT-CC efficiency is substantially higher than the SCGT-CC efficiency.

Finally, Figure 17 shows conceptually how the E^3 aircraft-gas turbine-development engine could be modified to obtain a steam-cooled-gas generator. The fan is removed and "zero" compressor staging is substituted. Cooling steam is introduced to the nozzle vanes and rotating blades through steam headers A, B and C and connecting-flexible-feed lines as shown.

Additional References

17 Hori, A., and Takeya, K., "Outline of Plan for Advanced Research Gas Turbine," ASME Paper No. 81-GT-28.

18 Rose, R. S., et al., "Application of Water Cooling for Improved Gas Turbine Fuel Flexibility and Reliability," ASME Paper No. 81-GT-68.

Downloaded 01 Jun 2010 to 171.66.16.62. Redistribution subject to ASME license or copyright; see http://www.asme.org/terms/Terms_Use.cfm

Full Potential Solution of Transonic Quasi-Three-Dimensional Flow Through a Cascade Using Artificial Compressibility

C. Farrell

J. Adamczyk

National Aeronautics
and Space Administration
Lewis Research Center
Cleveland, Ohio 44135

A reliable method is presented for calculating the flowfield about a cascade of arbitrary two-dimensional airfoils. The method approximates the three-dimensional flow in a turbomachinery blade row by correcting for streamtube convergence and radius change in the throughflow direction. The method is a fully conservative solution of the full potential equation incorporating the finite volume technique on a body-fitted periodic mesh, with an artificial density imposed in the transonic region to ensure stability and the capture of shock waves. Comparison of results for several supercritical blades shows good agreement with their hodograph solutions. Other calculations for these profiles as well as standard NACA blade sections indicate that this is a useful scheme for analyzing both the design and off-design performance of turbomachinery blading.

Introduction

Some very useful tools for the study of transonic flows have been developed during the last few years. Conservative schemes, finite volume, and artificial density have all contributed to accelerating progress in this area. Each has been applied to the analysis of external flow over isolated airfoils in two and three dimensions with promising results.

In the area of internal flows the need to design lighter, more efficient turbomachine components has led to consideration of machines with fewer stages, each with blades capable of higher speeds and higher loading. As speeds increase, the numerical problems inherent in the transonic regime have to be resolved. These include the calculation of imbedded shock discontinuities and the dual nature of the governing equations, which are elliptic in the subcritical flow regions but become hyperbolic for supersonic zones. The development of supercritical blade design has eliminated some of these difficulties by returning to the hodograph plane and explicitly designing blades that will be shock free. However, unlike the case of external wing aerodynamics, undesirable off-design conditions can develop much faster in turbomachinery flows and are not readily controlled or easily corrected. For these reasons the study of off-design conditions (high incidence, shocks, etc.) will remain a major requirement for internal flows. In addition, the periodic nature of the geometry for turbomachine components adds another degree of complexity which contributes to the importance of grid generation as another area of study in its own right.

Contributed by the Gas Turbine Division and presented at the International Gas Turbine Conference and Products Show, Houston, Texas, March 9-12, 1981, of THE AMERICAN SOCIETY OF MECHANICAL ENGINEERS. Manuscript received at ASME Headquarters, December 8, 1980. Paper No. 81-GT-70.

The present analysis combines some of the most promising transonic analysis techniques to calculate the flowfield surrounding a cascade of airfoils. The full potential equation in conservative form has been discretized at each point on a body-fitted periodic mesh and a mass balance calculated through the finite volume surrounding the point. Each local volume is corrected in the third dimension for any change in streamtube thickness along the streamtube. Each is also corrected in the tangential $y\,(r\theta)$ direction due to any change in the radial position of the streamtube from upstream to downstream. The final result is a tridiagonal matrix formulation involving potential corrections at each grid point as the unknowns. The right hand side of each equation is equal to the net mass flux through a volume. The resulting system of equations is solved along each grid line by an SLOR procedure. At points where the Mach number exceeds unity, the density at the forward (sweeping) edge of the volume is replaced by an artificial density as suggested in reference [1]. This artificial density is a function of the real gas density and its streamwise derivative.

In the following sections, two body-fitted mesh generators that were incorporated into the resulting computer code are discussed. The full potential equation in finite difference form is also reviewed along with details on the solution method employed. Subsonic and transonic calculations using this method on a NACA 0012 profile are compared to other computational procedures. Results for several supercritical blade designs of Sanz are compared to their hodograph solutions. The quasi-three-dimensional capabilities of the method are compared to results from reference [9].

Mesh Generation

The flowfield is discretized using a body-fitted, periodic 0-

Copyright © 1982 by ASME

Downloaded 01 Jun 2010 to 171.66.16.62. Redistribution subject to ASME license or copyright; see http://www.asme.org/terms/Terms_Use.cfm

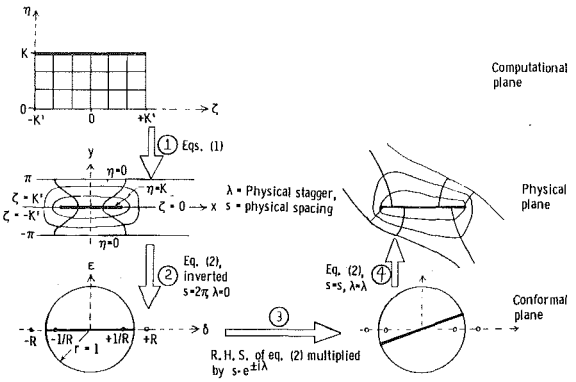


Fig. 1(a) Analytical transformation steps for near-orthogonal grid development

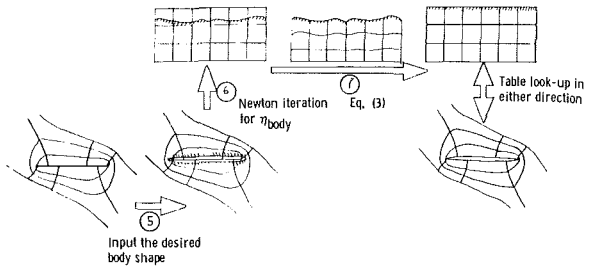


Fig. 1(b) Interpolation and shear transformation steps for near-orthogonal grid development

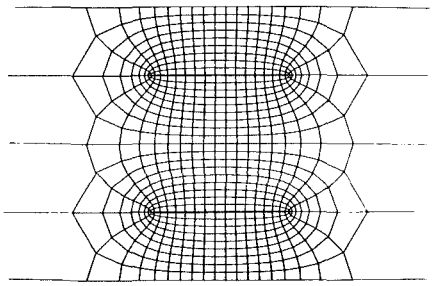


Fig. 2 Flat plate casade at zero stagger

type mesh. Two techniques were developed to generate computational grids. The original grid generation technique, referred to here as the interpolation scheme, is near-orthogonal and combines the use of analytical functions, interpolations, and simple stretchings. No numerical system must be solved for the generation of the grid. The second method, an electrostatic analog, was developed when the grids generated by the interpolation scheme were found to be unsatisfactory for cascades of high camber, thickness, and solidity.

Interpolation Scheme. A summary of this procedure is shown in Fig. 1. As suggested in reference [2], beginning with the orthogonal, computational plane,

$$-K' < \zeta < +K' \qquad 0 < \eta < K$$

the transformation to a physical (x,y) plane as described by the Jacobian elliptic functions, *sn*, *cn*, and *dn*(3), is given as:

Nomenclature

A = (equations (20), (22)), variable coefficient of change in potential for field equation (equations (27), (28)), flow area normal to the streamchannel direction

A_E = (equation (19)), total surface area of finite volume element

a = contravariant velocity component (η direction) in computational space

b = contravariant velocity component (ζ direction) in computational space

C = circulation about the airfoil as defined by the given values of flow angle

c = blade chord

c_x = length of passage along x-axis, from leading edge to trailing edge when blade is at setting angle

F = tabular function of body shape (x, y) pairs

G = transposed terms in field equation involving known (previously determined) potential corrections

h = local streamtube height normalized to unity far upstream

K = complete elliptic integral of the first kind for (k^2)

$$\int_0^{\pi/2} dt/\sqrt{1-k^2 \sin^2 t}$$

K' = complete elliptic integral of the first kind for $(1-k^2)$

$\mathcal{K}$ = complex electro-static potential field generated by infinite array of point charges

k = $e^{-(\pi c)/(s \cos \lambda)}$ parameter, defined by cascade geometry, for obtaining Jacobian elliptic functions

L = full potential operator, (equation (17))

ℓ = length of bounding surfaces for finite volume (see Fig. 8)

M = Mach number

m = k^2

$\hat{n}$ = unit vector, normal to airfoil surface

q = magnitude of flow speed, normalized to unity at far upstream conditions

R = residual net mass flow out of a finite volume using potential values from previous iteration, (equation (19))

$\mathcal{R}$ = $R + G$, total residual right hand side for field equation at each volume

r = local spanwise radial position of streamchannel normalized to unity far upstream

S = flow direction as defined by contravariant velocities a and b in equation (25)

s = blade spacings

T = a combination of Jacobian elliptic functions, defined in equation (1)

u = x-component of velocity in the physical plane

V = total physical velocity vector, $u\hat{i} + v\hat{j}$, (equation (31))

v = y-component of velocity in the physical plane

X = physical position coordinate along a line of constant η

x = streamwise position coordinate, i.e., in Fig. 4 x-axis is horizontal

Y = physical position coor-

Downloaded 01 Jun 2010 to 171.66.16.62. Redistribution subject to ASME license or copyright; see http://www.asme.org/terms/Terms_Use.cfm

$$x = \frac{s}{2\pi}\left[\ln\frac{1}{k} - 2\ln\frac{T}{\Gamma}\right]$$

$$y = \frac{s\Omega}{\pi}$$

where

$$k = e^{-\frac{\pi c}{s\cos\lambda}}$$

and

λ = stagger angle
s = blade spacing
c = chord

$$T = [(sn(\eta,m)\cdot dn(\zeta,m_1))^2 + (cn(\eta,m)\cdot dn(\eta,m)\cdot sn(\zeta,m_1)\cdot cn(\zeta,m_1))^2]^{1/2}$$

$$\Gamma = cn^2(\zeta,m_1) + m\cdot sn^2(\eta,m)\cdot sn^2(\zeta,m_1)$$

$$\Omega = \tan^{-1}\left\{\frac{cn(\eta,m)\cdot dn(\eta,m)\cdot sn(\zeta,m_1)\cdot cn(\zeta,m_1)}{sn(\eta,m)\cdot dn(\zeta,m_1)}\right\}$$

$$m = k^2$$

$$m_1 = 1 - k^2$$

(1)

with K, the complete elliptic integral of the first kind for m,$K(m)$ and

$$K' = \int_1^{1/k} \frac{dt}{\sqrt{(t^2-1)}\sqrt{1-k^2t^2}} = K(m_1)$$

The specified geometric parameters of chord, stagger angle, and blade spacing are sufficient to perform the analytical transformations described by equations (1). After computing K and K' for a blade spacing of $s = 2\pi$ and for zero stagger, values of η and ζ are then selected at equal intervals (or at

Nomenclature (cont.)

dinate along a line of constant ζ
y = tangential position coordinate, i.e., in Fig. 4 y-axis is vertical
z = coordinate to transform a physical point to complex plane, $z = x + iy$
z_a = coordinate of beginning of one line segment. Blade is divided into segments in solving for electrostatic analog grid.
z_b = coordinate at the end of a segment of the blade surface
z_0 = coordinate of zeroth charge for electrostatic analog
α = incidence angle of flow as measured from chordline of blade
β = angle of flow as measured from x-axis
γ = ratio of specific heats
$\gamma(z_0)$ = (electrostatic analog grid procedure); source density distribution
Γ = defined in equation (1)
δ = abscissa coordinate in the plane of the conformal circle transformation (interpolation scheme, equation (2))
$\delta\phi$ = change in the local potential field, the unknowns in equation (18)
ϵ = ordinate in conformal transformation plane (equation (2))
ζ = coordinate in computational space whose contours in physical space radiate from the blade and terminate on the periodic boundary
η = coordinate in computational space whose physical contours surround the airfoil
θ = tangential coordinate in radians, $y = r\theta$
λ = stagger or setting angle of the blade row, as measured from x-axis to chordline
μ = switch function to control the artificial density modification (equation (24))
π = 3.14159265
ρ = physical density
$\tilde{\rho}$ = artificial density as described in equation (23)
ϕ = flow velocity potential function
ψ = electrostatic potential function due to charge distribution on blade surface (equation (6))
ω = over-relaxation parameter, $1 < \omega < 2$
Ω = defined in equation (1)

Subscripts

i = position on computational plane in ζ-direction
j = position on computational plane in η-direction
x = differentiation with respect to streamwise position coordinate, x
y = differentiation with respect to tangential coordinate, y
ζ = differentiation with respect to ζ
η = differentiation with respect to η
$-\infty$ = conditions at far upstream station
$+\infty$ = far downstream conditions

Superscripts

n = artificial time step (iteration level)
$-$(bar) = (equation (19) and Fig. 8) average over the length, ℓ, of the velocity component normal to the element surface along ℓ

Downloaded 01 Jun 2010 to 171.66.16.62. Redistribution subject to ASME license or copyright; see http://www.asme.org/terms/Terms_Use.cfm

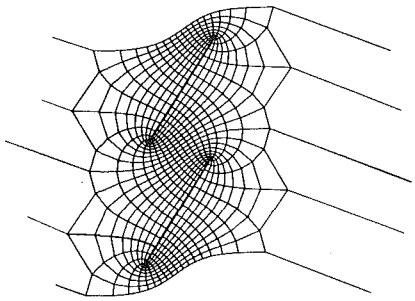


Fig. 3 Flat plate cascade rotated to desired stagger angle

weighted intervals if the grid is to be dense near the body or at the trailing edge). Tables of (x,y) for corresponding (ζ,η) points are generated using equations (1). In the Cartesian plane this gives an orthogonal coordinate system about a cascade of flat plates at zero stagger. An example is shown in Fig. 2. From this, the conformal transformation to a circle is [4],

$$z=x+iy=\frac{s}{2\pi}\left[e^{-i\lambda}\ln\left(\frac{\xi+R}{\xi-R}\right)+e^{i\lambda}\ln\left(\frac{\xi+1/R}{\xi-1/R}\right)\right] \quad (2)$$

where $\xi = \delta + i\epsilon$ in the circle plane, and the stagger, λ, is zero.

Equation (2) is easily inverted to obtain (δ,ϵ) tables if

$$\lambda=0$$

$$s=2\pi$$

which was the justification for the original calculations of K and K' noted above. The parameter R in equation (2) represents the locations of the up-stream and downstream infinity points in the conformal plane. It is a function of cascade solidity (c/s) and stagger angle and can be interpolated from information in reference [4] for the specified values of stagger and spacing. This same R is used in calculating (δ,ϵ) for the zero stagger transform.

The resulting circle is then rotated by applying the exponential terms with the correct stagger and desired spacing, s, to equation (2). The calculated values of z in the Cartesian plane then give an orthogonal grid about a flat plate cascade at the desired stagger angle and solidity. Figure 3 is an example of such a mesh.

The final step in generating this computational mesh is the adjustment of the flat plate grid so that the innermost ellipse coincides with the specified blade shape. This is accomplished by performing a straightforward Newton iteration along each line of constant ζ which intersects the flat plate. The three unknowns to be determined at the intersection of each ζ-line and the body are x, y, and η. The three equations required are equations (1) and

$$y=F(x)$$

where F is a tabular function giving the specified body shape.

A successful iteration yields $(x,y)_{\text{body}}$ and η_{body} where

$$0<\eta_{\text{body}}<K$$

for most blades surfaces, or

$$0<K<\eta_{\text{body}}$$

for the pressure surface of blades whose chordline lies outside the blade. The coordinates $(x,y)_{\text{body}}$ replace the point on the flat plate where the ζ-line ended. All other grid points on this ζ-line are shifted by means of a simple linear stretching function that reflects the revised length of the ζ-line:

$$x_i=\frac{K-\frac{\eta_{\text{body}}}{K}\cdot\eta_i}{K-\eta_i}(x_i-x_{\text{plate}})+x_{\text{plate}} \quad (3)$$

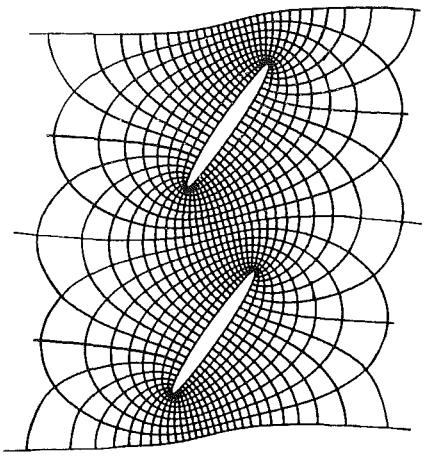


Fig. 4 Near-orthogonal mesh for a symmetric blade

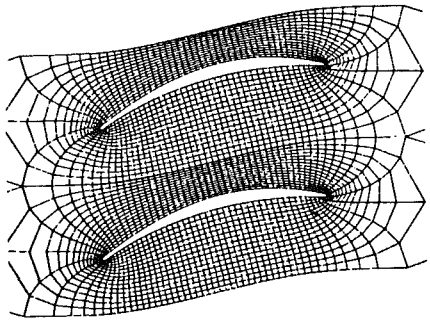


Fig. 5 Near-orthogonal mesh for a double circular arc compressor stator

and similarly for each y_i. Completed grids are seen in Figs. 4 and 5 for several typical blade shapes. This mesh generation scheme has no problem with larger stagger angles ($\simeq$75 deg) nor with high solidities. Cases with $c/s = 1.45$ have been attempted with good results. However, if the turning angle or camber of the blade is high, while at the same time, stagger and solidity are near the limits mentioned above, the grid lines may become crowded on the suction surface. This is common for turbine blade geometries.

Electrostatic Analog. An electrostatic analog has been developed to generate body-fitted orthogonal grids for cascades of large turning thickness and solidity. The development of this grid generation scheme begins by considering the potential field generated by an infinite spacial array of point charges in free space. The density of the charges is assumed to alternate between plus and minus one. The mathematical expression for this field is given by

$$\mathcal{K}(z-z_0)=\sum_{n=-\infty}^{\infty}(-1)^n\ln(z-z_0-\text{ins}) \quad (4)$$

where $\mathcal{K}(z-z_0)$ is the complex potential, $z = x + iy$, z_0 the location of the 0^{th} charge, $i=\sqrt{-1}$, and s the distance between charges. Equation (4) can be evaluated in closed form by utilizing the theory of calculations of residues [5]. The result is

$$\mathcal{K}(z-z_0)=\sum_{n=-\infty}^{\infty}(-1)^n\ln(z-z_0-\text{ins})=\ln\tanh\frac{(z-z_0)\pi}{2s} \quad (5)$$

Downloaded 01 Jun 2010 to 171.66.16.62. Redistribution subject to ASME license or copyright; see http://www.asme.org/terms/Terms_Use.cfm

(Note that this expression is periodic in y with period $2s$.) The potential field generated by distributing these fundamental solutions over the surface of an airfoil in the cascade is given by the integral

$$\psi(z) = \int_L \gamma(z_0)\mathcal{K}(z-z_0)dz_0 \tag{6}$$

where $\gamma(z_0)$ is the yet unknown source density distribution. On the surface of the airfoil (i.e., $z\epsilon L$) the real part of ω, ζ, will be set equal to one,

$$\text{Real}\,\psi(z) = 1 \quad z\epsilon L \tag{7}$$

At large distances upstream and downstream of the cascade $\zeta(z)$ is assumed to approach zero. This far-field condition imposes the requirement that

$$\text{Im}\int_L \gamma(z_0)dz_0 = 0 \tag{8}$$

Equation (6) evaluated on the airfoil surface in conjunction with equations (7) and (8) form the integral equation

$$1 = \text{Real}\left\{\int_L \gamma(z_0)\mathcal{K}(z-z_0)dz_0\right\}, \; z\epsilon L$$
$$0 = \text{Im}\int_L \gamma(z_0)dz_0 \tag{9}$$

for the source density function. Once γ is known, the entire potential field can in theory be computed by direct integration of equation (6).

Equation (9) is a singular integral equation, which can be solved by paneling procedures similar to those used in solving potential flow problems. To employ these procedures one must first factor out of the integral equation its singular behavior. For this problem the factor form of equation (9) is

$$1 = \text{Real}\left\{\int_L \gamma(z_0)\ln\frac{(z-z_0)}{2s}dz_0 + \int_L \gamma(z_0)\ln\frac{2s}{(z-z_0)\pi}\tanh\frac{(z-z_0)\pi}{2s}dz_0\right\} \tag{10}$$

Next the airfoil surface is divided into a series of line segments. Over each of these segments $\gamma(z_0)$ and $\ln[2s/(z-z_0)\pi]\tanh[(z-z_0)\pi/2s]$ are approximated by their value at the midpoint of the segment. The singular part of equation (10) is thus approximated as

$$\int_{z_a}^{z_b}\gamma(z_0)\ln\frac{(z-z_0)}{2s}dz_0 \simeq \gamma\left(\frac{z_b+z_a}{2}\right)\left[(z-z_b)\ln\frac{(z-z_b)\pi}{2s} - (z-z_a)\ln\frac{(z-z_a)\pi}{2s}\right] \tag{11}$$

with the regular part approximated by

$$\int_{z_a}^{z_b}\gamma(z_0)\ln\frac{2s}{(z-z_0)\pi}\tanh\frac{(z-z_0)\pi}{2s}dz_0 \cong \gamma(z_0)(z_b-z_a)\ln\frac{2s}{(z-z_0)\pi}\tanh\frac{(z-z_0)\pi}{2s}\Bigg|_{z_0=\frac{z_b+z_a}{2}} \tag{12}$$

The auxiliary condition is approximated by

$$\text{Im}\int_{z_a}^{z_b}\gamma(z_0)dz_0 \cong \text{Im}\left\{\gamma\frac{z_b+z_a}{2}(z_b-z_a)\right\} \tag{13}$$

Introducing equations (11), (12), and (13) into (10) and restricting the value of z to the mid-point of each line segment leads to a system of linear algebraic equations for the source density distribution. The solution of these equations can be obtained by standard matrix methods. With γ known, the complex field surrounding the cascade can be determined from equation (6). The real part η and the imaginary part ζ of this field form a periodic orthogonal body-fitted coordinate system. A typical coordinate system is shown in Fig. 6. The contours η = constant enclose the airfoil, while the curves ζ = constant project from the airfoil to the periodic boundary η = 0. The line extending to upstream and downstream infinity are $\zeta = \pm L$, and $\zeta = 0$, respectively.

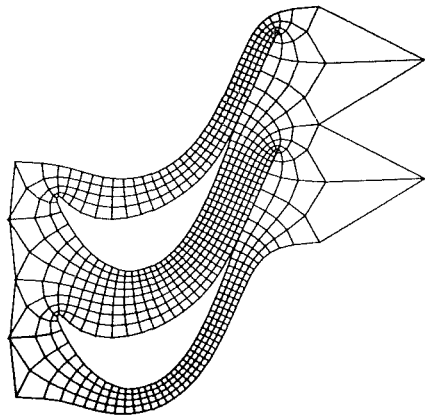


Fig. 6 Typical mesh generated by electro-static analog procedure for a turbine blade with trailing extension

Presently this grid generation scheme utilizes the direct integration procedure outlined above for constructing the bounding curvilinear coordinate. For the other grid lines, on the interior of the mesh, however, the direct procedure proved to be inefficient because of slow convergence. To overcome this difficulty an inverse procedure was developed in which ζ,η become the independent variables and x,y the dependent variables. This inverse procedure is constructed by first noting that the field conversion for the electrostatic potential and flux is the Laplace equation

$$\nabla^2\zeta = 0, \nabla^2\eta = 0 \tag{14}$$

Inverting this equation yields

$$\left.\begin{aligned}\frac{\partial^2 x}{\partial\zeta^2} + \frac{\partial^2 x}{\partial\eta^2} &= 0\\ \frac{\partial^2 y}{\partial\zeta^2} + \frac{\partial^2 y}{\partial\eta^2} &= 0\end{aligned}\right\} \tag{15}$$

as the governing equations for the inverse mapping (i.e., $x = x(\zeta,\eta)$, $y = y(\zeta,\eta)$).

The solution of the field equation (15) subjected to boundary conditions consistent with the coordinates of the bounding curvilinear curves yields the desired interior coordinate curves. A second sample grid for a highly cambered thick turbine blade generated by the above procedure is shown in Fig. 7. It is seen that the grid is highly regular with clustering of grid points in regions of rapid flow variations. The periodicity of the grid is quite apparent and leads to a simple numerical approximation of flow variables in the neighborhood of the periodic boundary. Flow computations applying this grid generation procedure are presented later in the paper.

Solution Method

Governing Equations. The equation to be solved is the two-dimensional steady, compressible full-potential equation in its conservation form

$$(\rho\phi_x)_x + (\rho\phi_y)_y = 0$$

Downloaded 01 Jun 2010 to 171.66.16.62. Redistribution subject to ASME license or copyright; see http://www.asme.org/terms/Terms_Use.cfm

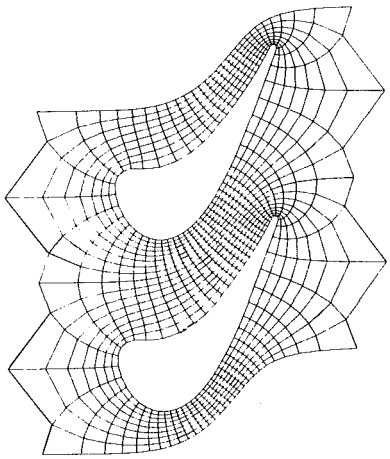


Fig. 7 Computational mesh developed by electrostatic analog procedure for another thick turbine blade

Similar to the approach taken by several others [7, 12], this equation is to be written at the finite volume element which surrounds each grid point.

With superscript n referring to the artificial time step, a typical formation at each grid location (i, j) is with,

$$\phi^{n+1}_{i,j} = \phi^{n}_{i,j} + \omega\delta\phi^{n}_{i,j} \tag{16}$$

then

$$L(\phi^{n+1}) = (\rho\phi^{n+1}_{x})_{x} + (\rho\phi^{n+1}_{y})_{y} = 0 = L(\phi^{n}) + L(\omega\delta\phi^{n}) = \nabla(\rho\phi^{n}) + \omega L(\delta\phi^{n}) \tag{17}$$

or

$$\omega L(\delta\phi^{n}_{i,j}) = -\nabla(\rho\phi^{n})_{i,j} = -\frac{R_{i,j}}{\mathcal{V}_{i,j}}$$

where $\mathcal{V}_{i,j}$ is the volume of the local element, ω is the over-relaxation parameter, $\delta\phi^{n}_{i,j}$ is the unknown change in the local potential field and $R_{i,j}$ is the residual net mass flow out of the finite volume surrounding the grid point. Expanding equation (17) in finite difference form:

$$L(\delta\phi^{n}_{i,j}) = \frac{\rho^{n}_{i+1/2,j}\left(\dfrac{\delta\phi^{n-1}_{i+1,j} - \delta\phi^{n}_{i,j}}{X_{i+1,j} - X_{i,j}}\right) - \rho^{n}_{i-1/2,j}\left(\dfrac{\delta\phi^{n}_{i,j} - \delta\phi^{n}_{i-1,j}}{X_{i,j} - X_{i-1,j}}\right)}{X_{i+1/2,j} - X_{i-1/2,j}} + \frac{\rho^{n}_{i,j+1/2}\left(\dfrac{\delta\phi^{n}_{i,j+1} - \delta\phi^{n}_{i,j}}{Y_{i,j+1} - Y_{i,j}}\right) - \rho^{n}_{i,j-1/2}\left(\dfrac{\delta\phi^{n}_{i,j} - \delta\phi^{n}_{i,j-1}}{Y_{i,j} - Y_{i,j-1}}\right)}{Y_{i,j+1/2} - Y_{i,j-1/2}} = -\frac{R_{i,j}}{\omega\mathcal{V}_{i,j}} \tag{18}$$

Each volume element is defined by the four surfaces parallel to and located halfway between neighboring grid lines as shown in Fig. 8. The thickness of the element (i.e., relative local streamtube height) is obtained from a specified height distribution or is set to unity for strict two-dimensional flow. Variations in the radial (spanwise) position, r, of the streamtube are accounted for by scaling all tangential $r\theta$ coordinates, (y) with a ratio of local radius, r, to a given upstream radius, $r_{-\infty}$. Then, over the area, A_E defined by the four surfaces of the volume element

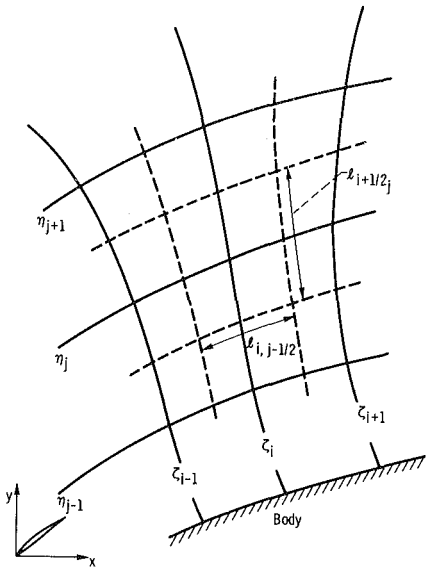


Fig. 8 Finite volume element in physical space

$$R_{i,j} = \int_{A_E} \rho\bar{u}dA = \sum (\rho^{n}_{i\pm1/2,j}\bar{u}^{n}_{i\pm1/2,j}\ell_{i\pm1/2,j}h_{i\pm1/2,j} + \rho^{n}_{i,j\pm1/2}\bar{u}^{n}_{i,j\pm1/2}\ell_{i,j\pm1/2}h_{i,j\pm1/2}) \tag{19}$$

where h is the local streamtube height normalized to unity far upstream. The velocities, $\bar{u}$, are normal to the element boundaries and located at the boundaries. Velocity, $\bar{u}$, and density, ρ, are calculated using the values of potential at the previous iteration.

Using equation (17) and isolating all unknown potential corrections on the left-hand side, equation (18) can be expressed in the form

$$A_{i,j+1}\delta\phi^{n}_{i,j+1} + A_{i,j}\delta\phi^{n}_{i,j} + A_{i,j-1}\delta\phi^{n}_{i,j-1} = \mathcal{R}^{n}_{i,j} \tag{20}$$

where

$$\mathcal{R}_{i,j} = R_{i,j} + G(\phi^{n}, \rho^{n}, \delta\phi^{n}_{i-1}) \tag{21}$$

and the coefficients

$$A = A(\rho^{n}, \Delta\zeta, \Delta\eta) \tag{22}$$

By writing equation (20) for each point on a grid line of constant ζ $(j = 1, J)$ a tridiagonal matrix system is formed which is then solved by the standard Thomas algorithm [6] for the potential corrections $\delta\phi^{n}$. New values of the field potential are obtained using equation (16) after all lines are solved $(i = 1, I)$.

Sweep Strategy. The grid lines are solved in order beginning with the line which goes to downstream infinity and then proceeding clockwise around the blade shape. This order results in a solution which sweeps against the flow direction on the bottom (pressure) surface of a compressor blade at positive incidence, where the flow is likely to be subcritical. This minimizes the chances of sweeping against a supersonic

Downloaded 01 Jun 2010 to 171.66.16.62. Redistribution subject to ASME license or copyright; see http://www.asme.org/terms/Terms_Use.cfm

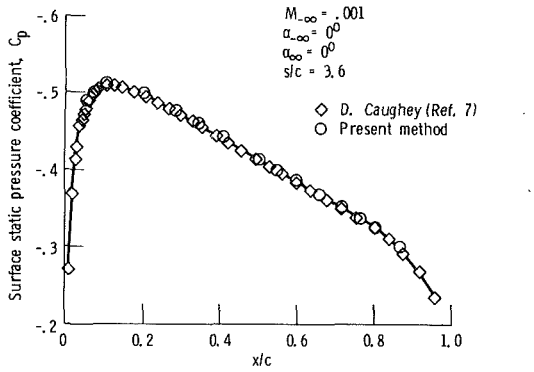


Fig. 9 NACA 0012 cascade nonlifting subsonic results

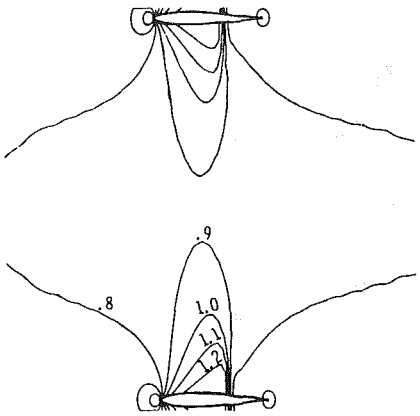


Fig. 11 Isomach map for NACA 0012 using present method

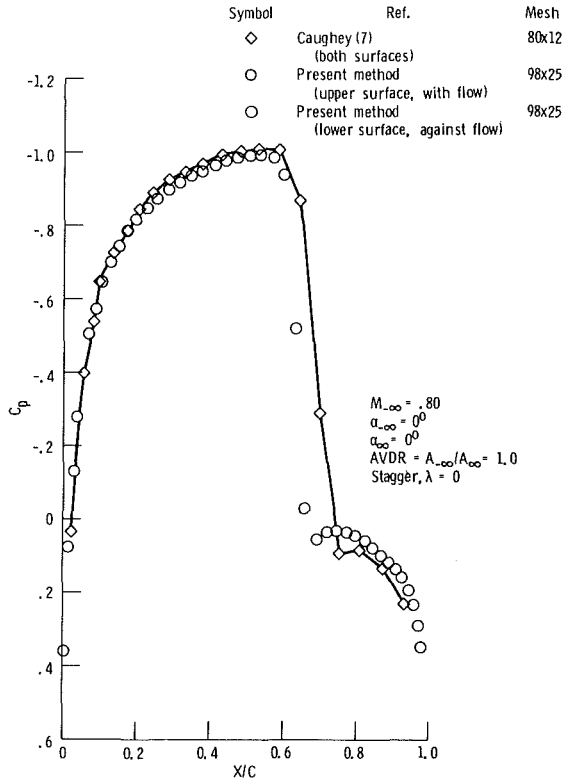


Fig. 10 NACA 0012 cascade nonlifting transonic results

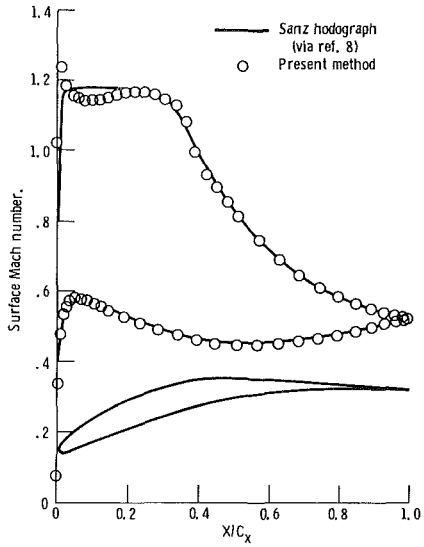


Fig. 12 Sanz supercritical stator tip section

flowfield. It became evident, when symmetric supersonic flows were successfully solved, that direction of sweep is not critical. The apparent reason is that additional damping is applied by the elliptic-like nature of the artificial density used in combination with the sweep strategy. More detail on this effect is described in the next section.

Artificial Density. In equation (18), there is no explicit artificial viscosity term necessary for stability in supercritical flow regions and for smearing shock jumps. As suggested by Hafez et al. [1], an implicit viscosity term is incorporated in the density. This modified density is used instead of the physical density in equation (18). The form of the modification is [1]

$$\tilde{\rho} = \rho - \mu \rho_S \Delta S \tag{23}$$

where μ is the switching function to eliminate the density modification in subsonic regions (M < 1)

$$\mu = \max\left(0, 1 - \frac{1}{M^2}\right) \tag{24}$$

and $\rho_S \Delta S$ is the total differential component of the density in the flow direction, S, defined by the contravariant velocity components a and b. Then:

$$\mu \rho_S \Delta S = \mu_a \frac{a}{q} \rho_\eta \Delta\eta + \mu_b \frac{b}{q} \rho_\zeta \Delta\zeta \tag{25}$$

where,

$$q = \sqrt{u^2 + v^2}$$

The switching function was split into two terms so that the effect of each component of the density change could be even more efficiently gauged in areas of high flow gradient. In addition, an upwind averaged Mach number was used:

$$\left.\begin{aligned} \mu_a &= \max\left(0, 1 - \frac{1}{M^2_{av_a}}\right), \text{ where } M_{av_a} = \frac{1}{2}(M_{i+1/2,j} + M_{i+1/2,j\pm1}) \\ \mu_b &= \max\left(0, 1 - \frac{1}{M^2_{av_b}}\right), \text{ where } M_{av_b} = \frac{1}{2}(M_{i+1/2,j} + M_{i+1/2\pm1,j}) \end{aligned}\right\} \tag{26}$$

Downloaded 01 Jun 2010 to 171.66.16.62. Redistribution subject to ASME license or copyright; see http://www.asme.org/terms/Terms_Use.cfm

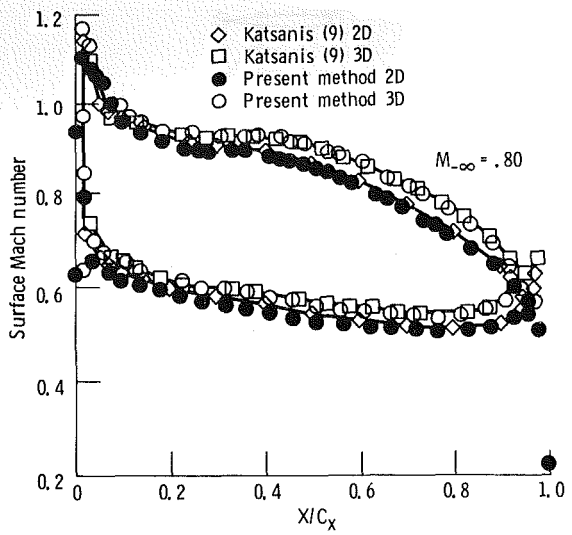


Fig. 13 Comparison of 2-D and 3-D results for DCA compressor stator

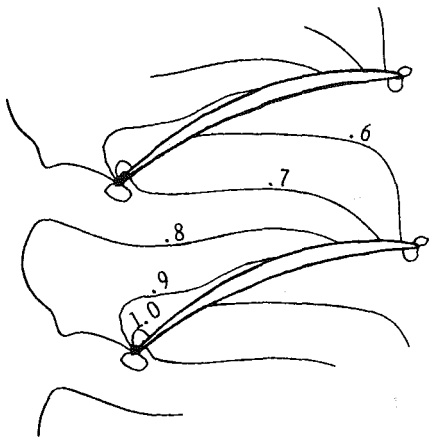


Fig. 14 Isomach map for quasi-3-D case of DCA stator using present method

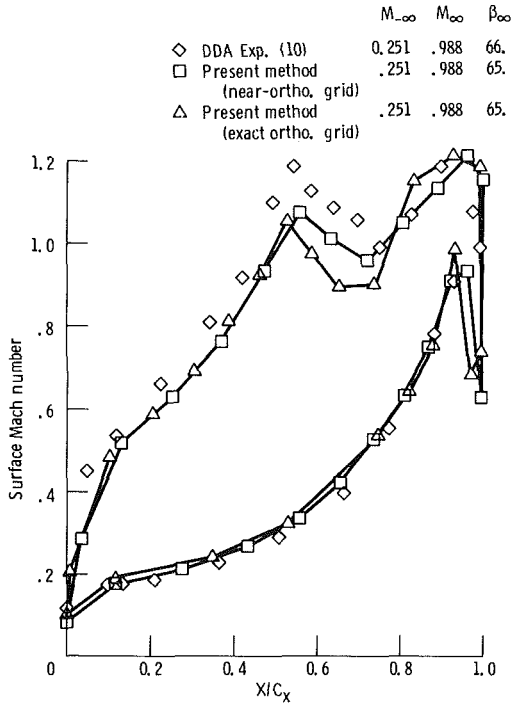


Fig. 15 Comparison of experimental and calculated results for turbine cascade, AACE (II)

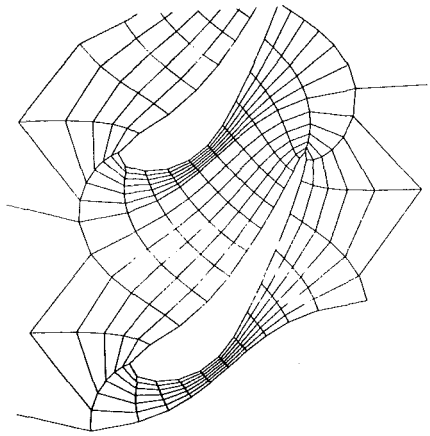


Fig. 16 Near-orthogonal coarse mesh for DDA AACE(II) turbine cascade

Similarly, upwind differencing is used for approximating ρ_ξ and ρ_η. The physical densities used to calculate ρ_ξ and ρ_η are updated as each line is reached. Implicit in this arrangement is the creation of a time-like cross derivative of density, ρ_{st}, when sweeping against the flow direction. This is because the density at the current line has been calculated using the values of potential and velocity at the latest iteration (i.e., artificial time step), while the values at the next upstream line, where the upwind differences are formed, remain at the previous time step until it in turn is solved. However, when sweeping with the flow, the upstream line from which the density gradients are formed has already been solved and updated. Thus this additional damping due to the time lag of densities is not present when solving with the flow and the artificial compressibility reduces to the original space-lag only.

Boundary Conditions. The boundary conditions applied to the solution system include a specified upstream axial mass flow in the form of an oncoming Mach number, plus incidence and stagger angles. Using global continuity,

$$\rho_{+\infty} u_{+\infty} A_{+\infty} = \rho_{-\infty} u_{-\infty} A_{-\infty} \tag{27}$$

where A is the flow area normal to the streamtube.

The specified flow angle at downstream infinity together with a simple iteration procedure on the isentropic density ratio gives the downstream Mach number boundary condition. For a stagger angle, λ, and upstream incidence (chordwise) of $\alpha_{-\infty}$, equation (27) can be rearranged to yield

$$M_\infty \left(\frac{1}{1+\frac{\gamma-1}{2} M_\infty^2} \right)^{\frac{\gamma+1}{2(\gamma-1)}} = F(M_\infty)$$

$$= \frac{A_{-\infty}}{A_{+\infty}} \frac{\cos\beta_{-\infty}}{\cos\beta_{+\infty}} M_{-\infty} \left(\frac{1}{1+\frac{\gamma-1}{2} M_{-\infty}^2} \right)^{\frac{\gamma+1}{2(\gamma-1)}} \tag{28}$$

where

$$\beta = \alpha + \lambda$$

Using a straightforward Newton iteration on equation (28) yields M_∞. From this the relative speed ratio is available as:

Downloaded 01 Jun 2010 to 171.66.16.62. Redistribution subject to ASME license or copyright; see http://www.asme.org/terms/Terms_Use.cfm

$$\frac{q_\infty}{q_{-\infty}} = \frac{M_\infty a_\infty}{M_{-\infty} a_{-\infty}} = \left(\frac{1 + \frac{2}{\gamma - 1} M_{-\infty}}{1 + \frac{2}{\gamma - 1} M_\infty^2} \right)^{1/2} \quad (29)$$

Periodicity is maintained in the tangential (y) direction by enforcing the relation

$$\phi(x, y+s) = \phi(x,y) + C \quad (30)$$

where s is the blade spacing and

$$C = \oint_{(x,y)}^{(x,y+s)} V \cdot d\hat{\ell} = v_{-\infty} s_{-\infty} \quad (31)$$

On the grid line defining the body, a standard zero normal flow condition is imposed

$$\nabla \phi \cdot \hat{n} = 0 \quad (32)$$

Results

Some results obtained from these methods are shown in Figs. 9 through 21. Verification of the code at low speed is provided in Fig. 9 by the comparison to the methods of Caughey [7] for the NACA 0012 blade shape. The transonic nonlifting case is shown in Fig. 10 for this same blade. The shock strength and location agree well with similar results using the methods of reference [7]. The solution is surprisingly symmetric, particularly in light of the fact that the solution on the lower surface was obtained by marching *against* the supersonic flow and the upper surface was obtained by marching *with* the flow. This relative shift in marching direction occurs because the solver was written such that it makes one continuous clockwise sweep of all grid lines around the airfoil. Thus there is a primary difference between this method and other transonic techniques. It is apparently insensitive to the relative direction of the supersonic flow. For the cases tested thus far, this insensitivity to flow direction does not seem to be affected by mesh size (down to $\Delta X \simeq 2$ percent chord). The symmetry of the solution can be seen very effectively in the isomach map of Fig. 11.

The sensitivity of the system to a near-shock condition can be seen in the results for the supercritical blade shown in Fig. 12. This is a compressor stator tip section designed for NASA-Lewis by Sanz using a method based on Bauer, et al. [8]. The trailing edge ends in a cusp. The fast compression is captured well without any over-reaction or steepening into a shock.

The capability to approximate moderate three-dimensional streamtube effects is demonstrated in Fig. 13 where both the strict two-dimensional flow and quasi-three-dimensional flow, as corrected for a given streamtube convergence profile, are compared for the double circular arc stator of Fig. 5. Agreement is excellent with results using the method of [9]. For this case there was a 7-percent gradual contraction in the streamtube from far upstream to far downstream. In addition, the streamtube varied its position along the span (radial shift) by 0.7 percent over the same distance, a negligible effect. The resulting isomach map is shown in Fig. 14.

A comparison of results for a typical turbine blade section is shown in Fig. 15. The blade used is designated as the AACE(II) airfoil by R. A. Delaney, to whom we are grateful for supplying the coordinates and experimental data [10]. Agreement is good on the pressure side, but the calculated envelope is slightly low on the suction surface. This is consistent with the metal blade coordinates used in this inviscid calculation. If a suitable boundary layer analysis were included and displacement thickness added to the profile, the suction surface calculation would more accurately match the experimental data. The location of each peak in speed is predicted accurately, even near the trailing edge, despite the inherent difficulty for potential flow methods to go around

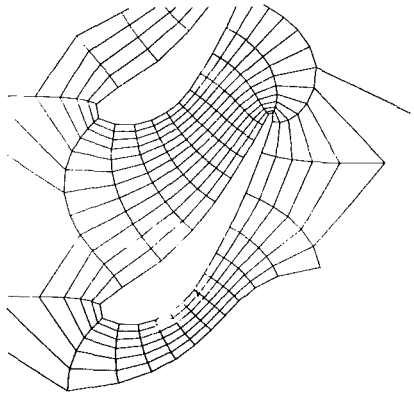


Fig. 17 Exact orthogonal coarse mesh for DDA AACE(II) turbine cascade

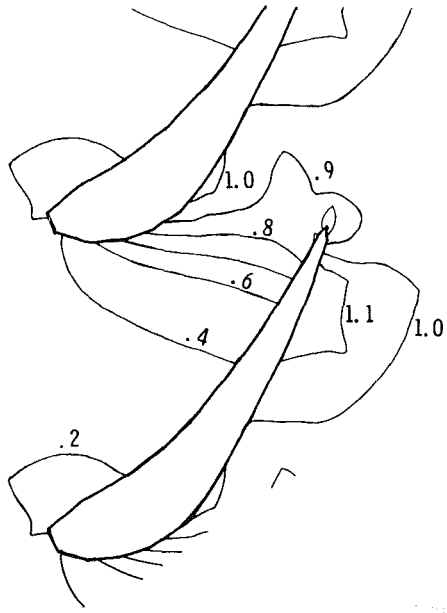


Fig. 18 Isomach map of DDA AACE(II) turbine using the near-orthogonal mesh

sharp bends at high velocity without some artificial limitation on calculated speeds. Such limits were not necessary for the coarse mesh used for Fig. 15 (26 points around the blade). However, finer meshes were unsuccessful without some artificial barrier imposed on Mach number.

Figure 15 also gives an interesting comparison between the two mesh generators described earlier. The results for both grids are virtually identical in the subsonic region as would be expected. In the high-speed region, the exact-orthogonal mesh (electrostatic analog) appears to be slightly more conservative overall than the near-orthogonal grid. Subsequent experience with other denser meshes showed that the exact-orthogonal mesh provided more stability in high gradient areas, such as the trailing edge. Figures 16 and 17 give views of the two grids used for the calculations of Fig. 15. An isomach map for the AACE(II) turbine, using the near-orthogonal grid, is shown in Fig. 18.

As a final example of the importance of streamtube effects on supercritical blade design, Fig. 19 shows a series of calculations performed on a thick compressor stator hub section developed for NASA-Lewis by Sanz (via [8]). The present method was first used to calculate the strict two-dimensional flow over the blade. This is seen to agree very

Downloaded 01 Jun 2010 to 171.66.16.62. Redistribution subject to ASME license or copyright; see http://www.asme.org/terms/Terms_Use.cfm

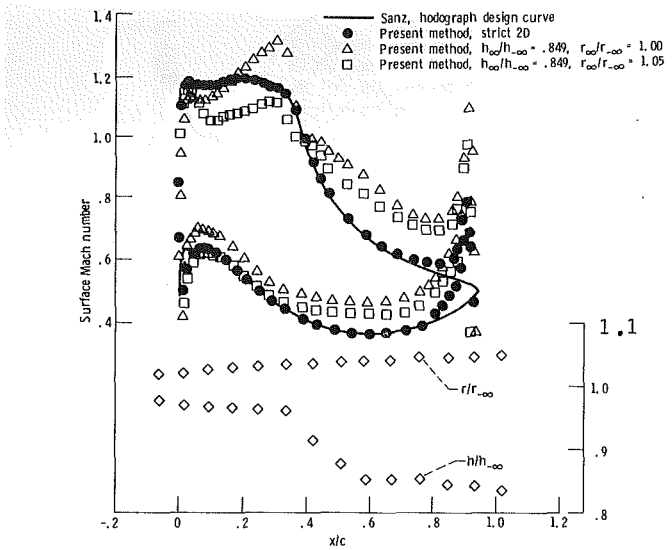


Fig. 19 Effect of streamtube's radial position and thickness on flow about a supercritical compressor stator hub section

well with the Sanz hodograph design envelope except at the trailing edge, where the idealized blade of infinite length (hodograph solution) was replaced by a cap of constant radius to connect pressure and suction surfaces for the present method. The remaining two curves are quasi-three-dimensional cases which highlight the effect of changes in spanwise (radial) position of the streamtube. Both cases involved a streamtube thickness change of about −14 percent (AVDR = 1.15). The axial distribution of this thickness change ($h/h_{-\infty}$) as well as the distribution of spanwise streamtube position ($r/r_{-\infty}$) as shown in Fig. 19 were obtained for this Sanz hub section by using the Katsanis meridional plane computer program [11]. The results are typical for a section near the hub wall with thickness decreasing, and spanwise position increasing about 5 percent. One quasi-three-dimensional case in Fig. 19 has only the thickness change applied, with radius held constant. The other case has both thickness and radius change. Note that the increasing radial position of the streamtube has a strong decelerating effect on the flow since the blade-to-blade passage now diverges ($r\theta$ larger at trailing edge than at leading edge). A design using this result could tolerate higher blade flow rates than one which ignored these radial effects.

Figure 20 shows the isomach map for the case of thickness variation only. The shock appears as expected near 40 percent chord. Figure 21 is for the case of both thickness and radius variation. Note that the shock has washed out and flow in the passage has decelerated.

Conclusions

A reliable method has been presented for calculating the flowfield about a cascade of arbitrary 2-D airfoils which can be made to approximate the three-dimensional flow in a turbomachinery blade row by correcting for streamtube convergence and radius shift. The method is a fully conservative solution of the full potential flow equation using a body-fitted periodic mesh, with an artificial density imposed in the transonic region to ensure the capture of shock waves. A computer code has been developed using the methods described above. It has been tested using a variety of turbomachinery and general blade profiles. The calculation of a shocked symmetric NACA blade has verified that this method is insensitive to the relative directions of supersonic flow and SLOR sweep. Comparison of results for several well-known supercritical blades has shown satisfactory agreement with their hodograph solutions. The approximation of moderate three-dimensional streamtube effects was demonstrated by a good comparison between this method and results using the Katsanis code on a DCA compressor stator. Two-dimensional and quasi-three-dimensional calculations for a supercritical compressor stator indicated that the moderate three-dimensional effects included in this method are important enough to radically affect design considerations in high-speed regions of the blade. These results all indicate that the method described is a useful one for analyzing off-design performance of turbomachinery blading.

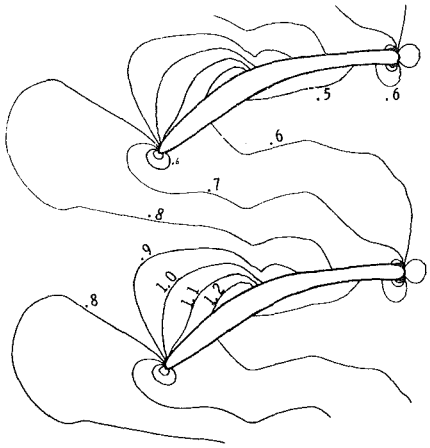


Fig. 20 Isomach map for Sanz stator with streamtube thickness variation and constant radius

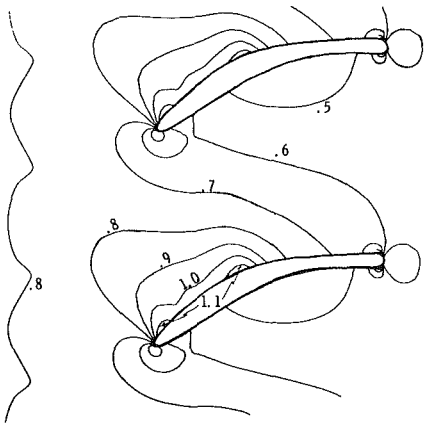


Fig. 21 Isomach map for Sanz stator with streamtube thickness variation and radius variation

References

1 Hafez, M., South J., and Murman, E., "Artificial Compressibility Methods for Numerical Solutions of Transonic Full Potential Equation," *AIAA Journal*, Vol. 17, No. 8, Aug. 1979, pp. 838–844.

2 Ives, D. C., and Liutermoza, J. F., "Analysis of Transonic Cascade Flow Using Conformal Mapping and Relaxation Techniques," AIAA Paper 76-370, July 1976.

3 Jahnke, E., and Emde, F., *Tables of Functions with Formulae and Curves*, 4th ed., Dover, New York, pp. 92–95.

4 Hawthorne, W. R., ed., *Aerodynamics of Turbines and Compressors*, Princeton University Press, Princeton, N.J., 1964, pp. 29–31.

5 Fuchs, B. A., and Shabat, B. V., *Functions of a Complex Variable and Some of Their Applications*, Vol. 1, Pergamon Press, New York, 1961, pp. 183–187.

6 Roache, P. J., *Computational Fluid Dynamics*, Rev. Printing, Hermosa Publications, Albuquerque, N.M., 1976, pp. 345–347.

7 Caughey, D. A., and Jameson, A., "Numerical Calculation of Transonic Potential Flow About Wing-Fuselage Combinations," AIAA Paper 77-677, June 1977.

8 Bauer, F., Garabedian, P., Korn, D., and Jameson, A., *Supercritical*

Downloaded 01 Jun 2010 to 171.66.16.62. Redistribution subject to ASME license or copyright; see http://www.asme.org/terms/Terms_Use.cfm

Wing Sections II, Lecture Notes in Economics and Mathematical Systems, Vol. 108, Springer-Verlag, New York, 1975.

9 Katsanis,T., "FORTRAN Program for Calculating Transonic Velocities on a Blade-to-Blade Stream Surface of a Turbomachine," NASA TN D-5427, Sept. 1969.

10 Huffman, G. D., McClure, R. B., Holtman, R. L., and Sinnett, G. T., "Results of a Two-Dimensional Turbine Cascade Test," Research Note 71-47, Detroit Diesel Allison, Indianapolis, Ind., 1971.

11 Katsanis, T. and McNally, W. D., "Revised FORTRAN Program for Calculating Velocities and Streamlines on the Hub-Shroud Midchannel Stream Surface of an Axial-, Radial-, or Mixed-Flow Turbomachine or Annular Duct," NASA TN D-8431, July 1977.

12 Caspar, J. R., Hobbs, D. E., and Davis, R. L., "The Calculation of Potential Flow in Cascades Using Finite Area Techniques," Paper 79-0077, AIAA 17th Aerospace Sciences Meeting, New Orleans, La., Jan. 1979.

Downloaded 01 Jun 2010 to 171.66.16.62. Redistribution subject to ASME license or copyright; see http://www.asme.org/terms/Terms_Use.cfm

Rotor-Tip Leakage: Part I—Basic Methodology

T. C. Booth

P. R. Dodge
Garrett Turbine Engine Co.,
Phoenix, Arz. 85010

H. K. Hepworth
Northern Arizona University,
Flagstaff, Arz. 86001

Blade tip losses represent a major efficiency penalty in a turbine rotor. These losses are presently controlled by maintaining close tolerances on tip clearances. This two-part paper outlines a new methodology for predicting and minimizing tip leakage flows. Part I of the paper describes a series of experiments and analyses which indicated a predominantly inviscid nature of tip leakage flow. The experiments were conducted on a series of three water flow rigs in which leakage quantities were measured over simulated blade tips. As a result of the experiments, a simple tip-leakage model is proposed that treats the normal velocity component in terms of discharge coefficient and conserves the tangential velocity (momentum) component. Identification of tip leakage controlled by a normal discharge coefficient suggests an optimum tip-treatment configuration may be designed through discharge testing of candidate configurations. A preliminary design optimization was conducted on the simple discharge rigs, and the results were evaluated on the water table cascade rig and on a turbine stage.

Introduction

The traditional approach for analyzing tip-clearance losses has concentrated upon measuring the effects of clearance on overall turbine performance and developing an approach which provides at best a semiempirical relationship between clearance and stage losses. With the advent of large-scale numerical techniques for solving the Navier-Stokes equations for rotor flows, the requirement arises for a solution to rotor tip flows that depends directly on the actual physics of flows leaking from the pressure to the suction side of a rotating turbine blade. The availability of a tip solution will not only supply a key boundary condition to the rotor analysis, but also will provide the means to design high performance tips that retain effective sealing at higher clearance levels.

Several models have been proposed for modeling tip flows at normal clearance levels. Papers written by Lakshminarayana [1] and Rains [2], although basically related to compressors, are also pertinent to the study objective of supplying accurate boundary conditions to a turbine-rotor Navier-Stokes solution.

The theory presented by Lakshminarayana [1] models the aerodynamic efficiency penalty due to tip clearance losses. By adding another model for the vortex-core radius and the circulation, a boundary-value problem was solved for the deviation field. The modeling was based on a solution for tip-leakage flow as related to an approximate blade boundary layer equation, with a closed-form solution in terms of the tip circulation deficit due to clearance. Although the model appeared to accurately predict losses, it had three major restrictions that precluded its application in supplying blade-tip boundary conditions for the rotor analysis. These are:

(1) the model supplies only an average uniform leakage,
(2) critical boundary layer parameters are supplied as a correlating constant, restricting extension to new blading, and
(3) the analysis may not readily be extended to a compressible form.

The work by Rains [2] presents an order-of-magnitude theory that suggested that the dominant flow mechanism is an inviscid balance. The modeling for this theory combined a local discharge in conjunction with preservation of tangential momentum, and as an overall result gave pausible leakage flows. In conjunction with a suitable loss model, Rains was able to predict accurate tip-clearance loss curves for two compressors. However, with the exception of tip-pressure measurements to measure unloading effects no detailed confirmation of the theory was provided. Therefore, it was not possible to verify that the success of the modeling could be attributed to accurate prediction of tip leakage flows or the loss model itself.

The two methods represent steps taken to quantify tip leakage flows. Neither approach is entirely satisfactory for supplying detailed boundary conditions for a rotor analysis. This paper describes a tip flow analysis that evolves from a consideration of the momentum balance supported by water rig discharge testing to model development. The test methodology is also applied to the design of new tip designs, one of which is tested in a stage.

Momentum Balance

At clearance levels typical of turbomachinery, flow over the rotor tip is viewed primarily as a pressure-driven

Contributed by the Gas Turbine Division of The American Society of Mechanical Engineers and presented at the International Gas Turbine Conference, Houston, Texas, March 8–11, 1981. Manuscript received at ASME Headquarters, December 11, 1980. Paper No. 81-GT-71.

Copyright © 1982 by ASME

Downloaded 01 Jun 2010 to 171.66.16.62. Redistribution subject to ASME license or copyright; see http://www.asme.org/terms/Terms_Use.cfm

Table 1 Water rig test capabilities

Parameter		Single-Side Discharge Rig	Double-Side Discharge Rig	Water Table Cascade Rig	Rotor Tip
Geometric Modeling	Tip Clearance / Chord	0.013	0.011	0.008	0.008
	Max. Thickness / Chord	0.058	0.083	0.109	0.109
Momentum Similarity	Pressure Across Tip / Dynamic Head	6.5	4.4	2.4	1.6
	Chord Reynolds Number	48,200	120,000	134,000	200,000
Driving Mechanisms	Pressure-Side Transverse Flow	X	X	X	X
	Suction-Side Transverse Flow		X	X	X
	Streamwise Pressure Distribution			X	X
	Moving End Walls				X

phenomenon. The dominant terms the momentum balance takes depends on the clearance level.

- At low clearance levels, shear forces directly balance pressure forces.
- At normal clearance levels, convection becomes dominant, with viscous effects becoming increasingly second order. In this regime, viscous effects are reduced to those creating separations and reattachments, and the tip can be modeled as a special kind of orifice. Streamwise momentum becomes nearly uncoupled from the leak processes and can be conserved with little axial influence.
- At high clearance levels, tip unloading becomes so great that pressure gradients become small. A strong interaction between streamwise momentum and leak momentum takes place, so that particles of fluid have a tendency of being swept downstream before they can migrate from the pressure to the suction surface. This process is dominant in wings, where clearance levels approach infinity.

It is apparent from blade-tip pressure loading distributions measured by high-response pressure transducers that rotor tips usually do not operate at high clearance levels; thus, pressure loading across the tip remains high. The tip flow in this case is dominated by either shear or convection, the latter of which would be modified by viscous-discharge effects.

Assessment of the applicability of a shear balance was deductive. The approach was to calculate the leakage flow with a slow-flow approximation that is similar to thin-film lubrication theory. The analysis predicted a leakage flow that would be 47 percent of full turbine flow – a value clearly too large. Therefore, the leakage flow was calculated with an inertial balance. The velocity was estimated from Bernoulli's equation with inlet pressure equal to the tip relative pressure and discharge pressure equal to an average suction-surface pressure. For a 1-percent clearance level, the calculated leak flow was approximately 2 percent of the turbine flow. This was consistent with the performance estimate of a 2-percent loss in efficiency/percent-of-clearance.

The preceding leakage analyses were indicative that in the range of tip clearances seen on turbines, the flow over the blade tip may be regarded as primarily inviscid. To support this concept, a series of simple tests was conducted on three flow rigs to actually measure leakage amounts over a simulated blade tip. For practical reasons, the tests were conducted in water. The sequence of testing progressed in complexity and effects demonstrated, as outlined in Table 1.

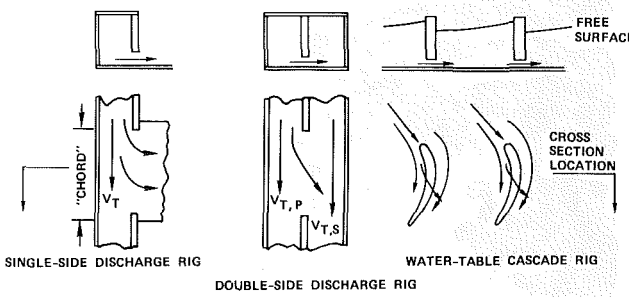


Fig. 1 Water rig configurations

The water rigs used for the tests are shown schematically in Fig. 1. For all three rigs, the fundamental quantities measured were gap leakage flow and driving pressure.

The first test series was conducted on the single-side discharge rig and was designed to measure the impact on gap leakage of:

- Pressure-side, transverse-flow velocity
- Gap pressure ratio
- Gap clearance height (thickness fixed)

The rig design was simple, with the gap pressure ratio and transverse velocity adjusted through columns of water upstream and downstream of the gap. The gap leakage flow was measured by recording the time needed to accumulate a quantity of the water leaking through the gap. This simplicity removed ambiguity from interpretation of the measurements.

The results of these first experiments indicated gap discharge coefficient was independent of:

- Gap clearance height
- Cross-flow velocity when the discharge coefficient is defined in terms of static pressure across the gap
- Inlet boundary layer – moving from near-zero boundary layer for cases with no cross flow, to large thicknesses when transverse flow levels were large.

Dye traces indicated that the major effect of transverse flows on the pressure side was to introduce a transverse momentum downstream of the gap. This suggested that transverse momentum would be preserved across the gap.

The effects of suction-side transverse velocity were not measured in the single-side discharge rig-test series. A new water rig was designed to properly simulate this effect.

Downloaded 01 Jun 2010 to 171.66.16.62. Redistribution subject to ASME license or copyright; see http://www.asme.org/terms/Terms_Use.cfm

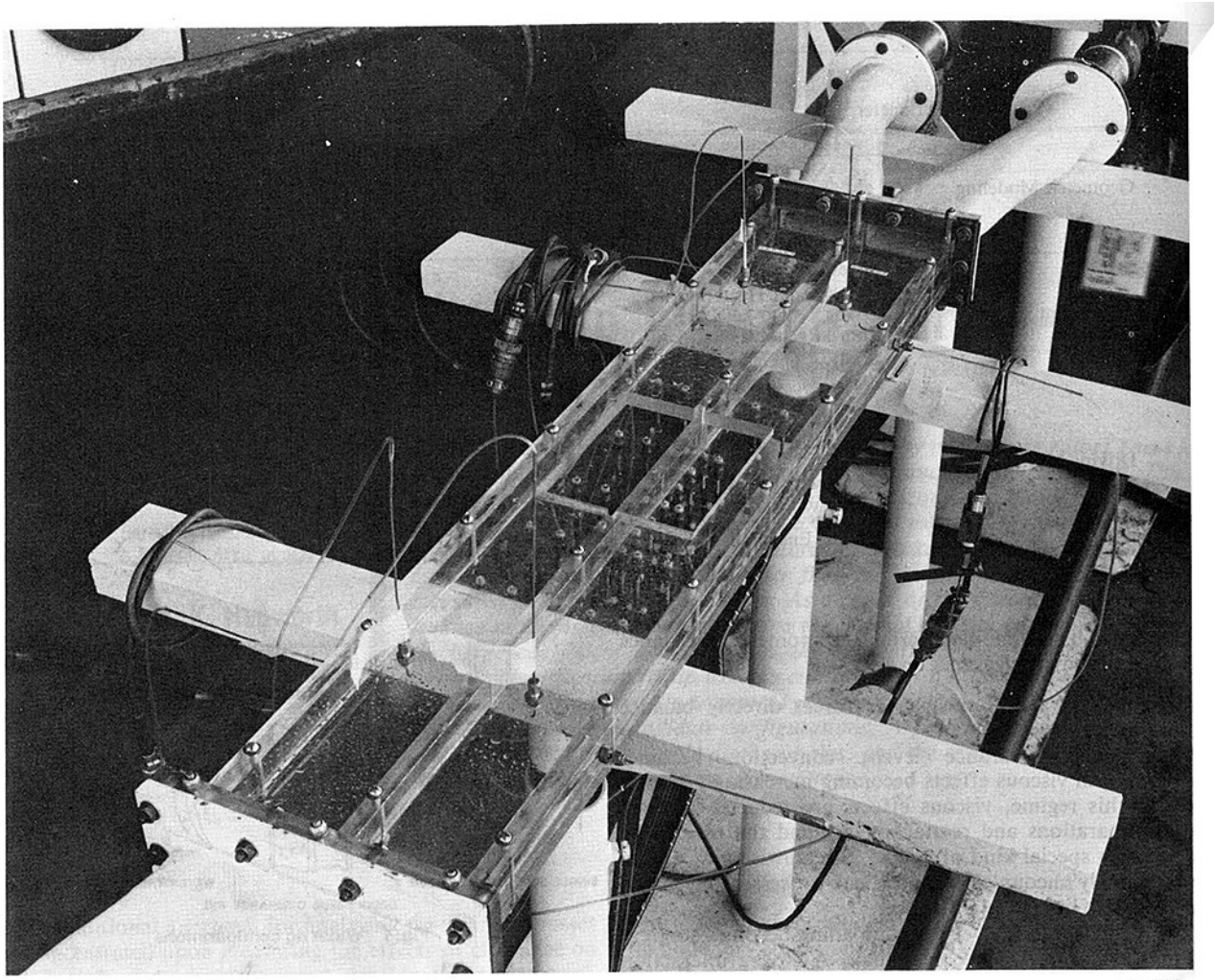


Fig. 2 Double-side discharge rig test section

Designated the double-side discharge rig, this rig produced transverse flows on both the pressure and the suction sides of the gap. A major feature of this rig was the ability to vary the transverse velocity and pressure level of each stream independently through four pinch valves. Redundant gap-leakage measurements were accomplished through a system of four Venturi meters. This system is shown in Fig. 2.

Data were collected over a range of transverse velocity levels, gap pressure levels, and gap clearance heights. For each gap height, the gap leakage was found to correlate with the gap pressure drop (as measured with wall taps at the inlet and exit). The data were taken for different values of pressure- and suction-side transverse velocity levels. There was no discernable trend to support a strong effect due to transverse velocity levels. The effect of gap height was merely that of a controlling flow area. This was reflected by the constancy of discharge coefficient; for a range of gap to thickness ratios between 0.134 to 0.260, discharge coefficient was 0.81 ± 0.01. The discharge coefficient was defined using

$$C_D = \frac{\dot{m}}{\rho A \sin \beta V_{\text{ideal}}},$$

where β is estimated from the measured gap velocity and pressure-side transverse velocity. The average was defined over all data for a given height.

The effects of transverse-velocity distributions along the gap (i.e., pressure-loading distribution) could not be simulated in the simpler rigs. To measure gap flows under this condition, a water table cascade, built at Northern Arizona University, was used to observe and measure leakage flows under a blade and later to determine the effectiveness of several tip treatments. The blade tip selected was that of the Garrett Low-Aspect-Ratio Turbine (LART)[3]. Testing was conducted for tip clearances of 0.043, 0.067, and 0.130 in. These are equivalent to clearances of 0.33, 0.52, and 1.00 percent of the blade height for an actual stage. Due to mechanical constraints in the water table, perfect Reynolds-number similitude was not obtained; the water-test and cold-air rig test Reynolds numbers were 134,000 and 200,000, respectively. The dynamic similarity, measured by $\Delta P/(1/2\ \rho v^2)$, was 2.4 and 1.6, respectively, where v was an average of the inlet and exit velocity, and ΔP was the average pressure loading.

The water table was used to measure the effect of pressure-side water height, which is directly analogous to the static pressure acting at the gap. This pressure was used to establish the pressure-loading distribution during the flow. Dye was injected into the water close to the blade surface to allow visual observation and photography of the leakage flow under the blade. A Hycam Model 41-004 high-speed camera (capable of up to 11,000 frames/s) was used to photograph the movement of dye clusters. The velocity and direction of the leakage flow was then determined by time, distance, and direction measurements using a film analyzer. Figure 3 illustrates the dye injection process used.

Test and design conditions were set at those of the LART

Downloaded 01 Jun 2010 to 171.66.16.62. Redistribution subject to ASME license or copyright; see http://www.asme.org/terms/Terms_Use.cfm

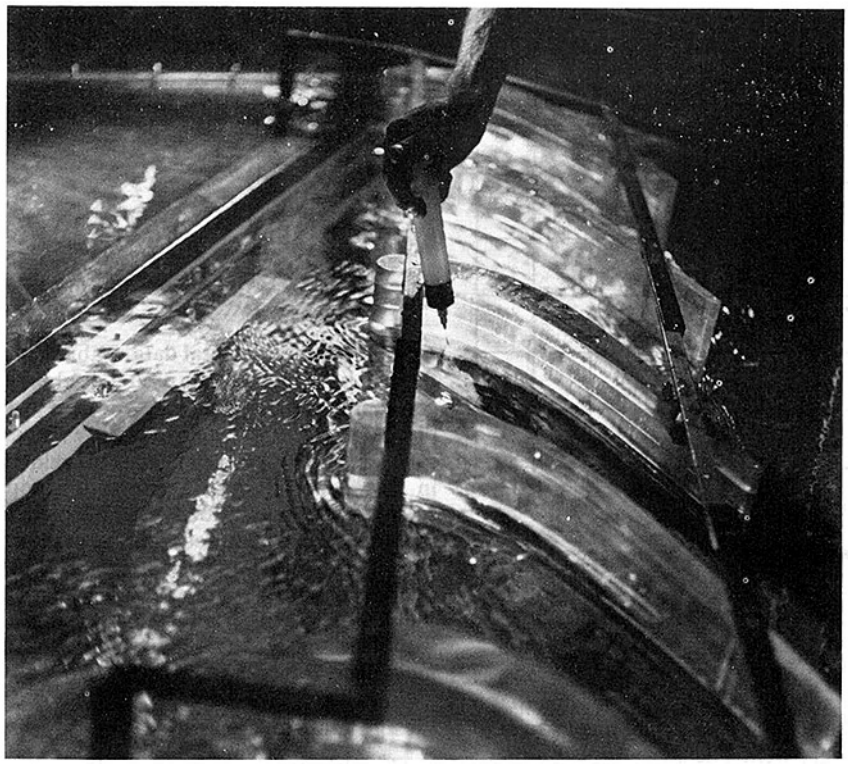


Fig. 3 Dye injected in to the water near the blade

cold-air rig test. All flow parameters were based on an average of inlet and exit conditions, except for ΔP, which represented an average loading. The test data consisted of:

- Anemometer measurements to establish cascade flow and to ensure blade-loading conditions
- Anemometer measurements to produce the velocity adjacent to the gap on the pressure-surface side, thus allowing evaluation of the applicability of Bernoulli's equation, as applied to leakage flow
- Water-height measurements (Δh) were made adjacent to the blade to confirm the transonic loading adjacent to the gap, and to evaluate the applicability of Bernoulli's equation applied to gap flow
- Leakage velocity vectors in the gap "over-the-tip" (Fig. 3).

Verification of the inviscid modeling was accomplished through evaluation of the applicability of Bernoulli's equation. The expression evaluated was:

$$V_B = \sqrt{2g\Delta h + V_{PS}^2}$$

where Δh was the blade-to-blade pressure drop evaluated along a measured leakage streamline, and V_{PS} was the pressure-surface velocity. This ideal prediction was compared to measured leakage velocities for all gaps. The results attained for a gap of 0.130 in. are presented in Fig. 4. Ideal velocities were generally quite close to the measured velocities. The fact that the measured velocity levels were not lower than calculated was simply due to dye traces that represented a maximum velocity midway between the blade tip and cascade floor (turbine shroud).

An important feature of the leakage flow was the linearity of the trajectory, indicating the conservation of tangential momentum as the flow is swept under the blade tip. Not only was this feature useful for data reduction, but it also provided an important clue for subsequent modeling.

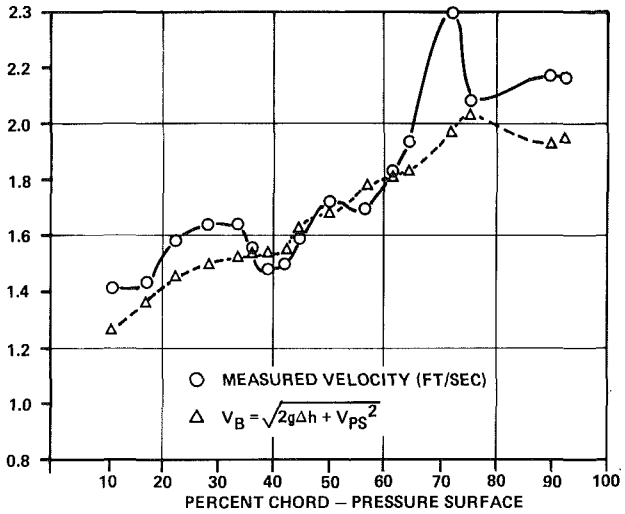


Fig. 4 Applicability of Bernoulli's equation to describe gap flow at 0.130-in. clearance

For model verification and performance rating, the gap leakage flow was computed by integrating the observed velocities. The mass flow obtained in this fashion was expected to be too high, because the dye velocity used probably corresponded to a peak velocity of a profile, rather than an average.

To summarize, a series of tests employing water rigs was conducted to demonstrate the flow physics of tip leakage flow. These tests showed the flow to be primarily inviscid, with high discharge coefficient characterizing the flow. Moreover, discharge coefficient may be insensitive to flow on the low-pressure (suction) side of the blade, as was shown in the double-side discharge rig for various transverse velocity ratios.

Downloaded 01 Jun 2010 to 171.66.16.62. Redistribution subject to ASME license or copyright; see http://www.asme.org/terms/Terms_Use.cfm

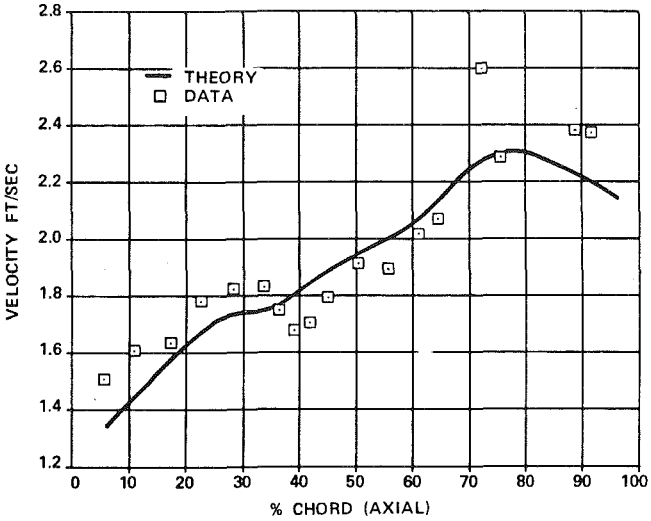


Fig. 5 Leakage velocity, 0.130-in. clearance

Leakage Model

Examination of the discharge rig data, as well as examination of the water-table cascade data, suggested that a simple leakage model following Rains [2] theory would describe the leakage flow very well. The basis for selection of such a model rested on three experimental observations. First, leakage flow stream tubes appeared to be straight; second, application of the Bernoulli equation seemed to predict the local leakage velocity well; and finally, flow angles observed could be closely predicted (assuming the tangential velocity is conserved). Based on these assumptions, a leakage flow could be predicted by using a simple iteration. The shroud-leakage algorithm used for this iteration was:

(1) Selection of a point on the pressure surface

(2) Determination of the tangential velocity and static pressure at a chosen point using experimental data or an analytical blade-to-blade calculation, or ultimately from a 3-D viscous solution in the channel

(3) Selection of a normal velocity component at a chosen point

(4) Determination of the flow angle from the known tangential velocity and the assumed normal velocity

(5) Construction of a straight line from the pressure-to-suction surface using the flow angle

(6) Determination of the static pressure found at the intersection point of the straight line and the suction surface

(7) Application of the Bernoulli equation in conjunction with a discharge coefficient yielding a new normal velocity on the pressure surface

(8) Repetition of steps (3) through (7) until there is no significant change in calculated normal velocity.

Table 2 Predictions of water-table cascade leakage rates

Clearance (in.)	Test Leakage (gal/min)	Model Leakage (gal/min)	Model Leakage / Test Leakage
0.043	3.83	3.56	0.93
0.086	7.71	6.58	0.85
0.130	10.397	9.51	0.91

This shroud-leakage algorithm was programmed and run for several water-table test cases. The pressure loading on the blade and the tangential velocity on the pressure side was taken from experimental data. Table 2 shows a comparison of the results. The analyses used a discharge coefficient of 0.80, corresponding to the data taken from the double-side discharge rig. The results were low, since the measured flow rate was computed using the peak velocities discussed earlier in this paper. Figure 5 shows a comparison between the calculated leakage velocity and the measured values. Figure 6 presents the measured and calculated flow directions. Considering the simplicity of the model, the results were quite good. Most of the errors between theory and data occurred in the leading- and trailing-edge regions, where 3-D effects would be the greatest, and where measurement errors were most likely to occur.

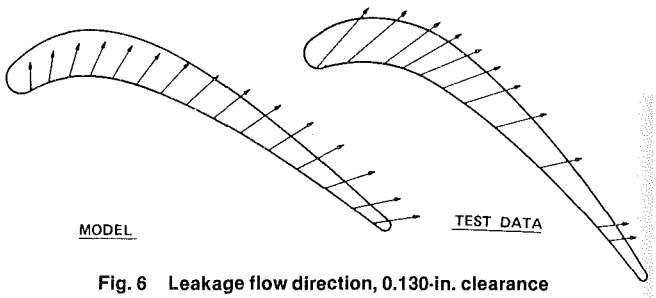


Fig. 6 Leakage flow direction, 0.130-in. clearance

Design Optimization

The ultimate application of the preceding methodology is its incorporation into a design system used to minimize tip losses – either by using it to supply a boundary condition to a 3-D rotor analysis or by using it to minimize the tip-leakage mass flow by adjusting the blade shape or loadings.

To demonstrate that reducing tip-leakage flow to reduce tip losses is a valid approach, the LART stage was used to test a flow-control sealing concept designed to minimize tip leakage mass flow. The level of tip clearance loss was demonstrated through a clearance test. During this test, the rotor tip was ground 0.026 in. to give a 3-percent clearance (0.039 in.). The tested total-to-total efficiency at the design point dropped from the original 92.0 to 89.0 percent, giving a 1.5-percent loss in efficiency for each percent of additonal clearance.

Four test series were conducted to develop a seal producing the minimum discharge coefficient. These were accomplished using the single-side discharge rig, the double-side discharge rig, and the water-table cascade. A final series of tests was then conducted on the single-side discharge rig to verify the design optimization. Testing in this hierarchal pattern allowed the opportunity of rapidly evaluating the maximum number of concepts requiring minimal time and cost – a practical design approach.

The configurations tested are shown in Figure 7. These configurations include a newly developed turbine concept called a "winglet." The idea behind the winglet design was to provide a large inlet-pressure drop by flow coming down over the sharp edge – with the potential for even greater improvement by reducing the surface-to-surface pressure drop with actual blading. The winglet produced about a 9-percent decrease in discharge coefficient relative to the flat tip. The results are shown in Fig. 8. Obviously, the greatest flow reduction is for a knife-edged tip. This exact configuration is impractical, however, due to mechanical and cooling constraints. The squealer design concept also proved to be a good performer. However, the strong dependence of performance on geometry and Reynolds number suggests that the squealer design can be haphazard. Good performance may be reliably obtained only through a viscous analysis or detailed testing.

An extensive series of tests was conducted using the double-side discharge rig. Altogether, 17 different configurations

Downloaded 01 Jun 2010 to 171.66.16.62. Redistribution subject to ASME license or copyright; see http://www.asme.org/terms/Terms_Use.cfm

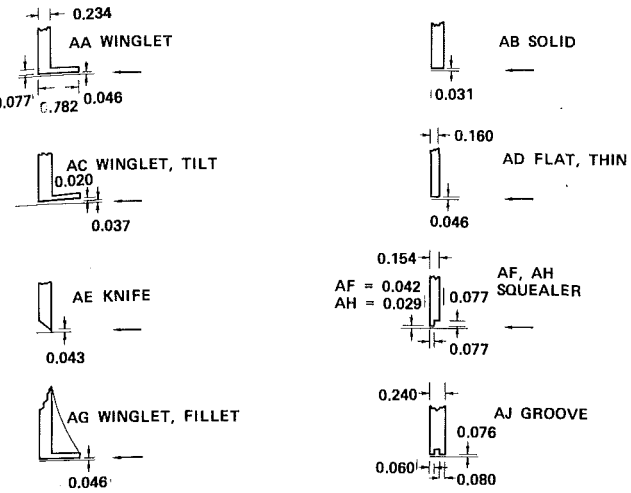


Fig. 7 Single-side discharge rig tested tip configurations

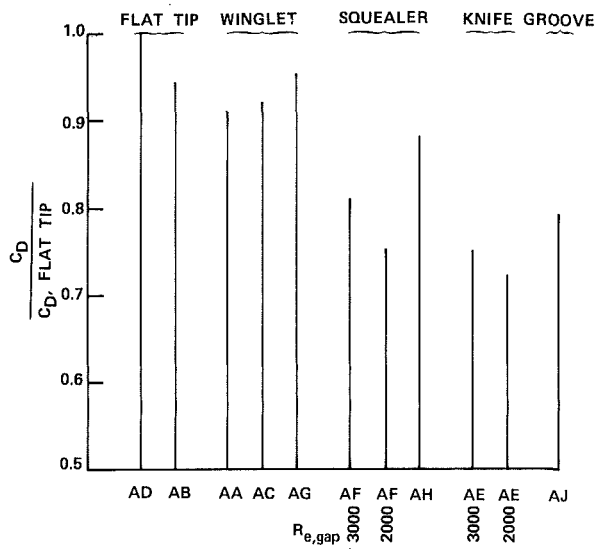


Fig. 8 Single-side discharge rig - series 2.

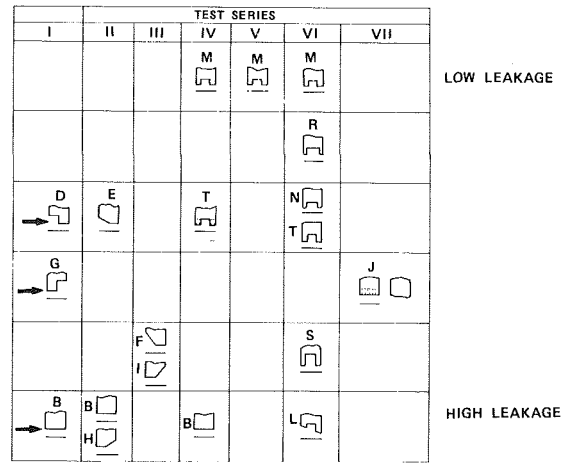


Fig. 9 Double-side discharge rig (test series and ranking)

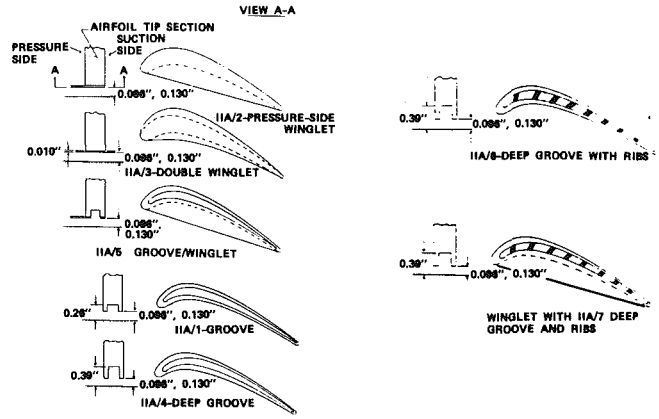


Fig. 10 IIA rotor-tip configurations

were tested. The configurations represented variants of "treated" flat tips, squealers, grooves, and winglets. More elaborate sealing configurations were possible on this rig, due to the thicker test section (0.500 versus 0.284 in.). The data from this test series are presented in Fig. 9. For purposes of comparison, there were seven test series conducted.

Table 3 lists the configuration ranking for the two discharge rigs of the three designs showing best results.

An evaluation of data taken from the test series indicates at first examination the superiority of grooves and squealers. However, both appear to be very sensitive to gap Reynolds number and configuration details, making it questionable as to whether design data for these configurations can be obtained directly from such simple experiments. One can anticipate that the effectiveness of grooves and squealers can vary widely depending on individual details of the application.

Ultimate verification of the optimal concept must be achieved over a blade tip with streamwise loading and pressure distributions inferred by the overall turning (circulation). The tests conducted on the water-table cascade rig provided this level of sophistication. The tips were designed to correspond to the best performers, as identified during the test series on the discharge rigs. These configurations are shown in Fig. 10.

Table 3 Configuration ranking

Rig Configuration	Ranking 1	2	3
Double-side discharge rig	Groove	Squealer	Bevel
Single-side discharge rig	Groove	Squealer	Winglet

The test results are shown in Fig. 11. The leakage flow rates measured for the grooved configurations may be slightly higher than presented. This is because the flow rate is calculated from the flow velocity, which in turn comes from a time-distance measurement; in the case of the groove configurations, the velocity levels are lower near the groove due to stream-tube expansion. In general, the leakage velocities were slightly higher than those achieved with winglets, so the groove-type configurations were not regarded as strong contenders for the candidate demonstration design. The distribution of leakage flow (with and without the winglet) is shown in Fig. 12. For the untreated IIA rotor tip, the leakage rates were highest near the trailing edge. The winglet, however, blocked this flow.

An additional element for this test series was the evaluation of a new blade tip. An additional design, designated IIC, was selected for which loading distribution was maintained, but with thickness reduced by 50 percent (maximum). The results of the IIC test (also shown in Fig. 11) indicated a performance degradation as thickness was reduced.

Downloaded 01 Jun 2010 to 171.66.16.62. Redistribution subject to ASME license or copyright; see http://www.asme.org/terms/Terms_Use.cfm

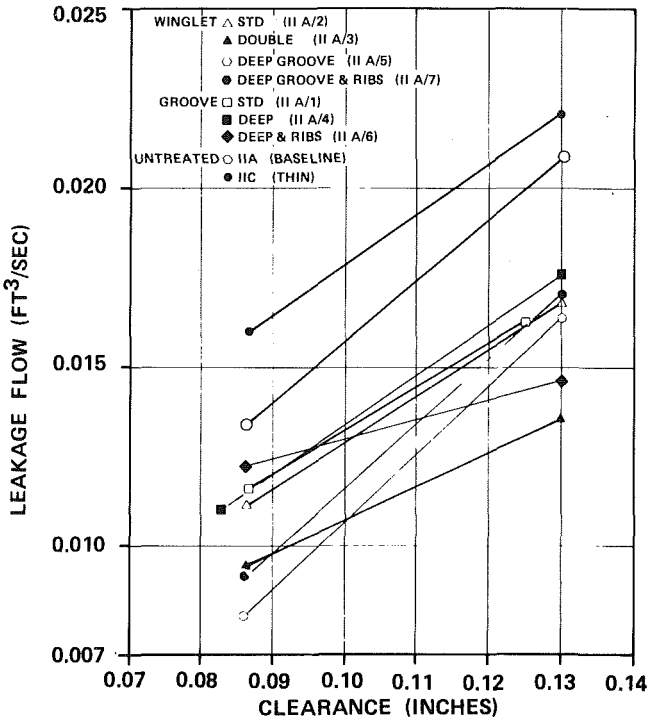


Fig. 11 Water-table cascade leakage results

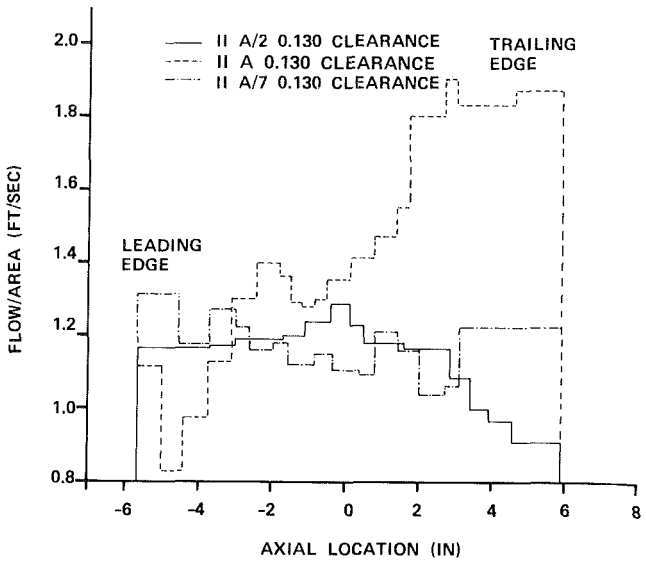


Fig. 12 Leakage mass flow distributions for winglet, baseline, and winglet with deep groove and ribs

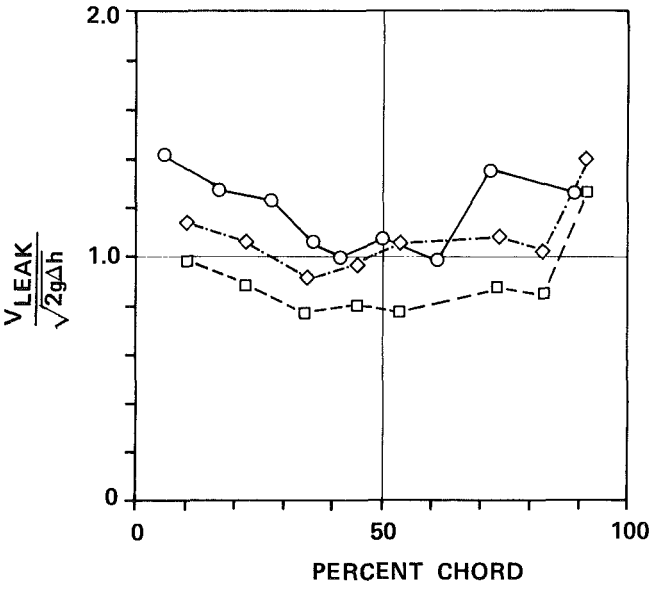


Fig. 13 Leakage discharge coefficient distribution

The cascade test indicated that winglets are somewhat superior to the grooved configuration – the high performers in the discharge rig tests. To understand this, one must realize that the winglet performance arises from a combination of reduced discharge coefficient and reduced pressure loading, whereas leakage reductions due to the groove are only due to the reduced discharge coefficient. To illustrate this point, a discharge coefficient distribution was defined in which the leakage velocity for several leak streamlines was normalized by the pressure head drop. Based on a full pressure drop, this distribution is plotted in Fig. 13 for both the winglet and baseline cases. Recall, however, that the winglet "sees" a reduced pressure drop across the tip, so a proper discharge coefficient must be based on the actual pressure drop across the tip. This distribution, based on a pressure drop inferred through interpolation of the pressure loading for the IIA baseline tip, gives a true discharge coefficient distribution for the winglet. The average performance improvement is 10 percent, a value entirely consistent with discharge rig results (Fig. 8).

To demonstrate the usefulness of tip treatment concepts for maintaining performance at high clearance levels, the rotor was tested with the winglet at a 3-percent clearance. The winglet-treated rotor showed efficiency gains of 0.6 (design point) to 1.05 percent at the extremes of speeds and pressure-ratio levels tested. These improvements yielded between a 11.5- and 20-percent improvement in comparison to flat tip efficiency-versus-clearance correlations. This compared to the anticipated 20-percent reduction in leakage flow based on the cascade tests.

Conclusions

The objectives of the tip-leakage studies were two-fold: first, an adequate model, directly compatible with the 3-D viscous solution, was needed; and second, improvements in tip-leakage configuratons were needed along with a systematic economical approach to developing such systems. The first objective resulted in a simple model ideally suited for interfacing with the 3-D viscous rotor analysis under development. The second objective was achieved by experimentally examining numerous tip configurations in simple test rigs.

Because of the nature of the leak processes, configurations tested thus far resulted only in limited improvements in leakage flow at the expense of considerable complexity in tip configurations. However, as a test of the concepts developed in the simple experiments, improvements predicted by simple discharge experiments were realized in both cascade tests and in a full-sized rotating turbine stage. Further improvements will result when complex configurations can be analyzed and the discharge coefficient predicted.

Downloaded 01 Jun 2010 to 171.66.16.62. Redistribution subject to ASME license or copyright; see http://www.asme.org/terms/Terms_Use.cfm

The relative motion of the blade was not addressed in the simplified experiments, since it is believed that the primary effect would be to alter the tip-periphery pressure-distribution (which drives the leakage flow), due to the scraping phenomenon in the rotor passage. However, wall motion must still be treated in the profile supplied to the appropriate rotor analysis. This subject will be discussed in Part II of this paper [4].

Acknowledgments

This work was supported by the Air Force Aero Propulsion Laboratory (AFAPL) Program for the Low-Aspect-Ratio Turbine, Part V, (Contract No. F33615-74-C-2017) under the direction of Dr. Kervyn Mach. The writers would like to thank Dr. Henry Woodard of Garrett Turbine Engine Company for his efforts in the testing and modeling activities, and Northern Arizona University students Lloyd Carleton, Bryon Cain, and Cheryl Aurand for their efforts in conducting the required water-table measurements. We would also like to thank Mr. Robert Boorman of Garrett for conducting the demonstration stage tests and Mr. Hsin-Chien Liu for the analysis of the stage-test results.

References

1 Lakshminarayana, B., "Methods of Predicting the Tip Clearance Effects in Axial Flow Machinery," ASME *Journal of Basic Engineering,* Vol. 92, pp. 467–482, 1970.

2 Rains, D. A., "Tip Clearance Flows in Axial Flow Compressors and Pumps," California Institute of Technology Report No. 5, June 1954.

3 Liu, H.C., T.C. Booth, and W.A. Tall, "An Application of 3-D Viscous Flows Analysis to the Design of a Low-Aspect-Ratio Turbine," ASME Paper 79-GT-53.

4 Wadia, A. R., and T. C. Booth, "Rotor-Tip Leakage, Part II — Basic Methodology," ASME Paper, Gas Turbine Conference, Mar. 1981.

Downloaded 01 Jun 2010 to 171.66.16.62. Redistribution subject to ASME license or copyright; see http://www.asme.org/terms/Terms_Use.cfm

Rotor-Tip Leakage: Part II—Design Optimization Through Viscous Analysis and Experiment

A. R. Wadia

T. C. Booth

Garrett Turbine Engine Co.
Phoenix, Ariz., 80501

Blade tip losses represent a major efficiency penalty in a turbine rotor. These losses are presently controlled by maintaining close tolerances on tip clearances. This two-part paper outlines a new methodology for predicting and minimizing tip flows, and focuses on the control of tip leakage through minimization of the discharge coefficient to control the normal leakage flow component. Minimization of the discharge coefficient was achieved through viscous analysis and was supported by discharge-rig testing. The analysis for the discharge cross-flow used a stream function-vorticity formulation. Support testing was conducted with a newly developed water table discharge rig in which tip-coolant discharge could also be simulated. Experimental and numerical tip-leakage results are presented on a discharge coefficient parameter for five different tip configurations. In addition, numerical studies were conducted for stationary and rotating blades with and without tip coolant injection.

Introduction

Part I [1] of this paper described an approach in which a balance of pressure and convection was found to dominate rotor-tip leakage. The flow was such that viscous effects were reduced, creating separations and reattachments. It was determined that the rotor tip could be modeled as a special orifice, and that even though streamwise momentum becomes nearly uncoupled during the leakage process, it is preserved across the gap.

The decoupling of streamwise and leak momentum implies that a low-leakage tip may be designed through consideration of the flow normal to the camberline. In Part I of this paper, two discharge rigs were described that measured the discharge coefficient of the normal flow component and steps were taken to determine an optimum rotor tip. In this paper, the decoupling principal was applied to the design of new flow-control configurations as part of a product improvement program. The key design element was the discharge coefficient; therefore, this study included the development of a two-dimensional viscous analysis for the perpendicular flow components, which was calibrated through a corresponding series of flow tests. A new single-side discharge rig was designed which has the added capability of rotor-tip discharge.

Numerical Analysis

Governing Equations. The basic incompressible-flow equations used are the vorticity transport equation in conservation form:

$$\frac{\partial \omega}{\partial t} = - \nabla \cdot (\mathbf{V}\omega) + \frac{1}{R} \nabla^2 \omega, \tag{1}$$

and the Poisson equation for the stream function

$$\nabla^2 \psi = \omega. \tag{2}$$

In the above equations, distance was normalized by the tip clearance, time by the advective constant $(L_g/\bar{U})$, velocity by the inflow velocity $(\bar{U} = \dot{m}/\rho L_g L_z)$, and vorticity by $(\bar{U}/L_g)$. As suggested by Roache [2], equation (1) was left in its unexpanded form, although the term $\nabla \cdot (\mathbf{V}\omega)$ could be reduced to $\mathbf{V} \cdot \nabla \omega$ by using the incompressible continuity equation. Proper finite differencing would then result in a conservative system [3].

Finite-Difference Approximation. The velocity components were obtained from the stream-function distribution by central differencing using unequal step sizes.

The vorticity was then advanced in time, as

$$\omega_{i,j}^{n+1} = \omega_{i,j}^{n} + \Delta t \Bigg[- \frac{u_R \omega_{R_1} - u_L \omega_{L_1}}{h_5} - \frac{v_R \omega_{R_2} - v_L \omega_{L_2}}{h_6} + \frac{1}{R} \Bigg\{ \frac{h_1 \omega_{i+1,j}^{n} - (h_1 + h_2)\omega_{i,j}^{n} + h_2 \omega_{i-1,j}^{n}}{0.5\, h_1 h_2 (h_1 + h_2)} + \frac{h_3 \omega_{i,j+1}^{n} - (h_3 + h_4)\omega_{i,j}^{n} + h_4 \omega_{i,j-1}^{n}}{0.5\, h_3 h_4 (h_3 + h_4)} \Bigg\} \Bigg] \tag{3}$$

where an upwind difference form [4,5] of the advection terms was used, and $h_1, h_2 \ldots h_6$ are defined in the Nomenclature. Also,

$$u_R = \frac{1}{2}(u_{i+1,j} + u_{i,j}),\ u_L = \frac{1}{2}(u_{i,j} + u_{i-1,j}),$$
$$v_R = \frac{1}{2}(v_{i,j+1} + v_{i,j}),\ v_L = \frac{1}{2}(v_{i,j} + v_{i,j-1}) \tag{4}$$

Contributed by the Gas Turbine Division of THE AMERICAN SOCIETY OF MECHANICAL ENGINEERS and presented at the Gas Turbine Conference & Products Show, March 9-12, 1981, Houston, Texas. Manuscript received at ASME Headquarters December 11, 1980. Paper No. 81-GT-72.

Copyright © 1982 by ASME

Downloaded 01 Jun 2010 to 171.66.16.62. Redistribution subject to ASME license or copyright; see http://www.asme.org/terms/Terms_Use.cfm

$$\omega_{R_2} = \begin{cases} \omega_{i,j}, \text{ if } v_R > 0 \\ \omega_{i,j+1}, \text{ if } v_R < 0 \end{cases} \qquad \omega_{R_1} = \begin{cases} \omega_{i,j}, \text{ if } u_R > 0 \\ \omega_{i+1,j}, \text{ if } u_R < 0 \end{cases} \tag{5a}$$

$$\omega_{L_2} = \begin{cases} \omega_{i,j-1}, \text{ if } v_L > 0 \\ \omega_{i,j}, \text{ if } v_L < 0 \end{cases} \qquad \begin{cases} \omega_{i-1,j}, \text{ if } u_L > 0 \\ \omega_{i,j}, \text{ if } u_L < 0 \end{cases} \tag{5b}$$

The Poisson equation for the stream function with the updated vorticity source term is solved using optimized successive over-relaxation by:

$$\psi_{i,j}^{(k+1)} = \psi_{i,j}^{(k)} + \omega_0 \left[\frac{h_1 h_2 h_3 h_4}{h_1 h_2 + h_3 h_4} \right] \left[\frac{h_1 \psi_{i+1,j}^{(k)} + h_2 \psi_{i-1,j}^{(k+1)}}{h_1 h_2 (h_1 + h_2)} \right.$$

$$\left. + \frac{h_3 \psi_{i,j+1}^{(k)} + h_4 \psi_{i,j-1}^{(k+1)}}{h_3 h_4 (h_3 + h_4)} - \frac{\omega_{i,j}}{2} - \frac{h_1 h_2 + h_3 h_4}{h_1 h_2 h_3 h_4} \psi_{i,j}^{(k)} \right] \tag{6}$$

The parabolic equation for the vorticity was solved by explicitly marching-in-time from an initial condition, with the steady-state solution attained as an asymptotic time solution. At each time step, the elliptic stream-function equation was iteratively solved using an optimized successive over-relaxation (OSOR) method. During the numerical experiments, the OSOR parameter, ω_0, was determined to be 1.75. For the Poisson equation, the iterative solution was not allowed to proceed more than ten iterations for the first hundred time steps, as the transient solution was of no practical importance for leakage analysis.

Mesh-Generation and Coordinate-Stretching Functions. As shown in Fig. 1, a linear-coordinate stretching function was used to obtain nonuniform spacing of the grid in the x and y directions with the mesh concentrated near the tip pressure and suction sides and on any other corners (i.e., winglet, squealer tip, etc.), and in the clearance region.

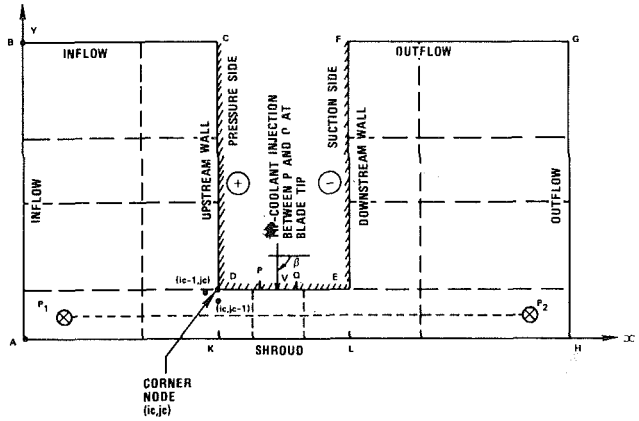


Fig. 1 Computational domain. Orientation is perpendicular to the camber line.

Sharp gradients required more mesh points within the tip clearance and near the sharp corners and solid boundaries. Upstream and downstream of the blade tip, the gradients were not large enough to warrant a closely spaced mesh. Therefore, large spatial steps were used in these regions. The size of the mesh typically consisted of 61 by 41 nodes. The minimum values of Δx and Δy (near corners or walls where sharp gradients exist) were 0.5 and 0.1, respectively.

Convergence Criteria and Error Analysis. Based on a stability analysis, the critical time step to avoid dynamic instability (Roache [2]) was 0.01 for calculations of Reynolds numbers between 400 to 10,000.

The criteria used to determine convergence for the solution of ψ at each time step and the asymtotic steady-state solution of ω were studied in detail. The criterion adopted was to limit fractional changes of ω to 0.001 and changes of ψ to 0.0001.

The truncation error in the upwind-difference formulation of the advection terms for $\omega \simeq$ constant was:

Nomenclature

β = tip-coolant velocity discharge angle
C_1 = constant depending on density and discharge area
C_D = discharge coefficient
Δn = normal distance from the wall to the first grid line adjacent to the wall
e = truncation error of upwind-differencing of advection terms
g = gravity constant
$h_1 = x_{i,j} - x_{i-1,j}$
$h_2 = x_{i+1,j} - x_{i,j}$
$h_3 = y_{i,j} - y_{i,j-1}$
$h_4 = y_{i,j+1} - y_{i,j}$
$h_5 = 0.5\,(h_1 + h_2)$
$h_6 = 0.5\,(h_3 + h_4)$
L_g = tip clearance, gap height
L_z = width in z direction (assumed to be unity)
$\dot{m}$ = mass flow rate
$\dot{m}_{lkg}$ = leakage mass flow rate
$\dot{m}_{pri}$ = mass flow rate at the entrance to the test section in the experiment
$\dot{m}_{sec}$ = secondary mass flow rate (tip injection)
$\dot{m}_{total}$ = total mass flow rate $(\dot{m}_{lkg} + \dot{m}_{sec})$
p = static pressure (normalized by $\rho \bar{U}^2$)
ΔP = pressure drop
R = Reynolds number $= \dfrac{\bar{U} L_g}{\nu}$
$\Delta\psi$ = change in stream function due to tip discharge
ψ = stream function
ρ = density
U_s = tip velocity
$\bar{U}$ = reference velocity $= \dfrac{\dot{m}_I}{\rho L_g L_z}$
t = time
μ = coefficient of viscosity
ν = kinematic viscosity
u,v = x,y components of velocity
$\mathbf{V}$ = (u,v)
W = weight
ω = vorticity
ω_0 = optimized successive over-relaxation parameter
x,y = cartesian coordinates
∇ = gradient (del operator)

Subscripts

D = downstream
I = inlet conditions (inflow)
i, j = node indexes in x,y directions
O = outflow conditions
U = upstream
WALL = wall values

Superscripts

k = iteration
n = time level

Downloaded 01 Jun 2010 to 171.66.16.62. Redistribution subject to ASME license or copyright; see http://www.asme.org/terms/Terms_Use.cfm

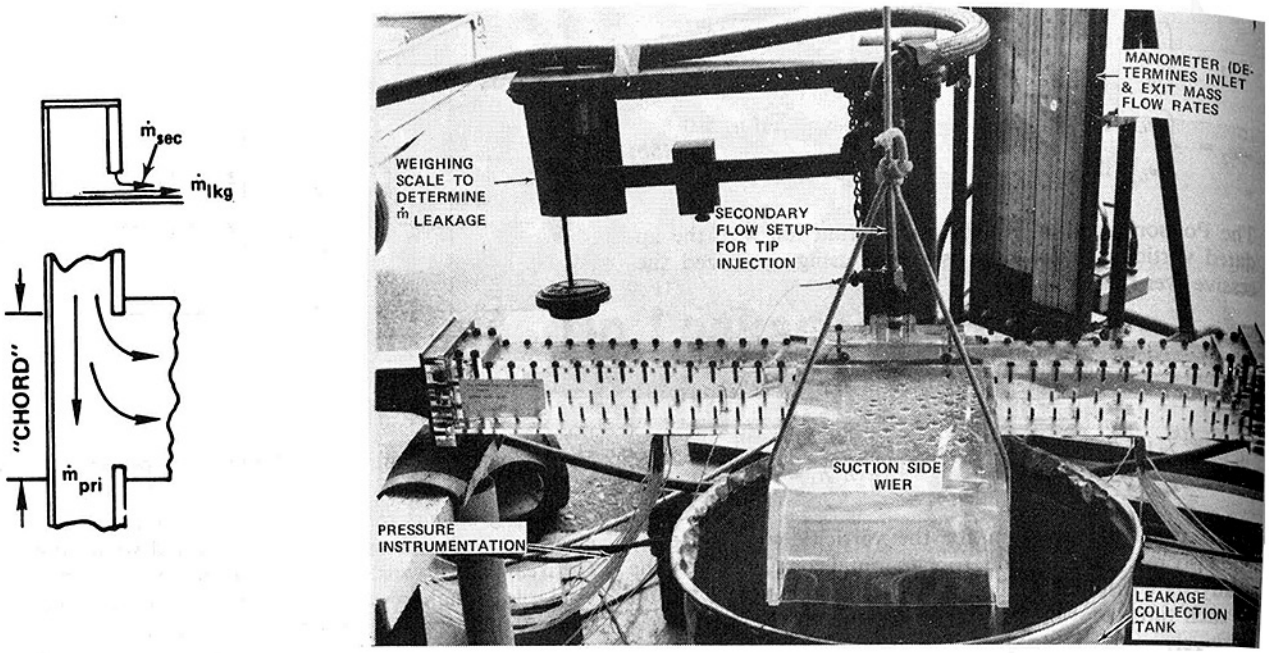


Fig. 2 Test rig

$$e = \frac{1}{h_1 + h_2}\left\{\left(\frac{h_1}{h_2} - 1\right)\left(u_{i+1} - u_i\right) + \left(\frac{h_2}{h_1} - 1\right)\left(u_i - u_{i-1}\right)\right\} \tag{7}$$

Within the clearance gap, $h = h_1 = h_2$ and e = zero, while far upstream and downstream of the blade, e is typically of order 10^{-4}.

Boundary Conditions. A major part of the present work involved the development of realistic, accurate, and stable boundary conditions.

Along the shroud end wall and the blade walls (Fig. 1), the boundary conditions specified are no slip, thus allowing specification of tip speed through a relative wall translation. Along the inflow and outflow boundaries, a radial potential flow solution was implemented. The validity of this boundary condition was based on the assumption that the inflow and outflow boundaries were "far" upstream and downstream from the viscous region within the tip clearance space.

The boundary conditions for tip-coolant discharge on PQ was produced by a parabolic velocity distribution. The leakage was specified by the stream function increment $\psi_Q - \psi_P = \Delta\psi$, the injection angle β, and the peak injection velocity.

Regardless of the wall orientation or the boundary value of ψ, the wall vorticity on all stationary walls (CD, DP, QE, EF) without mass injection is:

$$\omega_{WALL} = \frac{2(\psi_{WALL+1} - \psi_{WALL})}{(\Delta n)^2} + 0(\Delta n) \tag{8}$$

where Δn was the normal distance from the wall node to the adjacent node. This first-order form was determined by Thom [6,7] and has been extensively used in other research. For the shroud, the vorticity was determined as:

$$\frac{2(\psi_{WALL+1} - \psi_{WALL} - U_s\Delta y)}{(\Delta y)^2} + 0(\Delta y) \tag{9}$$

Along the surface of tip discharge, the vorticity was computed by:

$$\frac{2(\psi_{WALL-1} - \psi_{WALL} + u\Delta y)}{(\Delta y)^2} + \frac{\partial^2\psi}{\partial x^2} \tag{10}$$

where $\partial^2\psi/\partial x^2$ was determined from the distribution of ψ across the tip injection area.

Based on the original idea of Thoman and Szewczyk [8], the boundary condition $\partial\omega/\partial n = 0$ was imposed on the vorticity at the inflow and outflow boundaries. Other vorticity conditions (Roache [2]) were investigated in detail; numerical experimentation suggested that the above Neumann condition gave the best results.

A number of alternatives are available in the open literature [2,9] for the treatment of vorticity at a sharp corner. Two of these alternatives were numerically investigated in detail. Both were first-order formulations for the corner vorticity, consistent with the wall equation (8). Referring to the corner point D in Fig. 1 and defining node as (ic, jc), the wall equation applied to the upstream wall gave:

$$\omega_U = 2(\psi_{ic-1,jc} - \psi_{ic,jc})/(\Delta x)^2 \tag{11a}$$

If applied to the downstream side, the wall equation yielded:

$$\omega_D = 2(\psi_{ic,jc-1} - \psi_{ic,jc})/(\Delta y)^2 \tag{11b}$$

This method produces two values of the corner vorticity. When the vorticity was used in a difference equation about node ($ic-1$, jc), the corner vorticity is set equal to ω_U. Similarly, when the vorticity was used in a difference equation about node (ic, $jc-1$), the corner vorticity was set equal to ω_D.

The other method studied attempted to force separation at a sharp corner by specifying $\omega_D = 0$. This separation model was subsequently studied for a pressure-side cut on the blade tip (Fig. 3). The results implied that the model is incapable of forcing any corner separation along the pressure-surface cut. Hence, it is preferable to use the discontinuous values of the corner vorticity, and to let the separation develop as a part of the numerical solution.

Discharge Coefficient and Pressure Solution. For a specified value of the inlet mass flow, the pressure drop across the width of the tip was computed, from which the discharge coefficient was calculated. Several definitions of the discharge coefficient were considered in the analysis. The definition determined to be most suitable was:

Downloaded 01 Jun 2010 to 171.66.16.62. Redistribution subject to ASME license or copyright; see http://www.asme.org/terms/Terms_Use.cfm

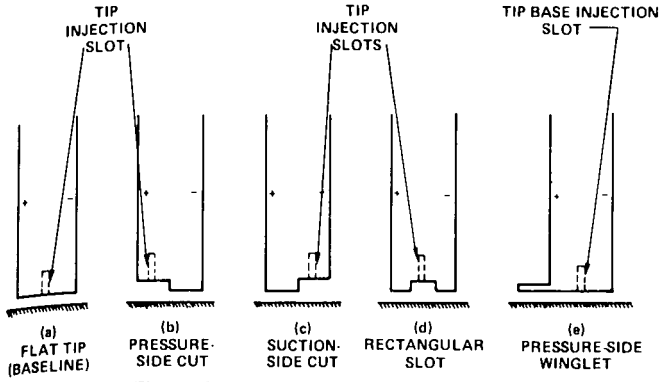


Fig. 3 Typical tip configuration concepts

$$C_D = \frac{(1.0 - \Delta\psi)}{\sqrt{2}(P_1 - P_2)} \tag{12}$$

This formula represents the ratio of the actual mass flow to the ideal mass flow, where the ideal mass flow was based on the pressure drop along a "y = constant line" in the middle of the clearance space (Fig. 1).

The pressure drop was obtained by numerically integrating the discretized equation for $\partial P/\partial x$ (x-momentum equation), while the velocity components were obtained from the stream-function solution. To reduce quadrature errors, the integro-differential equation was discretized in a conservative form for the x components and in nonconservative form for the y components as:

$$\frac{\partial p}{\partial x} = \frac{\partial f_1}{\partial x} + f_2 \tag{13a}$$

where

$$f_1 = \frac{1}{R}\frac{\partial u}{\partial x} - \frac{u^2}{2}; f_2 = -v\frac{\partial u}{\partial y} + \frac{1}{R}\frac{\partial^2 u}{\partial y^2} \tag{13b}$$

The finite-difference approximation to f_2 was obtained using second-order central difference formula for unequal node spacing. The f_1 in equation (13b) was differenced to be compatible with the quadrature formula used. The pressure was obtained using the trapezoidal rule.

The total pressure gradients could also be obtained from the vorticity values (see Ghia, et al. [10]) as:

$$\frac{\partial P_0}{\partial x} = -v\omega + \frac{1}{R}\frac{\partial \omega}{\partial y} \tag{14}$$

Using central differences to compute the derivatives in equation (14), the total pressure along the path P_1P_2 (Fig. 1) was obtained using the same quadrature formula as before. The results for the static pressure using equation (14) are in excellent agreement with those obtained using equation (13).

Experimental Investigation

As discussed in Part I of this paper, the flow conditions near a typical turbine rotor tip are such that a scaled test could be performed on a simplified water-table test rig. This test could be designed to reproduce the critical nondimensional groups (Reynolds number, pressure drop scaled to dynamic head, geometric ratios, etc.).

The double-side discharge rig developed for the first test series in Part I of this paper was designed around a system of four Venturis. Once the through-flow had been determined, gap leakage flow could be inferred through subtraction. This data acquisition technique places stringent constraints on the level of permissible error in each Venturi measurement. Using this technique, the leakage flow levels approached the error tolerance band.

To overcome this, a new test rig was designed with a primitive but accurate measurement capability for leakage flow. The results obtained in Part I of this two-part paper showed that the suction-side velocity had a second-order effect on leakage. Based on this fact, the rig design for the tests reported herein had only a pressure-side transverse velocity, and the suction side of the leakage gap was a "dump". Thus, leakage could be measured by simply collecting the leakage flow and measuring the discharge time – an accurate procedure.

The water-table test rig was designed based on the flow and geometric parameters of a typical Garrett turbine rotor. An important new feature designed into the rig was a provision for tip injection. In addition, careful attention was paid to providing dense instrumentation for measuring the gap static pressure distribution.

Rig Design and Features. The test section geometry was:

Axial chord = 10.36 cm
Blade thickness (based on maximum thickness) = 1.59 cm
Tip clearance = 0.254 cm
Test section flow area = 30.49 cm^2
Test section height = 5.72 cm
Test section width = 5.33 cm

The Reynolds number based on chord (1.9×10^5) was obtained from the rotor velocity diagram. The tip-injection parameters were scaled to correspond to actual engine coolant discharge conditions, i.e., a 1 percent leakage on the rig is equivalent to a 1 percent rotor-tip discharge flow relative to the primary flow.

Figure 2 shows the assembled rig with a 12-in. long suction-side wier. The injection provisions are shown schematically in Fig. 3.

Tip Configurations. Five basic types of tip configuration concepts were studied analytically and experimentally, and are shown in Fig. 3. Pressure taps were located under the blade tip and within the through-flow region near the pressure surface of the tip across the length of the test section. The pressure was measured using a scani-valve setup with an automatic digital recorder unit.

Summary of the Test Procedure. Using the test assembly shown in Fig. 2, the mass flow discharging from under the tip was collected for a specified time and the leakage flow rate was computed. The pressure drop was based on the upstream gauge pressure – the discharge was ambient.

For tip injection studies, the leakage mass-flow rate is computed by:

$$\dot{m}_{\text{lkg, actual}} = \dot{m}_{\text{total}} - \dot{m}_{\text{sec}} \tag{15}$$

$$C_D = \frac{\dot{m}_{\text{lkg, actual}}}{\dot{m}_{\text{lkg, ideal}}} \tag{16}$$

where $\dot{m}_{\text{sec}}$ is the tip discharge. The ideal leakage flow rate is computed using Bernoulli's equation and preserving tangential momentum.

Experimental Data Error Analysis. The experimental discharge coefficient can be simplified to the form

$$C_D = C_1 \frac{W}{t\sqrt{P}} \tag{17}$$

where W is the total weight of the leakage flow, t is the measured time, P is the pressure drop, and C_1 is a constant. Let δC_D, δW, δt, and δP be the errors associated with the measurements and the computed coefficients. This results in

$$C_D \pm \delta C_D = C_1 \frac{(W \pm \delta W)}{(t \pm \delta t)(P \pm \delta P)^{1/2}} \tag{18}$$

Downloaded 01 Jun 2010 to 171.66.16.62. Redistribution subject to ASME license or copyright; see http://www.asme.org/terms/Terms_Use.cfm

Using the binomial expansion and neglecting second and higher-order terms, equation (18) reduces to:

$$\frac{\delta C_D}{C_D} \sim \left|\frac{\delta W}{W}\right| + \left|\frac{\delta P}{2P}\right| + \left|\frac{\delta t}{t}\right| \tag{19}$$

From the accuracy of the measurements, $\delta W \simeq 0.1134$ kg, $\delta P \simeq 3.5154$ kg/m^2 and $\delta T \simeq 1$ second. For a typical case of the flat tip with $W \simeq 45.3$ kg, $P \simeq 315$ kg/m^2, $t \simeq 83$ sec, and $C_D \simeq 0.83$, the maximum error is:

$$\delta C_D \simeq 0.01678 \tag{20}$$

Experimental and Numerical Results

Table 1 shows the numerical and measured values of the discharge coefficient for no pressure-side through-flow tangential to the gap (i.e., $\dot{m}_{pri} = 0$) with no tip injection.

Table 1 Experimental and numerical results (no tip injection)

Experiment (No Through-Flow)	Analysis
Pressure-Side Winglet [R = 5840; C_D = 0.746]	Pressure-Side Winglet [R = 5840; C_D = 0.846]
Rectangular Slot [R = 6080, C_D = 0.794]	–
Suction-Side Cut Tip [R = 6331, C_D = 0.822]	Suction-Side Cut Tip [R = 6331; C_D = 0.887]
Flat Tip [R = 6523; C_D = 0.851]	Flat Tip [R = 6523, C_D = 0.864]
Pressure-Side Cut Tip [R = 7263; C_D = 0.925]	Pressure-Side Cut Tip [R = 7263; C_D = 0.956]

Experimental and analytical results suggest that the winglet configuration shows superior leakage performance. The analytical results, which agreed well with trends of the experimental results, showed the best agreement with the flat tip. Figure 4 shows a static pressure distribution across the width of the tip obtained numerically and by experiment for R = 5995. The analysis showed a greater drop in pressure near the inlet than the experimental results suggested. Pressure recovery outside the clearance space was quite small.

The analysis appears to predict a higher value of the discharge coefficient when compared to the water table experimental data. The maximum discrepancy between the viscous analysis and the experiment was observed for the case of the winglet (13 percent), and the minimum discrepancy occurs in the case of the flat tip ((1.5 percent) baseline configuration). It is believed that this particular behavior can be attributed to the numerical treatment of the singularity that exists at the sharp corners. The streamfunction at the sharp corner presents no problem, but there are several alternatives for the evaluation of the corner vorticity. In the present analysis, the discontinuous values of the corner vorticity are used. It appears that the error between the experiment and the analysis is a function of the number of corners being considered, the type of corner present, and the proximity of the corner nodes to each other (i.e., the resolution of the grid near the corners). Of the five tip configurations studied, the baseline configuration two corner nodes are placed the farthest apart. Both the squealer tips and the winglet have four corners. In the case of the winglet, two nodes are very close to each other. With the machine core requirement limitations, it was not possible to define the corner nodes at the tip of the winglet as accurately as for the flat tip and the two squealer tips. Both the experiment and the analysis indicate that the leakage is a strong function of the sharp gradients at the inlet. This suggests that to obtain good numerical results, two items become critical: (1) fine resolution of the grid near the corner node and (2), a fairly accurate treatment of the corner vorticity modeling [13]. For most of the configurations, the first item criterion was met reasonably well. The velocity profiles at the inlet of the clearance space suggest that even though the discontinuous treatment of the vorticity at the corners produces good results, there is still enough scope to improve the numerical model at the corners.

Supplemental analyses showed a sharp reduction in discharge coefficient with increasing cut height. Furthermore, analysis indicated that a longer, thinner pressure-side winglet tends to reduce the discharge coefficient slightly.

The average discharge coefficient with through-flow ($\dot{m}_{pri}$ = 1.39 kg/s) was about 2 to 4 percent less than the discharge coefficient with $\dot{m}_{pri}$ = 0.0. For example, the discharge coefficient for the flat tip decreased to 0.834.

Experimentally, the effect of tip injection for a flat tip (stationary blade) is to reduce the leakage discharge coefficient from 0.851 to 0.786 (as shown in Table 2). This reduction, predicted by the analysis, is also shown in Table 2.

The effect of increasing tip injection velocity was to reduce the discharge coefficient from 0.786 to 0.761. The analysis did not predict this reduction and had indicated no change. This discrepancy is believed to be due to a coarse computational mesh in the transverse direction. The results of the analysis show that at least five grid points are necessary across the

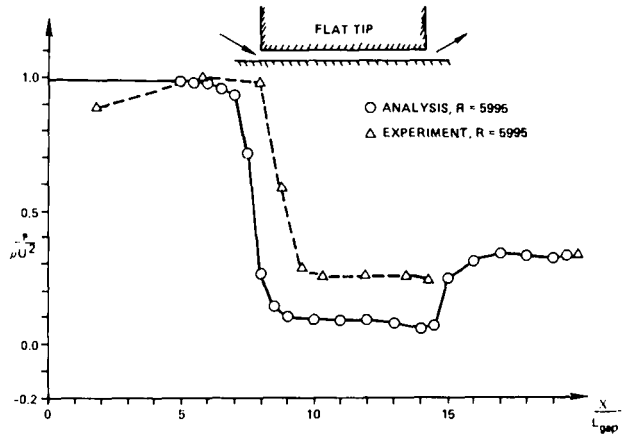


Fig. 4 Pressure distribution across the blade tip

Table 2 Experimental and numerical results (tip injection)

$\dot{m}_{sec}/\dot{m}_{pri}$	Experiment (No through-flow)	Analysis
0.0 percent	Flat Tip, R = 6523, C_D = 0.851	Flat Tip, R = 6523, C_D = 0.864
2.5 percent	Flat Tip R = 5112, C_D = 0.786	Flat Tip R = 5112, C_D = 0.796
5 percent	Flat Tip R = 5043, C_D = 0.781	Flat Tip R = 5043, C_D = 0.781

Downloaded 01 Jun 2010 to 171.66.16.62. Redistribution subject to ASME license or copyright; see http://www.asme.org/terms/Terms_Use.cfm

secondary flow area to have a decent resolution of the secondary flow velocity. This is the most probable reason why the analytical results for a flat tip with two different slot areas show almost negligible differences in discharge coefficient. For the case of the narrow slot, only a three-point grid was used across the slot resulting in a crude modeling of the physical injection conditions. This three-point grid resulted in a triangular-shaped profile rather than a parabolic profile, and the sharp discontinuity in slope at the middle node caused propagation of numerical errors into the clearance gap downstream from the point of injection.

Figure 5 shows the measured discharge coefficients for different tip discharge rates. Normally, the tip discharge rate at actual engine conditions is about 1 to 2 percent of the primary flow rate through the blade row. In this range, results showed that the performance increment at the 2 percent level

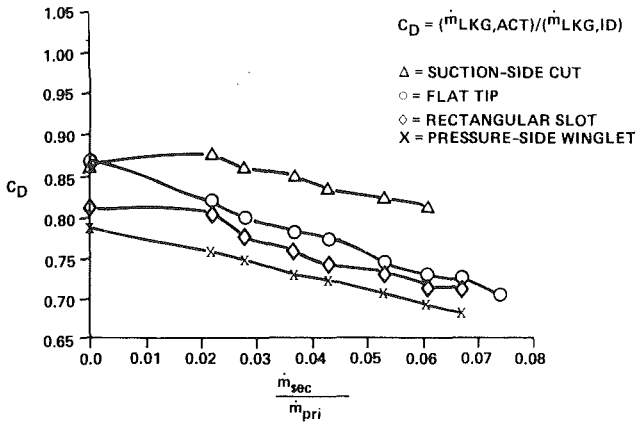


Fig. 5 Measured discharge coefficients for tip discharge configurations

is roughly equivalent between the flat tip, pressure-side winglet, and pressure-side cut.

It is obvious that this analysis technique is extremely powerful, and is capable of predicting a broader range of tip flow conditions than the current test rig permits. A primary example of this is the inability to measure effects of relative wall motion. The analysis was applied to predict the mutual effects of discharge, discharge angle, and relative wall speed. The flat tip results are summarized in Table 3.

The discharge coefficients were reduced due to wall motion. In a turbine, where the suction side leads in the rotation, the leakage flow opposes the shear flow. Therefore, this flow has a retarding effect on the "pressure drop" leakage flow and results in a reduction of the discharge coefficient. Similarly, in a compressor (where the pressure side of the blade leads in the rotation), the viscous drag of the stationary wall moving relative to the blade tip causes a flow relative to the blade tip from the pressure to the suction side, thus producing an increase in discharge coefficient.

The effect of the wall speed on the performance of the other tips, causes them to retain the same order as those with no wall speed (Table 1). The data obtained from the analysis for different tip injection angles, β, are summarized in Table 3.

Table 3 Predicted effects of injection and wall motion on discharge coefficient for the flat tip

Injection Angle β	Injection Fraction $\Delta\psi$	Wall Speed U_s	C_D
90 deg	0	0	0.851
45 deg	0.047	0	0.798
90 deg	0.047	0	0.797
135 deg	0.047	0	0.796
90 deg	0	−1.000	0.691
90 deg	0.047	−1.000	0.691

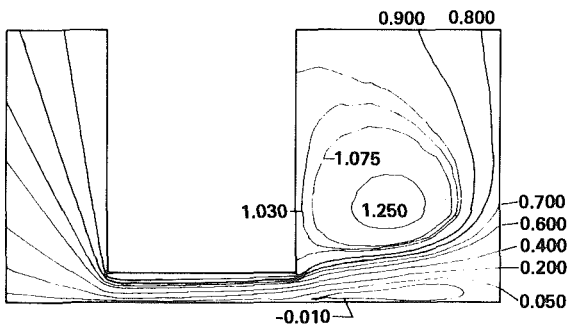


Fig. 6(a) Stationary blade, no tip injection

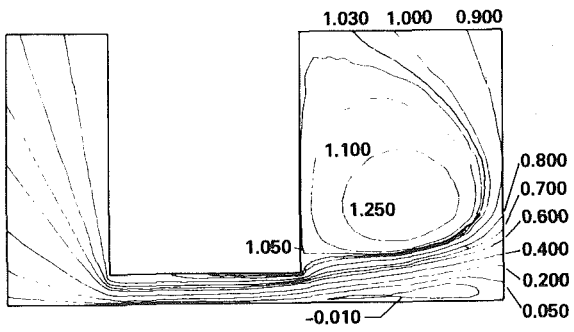


Fig. 6(c) Stationary blade, 2.5 percent tip injection

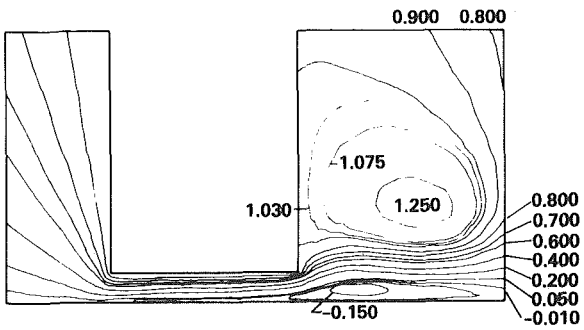


Fig. 6(b) Moving shroud, no tip injection

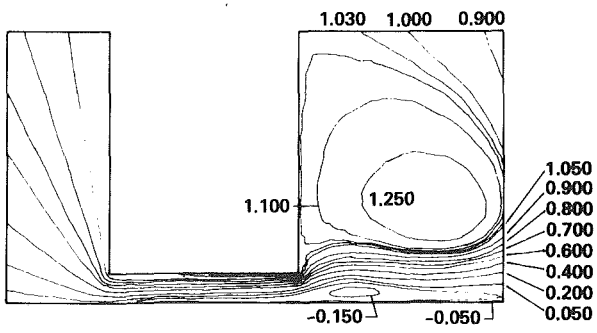


Fig. 6(d) Moving shroud, 2.5 percent tip injection

Fig. 6 Streamline patterns for the flat tip

Downloaded 01 Jun 2010 to 171.66.16.62. Redistribution subject to ASME license or copyright; see http://www.asme.org/terms/Terms_Use.cfm

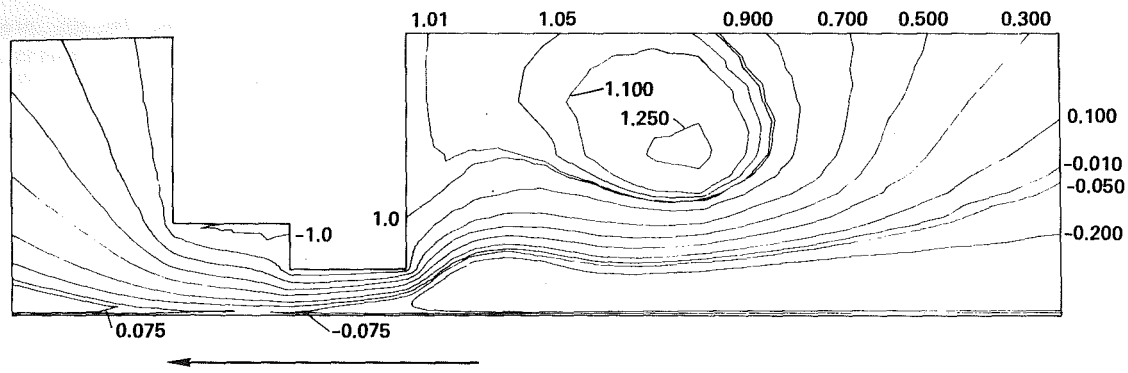


Fig. 7 Streamline pressure-side cut

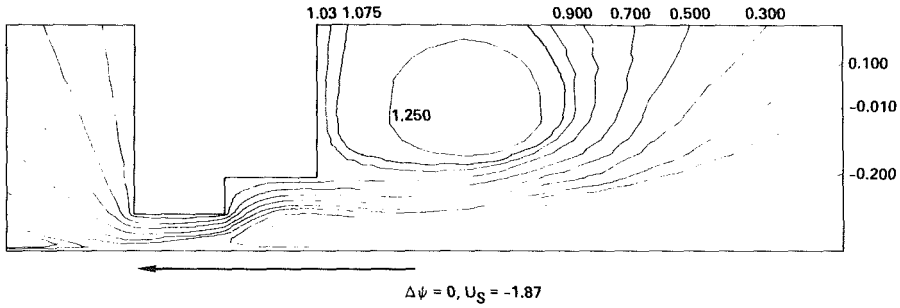


Fig. 8 Streamline suction-side cut

Injection angle is predicted to have a minimal effect for small tip discharge flow rate. Experimental correlation is not possible for these two cases, as no data are available at present.

The viscous effects of tip leakage flow are manifested in three ways and are shown in the stream function plots for the flat tip configuration under different conditions, Figs. 6(*a*) through 6(*d*):

- There is a resistance to the flow in the clearance
- The no-slip condition on the blade tip requires that the fluid be "pulled" with the blade as it rotates
- The case wall boundary layer flow impinges on the rotating blade.

Only part of the computational domain upstream and downstream of the blade tips is shown in each figure, and the different tip configurations with wall motion are shown in Figs. 7 – 10. With tip injection for a stationary blade, the analysis shows that tip separation is accelerated, resulting in a larger separation bubble for the pressure- and suction-side cut blade tips. However, this separation bubble is not so predominant for the flat-tip stationary blade with tip injection (Fig. 6(*c*)). With a moving end wall (relative frame of reference), the dividing streamline along the suction surface side at the tip is pushed vigorously upwards into the flow field away from the shroud, and the shape of the discharge jet as the fluid exits from within the clearance gap is altered considerably. While the discharge jet flares for a stationary blade, rotation tends to reduce the flare (Figs. 6(*c*) and 6(*d*)). Wall motion appears to separate the flow further, as indicated by the larger separation bubble on the pressure surface of the pressure-side cut (Fig. 7), while the separation region is greatly reduced on the suction surface of the suction-side cut (Fig. 8).

While tip injection with wall motion increases the size of the inlet separation from the pressure-side cut blade tip for all configurations, wall motion tends to strongly suppress the suction-side discharge effects.

Though no flow visualization experiments were conducted on the water rig, the stream function plots (Figs. 6(*a*) through 6(*d*)) show that the tip flow forms a thin jet that streams out into the main flow (suction side), maintaining its identity until it is rolled back by the main flow. It can be seen that after the jet is turned, it becomes a part of a turbulent cone flow (shown by analysis to be a vortex).

Conclusions

A numerical optimization technique and results for incompressible, laminar flow within tip clearance spaces of a conventional flat tip and four new tip configuration concepts using time-dependent finite-difference equations were determined. Conservative forms of the governing equations were used, with upwind-differencing for the advection terms. The transportive property of the differencing scheme was used to maintain the integral kinematic properties of the continuum solution. Particular attention was given to the boundary conditions – especially the vorticity at the sharp corner and the inflow and outflow boundaries. Using a water table rig, these results, with and without tip discharge for stationary blades were compared with those obtained by experiment on a scaled version of the blade tips. Typical streamline and velocity distributions were obtained for each of the different blade tip shapes. The separation patterns and vortex formation obtained agree well with those visualized experimentally by Rains [11].

The modeling for the analysis approach was developed within a simplified framework. Simplifying elements included streamwise momentum decoupling, laminar flow, and decoupling from far-field boundary conditions (such as the annulus boundary layer, etc.). These simplifications were made consistent with the ability to verify the details of the solution.

Downloaded 01 Jun 2010 to 171.66.16.62. Redistribution subject to ASME license or copyright; see http://www.asme.org/terms/Terms_Use.cfm

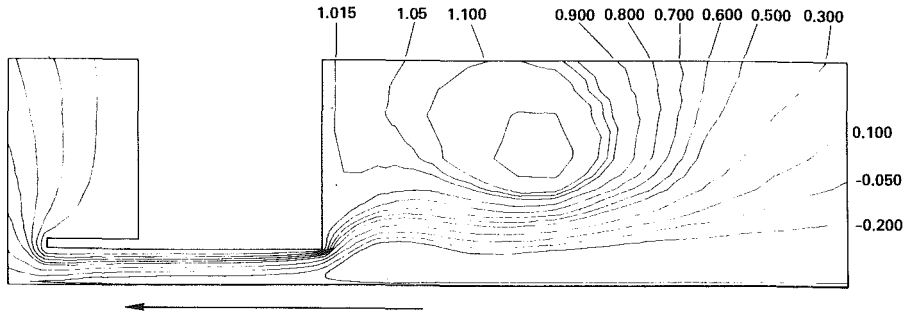


Fig. 9 Streamline pressure-side winglet

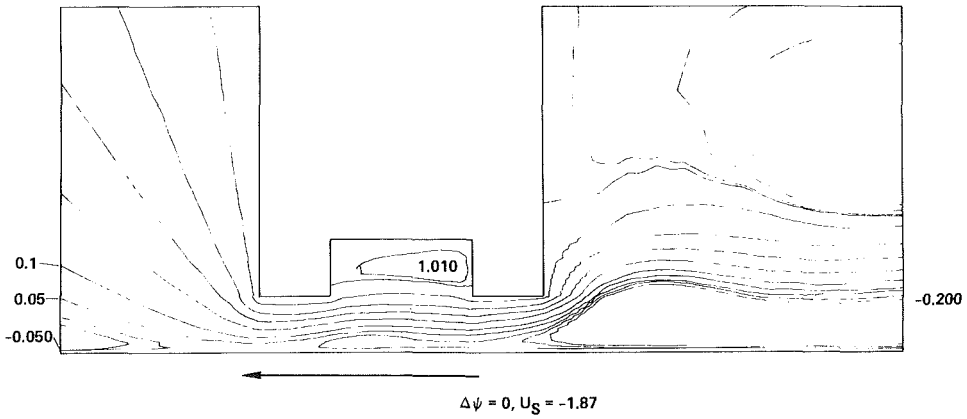


Fig. 10 Streamline pattern for a blade tip with a rectangular slot

The current analysis is now properly viewed as a starting point from which a more sophisticated rotor tip analysis may be developed. Refinements would include treating arbitrary wall motion, supplying an appropriate turbulence model, and introducing compressibility. Such additions must be accompanied by definitive experiments in which the overhead of the added sophistication may be verified and justified. This was sharply pin-pointed during the studies when an effort was made to predict the effect of turbulence on the flow. Increasing the viscosity by a factor of 50 in the separated zone for the suction-side squealer led to an increase of 0.01 for discharge coefficient. Thus, the additional sophistication of modeling afforded by an advanced turbulence model would not have been verifiable in the current study.

The numerical and experimental results suggest superior performance with the winglet configurations. This has been supported by experimental investigations [1,12]. The baseline numerical results showed excellent agreement with the water rig experiments. In general, the analysis showed similar qualitative trends as predicted from the experiment for all tip configurations. Tip discharge has a tendency to slightly reduce leakage flow. The tip discharge coefficient does not change significantly with tip injection angle. An increase in tip discharge velocity showed a slight decrease of the discharge coefficient. The analysis indicated that for the case of a turbine rotor, rotation will reduce leakage.

Acknowledgments

The authors would like to acknowledge the help of Mr. Gary Betzer, Mr. Norm Schoffield, and Mr. Nathan Adams for the design, fabrication, and assembly of the experimental setup.

References

1 Booth, T.C., Dodge, P.R. and Hepworth, H.K., "Rotor Tip Leakage: Part I-Basic Methodology," ASME Paper, Gas Turbine Conference, Mar. 1981.

2 Roache, P.J., *Computational Fluid Dynamics,* Hermosa Publishers, 1976.

3 Roberts, K.V. and Weiss, N.O., "Convective Difference Schemes," *Mathematics of Computations,* Vol. XX, No. 94, Apr. 1966.

4 Torrance, K.E., "Comparison of Finite Difference Computations of Natural Convection," *Journal of Research of the National Bureau of Standards,* Vol. 72B, No. 4, 1968, pp. 281-301.

5 Gentry, R.A., Martin, R.E. and Daly, B.J., "An Eulerian Differencing Method for Unsteady Compressible Flow Problems," *Journal of Computational Physics,* Vol. 1, 1966, pp. 87-118.

6 Thom, A., "An Investigation of Fluid Flow in Two Dimensions," ARC, R and M, No. 1194, United Kingdom, 1928.

7 Thom, A., "The Flow Past a Circular Cylinder at Low Speeds," *Proceedings of the Royal Society of London,* A141, pp. 651-666, 1933.

8 Thoman, D. and Szewczyk, A.A., "Time Dependent Viscous Flow over a Circular Cylinder," *The Physics of Fluids Supplement II,* pp. 76-87, 1969.

9 Gosman, A.D., Pun, W.M., Runchal, A.K., Spalding, D.B., and Wolfstein, M., *Heat and Mass Transfer in Recirculating Flow,* Academic Press, New York, 1969.

10 Ghia, U. and Goyal, R.K., "A Study of Laminar Incompressible Recirculating Flow in a Driven Cavity of Polar Cross-section," Numerical/Laboratory Computer Methods in Fluid Mechanics, Ed. A.A. Pouring and V.L. Shah.

11 Rains, D.A., "Tip Clearance Flow in Axial Flow Compressors and Pumps," California Institute of Technology, Hydrodynamics and Mechanical Energy Lab., Report No. 5, June 1954.

12 Patel, K.V., "Research on a High Work Axial Gas Generator Turbine," SAE Paper N o. 800681, 1980.

13 Lakshminarayana, B., Private Communication on Corner Vorticity Modeling, Under Investigation, 1980.

Downloaded 01 Jun 2010 to 171.66.16.62. Redistribution subject to ASME license or copyright; see http://www.asme.org/terms/Terms_Use.cfm

A Simple Model for Compressor Stall Cell Propagation[1]

N. A. Cumpsty
University Engineering Department,
Cambridge University,
Cambridge, England

E. M. Greitzer
Department of Aeronautics and Astronautics,
Massachusetts Insitute of Technology,
Cambridge, Mass.

A simple model for full-span stall cells in axial compressors has been formulated. The sudden changes in velocity across blade rows as the blade passages enter and leave the stall are shown to have important dynamical consequences for the stall flow field. The one empirical constant needed in the analysis is determined using the data of Day [1]. From this, reasonable predictions of stall cell speed and trends in speed have been obtained for a number of different compressors. From the satisfactory comparison between predicted and measured stall cell speeds, it is tentatively concluded that the model contains the essentials of a correct description of the controlling mechanism of full-span rotating stall.

Introduction

Not very much is known about the mechanism of rotating stall in axial compressors despite considerable work on this problem over the last three decades. One reason for the small amount of knowledge has undoubtedly been the difficulty in obtaining definitive information about the flow within the rotating stall cell. This hurdle was overcome by Day [1], and detailed measurements of velocity (magnitude and direction), static pressure, and total pressure throughout the stalled operating range of multi-stage axial compressors have been obtained. Some of these results have been published by Day and Cumpsty [2].

Even when the information about the physical quantities inside the cell is available, the mechanism is by no means obvious or clear. In reference [2], certain kinematic aspects of the flow were pointed out and their consequences elaborated upon. However, no explanation for the type of flow was offered there, and it has remained a mystery what determines the stall cell speed and why this varies in the way it does with parameters such as the number of stages, as shown in Fig. 1, which is taken from reference [1]. (Details of the geometry are also given in reference [3].)

The marked trends in stall cell speed with number of stages shown in this figure suggested that the controlling mechanism for some aspects could be inferred from the changes in the operating point of a given compressor as the number of stages was altered. The effect of changing the number of stages has been found to be very significant in determining the overall stalled compressor performance, as shown by Day, et al. [3]. The additional information which had been measured by Day [1], but not used in attempting to describe the stalled behavior up to now, was the circumferential variation in static pressure at the outer wall. It is the wall static pressures which form the main consideration of the present paper.

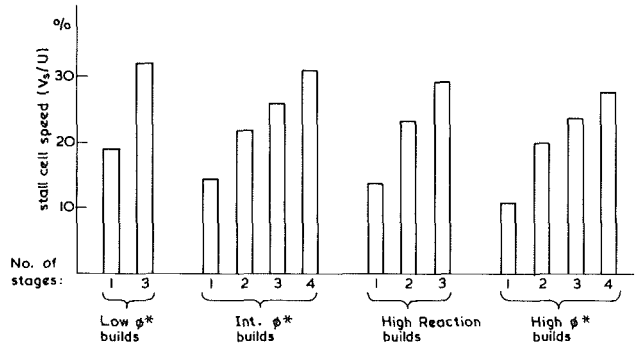


Fig. 1 Rotating stall cell propagation speed (Cells covering 50 percent of annulus; compressor builds tested by Day [1])

One of the principal flow quantities that has been examined in almost all analyses of rotating stall is the stall cell speed. The present paper also considers this aspect, not because the speed is of great practical importance, but because it is such a readily identifiable property of the process. The aim here is not so much to provide a method for determining stall cell speed, but to provide an overall, if approximate, description of the determining effects in full-span rotating stall. Two comments therefore seem appropriate at the outset. First, there is not enough information about the process in the stall cell to proceed without making some rather gross assumptions. Secondly, the detailed process in any stall phenomena is very complex and one should not therefore assess the results with the same rigor that would be applied to a description of unstalled flow.

In addition to the above general comments, it is also useful to preface the description of the model with several more specific statements concerning the background and scope of the present work. It is to be emphasized that the model developed below applies to *full-span* rotating stall, i.e., to the situation where there is a single stall cell extending from hub to tip over some fraction of the circumferential extent of the flow annulus. (This is in fact the more common situation in multistage compressors at speeds near design.) The part-span

[1] This work was partially supported under NASA Grant NSG 3208, J.J. Adamczyk, Contract Monitor.

Contributed by the Gas Turbine Division of THE AMERICAN SOCIETY OF MECHANICAL ENGINEERS for presentation at the Gas Turbine Conference & Products Show, March 9-12, 1981, Houston, Texas. Manuscript received at ASME Headquarters December 11, 1980. Paper No. 81-GT-73.

Copyright © 1982 by ASME

Downloaded 01 Jun 2010 to 171.66.16.62. Redistribution subject to ASME license or copyright; see http://www.asme.org/terms/Terms_Use.cfm

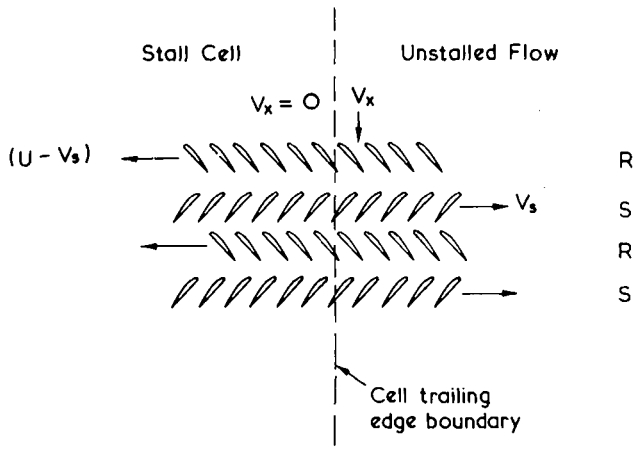


Fig. 2 Conditions at stall cell trailing edge (Drawn in system *fixed to stall cell*)

type of stall cell, which tends to occur in fans and multistage high pressure ratio compressors at part speed, is not considered. Further, it will be seen that much of the data presented below show propagation speeds in the range of 30 to 40 percent of rotor speed rather than 50 percent, a figure that is often quoted. If one examines the published stall data, however, it is observed that it is, in fact, the part span type of stall which is associated with this higher stall cell speed, and that the figure of 50 percent cannot be applied to the full span stall situation as a general rule.

In the next section the main points of Day and Cumpsty [2] relevant to the present work are recalled and some ramifications considered. The static pressure distributions measured by Day are then discussed with respect to the ideas inferred from the kinematics. Using these ideas and considering the overall dynamical aspects of the flow, an equation for the speed of full-span cells in terms of number of stages, axial velocity parameter and blade solidity is obtained. The remainder of the paper is discussion and consideration of the results of such predictions.

General Features of the Rotating Stall Flow Field

Day and Cumpsty [2] give a number of kinematic aspects of full-span stall cells in multistage compressors. Of particular significance to the present work are:

1 The stall cell is *axial* through the machine, it does not form a helix. The edges of the cell are generally very abrupt, this being particularly marked on the *trailing* edge of the stall cell.

2 Although the axial velocities are very much smaller in the stall cell than elsewhere, the tangential velocities are large, particularly upstream of the rotor. The notion of a "dead wake" type of cell, resembling a wake behind a large obstruction, is not tenable.

3 For the cases observed, flow enters the cell on the trailing side and leaves on the leading side. This is because the stall cell speeds were always less than half the blade speed, while the mean swirl velocity of a 50 percent reaction compressor is half the blade speed, so that fluid particles in the unstalled region are always "overtaking" the stall cell in the circumferential direction.

Figure 2 shows schematically the trailing edge of the stall cell. The stall cell is moving with circumferential speed V_s, and the rotor with velocity U (typically U is between two and five times V_s) in the same sense. As shown in the figure, it is convenient to adopt a frame of reference fixed to the stall cell, in which case the rotor blades are *entering* the cell with velocity U-V_s and stator blades are *leaving* with velocity V_s. This means that over a short circumferential distance, which data indicates are on the order of one or two blade pitches, the rotor blades are going from unstalled flow to stalled flow. Conversely the stator blades are changing from stalled flow to unstalled flow at the cell trailing edge. This means that the flow velocity in the rotor blade passage is changing suddenly from a large value to close to zero.

Because these changes will be quite abrupt, it seems likely that unsteady inertial effects will be locally dominant, and the pressure difference across the blade row, Δp, will be directly related to $\partial/\partial t$ (velocity in the blade passage). The partial derivative $\partial/\partial t$ may be expected to be proportional to the velocity with which the blade row crosses the stall cell boundary. It is thus expected that at the stall cell trailing edge there will be a *local* positive peak in pressure rise across the rotor and negative peak across the stator. Other things being equal, one should therefore expect the peak across the rotor row to be larger than across the stator because $U > 2V_s$. For example, with $V_s = 0.25U$, it follows that $U - V_s = 3V_s$ and so

$$\left(\frac{\partial}{\partial t}\right)_{\text{rotor}} = 3\left(\frac{\partial}{\partial t}\right)_{\text{stator}}$$

The overall pattern of local positive and negative pressures is thus illustrated schematically in Fig. 3. (By the same

Nomenclature

b = blade spacing (pitch) at mean radius
c = blade chord at mean radius
K = constant associated with unsteady pressure differences; defined in equation (4)
ℓ = distance along streamwise direction
N = number of stages
p = static pressure
p_T = total pressure
Δp = unsteady static pressure difference
Δp_{IGV} = unsteady static pressure difference across inlet guide vane row
Δp_r = unsteady static pressure difference across rotor row
Δp_{st} = unsteady static pressure difference across stator row
R = mean radius of compressor
t = time
U = rotor speed at midspan
V = velocity in streamwise direction
V_s = magnitude of stall cell propagation velocity
v_x = axial velocity
V_x = magnitude of axial velocity
x = axial coordinate
α_{IGV} = inlet guide vane stagger angle
α_r = rotor stagger angle
α_{st} = stator stagger angle
ρ = density
$\phi\left(= \frac{V_x}{U}\right)$ = axial velocity coefficient in stalled region
ϕ^* = design axial velocity coefficient
θ = circumferential position

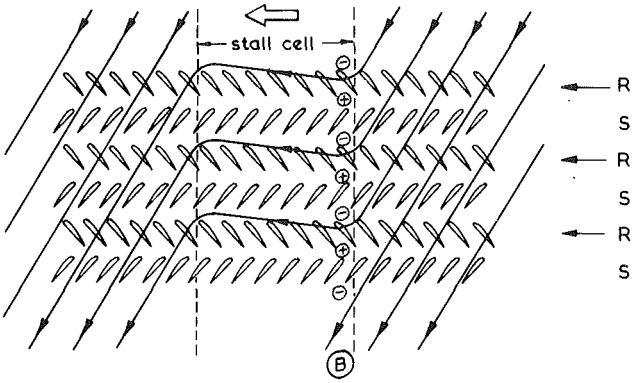
Superscripts

$(\bar{\ })$ = circumferential average

Subscripts

B = at trailing edge of stall cell
exit = at exit of compressor
inlet = at inlet of compressor

Downloaded 01 Jun 2010 to 171.66.16.62. Redistribution subject to ASME license or copyright; see http://www.asme.org/terms/Terms_Use.cfm



Note: ⊕ and ⊖ show relative levels of static pressure at cell trailing edge.

Fig. 3 Sketch of stall cell structure (Drawn in absolute reference frame)

arguments one might also expect that at the stall cell *leading edge* there would be a local negative peak across the rotor and a positive peak across the stator. The data, however, indicates that the axial velocity discontinuity is much less abrupt at the cell leading edge, and hence the pressure spikes should be much less evident.)

Before elaborating or becoming quantitative, it is appropriate to examine the measurements to establish whether spikes do appear at the edge of the stall cells in the measured pressure differences across the blade rows. When the wall static pressure distributions were measured the present use for them was not envisioned. Hence the pressure differences had to be obtained by measurement from the original pressure traces given in [1]. Despite this, the accuracy is quite sufficient for the purposes of this paper. Figure 4 shows the pressure changes across the blade rows for the three-stage, intermediate design flow coefficient ($\phi^* = 0.55$) machine; very similar effects are seen for the other builds. The plots show considerable variation in the pressure changes across blade rows in the middle of the stall cell but relatively little in the middle of the unstalled flow. Most remarkable are the strong, consistent, and nearly equal amplitude peaks at the trailing edge of the stall cell. These show, as expected, positive peaks across the rotor and negative peaks across the stator, with the latter being approximately 1/3 of the amplitudes of those across the rotor.

Fluid Dynamic Model

The previous section demonstrated that the dynamic consequences of the stall cell flow field, namely pressure spikes, can be seen in the measurements on the cell trailing edge. To make use of this the ideas must be quantified and the magnitudes related to other pressure changes in the flow.

Static Pressure Change at the Stall Cell Trailing Edge. Consider a rotor row entering the stall cell at the trailing edge; see for example Fig. 2. A short distance to the right of the cell the flow in the blade passages is high, while a very short time after entering the cell the velocity in the passage is approximately zero. It is appropriate to apply the unsteady Bernoulli equation

$$\frac{\partial V}{\partial t} + V\frac{\partial V}{\partial \ell} = -\frac{1}{\rho}\frac{\partial p}{\partial \ell} \tag{1}$$

assuming incompressible flow and neglecting shear stresses. Here ℓ is the coordinate along the direction of flow, which, as a reasonable approximation, will be the blade stagger line, and V is the velocity in the direction of ℓ. It is a fundamental postulate of the present work that local unsteady accelerations

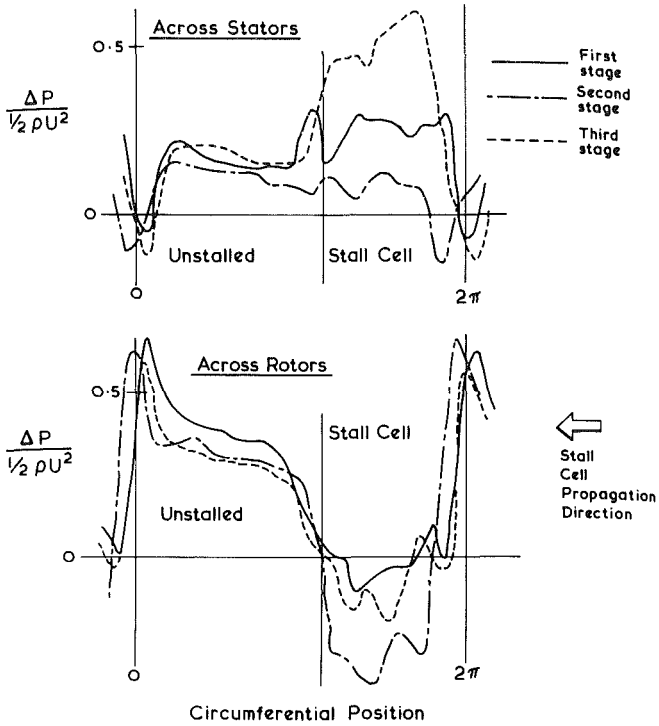


Fig. 4 Pressure differences across blade rows (three-stage compressor, $\phi^* = 0.55$)

are larger than convective accelerations

$$\left(\frac{\partial V}{\partial t} >> V\frac{\partial V}{\partial \ell}\right)$$

in the immediate vicinity of the stall cell edge. Then, integrating over the blade passage and taking V to be the average velocity over the passage cross section,

$$c\frac{\partial V}{\partial t} \approx -\frac{1}{\rho}\Delta p_r, \tag{2}$$

where c is the passage (i.e., chord) length and the abbreviation Δp_r is used for the pressure difference across the rotor row. In the unstalled flow $V \simeq V_x \text{ s } \alpha_r$, where V_x is the *unstalled* axial velocity and α_r the rotor stagger angle. During the deceleration process V changes from $V_x \text{ s } \alpha_r$ to zero over a circumferential distance of the order of a blade pitch, b. Since the rotor speed relative to the stall cell is $(U - V_s)$, it is then possible to write

$$\frac{\partial V}{\partial t} \approx -(V_s \sec\alpha_r)\frac{(U - V_s)}{b}. \tag{3}$$

so that the pressure spike across the rotor at the cell trailing edge will therefore be given by

$$\Delta p_r = K\rho\frac{c}{b}(V_x \sec\alpha_r)(U - V_s). \tag{4}$$

The nondimensional parameter K has been introduced to accommodate the uncertainties in the formulation. In particular the precise length to be used for integration of Bernoulli's equation in the streamwise direction is not necessarily the chord length, c, and the rate of change of velocity, $\partial V/\partial t$, will not be given precisely by assuming a linear change over exactly one blade pitch. (It can be remarked that one might expect more uncertainty about the circumferential distance associated with the change in velocity than about the relevant streamwise distance to be used, since the experiments of Nagano, Machida, and Takata [4] indicate the latter to be in the neighborhood of a chord.) From examination of the high

Downloaded 01 Jun 2010 to 171.66.16.62. Redistribution subject to ASME license or copyright; see http://www.asme.org/terms/Terms_Use.cfm

response data discussed in (2), the value of K is expected to be of order, but somewhat less than, unity.

The corresponding pressure spike across a stator row will be

$$\Delta p_{st} = -K\rho \frac{c}{b} (V_x \sec\alpha_{st}) V_s. \tag{5}$$

For the inlet guide vanes the chord and stagger angle, α_{IGV}, may be different, but, provided the difference is small, it may suffice to treat the pressure spike as equal to that from a stator row.

It is convenient to assume that $\alpha\hat{r}$ and α_s are the same for all stages and that the solidity, c/b, is equal for all the blade vows of the compressor. It then follows that for an N-stage compressor the sum of the pressure spikes from inlet to outlet is given by:

$$N\Delta p_r + N\Delta p_{st} + \Delta p_{IGV} =$$

$$\left[(U - V_s)\sec\alpha_r - V_s \sec\alpha_{st} - \frac{V_s \sec\alpha_{IGV}}{N} \right] NK\rho V_x \left(\frac{c}{b}\right) \tag{6}$$

Overall Pressure Rise for the Compressor. It has been verified, reference [3], that the total-to-static pressure rise across an N stage compressor in full span rotating stall can be given approximately by $0.11\ \rho U^2 N$, independent of unstalled pressure rise. The choice of specifying this empirical result in terms of total-to-static (instead of total-to-total or static-to-static) is that this particular quantity remains more or less constant from shut-off (i.e., no flow) up to mass flows just below that at which the compressor unstalls [3]. Nevertheless the total-to-static is somewhat inconvenient for the present purpose. The sum of the spikes along the trailing edge given above is a static-to-static pressure rise, which must be equated to the overall static-to-static pressure rise, not to the overall total-to-static pressure rise from the correlation.

Using the subscript B to designate pressures at the trailing edge boundary of the cell we may write

$$N\Delta p_r + N\Delta p_{st} + \Delta p_{IGV} = [p_{exit} - p_{inlet}]_B \tag{7}$$

The right hand side may be expanded as

$$[p_{exit} - p_{inlet}]_B = [(p_{exit})_B - \bar{p}_{exit}] -$$

$$- [(p_{inlet})_B - \bar{p}_{T_{inlet}}] + [\bar{p}_{exit} - \bar{p}_{T_{inlet}}] \tag{8}$$

where the overbar ($\bar{}$) designates a circumferential average. The last term on the right-hand side is the overall total-to-static pressure rise of the compressor which is given approximately by $0.11\rho U^2 N$. The previous two terms need to be found.

The precise determination of $[(p_{exit})_B - \bar{p}_{exit}]$ and $[(p_{inlet})_B - \bar{p}_{T_{inlet}}]$ is not simple and indeed sufficient information is not available to find them precisely. An estimate for the magnitude of these terms can be obtained by representing the velocity distribution upstream and downstream as a sinusoid of wavelength equal to the annulus circumference and taking $V_x/2$ to be the amplitude of the disturbance. In addition, in the *downstream* flow field, a linearized analysis is used to describe the static pressure nonuniformity. The procedures are described in more detail in the Appendix. The resulting expressions are

$$(p_{exit})_B - \bar{p}_{exit} = \rho V_s \frac{V_x}{2} \tag{9}$$

$$(p_{inlet})_B - \bar{p}_{T_{inlet}} = -\rho \frac{V_x}{2} V_s - \frac{1}{4}\rho V_x^2 \tag{10}$$

Thus equating the sum of the pressure spikes at the boundary to the other expression for the quantity $[p_{exit} - p_{inlet}]_B$:

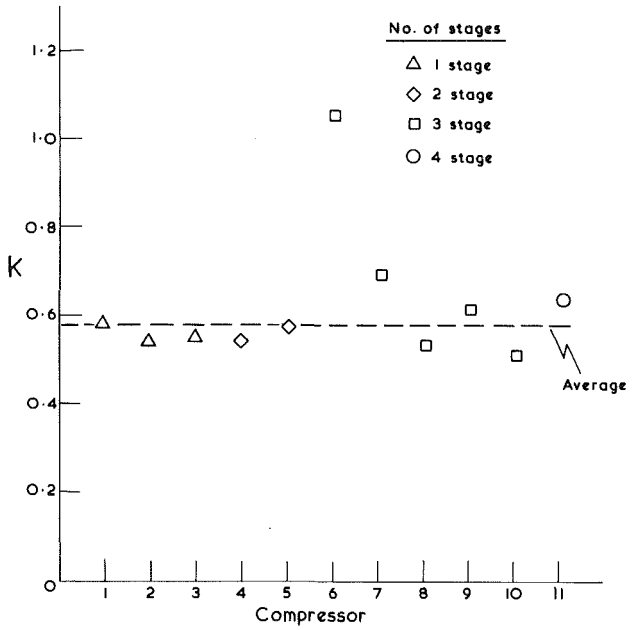


Fig. 5 Correlation for K parameter

$$N\Delta p_r + N\Delta p_{st} + \Delta p_{IGV}$$

$$= \rho U^2 \left[\frac{V_s}{U}\frac{V_x}{U} + \frac{(V_x/U)^2}{4} + .11N \right] \tag{11}$$

Substituting in for Δp_r, Δp_{st} and Δp_{IGV} and introducing $\phi = V_x/U$ gives

$$\frac{KN}{b/c}\left\{ \left(\phi - \frac{V_s}{U}\phi\sec\alpha_r - \frac{V_s}{U}\phi\sec\alpha_{st} \right.\right.$$

$$\left.\left. - \frac{1}{N}\frac{V_s}{U}\phi\sec\alpha_{IGV} \right\} = .11N + \frac{V_s}{U}\phi + \frac{\phi^2}{4} \right. \tag{12}$$

This can also be written to give an expression for the stall cell speed, nondimensionalized with respect to blade speed;

$$\frac{V_s}{U} = \frac{\phi\sec\alpha_r - \left(\frac{\phi^2}{4} + 0.11N\right)\frac{b}{c}\frac{1}{KN}}{\phi\left(\sec\alpha_r + \sec\alpha_{st} + \frac{1}{N}\sec\alpha_{IGV} + \frac{b/c}{KN}\right)} \tag{13}$$

The Determination of K. Before the expression for the stall cell speed can be used it is necessary to obtain an estimate for K. This has been done by using the stall-cell speeds in full span stall measured by Day [1] (these are also given in reference [2], together with estimates for the values of flow coefficient[2] at the condition for which the meaurements were made). Eleven different builds of compressor tested by Day [1] were used, with from one to four stages and values of design flow coeficient, ϕ^*, ranging from 0.35 up to 1.00. The values of K obtained in this way are shown in Fig. 5, and with one exception the data collapses satisfactorily. The anomalous value, $K = 1.05$, is for the highest stagger (low ϕ^*) build in which unusually large gaps exist between the blade rows. With the very large gaps the flow pattern is likely to be modified and a somewhat different value for K is to be expected; indeed, for a test using the same blading but reduced axial gaps the value obtained, $K = 0.69$, is more typical. The average value (excluding the very large gap results) of $K = 0.58$ was used in the calculations described below.

[2] The flow coefficient used is the average value in the unstalled portion of the compressor.

Downloaded 01 Jun 2010 to 171.66.16.62. Redistribution subject to ASME license or copyright; see http://www.asme.org/terms/Terms_Use.cfm

Table 1 Compressor geometries

Reference	$\left(\frac{V_s}{U}\right)$meas. from Fig. 6	Number of Stages	Stagger angle rotor/stator	Camber angle rotor/stator	Average solidity	Hub/tip ratio
5,6	0.10	1	44°/29°	20°/30°	0.89	0.6
	0.28	3	44°/29°	20°/30°	0.89	0.6
	0.19	3	44°/29°	20°/30°	0.44	0.6
	0.11	1	37°/35°	24°/25°	0.96	0.6
7	0.29	3	26°/30°	39°/10°	1.24	0.7
8	0.35	6	47°/47°	31°/30°	1.18	0.75
	0.35	6	27° – 47°/31° – 47°*	31°/30°	1.18	0.75
	0.35	6	37° – 47°/39° – 47°*	31°/30°	1.18	0.75

*Varying from front to rear stages

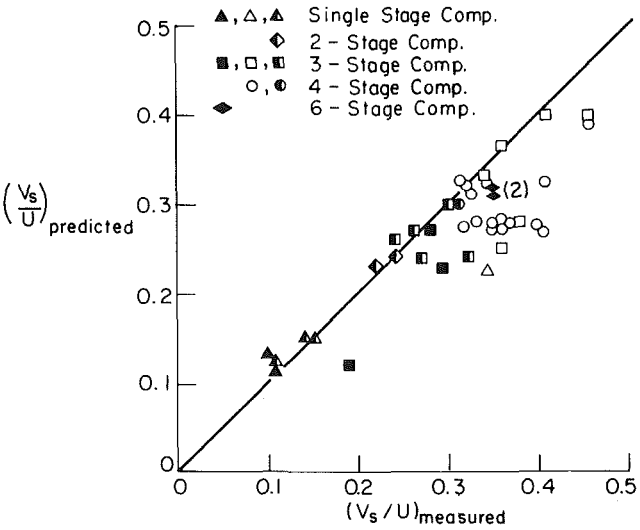


Fig. 6 Prediction of stall cell speed (Single and multistage compressors)

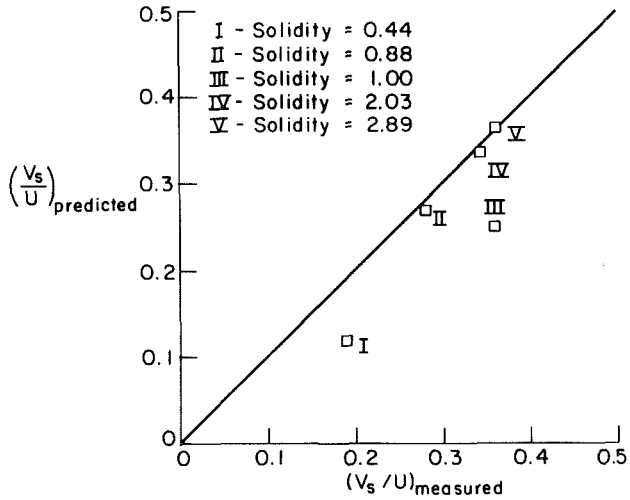


Fig. 7 Effect of Solidity on stall cell speed (three-stage compressors)

The comparatively small spread in the values of K (±15 percent), compared with the variation in stall cell speed of a factor of more than 3, gives support to the model of the flow. Similarly, the value of K is, as expected, near to, but less than, unity. It should be mentioned that if one considers an alternative hypothesis, in which the flow at the stall cell boundary produces the pressure rise in the rest of the flow ($p_{\text{exit}} - p_{T_{\text{inlet}}} = 0.11\,\rho U^2 N$) as well as the spikes, it is found that the values of K are congregated around 0.1. This is incompatible with the observations of a very abrupt change at the boundary. It does seem probable, however, that there is some small pressure rise at the boundary in addition to the spikes but less than that of the remainder of the flow; without any way of estimating its magnitude it is omitted.

Prediction and Discussion

In order to establish whether the ideas presented here have a more general validity, the expression derived for stall cell speed has been used to calculate the value for a number of *other* compressors on which the speed of full span stall cells had been measured. Where possible the stall cell speed is taken at a blockage of 50 percent, but available data (e.g.[5, 6]) indicate that for full span stall the speed is only weakly affected by operating point. Such data have been published by Iura and Rannie [5, 6], Greitzer [7], and Turner and Burrows [8], and characteristic quantities associated with each case are tabulated in Table 1. In addition, Seidlecki and Smith [9] have provided data from over 20 additional compressors operating in full span rotating stall. These latter data cover builds with one, three and four stages, hub/tip radius ratios of 0.5 to 0.85 and (estimated) flow coefficients in the unstalled part of the flow from 0.49 to 1.01.

A comparison of the predicted stall cell speed with the measurements is shown in Fig. 6. The horizontal axis is the measured nondimensional stall cell speed (V_s/U) and the vertical axis is the predicted speed given by equation (13), using the value of $K = 0.58$ derived from the data of Day. The symbol shape designates the number of stages (from one to six) as indicated in the figure. Solid symbols are used for the builds for which the geometry is given in Table 1, and open symbols are used for the General Electric data given by Seidlecki and Smith. The half-solid symbols denote the data of Day. It is to be emphasized that Fig. 6 truly does show the *prediction* of all the points indicated by the solid and open symbols, since these represent different compressors from those used to obtain the value of K. (In contrast the half-solid symbols represent correlation rather than prediction, since this data were used in the determination of K.) The total data shown in the figure represent tests from over 40 different compressor builds. (The single point representing the low solidity Iura and Rannie Compressor in Fig. 6 (and 7) is based on our calculation of the unstalled performance of this compressor. However, it should be noted that varying the assumptions used in carrying out this calculation over a large range results in only small changes in the ordinate of this point.)

It can be seen from Fig. 6 that the value of nondimensional stall cell speed is reasonably well predicted by the present model for a range of speeds from ten to 45 percent, and a wide variety of compressors. In almost all cases, the speed is

Downloaded 01 Jun 2010 to 171.66.16.62. Redistribution subject to ASME license or copyright; see http://www.asme.org/terms/Terms_Use.cfm

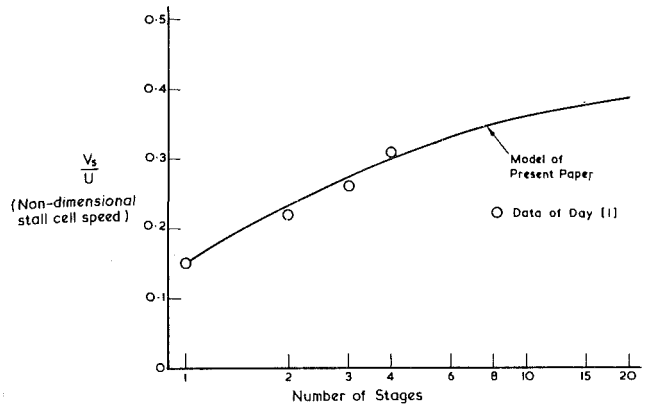


Fig. 8 Effect of number of stages on stall cell speed ($\phi^* = 0.55$, 50 percent reaction)

calculated as somewhat too high and a better prediction (or, more precisely, correlation) would be possible if the additional data were used to modify the value of K. However this is not the main purpose of the present paper, and the central idea, that the stall cell speed is determined by unsteady effects at the cell boundary, appears to be well supported by the figure. A particularly encouraging feature is seen in the three-stage results (the squares) where the measurements show trends that are predicted quite well by the theory for a range of stall cell speeds differing by a factor of more than two. It should also be remarked that it would be unrealistic to expect perfect agreement between measured and predicted speeds, since so many details have been omitted. In particular, details of the flow in the cell, notably the known radial variations, as well as the influence of compressor geometrical parameters, for example hub/tip ratio, have been neglected.

The expression for stall cell speed indicates a dependence of blade row solidity. Iura and Rannie [5] tested a three-stage compressor with solidity close to unity and, having every other blade removed, with a solidity close to one half. General Electric data include a three-stage compressor which was tested with solidities of 1.00, 2.03, and 2.89. All of these results are shown in Fig. 7, in which, as in Fig. 6, the predicted stall cell speed is plotted versus the measured speed. The Roman numerials refer to the different compressor builds. It can be seen that for the Iura and Rannie data the overall trend of increasing stall cell speed with increasing solidity is correctly predicted; the General Electric data, however, show virtually no change in measured stall cell speed as the solidity is changed. Thus, while the simple flow field description presented here does model many of the important features of the phenomenon correctly, there are some aspects which need further investigation.

It will be recalled that the striking trend of speed with number of stages found in Day's data had contributed to the motivation for this work. Using equation (13), the trend in predicted cell speed with number of stages is shown in Fig. 8 for one design of compressor used by Day (design flow coefficient $\phi^* = 0.55$, 50 percent reaction). In order to use equation (13) the unstalled characteristics are required to determine ϕ in the unstalled part of the flow, and this value will change with the number of stages. The characteristics were generated using efficiency trends taken from similar low-speed compressors, but it should be noted that the predicted cell speed is not sensitive to the precise method used to calculate the characteristic shape. In addition, the change in ϕ for the unstalled flow as a function of the number of stages become very small when the number of stages is large. Superimposed on the curve in Fig. 8 are the appropriate values measured by Day. (Since these data have been used in arriving at the value of the parameter K, this comparison is more in the nature of a correlation rather than a prediction.) It is clear from the figure that the change in stall cell speed becomes progressively less as the number of stages increases and that, for this compressor, an asymptotic value of approximately 40 percent seems to be indicated.

Conclusion

A model has been developed to predict the propagation speed of full-span rotating stall cells in single and multi-stage compressors. In view of the undoubted complexity of stalled flow in compressors, the present model is extraordinarily simple. However, by successfully predicting the trends in cell speeds in most cases, the principles behind the model appear to be supported. In this, attention is directed to the crucial aspects of the unsteadiness around the cell trailing edge (on which boundary the unstalled flow enters the cell) in determing the cell speed and more generally the overall characteristics of the stall flow field.

Acknowledgments

The authors greatly appreciate the interest shown in this work by W. F. Siedlecki, Jr. and L. H. Smith, Jr., of the Aircraft Engine Group, General Electric Company, who furnished the compressor data which appears in Figs. 6 and 7. The comments of R. S. Mazzawy and J. P. Nikkanen of Pratt & Whitney Aircraft are also gratefully acknowledged.

APPENDIX

Inlet and Exit Velocity Field Description. The treatment of the flow upstream and downstream of the compressor on a two-dimensional basis is given here in outline. The details for the inlet flow may be found in reference [1] and for the downstream flow in reference [10]. The rotating stall velocity field is represented by a cosinusoidal distortion of amplitide $V_x/2$, where V_x is the maximum axial velocity in the unstalled zone, the minimum velocity being zero.

Thus at the compressor inlet and exit

$$v_x = \frac{V_x}{2} \cos\left(\theta - \frac{V_s t}{R}\right) \tag{A-1}$$

where θ is the circumferential coordinate. Upstream of the compressor we take the flow to be irrotational and define a velocity potential ϕ.

The first integral of the momentum equation can thus be written

$$\frac{\partial \phi}{\partial t} = -\left(\frac{p_T - \bar{p}_T}{\rho}\right) \tag{A-2}$$

where $\bar{p}_T$ is a mean value of the upstream total pressure. Since ϕ obeys Laplace's equation, its form can readily be determined, leading to an equation for p_T at the compressor inlet

$$\frac{p_T}{\rho} = \frac{\bar{p}_T}{\rho} - \frac{V_x V_s}{2} \sin\left(\theta - \frac{V_s t}{R}\right) \tag{A-3}$$

What is needed, however, is the difference between the local static pressure, p_B, (at the stall cell trailing edge) and $\bar{p}_T$.

$$p_B - \bar{p}_T = p_B - \bar{p} + (\bar{p} - \bar{p}_T) \tag{A-4}$$

Using the definition of the total pressure and the compressor inlet axial velocity distribution given in (A-1) this can be found to be

$$p_B - \bar{p}_T = -\rho V_x \frac{V_s}{2} - \frac{1}{4}\rho V_x^2 \tag{A-5}$$

where use is made of the fact that the axial velocity perturbation is zero at B.

Downloaded 01 Jun 2010 to 171.66.16.62. Redistribution subject to ASME license or copyright; see http://www.asme.org/terms/Terms_Use.cfm

At the exit of the compressor the same axial velocity profile is assumed. In addition, the leaving angle is assumed constant around the circumference. The momentum equation in the axial direction is thus

$$\left(\frac{1}{\rho}\frac{\partial p}{\partial x} = -\frac{\partial v_x}{\partial t}\right)_{\text{at exit}} \tag{A-6}$$

This provides a boundary condition for the downsteam pressure field. In general, however, this pressure field cannot be found without calculating the velocity field in the downstream region as well. While this could be done numerically, such procedures are not warranted here in view of the other simplifications that have been made. More significantly, the measured pressure perturbation during rotating stall are considerably smaller at exit than at inlet over most of the range of relevant parameters. Because of this, it is reasonable to expect that they could be estimated reasonably well using a linearized description.

A linearized analysis of the exit pressure field is therefore employed, with the observation that what is being determined here is really a relatively small correction to the main pressure rise and that errors in determining it will not be very significant.

Doing this, it can readily be found that

$$p_{\text{exit}_B} - \bar{p}_{\text{exit}} = \rho V_s \frac{V_x}{2} \tag{A-7}$$

The final step is to use the result $\bar{p}_{\text{exit}} - \bar{p}_{T_{\text{inlet}}} = 0.11\ \rho U^2 N$, presented in reference [3], and equation (11) follows.

References

1 Day, I.J., "Axial Compressor Stall," Ph.D. Dissertation, University of Cambridge, 1976.

2 Day, I.J. and Cumpsty, N.A., "The Measurement and Interpretation of Flow withn Rotating Stall Cells in Axial Compressors," *Journal Mechanical Engineering Science,* Vol. 20, 1978, pp. 101-114.

3 Day, I.J., Greitzer, E.M. and Cumpsty, N.A., "Prediction of Compressor Performance in Rotating Stall," ASME JOURNAL OF ENGINEERING FOR POWER, Vol. 100, 1978, pp. 1-14.

4 Nagano, S., Machida, Y., and Takata, H., "Dynamic Performance of Stalled Blade Rows," Japan Society of Mechanical Engineers, Paper #JSME 11, presented at Tokyo Joint International Gas Turbine Conference, Tokyo, Oct. 1971.

5 Iura, T. and Rannie, W.D., "Experimental Investigation of Rotating Stall," *Trans. ASME,* Vol. 76, Apr. 1954, pp. 463-471.

6 Iura, T. and Rannie, W.D., "Observations of Propagating Stall in Axial-Flow Compressors," California Inst. of Tech., Mechanical Eng. Lab. Report No. 4, Apr. 1953.

7 Greitzer, E.M., "Surge and Rotating Stall in Axial Flow Compressors: Part II, Experimental Results and Comparison with Theory," ASME JOURNAL OF ENGINEERING FOR POWER, Vol. 98, 1976, pp. 199-217.

8 Turner, R.C. and Burrows, R.A., "An Experimental Investigation of the Effects of Stage Matching in Compressor Surge," Aeronautical Research Council Current Paper No. 548.

9 Seidlecki, W.F. and Smith, L.H., Personal communication.

10 Greitzer, E.M., "A Note on Compressor Exit Static Pressure Maldistributions in Asymmetric Flow," Cambridge University Engineering Department Turbomachinery Report, CUEDA/A-Turbo/TR79, 1976.

Downloaded 01 Jun 2010 to 171.66.16.62. Redistribution subject to ASME license or copyright; see http://www.asme.org/terms/Terms_Use.cfm

A Comparison of Two Alternative Methods for Defining Fan Performance

P. M. Gerhart
University of Akron,
Akron, Ohio

R. Jorgensen

J. Kroll

Buffalo Forge Co.,
Buffalo, N.Y.

PTC 11 Committee, the ASME Performance Test Code Committee charged with producing a new test code for large industrial fans, has decided to present code users with two options for expressing fan performance. While one of these options is representative of current U.S. practice, the other option appears to be quite different. The differences center around the definitions of fan flow rate and fan output. Historically, fan flow rate has been defined as the volume flow rate at the fan inlet, and fan output has been defined as either the rise in total pressure across the fan or as the rise from the total pressure at the inlet to the static pressure at the outlet. The alternative method uses the mass flow rate and the "fan specific energy" as the performance variables. If the fan process is incompressible, the two sets of variables produce easily reconciled values; however, if compressibility must be accounted for, subtle differences may arise. This paper examines the assumptions and developments of the two alternative methods of expressing fan performance.

Introduction

ASME Performance Test Code Committee Number 11 is charged with the responsibility of producing a code for the field testing of large industrial fans. A fan is defined as "an air or gas-moving device of one or more stages, but without interstage cooling" [1]. An alternative definition is: "a fan is a device for moving air, which utilizes a power driven rotating impeller" [2]. Fan performance is defined in terms of three primary variables, which are indicative of (*a*) the quantity of fluid (air or gas) passing through the fan in unit time, (*b*) the "useful," "ideal," or "mechanical" specific (per unit mass or volume) energy imparted to the fluid by the rotor, and (*c*) the mechanical power required to drive the fan. These variables can be used to define (or can be derived from) a fan output power that is the product of the flow rate and the useful specific energy (in consistent units) and a fan efficiency that is the ratio of fan output power to fan input power. Although simple in concept, the only one of these performance variables that can be defined without some ambiguity for all cases is the driving power. The flow rate must be given in either mass or volumetric terms. However, there are a variety of choices for the "specific energy" including total-to-static pressure changes, total-to-total pressure changes, or changes of energy per unit mas. The amount of useful energy imparted to the fluid also depends upon exactly which forms of energy are considered to be useful.

Fan engineers in the U.S. have customarily described fan performance in terms of volumetric flow rate and pressure rise across the fan [2]. On the other hand, European engineers often adopt the mass flow rate and a quantity that will be called the fan specific energy, which is equal to "the work per unit mass in an ideal (frictionless) transition between the actual inlet and outlet states" [1]. The mass flow rate and fan specific energy form the basis of a fan test code currently being drafted by the International Standards Organization (ISO) [3]. After deliberating the relative merits of these approaches to the definition of fan performance, the PTC-11 Committee decided to include both methods in PTC-11 and to allow the user the choice between the methods.

The purpose of this paper is to examine both methods as to their theoretical basis and their practical utility. The first section of the paper will deal with those characteristics of fans and fan performance that set fans apart from other types of flow machinery. Following this, an outline of the development of both methods of defining performance will be given. Finally, the two methods will be compared by means of a numerical example.

Before proceeding, it should be pointed out that the source documents for both methods of defining performance presume a laboratory-type test rather than a field test [2, 3]. It is assumed that pressures and densities are uniform across measurement planes and that measurements are made at stations where the velocity is reasonably uniform and parallel. In field testing, it is often more practicable to make measurements in regions of nonuniform pressure, density, and velocity, often at or near fan inlet and outlet boundaries. This paper is not intended to deal specifically with these difficulties, since they have been treated elsewhere [4, 5]. It shall be assumed that suitable average values are used whenever a uniform pressure, temperature, or density is needed.

Contributed by the Power Division of THE AMERICAN SOCIETY OF MECHANICAL ENGINEERS and presented at the Winter Annual Meeting, Chicago, Ill., November 15-20, 1980. Manuscript received at ASME Headquarters, August 25, 1980. Paper No. 80-WA/PTC-1.

Copyright © 1982 by ASME

Downloaded 01 Jun 2010 to 171.66.16.62. Redistribution subject to ASME license or copyright; see http://www.asme.org/terms/Terms_Use.cfm

Characteristics of Fans Relevant to Defining Fan Performance Variables

Fans are used to produce relatively large flow rates of air or gas at small velocities (typically at Mach numbers less than 0.3) and with relatively small energy addition per unit mass of fluid moved. The technological objective is the movement (displacement) of the fluid rather than the addition of the energy. The fan is a mechanical device in that it produces movement of fluid particles by exerting a force on them; however, it is also a thermodynamic device since it converts mechanical work into energy in the fluid.

It is a paradox of fan engineering that, although fans handle fluids (air or gas) that are highly compressible, a fan is often assumed to be an incompressible-flow machine. Therefore, equations and methodology from incompressible-fluid mechanics are often used in analyzing fans and in defining their performance. Such methods are quite accurate in low-pressure fans but for high-pressure fans, fluid compressibility may be significant. A definition of fan performance that will be applied to all fans must include some means of accounting for the effects of fluid compressibility.[1] Usually a "compressibility correction" of some form is applied to the performance variables. One means of developing such corrections is to effectively consider a fan as a very low-pressure compressor and to adapt compressor analysis methods that are largely based on a thermodynamic approach rather than a mechanical approach [2, 6]. A cornerstone of this approach is combining the fluid kinetic energy (per unit volume) with the pressure and then using the resulting stagnation pressure as if it were a purely thermodynamic variable (for example, by assuming that the fan process can be approximated by a polytropic law involving the stagnation properties ($p_{02}/p_{01} = (\rho_{02}/\rho_{01})^n$).

Such an approach is quite common in compressor engineering where it works quite well because the kinetic energy per unit volume (the velocity pressure) is quite small when compared with the static pressure. This latter fact is not generally true in fans where the kinetic energy is a significant fraction of the total energy. It follows that a strong argument can be made for the need for compressibility correction methods that handle the thermodynamic properties (e.g., static pressure) and the mechanical energies (e.g., kinetic and potential energies) separately rather than lumped together [3, 7].

The appearance of a significant portion of the energy added by a fan in the kinetic form demands a careful accounting of this form of energy in any fan performance definition. If we examine, for example, the flow near the outlet of a fan, we find that the static pressure of the fluid is usually closely uniform over the outlet plane; however, the velocity of the fluid is seldom closely uniform nor is it parallel to the main flow direction. The velocity is in general a three-dimensional vector with components transverse to the main flow direction as well as along it. The kinetic energy of each fluid particle is simply the square of its speed, independent of the actual direction of the velocity vector

$$\tilde{e}_K \equiv \frac{\tilde{V}_x^2 + \tilde{V}_y^2 + \tilde{V}_z^2}{2}$$

Since the primary purpose of a fan is to move air, the energy represented by $\tilde{V}_x^2/2$ is useful energy. The energy represented by $1/2(\tilde{V}_y^2 + \tilde{V}_z^2)$, however, is only useful if it can be converted into pressure. (In an axial fan, flow straightener vanes are provided for this very purpose.) Consider a flow without straightener vanes (or downstream of any vanes that are present). If we go far enough downstream (say 5-10 equivalent diameters, possibly passing through a flow straightener), we find that the velocity components in the cross-sectional plane (crudely, the swirl velocity) have disappeared. Unquestionably, a significant portion of the kinetic energy involved has been dissipated into heat; however, it is also true that some of it may show up as pressure. Of course, the actual pressure at our downstream location may be lower because of the pressure drop associated with the intervening ductwork. The fraction of the swirl kinetic energy converted to pressure is unknown and, of course, depends heavily on the geometry of the downstream ductwork.

In defining fan performance, it is necessary to make a somewhat arbitrary decision concerning exactly what components of the kinetic energy are to be credited to the fan's performance. The PTC-11 Committee has decided to credit to the fan only the kinetic energy due to velocity along the main flow path.

[1] The first American fan test code to consider compressibility effects was the fifth edition of AMCA Bulletin 210, published in 1960! See Appendix for other historical information about fan test codes in the U.S.

Nomenclature

A = cross-sectional area
C_p, C_v = specific heats at constant pressure, volume
D = impeller diameter
e_K = kinetic energy per unit mass, $\frac{V^2}{2}$
e_p = potential energy per unit mass
h = enthalpy
k = ratio of specific heats
K_p, K_ρ = compressibility coefficients
M = Mach number
$\dot{m}$ = mass flow rate
N = speed of rotation
n = polytropic exponent
p = pressure
p_t = total pressure
p_0 = stagnation pressure
p_F = fan pressure rise
p_{Fs} = fan static pressure
p_{FT} = fan total pressure
$\mathcal{P}$ = impeller power (fan input power)
$\mathcal{P}_f$ = friction power
$\mathcal{P}_0$ = fan output power
Q = volume flow rate
Q_F = fan flow rate
$\dot{Q}$ = heat loss from fan
R = specific gas constant
s = specific entropy
T = absolute static temperature
T_0 = stagnation temperature
T_t = total temperature
u = internal energy
$V, \tilde{V}$ = velocity, velocity vector
$\forall$ = volume
y_F = fan specific energy
α = kinetic energy correction factor, $\alpha \equiv \frac{\int \tilde{V}_x^3 dA}{V_x^3 A}$
η = fan efficiency
η_s = fan static efficiency
η_t = fan total efficiency
ρ = density
ρ_m = fan mean density
ρ_0 = stagnation density
ρ_t = total density
∇ = gradient operator

Subscripts and Superscripts

a,b = operating conditions
x,y,z = components in x,y,z directions
1 = average value at fan inlet plane
2 = average value at fan outlet plane
$\tilde{\ }$ = unaveraged (point) value

Downloaded 01 Jun 2010 to 171.66.16.62. Redistribution subject to ASME license or copyright; see http://www.asme.org/terms/Terms_Use.cfm

Even if all velocity vectors are parallel to the flow direction, there will still be a distributional effect in the kinetic energy. Performance variables are defined in terms of average values at measurement planes [5]. The average kinetic energy of the fluid is always greater than one-half the square of the average velocity of the fluid due to the distributional effect (i.e., $\alpha > 1.0$). Since α_1 and α_2 are often about 1.0 and 1.1, a fan in which kinetic energy accounts for one-half of the total energy will not be given credit for five percent of its energy rise if the distributional effect is neglected. For this reason, the PTC-11 Committee has decided to credit the distributional effect to the fan's performane. Thus,

$$e_K \equiv \alpha \frac{V_x^2}{2} \tag{1}$$

Assumptions and Equations Pertinent to the Definition of Fan Performance

The Incompressible Flow Assumption. It is common practice in fan engineering to assume that the process of flow through a fan is incompressible; that is, the effects of density changes are ignored. However, this assumption has further ramifications.

If the density is assumed constant under all circumstances, then it follows that [8]

1 fluid internal energy is a function of temperature only, and

2 pressure does not depend on either the density or the temperature; i.e., p, ρ, T are uncoupled.

This permits, indeed dictates, the division of the fluid properties into the thermal properties u and T and the mechanical properties p and ρ. Because of this division, it is customary to treat the mechanics and thermodynamics of incompressible flow separately.

Consider the addition of a quantity of energy to a fluid by means of doing mechanical work on the fluid. According to the general energy equation of thermodynamics, this results in an increase in the enthalpy of the fluid[2]

$$\Delta h = \Delta(u + p/\rho)$$

We identify p/ρ as the mechanical or displacement energy[3] and u as the thermal energy. If the process takes place in a compressible fluid that can be modeled by the ideal gas law, the ratio of these energy forms is

$$\frac{\Delta u}{\Delta(p/\rho)} = \frac{C_v \Delta T}{R \Delta T} = \frac{C_v}{R} = \text{Constant}.$$

That is, the energy is apportioned between mechanical and thermal forms in a constant ratio, and one form cannot be obtained without the other. In such a process, we could not say that thermal energy is undesirable because without it there would be no mechanical energy.

Considering the division of energy in an incompressible process

$$\frac{\Delta u}{\Delta(p/\rho)} \sim \frac{\Delta u}{\Delta p} \sim \frac{\Delta T}{\Delta p}$$

Since ΔT and Δp are independent, we expect (under ideal conditions) to increase the mechanical energy only, without a corresponding increase in thermal energy. Thus, in an incompressible flow, if temperature risees result from performing work on the fluid, we must count these thermal effects as lost energy.

Total and Stagnation Properties. Total (stagnation) properties are thermodynamic properties in which kinetic effects are lumped together with the true thermodynamic property.

The words total and stagnation are often used interchangeably; however, as used at times in fan engineering and particularly in this paper, there is a slight difference. Stagnation properties (pressure, density, temperature) are defined as those properties that would be obtained in an isentropic-workless deceleration from the actual fluid state to a state with zero velocity.[4] Total properties, on the other hand, are defined as those properties corresponding to the sum of the static property and its consistent kinetic energy counterpart. Thus,

$$p_t = p + \rho e_K \tag{2}$$

$$T_t = T + \frac{e_K}{C_p}, \text{ and} \tag{3}$$

$$\rho_t = p_t / R T_t \tag{4}$$

For incompressible flow, total and stagnation properties are identical. For compressible flows, they are different.

The Continuity Equation. In this and all other equations, it is assumed that the fan flow process is steady:

$$\dot{m}_1 = \dot{m}_2 = \dot{m}, \text{ or} \tag{5}$$

$$\rho_1 Q_1 = \rho_2 Q_2 = \dot{m}, \text{ or} \tag{6}$$

$$\rho_1 V_1 A_1 = \rho_2 V_2 A_2 = \dot{m} \tag{7}$$

The General Energy Equation (First Law of Thermodynamics)

$$\mathcal{P} - \dot{Q} = \dot{m}_2 \left(u_2 + \frac{p_2}{\rho_2} + e_{K_2} + e_{p_2} \right) - \dot{m}_1 \left(u_1 + \frac{p_1}{\rho_1} + e_{K_1} + e_{p_1} \right) \tag{8}$$

In fan engineering, it is customary to ignore changes in potential energy and heat losses so this equation, with the use of equation (5) and the ideal gas assumption, becomes

$$\mathcal{P} = \dot{m} \left[C_v (T_2 - T_1) + \frac{p_2}{\rho_2} - \frac{p_1}{\rho_1} + e_{K_2} - e_{K_1} \right]. \tag{9}$$

The Mechanical Energy or "Generalized Bernoulli" Equation [3]. This equation is derived entirely from Newton's second law of mechanics (in the form of the Navier-Stokes equations) and is

$$\mathcal{P} - \mathcal{P}_F = \iiint (\bar{V} \cdot \bar{\nabla} p) \, d\forall + \dot{m}[(e_{K_2} - e_{K_1}) + (e_{p_2} - e_{p_1})] \tag{10}$$

where $\mathcal{P}_F$ is the friction power or the irreversible conversion of mechanical energy into heat (also called the lost work). By considering the flow along various streamlines through the fan and ignoring potential energy changes, this equation can be written

$$\mathcal{P} - \mathcal{P}_F = \dot{m} \left[\int_1^2 \frac{dp}{\rho} + e_{K_2} - e_{K_1} \right] \tag{11}$$

where the integral is a thermodynamic-path integral between the inlet and outlet states. Since the ideal fan has $\mathcal{P}_F = 0$, the right-hand side of this equation is the fan output power.

All the above equations are valid for either compressible or

[2] Increases in velocity and elevation are ignored for this discussion.

[3] Note that p/ρ is actually a mechanical work term representing work done in the process of fluid motion.

[4] The defining equations for stagnation properties are:

$$p_0 = p \left(1 + \frac{k-1}{2} M^2 \right)^{k/k-1}$$

$$T_0 = T \left(1 + \frac{k-1}{2} M^2 \right)$$

$$\rho_0 = \rho \left(1 + \frac{k-1}{2} M^2 \right)^{1/k-1}$$

Downloaded 01 Jun 2010 to 171.66.16.62. Redistribution subject to ASME license or copyright; see http://www.asme.org/terms/Terms_Use.cfm

incompressible flow; however, if the process is incompressible ($\rho_1 = \rho_2 = \rho$) then equation (11) can be subtracted from (8) with this result:

$$\mathcal{P}_F - \dot{Q} = C_v (T_2 - T_1) \tag{12}$$

For an incompressible flow, equation (6) becomes

$$\rho Q = \dot{m} \tag{13}$$

and equation (11) becomes

$$\mathcal{P} - \mathcal{P}_F = Q[(p_2 + \rho e_{K_2}) - (p_1 + \rho e_{K_1})]$$

or

$$\mathcal{P} - \mathcal{P}_F = Q[p_{t_2} - p_{t_1}] \tag{14}$$

which is the familiar form of the fan output power equation.

Definitions of Fan Performance Variables

Recall that the performance variables consist of (*a*) a flow rate, (*b*) an ideal specific energy rise and (*c*) the driving power ($\mathcal{P}$). The continuity equation is obviously the basis for definitions of flow rate. Since the ideal fan flow process is without friction ($\mathcal{P}_F = 0$), and since the friction-loss terms appears explicitly in equation (11), this equation is the basis for definition of ideal energy rise and, hence, fan output power as well.

Volume Flow Rate – Pressure Approach to Defining Fan Performance Variables [2, 6]. This method has been used almost exclusively in the U.S. and selects the volume flow rate (Q_F) and total[5] pressure rise (called fan total pressure, p_{Ft}) as the primary performance variables (pressure can be conceived of as a type of energy per unit volume). The fan total pressure is computed by

$$p_{Ft} = (p_2 + \rho_2 e_{K_2}) - (p_1 + \rho_1 e_{K_1}) \tag{15}$$

If the density changes across the fan, the volume flow rate is different at the inlet and outlet. In this case the method defines a fan flow rate, which is the mass flow rate divided by the inlet total[5] density

$$Q_F = \frac{\dot{m}}{\rho_{t_1}} \tag{16}$$

If the flow is incompressible ($\rho_2 = \rho_1 = \rho_{t_1}$), the fan output power is equal to the product of p_{Ft} and Q_F. If compressibility effects are present, the fan output power is computed by using a compressibility coefficient (K_p):

$$\mathcal{P}_0 \equiv \dot{m}\left[\int_1^2 \frac{dp}{\rho} + e_{K_2} - e_{K_1}\right] \simeq K_p Q_F p_{Ft} \tag{17}$$

The compressibility coefficient is computed by lumping the kinetic energy terms into the pressure-density integral by means of total properties, thus

$$\int_1^2 \frac{dp}{\rho} + e_{K_2} - e_{K_1} \simeq \int_1^2 \frac{dp_t}{\rho_t} \tag{18}$$

so that

$$K_p = \frac{\rho_{t_1}}{p_{Ft}} \int_1^2 \frac{dp_t}{\rho_t} \tag{19}$$

The integral is evaluated by assuming a polytropic process between the inlet and outlet total states (Fig. 1). Consult reference [2] for further details of the development as well as working formulae and charts for K_p.

The fan total efficiency is defined by

$$\eta_t = \frac{\mathcal{P}_0}{\mathcal{P}} = \frac{K_p Q_F p_{Ft}}{\mathcal{P}} \tag{20}$$

[5] The words total and stagnation seem to be used interchangeably in this approach [2, 6].

This method also defines a fan static pressure, which is equal to the difference between the outlet static pressure and the inlet total pressure,

$$p_{F_s} = p_2 - (p_1 + \rho_1 e_K), \tag{21}$$

and a fan static efficiency

$$\eta_s = \eta_t \frac{p_{F_s}}{p_{F_t}}.$$

Mass Flow Rate – Specific Energy Approach to Defining Fan Performance Variables [3]. In this method, the mass flow rate ($\dot{m}_F$) is selected as the flow rate parameter. A quantity that can be called the "fan work per unit mass" or fan specific energy (y_F) is selected as the "useful" energy-rise parameter. From equation (11),

$$y_F = \int_1^2 \frac{dp}{\rho} + e_{K_2} - e_{K_1} \tag{23}$$

If the density is constant, then

$$y_F = \frac{p_2 - p_1}{\rho} + e_{K_2} - e_{K_1} = \frac{p_{F_t}}{\rho} \tag{24}$$

If the density varies, then a means for approximating the pressure-density integral is needed. In this method, the integral is evaluated by defining a fan mean density such that

$$\int_1^2 \frac{dp}{\rho} = \frac{p_2 - p_1}{\rho_m} \tag{25}$$

The fan mean density is approximated by the simple arithmetic mean of inlet and outlet densities.[6]

$$\rho_m \simeq \frac{\rho_1 + \rho_2}{2} \tag{26}$$

The fan output power for both compressible and incompressible cases is

$$\mathcal{P}_0 = \dot{m} y_F = \dot{m}\left[\frac{p_2 - p_1}{\rho_m} + e_{K_2} - e_{K_1}\right] \tag{27}$$

and the fan efficiency is

$$\eta = \frac{\mathcal{P}_0}{\mathcal{P}} = \frac{\dot{m}\left[\frac{p_2 - p_1}{\rho_m} + e_{K_2} - e_{K_1}\right]}{\mathcal{P}} \tag{28}$$

If desired, one could define a fan pressure rise by

$$p_F = \rho_m y_F = p_2 - p_1 + \rho_m e_{K_2} - \rho_m e_{K_1} \tag{29}$$

PTC-11 will not include this quantity as one of the fan performance variables. It is shown here only to demonstrate a consistent relationship between pressure and specific energy.

Fan Law's and Conversion Calculations. The fan laws are similarity laws that can be derived from dimensional analysis. These laws are useful for extrapolating performance points of geometrically similar fans or for converting performance data of a given fan to different conditions of rotative speed and different gas-inlet properties. In fan engineering, it has been customary to ignore Reynolds number effects in applying fan laws.[7] If we consider two geometrically similar fans *a* and *b* operating under different conditions, the fan laws become

Volume Flow-Pressure Approach [2, 5]:

$$\frac{K_{pa} Q_{Fa}}{N_a D_a^3} = \frac{K_{pb} Q_{Fb}}{N_b D_b^3}, \tag{30}$$

[6] It is possible to conceive of other means of evaluating ρ_m, for example, by assuming a polytropic process between inlet and outlet states. The arithmetic mean density corresponds to a polytropic process with $n = 2$.

[7] Reynolds number effects may be important, particularly at low values, and should not always be ignored.

Downloaded 01 Jun 2010 to 171.66.16.62. Redistribution subject to ASME license or copyright; see http://www.asme.org/terms/Terms_Use.cfm

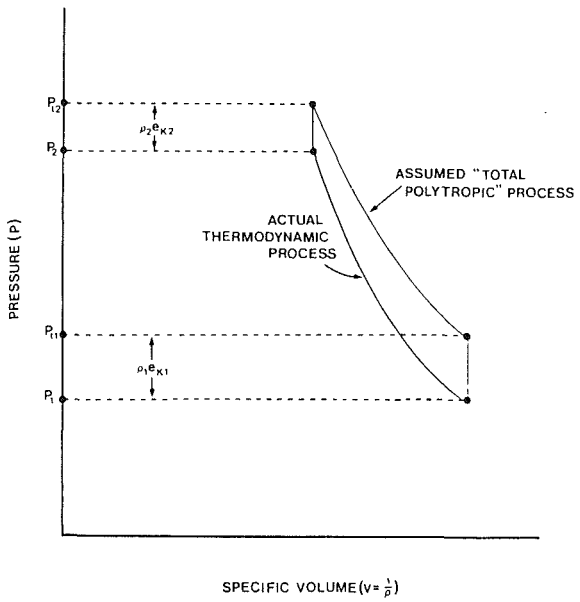


Fig. 1 Total polytropic process for evaluation of K_p

Table 1 Typical values of basic (measured) quantities for two fans

		Low-Pressure Fan	High-Pressure Fan
A_2	(ft^2)	100.0	100.0
V_2	(ft/min)	3000.0	7500.0
p_2	(in. wg)	5.0	50.0
T_2	(°F)	75.0	95.0
p_1	(in. wg)	0.0	0.0
T_1	(°F)	70.0	70.0
V_1	(ft/min)	0.0	0.0
$\mathcal{P}$	(hp)	320.0	7650.0

$$\frac{K_{pa}p_{Fta}}{\rho_{t_1}aN_a^2D_a^2} = \frac{K_{pb}p_{Ftb}}{\rho_{t_1}bN_b^2D_b^2} \tag{31}$$

$$\frac{K_{pa}\mathcal{P}_a}{\rho_{t_1}aN_a^3D_a^5} = \frac{K_{pb}\mathcal{P}_b}{\rho_{t_1}bN_b^3D_b^5} \text{ and} \tag{32}$$

$$\eta_{ta} = \eta_{tb} \tag{33}$$

Mass Flow-Specific Energy Approach [3]:

$$\frac{K_{pb}\dot{m}_a}{\rho_{1a}N_aD_a^3} = \frac{K_{\rho b}\dot{m}_b}{\rho_{1b}N_bD_b^3} \tag{34}$$

$$\frac{y_{Fa}}{N_a^2D_a^2} = \frac{y_{Fb}}{N_b^2D_b^2} \tag{35}$$

$$\frac{K_{\rho a}P_a}{\rho_{1a}N_a^3D_a^5} = \frac{K_{pb}P_b}{\rho_{1b}N_b^3D_b^5} \text{ and} \tag{36}$$

$$\eta_a = \eta_b \tag{37}$$

where

$$K_\rho \equiv \frac{\rho_1}{\rho_m} = \frac{2\rho_1}{\rho_1 + \rho_2} \tag{38}$$

These equations can be used for conversion calculations provided that a relationship between K_{pa} and K_{pb} or K_{pa} and K_{pb} is established. These relationships can be established with the aid of the general energy equation (9) and are available elsewhere [1–3].

Comparison and Evaluation of the Two Approaches to Defining Performance Variables

To some, it might appear that there is a considerable difference between the two approaches to defining performance variables, although to others it may seem that there is very little difference. This latter conclusion might be most obvious upon examining the fan laws, equations (30–38), and noting that K_p and K_ρ are usually slightly less than 1.0 and typically differ from each other in the third decimal place [3]. Upon close examination, it is noted that the two methods are essentially equivalent for incompressible flow, since the mass flow differs from the volume flow by the constant density and the total-pressure rise is simply the fan specific energy multiplied by the constant density. The coefficients K_p and K_ρ are both unity for incompressible flow, and the inlet static and total densities are equal, so the fan laws are identical for both. *The only real differences between the two methods arise when compressibility effects are present.*

At this point, two numerical examples are introduced to form the basis of further comparisons. Table 1 presents a set of typical values of velocities, pressures, temperatures, and densities for both a low-pressure and a high-pressure fan. (These are assumed to be appropriate average values [5].) Performance variables for these two fans, as computed by both approaches, are given in Table 2. Table 2 also includes two columns in which the outlet kinetic energy factor has been assumed to be unity rather than its true value.

Comparing the entries in the tables, observe that the differences are small but noticeable. In particular, note that the efficiency of fans is slightly lower when computed by the volume flow-pressure approach. Reference [3] considers 12 such examples and finds that the efficiency is lower when using the volume flow-pressure approach in ten of them, without change in one case, and higher in only one case. In most, if not all, real situations, the efficiency will be greater when calculated by the mass flow-specific energy approach. It can be shown [3] that the volume flow-pressure approach calculates a fan output power that is less than that calculated by the mass flow-specific energy approach by an amount that is proportional to the thermodynamic path integral:

$$\int_1^2 (T_0 - T)\,ds.$$

This integral increases with increasing compressibility, ($T_0 - T$) greater, and also with larger net entropy changes. This latter fact shows that the more inefficient the fan (larger Δs), the more the output power is lowered and the larger the difference between the efficiencies computed by the two methods.

Considering the conversion calculations, examining the fan law equations (30-38) reveals that the difference in converted performance variables arises because of the difference between K_p and K_ρ and because of the differences between ρ_1 and ρ_{t_1}. Note that:

$$\frac{Q_F}{ND^3} = \frac{\dot{m}_F}{\rho_{t_1}ND^3} \tag{39}$$

Note also that any differences in converted efficiencies are due to original differences in these quantities, since both fan total efficiency and fan efficiency are converted without change.

The final task remaining is to explain the reason for the existing differences between the two methods. The salient differences reduce to two:

1 The volume flow-pressure method lumps kinetic energy together with thermal energy by the use of total properites when evaluating the right-hand side of the mechanical energy equation. The mass flow-specific energy approach does not

Downloaded 01 Jun 2010 to 171.66.16.62. Redistribution subject to ASME license or copyright; see http://www.asme.org/terms/Terms_Use.cfm

Table 2 Fan performance variables for the data of Table 1

		Low-Pressure Fan		High-Pressure Fan	
α_2		1.0	1.1	1.0	1.1
ρ_2	(lb_m/ft^3)	0.07521	0.07521	0.08042	0.08042
ρ_1	(lb_m/ft^3)	0.075	0.075	0.075	0.075
ρ_m	(lb_m/ft^3)	0.07511	0.07511	0.07771	0.07771
$\dot{m}$	(lb_m/s)	376.05	376.05	1005.3	1005.3
Q_F	(CFM)	300840	300840	804210	804210
e_{K2}	(ft lb/lb_m)	38.851	42.736	242.82	267.10
e_{K1}	(ft lb/lb_m)	0	0	0	0
y_F	(ft lb/lb_m)	384.54	388.43	3584.1	3608.4
$\rho_2 e_{K_2}$ *	(in. wg)	0.56268	0.61894	3.760	4.136
p_{t_2}	(in. wg)	5.56268	5.61894	53.760	54.136
p_{Ft}	(in. wg)	5.56268	5.61894	53.760	54.136
p_F	(in. wg)	5.56187	5.61814	53.634	53.997
K_p	-	0.99558	0.99551	0.96126	0.96109
K_ρ	-	0.99854	0.99854	0.96513	0.96513
P_0 (1)	(hp)	262.21	264.84	6540.7	6585.3
P_0 (2)	(hp)	262.92	265.58	6551.1	6595.5
η_t	% -	81.94	82.76	85.50	86.09
η	% -	82.16	82.99	85.64	86.22

(1) Volume flow-pressure
(2) Mass flow-specific energy.
*Velocity pressure at 2.

Table 3 History of fan test codes in the U.S.

Year	Publisher	Number	Writers/Sponsors	Edition	Output
1923	NAFM		NAFM and ASHVE	1st	$Q_1 p_{Ft}$
	"Standard Code for the Testing of Centrifugal and Disc Fans"				
1932	NAFM		NAFM and ASHVE	2nd	$Q_1 p_{Ft}$
	"Standard Code for the Testing of Centrifugal and Disc Fans"				
1938	NAFM		NAFM and ASHVE	3rd	$Q_2 p_{Ft}$
	"Standard Code for the Testing of Centrifugal and Axial Fans"				
1946	ASME	PTC-11-1946	ASME	1946	$Q_1 p_{Ft}$
	"Test Code for Fans"				
1949	NAFM	Bulletin No. 103	NAFM and ASHVE	4th	$Q_2 p_{Ft}$
	"Standard Code for the Testing of Centrifugal and Axial Fans"				
1952	NAFM	Bulletin No. 110	NAFM and ASHVE	4th	$Q_2 p_{Ft}$
	"Standard Test Code for Centrifugal and Axial Fans"				
1953	NAFM	Bulletin No. 116	NAFM	1st	$Q_1 p_{Ft}$
	"Standard Code for Testing Centrifugal, Axial and Propeller Fans (Having Wheels Less Than 12″ Diameter)"				
1960	AMCA	Bulletin 210	AMCA	5th	$Q_1 p_{Ft} K_p$
	"Standard Test Code for Air Moving Devices"				
1962	AMCA	Bulletin 210	AMCA	5th rev	$Q_1 p_{Ft} K_p$
	"Standard Test Code for Air Moving Devices"				
1967	AMCA	Standard 210-67	AMCA	6th	$Q_1 p_{Ft} K_p$
	"Test Code for Air Moving Devices"				
1974	AMCA	Standard 210-74	AMCA and ASHRAE	1974	$Q_1 p_{Ft} K_p$
1975	ASHRAE	Standard 51-75	AMCA and ASHRAE	1975	$Q_1 p_{Ft} K_p$
	"Laboratory Methods of Testing Fans for Rating"				
1982*	ASME	PTC-11-1982	ASME	1982	$Q_1 p_{Ft} K_p, M_F Y_F$
	"Test Code for Large Industrial Fans"				

but treats thermal and mechanical (kinetic) energy terms separately. This results in an approximate treatment of kinetic energy in the former method as opposed to an exact treatment in the latter.

2 The volume flow-pressure approach uses a polytropic process between the actual end states for evaluating the thermodynamic-path integrals. The mass flow-specific energy approach simply uses a mean density (which is exact for a polytropic with $n = 2$). If the processes (total process in the one case and static process in the other) were truly polytropic, this leads to an approximation in the latter but not in the former.

The analysis of reference [3] demonstrates that the dominant factor causing differences between the two methods is the kinetic energy treatment rather than the different path approximations. It is shown that the volume flow-pressure approach actually introduces an error in the mechanical energy equation (11). This is deemed sufficient cause for rejecting the volume flow-pressure approach (for compressible cases) by the author(s) of reference [3]; however, the PTC-11 Committee does not support this conclusion. Accordingly, the forthcoming ASME *Performance Test Code Number 11—Large Industrial Fans* will permit code users to choose between the two methods of expressing fan performance. Hopefully, this paper will help prospective users to make an informed choice between the two methods of defining fan performance.

References

1 *ASME Performance Test Code No. 11—Large Industrial Fans*, Draft Copy, 1981.

2 "Laboratory Methods of Testing Fans for Rating," ASHRAE Standard 51-75/AMCA Standard 210-74, American Society of Heating, Refrigerating, and Air Conditioning Engineers and Air Moving and Conditioning Association, 1975.

3 "Fan Pressure and Fan Air Power where ρ_2 Differs from ρ_1," ISO/TC117/SC1-85E, Paris, Aug. 1978.

Downloaded 01 Jun 2010 to 171.66.16.62. Redistribution subject to ASME license or copyright; see http://www.asme.org/terms/Terms_Use.cfm

4 Gerhart, P., Nuspl, S., Wood, C., and Lovejoy, S., "An Evaluation of Velocity Probles for Measurement of Nonuniform Flow in Large Ducts," ASME JOURNAL OF ENGINEERING FOR POWER, Oct. 1979.

5 Gerhart, P. M., "Averaging Methods for Determining the Performance of Large Fans from Field Measurements," ASME Paper No. 80-JPGC/Pwr-1, 1980.

6 Jorgensen, R., and Bohannon, H. R., "Compressibility and Fan Laws," ASHRAE Technical Paper 2333, 1975.

7 Patigny, J., "Fans and the Laws of Thermodynamics," ISO/TC/117/SC 1(B), Paris, Feb. 1978.

8 Reynolds, A. J., *Thermofluid Dynamics*, Wiley Interscience, New York, 1971, pp. 65 67.

APPENDIX

The history of fan test codes in the U.S. is summarized in Table 3.

The 1923 NAFM Standard defined output power as the product of capacity (volume flow rate) and total pressure. Only by examining the calculation procedure does one discover that capacity is measured at fan inlet conditions. This was unchanged in the 1932 edition. However, the 1938 edition defined capacity as the volume flow rate at the outlet of the fan for reasons which were not stated. This was continued in the 1949 and 1952 editions. Meanwhile, the ASME in 1946 defined capacity as the volume flow rate at the inlet of the fan. All of these standards ignored the compressibility of the air even though higher and higher pressure rise machines were being called fans.

The 1960 AMCA Standard introduced compressibility considerations into fan test codes. At the same time, it returned to the original (1923) definition of capacity. The 1960, 1962, and 1967 AMCA Standards all continued these practices as did the 1974/1975 joint AMCA/ASHRAE Standard [2].

None of the above standards included provisions for evaluating the effects of velocity distribution on the kinetic energy terms. And, of course, none of them included any reference to mass flow rate or specific energy as will be done in the 1982 ASME Code.

Downloaded 01 Jun 2010 to 171.66.16.62. Redistribution subject to ASME license or copyright; see http://www.asme.org/terms/Terms_Use.cfm

Endwall Boundary Layer Flows and Losses in an Axial Turbine Stage

I. H. Hunter[1]
Scientist,
Thornton Research Centre,
Shell Research Ltd.,
Chester, England

In order to gain an insight into boundary layer phenomena in axial flow turbines, experimental studies were carried out on a large-scale, low speed, single stage machine. Low and high frequency instrumentation supplemented by flow visualizations were used to determine the details of the flows and losses in the stator and rotor blade rows. Measurements of the turbine stator flows, which were obtained at two different inlet wall boundary layer thicknesses, were generally consistent with typical linear cascade observations. A major difference concerned the presence of appreciable radially directed flow. Hot-wire anemometry measurements at the turbine rotor exit, revealed strong secondary flows at the high turning hub section. The flow pattern was seen to be influenced by the spacing between the two rows of blades and by the rotor's instantaneous position with respect to the periodic flow field arising from the upstream stator row.

Introduction

The efficiency of an axial flow turbine is controlled largely by viscous and turbulent phenomena in the boundary layers which develop on the blade surfaces and on the hub and casing walls of the annulus. Secondary losses (the term is somewhat inappropriate in view of their considerable magnitude) are the irreversibilities associated with the complex, three-dimensional flows which are generated by the annulus wall boundary layers as they pass through the blade rows. Within these endwall regions, the flow is known to deviate markedly from the distribution predicted by potential flow calculations. This behavior may impair both local work transfer and the development of the flow in subsequent blade rows. It can be appreciated, therefore, why there is considerable interest in understanding, predicting and controlling endwall boundary layer behavior.

Research into this aspect of turbomachinery aerodynamics has been in progress for many years yet much remains unclear. Since the flows present a formidable analytical problem, most effort has been directed along experimental lines in order to gain a physical insight into the nature of secondary flows and losses. Much of this work has been concerned with stationary linear cascades which have formed the basis of a number of excellent flow studies including Sjolander [1], Langston, et al. [2], Marchal and Sieverding [3] and Carrick [4]. Nevertheless, important turbomachinery effects are missing from the conventional model and there is a need to investigate endwall boundary layer phenomena in much more realistic environments.

At present, the available data regarding the aerodynamics of turbine stages, as opposed to cascades, are very limited and much of those which have actually been reported tend to be considerably less detailed than cascade work. As a contribution towards improving this situation, an experimental program has begun on a large-scale, low speed axial turbine recently built at the Whittle Laboratory, Cambridge. A particular objective of the present work being to highlight the similarities and differences between actual machines and cascade models.

Experimental Rig and Instrumentation

The experimental equipment is described fully in Hunter [5], so only a brief account will be given here.

A large centrifugal fan draws air into the tunnel via an inlet contraction with honeycombs and screens and through a single-stage research turbine, Fig. 1. Flow rate is controlled by a series of adjustable inlet guide vanes which preceed the auxilliary fan and serve as a throttle. The turbine rotor is coupled by way of a hydraulic pump and motor set to a primary, constant speed induction generator/rotor which feeds power into the fan drive. The outer diameter of the working section of the tunnel is 1524 mm and the inner diameter 1069 mm giving an annulus height of 229 mm and hub to tip ratio of 0.7.

The turbine stage comprises a stator row of 36 blades of 152 mm chord and a rotor row of 51 blades of 114 mm chord. The design of the turbine was such as to keep the fluid dynamics relatively simple by the adoption of a parallel annulus configuration, a free-vortex distribution of swirl velocities after the stators and axial leaving velocity. The important blading details are summarized in Table 1.

The blade profiles were formed from the thickness distribution given by Smith and Johnson [6] combined with a

[1] Formerly Research Student, Whittle Laboratory, Engineering Department, University of Cambridge, England.

Contributed by the Gas Turbine Division and presented orally at the International Gas Turbine Conference and Products Show, Houston, Texas, March 9-12, 1981 of THE AMERICAN SOCIETY OF MECHANICAL ENGINEERS. Revised manuscript received at ASME Headquarters March 4, 1981.

Copyright © 1982 by ASME
Downloaded 01 Jun 2010 to 171.66.16.62. Redistribution subject to ASME license or copyright; see http://www.asme.org/terms/Terms_Use.cfm

parabolic arc camber line with the maximum camber at 40 percent chord from the leading edge. Surface velocity distributions were checked by a Martensen type calculation and found to be satisfactory. The blades were manufactured in epoxy resin reinforced with glass fibre.

By altering the axial positions of the stators, the spacing of the two blade rows may be varied over a wide range. Two builds of the turbine corresponding to different inter-blade gaps, were used in the experiments described in this paper. These are indicated in Fig. 1.

Build 1 is considered to represent the basic build of the turbine, the axial spacing of the blade rows being 155 mm at mid-span. This gap size is slightly larger than may be encountered in practice due to the presence of a probe traversing ring in the tunnel casing between the two rows of blades.

In Build 2, the stators were placed 700 mm from the rotor. This unusually large spacing provides a long path in which circumferential non-uniformities in the flow leaving the upstream blade row substantially mix out and the performance of the rotor could be examined under conditions of reduced inlet circumferential variation.

The tunnel casing is provided with extensive facilities for traversing the flow in the annulus. Combined circumferential and radial flow surveys may be made within the inter-blade space and immediately downstream of the rotor.

The rotor was run at a constant speed of 525 rpm and the design operating flow rate determined by noting when the fluid at mid-span left the turbine stage with zero swirl. The resultant Reynolds Numbers, based upon blade chord and mid-span relative exit velocity, are given in Table 1. These values being typical of modern gas turbine practice.

Measurements of the wall boundary layers in the flow approaching the turbine, were taken at a location 143 mm in front of the leading edge of the stator blade row, using a three-tube pressure probe of head thickness 0.7 mm.

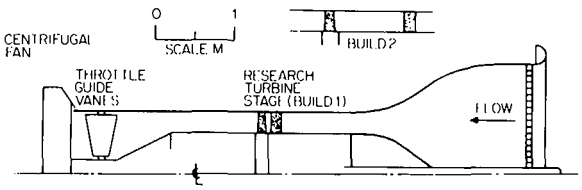


Fig. 1 Research turbine wind tunnel and stage builds

In the main series of experiments, the stator outlet flow field was measured at two planes 48 mm and 104 mm axially downstream of the trailing edge plane. Data were obtained by means of a five-hole pressure probe of head diameter 1.9 mm. The probe was traversed circumferentially over two blade pitches at fixed radial positions in order to build up ports full area surveys of the stator exit flow. To assist in the data collection, the probe pressure parts were connected to a solenoid operated, pneumatic scanning valve which could sequentially connect these to a manifold containing a small differential pressure transducer. The laboratory's PDP-12 computer was programmed to operate the valve, sample the transducer outputs and record these for subsequent processing.

side of the turbine rotor to obtain "time averaged" data concerning the flow leaving the moving blade row. The most important aspect of the turbine rotor studies were measurements of the outlet flow by hot-wire anonometry. The technique used was an extended version of that developed originally by Whitfield, et al. [7] and involving a single hot-wire sensor inclined at 54.7 deg to the probe axis. The probe is rotated through successive 120 deg increments and data obtained for each of three mutually orthogonal orientations of the wire sensor. From these measurements, the three components of the flow velocity may be evaluated.

The hot-wire probe assembly consisting of a 2 mm length of 5μ mm platinum coated tungsten wire between two steel prongs set in a 5 mm dia stem, was introduced radially into the tunnel behind the rotor where its axial distance from the trailing edge was 27 mm and 51 mm at the hub and tip, respectively.

To produce measurements of the blade to blade structure of the rotor exit flow, the inclined hot-wire technique was used in conjunction with the laboratory PDP-12 computer which provided on-line data acquisition and processing. The procedure makes use of phase-lock sampling which is now a well established technique in turbomachinery research, e.g., Gostelow [8]. The recording of the linearized hot-wire output voltage was initiated once every revolution of the rotor by a reference pulse. A total of 100 samples each of 256 discrete measurements covering the progress of three complete blade passages, were taken and corresponding values arithmetically averaged to produce a single ensemble averaged result which corresponded to the velocity signal linked solely to the passing of the rotor blades.

Table 1 Blading details

			STATOR			ROTOR
Aspect ratio, h/c			1.5			2.0
Reynolds Number, Re			4.39×10^5			3.29×10^5
Stage loading, $\Delta H/U_M{}^2$						1.0
Flow coefficient, Vx/U_M						0.49
	HUB	MEAN	TIP	HUB	MEAN	TIP
Pitch chord ratio, S/C	0.611	0.742	0.873	0.575	0.698	0.821
Flow turning	69.0 deg	65.0 deg	61.3 deg	100.8 deg	65.0 deg	33.3 deg

Nomenclature

C = blade chord
h = blade span
s = blade pitch
C_L = lift coefficient
R_e = Reynolds number
ΔPo = total pressure change
q = inlet flow dynamic head = $\frac{1}{2}\rho V_1{}^2$
V = velocity
U = blade speed
α = absolute tangential flow angle
β = relative tangential flow angle
η = efficiency
Y = loss coefficient
δ = boundary layer thickness
δ^* = boundary layer displacement thickness
H = boundary layer shape factor

Subscripts

X = axial direction
1 = upstream (of stators)
2 = downstream
tt = total to total
R = rotor
m = mean
M = mid-span

Downloaded 01 Jun 2010 to 171.66.16.62. Redistribution subject to ASME license or copyright; see http://www.asme.org/terms/Terms_Use.cfm

Results and Discussion

The experimental results are described in two parts concerning the aerodynamics of the stator and rotor blade rows respectively for each configuration of the turbine. The flows associated with the stator are dealt with first of all, and these then represent the inputs to the moving blade row where the subsequent interactions are a particularly important aspect of the research.

Stator Flows.

Build 1. Details of the wall boundary layers in the flow approaching the stator blade row are given in Table 2. The boundary layers on the hub and casing walls are very similar and in the second series of experiments the layers were artificially thickened to approximately 2½ times their natural thickness. In connection with the flow measurements downstream of the stators, a hot-wire probe introduced into the inter-blade space revealed that velocity fluctuations linked to the passing of the rotor blades were practically undetectable at the five hole probe traversing planes. This is taken to indicate that this instrument should not be affected by errors due to flow unsteadiness.

Considering first of all, the natural inlet boundary layer case and the traverse plane closest to the stator trailing edge, Fig. 2 shows the total pressure deficit distribution in both contour and circumferentially mass-averaged form. It is observed that large areas of the flow are virtually loss free while significant losses occur within the blade wakes and in the regions close to the hub and casing walls. The wakes do not follow the radial direction of the blade trailing edge from which they are shed, but are inclined due to the spanwise variation in the swirl velocity downstream. At the mid-span position where the flow is nominally unaffected by the behavior near the walls, the averaged total pressure deficit corresponds to a comparatively low value of profile loss coefficient of 1.4 percent. This is a result of a large amount of laminar boundary layer flow on the blade, thought to be related to the low free stream turbulence level (0.4 percent) in the working section of the tunnel. Further details of this aspect of the flow are considered later with regard to surface flow visualization tests.

The total pressure distribution, which it is emphasised includes the losses already present in the upstream wall boundary layers, shows clearly the expected increase in loss towards the endwalls due to secondary flows. The peaks in the loss distribution are typical of such measurements and correspond to the secondary vorticies. The loss peak observed near the hub in the corner between the suction side of the wake and the endwall, is particularly pronounced whilst the losses in the outer region appear to be concentrated actually within the wake rather than to the edge of it. The accumulation of low total pressure fluid in the inner half of the blade span is approximately 60 percent larger than in the outer portion of the annulus. A similar value was obtained by Allen, et al. [9] in an annular cascade and was explained largely by the inward migration of low energy fluid under the influence of the spanwise pressure gradient. The occurrence of such flows in the present turbine stator are considered later.

The circumferentially averaged plot of blade exit flow angle, Fig. 3(*a*), exhibits a pattern familiar in secondary flow studies, in which the fluid close to the endwell is overturned relative to the design flow and underturned further away from the wall. The basic pattern is the same at either endwall and it

Table 2 Inlet boundary layer parameters

	Naturally developing inlet boundary layers		Artificially thickened inlet boundary layers	
	Inner wall	Outer wall	Inner wall	Outer wall
Thickness, δ (mm)	21.3	22.1	55.9	52.8
Displacement thickness, δ^*(mm)	2.75	2.87	4.62	4.97
Shape factor, H	1.44	1.43	1.27	1.31

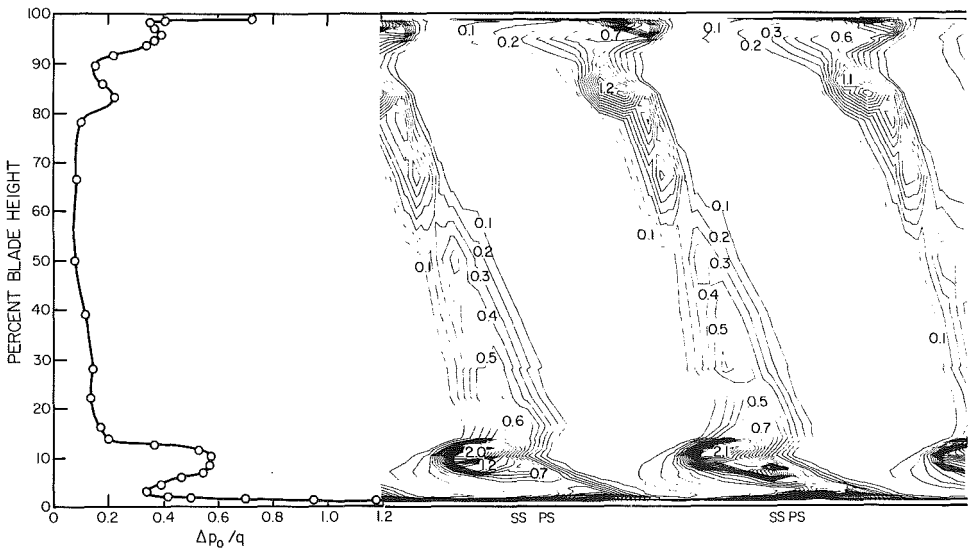


Fig. 2 Circumferentially averaged and contour distributions of total pressure deficit, 48 mm downstream of stators; natural inlet boundary layers

Downloaded 01 Jun 2010 to 171.66.16.62. Redistribution subject to ASME license or copyright; see http://www.asme.org/terms/Terms_Use.cfm

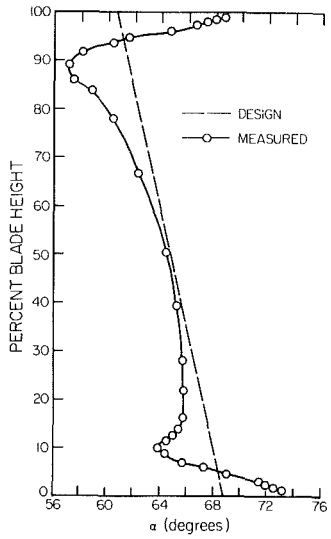


Fig. 3 (*a*) Flow angle

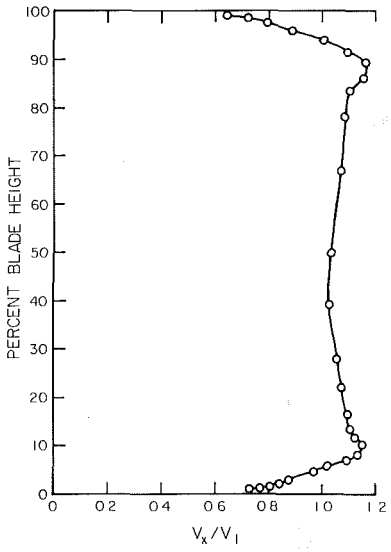


Fig. 3 (*b*) Axial velocity

Fig. 3 Circumferentially averaged flow distribution, 48 mm downstream of stators; natural inlet boundary layers

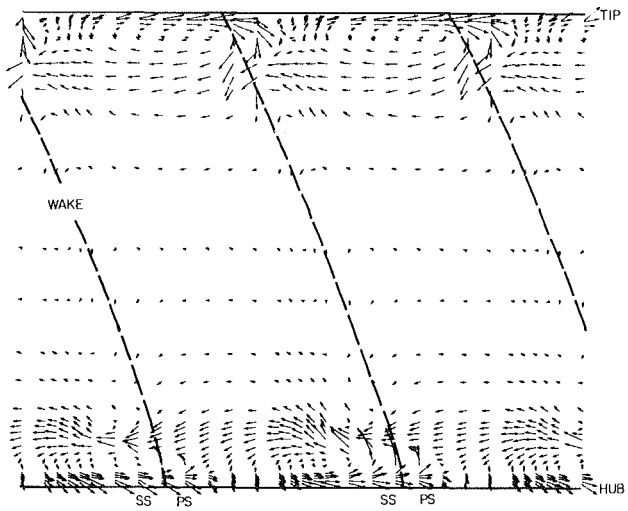


Fig. 4 Distributions of secondary flow velocities, 48 mm downstream of stators; natural inlet boundary layers

is noted that the maximum underturning occurs at a radial position which roughly coincides with the edge of the incoming wall boundary layer.

The axial velocity distribution in Fig. 3(*b*), has a noticeably concave freestream profile and peaks which are associated with the regions of flow underturning. The wall boundary layers have apparently undergone little axial thinning in their progress through the blade row. The secondary velocity diagram, Fig. 4, supplements the tangential flow angle plot and demonstrates the important three dimensional aspects. The velocity components represent the departures from the potential flow field and were derived by resolving the measured stator outlet flow in plane perpendicular to the design (free-vortex) distribution. The normalizing factor is the averaged resultant velocity at the mid-span position. At both ends of the blade it is possible to observe areas of circulating flow consistent with secondary streamwise vorticity. The vortex near the hub is the more intense and concentrated and coincides with the loss core in the suction side-endwall corner. Further inspection of Fig. 4 reveals that at this downstream position there is no continuous distribution of inwardly directed velocities within the blade wake regions which could account for the larger accumulation of low total pressure fluid at the hub endwall. The large radial velocity components observed at around 80 percent blade height, appear to be linked with movement of endwall losses away from the casing and into the blade wakes. This behavior plays an important role in the development of the flow as it proceeds further downstream.

Between the two traverse planes downstream of the stators, most reorganisation has taken place in the distribution of total pressure, Fig. 5. As the flow moves further from the blades, the spanwise swirl gradient is felt more and the wakes become more inclined. Additionally the traverse components of the secondary flow tend to twist the wakes, particularly in the outer portion of the annulus. The loss at mid-span is less than that at the previous traverse position and as a consequence the wakes appear parted in the middle. There is an overall increase in total pressure deficit of 21 percent between the two measurement planes, most of which appears to have arisen from further boundary layer growth on the endwalls, notably at the hub.

Examination of the secondary velocity distribution indicates that the intense circulating motion at the endwall has been effectively dissipated though the corresponding feature at the casing is still discernable. On a circumferentially averaged basis, the flow angle and axial velocity distributions are virtually the same as at the previous traverse station.

For the case with artificially thickened inlet wall boundary layers, the stator outlet flow was only examined at the traverse plane nearest to the blades. In contour form, Fig. 6, the total pressure distribution is very similar to that observed with thinner incoming boundary layers. The loss in central portion of the flow is virtually identical to that obtained before, as expected, and demonstrates the repeatability of the measurements. At the endwalls, however, the losses differ in the two cases. The loss regions are now of roughly equal size and it is noticed how losses are observed across the complete passage width.

The amounts of overturning and underturning in the stator outlet flow, Fig. 7(*a*), are decreased due to reduction in the inlet normal vorticity associated with the thicker and more rounded velocity profiles. The positions of the maximum underturning are practically the same as for the thinner inlet boundary case.

The reductions in the degree of underturning are reflected in the absence of peaks in the axial velocity profile, Fig. 7(*b*).

Downloaded 01 Jun 2010 to 171.66.16.62. Redistribution subject to ASME license or copyright; see http://www.asme.org/terms/Terms_Use.cfm

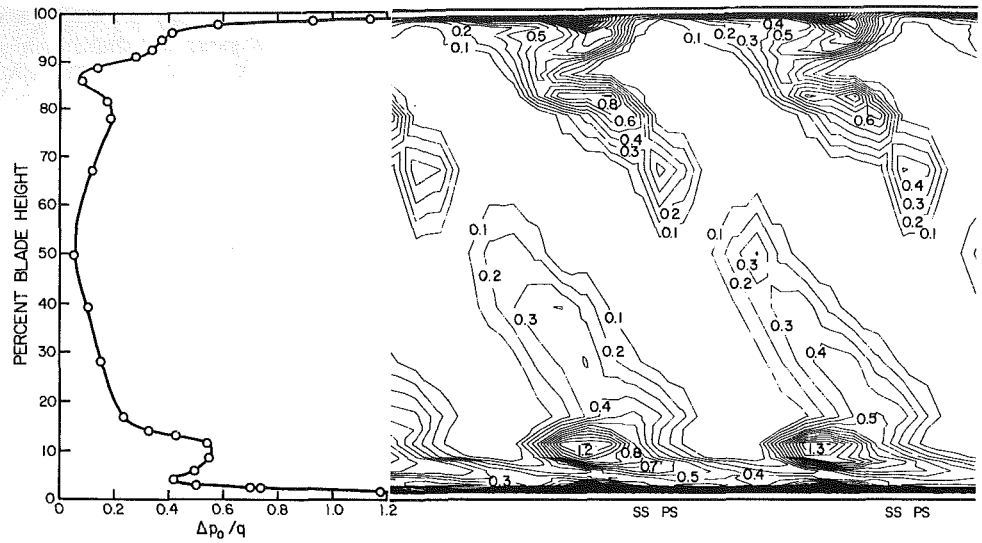


Fig. 5 Circumferentially averaged and contour distributions of total pressure deficit, 104 mm downstream of stators, natural inlet boundary layers

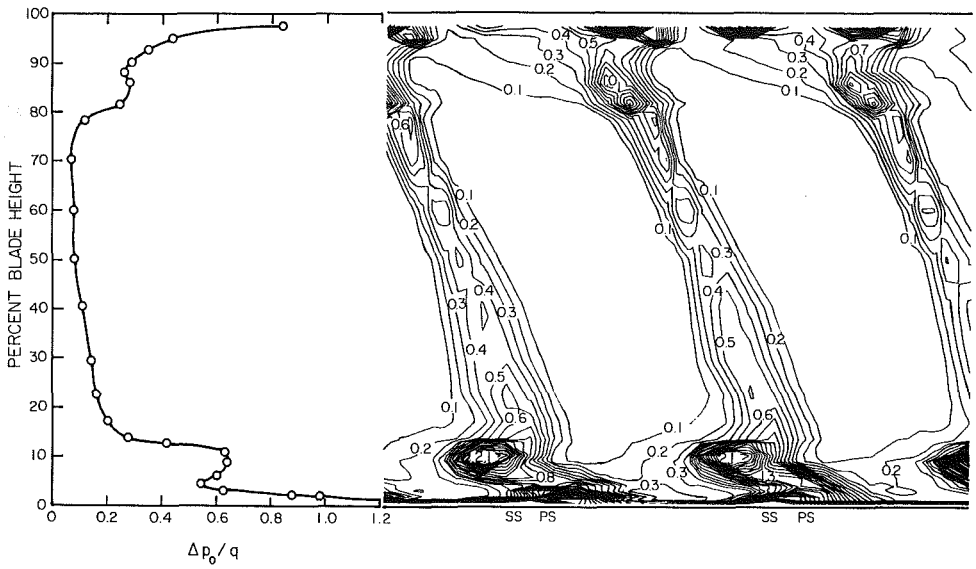


Fig. 6 Circumferentially averaged and contour distributions of total pressure deficit, 48 mm downstream of stators; thickened inlet boundary layers

Build 2. Traverses of the stator exit flow just in front of the rotor, showed that the flow in the annulus was sensibly uniform in the circumferential direction thus indicating that the large inter-blade spacing had promoted complete mixing.

The endwall losses, Fig. 8(*a*), are considerably greater than in Build 1 due to the longer contact path though the total pressure profile is free from the irregularities observed closer to the blade exit plane. The boundary layer at the hub is also appreciably thicker than on the outer endwall. This is thought to be due to the differing effects of streamline curvature on the growth of the layers on the convex and concave surfaces.

Overall Secondary Losses. The circumferentially mass-averaged total pressure data at the traverse positions closest to the stator blades have been integrated in the spanwise direction in order to obtain the overall secondary loss coefficients.

In Fig. 9 the measured gross secondary loss coefficients, corrected for aspect ratio and blade loading, are compared with the linear cascade correlation of Morris and Hoare [10]. In view of the scatter normally in evidence with measurements and predictions of secondary loss, the agreement of the predictions with the turbine data is considered satisfactory. The values in Fig. 9 are inclusive of the upstream boundary layer loss and in Table 3 the secondary losses are broken down so as to demonstrate how much of these actually occur within the blade row. The net or pure secondary loss is seen to increase with inlet boundary layer thickness which is consistent with Came's [11] linear cascade findings. It is interesting that the apparent reduction in the intensity of the secondary flow brought about the thicker inlet boundary layers, is not accompanied by a corresponding reduction in the net secondary loss.

Flow Visualization. To assist in the interpretation of the aerodynamic measurements downstream of the stator row, a

Downloaded 01 Jun 2010 to 171.66.16.62. Redistribution subject to ASME license or copyright; see http://www.asme.org/terms/Terms_Use.cfm

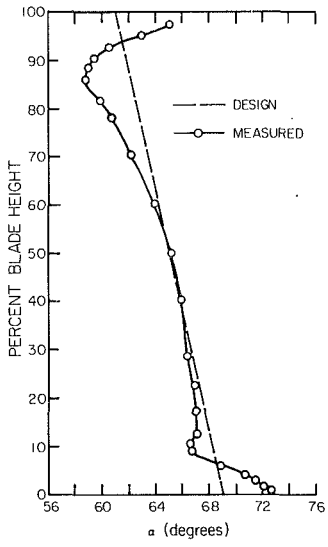


Fig. 7 (*a*) Flow angle

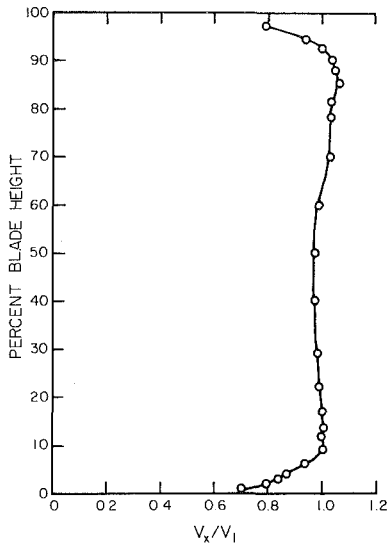


Fig. 7 (*b*) Axial velocity

Fig. 7 Circumferentially averaged flow distribution, 48 mm downstream of stators; thickened inlet boundary layers

mixture of gas-oil and fluorescent dye was used to reveal the surface flow patterns on the blades and endwalls. The results obtained for the natural and artificially thickened inlet boundary layers were as far as could be seen, identical.

The flow behavior observed on the endwalls was essentially the same at both hub and casing. The tendency for the surface fluid to move rapidly towards the suction side of the passage was clearly seen and in fact, at the blade exit plane the surface streamlines were almost tangential in direction.

On the blade pressure surface no significant interaction with the endwall flow was evident, indeed the flow appeared to be practically two-dimensional. The oil-dye tests on the suction surface, however, revealed a number of interesting features.

Figure 10 presents photographs of the suction side patterns on blades at two different circumferential positions around the annulus. The surface textures indicate a large amount of laminar flow on the blade. This is a result of the low free stream turbulence level in the working section of the tunnel and helps to explain the low profile loss measured at the centre of the blade span. Appreciable radially inward directed blade surface flow is apparent in these laminar regimes. A laminar separation bubble forms at about two-thirds of chord and there is strong radial flow within this as shown by Fig. 10(*b*). Fluid is also observed to pass along the blade trailing edge from the outer to inner endwall and in doing so is involved in a curious flow reversal, marked *R* on the photographs, back up the suction surface where the separation bubble intersects the trailing edge. In view of the above observations, it is probable that in addition to inlet boundary layer fluid and material entrained from the suction surface, the pronounced passage vortex at hub endwall will contain a certain amount of low energy fluid originating from the outer portion of the annulus.

The significance of laminar blade boundary layer flow was emphasised when "trips" of coarse sandpaper were secured spanwise to the blade surfaces close to the leading edge, and the flow visualisation tests repeated. In these circumstances with a wholly turbulent boundary layer, the blade surface flow was observed to be effectively two-dimensional away from the trailing edge and endwall regions. Evidently with the "fuller" velocity profile of the turbulent layer and with no separation bubble, the surface flow is much less susceptible to radial migration under the influence of the spanwise pressure gradient.

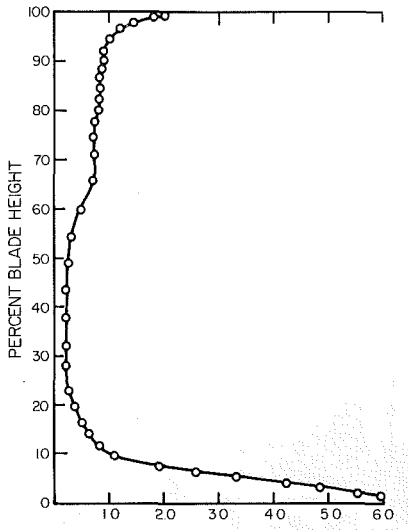


Fig. 8 (*a*) Total pressure deficit

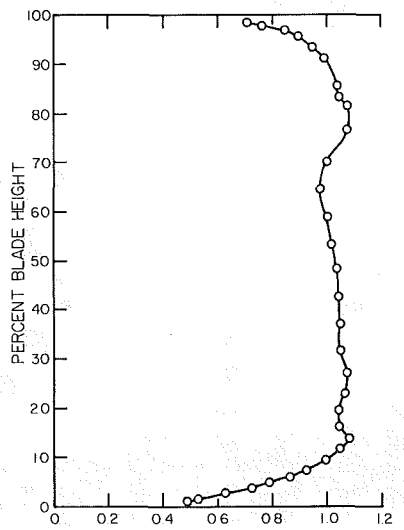


Fig. 8 (*b*) Axial velocity

Fig. 8 Flow distribution, 675 mm downstream of stators; Build 2

Downloaded 01 Jun 2010 to 171.66.16.62. Redistribution subject to ASME license or copyright; see http://www.asme.org/terms/Terms_Use.cfm

Table 3 Stator secondary losses

	Naturally developing inlet boundary layers		Artificially thickened inlet boundary layers	
	Inner wall	Outer wall	Inner wall	Outer wall
δ_1^*/C	0.0180	0.0189	0.0303	0.0326
Gross secondary loss coefficient, Y_{SG}	0.0154	0.0148	0.0213	0.0315
Percent gross secondary loss present in inlet layer	29	55	41	53
Net secondary loss coefficient, Y_S	0.0110	0.0066	0.0126	0.0147

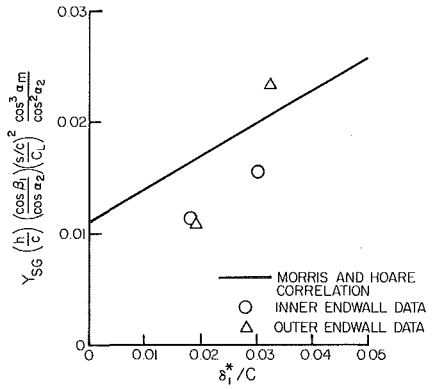


Fig. 9 Comparison of stator secondary losses with cascade correlation

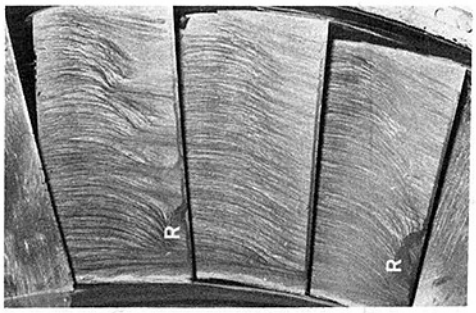


Fig. 10 (a) Flow visualization on stator suction surfaces

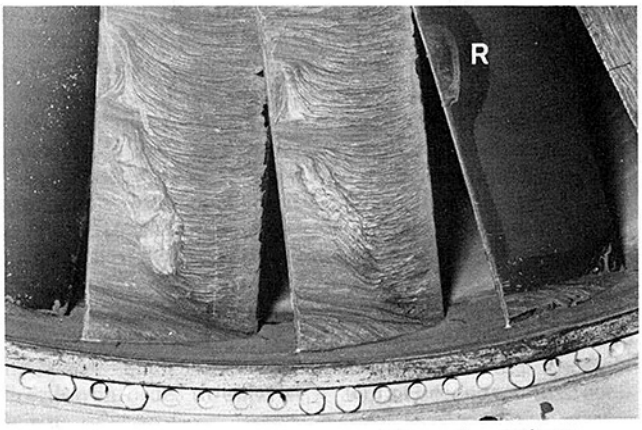


Fig. 10 (b) Flow visualization on stator suction surfaces

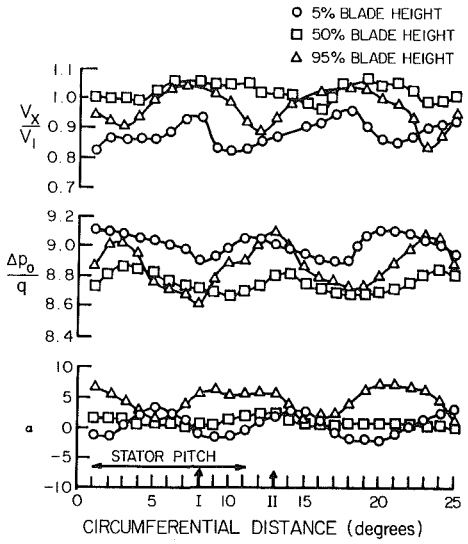


Fig. 11 Stationary flow field just downstream of rotor; Build 1

The regions of the flow where the boundary layers on the endwalls and blade suction surface interact are clearly visible in Fig. 10. The affected zones on the suction surface occur in a region of decelerating flow and are essentially triangular in shape with the apex on the junction with the endwall at about the position of maximum blade camber. The feature is most prominent at the outer endwall where it is likely that the spanwise pressure gradient is affecting a shift of the passage vortex away from the casing endwall.

Rotor Flows.

Build 1. The results obtained at the rotor exit for natural and artificially thickened inlet boundary layers were very similar and those actually presented here correspond to the first of these cases.

Surveys of the stationary flow field just behind the turbine rotor by five hole probe, Fig. 11, show that the circumferential variations imposed by the stators persist through the moving blade row. In accordance with the flow distribution upstream, these nonuniformities are most pronounced near the endwalls.

Indicated on Fig. 11 are two circumferential positions, 5 deg or half a stator pitch apart, where the flow was traversed by the hot-wire probe. This was done in order to obtain the outlet flow field with the rotor blades effectively "frozen" in different positions relative to the stators. The measured distributions of relative dynamic head (relative velocity squared) and secondary flow velocities in the moving frame of reference, are presented in Fig. 12. The nondimensionalizing factors are the mid-span, circumferentially averaged, relative velocity squared and relative velocity respectively.

Downloaded 01 Jun 2010 to 171.66.16.62. Redistribution subject to ASME license or copyright; see http://www.asme.org/terms/Terms_Use.cfm

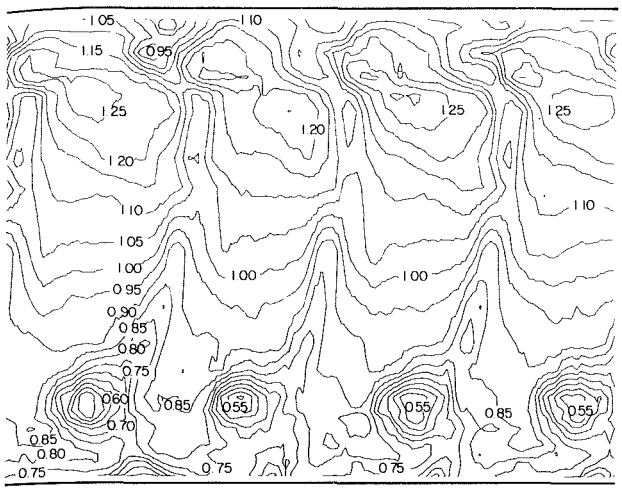


Fig. 12 (*a*) Relative dynamic head

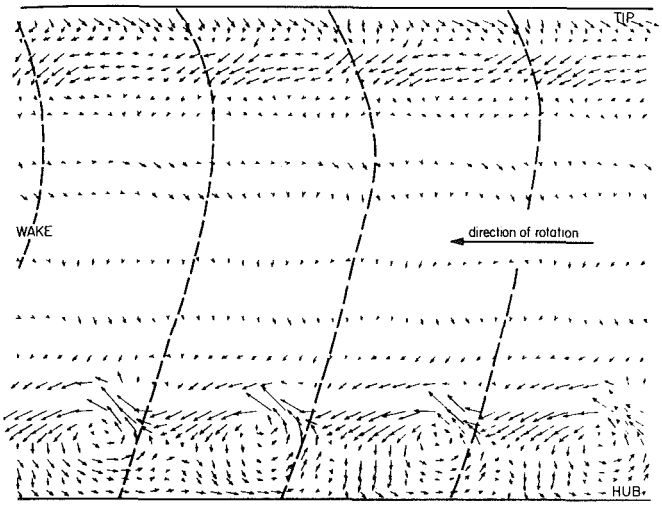


Fig. 12 (*b*) Relative secondary velocities

Fig. 12 Distribution of rotor exit flow, position I; Build 1

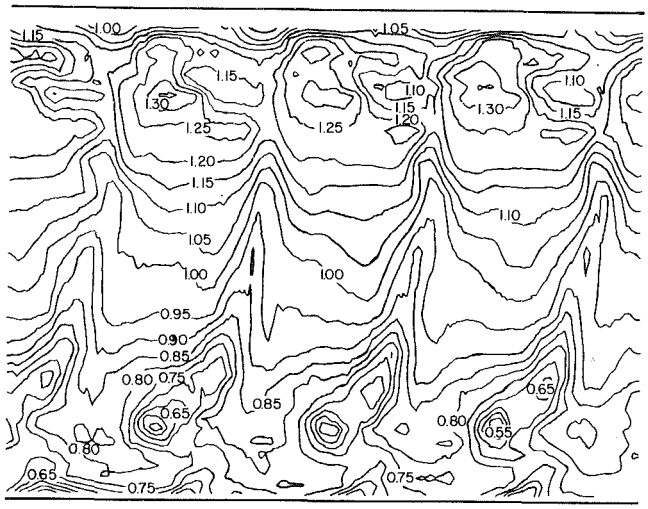


Fig. 13 (*a*) Relative dynamic head

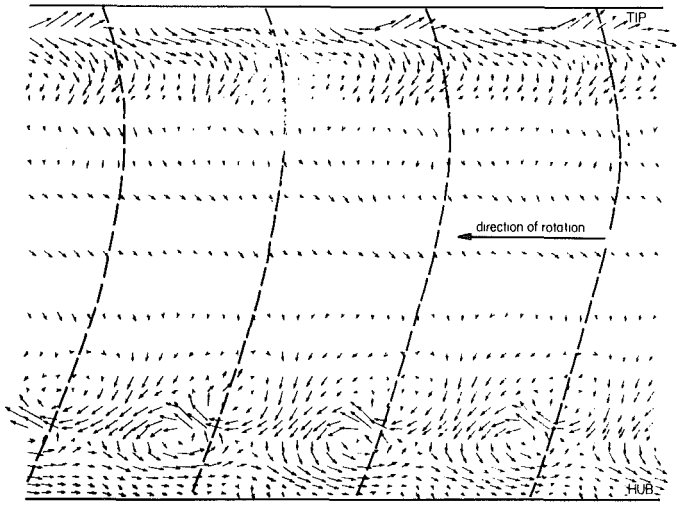


Fig. 13 (*b*) Relative secondary velocities

Fig. 13 Distribution of rotor exit flow, position II; Build 1

Before discussing the structure of the flow for the two cases, some further explanation of what these diagrams actually represent will be given.

At any instant, the rotor exit flow pattern is different from blade passage to blade passage since the numbers of rotating and stationary blades are not the same. While the hot-wire does indeed record the flow from four different passages, as they pass the sensor they are in the same position relative to the periodic stator flow field. Hence, the flow patterns appear the same in adjacent blade passages.

Examination of Fig. 12(*a*) for the rotor in position I shows that near the hub, which is the region of particular interest for this blade row, low energy fluid accumulates in a pronounced core towards the suction side of the passage. This is expected in view of the high turning here (100 deg) and the skewed nature of the boundary layer flow at inlet. It is noticeable that whereas at the stator hub the loss accumulation was located practically on the endwall, the corresponding flow feature in the rotor is displaced outwards appreciably, to almost 20 percent blade height, allowing freestream fluid to move in between it and the hub surface. The secondary velocity vector diagram, Fig. 12(*b*), reveals an intense passage vortex between the blade wakes at the hub. No such feature is apparent at the rotor tip, nor is there evidence of radial flow of blade wake fluid in the central portion of the annulus.

Comparing the above with corresponding data for position II, Fig. 13, it is seen that the most significant change in the flow pattern between the two instantaneous positions of the rotor, is at the hub in the structure of the vortex and concentration of low energy fluid. According to Fig. 13(*a*), the previously almost circular core has been drawn out along the blade wake and divided into two.

The distributions of circumferentially averaged relative outlet flow angle in Fig. 14(*a*), exhibit a number of similar features to those obtained for the stationary blades, notably the two peaks of underturning. Surprising, however, the flow overturning is very small at the rotor hub.

As before, the regions of underturned flow result in maxima in the axial velocity profiles, Fig. 14(*b*).

It is evident that the flow in the turbine hub region is being severely disturbed during its passage through the rotor. Some insight into this behavior was given by simple flow visualization tests in which numerous small tufts of goosedown were secured to the blade and hub endwall surfaces and a strobescope used to illuminate the resultant patterns in the running machine.

Observation of tufts on the hub suggested that the original inlet wall boundary layer was transported to the suction side of the passage after only about half the total angle of turn. Downstream of this point the tufts followed a direction roughly parallel to the blade camber. This indicates that the new wall boundary was not allowed to develop to any appreciable thickness since low energy fluid is continuously swept from the hub surface to be eventually discharged some

Downloaded 01 Jun 2010 to 171.66.16.62. Redistribution subject to ASME license or copyright; see http://www.asme.org/terms/Terms_Use.cfm

radial distance from it after the trailing edge. The flow visualization on the blade suction surface showed that the regions affected by secondary flows on the hub endwall, extended radially to a maximum of about 35 percent blade height at the trailing edge which agreed with the mesurements downstream of the blade row, Fig. 14(*a*). Elsewhere on the suction surface, the flow appeared to be closely two-dimensional with no evidence of centrifuging of boundary layer fluid which has frequently been suggested to occur in turbomachinery rotors.

The radial distributions of rotor loss coefficient, and total-total turbine efficiency, are shown in Fig. 15. In obtaining these quantities, the assumption was made that the flow was distributed on axisymmetric stream surfaces. The loss coefficient was evaluated from the difference in relative total pressure at rotor inlet and outlet, whilst efficiency was derived from the change in angular momentum and the isentropic work from the overall drop in total pressure. The results indicate as before, very low profile losses but pronounced loss peaks near the endwalls associated with the passage vorticity. Interestingly, the magnitude of the secondary losses are similar at both ends of the blade despite the nominal flow turning at the tip being only a third of that at the hub. On approaching the endwalls it is noticed that the loss coefficient and efficiency take on unrealistic values. The most likely explanation for this is that low energy fluid near the hub or tip, produced by both stator and rotor secondary losses, is drawn up by the passage vortex and is shed from the blade row some distance from the endwall. Such transverse flows violate the assumption that the flow is confined to surfaces of revolution which was used in the calculations. Despite these shortcomings in obtaining the local values, the overall turbine efficiency of 94 percent (±3 percent), is in reasonable agreement with through-flow calculations which predict around 91 percent using the Craig and Cox [12] correlations to estimate all losses.

Build 2. In this build, the rotor flow was considered to be steady in the moving frame of reference and a single radial traverse the outlet flow is representative of the overall pattern.

With the thick boundary layer on the hub endwall, Fig. 8, there is an increased tendency for adjustments of the incoming flow profile as it passes through the rotor. This is apparent in the unusual outlet axial velocity distribution, Fig. 16(*a*). The results show that the passage vortex is smaller than in Build 1, but is more intense.

The turbine efficiency, Fig. 16(*b*), falls off rapidly away from the centre of the span and the overall value of 90.6 percent is 3.2 points down on the build with the more realistic blade spacing. It is noteworthy, however, that the efficiency around mid-span is virtually unchanged suggesting that the rotor profile losses were not significantly affected by unsteadiness arising from the circumferentially nonuniform nature of the stator exit flow.

Concluding Remarks

The results presented here form only a small part of those obtained and described fully in reference [5]. On the basis of the overall experimental study, the following conclusions can be drawn.

The behavior of the endwall flow in the stators was largely consistent with that which has been observed in conventional linear cascades. The presence of a spanwise pressure gradient in the annular geometry, promotes a migration of boundary layer fluid towards the hub via the blade trailing edge and on the suction surface in the laminar regions. The extent of the laminar boundary layer flow on the research turbine stator may not be typical of practical machines, but it does have an important effect on the spanwise flow.

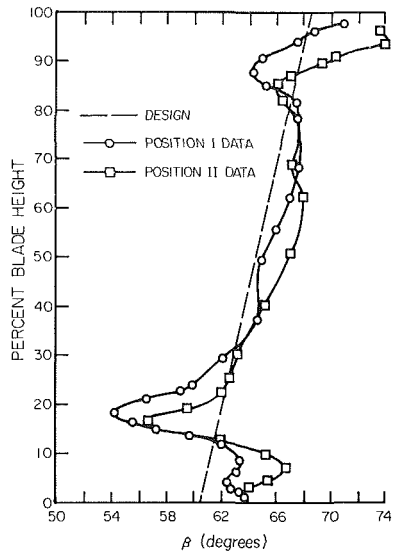


Fig. 14 (*a*) Relative outlet angle

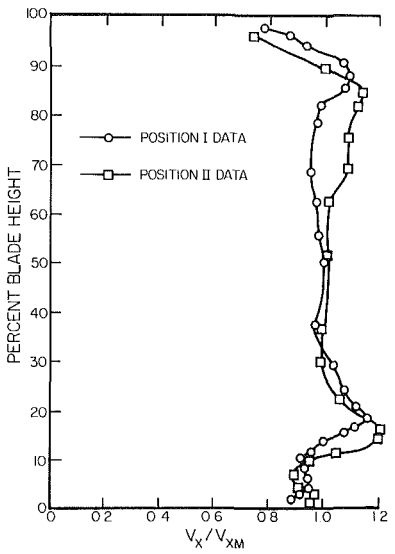


Fig. 14 (*b*) Axial velocity

Fig. 14 Circumferentially averaged rotor exit flow distributions positions I and II; Build 1

The secondary flows in the rotor blade row, notably at the high turning hub section, were considerably more complex than in the stators. Most significantly, the passage vortex and loss accumulation was observed to undergo appreciable changes in structure and position as a result of the unsteady flow relative to the rotor.

The aerodynamics of the turbine rotor hold much scope for further detailed study. In this repsect there is a need to measure the rotor losses more directly and with greater accuracy, and also to ascertain the state of the boundary layers on the blade surfaces.

The work reported in this paper has been restricted to a single-stage machine of comparatively simple geometry and whilst some specific results may be peculiar to this turbine, the data can provide a framework in which to understand the even more complex flow processes in practical, multi-stage machines.

Acknowledgments

The author would like to thank Dr. J. D. Denton for his supervision of the work which forms the basis of this paper.

The financial support of the Central Electricity Generating Board is also gratefully acknowledged.

Downloaded 01 Jun 2010 to 171.66.16.62. Redistribution subject to ASME license or copyright; see http://www.asme.org/terms/Terms_Use.cfm

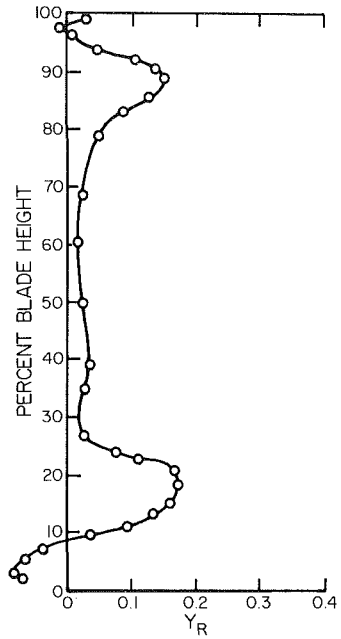


Fig. 15 (*a*) Rotor loss coefficient

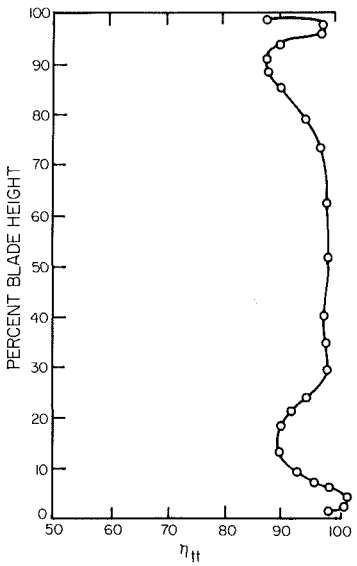


Fig. 15 (*b*) Turbine efficiency

Fig. 15 Rotor loss and turbine efficiency; Build 1

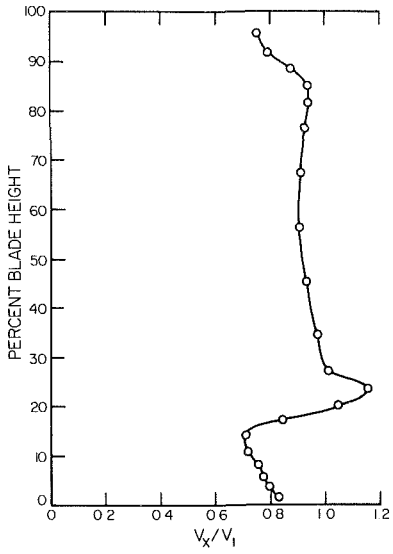


Fig. 16 (*a*) Axial velocity

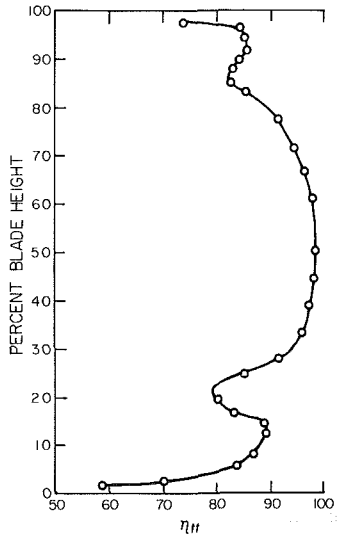


Fig. 16 (*b*) Turbine efficiency

Fig. 16 Flow distribution downstream of rotor; Build 2

References

1 Sjolander, S. A., "The Endwall Boundary Layer in an Annular Cascade of Turbine Nozzle Guide Vanes," Carleton University Msc Thesis, 1975.

2 Langston, L. S., Nice, M. L. and Hooper, R. M., "Three Dimensional Flow within a Turbine Cascade Passage," ASME Paper No. 76-GT-50, 1976.

3 Marchal, Ph., and Sieverding, C. H., "Secondary Flows within Turbomachinery Bladings," *Secondary Flows in Turbomachines*, AGARD, 1977.

4 Carrick, H. B., "Secondary Flow and Losses in Turbine Cascade with Inlet Skew," University of Cambridge PhD Thesis, 1975.

5 Hunter, I. H., "Endwall Boundary Layer Flows and Losses in Axial Turbomachines," University of Cambridge PhD Thesis, 1979.

6 Smith, D. J. T. and Johnson, J. H., "Investigation on an Experimental Single-Stage Turbine of Conservative Design," ARC R & M No. 3541, Jan. 1967.

7 Whitfield, C. E., Kelly, J. C., and Barry, B., "A Three Dimensional Analysis of Rotor Wakes," *Aeronautical Quarterly*, Nov. 1972, pp. 285–300.

8 Gostelow, J. P., "A New Approach to the Experimental Study of Turbomachinery Flow Phenomena," ASME Paper No. 76-GT-47, 1976.

9 Allen, H. W., Kofskey, M. G., and Chammers, R. E., "Experimental Investigation of Loss in an Annular Cascade of Turbine Nozzle Blades of Free-Vortex Design," NACA TN 2871, 1953.

10 Morris, A. W. H., and Hoare, R. G., "Secondary Loss Measurements in a Cascade of Turbine Blades with Meridional Wall Profiling," ASME Paper No. 74-WA/GT-13, 1975.

11 Came, P. M., "Secondary Loss Measurements in a Cascade of Turbine Blades," Institution of Mechanical Engineers Conference Publications No. 3, 1973, pp. 75–83.

12 Craig, H. R. M., Cox, H. J. A., "Performance Estimation of Axial Flow Turbines," *Proceeding of the Institution of Mechanical Engineers 185*, 1970–71.

Downloaded 01 Jun 2010 to 171.66.16.62. Redistribution subject to ASME license or copyright; see http://www.asme.org/terms/Terms_Use.cfm

R. K. Agrawal
Senior Performance Analyst,
Assoc. Mem. ASME

M. Yunis
Computing Analyst

Pratt & Whitney Aircraft of Canada Ltd.,
Longueuil, Quebec, Canada

A Generalized Mathematical Model to Estimate Gas Turbine Starting Characteristics

The paper describes a generalized mathematical model to estimate gas turbine performance in the starting regime of the engine. These estimates are then used to calculate the minimum engine starting torque requirements, thereby defining the specifications for the aircraft starting system. Alternatively, the model can also be used to estimate the start up time at any ambient temperature or altitude for a given engine/aircraft starting system combination.

Introduction

This paper describes a mathematical model developed to estimate gas turbine performance in the starting regime. Starting regime, here, is defined as that part of the operating range which lies between zero and engine idle speed.

Estimation of engine performance requires detailed performance maps for the various components in the engine. These maps, however, generally start to get well defined only beyond the engine idle speed and are therefore of not much use in the starting regime. In addition, differences in characteristics of individual component types from one engine to another, which are so pronounced at higher speeds, have been found to become relatively small at the low speeds encountered in starting regime. It is thus possible to generalize the performance of a given component type, e.g., compressor, by a single generalized map without introducing gross errors. Using these generalized maps, it is then possible to carry out transient performance analysis to estimate the engine starting characteristics. This, then, is the approach followed in this model.

An Overview of the Model

Generalized Component Characteristics.

Compressor. The compressor as well as other engine component characteristics the compressor used in the model are presented in the form of normalized parameters defining the performance of that component. Thus, for the compressor, these parameters would be flow, specific work and efficiency as functions of speed. To obtain these functional relationships, aero/thermodynamic analyses of these components were carried out. The compressor flow relation, for example, is derived as follows:

The compressor mass flow through an annulus of Area A_{ann} is given by

$$m = \rho A_{ann} V_a = \frac{p}{Rt} A_{ann} V_a \qquad \text{(i)}$$

where V_a is the axial flow velocity and is related to the compressor flow factor (ϕ), speed (N) and diameter (D_c) by

$$V_a = \frac{\pi N D_c \phi}{720} \qquad \text{(ii)}$$

From (i) and (ii) and normalizing p and t

$$m = \frac{\delta}{\theta} \cdot \frac{A_{ann}\pi N D_c \phi}{720R} \cdot \frac{14.696}{518.7} \qquad \text{(iii)}$$

Denoting the parameters in (iii) with a subscript R at a given engine reference condition,

$$m_R = \frac{\delta_R}{\theta_R} \cdot \frac{A_{ann}\pi D_c}{720\,R} \cdot \frac{14.696}{518.7} \cdot N_R \phi_R \qquad \text{(iv)}$$

From (iii) and (iv) then,

$$\frac{\left(\frac{m\sqrt{\theta}}{\delta}\right)}{\left(\frac{m\sqrt{\theta}}{\delta}\right)_R} = \frac{(N/\sqrt{\theta})}{(N/\sqrt{\theta})_R} \cdot \frac{\phi}{\phi_R} = K_\phi \cdot \frac{\left(\frac{N}{\sqrt{\theta}}\right)}{\left(\frac{N}{\sqrt{\theta}}\right)_R} \qquad (1)$$

Figure 2 shows this relation plotted based on steady state data from a number of engines.

Similarly, it can be shown that the steady state compressor work and efficiency will be represented by:

$$\frac{\Delta h_c/\theta}{(\Delta h_c/\theta)_R} = K_{\psi_c}\left[\frac{\left(\frac{N}{\sqrt{\theta}}\right)}{\left(\frac{N}{\sqrt{\theta}}\right)_R}\right]^2 \qquad (2)$$

and

$$\frac{(\eta_c)}{(\eta_c)_R} = K_{\eta_c}\left[\frac{\left(\frac{N}{\sqrt{\theta}}\right)}{\left(\frac{N}{\sqrt{\theta}}\right)_R}\right] \qquad (3)$$

Contributed by the Gas Turbine Division of THE AMERICAN SOCIETY OF MECHANICAL ENGINEERS and presented at the Gas Turbine Conference and Products Show, March 9-12, 1981, Houston, Texas. Manuscript received at ASME Headquarters December 22, 1980. Paper No. 81-GT-202.

Copyright © 1982 by ASME

Downloaded 01 Jun 2010 to 171.66.16.62. Redistribution subject to ASME license or copyright; see http://www.asme.org/terms/Terms_Use.cfm

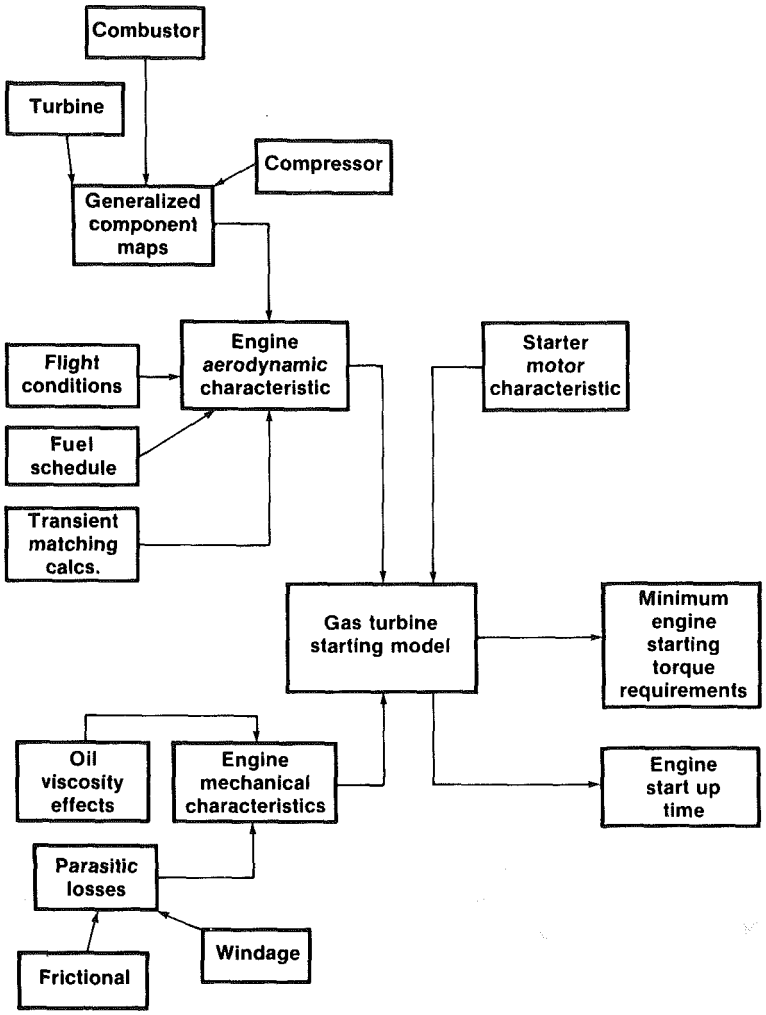


Fig. 1 An overview of the model

The functions $K\psi_c$ and $K\eta_c$ are once again determined empirically.

It should, however, be noted that since the engine does not operate at the steady state condition in the starting regime, the values obtained from equations (1-3) are used only as the first guess values in the engine performance calculations. The final values have to be obtained based on the flow match between the turbine (s) and the nozzle areas as will be described later.

Equations (1-3) now define the equations governing the performance of the compressor and are used to calculate the compression pressure ratio, total compressor aerodynamic work and torque required which is to be supplied either by the starter motor or the turbine or both.

Combustor. The main performance parameters here are the combustion efficiency and the combustor pressure drop.

The combustor pressure drop value is established based on data from a number of combustors and is presented to the model as a constant percentage of the combustor inlet pressure.

In addition, an estimate of the combustion efficiency is required, after the engine is lit up, to calculate the turbine inlet temperature. It was found that this could best be correlated as a function of the combustor air loading parameter and the fuel/air ratio. Thus,

$$\eta_{\text{comb}} = fn\left(\frac{\Omega}{\Omega_R}, f/a\right) \tag{4}$$

where, f/a is the fuel air ratio and is calculated from the prescribed fuel flow schedule, and Ω is defined as

$$\Omega = \frac{m}{P^{1.8} V_{\text{comb}} e^{T/540}}$$

Nomenclature

m = mass flow
N = rotational speed
p = static pressure
P = total pressure
PR = pressure ratio
R = gas constant
t = static temperature
T = total temperature
δ = corrected pressure
Δh = specific work
η = efficiency
θ = corrected temperature
ρ = static density
ζ = torque

Subscripts

amb = ambient
ACCEL = acceleration
c = compressor
comb = combustor
HPC = high pressure compressor
R = reference
t = turbine

Downloaded 01 Jun 2010 to 171.66.16.62. Redistribution subject to ASME license or copyright; see http://www.asme.org/terms/Terms_Use.cfm

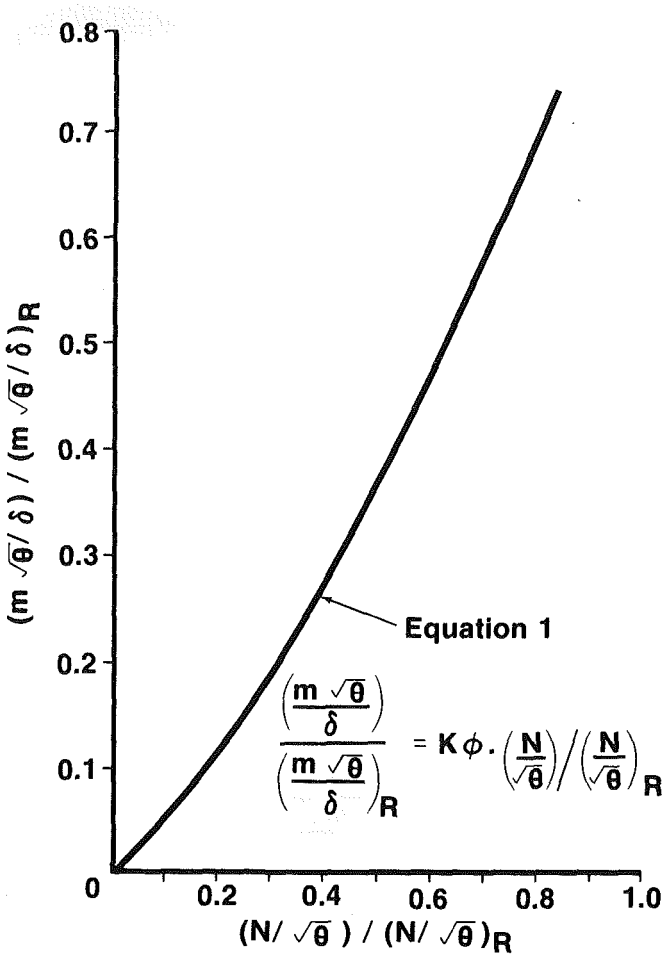


Fig. 2 Compressor inlet flow variation

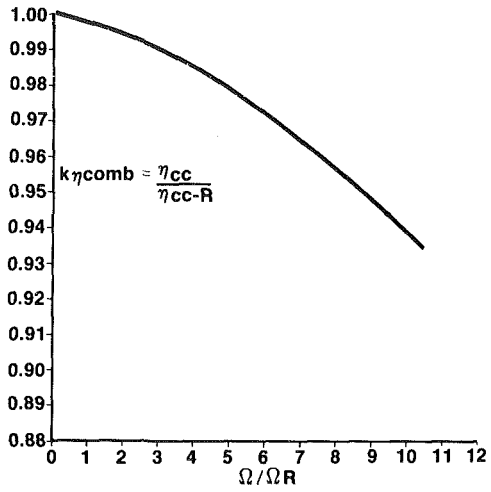


Fig. 3 Combustion efficiency variation with Ω

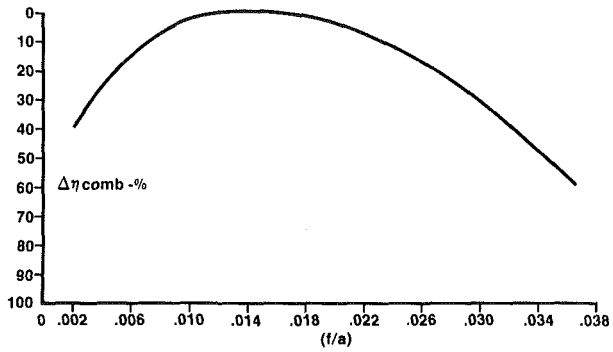


Fig. 4 Combustion efficiency correction for fuel air ratio

where m, P and T are the combustor inlet mass flow, pressure and temperature and V_{comb} is the combustion chamber volume.

The functional relationships were once again obtained empirically and are shown in Fig. 3 and 4. The combustion efficiency is then calculated from:

$$\eta_{comb} = K_{\eta_{comb}} (\text{from Fig. 3}).\eta_{comb-R} - \Delta\eta_{comb} (\text{Fig. 4}) \quad (5)$$

where η_{comb-R} is the combustion efficiency of the engine being analyzed at a known reference point, e.g., the engine Take Off condition.

Turbine. Since the engine in the starting sequence is not in steady state, the turbine work is not equal to the compressor work as is the case for steady state operation. Thus, the turbine work and hence PR cannot be determined from the knowledge of compressor work alone.

In this model, the turbine PR is obtained by the following method:

$$PR_t = \frac{P_4}{P_5} = \frac{P_1}{P_0} \cdot \frac{P_3}{P_1} \cdot \frac{P_4}{P_3} \cdot \frac{P_7}{P_5} \cdot \frac{P_0}{P_7} \quad (6)$$

In this identity:

P_1/P_0 = inlet pressure ratio; P_3/P_1 = compressor pressure ratio (PR_c); P_4/P_3 = combustor pressure loss (assumed constant), P_5/P_7 = power turbine or second turbine pressure ratio; and P_7/P_0 = nozzle pressure ratio.

For a single spool gas generator, $P_1/P_0 = P_7/P_0 \simeq 1.0$ (for a two-spool gas generator, P_1/P_0 is obtained as described in a later section). Also, as shown in Fig. 5, since the turbines and nozzles are operating in series, the flow match between the turbines and the nozzle result in a unique value of P_5/P_7 for each value of P_4/P_5. Thus, for each compressor pressure ratio, PR_c, there is a unique value of PR_t which satisfies the engine area restrictions. PR_t can then be expressed as:

$$PR_t \propto PR_c$$

or,

$$\frac{PR_t}{PR_{t-R}} = K_{P1} \frac{PR_c}{PR_{c-R}}$$

or,

$$\frac{PR_{t-1}}{PR_{t-R} - 1} = K_P \frac{PR_c - 1}{PR_{c-R} - 1} \quad (7)$$

This relation is plotted in Fig. 6 for various engines with differing design compressor pressure ratios. From this figure, it is clear that the value of K_p in equation (7) is a function of the design compressor pressure ratio. In this mathematical model, therefore, a series of these lines have been built to cover a wide range of present and probable future gas turbine engines.

The variation of the turbine flow corresponding to the pressure ratio used in equation (7) is shown in Fig. 7. This flow map was generated at varying power turbine or the second turbine speed (in case of a two-spool gas generator) to simulate the operation in the starting regime where the second turbine operates at only a fraction of its design speed. This map should therefore be representative of the operation of two turbines in series in the starting region and is assumed as the generalized turbine flow map in the model.

The only other parameter required to assess the turbine performance is the turbine efficiency. This correlates best

Downloaded 01 Jun 2010 to 171.66.16.62. Redistribution subject to ASME license or copyright; see http://www.asme.org/terms/Terms_Use.cfm

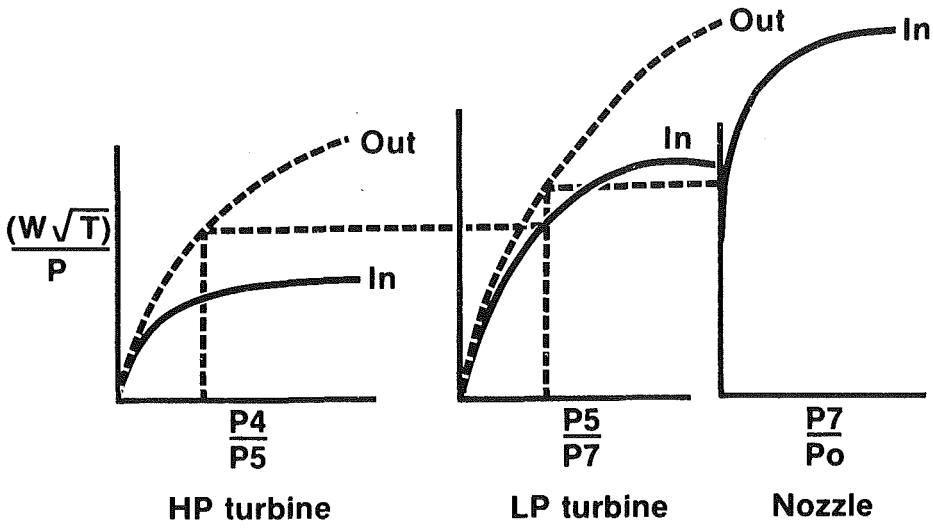


Fig. 5 Series operation of turbine (s) and nozzle

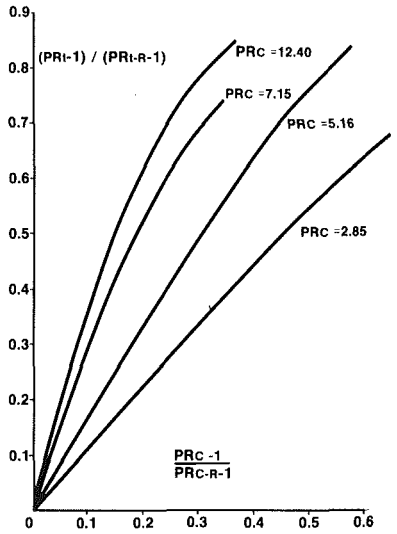


Fig. 6 Turbine *PR* variation with compressor *PR*

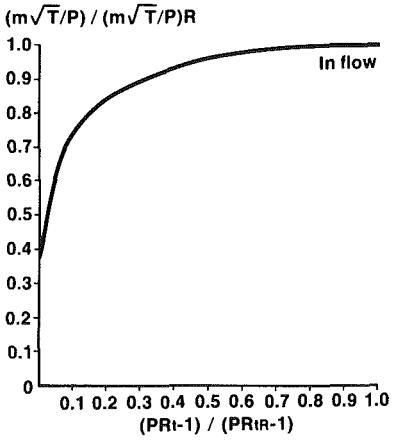


Fig. 7 Turbine flow variation with pressure ratio

against the turbine Pressure Ratio and is given by:

$$\frac{\eta_t}{\eta_{t-R}} = K_{\eta_t} \frac{(PR_{t-1} - 1)}{(PR_{t-R} - 1)} \tag{8}$$

Equations (7) and (8) now enable the calculation of the Turbine total aerodynamic work and the Torque which is supplied by the engine.

Two-Spool Gas Generator. It was found that, in the starting region, the *LP* spool, which is only aerodynamically coupled to the *HP* spool, has only a small effect on the starting of the engine. In this model, this effect is accounted for by modifying the pressure and temperature into the *HP* compressor as per the following relationships:

$$\left[\frac{\frac{\delta_{in}}{\delta_{amb}} - 1}{\delta_R}\right]_{HPC} = K_\delta \frac{\left(\frac{N}{\sqrt{\theta}}\right)_{HPC}}{\left(\frac{N}{\sqrt{\theta}}\right)_{HPC_R}} \tag{9}$$

and,

$$\left[\frac{\frac{\theta_{in}}{\theta_{amb}} - 1}{\theta_R}\right] = K_\theta \frac{\left(\frac{N}{\sqrt{\theta}}\right)_{HPC}}{\left(\frac{N}{\sqrt{\theta}}\right)_{HPC_R}} \tag{10}$$

where δ_R and θ_R are the normalized pressure and temperature to the *HP* compressor inlet at the engine reference point. K_δ and K_θ are once again determined empirically.

Transient Matching Calculations. The transient matching calculations essentially involve matching the turbine flow with the compressor flow. The turbine flow is a function of the turbine pressure drop (Fig. 7) which in turn is a function of the compressor pressure ratio (Fig. 6). At any instant of time, both the compressor pressure ratio and flow are dependent on the engine operating point at that time. As shown in Fig. 8, in general during starting, the engine operates closer to choke when being cranked and closer to surge when lit up. The problem then is to find the position of this operating point on the compressor map.

Now, the compressor map as defined by equations (1–3) is based on steady-state engine data. Since, as shown in Fig. 8, the engine is not operating on steady-state, the map has to be modified as the engine moves away from the steady-state operations. For the compressor efficiency, the steady state to transient modifier is correlated as:

Downloaded 01 Jun 2010 to 171.66.16.62. Redistribution subject to ASME license or copyright; see http://www.asme.org/terms/Terms_Use.cfm

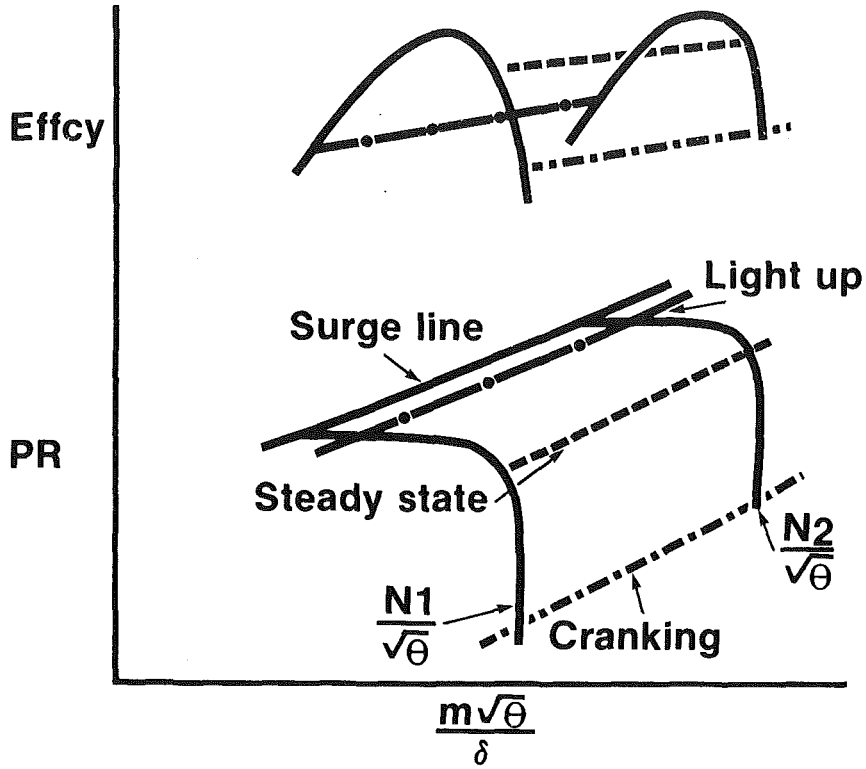


Fig. 8 Engine operating lines on compressor map

$$\eta_c(\text{mod}) = K'_{\eta_c}\left[\frac{\left(\frac{m\sqrt{\theta}}{\delta}\right)_{\text{transient}}}{\left(\frac{m\sqrt{\theta}}{\delta}\right)_{\text{steady-state}}}\right] \tag{11}$$

and

$$\eta_c(\text{transient}) = \eta_c \underset{-\text{equation (2)}}{(\text{steady state})} \cdot \eta_c(\text{mod}) \tag{12}$$

where the transient $(m\sqrt{\theta}/\delta)$ has to be obtained through iteration to match the compressor and turbine mass flows.

When the engine is cranking (near choke), the compressor steady state specific work is modified similar to the efficiency, so that,

$$\left(\frac{\Delta h_c}{\theta}\right)_{\text{tran}} = \left(\frac{\Delta hc}{\theta}\right)_{\substack{\text{steady-state}\\(\text{equation (3)})}} \cdot \left(\frac{\Delta hc}{\theta}\right)_{\text{mod}} \tag{13}$$

where

$$\left(\frac{\Delta hc}{\theta}\right)_{\text{mod}} = K'_{\psi c}\left[\frac{\left(\frac{m\sqrt{\theta}}{\delta}\right)_{\text{transient}}}{\left(\frac{m\sqrt{\theta}}{\delta}\right)_{\text{steady-state}}}\right] \tag{14}$$

Equations (12) and (13) then give the transient compressor pressure ratio when the engine is cranking.

For the situation when the engine is lit and the compressor is operating near surge, it was found that the compressor *PR* remains approximately constant at the steady state value (implying a horizontal speed line as shown in Fig. 8). For these cases then, the model assumes the compressor *PR* calculated using steady state values of compressor efficiency and work constant for all transient calculations and the transient work $(\Delta hc/\theta)_{\text{tran}}$ is calculated using this *PR* and the transient efficiency from equation (12).

The transient matching calculations then comprise changing the compressor inlet flow, m_c, with corresponding changes in Δhc, η_c, PR_c, compressor delivery temperature (T_3), η_{comb}, turbine inlet temperature (T_4), calculated turbine inlet flow and PR_t. With this PR_t, the turbine map (Fig. 7) gives the allowable turbine inlet flow. This then has to be matched with the calculated turbine flow to give the final engine operating point.

Engine Mechanical Characteristics

The engine mechanical configuration gives rise to mechanical losses which add to the compressor aerodynamic torque requirements to result in the total engine torque requirements to be supplied either by the starter or the turbine or both.

Mechanical losses in the engine are incurred due to mechanical frictional loss in bearings and gears and aerodynamic windage loss in the compressor and turbine disks as well as on the impeller face. In addition, some work is also required to power the fuel control unit, fuel pump and the oil pump. However, except at very low ambient temperatures, the proportion of the mechanical loss is generally less than 5 percent of the compressor aerodynamic power requirement and is sometimes ignored in calculating engine starting torque requirements. In this model, however, this is not the case and the mechanical losses are accounted for by splitting them into two categories:

(i) Basic parasitic loss, at normal operating temperatures (oil at temperatures above 130°F).

(ii) Additional viscosity effects to account for low oil temperatures.

Basic Parasitic Loss. These are further divided into two components – frictional and windage – where the frictional losses would be a function of the engine mechanical speed and the windage loss that of the aerodynamic speed. Additionally, in this model, the parasitic losses are correlated as a fraction of the required compressor torque calculated in the previous sections. Thus,

$$(\tau/\tau_{\text{comp}})_{\text{WINDAGE}} = A_0 + A_1\chi + A_2\chi^2 \tag{15}$$

Downloaded 01 Jun 2010 to 171.66.16.62. Redistribution subject to ASME license or copyright; see http://www.asme.org/terms/Terms_Use.cfm

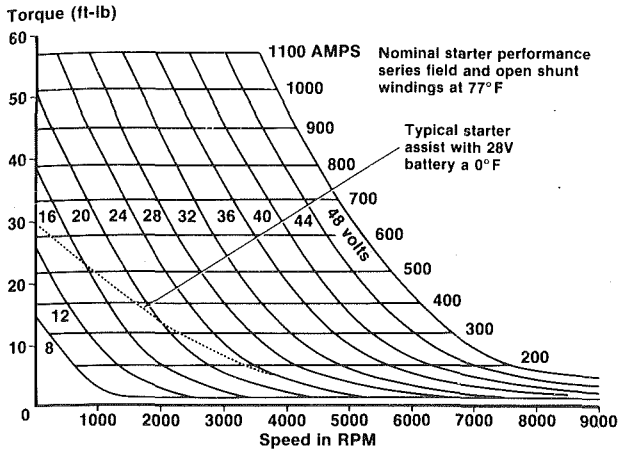


Fig. 9 Starter motor performance grid

$$(\tau/\tau_{\text{comp}})_{\text{FRICTION}} = B_0 + B_1 y + B_2 y^2 + B_3 y^3 \tag{16}$$

and,

$$\tau_{\text{parasitic}} = \tau_{\text{WIND}} + \tau_{\text{FRIC}} \tag{17}$$

where,

$$\chi = (N/\sqrt{\theta})/N/\sqrt{\theta})_R$$

and

$$y = N/N_R$$

The polynomial coefficients A_0 through A_2 and B_0 through B_3 are based on experimental data.

Additional Viscosity Effects. These were obtained empirically from cold day tests. The additional viscosity effects are to simulate the increase in the engine mechanical torque requirements as the drag resistance in the engine increases with reducing ambient temperatures and were, therefore, correlated as a function of the ambient temperature. This is then used as a multiplier on the basic parasitic loss calculated from equation (17) to give the final engine Mechanical Torque.

The total torque required by the engine and to be supplied by either the starter or the turbine or both at any given speed (N) is then given by:

$$\tau_{\text{ROTOR}} = \tau_{\text{comp}} + \tau_{\text{MECH}} \tag{18}$$

Starter Motor Characteristic

This information is required when an existing starter motor is to be used and the starting time to bring the engine from rest to a given speed, e.g., the ground idle speed is to be estimated using this starter motor.

The motor characteristic is obtained from the performance grid, such as that shown in Fig. 9, and is supplied by the motor manufacturer. From this grid, the torque versus speed curve for the given motor/battery combination can be obtained. This then is the torque supplied to the engine by the starter which, in conjunction with the positive turbine torque, overcomes the negative rotor (equation (18)) and provides a positive acceleration torque (τ_{ACCEL}) to accelerate the engine from rest.

Starting Time Estimation

The starting time is the total time required to bring the engine from rest to a given speed, e.g., the ground idle speed.

Now, at any instant of time, the acceleration torque is given by:

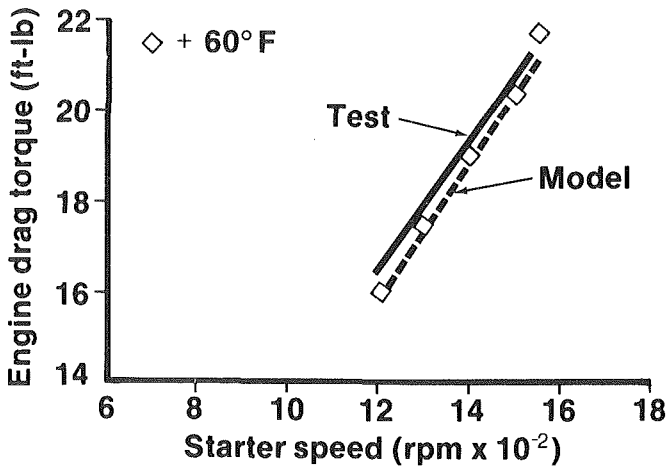


Fig. 10 Engine I – starting tests

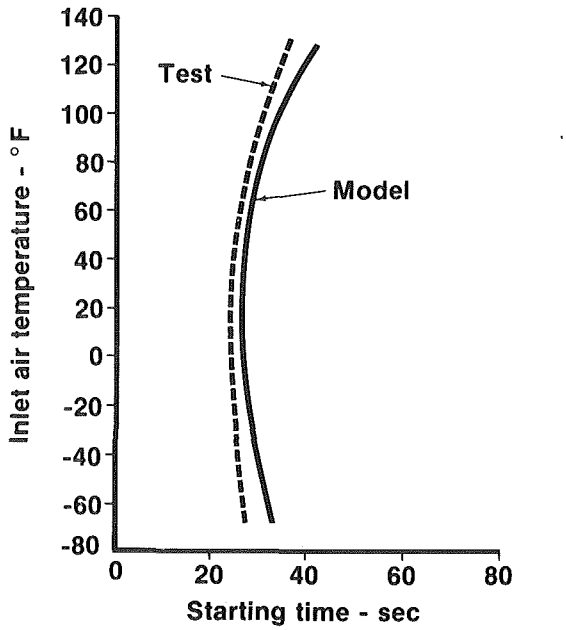


Fig. 11 Engine II – starting time versus inlet air temperature

$$d\tau_{\text{ACCEL}} = I_p \cdot \frac{d\omega}{dt} = 2\pi I_p \cdot \frac{dN}{dt}$$

and from this,

$$t = \int_{N=0}^{N_{\text{FINAL}}} 2\pi I_P \cdot \frac{dN}{d\tau_{\text{ACCEL}}} \tag{19}$$

where: t = total starting time; I_p = polar moment of inertia of the rotating components on the start shaft; and N_{FINAL} = final speed in the start cycle.

The starting time is then calculated by the numerical integration of equation (19).

Model Validation

The model was validated against data available from starting tests on three different types of engines – labeled here Engine I, Engine II, and Engine III – representing powerplants for turbojets, turboprops and helicopters.

Engine I. Starting tests on this turbofan engine were conducted at the Low Temperature Laboratory of the National Research Council of Canada.

Figure 10 shows the test and the corresponding model data

Downloaded 01 Jun 2010 to 171.66.16.62. Redistribution subject to ASME license or copyright; see http://www.asme.org/terms/Terms_Use.cfm

at one representative ambient temperature. The model output can be seen to have a close agreement with the test data.

Engine II. Tests on this turboshaft engine covered a temperature range of −65–130°F and gave total start time for bringing the engine from rest to idle speed. The start time was recorded with the engine fired at representative firing speed, e.g., 10 percent of the gas generator design speed. The model was then used to exactly duplicate this start sequence and estimate the starting time requirements.

Figure 11 shows the comparison of the model and test starting time requirements at various inlet air temperatures. It can be seen that in all cases the model was able to estimate the start time within 5 with the model being conservative.

Engine III. This, like Engine I, is a twin spool gas generator used in a turboprop application. Cranking tests on this engine were conducted and covered a speed range of 10–22 percent of the design speed.

Figure 12 shows the plot of the test and corresponding model data. The model was found to be within 10 percent of the test data – this time the model being optimistic. It should, however, be noted that these tests were conducted with an uncalibrated starter and the starting torque value for the starter motor was obtained from the speed and current measurements using the performance grid supplied by the manufacturer. This grid assumes new motor efficiencies. The motor performance, however, deteriorates wwith usage, thereby reducing the actual torque output for given starter and speed values. Thus it is possible that the test torque values shown on Fig. 12 may not be those actually supplied to the engine, but are on the higher side which will then close some of the gap between the test data and the model estimates.

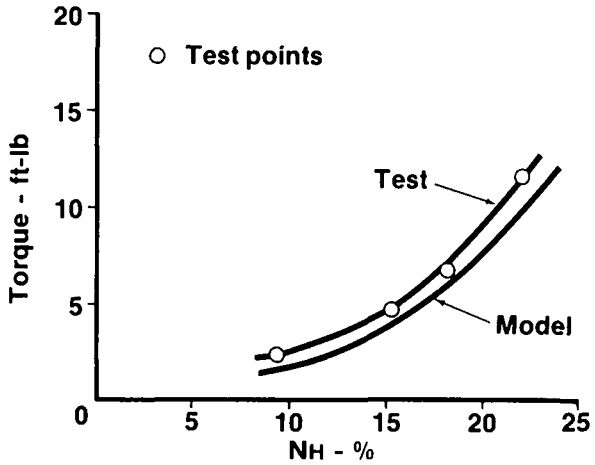


Fig. 12 Engine III – cranking torque

Sample Results

The model was used to generate starting characteristics for a hypothetical engine, labeled Engine IV. This engine had a twin spool gas generator with the high spool being motored by the starter.

Figure 13 shows the preliminary starting characteristics for the engine at sea level static condition. The torque requirements were estimated at three ambient temperatures (+130F, 59F, −65°F). The minimum firing speed was taken as 10 percent and a constant fuel schedule was assumed with a minimum fuel flow setting of 100 lb/hr.

Discussions of the Results. During cranking, i.e., when the engine is not fired, the engine starting torque requirements reduce with increasing ambient temperatures. This is to be expected since at any given rotational speed, the engine operates at lower aerodynamic speed as the ambient temperature is increased, thereby reducing the required compression work.

The engine torque requirements fall, giving a saw tooth

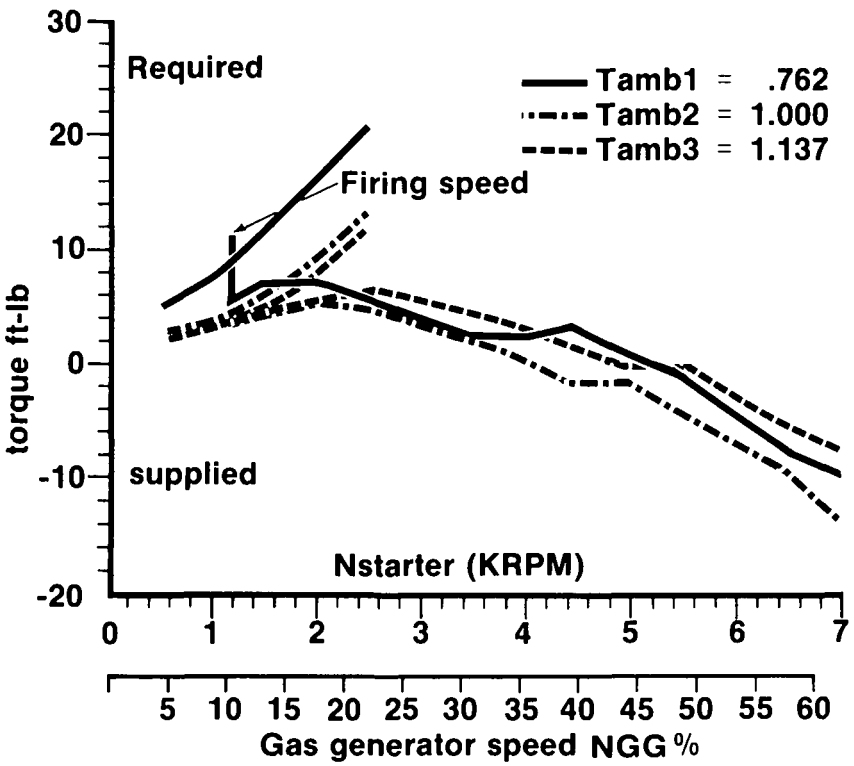


Fig. 13 Engine IV – starting characteristics

Downloaded 01 Jun 2010 to 171.66.16.62. Redistribution subject to ASME license or copyright; see http://www.asme.org/terms/Terms_Use.cfm

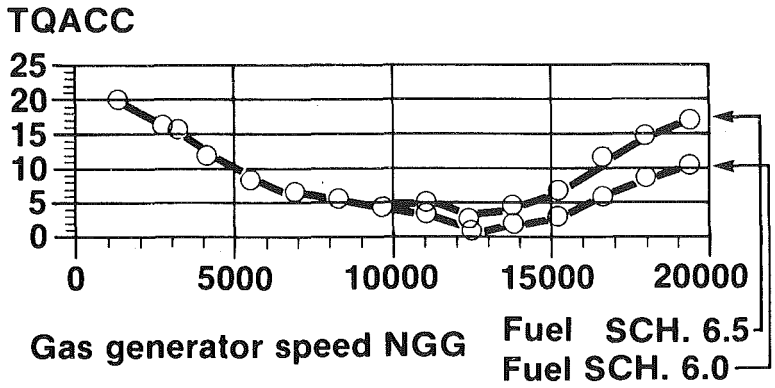


Fig. 14 Effect of fuel schedule variation on τ_{ACCEL}

characteristic, when the engine is fired. However, as the engine is sped up, the required torque rises momentarily before the assist from the engine turbine is able to more than offset the increase in compression work. This rather peculiar characteristic could be due to relatively low design *PR* on the high spool. This is because at very low *HP* spool speed, when the *LP* spool is not providing any compression, the *PR* on the *HP* spool is very low and although the TIT is relatively high, the turbine does not have enough *PR* to convert this into useful turbine work. This situation is especially pronounced at higher ambient temperatures where, for a given speed, the available *PR* is lower still.

Another peculiar feature of these characteristics seems to be that the torque required by the engine goes up between 30 and 40 percent N_H at all the three ambient temperatures. This was because in this speed range the specified fuel schedule does not provide enough fuel, thereby limiting the TIT. Before 30 percent N_H, the engine operates on the minimum fuel flow setting and after 40 percent, P_3 is sufficiently high to insure adequate fuel supply. As a result, as shown in Fig. 14, the available accelerating torque takes a dip between this speed range and the engine requires about 30 s to get through this dip. It can be seen from the figure that tuning the fuel schedule did reduce that dip which, at $-65°$F ambient temperature, resulted in a reduction of 30 s in the estimated start time.

Finally, for this particular engine, with 10 percent firing speed, the estimated maximum torque required by the engine was about 8.2 lb-ft. The minimum starter torque will therefore have to be greater than this and such as to provide adequate acceleration torque. In addition, for a successful start, the starter motor will have to provide some assist all the way up to about 40 percent N_{GG}. These two requirements would then govern the sizing of the host aircraft starting system.

Conclusions

The mathematical model described in this paper, although based on generalized component characteristics as well as a number of simplifying assumptions, does give fairly good preliminary estimates of gas turbine starting characteristics. These estimates could be especially useful when assessing the overall performance of an engine starting system in a new engine/aircraft development stage and could possibly *reduce* the number of test iterations required to arrive at the best engine/start system combination. The emphasis on reduction is intentional since the model, being based on generalized characteristics, is not expected to simulate individual engine/aircraft peculiarities and hence can be used only as a first go at getting the desired aircraft starting system.

Downloaded 01 Jun 2010 to 171.66.16.62. Redistribution subject to ASME license or copyright; see http://www.asme.org/terms/Terms_Use.cfm

Rotor Wake Mixing Effects Downstream of a Compressor Rotor

A. Ravindranath[1]
Graduate Assistant.

B. Lakshminarayana
Director of Computational Fluid Dynamics Studies and Professor of Aerospace Engineering

The Pennsylvania State University, University Park, Pa.

An experimental study of rotor wake was conducted in the trailing-edge and near-wake regions of a moderately loaded compressor rotor blade using a rotating tri-axial hot-wire probe in a rotating frame of reference. The flow-field was surveyed very close to the trailing-edge as well as inside the annulus and hub-wall boundary layers. The large amount of data acquired during this program has been analyzed to discern the decay effects as well as the spanwise variation of three components of velocity, three components of intensities and three components of shear stresses. The data set also include extensive information on the variation of the flow properties downstream. The other derived quantities include wake momentum thickness and deviation angles at various spanwise and downstream locations. These data are presented and interpreted, with emphasis on the downstream mixing as well as endwall-wake interaction effects.

Introduction

The complexity of a turbomachinery rotor-wake arises due to the three-dimensionality introduced by the effects of rotation, curvature, radial variation in circulation, trailing and tip vortices, and other effects. Considerable work has been done to understand, through measurement and analysis, the wake far downstream, outside the end-wall boundary-layers. Literature is scarce for the wakes inside the end-wall boundary layers, near-wake and wake-boundary-layer interaction. A thorough knowledge of the wake in these regions is also essential in understanding the stall and surge, unsteady flow in stators, aerodynamic losses and off design operation.

The rotor-wake is very strongly dependent on many aerodynamic and blade parameters such as solidity, aspect ratio, rotor-stator spacing, rotation, curvature, three-dimensional pressure gradients, inlet-turbulence and its general structure and level. A systematic attempt to study the effects of these parameters is being made at the Department of Aerospace Engineering at The Pennsylvania State University.

The data presented in this paper were obtained in a moderately-loaded, low-speed single-stage compressor using a rotating tri-axial hot-wire probe. Description of the facility and measuring techniques are provided in references [1] and [2]. The wake profiles and their decay with streamwise distance near the mid-radius were described in earlier papers [3,4]. Radial variations of wake properties and the wake boundary-layer interactions are dealt with in this paper. Wake data in the trailing edge, near-wake and far-wake regions are also presented in this paper. All the velocities given here are relative velocities and are normalized by the free-stream axial velocity unless otherwise stated.

In the earlier papers [3,4], the decay of the wake properties as a function of the downstream distance from the trailing-edge was presented with emphasis on the mid-radius data. In a later study, it was realized that the wakes differ considerably in the radial direction with regard to their profile and decay. This necessitated a study of the variation of the wake properties in the radial direction. Further understanding of the spanwise gradients in wake properties is essential in proper and improved design of blade elements from hub to tip. The wake data from hub to tip presented in this paper should be extremely useful to aerodynamicists, acousticians, and designers in the prediction and design of hub to tip blade section.

Facility Description, Probes, and Experimental Program

Measurements reported in this paper were obtained using the axial-flow-compressor facility, data transmission, and the data acquisition systems described in reference [1].

A general description of the compressor stage is given by Smith [5] and a detailed discussion of the facility is given by Lakshminarayana [1]. Good peak efficiencies are exhibited by the rotor. The hub/annulus wall diameter ratio of the facility is 0.5, with the diameter of the annulus wall equal to 0.932 m. The inlet guide vane row, which consists of 43 blades, is followed by the 21-bladed rotor. The rotor is driven by a 37.29 kw variable speed motor through a belt and pulley system. The rotor is followed by a stator vane row of 25 blades. Downstream of the stator is located a Joy axial flow fan with variable blade setting for the variation of pressure rise and mass flow. The facility is terminated downstream by an aerodynamically designed throttle which provides additional control of the stage operating characteristics. Some

[1] Presently at Garrett Turbine Engine Division, Phoenix, AZ.

Contributed by the Gas Turbine Division of THE AMERICAN SOCIETY OF MECHANICAL ENGINEERS and presented at the Gas Turbine Conference and Products Show, March 9-12, 1981, Houston, Texas. Manuscript received at ASME Headquarters December 11, 1980. Paper No. 81-GT-98.

Copyright © 1982 by ASME

Downloaded 01 Jun 2010 to 171.66.16.62. Redistribution subject to ASME license or copyright; see http://www.asme.org/terms/Terms_Use.cfm

of the other operating conditions and rotor specifications are as follows: inlet velocity, 29.04 m/s; flow coefficient based on tip speed, 0.56; stage loading coefficient based on tip speed, 0.4864; speed of rotor, 1066 rpm; and tip clearance, 0.25-0.3 cm. Blade element data at the tip are NASA 65 series, chord 15.41 cm, spacing 14.12 cm, maximum thickness 5.10 percent of chord, stagger angle 45.0 deg, camber 8 percent chord. The blade profile near the tip section is given in references [1] and [5]. The pressure rise and efficiency characteristics of this rotor are given in references [1] and [3]. The radial variation in flow properties upstream of the rotor (or downstream of the IGV) is shown in Fig. 1.

Wake properties were measured at various axial and radial locations using a rotating tri-axial hot wire probe. The matrix of the measurement locations are tabulated in Table 1 of reference [3]. The measurement included the study of the wake properties in the trailing-edge, near-wake and far-wake regions, as well as inside the annulus and hub-wall boundary layers.

Experimental Results, Interpretation, and Correlation

The wake properties near the mid-span of the blade row, such as the velocity profiles, turbulence intensity profiles, decay of the wake with downstream distance, similarity laws for profiles, decay of the wake with downstream distance, similarity laws for profiles, and wake decay correlations were covered in the earlier papers [3,4]. In this paper, the spanwise variations in wake properties are presented and interpreted. The streamwise variation of momentum thickness and shape factor in the wake is presented. The incidence changes for various stator locations are also estimated.

Wake Momentum Thickness. The momentum thickness implies the loss of momentum in the boundary layer and the wake, as compared to the potential flow. In the case of the rotor-wake, this loss of momentum is defined in the wake, with the integration carried across one blade spacing and is given by

$$\theta^* = \frac{1}{S}\int_0^S \frac{W}{W_0}\left(1 - \frac{W}{W_0}\right) r d\theta. \qquad (1)$$

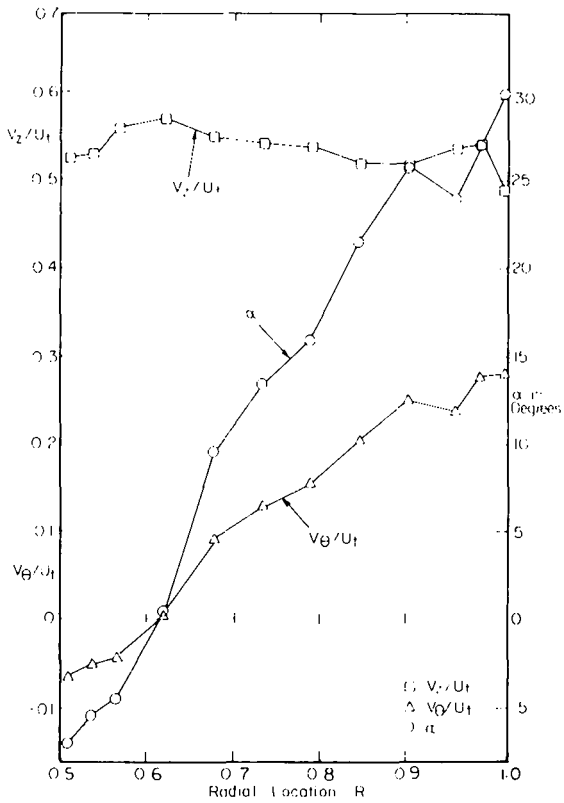


Fig. 1 Radial variation of axial and tangential velocity and outlet angle at the exit of the inlet guide vane ($\phi = 0.56$)

The experimental variation of the wake momentum thickness with downstream distance is shown plotted in Fig. 2 for various radial locations. The momentum thickness (θ^*) is found to vary appreciably from one radius to another. These variations can be explained on the basis of conventional boundary layer momentum equation (two-dimensional) with zero shear stress as follows:

Nomenclature

c = blade chord length
C_d = section drag coefficient based on mean velocity
H = wake shape factor = δ^*/θ^*
i_0 = stator incidence angle based on local free stream velocity
i_c = stator incidence based on the wake center line velocity
L = $(L_s + L_p)/S$ = sum of the characteristic length on the suction and pressure surfaces normalized by blade spacing
L_s, L_p = wake width at half the depth on rotor blade suction and pressure-surface of the wake, respectively
R = radius ratio = (r/r_t)
r = local radius, radial direction
(r,θ,z) = rotating cylindrical coordinate system (radial, tangential, and axial coordinate directions)
S = blade spacing
(s,n,r) = natural coordinate system (streamwise, normal, and radial coordinate directions)
U = blade speed
V = local absolute velocity
W = total relative velocity
w = defect in relative velocity
w' = fluctuating component of relative velocity
Z = axial distance from blade trailing-edge normalized by rotor blade chord at the tip
Ω = speed of rotation of rotor blade
β_0 = blade outlet angle
β = air outlet angle
β_m = mean air angle $[\tan^{-1}(\tan\beta_1 + \tan\beta_2)/2]$
δ = deviation angle
δ^* = displacement thickness $= \frac{1}{S}\int_0^S \left(1 - \frac{W}{W_0}\right) r d\theta$
ϕ = flow coefficient based on blade tip speed
θ^* = momentum thickness, equation (1)
$\tau_z, \tau_r, \tau_\theta$ = normalized turbulence intensities in the axial, radial, and tangential direction, respectively $(\sqrt{\overline{w_z'^2}}/W, \sqrt{\overline{w_r'^2}}/W, \sqrt{\overline{w_\theta'^2}}/W)$

Subscripts

c = value at the wake center
m,max = maximum value in the wake
0 = value at wake edge/free-stream value
p = pressure side
(r,θ,z) = values in the radial, tangential, and axial coordinate directions, respectively
(s,n,r) = values in the streamwise, normal, and radial coordinate directions, respectively
s = suction side, blade spacing
t = tip
1 = inlet of rotor
2 = exit of rotor

Downloaded 01 Jun 2010 to 171.66.16.62. Redistribution subject to ASME license or copyright; see http://www.asme.org/terms/Terms_Use.cfm

Table 1 Blade element details

Particulars	Radius Ratio																	
	Inlet-Guide-Vane						Rotor						Stator					
Radius Ratio	0.5	0.6	0.7	0.8	0.9	1.0	0.5	0.6	0.7	0.8	0.9	1.0	0.5	0.6	0.7	0.8	0.9	1.0
Chord, cm (in)	5.19 (2.04)		7.64 (3.01)		9.80 (3.86)		12.39 (4.88)		13.25 (5.22)		14.41 (5.67)		8.83 (3.48)		10.37 (4.08)		12.39 (4.88)	
	6.63 (2.61)		8.64 (3.40)		10.95 (4.31)		12.68 (4.99)		13.68 (5.39)		15.41 (6.07)		9.80 (3.86)		10.95 (4.31)		13.97 (5.50)	
Spacing, cm (in)	3.46 (1.36)		4.90 (1.93)		6.05 (2.38)		6.91 (2.72)		9.80 (3.86)		12.68 (4.99)		5.76 (2.27)		8.35 (3.29)		10.66 (4.20)	
	4.61 (1.82)		5.47 (2.16)		6.91 (2.72)		8.35 (3.29)		11.24 (4.42)		14.12 (5.56)		6.91 (2.72)		9.51 (3.74)		11.67 (4.59)	
Camber Angle (c_{L_0} for Rotor & Stator)	-5.0 (deg)		16.0 (deg)		32.0 (deg)		1.35		1.5		1.48		1.7		1.05		0.5	
	6.0 (deg)		24.0 (deg)		45.0 (deg)		1.45		1.5		1.32		1.4		0.8		0.4	
Thickness (t/c x 100)	13.0		10.5		8.5		9.50		7.6		5.9		9		9		7.0	
	12.0		9.5		8.0		9.1		6.5		5.1		9		7.6		6.2	
Chord Angle, ° (Stagger)	0		6		18		22.5		28.5		39.0		16.5		31.0		42.0	
	5		14		22		26.0		34.0		45.0		24.0		37.0		50.0	
Air Outlet Angle, °	0		15		27		19.5		16.0		26.0		0		24		40	
	8		20		35		13.5		19.5		33.5		17		32		55	

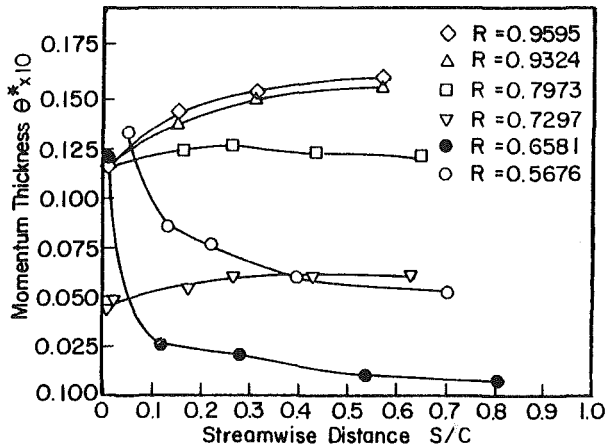


Fig. 2 Streamwise and radial variation of momentum thickness in the rotor wake

$$\frac{d\theta^*}{ds} + (H+2)\frac{\theta^*}{W_0}\frac{dW_0}{ds} = 0 \qquad (2)$$

From this equation, it is clear that the value of θ^* increases if W_0 decreases and decreases if W_0 increases. A knowledge of the freestream velocity variation will thus enable the determination of θ^* variation. A plot of this free-stream velocity variation with downstream distance is shown in Fig. 3. A comparison of this figure with Fig. 2 shows that the aforesaid reasoning is valid except in the trailing-edge and annulus-wall boundary layer regions.

As seen from Fig. 2, for a moderately loaded compressor rotor, most of the increase in momentum thickness occurs very close to the trailing-edge where the change in shape factor, and consequently the displacement thickness, is greatest. For $s/c>0.2$, very little change in θ^* occurs indicating approximately constant free-stream velocity. Very close to the trailing-edge, θ^* variations may not conform with the free-stream velocity variation due to the three-dimensional nature of the flow, the static-pressure gradients and the curvature induced Coriolis and centrifugal forces.

The wake inside the annulus-wall boundary layer behaves quite differently from that at other radii. Here the momentum thickness increases by nearly 16 percent until 0.4 chords downstream, beyond which it stays nearly constant. This large momentum thickness might be attributed to the tip-vortex (leakage vortex) which might be continuously contributing to the wake deficit. Beyond 0.4 chords, the strength of the tip-vortex might be very weak and the flow is dominated by the wake.

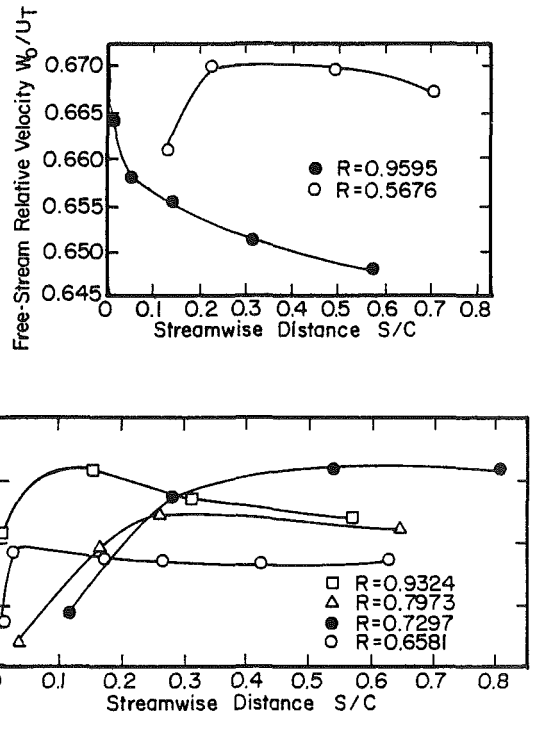


Fig. 3 Freestream relative velocity variation with streamwise distance

The effect of blade loading can be observed by comparing Fig. 2 with the data of reference [6]. At the same Z-location, say $Z=0.25$, $R=0.7297$, for a moderately loaded compressor rotor, the non-dimensionalized momentum thickness is 0.06 while for a lightly loaded rotor the value is only 0.02.

The momentum thickness is very high in the endwall regions (Fig. 2) and decreases toward the mid-radius. With increased blade loading, there will be greater radial outward transport of momentum and energy and consequently larger momentum deficit.

Wake Shape Factor. The wake shape factor (H) is defined as the ratio of the displacement thickness to momentum thickness and is uniquely related to the velocity profile. The variation of the shape factor with downstream distance for all

Downloaded 01 Jun 2010 to 171.66.16.62. Redistribution subject to ASME license or copyright; see http://www.asme.org/terms/Terms_Use.cfm

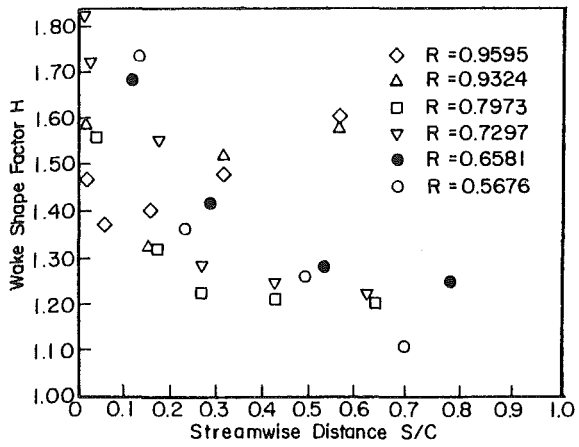


Fig. 4 Streamwise and radial variation of shape factor for the rotor wake

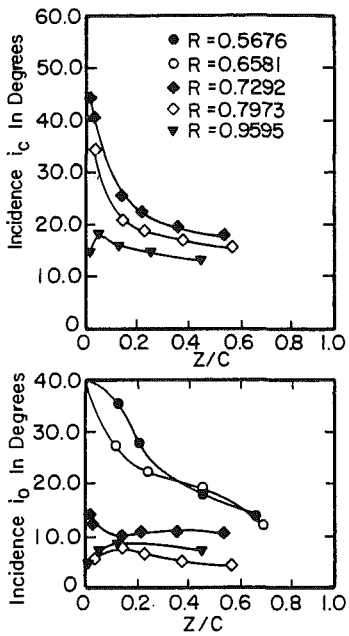


Fig. 5 Axial variation of stator incidence angle based on free stream velocity (i_0) and wake centerline velocity (i_c) at various radial locations

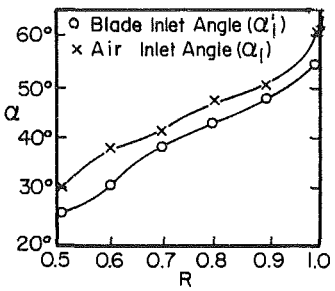


Fig. 6 Blade and air inlet angle (design) to stator

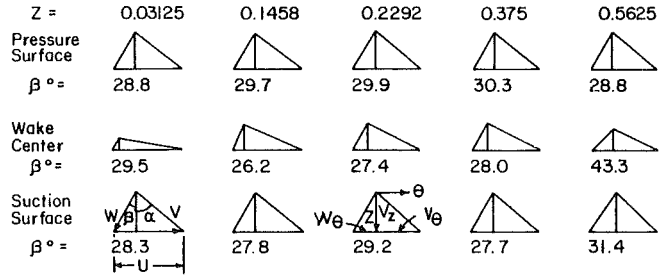


Fig. 7 Velocity triangles at several axial locations for $R=0.7973$, $\phi=0.56$

the radii is shown plotted in Fig. 4. For the wake outside the annulus-wall boundary layer, the shape factor, shown in Fig. 4, monotonically decreases with increasing distance from the trailing-edge and asymptotically approaches the value of 1.1 to 1.2 at far downstream locations. This is consistent with the shape factor distribution reported by Kool, et al. [7]. In the hub-wall boundary layer region, it is noted that the value of the shape factor is very high and this may be attributed to the pressure gradients. In the trailing-edge region for $R=0.7297$, the value of the shape factor is greater than 1.8 which indicates that the flow shows a tendency to separate. For the wake inside the annulus-wall boundary layer, the shape factor shows a very interesting trend. It initially decreases and beyond $Z=0.1$, it starts to increase. This might be due to the merger of the tip-vortex with the wake. As the wake travels downstream from the trailing edge, the vortex dominates the flow initially and later, as the vortex disssipates, the secondary flow and boundary layer flow dominate the flow. This may account for the unusual behavior of the shape factor variation in this region. It can thus be concluded that for the wakes inside the annulus and hub-wall boundary layers, the variation of the shape factor is no longer controlled by the variation of the momentum thickness or the free-stream velocity variation.

Comparison of the data from Reynolds and Lakshminarayana [6] with the present data (Fig. 4) indicates the effect of loading on the shape factor. The higher the loading, the higher the shape factor. Compared to a lightly loaded blade, the shape factor for a heavily loaded rotor decays much more slower. Thus the effect of loading is to slow down the decrease of the shape factor.

Change in Stator Incidence Due to Rotor Wake. In the present day turbomachines, the overall length and weight of the compressor is of major concern. A rotor-wake would strongly influence the incidence to the downstream stator. Large incidence results in high aerodynamic losses and consequently would affect the stage performance. The stator is usually designed for an incidence at which the drag is minimum. To evaluate the actual incidence to the stator located at different distances from the rotor trailing edge, the wake data was utilized to derive the rotor outlet angle and the stator inlet angle as function of downstream distance. Such a plot is shown in Fig. 5, where the stator incidences based on wake-edge and wake centerline velocities are shown. The blade and air inlet angle (design) to the stator is shown in Fig. 6. It is clear that the incidence to the stator would be unacceptably high should the rotor-stator spacing be very close. Based on both the wake-edge and the wake-centerline velocity, the plots indicate that a distance of a chord downstream from the rotor trailing-edge would be the ideal location or the stator should be designed taking into account the incidence changes due to rotor wake. In view of the modern trend towards close blade row spacing, it is essential to predict or measure the rotor wake structure and incorporate the incidence changes due to this in the design of the stator blade.

The velocity triangles that would exist at various distances from the rotor trailing edge is shown in Fig. 7. Near the trailing edge, the relative air flow angle is nearly constant and the absolute flow angle varies considerably across the wake. Far downstream, this trend is reversed, with large variation in relative flow angle and nearly constant absolute flow angle.

Downloaded 01 Jun 2010 to 171.66.16.62. Redistribution subject to ASME license or copyright; see http://www.asme.org/terms/Terms_Use.cfm

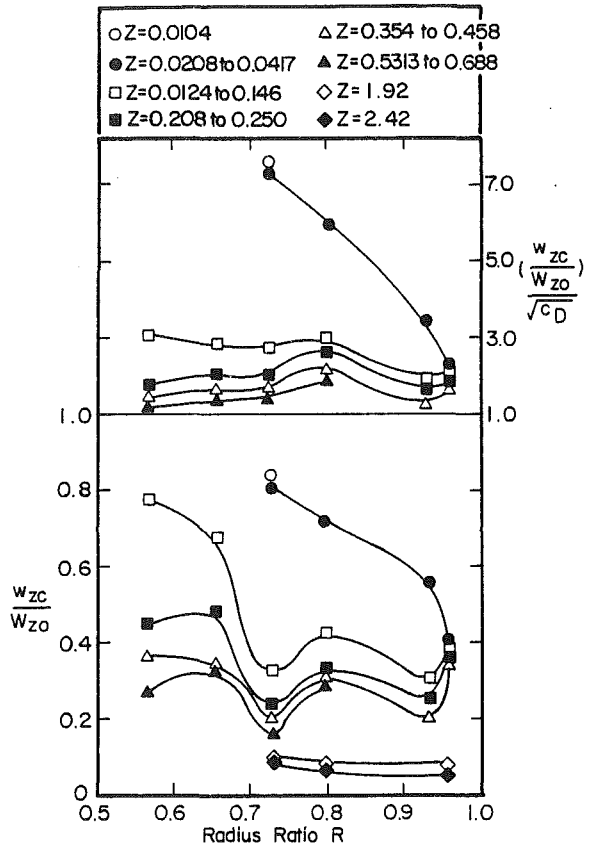


Fig. 8 Radial variation of axial mean velocity defect in the rotor wake at various axial locations

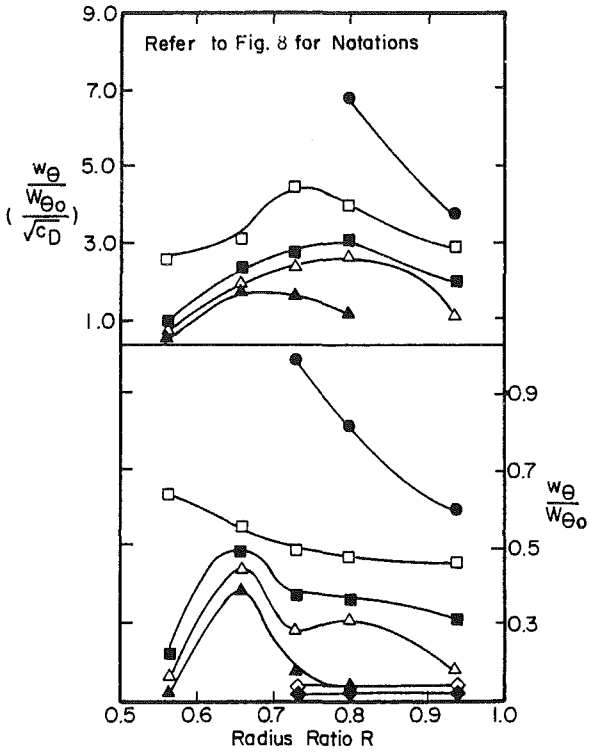


Fig. 9 Radial variation of tangential mean velocity defect in the rotor wake at various axial locations

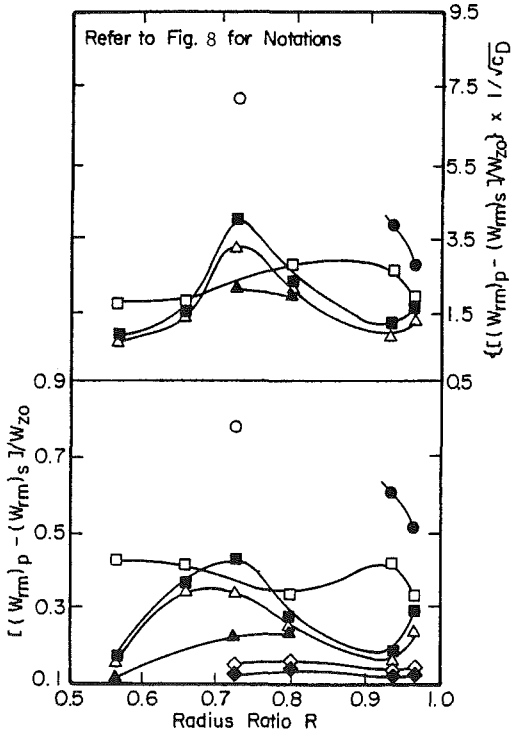


Fig. 10 Radial variation of radial mean velocity in the rotor wake at various axial locations

Radial and Axial Variation of the Characteristic Velocity in the Wake. The wake profiles, as well as their decay characteristics, vary considerably in the spanwise direction. This results from the variation of the blade geometry and blade loading, as well as three dimensionality in the blade boundary layer. A knowledge of the spanwise variation of these wake properties is essential in the three dimensional analysis and design of turbomachinery. The defect in the velocity at the centerline of the wake (w_c) is a parameter characterizing the properties of the wake. The radial variation of this property will be discussed in this section.

Radial variations of the maximum axial and tangential velocity defects and the maximum radial velocity of the rotor-wake are shown plotted in Figs. 8–10. Figure 11 shows the variation of the maximum velocity defects and the maximum radial velocity with radius for the station about 0.12 chords downstream of the blade trailing-edge. The proper parameter to be employed is the streamwise distance, s/c. The data points shown in Figs. 8–10 are at Z-locations shown in Fig. 8. Variations of β_0 at various radial locations are given in Table 1. It is seen from Fig. 8 that the velocity defect is maximum near the hub and decreases with increasing radius. The variation is not appreciable beyond $R=0.7$ and the defect remains fairly constant as the wake decays along the relative streamlines. At higher radii, the streamwise distance downstream of the rotor in the relative frame of reference is higher. Hence the defect tends to be lower. For the same reason, at lower radii the defect will be larger. Inside the annulus and hub-wall boundary layers, the wake is greatly influenced by the secondary flows (and the tip-leakage flows in the annulus-wall region) where the reasoning cited earlier may not apply.

Variation of the tangential velocity defect with radius is shown in Fig. 9. The velocity defect increases with increasing radius up to 0.73 and starts to decrease beyond that. This clearly indicates the effect of the three-dimensional nature of the flow as well as the effect of secondary flow (tip-vortex in the case of annulus-wall region). The lower tangential velocity defects near the hub and annulus-wall can be attributed to the rapid decay of the wake caused by the tip-vortex and secondary vortex.

Downloaded 01 Jun 2010 to 171.66.16.62. Redistribution subject to ASME license or copyright; see http://www.asme.org/terms/Terms_Use.cfm

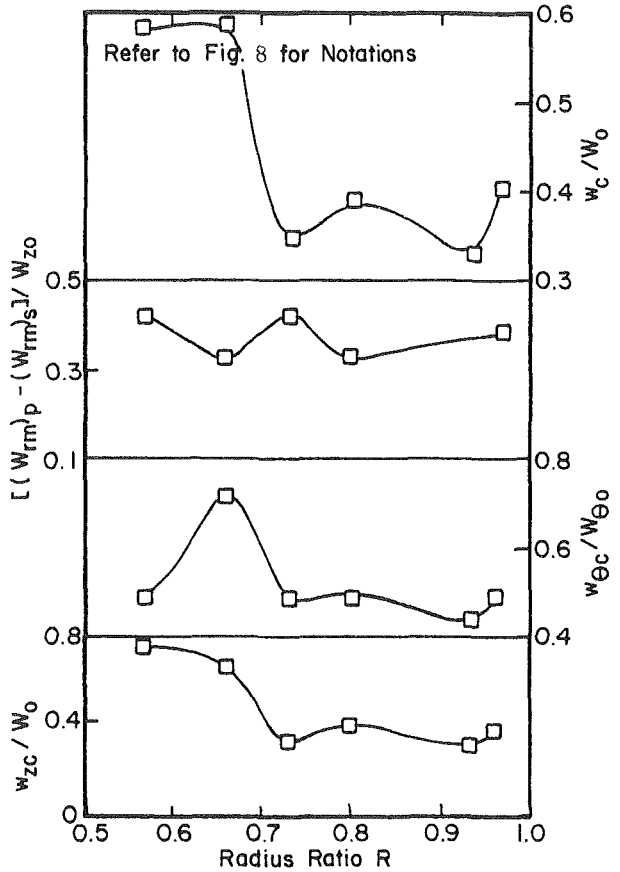


Fig. 11 Radial variation of mean velocities in the rotor wake at $Z = 0.12$

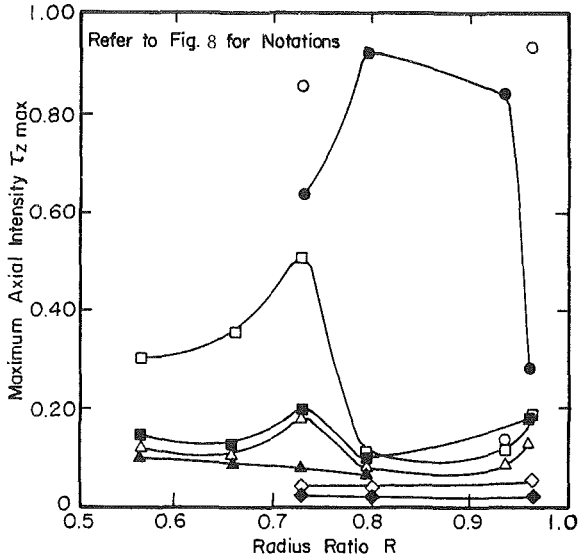


Fig. 12 Radial variation of maximum axial turbulence intensity in the rotor wake at various axial locations

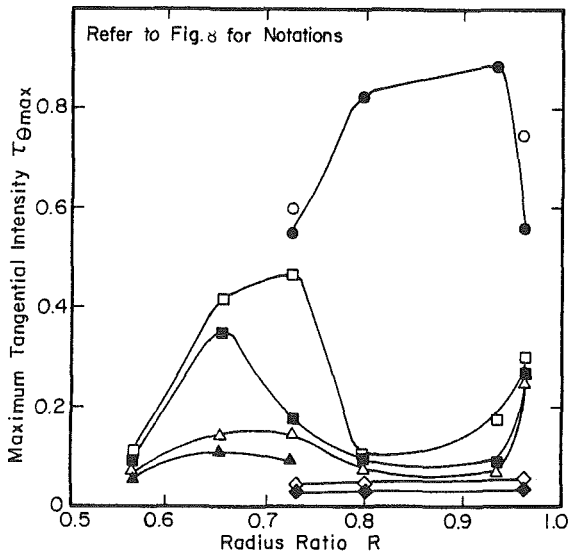


Fig. 13 Radial variation of maximum tangential turbulence intensity in the rotor wake at various axial locations

The effect of blade loading on the tangential velocity defect can be discerned by comparing this figure with that of reference [6]. Higher loading seems to give higher tangential defects. Comparing the two radii $R = 0.7297$ and 0.9595, at the same Z-location of 0.0104, it is noticed that at the lower radius, the tangential velocity defect is larger. The same is true as the hub-wall is approached; in fact, the tangential velocity defects are much more pronounced than the axial velocity defects.

The radial variation of the maximum variation in velocities $[(W_{rm})_p - (W_{rm})_s]/W_{z0}$ is shown plotted in Fig. 10. As mentioned earlier, the radial velocities are significant in the rotor-wakes and vary considerably in the radial direction. Secondary flow, tip-leakage (and the associated tip-vortex), and the trailing-vortex system greatly influence the radial flows. The radial velocities are also influenced by the centrifugal and Coriolis forces which are not only a function of speed of rotation, but also the radius. Radial velocities will also be induced by the trailing-shed-vortices and the unbalanced pressure gradients in the radial direction. The effect of all this is to make the radial variation of the radial velocity highly complex. Near the hub-wall boundary layer, radial velocities are inward in nature (influence of secondary flows) and at higher radii, the effect of secondary flow vanishes and the radial transport of mass, momentum, and energy influenced by the centrifugal forces dominates. As the annulus-wall region is approached, the radial outward velocities have to vanish and may result in radially inward velocity. The effect of these on radial velocities can be seen in Fig. 10.

The wake property, especially those of the far wake, is strongly dependent on the blade section parameters, the predominant one being the section drag coefficient. Schlichting [8] has theoretically correlated the wake properties using the drag coefficient and collapsed the mean velocity data from different configurations onto a single curve. The functional dependency, valid for the far wake of a single airfoil, is given by

$$\frac{w_c}{W_0} = \sqrt{C_D}\, f(s/c) \tag{3}$$

where s is the streamwise distance. This correlation has been tried for all the velocity components of the rotor wake and shown in Figs. 8–10. The drag coefficient for the rotor blade was derived from the following expression

$$C_D = \frac{2(P_{02} - P_{01})_{\text{rel}}}{\rho w_1^2} \frac{S}{c} \frac{\cos^3 \beta_m}{\cos^2 \beta_1} \tag{4}$$

where $(P_{02} - P_{01})_{\text{rel}}$ is the stagnation pressure loss in relative flow. This was derived from the hot wire and static pressure probe measurements. The correlation based on equation (3), at any given Z, seems to be satisfactory for the axial and radial components except very near the trailing edge (Figs. 8–10). Maximum departure is observed for the tangential velocity component, especially near the outer radius, as

Downloaded 01 Jun 2010 to 171.66.16.62. Redistribution subject to ASME license or copyright; see http://www.asme.org/terms/Terms_Use.cfm

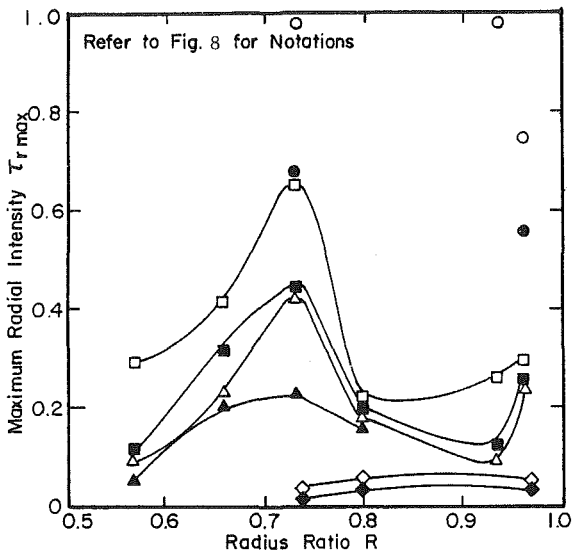


Fig. 14 Radial variation of maximum radial turbulence intensity in the rotor wake at various axial locations

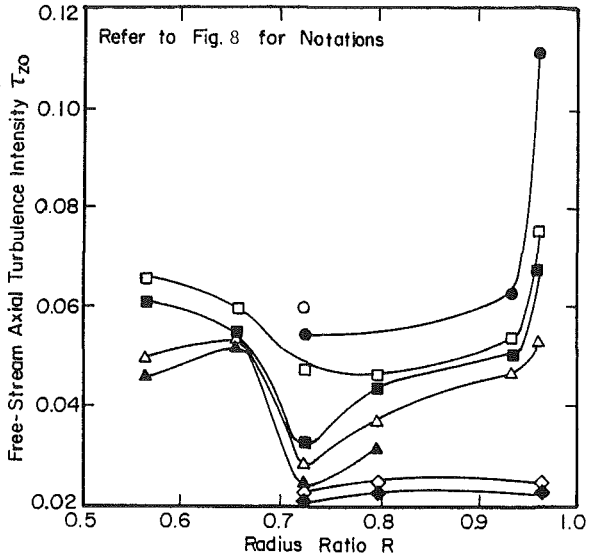


Fig. 15 Radial variation of free-stream axial turbulence intensity at various axial locations

shown in Fig. 9. This may have been caused by the effect of the wake curvature, which is not included in the correlation.

The total velocity defect, as well as the defect in components plotted for $Z=0.12$ in Fig. 11, shows that the defect is maximum near the hub walls, where the wakes are thin and are influenced by hub wall boundary layer. It should be remarked here that the wakes at different radii have had differing history, such as blade loading, streamwise distance, initial boundary layer growth, etc., and this should be kept in mind while interpreting these results. Nevertheless, it is clear that for rotor flows, the wakes differ considerably with radius in thickness, profile, and defect. This complicates the analysis of flow field as well as acoustic field resulting from these wakes.

Radial and Axial Variation of the Maximum Turbulence Intensity in the Wake. The radial variation of maximum axial, tangential, and radial turbulence intensities in the wake is shown in Figs. 12–14.

Measurements in the trailing-edge region show that the turbulence intensities are maximum at the wake center. Such high intensity may also have been caused by an unsteady phenomena near trailing edge, which is sensed as random fluctuation by the probe. These intensities are an order of magnitude higher than those that were measured in the near and far-wake regions. These high intensities are attributed to the trailing vortex system that dominates the flow at these locations. But the trailing-vortex's contribution to the wake-turbulence decays very rapidly and the wake-turbulence dominates the vortex-turbulence beyond this downstream location.

Considering only the wake-turbulence, it is noted that the turbulence intensity is high at the annulus wall region and decreases steadily to a minimum at the mid-radius and starts to increase again towards the hub-wall region. This is true for only the near and far-wake regions. For the trailing-edge locations, the trailing-shed vortex contribution is substantial and may offset the foregoing trend. This trend can be explained based on the tip-leakage-vortex, secondary flow, annulus and hub-wall boundary layer, and its interaction with the wake. Thus the intensities are fairly constant over a very narrow region across the annulus.

Of the three components of intensity the largest component is the radial intensity. Very close to the trailing-edge and in the near-wake regions, the turbulence is highly anisotropic and has a tendency to become isotropic at far-downstream locations. Even though the turbulence structure was radially

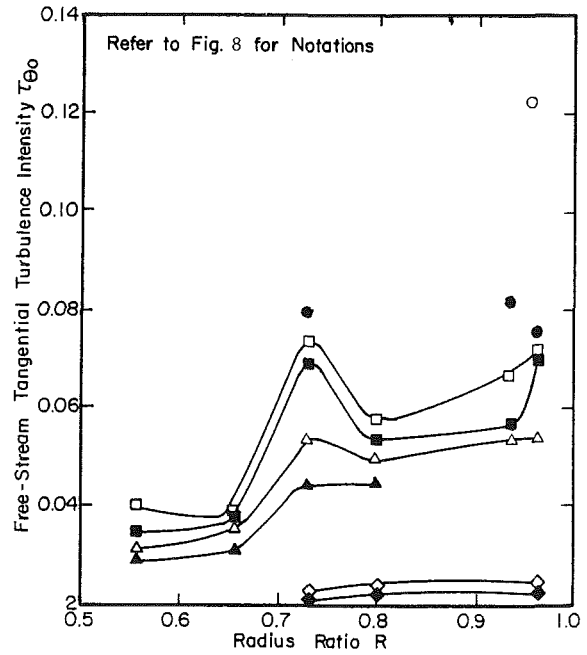


Fig. 16 Radial variation of tangential turbulence intensity in free stream at various axial locations

varying, free-stream turbulence for all the wakes outside the end-wall region was around 4–5 percent. The presence of maximum radial intensities of an order equal to or greater than that of axial and tangential components indicates the three-dimensional nature of the turbulence structure. This characteristic becomes less pronounced beyond 0.5 chords downstream. Reynolds and Lakshminarayana [7] also measured high radial intensities even at far downstream locations. This might reflect on the effect of loading on the three-dimensionality of the turbulence structure. The higher the loading, the faster is the tendency for the turbulence to tend towards isotropy.

Radial and Axial Variation of the Free-Stream Turbulence Intensity. Variations of the free-stream axial, tangential, and radial turbulence intensities are shown plotted in Figs. 15–17. Here again, the radial intensity is at a maximum, confirming the effect of rotation on the turbulence structure.

Downloaded 01 Jun 2010 to 171.66.16.62. Redistribution subject to ASME license or copyright; see http://www.asme.org/terms/Terms_Use.cfm

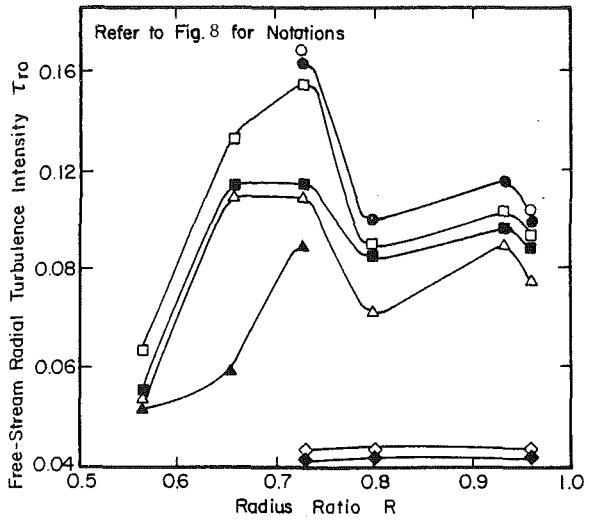


Fig. 17 Radial variation of radial turbulence intensity in free stream at various axial locations.

It is of interest to note the turbulence amplification through the blade row. A 2 percent free-stream axial and tangential intensity and a less than 1 percent radial intensity measured ahead of the blade row show up as rather high values in the free-stream after passing through the blade row. This amplification is probably caused by the blade force acting on the fluid.

In the case of radial intensity (Fig. 17), a less than 1 percent turbulence intensity in front of the rotor gets amplified to nearly 16 percent in the trailing-edge region for $R=0.7297$ and it drops off rather quickly to less than 8 percent in half-a-chord downstream. The same is true at other radii except for those inside the annulus-wall boundary layer. Here, the overall radial turbulence level was within the range of 8–11 percent indicating the effect of secondary flow and the tip-vortex on the turbulence structure. In the hub-wall region, as no trailing-edge measurements are available, the radial turbulence intensity remained fairly low in the range of 2.5–4.6 percent. All this clearly indicates the effect of centrifugal and Coriolis forces on the radial turbulence intensity.

A 2 percent axial and tangential intensity measured ahead of the rotor is found to have been amplified to nearly 8 percent in the free-stream in the trailing edge and near-wake regions and drops off to around 2 percent in the far-wake region. So the free-stream axial and tangential turbulence intensity are of the same order of magnitude while the radial intensity is nearly twice the value of the axial and tangential components.

The free-stream turbulence structure does affect the wake characteristics. A knowledge of this is helpful to the areodynamicists and aeroacousticians in evaluating the inlet flow conditions to a subsequent stage. As explained earlier, the axial and tangential components are of the same order while the radial turbulence structure is greatly affected by centrifugal forces. Near the hub and annulus-wall, because of interactions of the wake, secondary flow, and the end-wall boundary layers, the level of turbulence is high. At the tip region added to the aforementioned is the effect of tip vortex.

Thus in a multi-stage machine, there will be a spanwise gradient in turbulence intensity which would alter the flow situation into a succeeding blade row and, consequently, there will be a spanwise gradient in noise generation and propagation.

Radial and Axial Variation of the Semi-Wake Width. The variation of the semi-wake width with radius is shown plotted in Fig. 18. It is seen that the wake width is a minimum in the mid-radius region and increases very rapidly towards annulus-wall and hub-wall region. This has to be expected as the radial transport of mass, momentum, and energy in the rotor-wake is toward the annulus-wall region and, also, the influence of the secondary flow (and the tip-leakage flow in the case of annulus-wall) on the wake is pronounced at these locations. Inside the annulus-wall boundary layer, the wake width covers the entire blade passage. This is believed to have been caused by the tip-vortex and secondary flow and their interaction with the wake. Again, as the hub-wall region is approached, the wake width starts to grow because of the interaction of the two shear layers, namely, the wake and the hub-wall boundary layer.

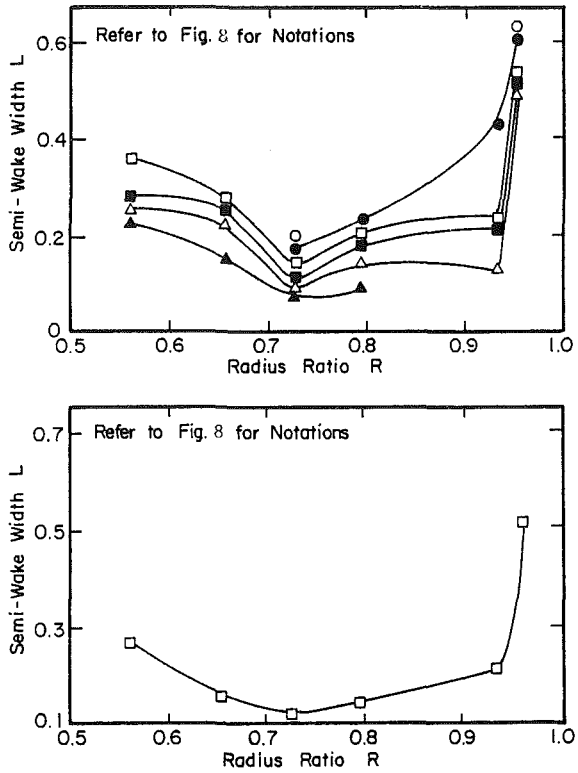


Fig. 18 Radial variation of semi-wake at various axial locations

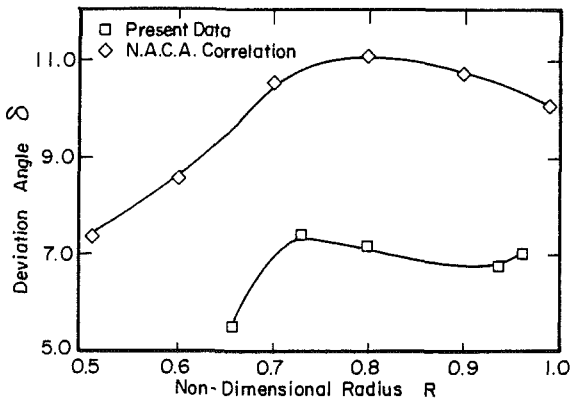


Fig. 19 Variation of deviation angle with radius

Semi-wake width is controlled by many parameters, the important ones being the section drag coefficient, blade spacing, and the rate of decay. In the case of an isolated airfoil, the wake has an infinite media in which it can expand. But in the case of a rotor, the wake growth is controlled by the adjacent blade wakes. Thus the wake growth is very rapid in the trailing-edge region and the growth slows down and becomes asymptotic in the far-wake region. It is also possible that the two adjacent wakes might merge together. In such an

Downloaded 01 Jun 2010 to 171.66.16.62. Redistribution subject to ASME license or copyright; see http://www.asme.org/terms/Terms_Use.cfm

event, the wake width would be greater than one blade passage and this is very clearly seen in Fig. 18, where, at the radius $R=0.9595$, the wake width is greater than one passage. Such a growth might also be assisted by the tip-vortex at these locations.

Radial Variation of Rotor Blade Deviation Angle. The deviation angle is defined as the angle between the average exit flow direction and the direction of a line tangent to the blade section camber line at the trailing-edge. A knowledge of the deviation angle is essential in predicting the losses and aerodynamic performance of compressors. Most of the compressor design done today is based on existing cascade correlations. Even the deviation angles are predicted based on cascade correlations. There may be a difference between the deviation angles derived from cascade correlation and the actual values in a rotor. In this section, an attempt is made to evaluate the applicability of cascade correlation to the actual compressor rotor-blade data. The NACA deviation angle correlation as given by Serovy [9] was employed to compare the results from the present experimental data. The NACA deviation angle correlation based on cascade data is given as:

$$\delta_{\text{ref}} = \delta_0 + \frac{m_{0=1}}{\sigma^b}\phi$$

where: δ_0 = deviation angle measured from chord line for zero camber cascade with same fluid inlet angle and solidity as the cambered cascade; δ_{ref} = cascade exit average deviation angle measured from tangent to blade trailing edge; $m_{\sigma=1}$ = rate of change of deviation angle with camber angle for cascade with solidity of 1.0; b = exponent to account for variable influence of solidity; σ = cascade solidity; and ϕ = blade section camber angle.

For the present rotor, the deviation angles were calculated using the foregoing equation. The actual deviation for the rotor-blade was obtained to be the difference between the blade outlet angle and the measured fluid outlet angle. The fluid outlet angle can be obtained from the mean velocity data presented earlier. Figure 19 shows the plot of this variation of the deviation angle from hub-to-tip of the machine. It is seen that the cascade correlation overpredicts the deviation angle by as much as 4–5 deg.

Thus it can be concluded that the deviation angles based on the cascade correlations will not yield true estimates in an actual rotor-blade. The failure of the cascade correlations to predict deviation angles correctly is the result of three-dimensional viscid and inviscid effects.

Radial Variation of Stator Incidence Angle. Radial variation of incidence to the downstream stator can be discerned from Fig. 5. Like deviation, a knowledge of the spanwise variation in the incidence angle is essential in predicting the losses and aerodynamic performance of stators. Since the rotor wake decays along streamwise direction, it is logical to assume that at any particular axial location, the wakes at higher radii would have decayed to a farther extent as compared to the wakes at lower radii. Therefore, at any axial location, the stator would encounter higher incidence at the hub than at the tip, generating varying off design conditions along the stator span. This is clearly seen in Fig. 5.

Conclusions

The characteristics of the wake of a moderately loaded compressor rotor blade were investigated. All the measurements were acquired in the rotor frame of reference using a three sensor hot-wire probe. Some of the important conclusions that can be drawn based on the results of the present investigation are as follows:

1 Very large velocity defects were measured in the trailing-edge region. The defect was found to decay very rapidly in the trailing-edge and near-wake regions.

2 The wake-width increases very rapidly in the trailing-edge region and the growth becomes very gradual in the far-wake region. Because of centrifugal effects, wake-width at higher radii is thicker. Inside the annulus and hub-wall boundary layers, the wake width is found to be very large due to the effect of secondary flow and tip-leakage flow.

3 For the wakes outside the end-wall boundary layers, the wake shape factor monotonically decreases with downstream distance. It reaches an asymptotic value of nearly 1.2 at far downstream location. In the trailing-edge region, the value is greater than 1.8, indicating the tendency of the flow to separate.

4 Variation of the momentum-thickness in the near and far-wake regions is in close conformity with the free-stream velocity variation. For the wakes inside the annulus-wall boundary layer, the momentum thickness grows very rapidly in the trailing-edge region and nearly remains constant in the far-wake region. This behavior is due to the tip-vortex and the secondary flow at these locations.

5 There is a marked variation in the wake properties from one radius to the other. Both the defects and decay rates vary from one radius to the other.

6 For the wakes outside the end-wall boundary layers, the wake decay and wake width differ in the radial direction, but they correlate reasonably well with $\sqrt{c_d}$.

7 The incidence to stator, placed at various axial locations downstream of the rotor, varies considerably from the design values. The section from hub to mid-radius encounters servere off design conditions.

8 The measured deviation angle for the rotor blade differs from the widely used NACA correlation.

9 The radial turbulence intensity is found to be maximum. The maximum value of all the components of intensities increase toward hub and annulus walls, except at the trailing edge where it is consistently higher at all radii.

10 The free-stream turbulence in the wakes outside the end-wall boundary layers is about the same at all radii. But for the wakes inside the annulus and hub-wall boundary layers, the magnitude of the free-stream turbulence is higher, indicating the influence of secondary and tip-leakage, as well as wall boundary layers on the turbulence intensity.

Acknowledgments

This work was supported by the National Aeronautics and Space Administration through Grant NSG 3012, with L. Shaw as the technical monitor.

References

1 Lakshminarayana, B., "An Axial Flow Research Compressor Facility Designed for Flow Measurement in Rotor Passages," in *Measurement Methods in Rotating Components of Turbomachinery*, New York, Mar. 1980, pp. 31–42.

2 Lakshminarayana, B., "Techniques for Aerodynamic and Turbulence Measurements in Turbomachinery Rotors," in *Measurement Methods in Rotating Components of Turbomachinery*, ASME, New York, Mar. 1980, pp. 5–31.

3 Ravindranath, A., and Lakshminarayana, B., "Mean Velocity and Decay Characteristics of the Near- and Far-Wake of a Compressor Rotor of Moderate Loading," ASME JOURNAL OF ENGINEERING FOR POWER, Vol. 102, No. 3, July 1980, pp. 535–548.

4 Ravindranath, A., and Lakshminarayana, B., "Structure and Decay Characteristics of Turbulence in the Near- and Far-Wake of a Moderately Loaded Compressor Rotor Blade," ASME JOURNAL OF ENGINEERING FOR POWER, Vol. 103, Jan. 1981, pp. 131–140.

5 Smith, L. H., "Three Dimensional Flow in Axial Flow Turbomachinery," WADC Technical Report 55-3480, 1956.

6 Reynolds, B., and Lakshminarayana, B., "Characteristics of Lightly Loaded Fan Rotor Blade Wakes," NASA CR 3188, Oct. 1979.

7 Kool, P., DeRuyck, J., and Hirsch, Ch., "Three Dimensional Flow in an Axial Plane Downstream of an Axial Flow Compressor Rotor," ASME Paper 78-GT-66, 1978.

8 Schlichting, H., *Boundary Layer Theory*, 6th ed., McGraw-Hill, 1968.

9 Serovy, G. K., "Deviation Angle/Turning Angle Prediction for Advanced Axial Flow Compressor Blade Row Geometries," Air Force Aeropropulsion Laboratory Report AFAPL TR-77-81, 1977.

Downloaded 01 Jun 2010 to 171.66.16.62. Redistribution subject to ASME license or copyright; see http://www.asme.org/terms/Terms_Use.cfm

Calculation of the Theoretical Critical Flow Rate of Saturated Steam

J. W. Murdock
Associate Professor,
Mechanical Engineering and
Mechanics Department,
Drexel University,
Philadelphia, Pa. 19104
Fellow ASME

This paper is concerned with the computation of the theoretical critical flow of dry saturated steam through passages over a range of 1 psia (7 kPa) to the critical pressure of 3208.2 psia (22.12 MPa). Two computational methods are used: a theoretical method using ideal gas relations, and a flow maximization method using actual saturated steam properties. An equation is developed and based on the theoretical equation that yields flow rates that have an average deviation of 0.1 percent and a maximum deviation of 0.3 percent from the flow rate found by flow maximization. It is also demonstrated that Napier's equation currently recommended by PTC 25.3-1976 "Safety and Relief Valves" is unsatisfactory for the calculation of theoretical critical flow rates.

Introduction

This paper was undertaken as a result of a series of discussions with some members of the ASME Performance Test Codes Supervisory Committee concerning the need for an accurate method of computing the theoretical flow of steam. The present Code and Safety and Relief Valves [1] in Par. 5.063 indicates that the theoretical critical flow of steam may be computed from page 301, Fig. 14, of the ASME Steam Tables [2]. For dry saturated conditions the Code goes on to state that

" . . . It is general engineering practice to use Napier's equation due to its simplicity and reasonable correlation with the theoretical method . . . "

Unfortunately Fig. 14 of reference [2] is hard to read with any degree of accuracy and Napier's equation is very inaccurate except at 100 psia and 1500 psia. Figure 1 shows the error due to use of Napier's equation for the calculation of critical theoretical flow of saturated steam. The range of error from about 12 percent at 1 psia to 26 percent at critical pressure mitigates against its use.

For calculations in the superheat region, data and equations were developed by Steltz [3] and Murdock and Bauman [4]. Additional information is given in reference [5] concerning use of the isentropic exponent in calculations. The material contained in these references are based on the steam property values given in the 1936 Keenan and Keyes Steam Tables [6]. It is intended that the calculation of the theoretical critical flow of superheated steam be the subject of a later paper to adjust available data to the presently accepted values of steam properties as given in reference [2].

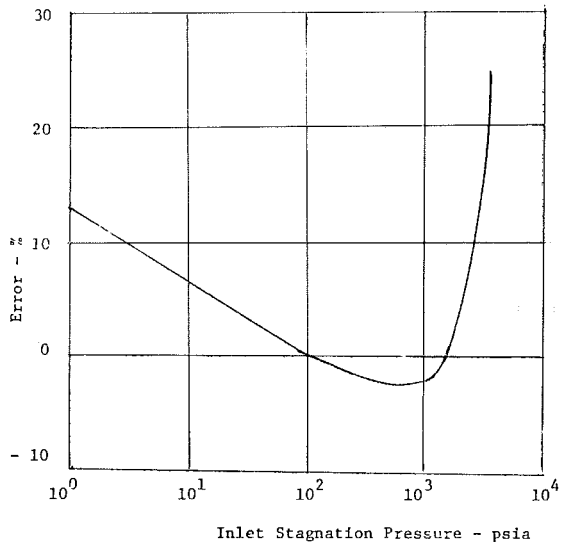


Fig. 1 Error in theoretical critical flow using Napier's equation

Theoretical Equation

This equation is derived on the basis of assuming frictionless adiabatic (isentropic) one-dimensional critical flow in a horizontal passage. With this assumption:

Equation of continuity:

$$G_t = V_2/v_2 \tag{1}$$

Acoustic velocity:

$$V_2 = \sqrt{144 g_c p_2 v_2} \tag{2}$$

Critical pressure ratio:

$$p_2 = p_1 \left(\frac{2}{k+1}\right)^{k/(k-1)} \tag{3}$$

Isentropic process:

$$v_2 = v_1 (p_1/p_2)^{1/k} = v_1 \left(\frac{2}{k+1}\right)^{1/(1-k)} \tag{4}$$

Contributed by the Performance Test Codes Committee of THE AMERICAN SOCIETY OF MECHANICAL ENGINEERS and presented at the Winter Annual Meeting Nov. 16-18 1980, Chicago, Illinois. Manuscript received at ASME Headquarters August 23, 1980. Paper No. 80-WA/PTC-3.

Copyright © 1982 by ASME

Downloaded 01 Jun 2010 to 171.66.16.62. Redistribution subject to ASME license or copyright; see http://www.asme.org/terms/Terms_Use.cfm

Substituting for V_2 from equation (2), p_2 from equation (3), and v_2 from equation (4) in equation (1) and simplifying, results in:

$$G_t = \sqrt{144 g_c \left(\frac{2}{k+1}\right)^{(k+1)/(k-1)}} \sqrt{p_1/v_1} \tag{5}$$

Let F_s (critical flow factor) be defined as follows:

$$F_s = 12\sqrt{g_c \left(\frac{2}{k+1}\right)^{(k+1)/(k-1)}} \tag{6}$$

Equation (5) then may be written as:

$$G_t = F_s \sqrt{p_1/v_1} \tag{7}$$

Flow Maximization

From the first law of thermodynamics for inlet stagnation conditions and steady horizontal flow:

$$v_x = \sqrt{2 g_c J (h_{gl} - h_x)_s} \tag{8}$$

and

$$G_x = V_x / v_x \tag{9}$$

Values of downstream pressure are selected until G_x reaches a maximum value so that:

$$G_{\max} = \sqrt{2 g_c J (h_{gl} - h_2)_s / v_2} \tag{10}$$

The critical flow factor then becomes

$$F_s = G_{\max} \sqrt{v_1 / p_1} \tag{11}$$

A detailed example of this type of calculation is given in reference [4]. For this paper, flow maximization from 1 psia to 3000 psia was accomplished on a Radio Shack TRS-80 microcomputer. Steam table data [2] were fed into the computer at 10°F intervals and interpolation was accomplished by appropriate techniques to limit interpolation error to within two of the least significant digit of the tabulated data. At the critical pressure a Texas Instrument SR 60A was programmed to compute G_x and data were fed directly from the steam tables [2] at various downstream pressures and plotted to obtain the maximum mass velocity. Spot checks were made at other inlet pressures to verify the results obtained with the TRS-80 microcomputer.

Isentropic Exponent

The value of the isentropic exponent needed for the solution of equation (6) was obtained from two sources, the first being from Fig. 11, page 298, of reference [2] and the second from data generated by flow maximization.

To obtain the average isentropic exponent from Fig. 11, a critical pressure ratio of 0.6 was assumed. A line was drawn on Fig. 11, representing a critical pressure equal to that of 60 percent of the saturation pressure. Values of the isentropic exponent were read from the saturation pressure line and the critical pressure line along a path of constant entropy. The values were averaged and are shown as a dashed line on Fig. 2.

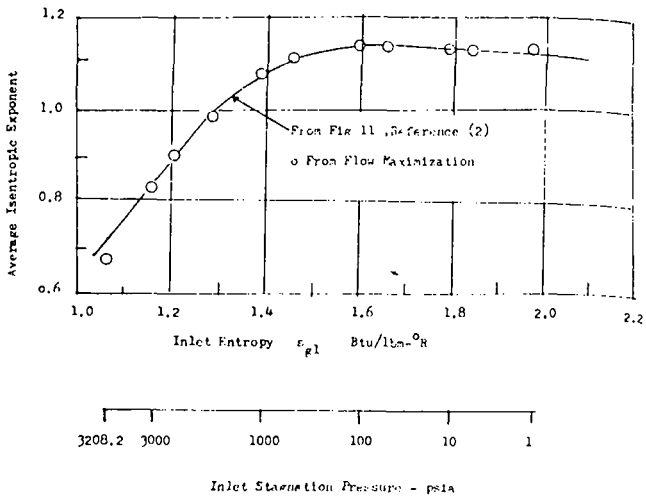


Fig. 2 Average isentropic exponent

For flow maximization two techniques were used as described by the following equations:

$$k = (\partial h/\partial u)_s \simeq (h_{gl} - h_2)/(u_{gl} - u_2) \tag{12}$$

$$k = \frac{-v}{p}\left(\frac{\partial p}{\partial v}\right)_s \simeq \log_e (p_1/p_2)/\log_e (v_2/v_1) \tag{13}$$

Equations (12) and (13) gave results that were in agreement with each other to within the third decimal place and selected values are plotted on Fig. 2.

The average isentropic exponent obtained from Fig. 11 was found to be in agreement with those obtained using equations (12) and (13).

Working Equations

A least squares curve fit of the data from flow maximization resulted in the following equation:

$$F_s = a + b s_{gl} + c s_{gl}^2 \tag{14}$$

where the values of a, b, and c are obtained from Table 1.

The average deviation between values of the critical flow factor obtained from equation (14) and those obtained from

Nomenclature

a = constant in equation (14)
a' = constant in equation (18)
A = passage area, ft^2
A' = passage area, m^2
b = constant in equation (14)
b' = constant in equation (18)
c = constant in equation (14)
c' = constant in equation (18)
F_s = critical flow factor as defined by equation (7) lbm$^{1/2}$-in./ft. $^1/_2$-lb$_f^{1/2}$-sec.
F_s' = critical flow factor as defined by equation (16) dimensionless
g_c = proportionality constant = 32.174 lbm-ft/lb$_f$-sec^2
g_c' = proportionality constant = 1 kg-m/(N•s^2)
G = mass velocity, lbm/ft^2-sec
G' = mass velocity, kg/(m^2•s)
h = enthalpy, Btu/lbm
J = mechanical equivalent of heat = 778.169 ft-lb$_f$/Btu
k = isentropic exponent, dimensionless
p = pressure, lb$_f$/in.^{2}
p' = pressure, Pa
r_c = critical pressure ratio, dimensionless
s = entropy, Btu/lbm-°R
s' = entropy, kJ/(kg•K)
T = thermodynamic temperature, °R
u = internal energy, Btu/lbm
v = specific volume, ft^3/lbm
v' = specific volume, m^3/kg
V = velocity, ft/sec
$\dot{w}$ = mass flow rate lbm/hr
$\dot{w}'$ = mass flow rate kg/s

Subscripts

cal = calculated value
f = saturated liquid
g = saturated vapor
max = maximum value
s = constant entropy
t = theoretical value
x = assumed exit state
1 = inlet stagnation state
2 = critical state

Downloaded 01 Jun 2010 to 171.66.16.62. Redistribution subject to ASME license or copyright; see http://www.asme.org/terms/Terms_Use.cfm

flow maximization was equal to 0.1 percent and the maximum to 0.3 percent as shown in Table 2. The agreement between the critical flow factor computed from Fig. 11 [2] and equation (6) is shown in Fig. 3. Again there is excellent agreement between the two methods.

For calculation of mass flow rate

$$\dot{w}_t = 3600\, G_t A \tag{15}$$

SI (Metric) Units

Although the present edition of PTC 25.3 does not require computation in SI (Metric) units, it is only a matter of time before SI computations will be required. For this reason the following equations for the computation of theoretical flow rate are presented:

For mass flow rate:

$$\dot{w} = G'_t F'_s A' \tag{19}$$

For mass velocity:

Table 1

p, psia	a	b	c
$p_1 < 300$	28.9005	17.0228	5.03362
$p_1 > 300$	41.4266	111.546	36.8296

$$G'_t = F'_s \sqrt{p'_1 / v'_1} \tag{16}$$

For critical flow factor:

$$F'_s = \sqrt{k g'_c \left(\frac{2}{k+1}\right)^{(k+1)/(k-1)}} \tag{17}$$

Working equation:

$$F'_s = a' + b' s'_{gl} + c' s'^{2}_{gl} \tag{18}$$

where values of a', b' and c' are obtained from Table 3.

Critical Pressure Ratio

The critical pressure ratio obtained from flow maximization and that obtained from using the average isentropic exponent and equation (3) is shown in Fig. 4. For inlet stagnation pressures below 1000 psia (7 Mpa) the critical pressure ratio obtained from the two methods agreed to within the third decimal place. For higher inlet pressures the flow maximization method gave critical pressure ratios lower than those from equation (3), ranging from about 1 percent at 2,000 psia (14 Mpa) to about 4 percent at critical inlet pressure. The use of equation (3) to calculate critical pressure ratio will produce a maximum error of 0.7 percent in mass velocity at 3208.2 psia, the error decreasing to zero at 1000 psia (7 Mpa). For checking to see if critical flow exists, the flow maximization pressure ratio curve of Fig. 4 should be used.

Table 2 Data Summary

Inlet stagnation pressure psia	Average isentropic exponent k	Mass velocity G_2 lbm/ft – sec	Critical Flow Factor: From flow maximization F_{smax}	Critical Flow Factor: Calculated from equation (14) F_{scal}	Difference – % $100 \times (1 - F_{scal}/F_{smax})$
1	1.113	2.353	42.96	42.88	0.19
2	1.118	4.607	43.02	43.03	0.02
3	1.121	6.840	43.07	43.10	−0.07
4	1.123	9.052	43.10	43.14	−0.09
5	1.126	11.24	43.13	43.17	−0.09
6	1.127	13.42	43.15	43.20	−0.12
7	1.128	15.59	43.17	43.21	0.09
8	1.129	17.75	43.17	43.23	0.14
9	1.129	19.90	43.19	43.24	0.14
10	1.130	22.03	43.20	43.25	−0.12
20	1.137	43.16	43.29	43.28	0.02
30	1.138	64.02	43.31	43.29	0.05
40	1.138	84.46	43.30	43.29	0.02
50	1.141	105.0	43.34	43.29	0.12
60	1.141	125.2	43.31	43.28	0.07
70	1.141	145.5	43.32	43.28	0.09
80	1.141	165.8	43.36	43.27	0.21
90	1.142	185.7	43.31	43.26	0.12
100	1.142	205.9	43.35	43.25	0.23
200	1.135	404.4	43.25	43.19	0.14
300	1.132	602.6	43.22	43.13	0.21
400	1.124	800.0	43.11	43.00	0.26
500	1.118	996.7	42.93	42.94	0.02
600	1.110	1198	42.91	42.86	0.12
700	1.102	1399	42.80	42.77	0.09
800	1.095	1601	42.70	42.68	0.05
900	1.086	1808	42.57	42.58	−0.02
1000	1.077	2013	42.44	42.46	−0.05
1100	1.070	2221	42.38	42.36	0.05
1200	1.065	2427	42.27	42.27	0.00
1300	1.054	2644	42.13	42.13	0.00
1400	1.045	2860	41.99	42.00	−0.02
1500	1.036	3078	41.85	41.87	−0.05
1600	1.026	3302	41.74	41.74	0.00
1700	1.016	3531	41.62	41.61	0.02
1800	1.005	3757	41.40	41.47	0.17
1900	0.996	3991	41.25	41.31	−0.15
2000	0.983	4242	41.18	41.15	0.07
2200	0.962	4725	40.68	40.78	−0.25
2400	0.932	5265	40.32	40.38	−0.15
2600	0.907	5810	39.78	39.89	−0.28
2800	0.870	6456	39.21	39.28	0.18
3000	0.831	8205	38.46	38.43	0.08
3208.2	0.670	8914	35.46	35.46	0.00

Downloaded 01 Jun 2010 to 171.66.16.62. Redistribution subject to ASME license or copyright; see http://www.asme.org/terms/Terms_Use.cfm

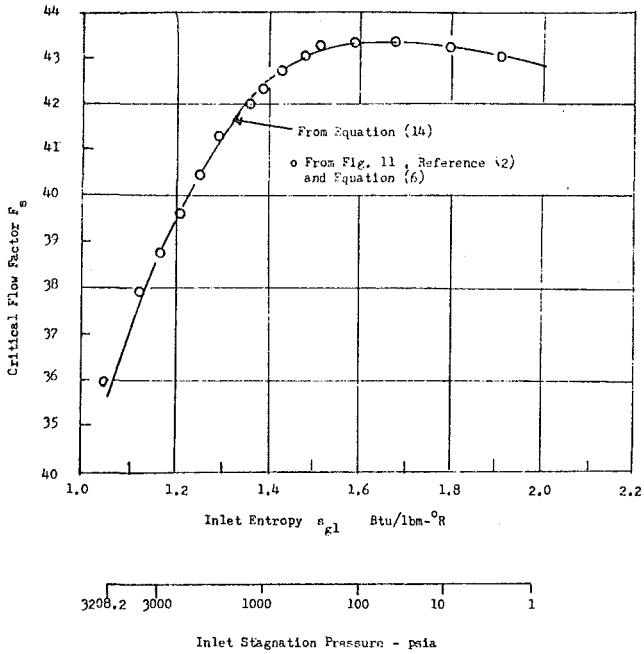


Fig. 3 Critical flow factor F_s

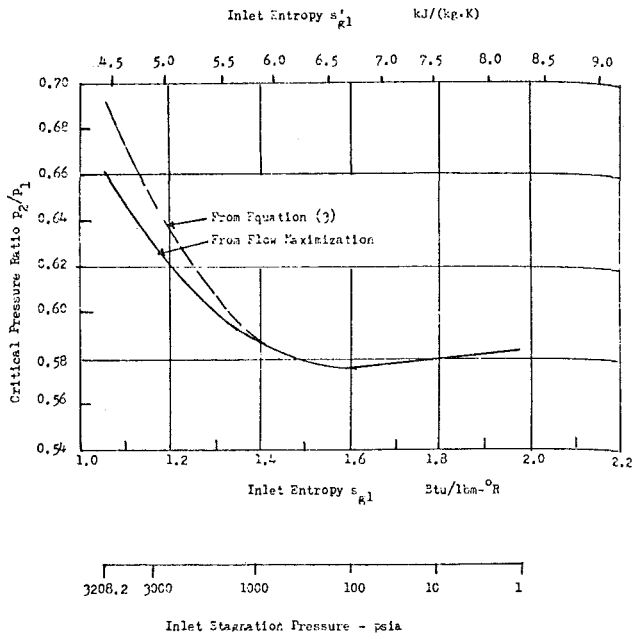


Fig. 4 Critical pressure ratio p_2/p_1

Table 3

p, kPa	a'	b'	c'
$p_1 < 2$ 100	0.424966	0.0597446	-4.220408×10^{-3}
$p_1 > 2$ 100	−0.60862	0.391491	−0.0308791

Sample Calculations

U.S. Units. A valve has a discharge area of 3 sq in. Dry and saturated steam is supplied at 1000 psia and discharge is into the atmosphere. Compute the theoretical critical flow rate.

(*a*) Steam properties from reference [2] at 1000 psia:

$v_{gl} = 0.44596$ ft^3/lbm

$s_{gl} = 1.3910$ Btu/lbm-°R

(*b*) Check for critical flow

$p_2/p_1 = 14.7/1000 = 0.015$

From Fig. 4 at $s_{gl} = 1.3910$, critical pressure ratio = 0.583

Since 0.015 is less than 0.583, flow is critical,

(*c*) Compute critical flow factor F_s

$$F_s = a + bs_{gl} + cs_{gl}^2 \tag{14}$$

From Table 1 (p_1 greater than 300 psia):

$F_s = -41.4266 + 111.546\,(1.3910) - 36.8296\,(1.3910)^2 = 42.47$

(*d*) Compute mass velocity:

$$G_t = F_s\sqrt{p_1/v_1} \tag{7}$$

$G_t = 42.47\,(1000/0.44596)^{1/2} = 2{,}011$ lbm/sec-ft^2

(*e*) Compute flow rate;

$$\dot{w} = 3600 G_t A \tag{15}$$

$\dot{w} = 3600x\,2011 \times (3/144) = 150{,}825$ lbm/hr

SI Units. A valve has a discharge area of 20 cm^2. Dry and saturated steam is supplied at 7 Mpa and discharge is into the atmosphere. Compute the theoretical critical flow rate.

(*a*) Steam properties from reference [7] at 7000 kPa:

$v'_{gl} = 0.027373$ m^3/kg

$s'_{gl} = 5.8162$ kJ/(kg•*K*)

(*b*) Check for critical flow:

$p'_2/p'_1 = 101.325/7000 = 0.015$

From Fig. 4 at $s'_{gl} = 5.8162$, critical pressure ratio = 0.583

Since 0.015 is less than 0.583, flow is critical.

(*c*) Compute the critical flow factor F'_s:

$$F'_s = a' + b's'_{gl} + c's'^2_{gl} \tag{18}$$

From Table 2 (p'_1 greater than 2 100 kPa):

$F'_s = -0.60862 + 0.391491\,(5.8162) - 0.0308791\,(5.8162)^2$

$F'_s = 0.6238$

(*d*) Compute mass velocity:

$$G'_t = F'_s\sqrt{p'_1/v'_1} \tag{16}$$

$$G'_t = 0.6238\,(7000 \times 10^3/0.02737)^{1/2} = 9975 \text{ kg/m}^2\text{•}s \tag{16}$$

(*e*) Compute mass flow rate:

$$\dot{w} = G'_t A'$$

$$\dot{w}' = 9975(20 \times 10^{-4}) = 19.95 \text{ kg/s} \tag{19}$$

Conclusions

The equation and data presented in this paper may be used to compute the theoretical critical flow of dry and saturated steam from 1 psia (7kPa) to critical pressure 3208.2 psia (21.12 Mpa) with an average error of within ±0.1 percent and a maximum error of 0.3 percent.

Napier's equation should not be used for the calculation of theoretical critical flow of dry and saturated steam for the purpose of establishing valve coefficients.

References

1 *Safety and Relief Values*, ASME Performance Test Code, ANSI/ASME PTC 25.3, 1976.

2 *Thermodynamic and Transport Properties of Steam*, ASME, N.Y., 1967.

3 Stelz, W. G., "The Critical and Two-Phase Flow of Steam," ASME JOURNAL OF ENGINEERING FOR POWER, Vol. 83, April 1961, pp. 145–154.

4 Murdock, J. W., and Bauman, J. M., "The Critical Flow Function for Superheated Steam," ASME *Journal of Basic Engineering*, Vol. 86, Sept. 1964, pp. 507–518.

5 "Flow Measurement," Chapter 4 of Part 5 "Measurement of Quantities of Materials," ASME Power Test Code Supplement on Instruments and Apparatus, PTC 19.5, 1959, pp. 4–19.

6 Keenan, J. H., and Keyes, F. G., *Themodynamic Properties of Steam*, John F. Wiley & Sons, Inc., New York, 1936.

7 "ASME Steam Tables in SI (METRIC) Units" ASME, N.Y., 1977.

Downloaded 01 Jun 2010 to 171.66.16.62. Redistribution subject to ASME license or copyright; see http://www.asme.org/terms/Terms_Use.cfm

Measurement of Heat Flux and Pressure in a Turbine Stage

M. G. Dunn
Aerodynamic Research Dept.,
Calspan Advanced Technology Center,
Buffalo, N. Y.

A. Hause
Aero-Propulsion Laboratory,
Air Force Systems Command,
Wright-Patterson Air Force Base, Ohio

Selected portions of the first stage stationary inlet nozzle, shroud, and rotor of the AiResearch TFE 731-2 turbine were instrumented with thin-film heat-transfer gages and heat-flux measurements were performed using a shock tunnel as a source of high-temperature, high-pressure gas. Experiments were performed over a range of Reynolds numbers, based on mid-annular stator chord, from 1.6×10^5 to 3.1×10^5 and corrected speeds from approximately 70-106 percent. The full-stage heat-flux results are compared to our previous measurements obtained with a stator only, in the absence of a rotor. The previous results are in good agreement with the full-stage data for the tip end-wall region, but they are significantly less than the full-stage results for the stator airfoil. Pressure measurements were obtained throughout the model and these results are shown to be in excellent agreement with the steady-state rig data supplied to us by AiResearch for this turbine. Heat-flux measurements are also presented for the stationary shroud as a function of rotor mid-annular chord. The shroud heat-flux data are shown to be in excess of the rotor blade results. Rotor-tip heat-flux measurements are shown to be slightly greater than the shroud results.

Introduction

The ability to predict accurately the heat-flux distributions for various engine components is an important consideration in gas turbine engine design. Three recent workshops [1-3] devoted to detailed discussions of the state-of-the-art of turbine heat-transfer predictive and/or experimental capability indicate the necessity for improvement in these areas. In addition to the work described in [1-3], several calculational techniques, e.g., Dodge [4], Katsanis [5], Wu [6], Smith [7], Horlock and Perkins [8], and Booth [9], have been developed. Dodge [10] has compared the results of his 3-D code to the heat-flux distributions for the early stator-only data [11]. Good agreement was demonstrated between his predictions and the experimental results.

Many different facilities are currently being used to perform turbine related studies. These include the long run-time cascade facilities, such as those used by Blair [12], Graziani et al. [13], and York [14], and the low speed rotating rig of Dring [15]. Also included in the long run-time facility class would be the new high pressure and temperature combustor and full-stage turbine test facility currently under development at NASA-Lewis as discussed by Stepka [1]. Many other groups have used, and are still using, short-duration facilities similar to that used in the present study. Louis [16, 17] has used thin-film, heat-transfer gages to obtain heat-flux measurements on turbine components with a blow-down facility as the source of test gas. Jones, Schultz et al. at Oxford University [18-21] have also used the thin-film, heat-transfer gage techniques but with a light-piston technique as the supply of test gas. This particular group has performed detailed aerodynamic measurements within their test environment in order to establish the validity of the short-duration technique.

All of the facilities and measurement techniques noted above have applicability to turbine technology development, as there is not a single facility that meets all of the needs of the turbine designer. The test apparatus used for the present experiments provides an experimental capability fitting between the well-known, cascade-type facility and the full-scale engine facility.

This paper describes heat-flux and pressure measurements that were obtained using state-of-the-art, shock-tube technology and well established transient-test techniques (thin-film gages and fast-response pressure transducers). These measurements were performed for a full turbine stage of the AiResearch TFE 731-2 engine. This work is an extension of earlier measurements reported in [11] and [22]. These earlier results, obtained for a single stator stage in the absence of a rotor, will be used extensively herein for comparison purposes.

The shock-tunnel facility used provides a clean, uniform, and well-known gas-dynamic condition at the inlet to the stationary nozzle. The experimental technique is not intended to duplicate every known parameter important to turbine heat-transfer studies, but the flow conditions are sufficiently well defined and enough parameters are duplicated so that the measured heat-flux distributions can be used to validate and improve confidence in the accuracy of full-stage design data and existing/advanced predictive techniques under development. In addition, these experimental results have been utilized in the placement of instrumentation for other on-going measurement programs.

Experimental Apparatus

The experimental apparatus sketched in Fig. 1 consists of

Contributed by the Gas Turbine Division of THE AMERICAN SOCIETY OF MECHANICAL ENGINEERS and presented at the Gas Turbine Conference and Products Show, March 9-12, 1981, Houston, Texas. Manuscript received at ASME Headquarters Dec. 11, 1980. Paper No. 81-GT-88.

Copyright © 1982 by ASME
Downloaded 01 Jun 2010 to 171.66.16.62. Redistribution subject to ASME license or copyright; see http://www.asme.org/terms/Terms_Use.cfm

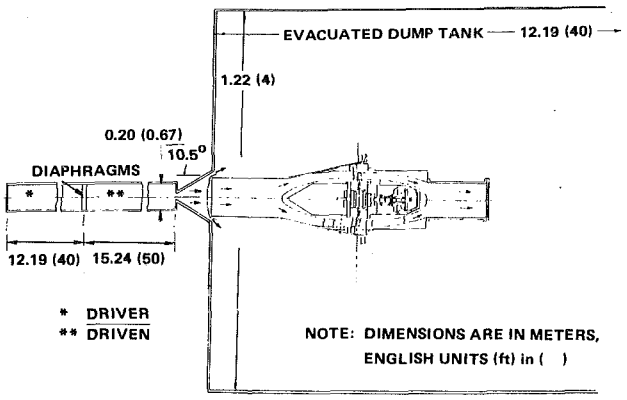


Fig. 1 Schematic of experimental apparatus

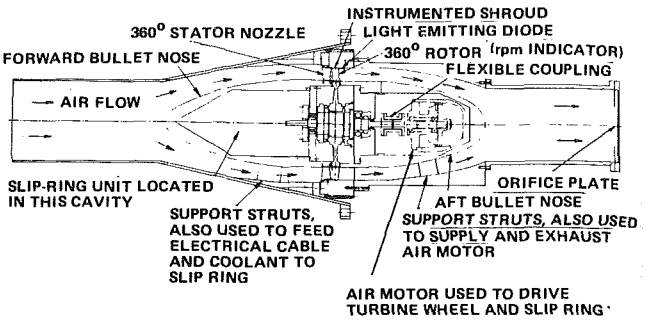


Fig. 2 Schematic of test section apparatus for full-stage turbine experiments

an 0.20 m (8-in.) i.d. helium-driven shock tube, consisting of a 12.19-m (40-ft) long driver tube and a 15.24-m (50-ft) long driven tube, as a short-duration source of high-temperature, high-pressure air, driving a test-section device mounted near the exit of the primary shock-tunnel nozzle. The receiver tank is initially evacuated to a pressure of approximately 5 torr in order to minimize the starting air load on the turbine wheel and to improve the flow establishment characteristics of the model. It was not possible to reduce further the initial pressure in the receiver because of air leakage from the slip-ring shaft seal. The combination of a large diameter driven tube and very long driver tube accounts for the long test times (~12 ms) obtained for this work. The test-section device sketched in Fig. 2 consists of a forward transition section with a circular opening facing the supersonic primary nozzle flow. The circular opening is followed by a complete 360-deg annular passage containing the nozzle stator, the rotor, and the shroud as can be seen in Fig. 2. The axial spacing between the stator and the rotor was approximately 0.18 c_s at mid-annulus. The rotor-blade tip-to-shroud clearance at 0 rpm was constructed to be 5.1×10^{-4} m (0.020-in.). Because the rotor will increase in diameter by about 2.0×10^{-4} m (0.008 in.) during operation, the actual clearance when the wheel is at full speed is on the order of 3.0×10^{-4} m (0.012-in.). Whenever possible, flight hardware, which was supplied to Calspan by AiResearch, was utilized in constructing the model. In order to minimize the flow establishment time in the test model, the approach previously used [11] for maintaining the cross-sectional area constant from the model inlet to the stator nozzle inlet and the exit area constant from the stator nozzle exit to the cylindrical section just upstream of the orifice plate was used in this design. The orifice plate is used to set the mass-flow rate through the device and thus to set the exit Mach number of the stator nozzle. This particular stator vane is designed to operate with a subsonic exit Mach number.

A photograph of one of the heat-transfer gages used in this work was taken through a Leitz microscope and is shown in Fig. 3. The technology used to construct these gages has been well established for many years, as described by Vidal [23]. The Pyrex insulating substrate for the metallic film is 9.7×10^{-4} m (0.38 in.) in diameter by 7.1×10^{-4}-m (0.028-in.) thick. The thin-film gage is made of platinum (~1000 Å thick) and is painted on the substrate in the form of a strip approximately 1.0×10^{-4}-m (0.004-in.) wide by about 5.1×10^{-4}-m (0.020-in.) long. The response time of these heat-transfer elements is on the order of 10^{-8} s [23]. A coating of magnesium fluoride (~1200 Å thick) is vapor deposited over the gage to protect against abrasion. These gages are very durable in a clean environment, and a very low loss rate of gages was experienced during the measurement program. A diamond drill was used to notch the substrate on each side so as to permit the lead wires access to the thin film without shorting as a result of contact with the metal nozzle. The gages are held in the turbine components using an epoxy

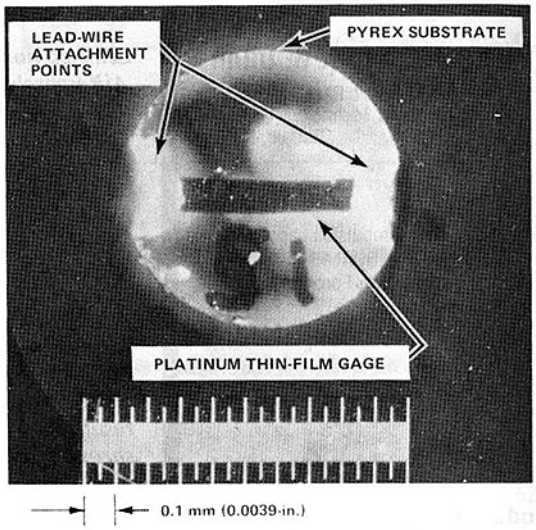


Fig. 3 Photograph of heat transfer gage taken through Leitz microscope

Nomenclature

A = stator inlet area
c_s = stator mid-annular chord length
c_r = rotor mid-annular chord length
H_0 = total enthalpy
H_w = wall enthalpy
$\dot{m}$ = physical mass-flow rate
N_{phy} = physical rotor speed
N_{corr} = corrected rotor speed, $N_{corr} = N_{phy}/\sqrt{T_0}/513$
$\%N_{corr}$ = $N_{corr}/[N_{corr}]$design
$\dot{q}$ = heat flux
$\mathrm{Re})_{c_r}$ = Reynold number based on rotor midchord, $\dfrac{\rho V c_r}{\mu}$
$\mathrm{Re})_{c_s}$ = Reynolds number based on stator midchord, $\dfrac{\rho V c_s}{\mu}$
T_0 = total temperature
μ = dynamic viscosity evaluated at T_0
τ_1 = defined in Fig. 12
τ = defined in Fig. 12
ρV = obtained from $(\dot{m}/A)$

Downloaded 01 Jun 2010 to 171.66.16.62. Redistribution subject to ASME license or copyright; see http://www.asme.org/terms/Terms_Use.cfm

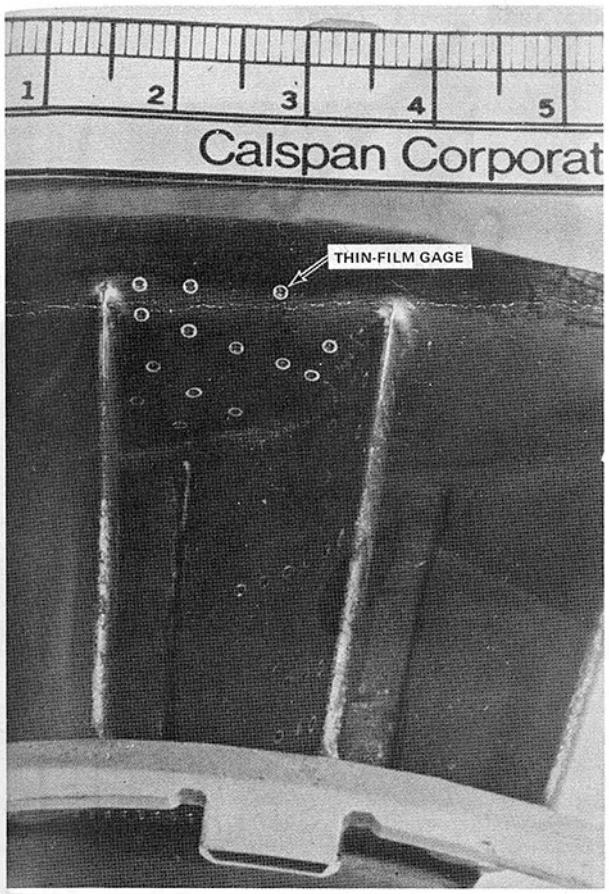


Fig. 4 Photograph of stator nozzle inlet

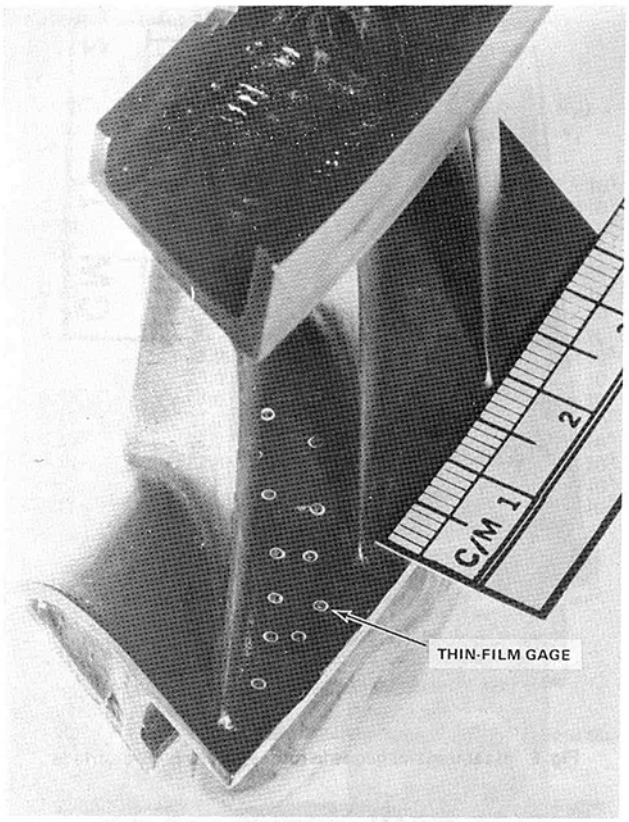


Fig. 5 Photograph of stator nozzle end wall

adhesive. They are installed under a microscope so as to ensure that they are flush with the local surface contour to within less than 1.3×10^5 m(0.0005 in.).

The temperature versus time histories of the thin-film gages located on the stator and the shroud were recorded directly on tape recorders with a frequency response of 20 KHz. These data were then processed through a standard analog heat-flux network (developed by Skinner [24]) and they were also were analyzed using a digital version of the heat-flux equation. The results of the two analysis techniques are consistent, but the digital version allows retention of the 20 KHz frequency response.

The temperature versus time histories obtained from the heat-transfer gages located on the rotating airfoils are transferred to the previously mentioned tape recorders by use of a slip-ring system. Each heat-transfer gage is a separate circuit with the power supply for the entire array located in the tunnel control room. During the experiments, a constant current of 1 mA was passed through each gage (which has room temperature resistance on the order of 50 to 100 Ω) via the slip rings. The resulting $i^2 R$ heating of the gage produced less than 0.1 percent of the gage ΔT experienced during an experiment. The slip ring was built by Poly Scientific Corporation but the assembly and associated cooling system were purchased from CTL Dixie Corporation. The slip-ring contact noise is on the order of 25μ volts compared to a heat-transfer gage output in the tens of millivolt range. These rotor heat-flux data were processed in the manner discussed above, but the tape recorder frequency response was not sufficient to resolve the rotor-blade passage phenomena that were anticipated as the rotor blades pass through the nozzle exit passages. This particular turbine has 78 rotor blades and 41 stator passages. In order to obtain these high-frequency data, a four-channel Biomation Waveform recorder (Model 2805) with a maximum frequency response of 1.2 MHz was used to obtain temperature versus time histories from four selected gages.

As previously noted, this experimental program utilized a full turbine stage with the stator nozzle, the shroud, and the rotor instrumented. Figures 4 and 5 are photographs of the instrumented stator nozzle end wall and airfoil. This instrumented stator was previously used to obtain the results presented in [11]. The stator contains approximately 58 heat-transfer gages at locations[1] discussed in detail in that reference. Figures 6–8 are photographs of the heat-transfer gage instrumentation located in the rotor pressure surface (12 gages), suction surface (7 gages), and tip (2 gages). Figure 9 is a photograph of the heat-transfer gages and pressure transducers installed in the shroud.

Pressure transducers (PCB Model 112M and 113M) were installed in the test model from the entrance section to the orifice plate in order to obtain detailed data on the starting process and the stage performance. In addition, three Kulite (XCR-080-300A) transducers were placed at the stator exit plane in the tip end wall, and six more Kulite transducers were installed at selected axial locations in the shroud above the rotor. The Kulite transducers have a frequency response on the order of 200 KHz and the PCB transducers have a frequency response on the order of 250 KHz. The Kulities were also used to help determine flow establishment time in the rotor region and to obtain stage performance data for comparison with the AiResearch steady-state rig data.

Experimental Results

Table 1 gives the experimental conditions at which heat-flux measurements were performed. The following data were obtained for corrected speeds ($N_{corr} = N_{phy}/\sqrt{T_0/513}$) rang-

[1] The locations selected for placement of these gages were mutually agreed upon by the AFAPL, Calspan and AiResearch. This particular stator has provision for trailing-edge cooling, but cooling gas was not utilized for the experiments discussed herein.

Downloaded 01 Jun 2010 to 171.66.16.62. Redistribution subject to ASME license or copyright; see http://www.asme.org/terms/Terms_Use.cfm

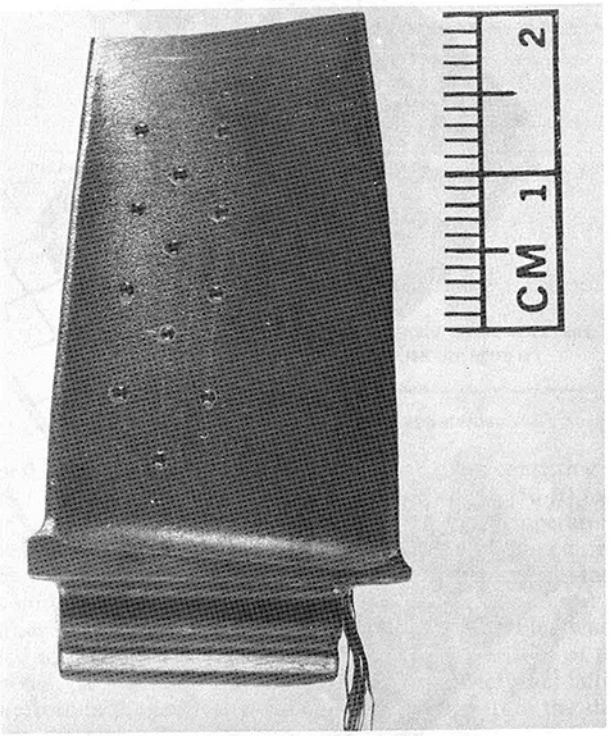


Fig. 6 Heat-transfer gages in rotor airfoil pressure surface

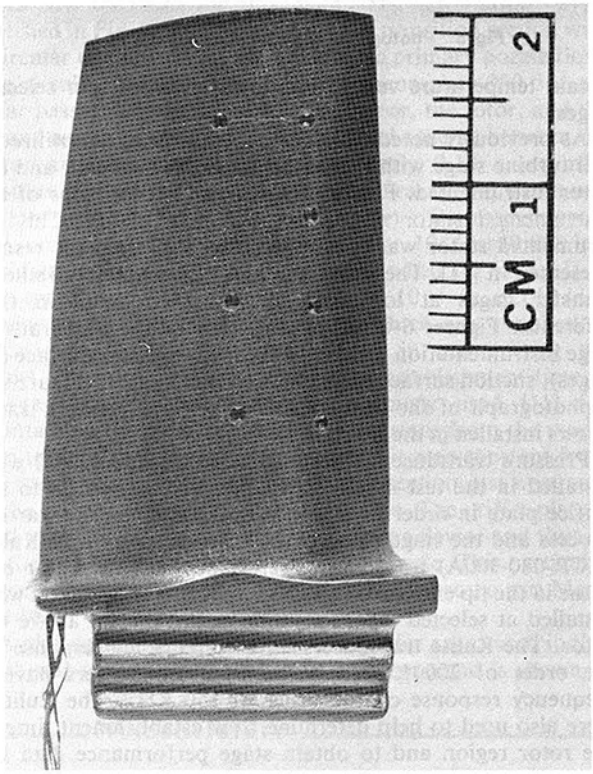


Fig. 7 Heat-transfer gages in rotor airfoil suction surface

ing from approximately 70 to 106 percent of design corrected speed: (*a*) the shock-tube, reflected-shock temperature and pressure, T_0 and P_0; (*b*) the weight flow; (*c*) Mach number at the start of the forward bullet nose; (*d*) the Mach number at the inlet to the stator nozzle/corresponding total pressure; and (*e*) the stator-nozzle inlet Reynolds number based on stator mid-chord, c_s. The engine idle condition is 78 percent corrected speed at sea level. As illustrated in Table 1, 16 separate experiments were performed. For most of the ex-

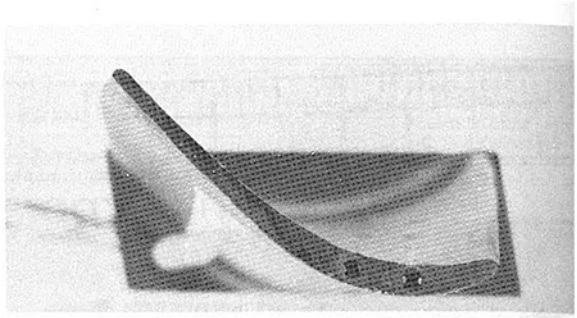


Fig. 8 Heat-transfer gages in rotor airfoil tip

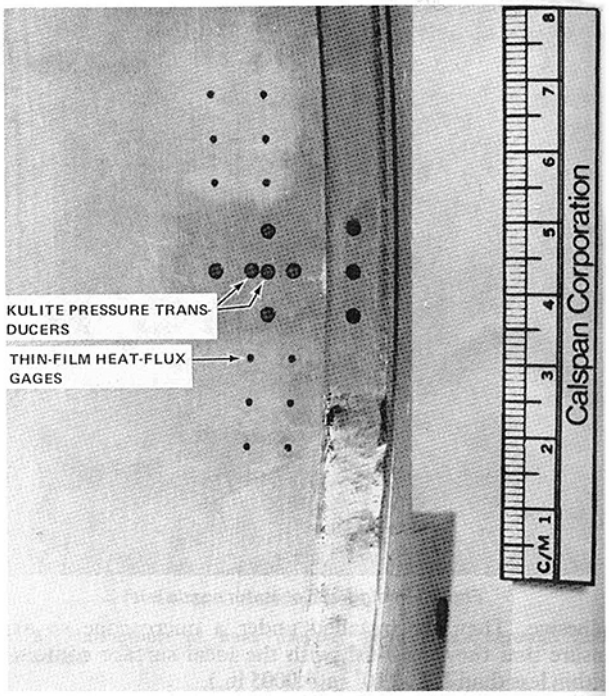


Fig. 9 Photograph of shroud heat-flux gages and pressure transducer locations

perimental conditions, approximately 90 heat-flux measurements were obtained. The different weight-flow rates were achieved by changing the model exit orifice plate shown in Fig. 2. The different total temperatures were obtained by changing shock-tube conditions.

Static pressure measurements were performed at several locations along the model and in the stationary shroud in the proximity of the rotor passage. These measurements allowed the determination of flow establishment time and the pressure change across the stage. Figure 10 illustrates the character of the model pressure histories obtained on the front portion of the inlet bullet nose, on the bullet nose just upstream of the stator inlet (hub wall) and in the exit section of the model. Typical data records obtained in the reflected-shock region for these test conditions were previously given in [22] and will not be repeated here. What appears to be noise on the pressure records is presumed to be associated with the presence of the rotor. The same pressure transducers were used at similar relative locations in the stator-only experiments [22], and the pressure records have significantly smaller fluctuations associated with them. It should also be noted that the pressure record obtained using the transducer located in the exit region is very similar to the corresponding record in the earlier experiments [22]. The early portion of the pressure record demonstrated a flow establishment time of approximately 5 to 7 ms, consistent with previous results [22] and with the estimated starting time calculated using one-dimensional gas dynamics. The exit section pressure history was used in conjuncton with known aft section physical dimensions and

Downloaded 01 Jun 2010 to 171.66.16.62. Redistribution subject to ASME license or copyright; see http://www.asme.org/terms/Terms_Use.cfm

Table 1 Experimental Conditions for Heat-Transfer Measurements

Run No.	T_0 °R	P_0 (Shock Tube) psia	N_{phy} rpm	$\%N_{corr}$ –	M) Start of Bullet Nose	$\dot{m}$ lb/sec	P_T) Stator Inlet psia	M) Stator Inlet –	R_E) c_s –
1	2970	1980	20,000	68	0.15	21.4	181	0.15	1.67×10^5
2	2970	1960	20,000	68	0.15	21.4	179	0.15	1.67×10^5
3	2970	1960	20,000	68	0.14	20.6	183	0.14	1.61×10^5
4	2580	1650	20,000	73	0.16	20.2	159	0.15	1.72×10^5
5	2600	1690	20,800	76	0.16	19.7	155	0.15	1.66×10^5
6	2710	1820	21,740	78	0.15	19.7	166	0.14	1.62×10^5
7	1370	1130	21,140	106	0.16	19.3	103	0.16	2.76×10^5
8	1600	1650	22,730	106	0.16	26.1	153	0.16	2.96×10^5
9	1600	1640	26,320	122	0.16	25.9	153	0.16	2.94×10^5
10	1620	1660	22,220	103	0.16	24.6	150	0.15	2.77×10^5
11	1620	1650	20,830	96	0.18	27.6	152	0.17	3.11×10^5
12	1620	1670	22,220	103	0.17	27.1	153	0.16	3.05×10^5
13	2620	1700	21,280	77	0.19	23.2	159	0.17	1.94×10^5
14	2620	1700	24,100	88	0.18	22.8	162	0.17	1.91×10^5
15	1620	1660	0	0	–	29.7	149	0.19	3.34×10^5
16	1600	1620	0	0	0.18	27.5	145	0.18	3.17×10^5

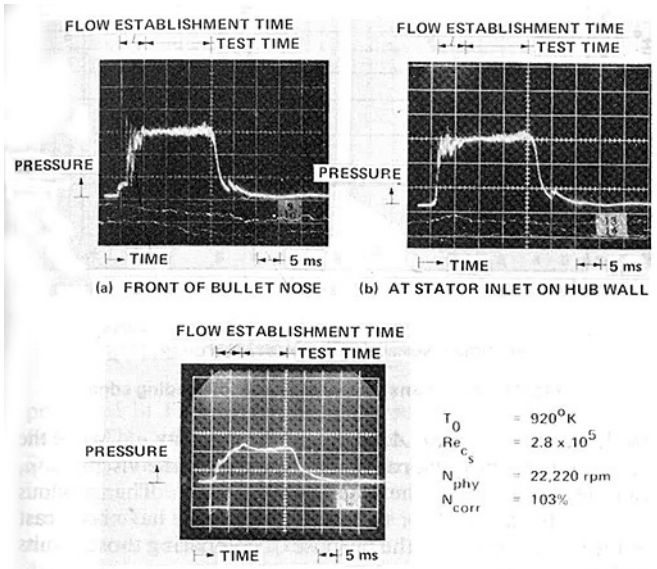


Fig. 10 Model pressure histories

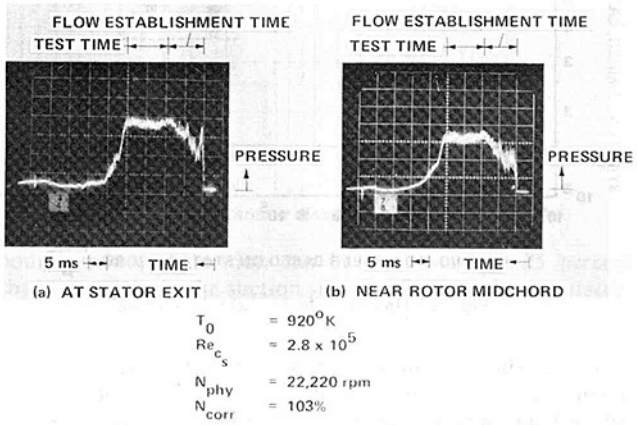


Fig. 11 Shroud pressure histories near rotor

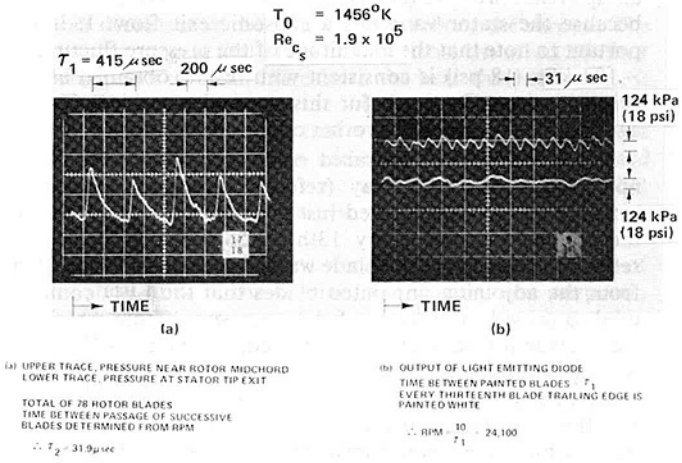


Fig. 12 Time-resolved showed pressure history and rotor speed

the shock-tube reservoir parameters in order to calculate the mass-flow rate at the orifice plate using isentropic relationships.

The pressure change across the turbine stage was found to be in agreement with the AiResearch rig-test results[2] over the entire speed range studied here. AiResearch measures the ratio of total pressure at stator entrance to total pressure at rotor exit to be equal to 1.45 for the 78 percent speed point (ground idle). The value of this ratio measured during these experiments was 1.46, which is within 1 percent of the steady-state rig data. Similar comparisons made at other operating conditions were within 2 to 3 percent.

Figures 11(*a*) and (*b*) present typical data obtained using the shroud pressure transducers for the stator exit pressure history and the pressure history near the rotor midchord. The flow establishment time within the stage is seen to be approximately 3 or 4 ms more than required for the remainder of the model and is felt to be the result of the much more complicated flow environment associated with the rotor-shroud interaction region. The pressure fluctuations observed during the test time were time resolved on a separate oscilloscope by using a delay generator on the oscilloscope sweep.

Figure 12(*a*) includes the two time resolved shroud pressure histories mentioned above for the rotor midchord and the stator exit regions. The mid-chord record shows a fluctuating pressure with a period approximately equal to the blade passage time, suggesting that the structure of the pressure history is a result of the rotor. The data shown on the lower trace of Fig. 12(*a*) were taken from a pressure transducer located at the stator exit in the tip end wall. The magnitude of the pressure variation is of the same order as that observed

[2] T. C. Booth, AiResearch Corporation, Phoenix, Arizona, private communication to M. G. Dunn, October 1980.

Downloaded 01 Jun 2010 to 171.66.16.62. Redistribution subject to ASME license or copyright; see http://www.asme.org/terms/Terms_Use.cfm

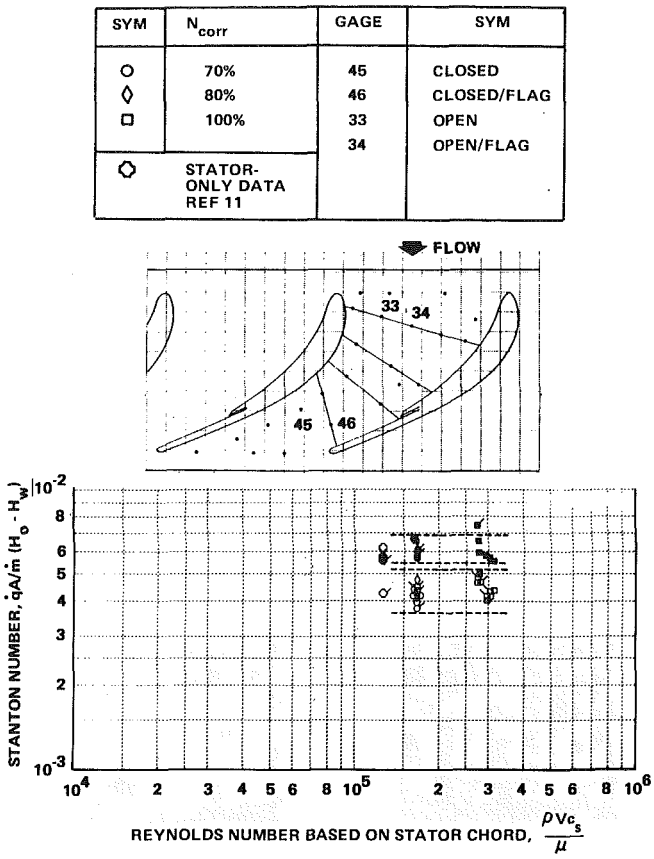


Fig. 13 Heat transfer to stator tip end wall

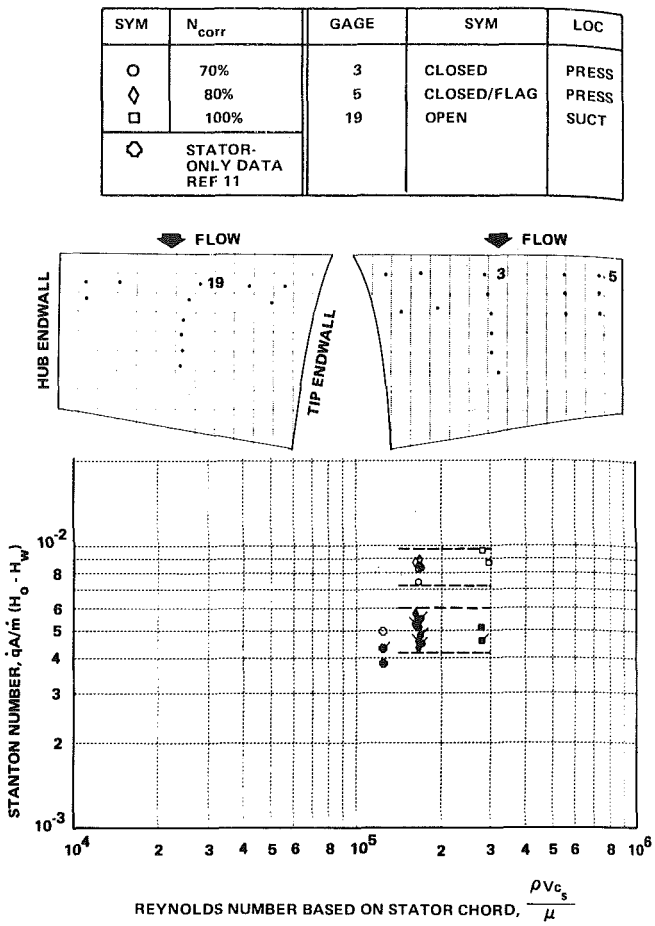


Fig. 14 Heat transfer near stator airfoil leading edge

from the shroud transducer in the immediate vicinity of the rotor, but the period is significantly different and the transition from pressure surface to suction surface is not as well defined. The measurement obtained at the stator exit suggests an upstream pressure influence at the tip end wall presumably because the stator vane has a subsonic exit flow. It is important to note that the magnitude of the pressure fluctuation ~124 kPa (18 psi) is consistent with results obtained at this condition by AiResearch for this particular turbine. Similar agreement was achieved at other operating conditions.

A gallium arsenide infrared emitting diode and a silicon npn photo-transistor array (referred to herein as a light emitting diode) were located just behind the rotor which had the trailing edge of every 13th blade painted white. The reflection from the white blade was so much greater than that from the adjoining unpainted blades that the LED could be used to provide a measure of the rotor speed from which the rotor-blade period could be calculated. A typical LED history is presented in Fig. 12(*b*). The unpainted blades can be seen as substructure on the record, but the white blades are obvious. For the case shown in Fig. 12(*b*), the average time between painted blades, τ_1, was approximately 415μ sec. Siunce there are 78 blades on the rotor, and one obtains 6 pulses every rotor revolution, the rotor speed can bew shown to be equal to RPM = $10/\tau_1$. Knowing the rotor speed and teh total number of blades on the rotor, the time between successive blade passages at a fixed point on the shroud, τ_2, was calculated to be approximately 32μs for the case given in Fig. 12(*b*).

The heat-flux data obtained in these experiments has been used to obtain plots of Stanton number, $St = \dot{q}A/\dot{m}(H_0 - H_w)$, versus Reynolds number based on mid-annular stator chord, $\rho\ Vc_s/\mu$. The Stanton number is obtained from the measured heat flux, $\dot{q}$, stator inlet area, A, the mass flow rate, $\dot{m}$, and the known enthalpy difference, $H_0 - H_w$. The Reynolds number is obtained by dividing the mass-flow rate by the stator inlet area, A, to obtain the quantity ρV, while the mid-annular stator chord, c_s, is known, and the viscosity, μ, can be evaluated at the total enthalpy, H_0. The previous stator-only data [11] for the same stator stage have been cast in the same format for the purpose of comparing those results with the full-stage results.

Figure 13 presents the data obtained for four specific gages on the stator-tip end-wall, two near the entrance to the passage (gages #33 and #34) and two further along in the channel (gages #45 and #46). The heat-flux gages selected for comparison in this discussion were chosen to be representative of the data. For comparison purposes, the previous stator-only data are included on this figure and those that follow. With the exception of the stator-only data of gage #33, the results obtained with or without the rotor are in good agreement. The stator-only data for gage #33 is the only end wall gage that deviated significantly from the corresponding full-stage data. The data presented on Fig. 13 suggest that the end-wall Stanton number is independent of Reynolds number and corrected speed over the range of those parameters investigated.

A similar plot is presented in Fig. 14 for gages located near the stator airfoil leading edge. The stator-only data of gages #5 and #3 are in reasonably good agreement with the full stage data, but the gage #19 stator-only heat flux is lower. In general, the stator-only data obtained on the suction surface near the leading edge from gage #19 towards the tip end-wall were consistent in that they were significantly lower than the full-stage data. By comparison, the results for gages located closer to the hub end wall were more consistent with the pressure surface result shown on Fig. 14 in that the stator-only data are within 15 percent of the full-stage results.

Data obtained for the aft portion of the airfoil are

Downloaded 01 Jun 2010 to 171.66.16.62. Redistribution subject to ASME license or copyright; see http://www.asme.org/terms/Terms_Use.cfm

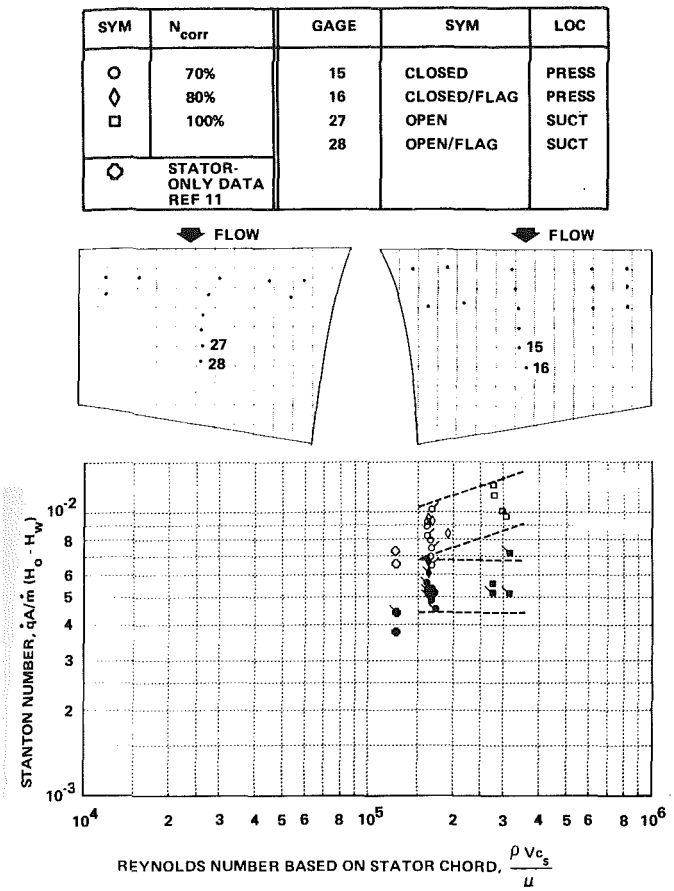


Fig. 15 Heat transfer aft of stator midchord

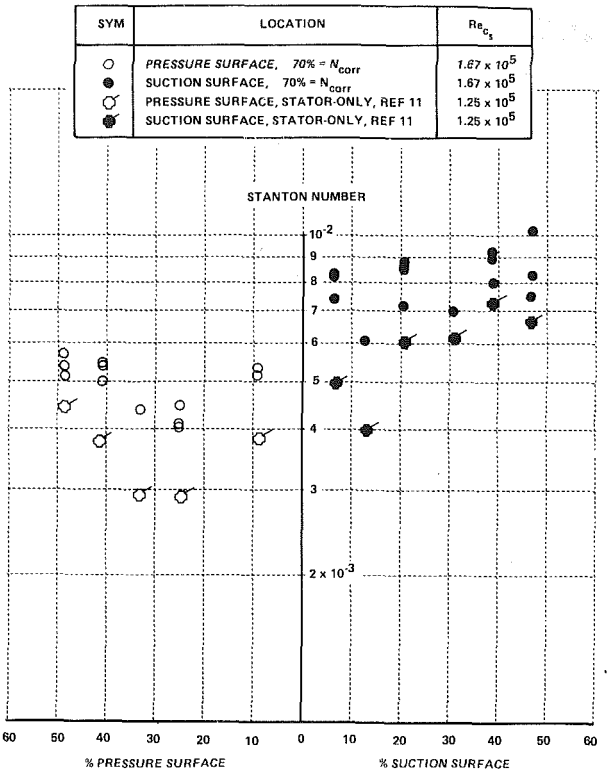


Fig. 16 Heat transfer distribution on stator airfoil

presented in Fig. 15 for both the suction and pressure surfaces. The suction surface results suggest an increasing Stanton number with increasing Reynolds number, perhaps indicating boundary-layer transition. A later plot (Fig. 16) compares the pressure surface and suction surface Stanton numbers as a function of chord position. The pressure surface data appear to be independent of both Reynolds number and corrected speed. The stator-only data were on the order of 20 percent below the full-stage data.

The data presented in Figs. 13–15 were also plotted as a function of the percent corrected speed and are given in [25]. When plotted in this manner, the stator-tip end-wall suggest that the end-wall, heat-flux values at selected locations are independent of rotor speed. With the exception of a single data point at 96 percent corrected speed, essentially the same result was found for the stator airfoil pressure surface. However, the data for the airfoil suction surface illustrate a somewhat different trend in that the heat-flux increases with increasing corrected speed. From Table 1 it can be observed that the Reynolds number was larger at the higher corrected speeds. Additional experiments are currently in progress for which the Reynolds number is being held constant while the rotor speed is varied from 78 to 100 percent in order to be more definitive about the cause of the increasing heat flux.

The data discussed above were also cast into a distribution of Stanton number over the airfoil midspan and the result is presented in Fig. 16 and compared to the stator-only result. Note that the Reynolds numbers for these two sets of data are slightly different. The 70 percent corrected speed data were selected for this comparison because of the comparable Reynolds numbers. The general shape of the distribution is qualitatively the same for both the stator-only experiments and the full-stage data, and is consistent with the distributions measured for a rotor blade by Martin et al. [26]. Evidence of boundary-layer transition can be seen near the 25 percent chord position on the suction surface. Once again, the stator-only data appear to indicate lower Stanton numbers than the corresponding full-stage data.

Heat-flux results for the rotor shroud and tip are presented in Fig. 17. The shroud region Stanton numbers are presented as a function of mid-annular rotor chord position, percent of c_r. These data, which were obtained from approximately 22 to 90 percent of the rotor chord, suggest that the Stanton number decreased in the axial direction along the shroud. The results also suggest that at a given location, the effect of rotor speed appears to be an increase in the heat flux. However, it should be noted that at the higher speed, the Reynolds numbers are also higher, so that what is observed is possibly a Reynolds number effect. In addition, the tip data presented on Fig. 17 indicate that the tip heat-flux values are somewhat greater than the shroud values, and also increase with increasing Reynolds numbers.

The shroud and tip regions were found to be the regions of highest heat flux in the turbine. For comparison purposes, one of the rotor suction surface measurements is presented in Fig. 18. Corresponding pressure surface data are presented in [25]. The resulting Stanton numbers for the blade surfaces are about 60 to 70 percent of the corresponding shroud value. These figures include typical heat-flux history records obtained from the analog network [24]. The fluctuations appearing on the heat-flux record of Fig. 18 are indicative of the flow environment and gage noise. The heat-flux measurements, for nominally the same flow conditions, are repeatable to within approximately ±5 percent. Note that the results presented in Figs. 13–17 were obtained at actual rotor speeds that were within ±3 percent of the nominal rotor speeds. The flow establishment time is noted on this record and is consistent with the values shown on the earlier shroud region pressure histories.

A comparison between the stator-only data reported in [11] and predictions obtained using flat-plate correlations, a 2-D parabolic boundary layer code (STAN 5), and a 3-D viscous code (NANCY) has recently been presented [27]. Results of

Downloaded 01 Jun 2010 to 171.66.16.62. Redistribution subject to ASME license or copyright; see http://www.asme.org/terms/Terms_Use.cfm

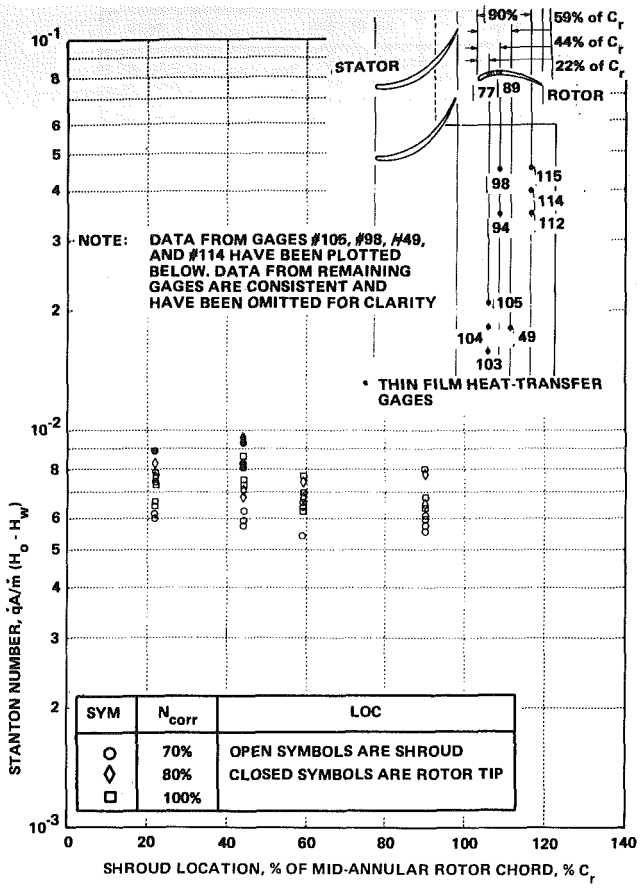


Fig. 17 Heat transfer to shroud and rotor tip

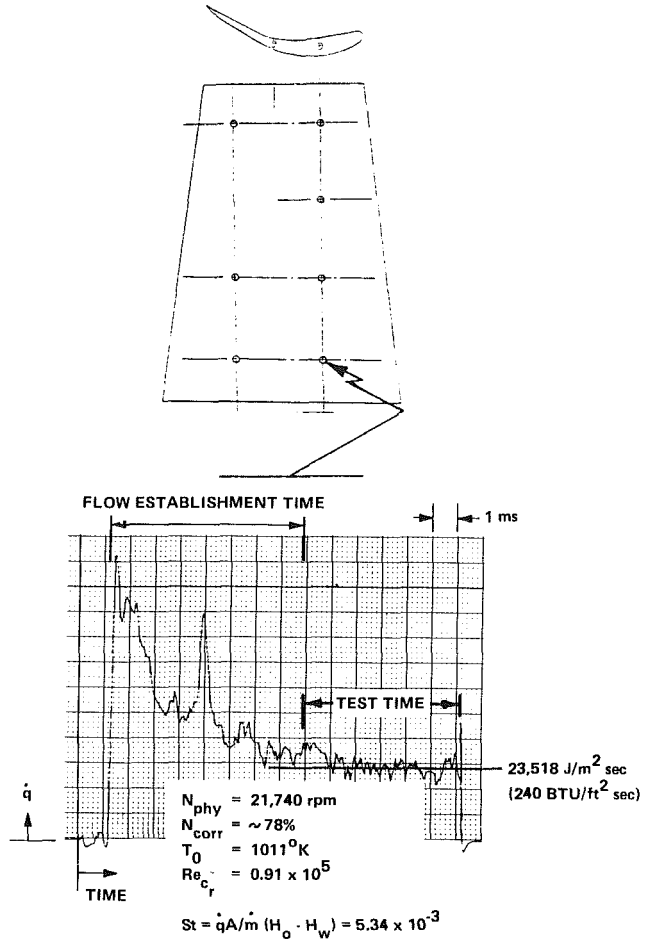


Fig. 18 Heat flux to rotor suction surface

this comparison indicated that turbulent flat-plate correlations and post-transition boundary-layer codes generally overpredict surface heat transfer, particularly on or near the vane suction surface. The 3-D calculation reasonably predicts the heat-transfer distribution on the end walls where transition is not a dominant factor.

Conclusions

Detailed heat flux and pressure data have been obtained for the full-stage AiResearch TFE 731-2 turbine using state-of-the-art shock-tube technology and transient-test techniques. The stage pressure data obtained in these experiments were found to be in good agreement with the steady-stage rig data obtained by AiResearch for this turbine. Comparisons are presented between the previous Calspan experiment with the TFE 731-2 stator-stage only and the current full-stage data. The stator end-wall Stanton number appears to be independent of stator-stage only or full-stage configuration, Reynolds number and corrected speed. The full-stage stator airfoil data demonstrate a significant influence of the pressure of the rotor at comparable Reynolds numbers, suggesting that caution should be exercised when applying stator-only results to full-stage predictions. For this turbine, the stator-only Stanton numbers for the stator airfoil are shown to be approximately 20 percent less than the corresponding full-stage results. The shroud heat flux was found to decrease with increasing axial rotor chord position, but increased with with increasing Reynolds number. The tip heat flux was found to be somewhat greater than the shroud heat flux and it also increased with Reynolds number.

Acknowledgments

This work was supported by the Air Force Aero-Propulsion Laboratory, Air Force Systems Command, Wright-Patterson AFB, Ohio, and the Naval Air Propulsion Center, Trenton, N.J., under Contract No. F33615-79-2075.

The authors are indebted to P. R. Dodge, R. W. Vershure, and T. C. Booth of the Garrett Corporation for supplying the engine hardware and for many helpful discussions regarding the stage operation. We are also indebted to J. C. Erickson, Jr., of Calspan for many helpful discussions during the course of this work.

References

1 Project SQUID Workshop on Cooling Problems in Aircraft Gas Turbines, Naval Postgraduate School, Monterey, Calif., Sept. 27-28, 1978.

2 Gas Turbine Heat Transfer and Cooling Technology—Current Status and Future Needs, Panel Discussion, 25th Annual International Gas Turbine Conference, New Orleans, La., Mar. 9-13, 1980.

3 Workshop on Fundamental Heat Transfer Research for Gas Turbine Engines, NASA-Lewis Research Center, Oct. 8-9, 1980.

4 Dodge, P. R., "Numerical Method for 2D and 3D Viscous Flows," *AIAA Journal*, Vol. 15, July 1977, pp. 961-965.

5 Katsanis, T., "Fortran Program for Calculating Transonic Velocities on a Blade-to-Blade Stream Surface of a Turbomachine," NASA Tech. Note D-5427, Sept. 1969.

6 Wu, C. H., "A General Theory of Three-Dimensional Flow with Subsonic and Supersonic Velocity in Turbomachines having Arbitrary Hub and Casing Shapes—Parts I and II," ASME Paper No. 50-A-79, 1950.

7 Smith, L. H., "Radial Equilibrium Equations of Turbomachinery," ASME 65-WA/GTP-1, 1965.

8 Horlock, J. H., and Perkins, H. J., "Annulus Wall Boundary Layers in Turbomachines," AGARD-AG-185, 1974.

9 Booth, T. C., "An Analysis of the Turbine Endwall Boundary Layer and Aerodynamic Losses," ASME Paper 75-GT-23, ASME Gas Turbine Conference, Houston, Tex., Mar. 2-6, 1975.

10 Dodge, P. R., "3-D Heat Transfer Analysis Program," Final Technical Report AFAPL-TR-64, Oct. 1977.

11 Dunn, M. G., and Stoddard, F. J., Measurement of Heat-Transfer Rate

Downloaded 01 Jun 2010 to 171.66.16.62. Redistribution subject to ASME license or copyright; see http://www.asme.org/terms/Terms_Use.cfm

to a Gas Turbine Stator," ASME JOURNAL OF ENGINEERING FOR POWER, Vol. 101, No. 2, Apr. 1979.

12 Blair, M. F., "An Experimental Study of Heat Transfer and Film Cooling on Large-Scale Turbine Endwalls," ASME *Journal of Heat Transfer*, Vol. 96, Nov. 1974, pp. 524-529.

13 Graziani, R. A. et al., "An Experimental Study of Endwall and Airfoil Surface Heat Transfer in a Large Scale Turbine Blade Cascade," ASME JOURNAL OF ENGINEERING FOR POWER, Vol. 102, Apr. 1980, pp. 257-267.

14 York, R. E., "Experimental Investigation of Turbine Endwall Heat Transfer," Detroit Diesel Allison, Final Report in preparation.

15 Dring, R. P. et al., "An Experimental Investigation of Film Cooling on a Turbine rotor Blade," ASME JOURNAL OF ENGINEERING FOR POWER, Vol. 102, Jan. 1980, pp. 81-87.

16 Louis, J. F., "Investigation of Factors Affecting Heat Transfer to Turbine End Walls," Air Force Aero-Propulsion Laboratory, TR-73-93, Oct. 1973.

17 Louis, J. F., "Heat Transfer in Turbines," Air Force Aero-Propulsion Laboratory TR-75-107, Sept. 1975.

18 Jones, T. V., and Shultz, D. L., "A Study of Film Cooling Related to Gas Turbines Using Transient Techniques," University of Oxford Report No. 1121/70, 1970.

19 Jones, T. V. et al., "Measurement of the Heat Transfer Rate to Turbine Blades and NGV's in the Transient Cascade," 6th International Heat Transfer Conference, Toronto, Canada, Paper EC-12, 1978.

20 Schultz, D. L. et al., "A New Transient Facility for the Measurement of Heat Transfer Rates," Conference Proceedings No. 229, *High Temperature Problems in Gas Turbine Engines*, Sept. 1977, pp. 31-1 to 31-27.

21 Smith, M. R., "A Study of Film Cooling Effectiveness with Discrete Holes and Slots," University of Oxford Report No. 1100/74, 1974.

22 Dunn, M. G., and Stoddard, F. J., "Development of a Shock-Tunnel Technique for the Measurement of Heat-Transfer Rate to Gas Turbine Components," 11th International Symposium on Shock Tubes and Waves, July 1977.

23 Vidal, R. J., "Model Instrumentation Techniques for Heat Transfer and Force Measurements in a Hypersonic Shock Tunnel," Cornell Aeronautical Laboratory Report No. AD-917-A-1, Feb. 1956, also WADC TN 56-315, AD97238.

24 Skinner, G. T., "Analog Network to Convert Surface Temperature to Heat Flux," Cornell Aeronautical Laboratory Report No. CAL-100, Feb. 1960; also *American Rocket Society Journal*, Vol. 30, No. 6, June, 1960, pp. 569-570.

25 Dunn, M. G., "Measurement of Heat Flux and Pressure in a Turbine Stage," AFAPL-TR-81-2055, Oct. 1980.

26 Martin, B. W. et al., "Heat Transfer to a PVD Rotor Blade at High Subsonic Passage Throat Mach Numbers," AGARD Conference Proceedings No. 229, *High Temperature Problems in Gas Turbine Engines*, Sept. 1977, pp. 1-32.

27 Winstanley, D. K., Booth, T. C., and Dunn, M. G., "The Predictability of Turbine Vane Convective Heat Transfer," Paper AIAA-81-1435, 17th Joint Propulsion Conference, Colorado Springs, Colorado, 27-30 July 1981.

Downloaded 01 Jun 2010 to 171.66.16.62. Redistribution subject to ASME license or copyright; see http://www.asme.org/terms/Terms_Use.cfm

A Simplified ASME Acceptance Test Procedure for Steam Turbines

B. Bornstein
Principal Engineer,
Bechtel Power Corporation,
San Francisco, Calif.
Mem. ASME

K. C. Cotton
Manager, Turbine Performance Engineering,
General Electric Large Steam Turbine
Department,
Schenectady, N.Y.
Mem. ASME

A simplified procedure is proposed, which reduces the cost of steam turbine acceptance testing without significantly affecting testing accuracy. This simplified acceptance test procedure is applicable to both fossil and nuclear power plants. It involves only the measurements required to calculate heat rate and required to compare the test value to guarantee. The object is to simplify the acceptance test and to reduce its cost to the extent that a no-tolerance acceptance test is conducted on every new, large steam turine-generator unit. While maintaining the traditional high level of testing accuracy, this method also facilitates periodic testing. The results of such tests can provide the information required for scheduling plant outages for maintenance or repair thus ensuring efficient operation of the steam turbine/feedwater cycle throughout the life of the turbine.

Introduction

The U.S. Test Code for Steam Turbines is set forth in the ANSI/ASME Performance Test Code PTC 6 [1]. The accuracy attainable by conformance to the provisions of this code is high enough not to require the application of any measuring tolerances to the test results.

Despite the fact that 1 percent in plant heat rate for a 1,000 MW unit is typically worth 10 million dollars [2], few U.S. utilities conduct turbine acceptance tests to verify guaranteed performance. This is presumably due to the complexity and cost associated with a full ASME acceptance test. In order to reduce both the complexity and the cost, without significantly affecting test accuracy, a simplified procedure is proposed. This procedure should result in an increase in the number of units tested and therefore in increased in the number of units tested and therefore in increased vendor accountability. On light water moderated nuclear plants it permits approaching the rated thermal output more closely. In addition, this method facilitates periodic testing, assures basic plant operation is correct and serves as a bench mark for analysis of future data.

ASME Committee PTC 6, in compliance with the PTC Supervisory Committee's instruction to evaluate alternative methods of testing, has examined both the costs and the cost effectiveness of various test methods. This paper presents the conclusions of the Committee's examination. It proposes, as an alternative to the full PTC 6 acceptance test, a turbine ASME acceptance test, here called "a simplified acceptance test," which involves considerably fewer measurements than does PTC 6. The simplified acceptance test does not provide as much information about cycle components as the full turbine acceptance test, nor is it quite as accurate; but it costs considerably less to perform, and is designed principally to determine plant heat rate without the need to apply any measuring tolerance to the test results.

Contributed by the Power Division of THE AMERICAN SOCIETY OF MECHANICAL ENGINEERS and presented at the Joint Power Generation Conference, Phoenix, Arizona, Sept. 28-Oct. 2, 1980. Manuscript received at ASME Headquarters July 2, 1980.

SI Units Conversion Table

Quantity	SI Units	Conversion factor
Temperature	°C	(°F − 32)/1.8
Pressure	kPa	6.894 × (psi)
Length	cm	2.54 × (in.)
Heat Rate	kJ/kWh	1.05516 × (Btu/kWh)

The Simplified Acceptance Test

In the simplified acceptance test, it is proposed that only the quantities necessary to calculate the actual and corrected cycle heat rate be measured. As will be shown, this test though much reduced in scope, will still answer the critical question of whether the turbine meets its guaranteed performance without application of any measuring tolerance to the results. Table 1 compares the total number of high accuracy instruments (see Fig. 3) that might typically be required for a full ASME acceptance test to that of the simplified acceptance test. The instrument count in Table 1 is based on a tandem-compound six flow turbine for a fossil fuel fired unit, rated at 770 MWe.

Reducing the scope of measurements does not eliminate the requirements for proper cycle isolation; nor does it abolish any of the other guiding principles given in the PTC6 code. It minimizes the number of high accuracy measurements and relies on station instrumentation for all other measurements. Reducing the number of measurements as just suggested should reduce the cost of the simplified acceptance test substantially when compared to the potential costs of a full ASME turbine acceptance test. Furthermore, if the connections between source point and test bench are permanently installed, the test can be repeated periodically. Information gathered from periodic tests can be used to schedule plant outages for maintenance and repair. This should reduce the frequency of plant forced outages and make for a more efficient operation of the power plant and a corresponding saving in fuel cost.

Copyright © 1982 by ASME
Downloaded 01 Jun 2010 to 171.66.16.62. Redistribution subject to ASME license or copyright; see http://www.asme.org/terms/Terms_Use.cfm

Table 1 Typical high-accuracy instrument requirements for a TC6F 770 MW fossil fuel fired unit

	Number of instruments	
	Full ASME acceptance test	Simplified acceptance test
Temperature	154	27(1)
Pressure	68	16(2)
Differential pressure	15	7(3)

(1) 3 condensate leaving condenser
8 top heater (total for 2 shells)
2 final feed
4 throttle
4 cold reheat
4 hot reheat
2 auxiliary turbine

(2) 2 top heater (total for 2 shells)
4 throttle
2 cold reheat
2 hot reheat
6 exhaust pressures

(3) 2 final feed
1 air preheater
2 auxiliary turbine
1 reheat spray
1 main steam spray

Primary Flow Measurement

One of the features that is fundamentally different in the simplified acceptance test is the location of the primary-flowrate measuring device. In the simplified acceptance test this device is welded into the high pressure feedwater line, downstream of the highest pressure heater, and directly measures feedwater flowrate to the steam generator. An accurate determination of primary-flowrate (i.e., feedwater flowrate to the steam generator) lies at the heart of any turbine acceptance test. In the past, however, this flowrate has not been measured directly. In order to determine the feedwater flowrate to the steam generator, the Code recommends the measurement of a (low pressure) condensate flowrate which, when measured in conjunction with various other flowrates, pressures and temperatures, permits the determination of the final feedwater flowrate. The principal reason for recommending this indirect measuring method is that in contrast to devices installed in high pressure welded pipe sections, a primary-flow measuring device installed in a low-pressure condensate line, can be removed for inspection both before and after the test. The criterion of permitting inspection of the primary-flow measuring device is fundamental to an acceptance test with no measuring tolerance.

At the time the test code was developed, the PTC 6 committee was not aware of any design that would permit the measurement of primary-flow with the accuracy required by the code and yet would permit inspection and cleaning of flow measuring devices welded into high pressure lines. More recently, however, a design has come to the committee's attention, which permits inspection of a primary-flow test section welded into the high-pressure feedwater piping run. This design provides a 4-in. access hole upstream of the flow nozzle as shown in Figs. 1 and 1(a).

The primary-flow section shown in this figure satisfies all code requirements for primary-flow measurement. To satisfy the inspection requirement, a 4-in. plugged inspection hole (see Fig. 1(*a*)) is provided (upstream of the nozzle in this case). Designs of this type are available for operating pressures of up to 5000 psig. Care must be exercised during an inspection that the device used (e.g., a borescope) not damage the sharp edges of the inspection hole and that the plug itself not be damaged so as not to disturb the flow profile of the water.

Flow test section cleaning can be accomplished by the use of supersonic high pressure water jet devices, which have proven very effective on similar applications.

Welding the primary flow test section into the high pressure feedwater line calls for a somewhat modified approach to the line flushing operation that normally precedes the commissioning of a plant. On fossil-fuel fired plants it is common to provide a connection just ahead of the stop check valve at the inlet to the steam generator, through which the high-pressure line is flushed back to the condenser. The steam generator is then cleaned separately. In order to minimize potential damage to the flow test section, it is suggested that the flushing connection be installed just ahead of the flow section instead of just ahead of the stop check valve. The line downstream of the flow test section can then be cleaned as part of the steam generator system.

On light-water moderated nuclear plants, each pipe section is usually cleaned separately before installation. Any subsequent flushing is therefore not likely to damage the flow test section.

If after installation, inspection reveals damage to the flow nozzle or to its throat taps, it may be possible to remedy the problem using the access provided by the inspection opening. This would depend on the type and extent of the damage, and would call for consultation and agreement between the parties to the test.

It is recognized that the newly suggested location of the

Nomenclature

h_1 = enthalpy of steam entering the main turbine
h_2 = enthalpy of steam at high pressure turbine exhaust
h_3 = enthalpy of steam entering intermediate pressure turbine
h_{11} = enthalpy of feedwater leaving feedwater system
HR_c = cycle heat rate
P_g = electrical power measured at the generator terminals
Q_c = Rate of heat input to the cycle
w_{fw} = feedwater flowrate to the steam generator
w_{rh} = steam flowrate through the reheater

Downloaded 01 Jun 2010 to 171.66.16.62. Redistribution subject to ASME license or copyright; see http://www.asme.org/terms/Terms_Use.cfm

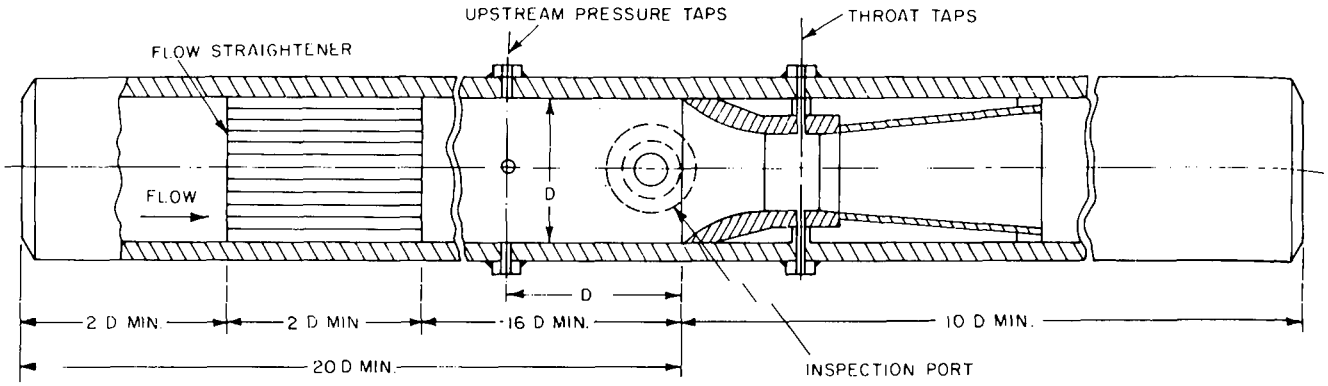


Fig. 1 Primary flow measurement section

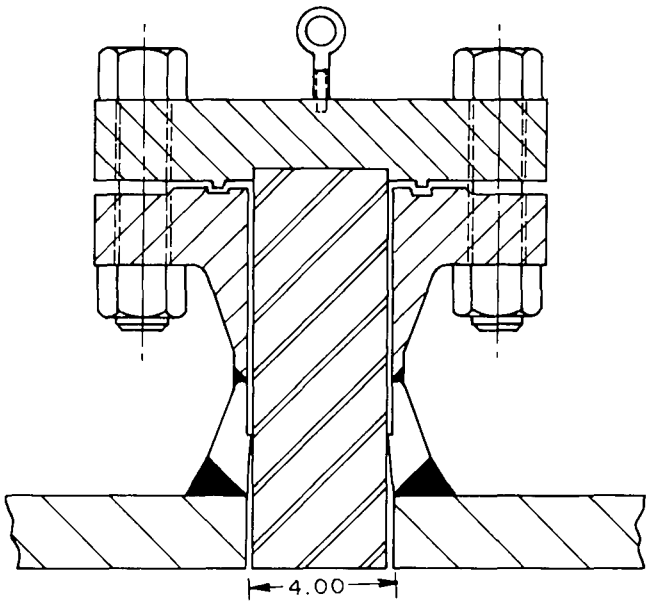


Fig. 1 (a) Inspection port

flow test section exposes it to temperatures considerably in excess of the 300°F recommended by paragraph 4.37 of the code. This paragraph seeks to minimize measurement errors due to flow nozzle distortion as well as errors that might result from the greater extrapolation of the coefficient of discharge which occur when operating at higher Reynolds numbers. An analysis of flow nozzle distortion at 5000 psig and 500 F, however, shows that a "worst case" differential expansion between pipe and nozzle results in a nozzle radial deflection of about 0.045 percent, and a more reasonable deflection expectation is 0.01-0.02 percent [3]. In other words, the incremental measuring error introduced by the elevated temperature in the flow test section is negligible.

A recent publication [4] shows that at high Reynolds numbers, the slope of the flow coefficient curve is very small. Thus, for instance, an increase in the Reynolds number from 20×10^6 to 40×10^6, increases the coefficient of discharge by less than .05 percent. Again, the elevated temperature does not introduce a significant flowrate measurement error.

Locating the flow test section in the high-pressure feedwater line will obviate the need for other flow measuring devices in that location. Total system pressure drop may therefore remain largely unaffected. If the test section does result in a slightly higher pressure drop, however, its cost is not expected to be significant. Thus, for instance, it has been calculated that for a fossil fuel fired unit, a 10 psi increment in high pressure system pressure drop will increase turbine heat rate by less than 0.5 Btu/kWh. For a 700 MW unit, this might translate into a capitalized annual cost of about $25,000 expressed in 1980 dollars (see Appendix 1).

As will be explained below, a test section located in a position to measure directly primary-flowrate to the steam generator is of great advantage because that is the quantity needed to establish station heat rate. Since no heater drains are introduced into the feedwater line downstream of the highest pressure heater, measuring the flow to the steam generator eliminates all errors in that flow measurement associated with possible heater tube leaks. Locating the primary-flow section as just described has additional benefits. On light-water moderated nuclear plants, thermal output is determined on the basis of the measured feedwater flowrate. If feedwater flowrate is measured with a substantial error such that the indicated value is higher than the true value, station electrical output may be needlessly curtailed because of the limit imposed on the thermal output of the reactor. Clearly, in such cases, as well as in many others, a high precision feedwater flowrate measurement is of great value to the owner.

Cycle Heat Rate

The simplified acceptance test takes the following approach: cycle heat rate HR_c, is defined as Q_c/P_g. In order to determine the rate of heat input to a cylce, the water and steam flowrates to and from the steam generator, as well as their associated enthalpies must be established.[1]

On light-water moderated nuclear plants, the cycle heat rate can be expressed as follows:

$$HR_c = \frac{w_{fw}(h_1 - h_{11})}{P_g}$$

Feedwater flowrate to the steam generator, possibly as modified by blowdown or by condensate flow to the control rod drives, is the only flow used in determining the rate of heat input to the cycle. The only other quantities required to establish this heat input are the enthalpies of the feedwater leaving the feedwater system and of the steam at the inlet to the turbine, that relate to the aforementioned flows (see Fig. 2).

On fossil fuel-fired single reheat units,[2] the cycle heat rate can be expressed as follows:

$$HR_c = \frac{w_{fw}(h_1 - h_{11}) + w_{rh}(h_3 - h_2)}{P_g}$$

[1] For certain cycles, ancillary heat inputs must also be established. For instance, in the case of cycles with motor driven feed pumps, the energy to drive the pumps is a heat input to the cycle. These are not central to the discussion at hand and will be ignored henceforth, however, with the understanding that in certain cycles the measurement of secondary flows, in addition to the ones discussed above, may be necessary for the determination of the total heat input. These secondary flows will be measured using station instrumentation calibrated in place.

[2] Turbines with two stages of reheating will not be considered here in detail although the method under discussion is equally applicable.

Downloaded 01 Jun 2010 to 171.66.16.62. Redistribution subject to ASME license or copyright; see http://www.asme.org/terms/Terms_Use.cfm

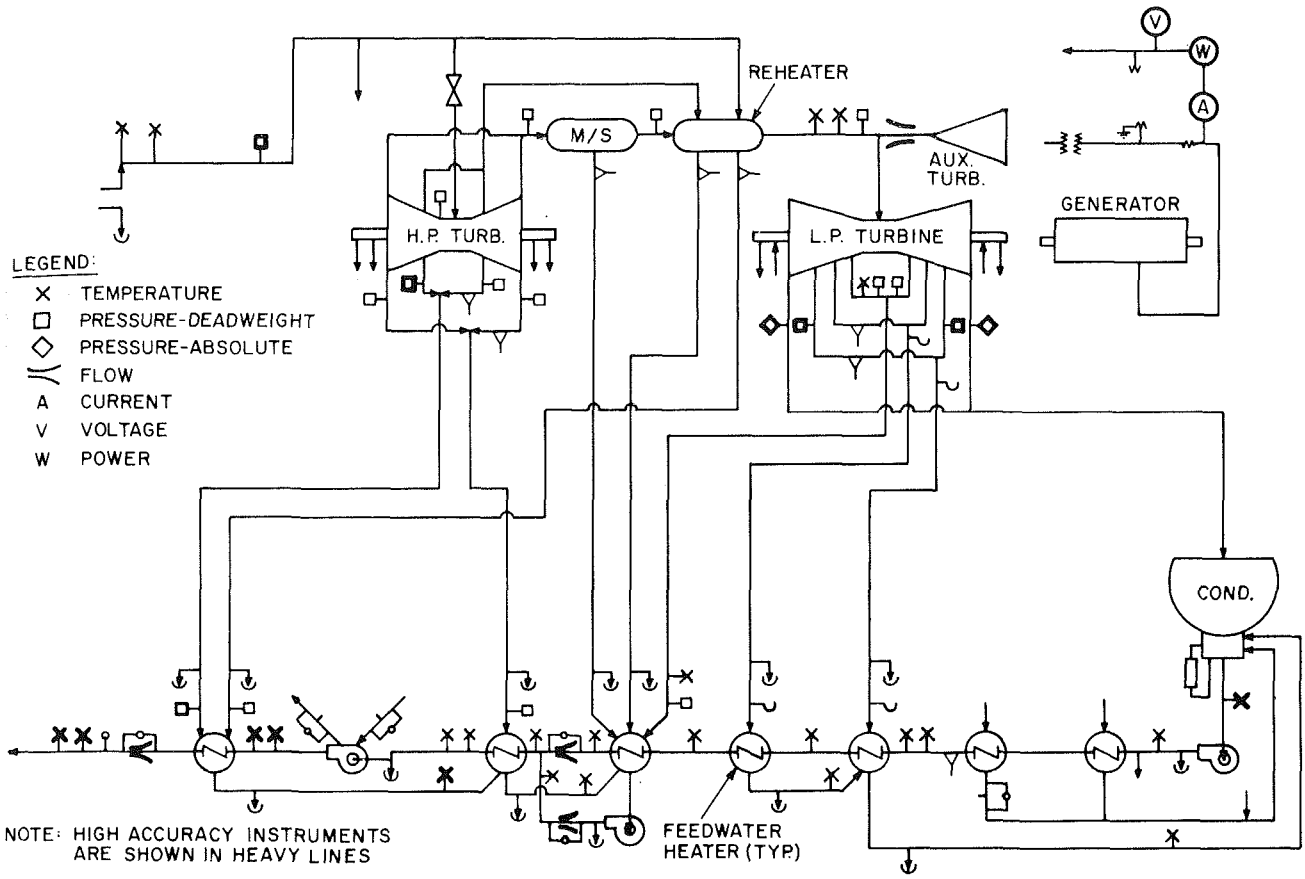


Fig. 2 Location and type of high accuracy test instrumentation for simplified acceptance test – nuclear

Both the main steam and the reheat flows, possibly as modified by desuperheater flows, are used in determining the rate of heat input to the cycle. Since reheat flow is difficult to measure accurately, the code recommends that the extraction flow to the high pressure heater be calculated on the basis of enthalpy measurements around that heater, and that reheat flow then be calculated by subtracting this extraction flow from main steam flow, with appropriate corrections for turbine leak-off and desuperheater flows[3]. The other quantities required to establish this heat input are enthalpies at the inlets and the outlets of the turbine, that relate to the aforementioned flows (see Fig. 3).

Figures 2 and 3 show all quantities that should be measured using high accuracy instrumentation in conformance with the code. They include:

(*a*) Feedwater flow to the steam generator but using the arrangement shown in Fig. 1

(*b*) All temperatures and pressures around the highest pressure heater, required to establish the complete performance of that heater

(*c*) Steam flow for auxiliary turbine drivers, if any. It is recommended that a flow measuring device with a measurement uncertainty of less than 1 percent for a fossil-fuel fired and less than 2 percent for a nuclear plant be used in this application.

(*d*) Plant electrical output

All other measurements, including those for Group 2 corrections (see paragraph 5.17 of code), can utilize station instrumentation calibrated in place.

Table 2 provides an error analysis comparison between the full ASME acceptance test and the simplified acceptance test. Table 2 shows that the uncertainty of the results established in this fashion is 0.38 percent compared to 0.27 percent (at the same confidence level) for the full ASME code test. This higher uncertainty level is still considered low enough to accept the test results without application of any measuring tolerance.

The Costs of Testing

The costs of conducting a steam turbine acceptance test may comprise one or more of the following three categories:

(*a*) Costs of power and replacement energy when the unit is shut down in preparation for the acceptance test. These costs are sometimes very high, and can become the most significant of the three categories.

(*b*) The installed cost of all test provisions (i.e., pressure taps, thermowells, flow measuring devices, isolation valves, etc.) and their associated instrumentation, specifically required, and needed only, to satisfy acceptance test requirements

(*c*) The costs of conducting the test proper and of evaluating test results. This includes the cost of calibrating the instruments; the cost of rental instruments and data processing equipment for the test, if any; the costs associated with the personnel who conduct and evaluate the test; and the costs of purchased power and replacement energy during the test, if any.

The actual cost of the test may be difficult to determine since it depends on the manner in which the individual cost components are apportioned. For instance, unit shutdown before the test might be scheduled to coincide with a plant outage that is required for other reasons. In this fashion, there may be no penalty; or a very small penalty would be assessed against the acceptance test for the outage. Similarly, if mutually agreed to by the parties, the post-test inspection outage might be delayed to coincide with another scheduled

[3] Cycles with high pressure heaters drawing extraction from the high pressure turbine proper (i.e., *above* the cold reheat) will not be considered here in detail although the method under consideration is equally applicable.

Downloaded 01 Jun 2010 to 171.66.16.62. Redistribution subject to ASME license or copyright; see http://www.asme.org/terms/Terms_Use.cfm

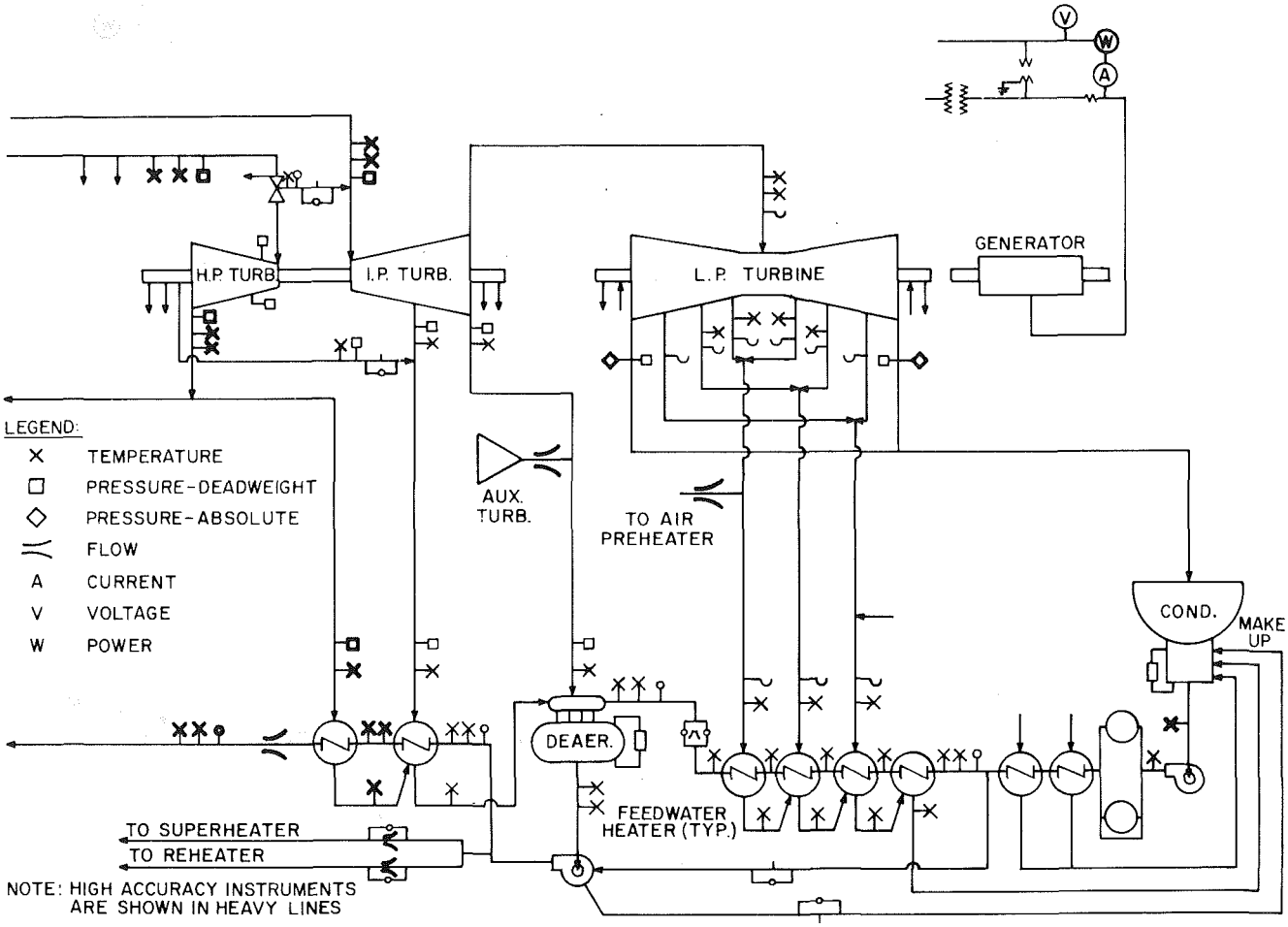


Fig. 3 Location and type of high-accuracy test instrumentation for simplified acceptance test – fossil

Table 2 Error Analysis

	Estimated Error – Percent Heat Rate	
	Full ASME acceptance test	Simplified acceptance test
Primary flow (1)	0.15	0.25(5)
Electrical output	0.15	0.15
Pressures and temperatures	0.05	0.05
Group I corrections (2)	0.15	0.22(6)
Isolation	0.05(4)	0.10(4)
Total Error (3)	0.27	0.38

(1) Laboratory calibrated
(2) See paragraph 5.15 of code
(3) Total is defined as square root of the sum of the squares of the individual errors.
(4) It is not expected that cycle isolation will be affected by the type of test conducted; however, an arbitrary penalty of 0.05 percent against the simplified test has been included.
(5) Flow will be measured at a higher temperature and therefore at a higher Reynolds number than in full ASME acceptance test. The added 0.10 percent represents an allowance for a possible extrapolation error in the nozzle flow coefficient at the higher Reynolds number; and for the added effect of nozzle distortion, if any. Note that no credit was allowed for the direct measurement, which eliminates errors in flow measurement due to possible heater tube leaks.
(6) For underlying assumptions, see Appendix 2.

plant outage, again completely eliminating or largely reducing the outage penalty charged to the test. Other testing costs, such as the costs for certain instruments, or the costs of calibrating plant instruments, may be similarly difficult to apportion between the acceptance test and other uses.

In order to minimize costs all test provisions required for the simplified turbine acceptance test should be made during plant design. Furthermore, if necessary, provisions should be made so that a full ASME turbine acceptance test is not precluded, should the need for such a test arise at a later time. For instance, a straight horizontal run having a minimum length of 30 pipe diameters, perhaps including also a removable pipe spool piece, should be provided in the condensate piping to allow for the future installation of a primary flow section in accordance with the Code.

It is estimated that the installed cost of permanent provisions for a full PTC 6 test on a light-water moderated nuclear turbine cycle is on the order of $500,000 (expressed in 1980 dollars). This figure includes only the cost of the pipe taps, the thermowells, and the necessary wiring, conduit and

Downloaded 01 Jun 2010 to 171.66.16.62. Redistribution subject to ASME license or copyright; see http://www.asme.org/terms/Terms_Use.cfm

tubing between the test points and convenient and safe test bench locations. It is noteworthy that the cost of the provisions just cited is highly sensitive to the distance between test points and test benches, since this distance affects the cost of the interconnecting wiring and tubing. On one boiling water reactor unit, it was estimated that about 70 percent of the total cost of PTC 6 test provisions was assignable to the installed cost of tubing alone. The simplified acceptance test, by minimizing the number of required test connections will reduce test costs by substantial margins. It is estimated that if temporary test connections are used, the simplified test will reduce the test cost by about $150,000 to $250,000 (see Appendix 3). If permanent test provisions are installed, these figures will substantially increase.

Electrical Output Measurement

In order to meter electrical output with the desired accuracy and without shutting down the plant for installation of the metering devices, it is recommended that the plant design incorporate separate potential transformers (PT's), the existing metering current transformers (CT's), wiring and associated electrical devices all dedicated to power metering, as well as connection points for plugging in a high accuracy test device which would be used to meter electrical output for the full ASME test or the simplified acceptance test.

Cycle Isolation

The cycle isolation requirements of PTC 6 are sometimes citied as contributors to the cost of an acceptance test. The provisions for detecting and minimizing the quantity of various vents and drains that bypass the normal flow path and leave the cycle during steady-state conditions, however, should be incorporated into the design of *any* plant, and thus the cost of such provisions should *not* be charged against the acceptance test. There are many piping systems, such as emergency drains, recirculation lines and auxiliary steam lines that are connected to the normal cycle but are required only during start-up and loading. However, because leakage in any of these lines will adversely affect performance, positive isolation of these systems is necessary. Modern plants are usually designed with isolation valves which can be used to isolate most of these systems adequately. Leaks can be detected by using tell-tale valves or by pipe temperature detection. Such detection can be effected by the use of strap-on RTD's. Alternatively, as an equally effective method for areas that are accessible and safe, a roving operator can check leaks by locating pipes that feel warm to the touch. This should be done just before an acceptance test is conducted and on a periodic basis, and is probably the most economical method for leak detection.

The simplified acceptance test, though relatively inexpensive, will answer the critical question of whether a turbine has met its guaranteed performance. If it is established that the turbine does not operate in accordance with guarantees, further measurements such as those needed to define the performance of the individual turbine-generator components may be needed. The extent of such further measurements could conceivably involve a full code acceptance test. In such an eventuality, however, this test would most likely be conducted by the manufacturer without charge to the owner.

Summary

The simplified turbine acceptance test, as distinguished from the full ASME turbine acceptance test, measures high pressure feedwater flow directly. This measurement, combined with a small number of other high-accuracy measurements, permits the determination of whether a turbine has met its performance guarantee. The accuracy of the simplified method is such that measuring tolerances should not be applied to the test results.

The substantial reduction in testing costs afforded by this method should make it economical for the owners to test every large steam turbine that they purchase, and evaluate its performance.

Since turbine test provisions can be permanently installed, turbine cycle performance can be monitored by repeating the test periodically, permitting the evaluation of performance trends at a relatively low cost.

The use of a laboratory calibrated flow test section, which measures feedwater flow directly, will permit the owners of light-water moderated nuclear plants to operate more closely to the full capacity of the licensed thermal output of their plant, without exceeding it.

Acknowledgment

In order to explore the feasibility and cost effectiveness of the simplified turbine acceptance test concept, the chairman of ASME Committee PTC 6 appointed a number of members to an ad hoc committee. The ad hoc committee consisted of the following members, listed alphabetically: H. S. Arnold, Public Service and Gas Co., Newark, N.J.; B. Bornstein, Bechtel Power Corp., San Francisco, CA.; W. A. Campbell, Philadelphia Electric Co., Philadelphia, PA.; K. C. Cotton, General Electric Co., Schenectady, N.Y.; N. R. Deming, Westinghouse Electric Corp., Lester, PA.; J. Greco, formerly with TVA, Chattanooga, TN.; D. L. Knighton, Black and Veatch Consulting Engineers, Kansas City, MO.; C. B. Scharp, Baltimore Gas and Electric Co., Baltimore, MD.

The authors are indebted to the various members of ASME Committee PTC 6, and in particular to their fellow members on the ad hoc committee, whose suggestions and criticisms helped shape this paper.

References

1 ANSI/ASME, PTC 6-1976 Steam Turbines.

2 Cotton, K. C. et al., "A Procedure for Determining the 'Optimum' Accuracy of an Acceptance Test on a Cost/Effectiveness Basis," *Proceedings of the American Power Conference*, Vol. 40, 1978, pp. 693-712.

3 General Electric Company Internal Report No. TR-58-I.S-6: "Flow Nozzle Analysis."

4 Benedict, R. P., "Generalized Fluid Meter Discharge Coefficient Based Solely on Boundary Layer Parameters," ASME JOURNAL OF ENGINEERING FOR POWER, Vol. 101, Oct. 1979, pp. 572-575.

APPENDIX 1

The cost of heat rate was calculated on the basis of the following assumptions:

Levelized fuel cost	$2.00/Million Btu
Levelized plant capacity factor	70 percent
Fixed charge rate	20 percent
Boiler efficiency	85 percent

For an electrical output of 700 MW, the cost of 0.46Btu/kWh in turbine heat rate is:

$$\frac{0.46\text{Btu/kWh} \times 7 \times 10^5\,\text{kW} \times (8760 \times 0.70)\text{h/yr} \times \$2.00/10^6\,\text{Btu}}{0.85 \times 0.20} = \$23{,}200$$

Note: This calculation is based on generating the same electrical output in the design with the higher pressure drop as in the design with the lower pressure drop. For the cycle under consideration, a 10 psi increase in high pressure system pressure drop increases the 4,000,000 lbm/h throttle flow by about 300 lbm/h. It was assumed that the higher pressure drop design would not affect piping and equipment sizes. Although it is recognized that some capital cost increase could result from the increased pressure drop, the magnitude of the cost increase is likely to be small. Therefore, no capital cost penalty was assessed against this design.

Downloaded 01 Jun 2010 to 171.66.16.62. Redistribution subject to ASME license or copyright; see http://www.asme.org/terms/Terms_Use.cfm

APPENDIX 2

The following analysis was conducted for a fossil fuel fired cycle with seven feedwater heaters, including a deaerator. The figures show the effect on turbine heat rate, caused by various deviations from contract cycle parameters, as listed:

Deviation from Contract Cycle	Estimated Error – percent of turbine heat rate	
5°F in heater terminal diff.	0.03	
5°F in heater approach temp.	0.004	0.08(1)
3 percent points in extraction line ΔP	0.02	
100 percent in boiler feed pump seal flow		0.07
20 percent in boiler feed pump enthalpy rise		0.12
Allowance for miscellaneous cycle components		0.15
$\Sigma X^2 =$		0.049
$\sqrt{\Sigma X^2} =$		0.22

(1) The 0.08 represents the combined effect of the items under consideration, and was arrived at in the following manner:

Since the highest pressure heater is accounted for in the test proper, its effect is not included herein. The deaerator is not subject to variations in terminal difference or approach temperature. The combined effect is therefore based on the individual effects of terminal differences and approach temperatures on five heaters, and on the effect of extraction line pressure drop on six heaters.

APPENDIX 3

The figures tabulated below give a comparison between the costs of performing full ASME acceptance tests and the simplified acceptance tests. The figures represent estimates of expenditures for conducting an acceptance test and are based on the use of temporary test connections. Costs are at 1980 price levels.

Comparative Testing Costs – 1000's dollars

	Full ASME acceptance test		Simplified acceptance test	
	Nuclear unit	Fossil unit	Nuclear unit	Fossil unit
Upgrade station instrumentation (1)	Base	Base	32	35
Radioactive tracer (2)	44	-0-	-0-	-0-
Turbine testing provisions	31	25	8	6
Test equipment (3)	68	68	8	11
Instrument installation & calibration	80	30	6	6
Data takers	50	50	5	5
Preparation of results (4)	57	55	14	18
Comparative totals – nuclear	330		73	
Comparative totals – fossil		228		81
Incremental test costs – nuclear	257		Base	
Incremental test costs – fossil		147		Base

(1) Includes incremental cost of primary flow nozzle
(2) Includes cost of technicians who operate radioactive tracer equipment
(3) Includes technicians' time for preparing, installing and removing test equipment
(4) Includes engineers' time for planning and analyzing results during and after test; also cost of computer programming and machine time

Downloaded 01 Jun 2010 to 171.66.16.62. Redistribution subject to ASME license or copyright; see http://www.asme.org/terms/Terms_Use.cfm

Performance Characteristics of the Lysholm Engine as Tested for Geothermal Power Applications in the Imperial Valley[1]

R. F. Steidel, Jr.
Mechanical Engineering,
University of California,
Berkeley, Calif.

H. Weiss
Mechanical Engineering,
University of California,
Lawrence Livermore National Laboratory,
Livermore, Calif.

J. E. Flower
Gibbs and Hill,
San Jose, Calif.

This is a description of the performance tests of a Lysholm engine completed at the Lawrence Livermore National Laboratory at the University of California. The Lysholm engine is a rotary displacement engine which can accept a low quality (vapor fraction) two-phase mixture. Generally, the well-head condition of geothermal fluids is a mixture of liquid and vapor, with quality up to 40 percent, although for most liquid dominated geothermal resources the vapor fraction is considerably less than 40 percent. As a thermodynamic process, using mixed phase flow has the potential for using significantly more of the available energy output per pound of fluid, as contrasted with other processes that either transfer heat energy to a second fluid, or use only the vapor fraction and discard the liquid. In our tests, the quality was varied between 8 and 27 percent. Our results indicate that the Lysholm engine can operate well with a two-phase mixture as a working fluid. The maximum observed engine efficiency was 53 percent at 8000 rpm, with an inlet pressure of 190.6 psia, 22.2 percent quality, and an exhaust pressure of 30.6 psia. The best results were observed at the higher speeds and with exhaust to an above-atmospheric back pressure.

Introduction

Geothermal fluids at wellhead conditions in the Imperial Valley, California, consist of a mixture of liquid and vapor, with a quality (vapor fraction) ranging to 40 percent. Pressure and temperature may be as high as 400 psia (2.75 MPa) and 450°F (382°C). Dissolved minerals are as much as 30 wt percent of the fluid. Because of the variety of thermodynamic states and chemistries in the geothermal resources of the Imperial Valley, we need complete technical and economic understanding of many different energy-conversion machines and systems to select the machine that will best produce usable energy. Thermodynamic performance evaluation, such as presented in this report, is a first step toward that understanding.

If all of the wellhead fluid is expanded in the energy conversion machine, there is significantly more potential for using all of the available energy in the geothermal fluid. This contrasts with other thermodynamic processes, such as the binary process or the flashed-steam process, that either transfer heat energy to a second fluid or use only the vapor fraction and discard the liquid [1].

The Lysholm engine or helical expander is an energy-conversion machine that can operate using a two-phase flow mixture. The expander consists of two side-by-side meshing, helical, counter rotating rotors (Fig. 1)[2]. It is a positive-displacement machine that takes in a discrete volume of fluid. The fluid then expands against the rotors, doing work. Physical contact between the rotors is prevented by a set of timing gears. The absence of internal wearing parts, the inherent mechanical balance, and the ability to operate at high rotary speeds are all attractive features of the Lysholm design. The rotors are basically rugged and their meshing action tends to keep them clean by continuous scraping that removes scale.

An expander and an engine carry slightly different connotations. In an expander, the primary objective is the expansion of a gas or fluid to a lower pressure. Power is recovered as a by-product. Expanders are used widely in cryogenic process engineering. The conversion of energy with the production of power is the primary objective of an engine. Lysholm referred to his design as an engine, and so do we.

The Lysholm design is perhaps better known as a gas compressor, and Lysholm compressors are manufactured in a wide range of sizes by a number of companies throughout the world. As either a compressor or an engine, its features are very attractive for severe environments.

The original development of the Lysholm design dates back over 40 years to when A. Lysholm designed and built the first

[1] This work performed under the auspices of the U.S. Department of Energy, Contract No. W-7405-Eng-48.

Contributed by the Energetics Division for publication in the JOURNAL OF ENGINEERING FOR POWER. Manuscript received at ASME Headquarters March 25, 1981.

[2] Reference to a company name does not imply approval or recommendation of the product by the University of California or the U.S. Department of Energy to the exclusion of others that may be suitable.

Copyright © 1982 by ASME

Downloaded 01 Jun 2010 to 171.66.16.62. Redistribution subject to ASME license or copyright; see http://www.asme.org/terms/Terms_Use.cfm

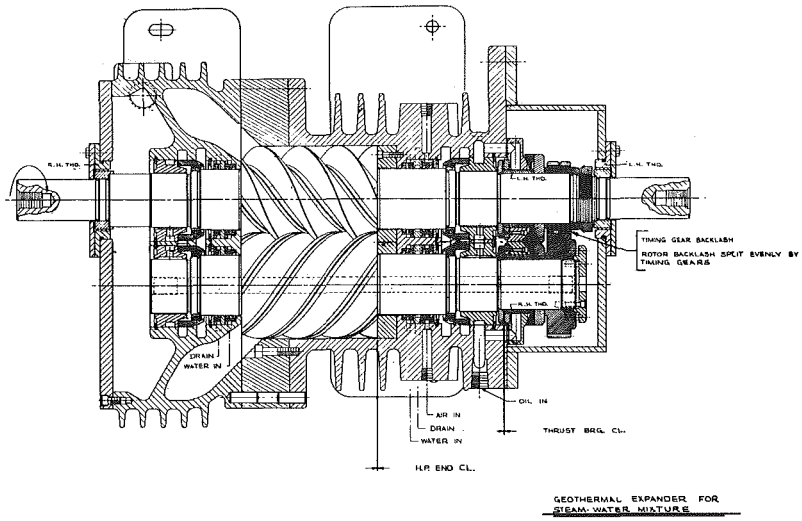


Fig. 1 Cross section of Lysholm engine (drawing by Gardner-Denver Company)

practical helical-lobe compressor. At that time, he was Chief Engineer of A. B. Ljungstroms Angturbin, which was the earlier name of Svenska Rotor Maskiner. His work is well documented by numerous patents [2] and by his paper [3] published by the Institution of Mechanical Engineers in 1943. In 1952, H. R. Nilssen patented a helical rotary engine [4]. In 1966, Lysholm described the application of the design as a screw engine [5]. In 1973, R. Sprankle patented the use of the Lysholm engine for a geothermal application where the geothermal fluid is predominantly water [6]. At Lawrence Livermore National Laboratory, the Lysholm engine has been studied extensively for high-temperature applications and as a topping engine for Rankine cycles [7]. The rugged characteristics of the engine for use in severe environments were recognized by Wells et al. [8].

The basic concept of the Lysholm engine for geothermal application has been demonstrated in field tests of a modified air compressor unit with 6 in. dia rotors by R. Sprankle of the Hydrothermal Power Company, Ltd. [9]. Tests have been conducted by the Hydrothermal Power Company at the Cerro Prieto field in Mexico and at the East Mesa geothermal field in the Imperial Valley of California. In both locations, the major limitations on the tests were the available wellhead conditions.

Tests of this same unit were conducted at Lawrence Livermore National Laboratory in April 1975 [10]. Tests were run at operating speeds of 3000, 4000, and 5000 rpm. However, the pressure and temperature measurements of the laboratory tests were at best crude. For example, the exhaust pressure was not measured. The inlet pressure was measured after the inlet port, rather than before, and thus the throttling losses through the inlet port were not charged to the engine. This resulted in a very generous and erroneous engine efficiency for that specific machine.

We realized that further and more complete testing of the Lysholm engine was necessary before any conclusions could be made about its applicability to geothermal energy conversion. The performance characteristics over a broader range of inlet and exhaust conditions needed to be determined, including both higher and lower back pressures and higher operating speeds. In this paper, we report the first results of a more complete and more accurate study of the performance characteristics of the Lysholm engine.

Lysholm Engine Data

The Lysholm engine that we tested (Fig. 1) was a modification of the basic air compressor manufactured by the Gardner-Denver Company (Gardner-Denver machine "SC-71"). The length of the rotors was increased by a half-diameter to give 320 deg wrap angle on the male rotor, permitting the use of built-in volume ratios above five.

Standard castings, bearings, seals, and gears were all used. A fabricated sandwich piece was mounted between cylinder and discharge housing to accommodate the longer rotor. Removable plates at the inlet permit simple changes in the built-in volume ratio. The rotors are made of stainless steel and coated with Teflon to provide safe operation with small clearances. The rotor housing was Teflon coated with sacrificial zinc inserts for improved corrosion protection.

The machine has a series of floating carbon ring seals at each end, separating the working fluid (vapor and liquid) from the lubricating oil. Water is pumped around the seals to maintain separation and to prevent excessive shaft heating. Air is introduced around the bearings, at the high-pressure end only, to help prevent seal water from entering the lubricating-oil passages.

To uniformly heat the engine on starting and to cool the engine on shutdown, a 1/8 hp turning motor was attached to the male-rotor shaft at the high-pressure end. This motor was set to turn at approximately 10 rpm.

The following are some of the basic data concerning the engine:

Rotor diameter	5.120 in. (130 mm)
Rotor length	6.519 in. (166 mm)
Male-rotor wrap angle	320 deg
Displacement (theoretical outlet volume)	0.0423 ft^3/rev (0.0012 m^3/rev)
Max recommended built-in volume ratio	5.3
Min recommended built-in volume ratio	1.6
Male-rotor shaft speed	2000-9000 rpm
Male-rotor tip speed	43-200 ft/s (13-61 m/s)
Max inlet pressure	250 psia (1.75 MPa)
Min outlet pressure	4 psia (0.03 MPa)
Max inlet temperature	500°F(260°C)

For reasons of safety, the engine was connected through a timing belt to the eddy-current brake. This allowed a 3:1 speed reduction and thus kept the brake speed below 2760 rpm.

Downloaded 01 Jun 2010 to 171.66.16.62. Redistribution subject to ASME license or copyright; see http://www.asme.org/terms/Terms_Use.cfm

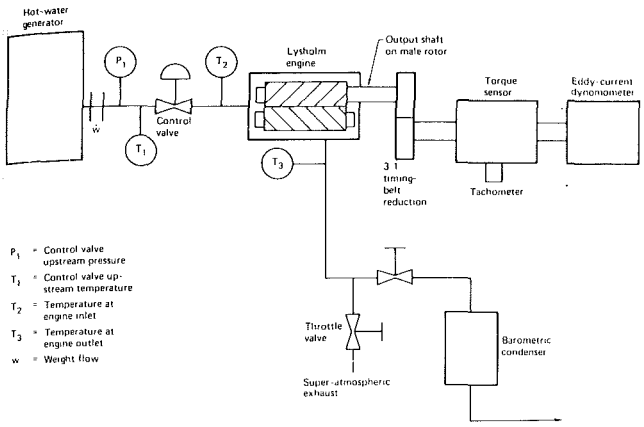


Fig. 2 Lysholm engine test setup

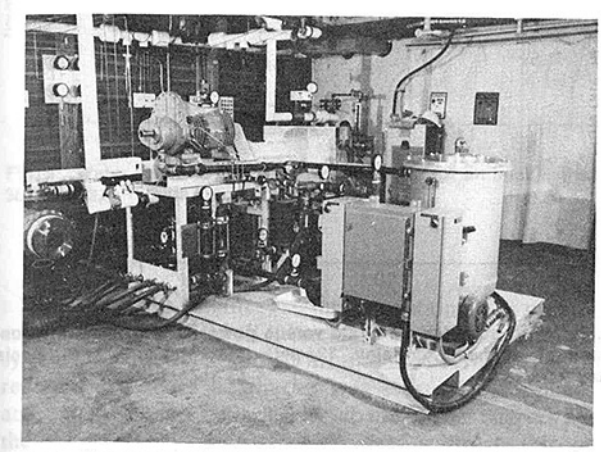


Fig. 3 Photograph of Lysholm engine installed on the test stand

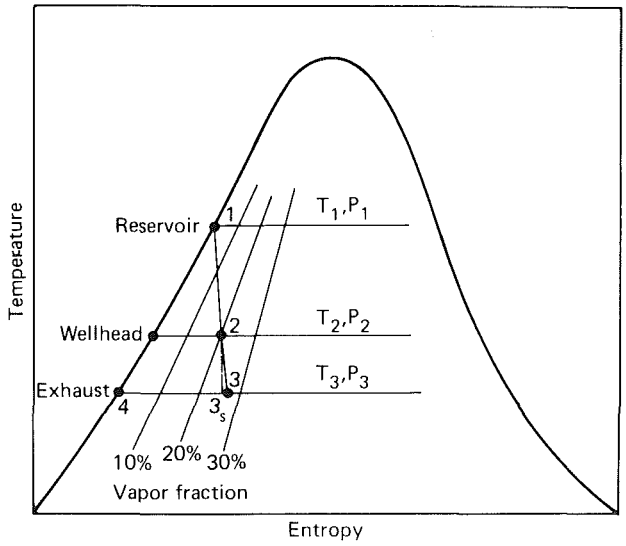


Fig. 4 Temperature-entropy diagram for water, showing reservoir, wellhead, and exhaust conditions

Test Description

A schematic diagram of the test setup is shown in Fig. 2, and a photo of the setup in Fig. 3. As indicated, we determined the performance of the engine by means of speed and torque measurements in conjunction with an eddy-current dynamometer. The mass flow rate, temperature, and pressure were measured in the compressed liquid state, just in front of the system control valve. Temperature was also measured at the exhaust of the engine; the exhaust pressure was derived

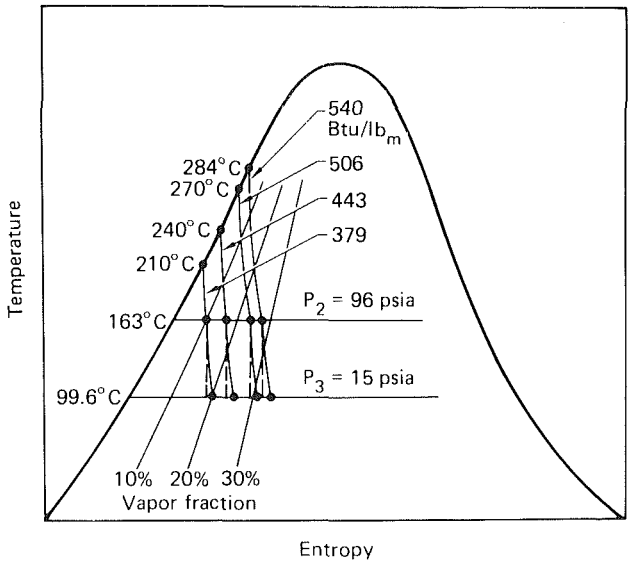


Fig. 5 Temperature-entropy diagram for water, showing four separate reservoir conditions for an inlet pressure of 96 psia and an outlet pressure of 15 psia

from the temperature. Inlet pressure to the rotors was varied from 25.9 psia (0.18 MPa) to 198 psia (1.39 MPa). The quality (vapor fraction) at the inlet to the rotors ranged from 6.7 to 27.3 percent. We varied the back pressure from a minimum of 4.9 psia (0.04 MPa) to a maximum of 34 psia (0.24 MPa). To obtain a desired speed, we adjusted the eddy-current brake and the mass flow rate.

Hot, pressurized water from the hot-water generator was throttled through a control valve and flashed to a two-phase fluid having the vapor fraction, temperature, and pressure (X_2, T_2, P_2) desired for the particular test being run. After passing through the engine, the fluid was either exhausted to the atmosphere or to a direct-contact condenser. Noncondensible gases were removed from the condenser by means of a water-seal-ring pump.

Figure 4 is a portion of the temperature-entropy diagram for water, showing the state points of the fluid at various locations. The fluid in a geothermal reservoir is actually a compressed liquid, but, because the enthalpy of a compressed liquid can be neglected, the fluid is simulated as a saturated liquid at point 1. The state conditions for any point 1 ("in the reservoir") were established by presetting the gas-fired, hot-water generator.

The hot-water generator can output 5500 lb_m/h at 5.5×10^6 Btu/h (2500 kg/h at 5.8 GJ) [11]. The temperature is maintained by air dampers and gas-control valves, and the pressure is controlled by a throttled by-pass valve. The maximum temperature and pressure of the hot water leaving the generator is 550°F at 1000 psia (288°C at 7 MPa). This means that the maximum enthalpy of the hot water leaving the generator is 549.3 Btu/lb_m. The maximum mass flow rate that can be maintained is 2.25 lb_m/s (1.01 kg/s). Safety features on the generator include low-water gas cut-outs, pressure-relief valves, and air-operated, quick-acting stop valves.

In a self-pumping mode of geothermal-well operation, the fluid emerges at the wellhead as a two-phase fluid. Point 2 simulates the wellhead condition. In operation, the hot water generator establishes state point 1 and throttling of the fluid through the control valve to a prescribed pressure defines state point 2. Expansion of the two-phase fluid through the engine occurs between points 2 and 3. The liquid phase, which constitutes about 80 percent of the mass flow, continues to evaporate during the expansion process. In this respect, the

Downloaded 01 Jun 2010 to 171.66.16.62. Redistribution subject to ASME license or copyright; see http://www.asme.org/terms/Terms_Use.cfm

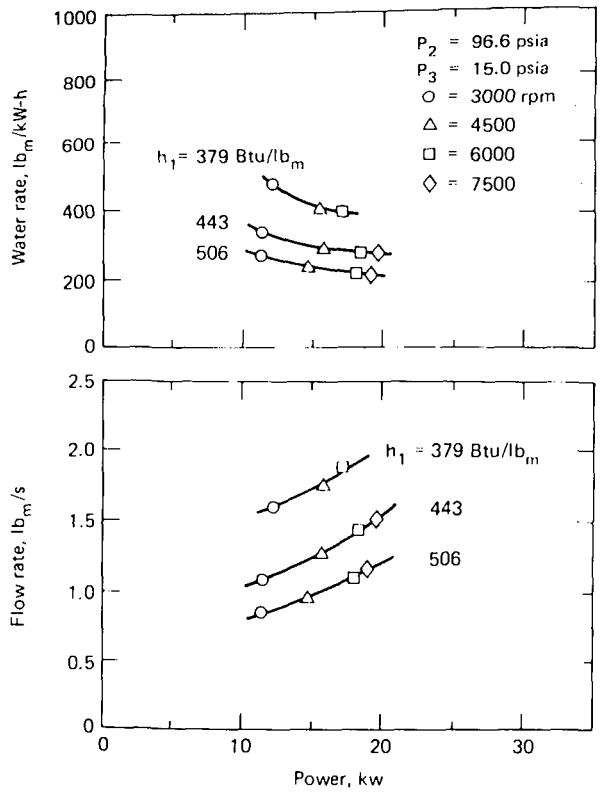


Fig. 6 Water rate and flow rate versus power for three separate conditions of wellhead enthalpy, 96-psia inlet pressure, and 15-psia exhaust pressure

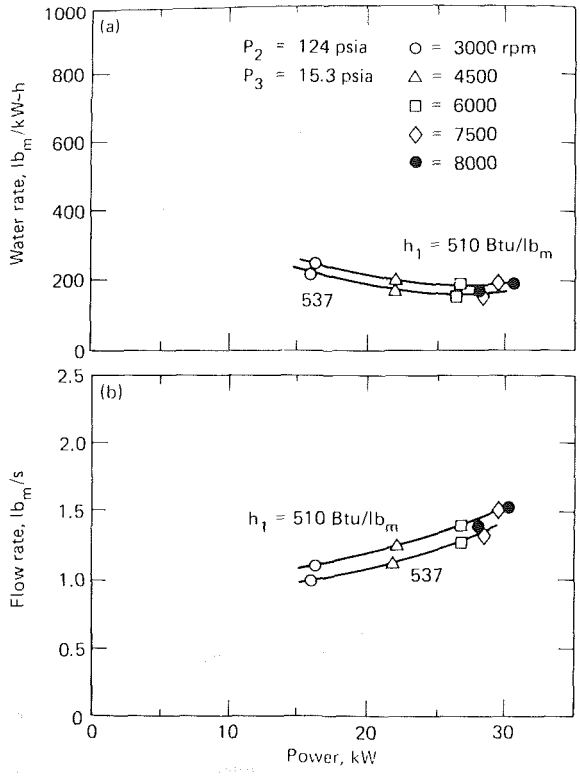


Fig. 7 Water rate and flow rate versus power for two separate conditions of wellhead enthalpy, 124-psia inlet pressure, and 15-psia exhaust pressure

process differs from the conventional steam turbine operating on saturated steam, in which condensation occurs during expansion. The exhaust vapor condenses from point 3 to point 4. The liquid is discarded in the sink condition at point 4.

After each test run, we adjusted the control valve, changing the inlet pressure P_2 and producing a different state condition for point 2. State point 1 or the outlet pressure P_3 was changed only after the range of inlet pressures had been covered. This procedure varied the pressure ratio for constant inlet enthalpy. Normally, only one hot-water generator setting (state point 1) was used in each series of runs, but the settings were changed from series to series. It would have been more conventional to vary enthalpy for a set inlet pressure, but this would have meant changing the generator setting for each run and waiting for stable conditions. By using the same series of inlet pressures with each generator setting, we obtained data for the same pressure ratio at different inlet enthalpy values. Figure 5 shows the four separate inlet enthalpy values for which a throttle pressure of 96 psia was tested.

Test Data and Computations

In the computations, we assumed that the inlet enthalpy to the expander is defined by the saturated liquid condition at state point 1 and that the process through the throttle control valve and the orifice plate is a pure throttling process, i.e., does not change enthalpy. The exhaust pressure P_3 was assumed to be the vapor pressure at the measured exhaust temperature T_3.

Referring to Fig. 4, the efficiencies are defined as follows:

$$\text{Engine efficiency, } n_e = \frac{h_2 - h_3}{h_2 - h_{3_s}} = \frac{0.948453\,\Pi}{\dot{w}(h_2 - h_{3_s})} \tag{1}$$

$$\text{Thermal efficiency, } \eta_T = \frac{h_2 - h_3}{h_2 - h_4} = \frac{0.948453\,\Pi}{\dot{w}(h_2 - h_4)} \tag{2}$$

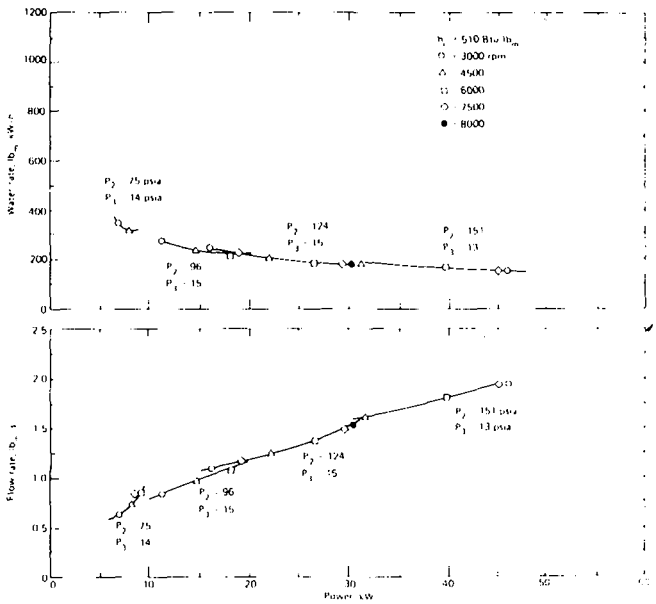


Fig. 8 Water rate and flow rate at one condition of inlet enthalpy for four separate inlet pressures and essentially atmospheric exhaust pressure

Here:

h_2 = enthalpy at engine inlet, Btu/lb$_m$
h_3 = enthalpy at engine outlet, Btu/lb$_m$
h_{3_s} = enthalpy at engine outlet assuming an isentropic drop, Btu/lb$_m$
h_4 = enthalpy of the feedwater at exhaust pressure P_3, Btu/lb$_m$
$\dot{w}$ = flow rate, lb/s
Π = power, kW net.

Downloaded 01 Jun 2010 to 171.66.16.62. Redistribution subject to ASME license or copyright; see http://www.asme.org/terms/Terms_Use.cfm

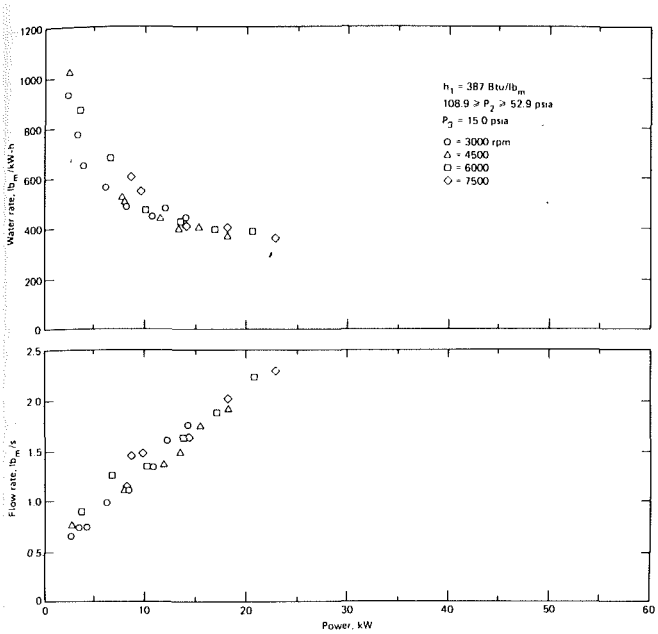


Fig. 9 Water rate and flow rate versus power for an inlet enthalpy of 387 BTu/lb$_m$, 15-psia exhaust pressure

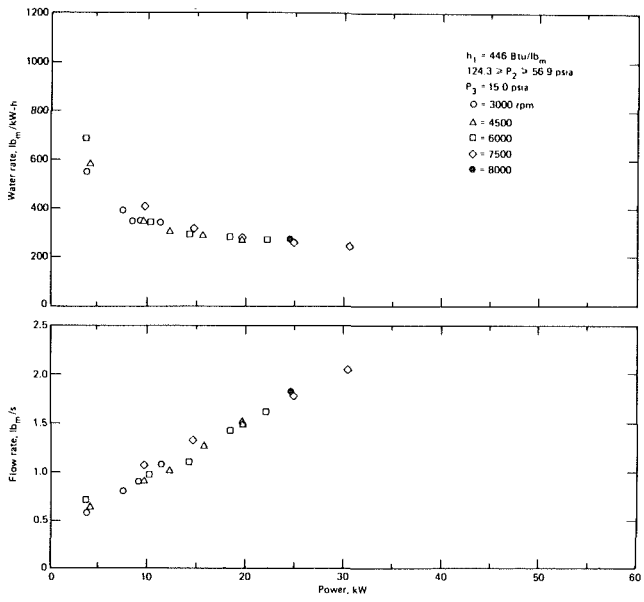


Fig. 10 Water rate and flow rate versus power for an inlet enthalpy of 446 Btu/lb$_m$, 15-psia exhaust pressure

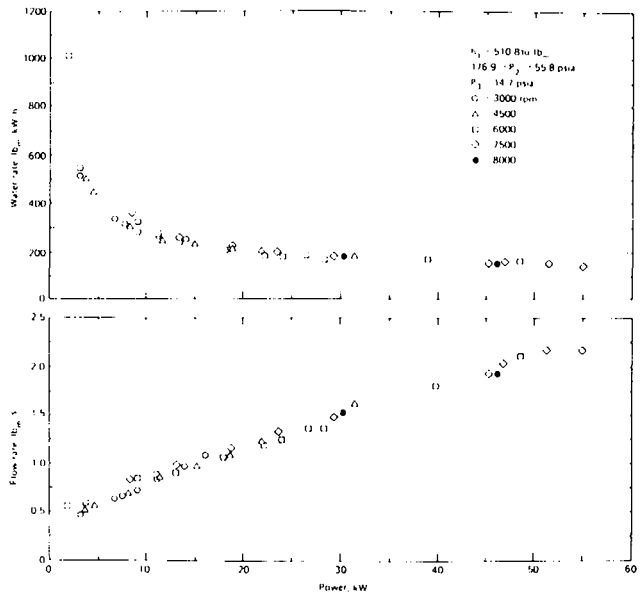


Fig. 11 Water rate and flow rate versus power for an inlet enthalpy of 510 Btu/lb$_m$ k 15-psia exhaust pressure

The Lysholm engine assembly contained a pump and supply system for the oil lubricating the bearings and supply systems for the water and air around the bearings. The power required for these auxiliaries was externally supplied. To account for these auxiliaries, which are proper charges against the engine efficiency, 0.155 kW was subtracted from the brake power, distributed as follows: 0.07 kW was allowed for the oil supply system (about 6 gpm against a 25-psig supply pressure), and 0.085 kW was allowed for the water supply system (about 3 gpm at an average supply pressure of 60 psig). The air required for the bearing seals came from the supply available in the laboratory. Very little was needed, and no accounting for it has been included in these calculations.

We found that, for any particular set of inlet and exhaust conditions, we could vary the engine power output as much as 4 percent by changing the seal water pressure. Also, the seal water became entrained in the lubricating oil when the water pressure became high enough to bypass the carbon seals. Oil was entrained in the working fluid when the seal water pressure was too low. In general, letting the working fluid pass by the seals seemed to increase power output. If the seal water mixed with the working fluid, the seal water decreased the power by cooling the working fluid. Also, the best seal water pressure varied as a function of rpm, internal pressure, and the mass flow rate.

We measured the losses in the timing belt, reduction gearing, and bearings separately by externally driving the Lysholm engine with an electric motor at 3000 rpm. The difference in torque measured with and without the timing belt was about 10 in.-lb (0.36 kW). We assumed these losses to vary linearly with speed and added them to the power measured at the brake to determine the net power output of the engine. The net output of the engine is the brake power, which we measured, plus the belt losses and minus the power required by the oil pump and seal water pump.

With η_e known from the net power output, the actual enthalpy drop can be calculated from equation (1):

$$h_2 - h_3 = \eta_e (h_2 - h_{3_s}) \tag{3}$$

which yields the actual enthalpy h_3:

$$h_3 = h_2 - \eta_e (h_2 - h_{3_s}) \tag{4}$$

From h_3, P_3, and T_3, the specific volume $\bar{v}_3$ at the exhaust condition can be found. This value is used in estimating the specific speed and specific diameter of the engine.

Results

The reduced data are tabulated in the Appendix. The following figures give plots of the data, showing the major characteristics we observed in the Lysholm engine performance.

In Fig. 6, data for three separate values of inlet enthalpy are included for one inlet pressure P_2 and one outlet pressure P_3. Note that the data are discriminate. The approximately linear increases of flow rate with power output are commonly called Willans' lines. The water rate or steam rate decreases with power output. Note also that performance improves with increased speed.

Downloaded 01 Jun 2010 to 171.66.16.62. Redistribution subject to ASME license or copyright; see http://www.asme.org/terms/Terms_Use.cfm

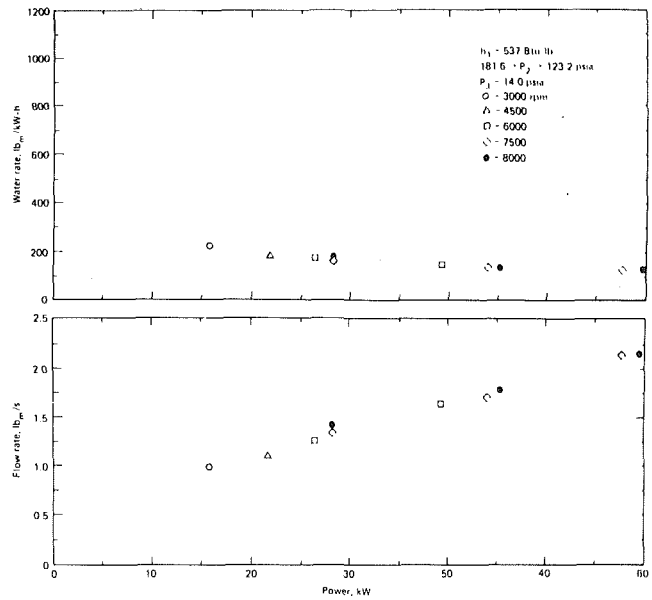


Fig. 12 Water rate and flow rate versus power for an inlet enthalpy of 537 Btu/lb$_m$, 14-psia exhaust pressure

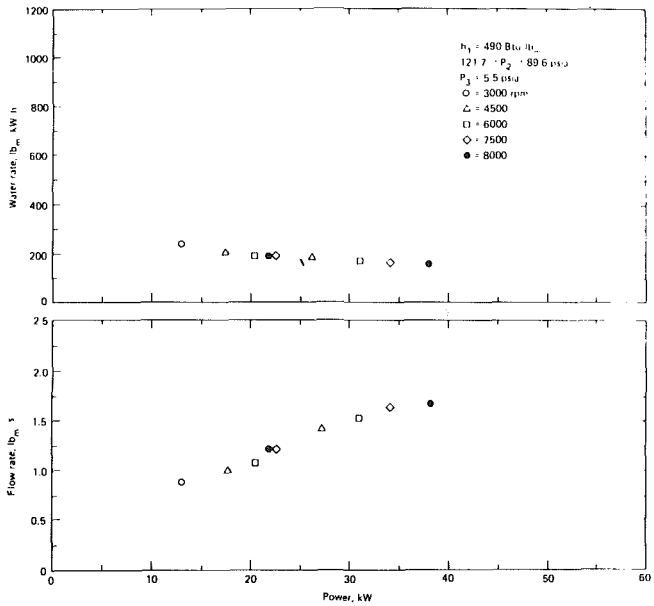


Fig. 13 Water rate and flow rate versus power for an inlet enthalpy of 490 Btu/lb$_m$, 5.5-psia exhaust pressure

Figure 7 shows performance at a higher inlet pressure, but the same outlet pressure for two other values of inlet enthalpy. Figure 8 shows data for four different inlet pressures, all with about the same inlet enthalpy, 505 to 510 Btu/lb$_m$. The data are all compatible, but these are really four sets of data for four different pressure ratios, i.e., four different Willans' lines.

Figures 9–12 show the effect of varying inlet enthalpy at an essentially constant exhaust pressure. The data are for average inlet enthalpies of 387, 446, 510, and 537 Btu/lb$_m$, respectively. The last value is near the upper limit of our test facility. As the inlet enthalpy was raised, the power output increased for a given fluid flow rate and the water rate decreased for a given power output. The rotational speed of the tests was limited by the timing belt in the power transmission train. The maximum flow rate of 2.25 lb$_m$/s was also a limit of the test facility.

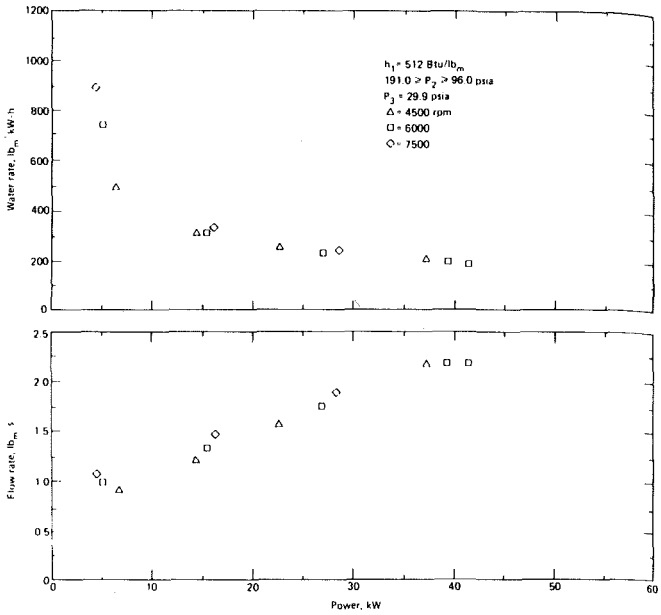


Fig. 14 Water rate and flow rate versus power for an inlet enthalpy of 512 Btu/lb$_m$, 29.9-psia exhaust pressure

In Figs. 9–12, we have not drawn lines through the data points. Each of these data points was taken under a different set of conditions, i.e., each data point is part of a separate Willans' line. The distinction is academic, but we have chosen to acknowledge it.

Figures 13 and 14 show the effect of varying the exhaust pressure (compare with Fig. 11). For a subatmospheric exhaust, both water rate and flow rate are lower at a given power. For exhaust above atmospheric pressure, the water rate and flow rate are higher.

Each of Figs. 15–20 shows data at constant speed and constant back pressure, but with varying inlet pressure and inlet enthalpy. These figures show the conventional performance characteristics: engine efficiency and thermal efficiency as a function of power output. As expected, engine efficiency increases with increased speed. Figures 15–18 show performance data for atmospheric exhaust. In all cases, the measured exhaust pressure was slightly higher than atmospheric because of the pressure drop in the exhaust pipe. Figure 19 shows data for a subatmospheric exhaust, and Fig. 20 is for an exhaust pressure of 2 atm (30 psia). The effect of varying the back pressure can be observed by comparing Figs. 18–20, all at 7500 rpm and for essentially the same inlet conditions, but with different exhaust conditions.

In all six cases, the variations in the inlet conditions appear as random differences in inlet pressure and in inlet vapor quality. Judging by the small scatter in the data, these variations have little effect on engine efficiency. Each graph is a smooth curve within the margin of error that is to be expected.

Specific Speed

Specific speed N_S and specific diameter D_S are parameters that represent significant fluid-dynamic aspects of fluid machines. The ratio of tip velocity to fluid velocity is directly related to N_S and D_S (see Baljé [12]). Because the engine efficiency is directly related to this ratio, it follows that engine efficiency is also directly related to specific speed and specific diameter.

For two-phase flow with mass flow $\dot{w}$ and the specific volume at the exhaust $\bar{v}$,

Downloaded 01 Jun 2010 to 171.66.16.62. Redistribution subject to ASME license or copyright; see http://www.asme.org/terms/Terms_Use.cfm

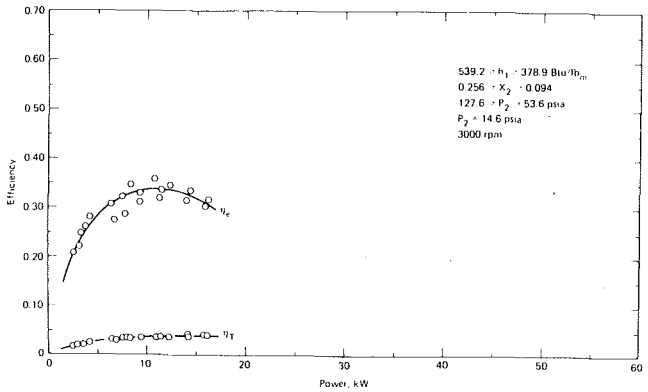


Fig. 15 Engine efficiency η_e and thermal efficiency η_T versus power for 3000 rpm, atmospheric exhaust

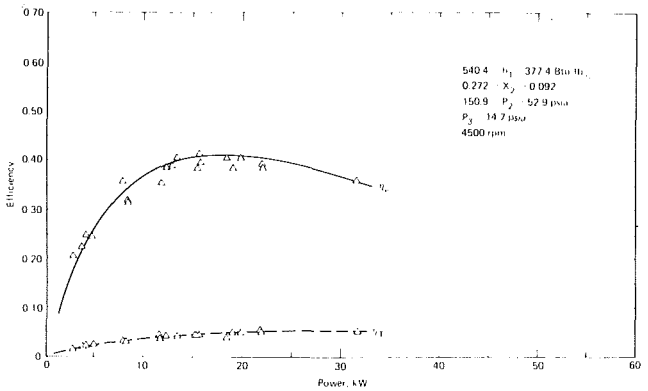


Fig. 16 Engine efficiency η_e and thermal efficiency η_T versus power for 4500 rpm, atmospheric exhaust

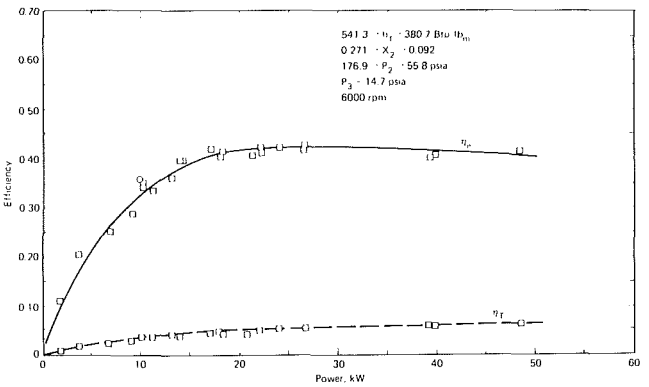


Fig. 17 Engine efficiency η_e and thermal efficiency η_T versus power for 6000 rpm, atmospheric exhaust

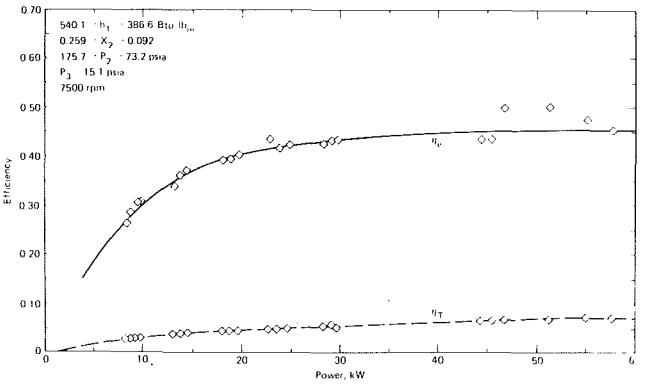


Fig. 18 Engine efficiency η_e and thermal efficiency η_T versus power for 7500 rpm, atmospheric exhaust

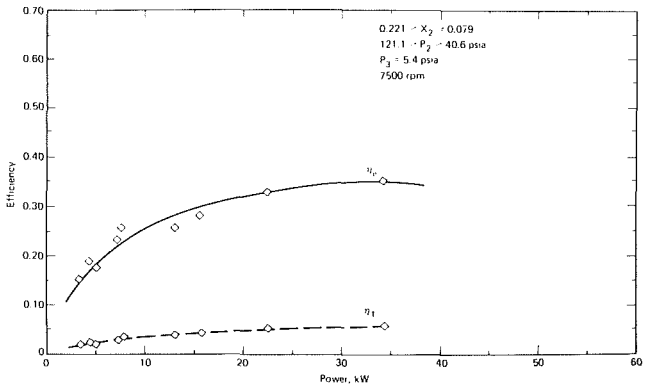


Fig. 19 Engine efficiency η_e and thermal efficiency η_T versus power for 7500 rpm, subatomospheric exhaust

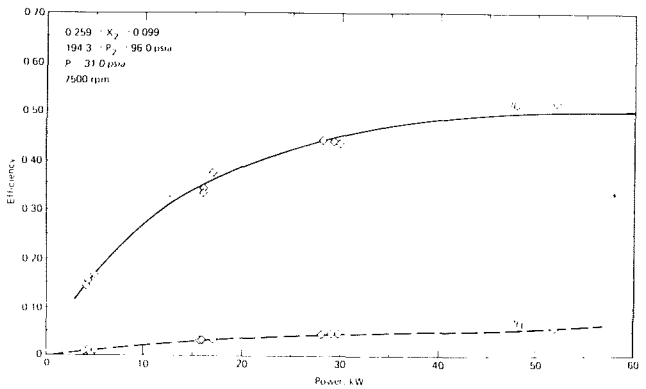


Fig. 20 Engine efficiency η_e and thermal efficiency η_T versus power for 7500 rpm, two atmospheres exhaust

$$N_S = \frac{N(\dot{w}\bar{v})^{1/2}}{(\Delta h)^{3/4}} \tag{5}$$

and

$$D_S = \frac{d(\Delta h)^{1/4}}{(\dot{w}\bar{v})^{1/2}}$$

In this equation, the head Δh equals $778(h_2 - h_{3_s})$, where $h_2 - h_{3_s}$ is the enthalpy change for an isentropic expansion through the rotor and is the maximum available energy to the fluid machine.

O. E. Balje, [12] has mapped performance characteristics on the basis of specific diameter and specific speed, and O. Cordier, [13] did the same a little earlier. The practice is established, although not commonly used. Specific diameter and specific speed are the most logical indicators of performance, since the first establishes physical size and the second the running speed. The only other meaningful combination would be specific power as a function of specific sound.

The Balje plot for the Lysholm engine is shown in Fig. 21 with the isoefficiency contours drawn. Our data fall between $N_S = 3$ and $N_S = 20$ and $D_S = 1$ and $D_S = 3$. In this plot, because specific speed and not absolute speed is the independent variable, all of the data are for one exhaust condition (atmospheric). Because both specific speed and specific diameter depend on $\bar{V}_3$, which is calculated and not measured, changing the exhaust pressure will affect specific speed and specific diameter.

The operating points at 3000, 4500, 6000, and 7500 rpm are bunched separately, and most of the higher-efficiency points are those for 7500 rpm. The maximum engine efficiency of 50

Downloaded 01 Jun 2010 to 171.66.16.62. Redistribution subject to ASME license or copyright; see http://www.asme.org/terms/Terms_Use.cfm

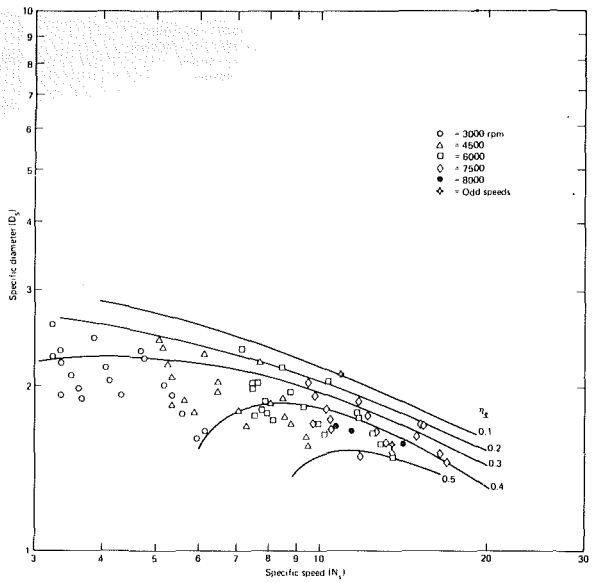


Fig. 21 Efficiency contours for various specific speeds and various specific diameters for all inlet conditions, atmospheric exhaust

percent is found at approximately $N_S = 11$ and $D_S = 1.7$. The data show the hill-shaped contours that Balje indicated. No specific diameter was observed below $D_S = 1$ for any specific speed.

Conclusions

Several specific statements can be made relative to the application of the Lysholm engine to geothermal energy conversion:

- The Lysholm engine can operate well with a two-phase mixture as a working fluid. Under the source conditions of these tests, it seems to perform best with qualities between 15 and 25 percent. An optimum quality was not determined, nor was it determined that an optimum exists. It was fairly obvious that engine operation was poorer for qualities below 15 percent.
- This Lysholm engine exhibits poorer performance at subatmospheric exhaust than at atmospheric and above-atmospheric exhaust. This is especially true of exhaust pressures below 7 psia. At the low exhaust pressures, there is a reduced mass flow because of the high specific volume, which in turn reduces the power output. The drag forces, which are always present, then become an increasingly greater fraction of the total power output and penalize the engine efficiency.
- The high performance characteristics for exhaust conditions above atmospheric pressure are a result of the high inlet pressures, low specific volume, and consequently high mass flow. This then reduces the effect of the overall parasitic losses.
- The best results were observed at the higher speeds, consistent with past experience with the Lysholm design used as a compressor.
- The maximum observed engine efficiency was $\eta_e = 53$ percent at 8000 rpm, with an inlet pressure of 190.6 psia, 22.2 percent quality, and an exhaust pressure of 30.6 psia. These conditions are for a pressure ratio of 6.23 and a volume ratio of 7.75.
- Our results show that, for low quality (on the order of 10 percent), engine efficiency is increased at low speeds. We believe that at low speeds, the liquid drag forces are less significant and rotor leakages are reduced. For low quality, engine efficiency is reduced at high speeds.

While these effects are inherent to this type of positive-displacement expander, it is possible that design changes that affect seals, bearings, case configuration, and exhaust porting could further improve performance.

Further Testing

From our tests of the performance of the Lysholm engine, we feel that there are four areas needing further testing:

- These tests were flow-limited. The physical maximum flow of the hot water generator was 2 lbm/s. For tests above 2 lbm/s, another facility would be required.
- All our test results indicate that engine efficiency increases with an increase in speed, so the engine should be tested at speeds higher than obtained here. The maximum engine speed for these tests was 8000 rpm. With modest changes in the power transmission assembly, our facility could achieve speeds from 9000 to 12,000 rpm.
- The bearings and seals are an obvious design deficiency, and they should be redesigned. This Lysholm design developed from the Lysholm air compressor, which is usually oil flooded. The bearings and seals were especially designed to prevent lubricating oil from mixing with the working fluid. Their design was not optimum. The bearing losses are properly charged to the machine, and they are considerable – approaching 7 kW at 8000 rpm. The engine efficiency could be improved 5 to 10 percent if the bearing losses could be halved.
- Interest in the performance characteristics of low-quality fluid suggests that further tests be performed at quality levels below 10 percent and speeds below 3000 rpm. Our results show that there is some evidence that the Lysholm engine can be operated quite credibly in this regime.

Acknowledgments

The authors acknowledge the support of Mr. Jay Schall in planning for the auxiliary equipment and laying out the test bed. Mr. Glen Lathrop and Mr. Don Podesta were invaluable in testing the machine, and their helpful suggestions were much appreciated.

The comments, criticism, and guidance of Dr. O. E. Baljé are acknowledged with thanks.

Complete data from the tests

Run	N rpm	h_1 Btu/lb_m	P_2 psia	X_2	P_3 psia	Flow rate lb_m	Power kW	Water rate lb_m/kW-h	η_e	T	N_S	D_S
1R	3000	390.7	53.6	0.148	14.18	0.676	2.49	978.1	0.195	0.016	4.69	2.32
2	3006	389.3	53.6	0.146	14.18	0.666	2.58	930.8	0.207	0.017	4.67	2.34
3	3018	386.6	71.5	0.124	14.33	0.995	6.40	560.2	0.304	0.029	5.14	2.01
4R	3030	383.6	70.5	0.122	14.33	0.997	6.33	567.2	0.307	0.029	5.22	2.01
5R	3006	388.7	73.0	0.125	14.28	0.992	6.35	562.9	0.295	0.029	5.05	2.01
6R	4524	391.7	75.2	0.126	14.49	1.176	8.24	514.0	0.316	0.031	8.11	1.86
7R	4512	391.9	75.4	0.126	14.49	1.178	8.25	514.2	0.316	0.031	8.09	1.86
8	4500	393.6	75.6	0.126	14.44	1.168	8.37	502.4	0.318	0.032	8.00	1.86
9R	5988	389.1	72.6	0.126	14.54	1.297	7.17	650.8	0.258	0.025	11.47	1.77
10	6000	386.2	71.9	0.123	14.54	1.287	6.81	680.3	0.253	0.024	11.57	1.78
11R	6009	383.8	71.5	0.121	14.54	1.307	6.68	704.8	0.248	0.024	11.76	1.77
12	3000	513.5	83.7	0.258	14.44	0.674	7.74	313.5	0.284	0.033	3.26	2.27
13R	3006	512.6	83.9	0.253	14.38	0.679	7.61	321.3	0.277	0.032	3.28	2.26
14	3003	510.7	127.6	0.221	14.85	1.100	16.13	245.5	0.313	0.042	3.68	1.89
15R	2991	509.8	129.1	0.219	14.85	1.114	16.15	248.4	0.309	0.042	3.65	1.88
16	4497	506.1	61.8	0.265	14.33	0.580	4.73	441.3	0.242	0.024	5.16	2.36
17	4506	507.6	100.1	0.235	14.75	0.960	15.11	233.5	0.364	0.045	5.55	1.96
18R	4491	508.7	98.2	0.238	14.70	0.966	14.66	237.3	0.359	0.044	5.52	1.97
19	6021	506.1	55.8	0.271	14.33	0.562	1.99	1015.5	0.132	0.010	7.15	2.35
20	6003	509.1	81.7	0.251	14.59	0.866	11.31	275.7	0.334	0.038	7.44	2.03
21R	5997	510.0	81.1	0.252	14.54	0.853	11.21	274.2	0.335	0.038	7.39	2.04
22R	6000	511.3	115.2	0.229	15.28	1.249	23.28	193.2	0.416	0.054	7.86	1.79
23	6003	511.1	115.7	0.229	15.23	1.271	23.90	191.4	0.421	0.054	7.94	1.78
24R	6060	510.9	123.7	0.224	15.45	1.386	28.31	176.2	0.449	0.059	8.19	1.73
25	2973	388.3	57.2	0.141	14.49	0.749	3.48	774.3	0.245	0.021	4.77	2.25
26R	3030	388.3	57.3	0.141	14.44	0.752	3.29	822.4	0.230	0.020	4.87	2.24
27R	3045	389.3	58.9	0.140	14.38	0.747	3.93	684.3	0.270	0.024	4.80	2.26
28	3018	389.7	59.3	0.140	14.38	0.748	4.12	652.9	0.281	0.025	4.75	2.26
29R	3051	383.2	58.8	0.134	14.44	0.758	4.12	662.0	0.290	0.025	4.91	2.26
30	4488	377.4	52.9	0.134	14.38	0.771	2.72	1021.1	0.207	0.017	7.72	2.21
31R	4518	372.1	52.3	0.129	14.38	0.783	2.60	1085.3	0.202	0.016	7.96	2.20
32	6015	397.8	58.9	0.149	14.54	0.901	3.72	871.5	0.204	0.018	10.21	2.05
33R	5994	396.4	58.8	0.148	14.54	0.913	3.71	686.7	0.202	0.016	10.29	2.04
34R	6018	388.5	75.4	0.122	14.80	1.350	9.94	489.1	0.344	0.034	11.58	1.76
35	6030	388.1	76.2	0.121	14.80	1.358	10.27	476.0	0.352	0.035	11.60	1.76
36	4485	387.5	82.2	0.115	14.80	1.372	11.77	419.8	0.389	0.039	8.49	1.77
37R	4485	385.8	81.3	0.114	14.80	1.365	11.52	426.4	0.388	0.039	8.53	1.77
38R	3006	385.2	89.9	0.105	14.80	1.355	10.88	448.3	0.357	0.037	5.56	1.79
39	2994	384.6	89.4	0.105	14.80	1.373	10.71	461.6	0.349	0.036	5.59	1.78
40R	3030	383.6	76.6	0.116	14.59	1.123	8.21	492.5	0.346	0.034	5.38	1.93
41	3024	384.8	76.6	0.117	14.54	1.117	8.26	486.9	0.347	0.034	5.34	1.93

(cont.)

The symbol R following a run number means that another run exists at those same test conditions.

Downloaded 01 Jun 2010 to 171.66.16.62. Redistribution subject to ASME license or copyright; see http://www.asme.org/terms/Terms_Use.cfm

Complete data, continued

Run	N rpm	h_1 Btu/lb$_m$	P_2 psia	X_2	P_3 psia	Flow rate lb$_m$/s	Power kW	Water rate lb$_m$/kW-h	η_e	η_T	N_S	D_S
42R	4518	385.6	86.7	0.109	14.91	1.502	13.32	406.0	0.400	0.041	8.84	1.71
43	4518	386.2	86.7	0.110	14.96	1.488	13.39	400.0	0.406	0.042	8.78	1.72
44R	5985	383.2	85.0	0.105	15.12	1.642	13.78	429.0	0.391	0.039	12.35	1.64
45	6000	383.0	85.0	0.108	15.07	1.633	13.86	424.3	0.395	0.040	12.35	1.65
46R	6012	383.6	95.5	0.099	15.45	1.905	17.35	395.4	0.412	0.043	12.90	1.56
47	5976	380.7	95.0	0.096	15.39	1.384	17.06	397.8	0.417	0.043	12.86	1.57
48	4461	377.7	96.5	0.092	15.28	1.747	15.51	405.6	0.413	0.043	9.31	1.63
49R	4407	376.0	94.1	0.092	15.23	1.311	14.87	438.6	0.389	0.040	9.48	1.59
50R	4488	375.0	92.2	0.092	15.12	1.774	14.75	432.9	0.398	0.041	9.63	1.60
51	2991	390.5	108.4	0.097	15.28	1.763	14.33	443.0	0.335	0.037	5.93	1.61
52R	3006	388.6	108.5	0.093	15.17	1.797	14.08	459.3	0.334	0.036	6.12	1.59
53	3027	378.9	96.0	0.094	15.01	1.517	12.12	480.5	0.343	0.036	6.11	1.67
54R	3045	377.9	96.5	0.092	15.07	1.550	12.28	483.9	0.343	0.036	6.21	1.65
55R	4449	374.6	67.8	0.115	14.64	1.165	7.75	541.3	0.353	0.032	8.53	1.89
56	4506	378.5	68.5	0.118	14.64	1.145	7.95	518.3	0.358	0.033	8.45	1.90
57	3009	444.0	56.9	0.202	14.38	0.579	3.78	551.6	0.260	0.023	3.87	2.43
58R	3024	444.7	57.2	0.202	14.38	0.585	3.83	549.6	0.259	0.023	3.90	2.42
59R	4506	446.3	57.0	0.204	14.38	0.664	4.03	593.7	0.238	0.022	6.18	2.27
60	4512	446.7	56.9	0.205	14.38	0.647	4.03	577.8	0.245	0.022	6.11	2.30
61R	4530	448.6	56.9	0.207	13.24	0.642	4.64	498.0	0.265	0.025	6.08	2.24
62R	6021	451.0	57.2	0.209	14.49	0.701	3.61	700.3	0.199	0.018	8.40	2.22
63	6012	451.4	57.3	0.210	14.49	0.716	3.77	684.5	0.203	0.018	8.46	2.19
64	6012	456.0	75.2	0.197	14.64	0.976	10.24	343.1	0.344	0.036	8.72	1.96
65R	6024	453.7	75.0	0.195	14.64	0.974	10.26	341.7	0.350	0.036	8.77	1.97
66R	4524	446.5	75.0	0.187	14.54	0.914	9.61	342.3	0.359	0.037	6.46	2.03
67	4515	443.6	75.4	0.183	14.54	0.920	9.61	344.7	0.360	0.038	6.49	2.03
68R	2994	441.4	74.4	0.182	14.49	0.805	7.46	388.4	0.324	0.034	4.08	2.16
69	3000	443.0	74.2	0.184	14.54	0.807	7.44	390.2	0.321	0.033	4.08	2.16
70	3006	447.9	84.5	0.180	14.59	0.913	9.31	353.0	0.328	0.036	4.12	2.05
71R	3030	448.8	84.7	0.181	14.59	0.917	9.47	348.5	0.330	0.036	4.16	2.05
72	4505	449.6	84.5	0.182	14.70	1.019	12.25	299.3	0.386	0.042	6.47	1.96
73R	4509	448.6	84.5	0.181	14.70	1.018	12.16	301.5	0.385	0.042	6.49	1.96
74	5994	445.3	85.8	0.176	14.85	1.131	14.30	297.3	0.396	0.043	9.25	1.84
75R	6006	444.3	85.6	0.175	14.85	1.186	14.06	303.7	0.390	0.043	9.32	1.84
76	6000	442.2	96.9	0.164	15.12	1.422	18.36	279.0	0.411	0.047	9.81	1.72
77R	6036	440.8	97.7	0.162	15.17	1.436	18.68	276.7	0.417	0.048	9.91	1.71
78	4494	440.0	95.7	0.162	14.91	1.268	15.62	292.2	0.396	0.045	7.02	1.80
79R	4506	439.5	95.7	0.162	14.96	1.256	15.52	291.4	0.398	0.045	7.01	1.81
80	2982	441.4	95.5	0.164	14.75	1.079	11.43	339.8	0.336	0.038	4.32	1.93
81	4524	443.3	110.0	0.156	15.28	1.481	19.69	270.8	0.404	0.048	7.27	1.70
82R	4536	443.4	110.5	0.156	15.28	1.512	19.88	273.7	0.399	0.048	7.36	1.69
83R	5970	442.8	108.6	0.156	15.56	1.609	22.05	262.6	0.424	0.050	10.00	1.65
84	5994	442.8	108.4	0.156	15.50	1.625	22.07	265.0	0.420	0.050	10.10	1.64
85R	4530	387.7	104.2	0.097	15.56	1.946	18.12	386.5	0.400	0.043	9.52	1.55
86	4524	389.1	105.0	0.098	15.56	1.924	18.37	377.1	0.405	0.044	9.40	1.56
87	6003	386.7	108.9	0.092	16.23	2.245	20.73	389.8	0.404	0.043	13.17	1.48
88R	6018	385.4	107.8	0.092	16.06	2.258	20.52	396.1	0.400	0.043	13.54	1.47
89	7506	386.9	73.2	0.123	14.91	1.445	8.62	603.8	0.286	0.027	15.13	1.71
90R	7539	386.7	73.4	0.122	14.91	1.463	8.86	594.0	0.291	0.028	15.28	1.70
91	7500	388.5	75.0	0.123	14.96	1.482	9.73	547.9	0.310	0.030	15.11	1.69
92R	7515	389.5	74.8	0.124	14.91	1.497	9.78	551.0	0.306	0.030	15.21	1.68
93	7470	397.6	84.7	0.124	15.23	1.650	14.29	415.6	0.371	0.038	14.93	1.63
94R	7530	384.4	85.6	0.108	15.23	1.761	13.81	459.0	0.364	0.037	15.98	1.59
95R	7542	387.1	85.4	0.112	15.28	1.750	13.95	451.6	0.364	0.037	15.86	1.60
96R	7515	387.7	96.9	0.103	15.61	2.047	18.38	400.9	0.396	0.042	16.43	1.51
97	7503	387.1	96.5	0.103	15.67	2.040	18.20	403.5	0.396	0.042	16.42	1.51
98	7482	388.6	108.6	0.092	16.28	2.303	22.93	361.5	0.438	0.047	16.81	1.47
99R	7479	385.2	108.1	0.091	16.40	2.303	22.71	365.0	0.440	0.047	16.88	1.47
100	7506	445.5	85.6	0.177	15.01	1.285	14.63	316.2	0.375	0.041	12.06	1.77
101R	7491	445.7	85.4	0.177	15.01	1.297	14.60	319.8	0.371	0.040	12.11	1.76
102	7500	447.1	96.9	0.169	15.28	1.516	19.61	278.3	0.405	0.046	12.52	1.67
103R	7521	446.7	96.7	0.169	15.34	1.526	19.43	282.7	0.401	0.046	12.61	1.66
104R	7536	446.9	110.0	0.160	15.67	1.763	24.58	258.2	0.423	0.050	13.04	1.58
105	7536	447.7	110.5	0.160	15.72	1.769	24.82	258.7	0.424	0.050	13.02	1.58
106	7527	448.4	123.4	0.152	16.23	2.021	29.86	243.9	0.433	0.053	13.42	1.51
107R	7536	448.2	124.3	0.152	16.17	2.046	30.49	241.6	0.438	0.054	13.50	1.50
108R	7518	446.7	75.2	0.187	14.64	1.108	10.06	396.7	0.310	0.032	11.77	1.86
109	7500	445.7	74.0	0.187	14.64	1.082	9.65	404.0	0.309	0.032	11.69	1.88
110R	7299	443.4	57.2	0.201	14.49	0.796	2.79	1026.3	0.140	0.013	10.95	2.09
111	7290	446.5	57.0	0.205	14.49	0.779	2.73	1026.8	0.138	0.012	10.79	2.11
112	7665	445.3	109.4	0.158	15.78	1.787	24.58	261.7	0.423	0.050	13.39	1.58
113	7971	444.7	110.5	0.157	15.83	1.814	24.66	264.9	0.418	0.049	14.00	1.57
114R	8004	444.3	110.0	0.157	15.83	1.830	24.60	267.7	0.415	0.049	14.15	1.56
115	2994	507.2	56.5	0.271	14.54	0.460	3.25	515.9	0.225	0.020	3.23	2.60
116R	2964	506.9	55.0	0.272	14.49	0.451	3.01	540.7	0.213	0.019	3.18	2.62
117	4503	508.9	57.7	0.272	14.54	0.525	3.76	502.9	0.221	0.021	5.07	2.46
118	6000	505.9	57.5	0.269	14.54	0.588	3.85	549.7	0.205	0.019	7.16	2.33
119	3051	514.8	111.6	0.236	14.85	0.974	13.99	250.9	0.317	0.041	3.61	1.98
120	4509	515.3	111.6	0.236	15.07	1.099	18.88	209.6	0.382	0.049	5.61	1.88
121	6033	513.7	110.2	0.235	15.28	1.214	22.10	197.7	0.412	0.052	7.89	1.81
122	7521	507.6	109.4	0.229	15.45	1.330	23.58	203.0	0.414	0.052	10.36	1.74
123R	7521	506.5	109.7	0.227	15.45	1.340	23.61	205.0	0.411	0.051	10.43	1.73
124R	7524	509.1	125.8	0.220	15.89	1.434	29.76	185.6	0.433	0.057	10.62	1.66
125R	7530	509.4	125.8	0.221	15.89	1.523	29.84	183.8	0.437	0.057	10.58	1.67
126	6000	508.9	123.4	0.222	15.56	1.383	26.52	187.8	0.427	0.056	8.13	1.73
127	4479	506.7	122.3	0.220	15.34	1.261	22.00	206.3	0.390	0.051	5.86	1.80
128	3009	505.0	96.5	0.235	14.75	0.845	11.29	269.6	0.323	0.039	3.51	2.10
129R	4515	504.3	97.4	0.233	14.85	0.973	15.34	228.3	0.383	0.046	5.60	1.97
130	6030	504.8	97.7	0.234	15.01	1.080	18.02	215.7	0.406	0.049	7.83	1.89
131	7506	504.3	97.9	0.233	15.23	1.178	18.92	224.3	0.394	0.047	10.15	1.82
132R	7509	503.5	98.4	0.232	15.12	1.189	18.87	226.8	0.388	0.047	10.20	1.81
133	3018	508.7	75.6	0.255	14.44	0.642	6.72	343.9	0.277	0.030	3.34	2.31
134	4512	509.4	74.4	0.257	14.44	0.704	8.30	305.3	0.313	0.034	5.24	2.20
135	6012	510.9	74.6	0.258	14.54	0.840	9.08	333.3	0.286	0.031	7.60	2.02
136R	7512	511.8	75.2	0.259	14.59	0.840	8.54	354.2	0.268	0.029	9.43	2.03
137	7500	511.5	75.0	0.259	14.59	0.846	8.46	359.7	0.265	0.029	9.46	2.03
138	7524	511.8	85.8	0.250	14.75	0.983	13.33	265.6	0.337	0.039	9.69	1.93
139R	7539	511.8	85.8	0.250	14.75	0.979	13.26	265.9	0.337	0.039	9.69	1.93
140	4527	512.4	85.6	0.251	14.64	0.911	13.23	247.9	0.360	0.041	7.49	1.99
141	4503	512.0	85.0	0.251	14.54	0.813	11.57	252.9	0.353	0.041	5.32	2.09
142	3009	511.5	85.8	0.250	14.49	0.729	9.19	285.8	0.311	0.036	3.37	2.20
143R	7503	514.6	123.7	0.228	15.67	1.480	28.85	184.6	0.426	0.056	10.40	1.68
144	7503	513.1	123.7	0.226	15.72	1.498	29.38	183.6	0.432	0.056	10.47	1.67
145R	8031	512.2	125.2	0.224	15.89	1.541	30.07	184.5	0.431	0.056	11.32	1.66
146	8019	512.2	125.2	0.224	15.89	1.544	30.18	184.2	0.432	0.056	11.31	1.66
147	2982	539.2	124.0	0.256	14.75	0.999	15.75	228.5	0.306	0.042	3.37	1.94
148R	3036	539.9	122.3	0.258	14.70	0.995	15.76	227.2	0.308	0.042	3.43	1.94
149	4509	540.4	123.2	0.258	14.91	1.114	21.92	182.9	0.384	0.052	5.34	1.85
150	6015	537.0	123.7	0.253	15.23	1.265	26.54	171.6	0.418	0.056	7.55	1.77
151	7509	535.6	122.9	0.252	15.45	1.360	28.37	172.5	0.421	0.056	9.77	1.72
152R	FAULTY THERMOCOUPLES											
153R	FAULTY THERMOCOUPLES											
154R	8022	536.0	125.2	0.251	15.61	1.426	28.48	180.2	0.402	0.054	10.61	1.69
155	8004	534.0	124.3	0.250	15.50	1.414	28.23	180.4	0.404	0.054	10.60	1.69
156R	FAULTY THERMOCOUPLES											
157	4515	529.7	123.2	0.245	21.92	1.160	19.51	214.1	0.418	0.049	5.27	2.12
158R	4491	531.1	122.6	0.248	21.99	1.153	18.98	218.7	0.409	0.047	5.23	2.13
159	6000	534.2	125.2	0.249	19.96	1.287	25.74	180.0	0.461	0.056	7.32	1.95
160	7500	535.1	122.6	0.252	20.92	1.338	26.29	183.2	0.468	0.055	9.33	1.95
161	7518	536.3	123.7	0.253	24.76	1.341	23.51	205.3	0.459	0.051	9.22	2.07
162	6006	539.5	123.2	0.257	23.04	1.231	22.71	195.2	0.457	0.052	7.09	2.10
163R	6024	540.4	122.6	0.258	22.96	1.217	22.89	191.4	0.465	0.053	7.07	2.10
164	4512	539.5	126.7	0.255	21.70	1.150	20.54	201.6	0.421	0.050	5.14	2.12
165R	6012	447.9	131.9	0.147	24.44	1.945	23.65	296.0	0.448	0.048	9.94	1.82
166	6006	448.6	131.9	0.147	24.12	1.972	24.10	294.6	0.445	0.048	9.99	1.80
167	5994	447.5	132.2	0.146	30.00	1.966	20.20	350.4	0.438	0.043	9.91	1.96
168	6012	449.0	149.5	0.137	30.29	2.250	26.76	302.8	0.478	0.049	10.13	1.87
169	5994	451.9	150.2	0.140	28.61	2.245	28.10	287.6	0.475	0.050	10.03	1.83
170	6015	451.9	150.9	0.140	25.00	2.250	30.71	263.8	0.474	0.053	10.15	1.73
171	7518	453.9	146.8	0.145	25.17	2.245	31.81	254.1	0.494	0.055	12.68	1.74
172	7491	449.0	146.4	0.139	33.87	2.251	23.81	340.3	0.466	0.045	12.68	1.95
173	5994	444.0	152.9	0.130	33.98	2.257	25.80	314.9	0.509	0.050	10.10	1.97
174	7524	510.9	145.4	0.211	23.89	1.787	30.68	209.7	0.448	0.053	10.42	1.83
175	7530	512.2	175.7	0.197	18.58	2.183	51.43	152.8	0.500	0.070	11.23	1.54
176	7515	512.2	151.2	0.210	24.20	1.871	35.95	187.4	0.495	0.060	10.46	1.81
177	5985	512.4	151.2	0.210	24.28	1.711	31.88	193.2	0.480	0.058	7.98	1.89
178R	7536	512.2	150.9	0.210	17.16	2.063	46.80	158.7	0.488	0.066	11.52	1.51
179	7494	512.4	141.5	0.215	17.10	2.056	46.84	158.0	0.499	0.067	11.63	1.50
180	4506	512.0	156.1	0.207	30.29	1.589	22.56	253.6	0.414	0.046	5.67	2.13
181	5991	511.3	155.0	0.207	29.35	1.764	26.93	235.9	0.439	0.049	7.96	2.00

Complete data, continued

Run	N rpm	h_1 Btu/lb$_m$	P_2 psia	X_2	P_3 psia	Flow rate lb$_m$/s	Power kW	Water rate lb$_m$/kW-h	η_e	η_T	N_S	D_S
182	7464	511.1	154.7	0.207	30.86	1.894	28.05	243.1	0.441	0.048	10.25	1.97
183	4515	512.0	122.9	0.225	29.26	1.221	14.24	308.9	0.376	0.038	5.50	2.32
184	5985	508.3	122.9	0.221	29.91	1.348	15.41	315.1	0.380	0.037	7.66	2.23
185	7491	509.8	132.2	0.217	29.63	1.473	16.04	330.5	0.343	0.035	9.71	2.15
186	4506	513.3	96.0	0.245	30.00	0.910	6.57	498.8	0.277	0.023	5.37	2.58
187	6015	512.9	96.7	0.243	28.61	1.032	5.00	742.9	0.178	0.015	7.59	2.39
188	7530	514.2	96.0	0.245	30.19	1.089	4.40	890.9	0.156	0.013	9.82	2.37
189	4545	511.5	199.0	0.186	29.07	2.180	37.13	211.4	0.438	0.055	6.21	1.84
190	4650	512.0	198.1	0.186	29.72	2.179	37.16	211.1	0.444	0.055	6.34	1.86
191	6003	513.1	191.0	0.191	30.57	2.180	41.46	189.2	0.509	0.062	8.19	1.88
192	4491	444.5	150.2	0.132	31.35	2.193	22.68	348.2	0.436	0.044	7.55	1.92
193R	4545	444.7	149.8	0.132	31.45	2.203	22.77	348.3	0.437	0.044	7.66	1.92
194	4509	445.3	123.7	0.149	31.54	1.709	14.86	414.1	0.404	0.037	7.20	2.12
195	6036	443.0	124.3	0.146	30.29	1.930	17.28	402.2	0.406	0.038	10.23	1.98
196	7512	447.9	123.2	0.152	29.91	1.993	16.98	422.5	0.375	0.035	12.85	1.93
197	4350	440.8	77.2	0.179	30.57	0.960	1.28	2708.3	0.086	0.006	6.82	2.55
198	4443	448.6	97.4	0.171	30.29	1.269	7.56	604.2	0.304	0.025	6.81	2.32
199	6006	448.8	96.9	0.171	29.53	1.269	7.48	610.7	0.295	0.024	9.17	2.30
200	7500	449.0	97.2	0.171	30.19	1.505	4.91	1102.6	0.166	0.013	12.52	2.12
201	4494	384.2	76.0	0.117	30.38	1.294	1.94	2397.6	0.138	0.009	9.21	2.32
202	4485	387.3	96.2	0.103	30.10	1.785	8.48	757.7	0.355	0.027	9.31	2.07
203	6042	387.3	96.9	0.102	30.00	1.927	7.29	951.9	0.281	0.021	12.99	1.99
204	7494	384.0	96.7	0.099	29.81	2.082	4.08	1836.1	0.148	0.011	16.95	1.91
205	4470	386.0	118.2	0.085	30.29	2.082	14.59	514.0	0.476	0.040	9.20	1.99
206	6000	384.2	111.0	0.088	30.57	2.315	11.80	706.1	0.366	0.029	13.45	1.88
207	6033	510.0	183.2	0.191	29.91	2.197	39.44	200.6	0.488	0.058	8.44	1.85
208	4485	539.9	124.3	0.256	29.72	1.128	14.26	284.8	0.368	0.037	5.05	2.38
209	6006	540.4	124.6	0.257	29.81	1.243	15.77	283.9	0.369	0.037	7.07	2.28
210	7515	542.2	125.2	0.259	29.35	1.348	15.83	306.5	0.335	0.034	9.16	2.18
211	7530	539.9	155.4	0.240	29.07	1.783	23.78	270.9	0.436	0.050	9.56	1.98
212	7518	541.3	156.1	0.241	30.29	1.731	29.26	213.0	0.439	0.050	9.46	2.01
213	6045	539.0	156.1	0.238	30.00	1.651	27.50	216.1	0.434	0.049	7.46	2.05
214	6201	541.5	188.9	0.226	30.77	2.096	38.97	193.6	0.447	0.055	8.03	1.88
215	7539	539.9	194.3	0.221	30.77	2.156	46.82	165.8	0.519	0.064	9.77	1.88
216	7980	539.0	190.6	0.222	30.57	2.155	47.49	163.4	0.531	0.065	10.41	1.87
217	4539	372.9	30.8	0.161	4.97	0.483	1.61	1081.9	0.125	0.013	7.90	1.75
218	4515	375.0	36.1	0.155	5.01	0.559	3.24	621.8	0.202	0.022	7.99	1.66
219	6000	376.4	35.7	0.157	5.05	0.629	2.22	1019.6	0.124	0.014	11.57	1.56
220	3960	374.2	26.3	0.171	4.90	0.401	1.04	1390.0	0.103	0.010	6.63	1.87
221	4524	431.0	35.7	0.215	4.95	0.448	3.44	469.3	0.208	0.024	6.63	1.77
222	6018	431.8	35.9	0.216	4.99	0.496	2.73	654.8	0.149	0.017	9.22	1.69
223	4500	429.4	30.8	0.221	4.99	0.380	2.23	613.6	0.172	0.019	6.38	1.90
224	5427	428.2	30.9	0.220	4.99	0.403	1.69	855.8	0.124	0.013	7.92	1.85
225	4320	426.6	26.4	0.226	4.97	0.332	1.16	1028.4	0.111	0.011	6.10	1.98
226	3003	324.9	36.6	0.101	4.97	0.708	3.56	716.3	0.233	0.024	6.65	1.53
227	4497	322.2	35.2	0.100	4.97	0.759	3.17	861.9	0.199	0.021	10.46	1.48
228	6021	321.8	36.1	0.098	5.01	0.866	2.06	1513.9	0.113	0.012	14.88	1.39
229	4500	323.0	31.1	0.108	4.88	0.658	2.04	1164.8	0.152	0.015	10.10	1.55
230	3003	323.5	30.6	0.110	4.90	0.565	2.34	870.1	0.204	0.020	6.27	1.67
231	3003	323.0	26.4	0.117	4.84	0.484	1.59	1095.9	0.172	0.016	6.09	1.77
232	3999	323.2	26.1	0.118	4.88	0.520	1.02	1837.3	0.103	0.010	8.43	1.71
233	2985	274.9	26.2	0.067	4.90	0.705	1.52	1667.7	0.165	0.014	8.40	1.55
234	3015	321.1	40.6	0.090	4.97	0.802	3.77	764.9	0.217	0.023	7.01	1.45
235	4494	324.7	40.2	0.094	5.05	0.873	3.96	793.1	0.206	0.022	10.77	1.40
236	6018	324.1	40.1	0.094	5.14	0.936	3.30	1022.0	0.162	0.017	14.90	1.36
237	6969	323.7	40.4	0.093	4.93	0.989	2.74	1298.4	0.125	0.014	17.82	1.30
238	3006	372.3	40.5	0.145	4.88	0.584	3.98	529.2	0.228	0.027	5.33	1.62
239	4497	373.6	40.0	0.147	4.97	0.641	4.62	499.3	0.243	0.028	8.31	1.56
240	5997	375.4	39.9	0.149	5.10	0.711	4.14	618.7	0.197	0.023	11.58	1.50
241	7482	376.6	40.6	0.150	5.05	0.764	3.52	782.4	0.153	0.018	14.85	1.45
242	3009	375.0	36.0	0.155	4.95	0.629	3.35	675.8	0.185	0.021	5.70	1.55
243	3006	374.6	30.5	0.164	4.99	0.409	2.39	617.6	0.218	0.023	4.82	1.90
244	3030	374.6	26.2	0.172	4.99	0.360	1.57	824.4	0.175	0.017	4.80	1.99
245	3009	430.6	40.5	0.208	4.95	0.474	4.18	408.0	0.228	0.028	4.38	1.74
246	4518	430.4	40.5	0.207	5.01	0.513	4.98	370.7	0.253	0.031	6.53	1.69
247

4 Nilsson, H. R., *Helical Rotary Engine*, U.S. Patent No. 2,622,687, Dec. 23, 1952.

5 Lysholm, A., *The Fundamentals of a New Screw Engine*, ASME Paper No. 66-GT-67, 1966.

6 Sprankle, R. S., *Electrical Power Generating System*, U.S. Patent No. 3,751,673, Aug. 7, 1973.

7 Wells, W. M., *On Central Station Application of Graphite Helical-Rotor Expanders*, Lawrence Livermore Laboratory Report UCRL-70258, Livermore, Calif., 1967.

8 Wells, W. M., Hanner, D. W., McElroy, J. L., and Robinson, E., *High Temperature Testing and Evaluation of Graphite Helical-Screw Expander and Compressors*, Lawrence Livermore Laboratory Report UCRL-14660, Livermore, Calif., 1966.

9 Sprankle, R. S., to McKay, R., *Memorandum of HPC Power System Evaluation*, Hydrothermal Power, Ltd., Pasadena, Calif., Aug. 21, 1974.

10 Weiss, H., Steidel, R., and Lundberg, A., *Performance Test of a Lysholm Engine*, Lawrence Livermore Laboratory Report UCRL-51861, Livermore, Calif., 1975.

11 Weiss, H., and Shaw, G., "Geothermal Two-Phase-Flow Test Facility," *Proceedings of the 2nd United Nations Symposium on the Development and Use of Geothermal Resources*, Lawrence Berkeley Laboratory, Berkeley, Calif., 1976.

12 Baljé, O. E., "A Study on Design Criteria and Matching Turbomachines, Part A—Similarity and Design Criteria of Turbines," ASME JOURNAL OF ENGINEERING FOR POWER, Vol. 84, 1962, pp. 83–102.

13 Cordier, O., *Aenlichkeitsbedingungen Fur Stromungsmaschinen*, V. D. I Berichte, Vol. 5, Brennstoff-Warme-Kraft, 1953.

Downloaded 01 Jun 2010 to 171.66.16.62. Redistribution subject to ASME license or copyright; see http://www.asme.org/terms/Terms_Use.cfm

M. A. Paolino
Associate Professor,
Department of Mechanics,
U.S. Military Academy,
West Point, N.Y.
Mem. ASME

M. D. Burghardt
Professor,
Department of Engineering,
U.S. Merchant Marine Academy,
Kings Point, N.Y.
Mem. ASME

Energy Conservation and Second Law Efficiency

Introduction

Energy conservation programs are of concern in both domestic and work environments. The quest is to improve the first law efficiency, η_1, defined as

$$\eta_1 = \frac{\text{output}}{\text{input}} \tag{1}$$

Typically, one seeks to maintain the same output and diminish the input by improving equipment efficiency, cleaning heat exchangers, and maintaining design conditions in rotative and reciprocating devices. Another method used in conservation programs is to reduce the input, such as using every other light; while the output in terms of illumination is reduced, the level is still acceptable. At home, thermostats have been lowered, reducing both the input and output. All these methods, and others, are practiced today to reduce our energy demands, thereby conserving energy for future use.

Few efforts address the quality of energy being used. The quality of energy may be defined as its available portion, that portion which may be used for work. Not only is it important that energy be conserved, but the manner in which energy is used must be examined. To use high quality energy for low quality energy tasks is wasteful. The first law efficiency for a task may be a maximum, but the effective use of energy quality may be low.

The second law efficiency, η_2, addresses the quality of energy. There are discussions in the literature [1, 2] that focus on second law efficiency. What follows in this article is a development of second law efficiency, for processes and cycles, based on fundamental thermodynamic concepts which are familiar to practicing engineers.

Second Law Process Efficiency

The second law efficiency for a process, η_2, may be defined as

$$\eta_2 = \frac{\text{change of available energy of the system}}{\text{change of available energy of the source}}$$

$$\eta_2 = \frac{(\Delta a.e.)_{\text{system}}}{(\Delta a.e.)_{\text{source}}} \tag{2}$$

Pumps and Compressors. Figure 1 illustrates the $T-s$ diagram for a fluid which passes through a pump or a compressor in a steady-state, steady-flow process from state 1 to state 2. In general, the process will be irreversible and is represented by a dotted line from 1-2, indicating an entropy increase. To accomplish this change of state, an amount of energy, w_{1-2}, was transferred to the device by an electric motor, for instance. This amount of energy, w_{1-2}, represents the change of available energy of the source

$$(\Delta a.e.)_{\text{source}} = w_{1-2} \tag{3}$$

Because of irreversibilities, the energy input, w_{1-2}, is greater than the minimum energy input required to change from state 1 to state 2 in a completely reversible manner. The series of processes, 1-*a*-*b*-2, shown in Fig. 1, represent the reversible path between states 1 and 2 which requires the minimum energy input [3]. The minimum energy input is equal to the change in available energy of the system. From classical thermodynamics concepts [4], the minimum energy input is called the reversible work, $(w_{1-2})_{\text{rev}}$, and it is also equal to the change in the availability property of the medium, $\psi_1 - \psi_2$. The change in the available energy of the system is calculated from the equation

$$(\Delta a.e.)_{\text{system}} = (w_{1-2})_{\text{rev}} = (h_1 - h_2) - T_0(s_1 - s_2) \tag{4}$$

where T_0 represents the temperature of the surrounding environment. The second law efficiency for a pump or compressor follows from equation (2) and is given by the equation

$$\eta_2 = \frac{(w_{1-2})_{\text{rev}}}{w_{1-2}} \tag{5}$$

Equation (5) is interpreted as the minimum energy input to change from state 1 to state 2, $(w_{1-2})_{\text{rev}}$, divided by the actual energy required to move from state 1 to state 2. The reversible power is calculated from equation (4) multiplied by the flow-rate, and the source power may be measured electrically or with a torque meter.

Contributed by the Energetics Division for publication in the JOURNAL OF ENGINEERING FOR POWER. Manuscript received at ASME Headquarters June 1, 1981.

Copyright © 1982 by ASME
Downloaded 01 Jun 2010 to 171.66.16.62. Redistribution subject to ASME license or copyright; see http://www.asme.org/terms/Terms_Use.cfm

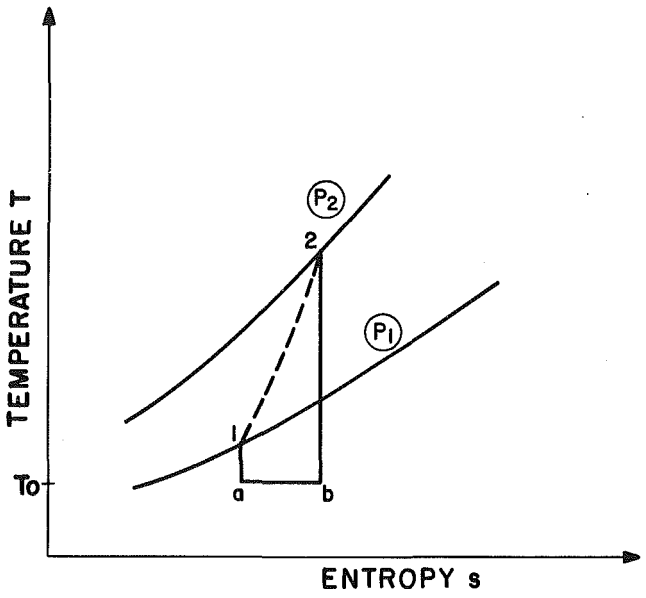


Fig. 1 A T-s diagram illustrating flow through a pump or compressor

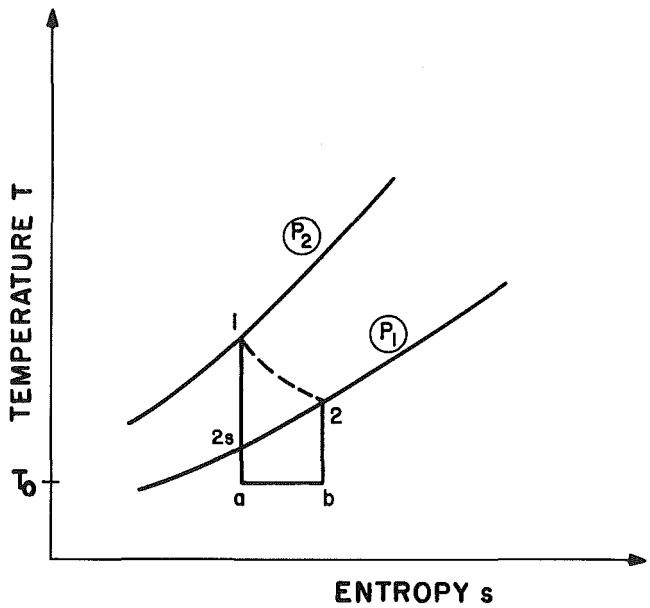


Fig. 2 A T-s diagram illustrating flow through a turbine

Turbines. Figure 2 illustrates the irreversible expansion of a fluid from state 1 to state 2 through a turbine. Again steady-state, steady-flow conditions apply. In this instance, the change of system available energy is represented by the actual work output of the device

$$(\Delta a.e.)_{\text{system}} = w_{1-2} \tag{6}$$

The actual output of the device is less than the maximum output that could be obtained from state 1 to state 2 if a series of completely reversible processes were used. The reversible path from state 1 to state 2 is shown in Fig. 2 by the processes, $1-a-b-2$. The maximum output represents the change in available energy of the source, $(\Delta a.e.)_{\text{source}}$, and is the reversible work, $(w_{1-2})_{\text{rev}}$. It is also equal to the change in the availability property of the medium, $\psi_1-\psi_2$. The change in available energy of the source is calculated as follows

$$(\Delta a.e.)_{\text{source}} = (w_{1-2})_{\text{rev}} = (h_1 - h_2) - T_0(s_1 - s_2) \tag{7}$$

The second law efficiency becomes

$$\eta_2 = \frac{w_{1-2}}{(w_{1-2})_{\text{rev}}} \tag{8}$$

Calculations may be made in an analogous manner to that described for pumps and compressors.

The concept of second law process efficiency is illustrated with the following example problem.

Example 1. A high pressure steam turbine receives 25 kg/s of steam at 16.5 MPa and 550°C and discharges it to the intermediate pressure turbine at 3 MPa and 313°C. The turbine's power meter reads 9800 kW. The surrounding environmental temperature is 25°C. Determine the second law efficiency of the turbine.

Solution. The appropriate state points are shown in Fig. 2. The values for the state point data are obtained from a Mollier chart or steam tables [5].

$$h_1 = 3432.4 \text{ kJ/kg}, \; s_1 = 6.4606 \text{ kJ/kg} \cdot \text{K}$$

$$h_2 = 3026.5 \text{ kJ/kg}, s_2 = 6.5957 \text{ kJ/kg} \cdot \text{K}$$

$$w_{1-2} = \frac{9800}{25} = 392.0 \text{ kJ/kg}$$

$$(w_{1-2})_{\text{rev}} = (h_1 - h_2) - T_0(s_1 - s_2)$$

$$(w_{1-2})_{\text{rev}} = (3432.4 - 3026.5) - 298(6.3606 - 6.5957)$$

$$(w_{1-2})_{\text{rev}} = 446.2 \text{ kJ/kg}$$

From equation (8)

$$\eta_2 = \frac{392.0}{446.2} = 0.878$$

Had a power meter not been available and the best available information on the actual turbine was, $w_{1-2} = h_1 - h_2$, the second law efficiency is, $\eta_2 = 0.910$. The second law efficiency is higher because the calculation of w_{1-2} does not reflect mechanical and gear losses.

Frequently engineers calculate the isentropic efficiency, η_s, of a turbine or pump. In this example, the isentropic efficiency is [6]

$$\eta_s = \frac{h_1 - h_2}{h_1 - h_{2s}}$$

$$\eta_s = \frac{3432.4 - 3026.5}{3432.4 - 2949.3} = 0.84$$

The second law efficiency and isentropic efficiency are different. While the isentropic efficiency is a common standard of comparison, it does not reflect the energy available from the source because the isentropic exit state point, 2s, in Fig. 2, is not the actual exit state point, 2. Thus, the second law efficiency is a true measure of the use of available energy.

In summary, for a medium in an open or closed system, undergoing a process which requires an energy input in the form of work or electrical energy, the second law efficiency is calculated from equation (5). For a substance in an open or closed system, undergoing a process where the output is work, the second law efficiency is calcuiated from equation (8). For a closed system, equation (9) is used to calculate the reversible work [4]

$$(w_{1-2})_{\text{rev}} = (u_1 - u_2) - T_0(s_1 - s_2) \tag{9}$$

Heating. Figure 3 represents the $T-s$ diagram for a solar collector which receives incident radiation, q_c, at tem-

Downloaded 01 Jun 2010 to 171.66.16.62. Redistribution subject to ASME license or copyright; see http://www.asme.org/terms/Terms_Use.cfm

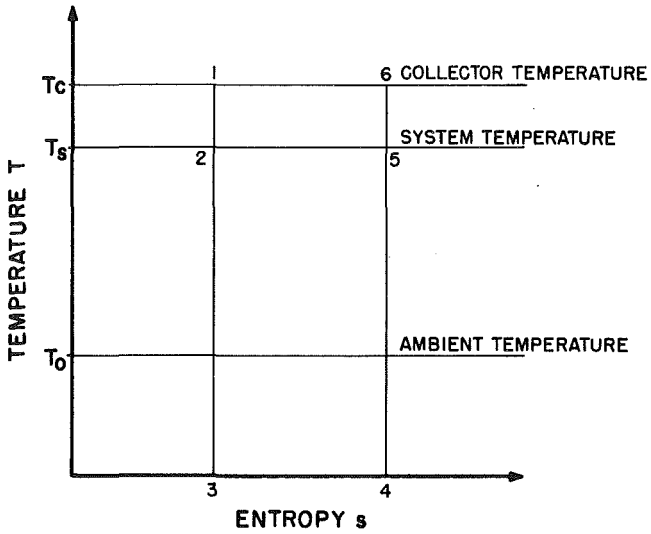


Fig. 3 A T-s diagram illustrating heat transfer in a solar collector

perature, T_c, and delivers q_s to the system, at temperature, T_s, for heating. The ambient temperature of the surroundings is T_0. The incident radiation, q_c, is represented by the area, 1-3-4-6. The portion of this energy that is available for use, the available energy of the source, is given by the equation

$$(\Delta a.e.)_{\text{source}} = q_c\left(1 - \frac{T_0}{T_c}\right)$$

The foregoing equation represents the output from a Carnot heat engine operating between the temperature limits of T_c and T_0 [6]. Some of the source available energy is lost by heat transfer and leakage to the surroundings. The remaining energy, q_s, is represented by the area, 2-3-4-5. The ratio of q_s/q_c represents the first law efficiency of the collector, η_1.

Not all of the energy, q_s, is available for use. The portion available for use, the available energy of the system, is given by the equation

$$(\Delta a.e.)_{\text{system}} = q_s\left(1 - \frac{T_0}{T_s}\right)$$

Again, the foregoing equation represents the output from a Carnot heat engine operating between T_s and T_0. With the use of equation (2), the second law efficiency for a solar collector becomes

$$\eta_2 = \eta_1 \frac{\left(1 - \frac{T_0}{T_s}\right)}{\left(1 - \frac{T_0}{T_c}\right)} \tag{10}$$

It is instructive to note that the upper limit for a solar collector is the first law efficiency and that the second law efficiency is maximized as the temperature difference between T_c and T_s decreases. The increase in η_2, resulting from the decrease in ΔT between T_c and T_s, is an example of matching the source energy quality to the task.

The following example problem illustrates these concepts.

Example 2. A homeowner wishes to heat water to 60°C for a domestic hot water system. Determine and compare the second law efficiency for a gas heater, $\eta_1 = 0.90$, and a solar collector, $\eta_1 = 0.65$. The temperature of the surroundings is 25°C.

Solution. For a flat plate collector, the collector temperature, T_c, is typically 366 K. From the specified data, $T_0 = 298$ K and $T_s = 333$ K. With the use of equation (10), the second law efficiency for the collector can be computed as

$$n_2 = 0.65 \frac{\left(1 - \frac{298}{333}\right)}{\left(1 - \frac{298}{366}\right)} = 0.368$$

For the gas heater, the temperature of the flame is approximately 1360 K. For the gas heater, T_c is the source temperature, 1360 K. The second law efficiency is

$$\eta_2 = 0.90 \frac{\left(1 - \frac{298}{333}\right)}{\left(1 - \frac{298}{1360}\right)} = 0.121$$

If the source temperature, T_c, is reduced to 1000 K, the second law efficiency increases to 0.135.

To complete this example, consider the situation where the water is heated by an electric heater with a first law efficiency, $\eta_1 = 0.99$. In this case, the second law efficiency is calculated by applying equation (2). Since all the electrical energy, q_c, is available energy

$$(\Delta a.e.)_{\text{source}} = q_c$$

As previously shown, the available energy of the system is

$$(\Delta a.e.)_{\text{system}} = q_s\left(1 - \frac{T_0}{T_s}\right)$$

Thus, the second law efficiency for an electric water heater is

$$\eta_2 = \frac{q_s\left(1 - \frac{T_0}{T_s}\right)}{q_c}$$

$$\eta_2 = \eta_1\left(1 - \frac{T_0}{T_s}\right)$$

$$\eta_2 = 0.99\left(1 - \frac{298}{333}\right) = 0.104$$

Thus, the solar collector with a comparatively poor first law efficiency is significantly better at matching source and system energy levels. As the adiabatic effectiveness of the collector rises, the first law efficiency and the second law efficiency will also rise.

Second Law Efficiency for Cycles

The second law efficiency for a cycle may be defined as [2]

$$\eta_2 = \frac{\text{the minimum available energy necessary to perform a given task}}{\text{the actual available energy required to perform a given task}}$$

$$\eta_2 = \frac{(a.e.)_{\text{min.}}}{(a.e.)_{\text{actual}}} \tag{11}$$

In the following development, it is necessary to keep in mind that for both the numerator and denominator of equation (11), the given task is the same.

Power Producing Cycle—Heat Engine

For a heat engine, the given task is to produce a certain

Downloaded 01 Jun 2010 to 171.66.16.62. Redistribution subject to ASME license or copyright; see http://www.asme.org/terms/Terms_Use.cfm

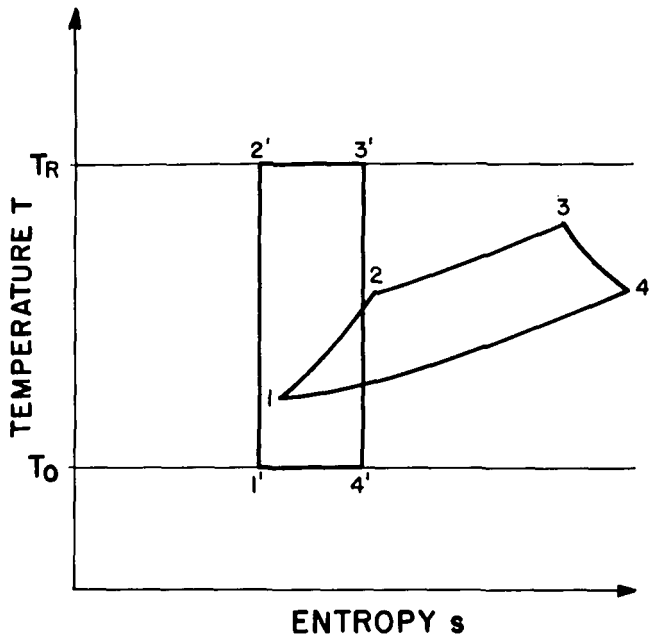


Fig. 4 A T-s diagram illustrating power producing cycles

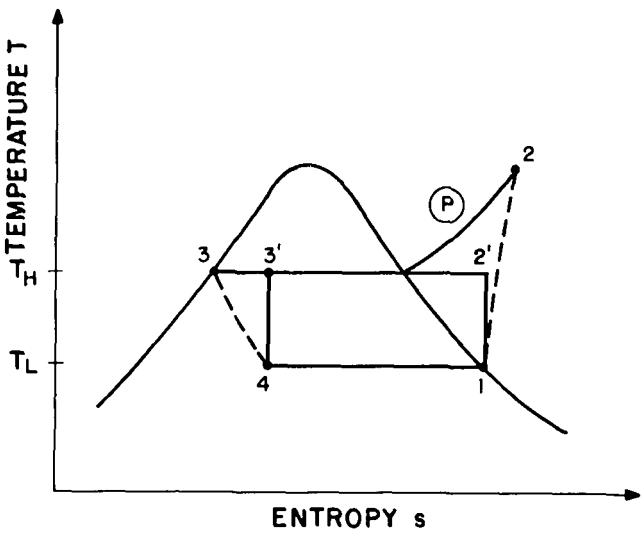


Fig. 5 A T-s diagram illustrating refrigeration cycles

output, w_{net}. Figure 4 illustrates an arbitrary heat engine, represented by the cycle, 1-2-3-4-1. The heat engine receives heat, q_R, from a high temperature reservoir at temperature, T_R. The surroundings are at temperature, T_0. The heat engine's temperature limits are T_1 and T_3. The actual available energy used by the heat engine is given by the equation

$$(a.e.)_{\text{actual}} = \left(1 - \frac{T_0}{T_R}\right) q_R \tag{12}$$

The output from the heat engine, w_{net}, is less than this amount of available energy owing to the irreversibilities in the heat engine. Nevertheless, the available energy given in equation (12) represents the actual use of energy, w_{net} plus irreversibilities, by the heat engine. The minimum available energy required to perform the fixed task of producing w_{net} would result from the use of a Carnot cycle, 1′-2′-3′-4′-1′, shown in Fig. 4. The area represented by 1′-2′-3′-4′ is equal to the output, w_{net}, of the irreversible engine and is also equal to the minimum use of available energy. That is

$$(a.e.)_{\min} = w_{net}$$

The second law efficiency for the heat engine follows from equation (11) and is given as

$$\eta_2 = \frac{w_{net}}{\left(1 - \frac{T_0}{T_R}\right) q_R}$$

Since the first law efficiency is

$$\eta_1 = \frac{w_{net}}{q_R}$$

and

$$\eta_{\text{Carnot}} = 1 - \frac{T_0}{T_R}$$

the second law efficiency for the heat engine may be expressed as

$$\eta_2 = \frac{\eta_1}{\eta_{\text{Carnot}}} \tag{13}$$

The following observings concerning equation (13) should be noted. If the actual cycle has irreversibilities, η_1 will be low and consequently η_2 will also be low. Also, as the temperature of the reservoir, T_R, approaches T_3, the peak temperature in the cycle, the Carnot efficiency, $(1 - T_0/T_R)$, decreases and the second law efficiency given by equation (13) increases. From a practical point of view, this increase in second law efficiency results from matching the quality of the energy source to the task. Less energy is made unavailable as the temperature difference between T_R and T_3 decreases. This is demonstrated by the following example.

Example 3. A steam power plant, operating on the Rankine cycle, generates saturated steam at 200°C. A parabolic solar collector with a focal point temperature of 450°C is used as the heat source. The Rankine cycle has a condensing pressure of 7.0 kPa. Assume the ambient temperature is 39°C. Determine the cycle's second law efficiency and the effect a reduction in collector temperature has on the second law efficiency.

Solution. From the given data, T_R = 723 K and T_0 = 312 K. Again, the values for the state point data are obtained from a Mollier chart and steam tables.

State point 3, turbine inlet, T_3 = 473 K, saturated steam
h_3 = 2792.6 kJ/kg, s_3 = 6.4326 kJ/kg • K
State point 4, turbine exit, P_4 = 7.0 kPa, $s_4 = s_3$
h_4 = 1995.7 kJ/kg
State point 1, condenser exit, $P_1 = P_4$, saturated liquid
h_1 = 162.4 kJ/kg
State point 2, pump exit, $P_2 = P_3$ = 1.9063 MPa
h_2 = 164.3 kJ/kg

To calculate the second law efficiency from equation (13), it is necessary to first calculate η_1 and η_{Carnot}.

$$\eta_1 = \frac{w_{net}}{q_R}$$

$$w_{net} = w_{3-4} - w_{1-2}$$

$$w_{net} = (h_3 - h_4) - (h_2 - h_1) = 795.0 \text{ kJ/kg}$$

$$q_R = (h_3 - h_2) = 2628.3$$

$$\eta_1 = 0.302$$

Downloaded 01 Jun 2010 to 171.66.16.62. Redistribution subject to ASME license or copyright; see http://www.asme.org/terms/Terms_Use.cfm

$$\eta_{\text{Carnot}} = 1 - \frac{T_0}{T_R} = 0.568$$

$$\eta_2 = \frac{0.302}{0.568} = 0.532$$

Table 1 shows the result of decreasing the collector temperature. The increase in second law efficiency is apparent. This is the result of matching the quality of the energy source with the task.

Table 1 The effect of T_R on η_2

T_R(K)	η_{Carnot}	η_2
723	0.568	0.532
673	0.536	0.563
623	0.499	0.605
573	0.455	0.663
523	0.403	0.749

Power Consuming Cycle—Refrigerator

Figure 5 illustrates an actual refrigeration cycle, 1-2-3-4-1, on a T-s diagram. In the case of a refrigerator, the given task is to produce a certain amount of cooling, q_{4-1}. To produce the specified amount of cooling, q_{4-1}, in the actual cycle, the available energy actually used is w_{net}. This is most often in the form of electrical energy input to the compressor motor. Thus

$$(a.e.)_{\text{actual}} = w_{\text{net}}$$

The minimum available energy required to perform the given task, removing heat q_{4-1}, would be the work input required to run the Carnot refrigerator represented by the cycle, 1-2′-3′-4-1. This minimum use of available energy is given by the equation

$$(a.e.)_{\text{min.}} = T_H(s_2' - s_3') - T_L(s_1 - s_4)$$

$$(a.e.)_{\text{min.}} = \left(\frac{T_H}{T_L} - 1\right) T_L \Delta s$$

$$(a.e.)_{\text{min.}} = \left(\frac{T_H}{T_L} - 1\right) q_{4-1}$$

where

$$\Delta s = (s_2' - s_3') = (s_1 - s_4)$$

With the use of equation (11), the second law efficiency is

$$\eta_2 = \frac{\left(\frac{T_H}{T_L} - 1\right) q_{4-1}}{w_{\text{net}}}$$

If β represents the coefficient of performance for a refrigerator

$$\beta = \frac{q_{4-1}}{w_{\text{net}}}$$

the second law efficiency becomes

$$\eta_2 = \frac{\beta}{\beta_{\text{Carnot}}} \tag{14}$$

It is interesting to note the effect of irreversibilities in the actual cycle. At the start of the cycle, the initial available energy is

$$(a.e.)_i = q_{2-3} - T_L(s_1 - s_4)$$

When the cycle is completed, the final available energy is

$$(a.e.)_f = q_{2-3} - T_L(s_2 - s_3)$$

The change in available energy is

$$\Delta(a.e.) = (a.e.)_i - (a.e.)_f$$

$$\Delta(a.e.) = T_L[(s_4 - s_3) + (s_2 - s_1)]$$

This change in available energy represents the loss of available energy due to irreversibilities in the actual cycle. In this case, these are from irreversible expansion and compression processes.

Example 4. A vapor compression refrigeration system uses R12 and operates with an evaporator temperature of −20°C and a peak cycle temperature and pressure of 67°C and 0.7 MPa. The condenser exit temperature and pressure are 27.82°C and 0.7 MPa. The evaporator inlet quality is 0.3. Calculate the second law efficiency for this refrigerator.

Solution. The appropriate state points are shown on Fig. 5. The values for the state point data are obtained from R12 tables or an R12, P-h plot [5].

$h_1 = 207.5$ kJ/kg, $s_1 = 0.8421$ kJ/kg • K

$h_2 = 255.7$ kJ/kg, $s_2 = 0.9072$ kJ/kg • K

$h_3 = 91.14$ kJ/kg, $s_3 = 0.3657$ kJ/kg • K

$h_4 = 94.8$ kJ/kg, $s_4 = 0.3967$ kJ/kg • K

From the given data, $T_L = 253$ K and $T_H = 300.82$ K.

To calculate the second law efficiency from equation (14), it is necessary to first calculate β and β_{Carnot}.

$$\beta = \frac{q_{4-1}}{w_{\text{net}}}$$

$$q_{4-1} = h_1 - h_4 = 112.7 \text{ kJ/kg}$$

$$w_{\text{net}} = h_2 - h_1 = 48.2 \text{ kJ/kg}$$

$$\beta = 2.34$$

$$\beta_{\text{Carnot}} = \frac{1}{\left(\frac{T_H}{T_L} - 1\right)} = 5.29$$

$$\eta_2 = \frac{2.34}{5.29} = 0.442$$

If the cycle were ideal, $s_1 = s_2$ and $h_3 = h_4$, the coefficient of performance, β, would increase and so would the second law efficiency. In this example problem, for the ideal cycle

$P_2 = 0.7$ MPa, $s_2 = s_1$, $h_2 = 234.6$ kJ/kg

$h_4 = h_3 = 91.14$ kJ/kg

$q_{4-1} = h_1 - h_4 = 116.4$ kJ/kg

$w_{\text{net}} = h_2 - h_1 = 27.1$ kJ/kg

$$\beta = \frac{q_{4-1}}{w_{\text{net}}} = 4.29$$

$$\eta_2 = \frac{4.29}{5.29} = 0.811$$

The increase in second law efficiency results from eliminating the irreversibilities in the cycle. That is, the expansion process from 3-4 is adiabatic and the compression process from 1-2 is isentropic.

Power Consuming Cycle—Heat Pump

Figure 6 illustrates an actual heat pump cycle, 1-2-3-4-1, on a T-s diagram. In the case of a heat pump, the given task is to produce a given amount of heat at T_H. This is shown in Fig. 6 as the heat removed in going from state 2 to state 3. The actual available energy required to accomplish this is

$$(a.e.)_{\text{actual}} = w_{\text{net}}$$

Downloaded 01 Jun 2010 to 171.66.16.62. Redistribution subject to ASME license or copyright; see http://www.asme.org/terms/Terms_Use.cfm

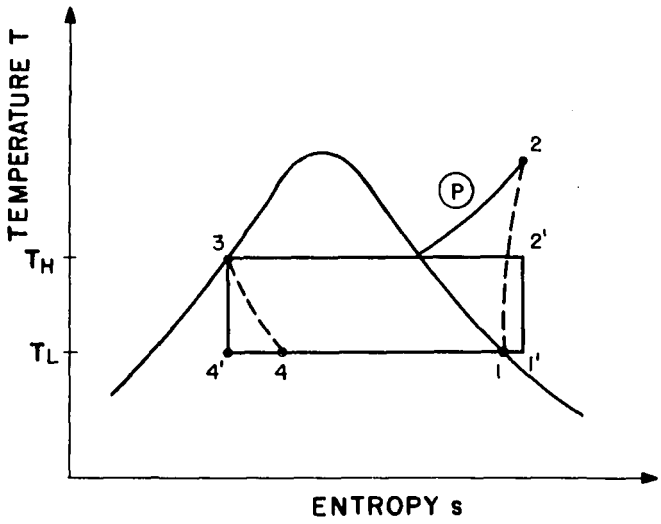


Fig. 6 A T-s diagram illustrating heat pump cycles

where w_{net} is the work required to run the compressor. The minimum available energy to accomplish the same task would result from the use of a Carnot heat pump operating between temperature limits T_H and T_L. The Carnot heat pump does not operate at state 2 because there would be a loss of available energy due to the irreversible heat transfer between T_2 and T_H. In this case, the areas under the curves 2–3 and 2′–3 must be equal since the given task is to provide heating, q_{2-3}. Thus,

$$q_{2-3} = T_H(s_2' - s_3)$$

The minimum available energy required to perform the given task is

$$(a.e.)_{\min.} = T_H(s_2' - s_3) - T_L(s_1' - s_4')$$

$$(a.e.)_{\min.} = \left(1 - \frac{T_L}{T_H}\right) T_{H\Delta S}$$

$$(a.e.)_{\min.} = \left(1 - \frac{T_L}{T_H}\right) q_{2-3}$$

where

$$\Delta s = (s_2' - s_3) = (s_1' - s_4')$$

With the use of equation (11), the second law efficiency is

$$\eta_2 = \frac{\left(1 - \frac{T_L}{T_H}\right) q_{2-3}}{W_{net}}$$

If β' represents the coefficient of performance for a heat pump

$$\beta' = \frac{q_{2-3}}{w_{net}}$$

and the second law efficiency becomes

$$\eta_2 = \frac{\beta'}{\beta'_{Carnot}} \tag{15}$$

Conclusion

Energy conservation demands that we examine quantity and quality. The first law efficiency helps in analyzing the former, the second law efficiency in analyzing the latter. Should an analysis show the second law efficiency is low, lower than current technology allows, the method of energy conversion must be examined to raise both efficiencies. As we progress, we should not only convert energy efficiently (η_1), but we should match the available energy sources to the task, improving η_2. To do otherwise is wasteful and only goes partway in saving energy for the future.

References

1 Berg, C. A., "A Technical Basis for Energy Conservation," *Mechanical Engineering*, May 1974.

2 Kreith, F., and Kreider, J. F., *Principles of Solar Engineering*, Hemisphere Publishing, Washington, 1978.

3 Paolino, M. A., and Kuspa, J. P., "A Simple Approach to the Concepts of Reversible Work, Availability and Irreversibility," *Mechanical Engineering News*, Vol. 17, No. 3, Aug. 1980.

4 Van Wylen, G. J., and Sonntag, R. E., *Fundamentals of Classical Thermodynamics*, Wiley, New York, 1976.

5 Reynolds, W. C., *Thermodynamic Properties in SI*, Stanford University, Stanford, 1979.

6 Burghardt, M. D., *Engineering Thermodynamics with Applications*, Harper and Row, New York, 1978.

Downloaded 01 Jun 2010 to 171.66.16.62. Redistribution subject to ASME license or copyright; see http://www.asme.org/terms/Terms_Use.cfm

Journal of Engineering for Power

Technical Briefs

Sizing Safety Valve Vent Pipes for Saturated Steam

H. E. Brandmaier[1]

An earlier one-dimensional ideal gas analysis was changed to incorporate equilibrium properties of steam as given by the 1967 ASME steam tables.

A generalized procedure based on pressure and entropy as independent variables is used to calculate choked flow conditions at the valve orifice, valve pipe outlet and vent pipe outlet. At the third location, the results are independent of whether flow in the vent pipe is supersonic or subsonic. An integral method is used to calculate the vent pipe length required to choke the flow.

Computed data are compared with ideal gas data. The vent pipe size, to prevent blowback into the powerplant, is less conservative using real steam data. The flow properties, particularly specific volume, are significantly different.

Nomenclature

A = one dimensional area ratio
D = internal pipe diameter
f = friction factor
G = specific mass flow
h = enthalpy
L = vent pipe length
M = Mach Number
P = pressure
S = entropy
T = temperature
U = one dimensional velocity
V = specific volume
γ = isentropic exponent

Subscripts

B = atmospheric conditions
SAT = saturation conditions
T = total or stagnation conditions
0 = valve orifice
1 = valve pipe outlet
2 = vent pipe inlet, flow reattachment point
3 = downstream of normal shock
4 = vent pipe outlet

Introduction

Sizing of steam safety valve vent pipes of the open type has been described in a number of recent papers [1-3]. The flow was assumed to be one-dimensional with steam modeled either as a perfect gas characterized by a suitable isentropic exponent [1] or partially as a perfect gas and partially as real steam [2, 3]. The one-dimensional analysis described herein is consistent in using the equilibrium properties of steam given in the ASME steam tables [4]. Specific application is to initially saturated steam.

The general flow characteristics were described in some detail by Brandmaier and Knebel [1]. Referring to Fig. 1, the features of the adiabatic flow model are:

1 Isentropic flow to a choked valve orifice at section 0
2 An increase in entropy between the valve orifice and valve pipe outlet, section 1, sufficient to choke the flow at the outlet
3 An underexpanded free jet leaving the valve pipe outlet and intersecting the vent pipe wall at section 2
4 Choked flow at the vent pipe outlet, section 4, due to shock interactions and pipe friction

The objective of the analysis is to determine the minimum vent pipe size to prevent blowback of the flow into the powerplant interior. The possibility of entrainment of air by the steam is not considered in this study.

The computer program used to calculate the data makes extensive use of the Regula Falsi iterative method [5]. Static pressure and entropy are considered the principal variables.

At the onset, it is recognized that the major problem is representation of a complex three-dimensional flow by a simple one-dimensional model.

Valve Pipe Flow

The usual assumption that the flow is choked at the valve pipe outlet presupposes a dissipative process sufficient to produce the required entropy increase between the safety valve orifice and the valve pipe outlet. Brandmaier and Knebel [1] opined that this assumption leads to a conservative vent pipe size. Regula Falsi is used to calculate the static pressure at which the flow velocity is sonic – the critical pressure – at a specified entropy. The entropy of saturated vapor is assumed at the valve orifice while Regula Falsi is also used to determine the entropy that chokes the flow at the larger valve pipe outlet area.

Figure 2 shows the relationship between the critical pressure and the ratio of valve orifice to outlet areas for saturation pressures of 250, 500 and 1000 psia. Table 1 gives factors to convert from US customary to SI units. For a perfect gas, the product of static pressure and area, is constant when the flow is critical [1]. Figure 2 shows that this linear relation approximates the behavior of saturated steam. The displacement of the straight lines at low area ratios appears to correspond to superheating at the valve pipe outlet. Assuming a minimum critical pressure equal to atmospheric produces the limit shown in Fig. 2.

[1] Manager, Engineering, Burns and Roe, Inc., Paramus, N. J. Mem. ASME

Contributed by the Power Division for publication in the JOURNAL OF ENGINEERING FOR POWER. Manuscript received at ASME Headquarters 21 July 1981.

Copyright © 1982 by ASME

Downloaded 01 Jun 2010 to 171.66.16.62. Redistribution subject to ASME license or copyright; see http://www.asme.org/terms/Terms_Use.cfm

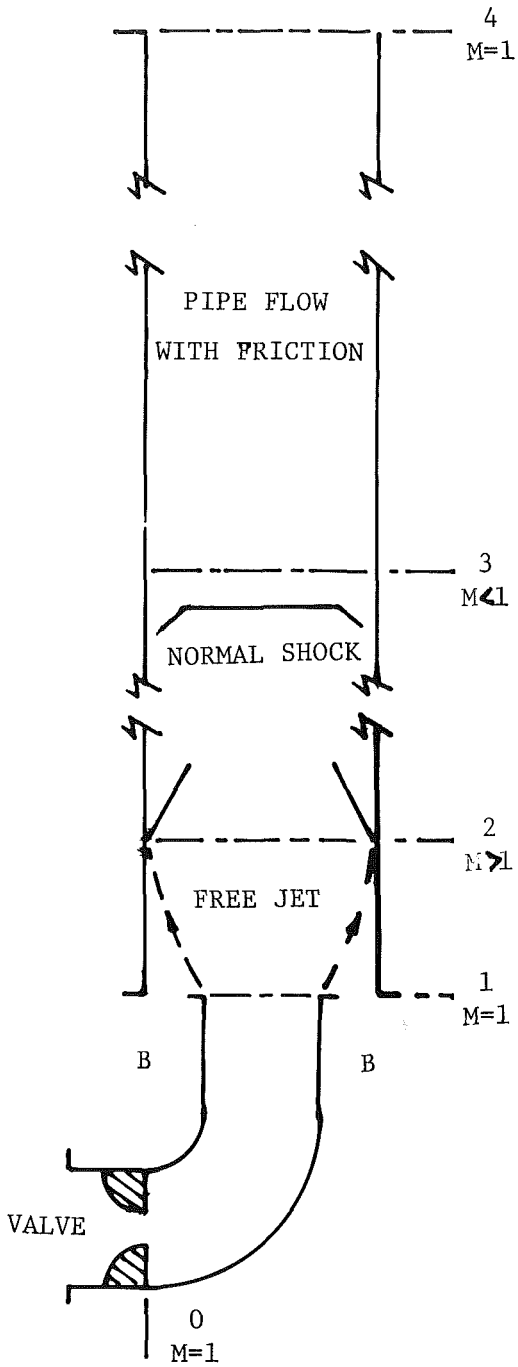


Fig. 1 Flow model

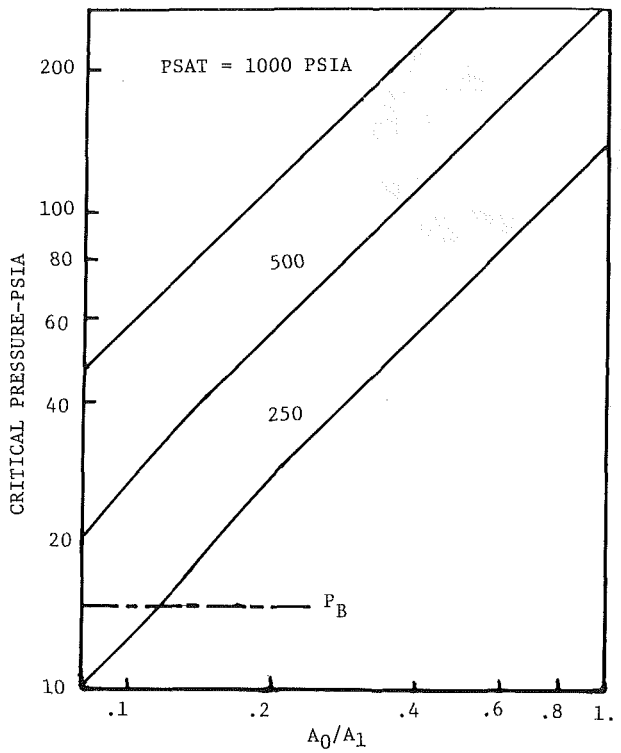


Fig. 2 Critical pressure data

Table 1 US customary to SI conversion (15)

Multiply	By	To Obtain
psi	6.894757	kPa
BTU/lb – °F	4.186800	k J/(kg – K)
ft^3/lb	6.242797×10^2	m^3/kg
ft/s	3.048000×10^{-1}	m/s
lb/ft^2-s	4.882428	kg/m^2-s

Vent Pipe Inlet

When the critical pressure at the valve pipe outlet is above atmospheric, the downstream flow corresponds to an underexpanded free jet. Its properties can be calculated using the Method of Characteristics [6]. Except at the boundary where mixing between steam and the surrounding air occurs, the flow is isentropic. The static pressure is constant along the boundary and equal to the surrounding atmospheric pressure. Along the free jet centerline, the pressure decreases from the valve pipe outlet pressure to pressures considerably below atmospheric. At a certain distance from the outlet, a normal shock, referred to as the Mach Disk [7] occurs. The basic supersonic wave interactions continue downstream of this point until the combination of shock interactions in the interior of the jet and mixing at the boundary complete dissipation of the jet.

It is significant that the free jet reaches a maximum diameter. Surrounding the free jet with the vent pipe has little effect on the flow until its diameter approaches this maximum. When this occurs, the dissipated jet fills the vent pipe and flows subsonically to the outlet. However, when the vent pipe diameter is less than the free jet diameter, an oblique shock is generated at the intersection of the jet boundary, the reattachment point, with the wall, as sketched in Fig. 1. Its initial strength, measured in terms of the pressure rise across it, depends on the Mach Number and flow direction at the boundary.

Within the context of a one-dimensional flow, the oblique shock at the reattachment point and subsequent shock interactions within the vent pipe must be replaced by a normal shock downstream of which the flow is subsonic. However, if the axial distance between the reattachment point and the point where the real flow becomes subsonic is greater than the vent pipe length, the vent pipe outlet flow will be supersonic.

The properties of an 'equivalent' one-dimensional supersonic flow just upstream of the attachment point can be evaluated by assuming a uniform average static pressure P_2, and applying conservation of mass, momentum, and energy between sections 1 and 2. It should be noted that the average P_2 is less than P_B at large ratios of A_2/A_1 and greater than P_B at small ratios. Kochendorfer and Rousso [8], in their investigation of aircraft ejectors, assumed $P_2 = P_B$ for all area ratios. The minimum value of P_2 corresponds to $S_2 = S_1$.

Barakauskas's pressure measurements for a similar flow geometry [9] showed that near section 1 the flow is similar to an unconfined, underexpanded free jet, while at section 2 the

Downloaded 01 Jun 2010 to 171.66.16.62. Redistribution subject to ASME license or copyright; see http://www.asme.org/terms/Terms_Use.cfm

pressure level approximates that in a nozzle of the same area ratio. Brandmaier and Knebel [1] assumed P_2 is determined by the pressure drop between sections 3 and 4 due to friction in the vent pipe, whereas Sale [2] and Liao [3] used a base pressure analysis to relate A_2/A_1 to P_1/P_B.

Figure 3 compares theoretical and experimental data [8, 10, 11, 12] for supersonic flow of air across an abrupt enlargement. It relates the pressure at the free jet boundary to the area ratio of the enlargement. The theoretical base pressure curve was determined using the method described by Korst [13] and approximate free jet boundary shapes based on Charwat [14]. Agreement between theory and experiment is reasonable. The difference between the two theoretical models is certainly consistent with the one-dimensional flow assumption.

One-dimensional flow properties at section 2 are determined by applying conservation of momentum between sections 1 and 2. Thus,

$$G_1A_1U_1 + P_1A_1 + P_B(A_2 - A_1) = G_2A_2U_2 + P_2A_2 \quad (1)$$

Using one-dimensional mass conservation to eliminate U_1 and U_2 and solving for A_1/A_2 results in,

$$V_2(A_1/A_2) = (1/2)(V_1 + (P_1 - P_B)/G_1^2) + ((1/4)(V_1 + (P_1 - P_B)/G_1^2)^2 - (P_2 - P_B)V_2/G_1^2)^{1/2} \quad (2)$$

For $P_2 = P_B$, equation (2) simplifies to,

$$V_2(A_1/A_2) = V_1 + (P_1 - P_B)/G_1^2 \quad (3)$$

The corresponding computer program assumes either P and S or P and h as independent variables and solves for the remaining thermodynamic and flow properties. The calculation procedure, subsequent to solving equations (2) or (3) for V_2A_1/A_2, is the following. From conservation of energy,

$$h_2 = h_T - (1/2)G_1^2(V_2A_1/A_2)^2;\ h_T = h_{SAT} \quad (4)$$

and from the thermodynamic properties of steam sub-routine,

$$S_2 = S_2(P_B, h_2) \text{ and } V_2 = V_2(P_B, h_2) \quad (5)$$

Finally,

$$A_1/A_2 = (V_2A_1/A_2)/V_2 \quad (6)$$

Simple iteration is used with equation (2) for a specified P_2 since V_2 appears on the right hand side. Equation (3) doesn't require an iterative solution. As P_2 is decreased below P_B, a value is reached for which $S_2 = S_1$. This is the thermodynamic limit described by Brandmaier and Knebel [1].

Figure 4 shows the variation of the vent pipe area ratio A_2/A_1 with the valve pipe area ratio A_1/A_0 for a number of cases. Consider the data for a 1000 psia saturation pressure. The maximum value of A_2/A_1 corresponds to the same entropy at sections 1 and 2, i.e., $S_2 = S_1$. However, the maximum free jet cross-sectional area, based on the method described by Charwat [14] is less than the $S_2 = S_1$ value and therefore is the real limit to the analysis described herein. The minimum value of A_2/A_1 was somewhat arbitrarily taken to correspond to $P_2 = P_B$. Between the maximum and minimum curves, A_2/A_1 is determined by the combination of shock interactions and fluid friction in the vent pipe. A_2/A_1 for $fL/D_1 = 4$, 8 and 16 are shown. These correspond to a normal shock near section 2, followed by subsonic acceleration, due to fluid friction, to choked flow at section 4. Finally, the effect of saturation pressure on A_2/A_1 is shown for $P_2 = P_B$. The value of A_1/A_0 at $A_2/A_1 = 1$ corresponds to $P_1 = P_B$ under which condition the free jet boundary is parallel to its axis, i.e., there is no free jet-vent pipe wall intersection.

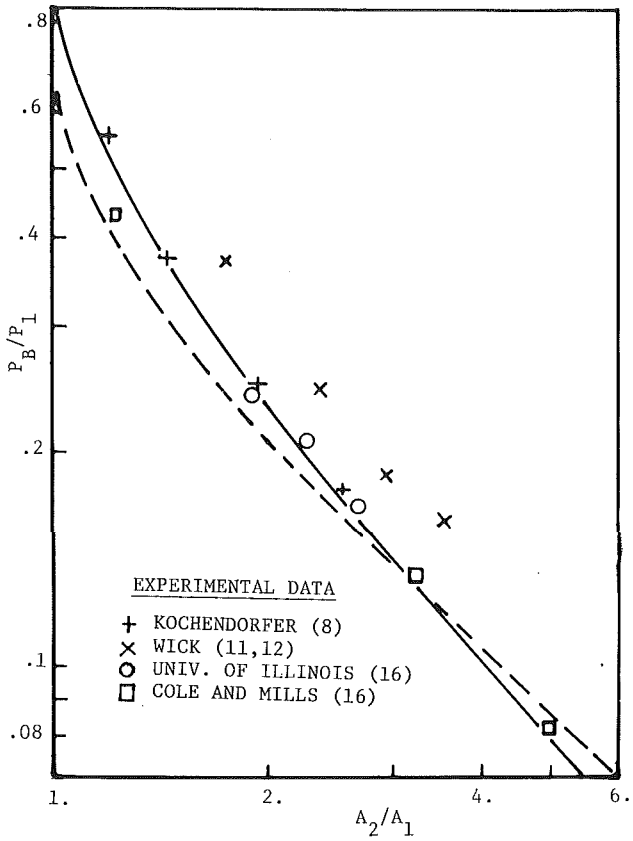


Fig. 3 Base pressure data for air _____ $P_2 = P_B$; · · · · · base pressure analysis

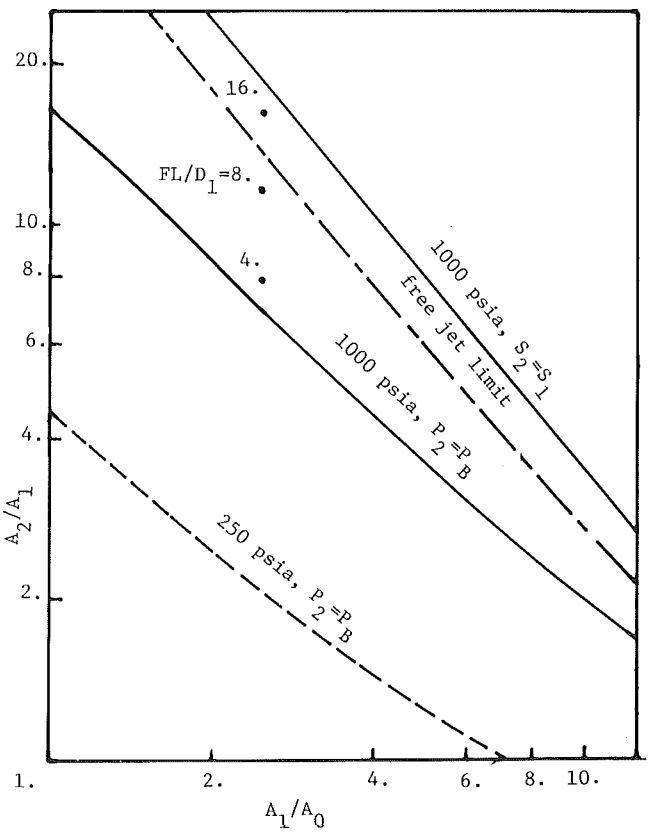


Fig. 4 Minimum vent pipe area to prevent blowback

Downloaded 01 Jun 2010 to 171.66.16.62. Redistribution subject to ASME license or copyright; see http://www.asme.org/terms/Terms_Use.cfm

Normal Shock

The maximum vent pipe length was shown [1] to correspond to subsonic flow downstream of a shock system which, within the one-dimensional model, is a normal shock. Conservation of mass, momentum, and energy across the normal shock between sections 2 and 3 in Fig. 1 results in the following equation for the specific volume downstream of the normal shock,

$$V_3 = V_2 + (P_2 - P_3)/G_2^2 \tag{7}$$

This is the same form as equation (3) except that $A_2 = A_3$. The computational procedure is also similar to equations (4) and (5) except that Regula Falsi is used to iterate on P_3 until V_3 from equation (7) approximates V_3 from the steam property sub-routine, i.e., $V_3 = V_3(P_3, h_3)$.

Vent Pipe Outlet

The maximum vent pipe length, for both subsonic and supersonic flow, corresponds to choked flow at the vent pipe outlet. For a constant area pipe and no elevational changes, conservation of mass and momentum can be written as,

$$dP = -G^2(dV - (f/2D)\,V dL) \tag{8}$$

as $V = V(P,S)$,

$$dV = (\partial V/\partial S)_s dP + (\partial V/\partial S)_p dS \tag{9}$$

using the identity

$$(\partial V/\partial S)_p = T(\partial V/\partial h)_p \tag{10}$$

equation (9) becomes,

$$dV = (\partial V/\partial P)_s dP + T(\partial V/\partial h)_p ds \tag{11}$$

From the First and Second Laws of Thermodynamics,

$$Tds = dh - Vdp \tag{12}$$

Substituting equation (12) for dp and $dh = -G^2 V dV$ from conservation of energy results in,

$$dS = (f/2D)\,(G^2 V^2/T)\,dL \tag{13}$$

Inserting equations (11) and (13) into equation (8) yields,

$$dP/dfL/D = (1/2)G^2 V(G^2 V(\partial V/\partial h)_p + 1)/(1 + G^2(\partial V/\partial p)_s) \tag{14}$$

The second term in the denominator is recognized as minus the square of the Mach Number. Equations (13) and (14) are integrated simultaneously using the Runge-Kutta or similar numerical method. Integration stops when the flow chokes or $M = 1$. From a computational viewpoint, this requires significantly reducing the integration step as M approaches 1.

Alternatively, the same approach can be used to determine the choked flow properties at section 4 as was used to determine the choked flow properties at section 1. It is interesting to note that these properties are the same for both subsonic and supersonic flow in the vent pipe. The corresponding vent pipe length in terms of fL/D_4 can be determined by dividing equation (8) by V and integrating. Thus,

$$fL/D_4 = -(2/G_4^2)\int_{P_3}^{P_4} dP/V - 2\,ln(V_4/V_3) \tag{15}$$

The integral is evaluated using Tchebycheff's nine point polynomial equation (5). Using Regula Falsi, the entropy required to maintain G constant at each of the nine pressures specified by the Tchebycheff method is calculated. Results using the differential and integral methods are close; differences are due to the approximations inherent in each numerical method.

Figure 5 shows A_2/A_1 as a function of fL/D_1 and A_1/A_0

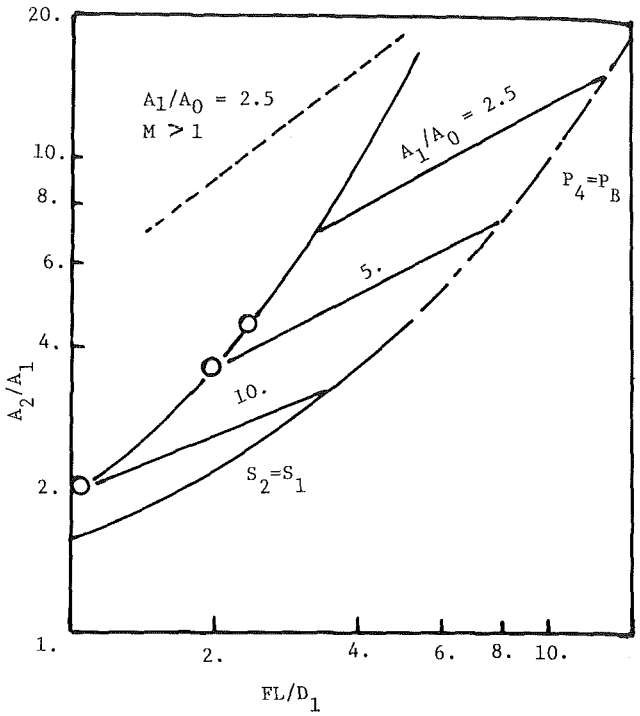


Fig. 5 Design data for 1000 psi saturation pressure and subsonic vent pipe flow

Table 2 Calculated data for 1000 psia saturation pressure

$P_2 = P_B$, $A_1/A_0 = 5$; $P_B = 14.69$ psia

Section	Units	0	1	2	3	4
Pressure	psia	586.3	114.3	14.69	57.84	30.42
Entropy	Btu/lb-°F	1.391	1.540	1.612	1.650	1.678
Specific volume	ft^3/lb	.732	3.722	24.13	7.482	13.36
Fluid velocity	ft/s	1472.	1497.	2644.	820.1	1464.
Sonic velocity	ft/s	1472.	1497.	1359.	1622.	1464.
Quality	%	92.63	95.31	89.99	Super	98.49
Specific mass flow	lb/ft^2-s	2012.	402.3	109.6	109.6	109.6

fL/D_1 for subsonic vent pipe flow = 2.009
fL/D_1 for supersonic vent pipe flow = 0.916

Table 3 Ideal gas data for 1000 psia saturation pressure

$\gamma = 1.1$, $P_2 = P_B$, $A_1/A_0 = 5$, $P_B = 14.69$ psia

Section		0	1	2	3	4
Pressure	psia	584.7	116.9	14.69	56.51	29.66
Entropy	Btu/lb-°F	1.391	1.568	1.654	1.689	1.720
Specific volume	ft^3/lb	.974	4.872	34.48	10.42	19.21
Fluid velocity	ft/s	1704.	1704.	3058.	965.5	1704.
Sonic velocity	ft/s	1704.	1704.	1607.	1733.	1704.
Specific mass flow	lb/ft^2-s	1749.	349.7	88.71	88.71	88.71

fL/D_1 for subsonic vent pipe flow = 1.855
fL/D_1 for supersonic vent pipe flow = 0.910

Downloaded 01 Jun 2010 to 171.66.16.62. Redistribution subject to ASME license or copyright; see http://www.asme.org/terms/Terms_Use.cfm

for $P_{SAT} = 1000$ PSIA. Similar plots appear in reference [1]. At a specified A_1/A_0 and fL/D_1, the plot gives the minimum A_2/A_1 for no blowback. For each A_1/A_0, limiting values were taken to correspond to $P_2 = P_B$ and $S_1 = S_2$. However, at some fL/D_1, $P_4 = P_B$, which limit is also shown. The circled data points correspond to $P_{SAT} = 250$ psia. That they lie along the $P_{SAT} = 1000$ psia curve is further evidence that the perfect gas analysis is generally satisfactory.

For a given A_2/A_1, the curve gives the maximum value of fL/D_1 for no blowback. This corresponds to an 'equivalent' normal shock near section 2 followed by subsonic acceleration, due to fluid friction, to choked flow at section 4. The dotted curve for $A_1/A_0 = 2.5$ represents the maximum fL/D_1 for shockless supersonic flow in the vent pipe. Because of the oblique shock at section 2, this maximum will never be realized. Between the subsonic and supersonic limits, the shock system in the vent pipe adjusts to produce subsonic flow at section 4 which results in $P_4 = P_B$.

Presentation of the data in the form used in Fig. 5 provides convenient design curves. These can be prepared using a computer program with a steam property sub-routine. If steam is modeled as a perfect gas, a programmable calculator program is all that is required. However, to be more correct, the effect of diameter on f should be included when calculating fL/D_1.

Finally, Tables 2 and 3 compare data at sections 1 to 4 for real steam and steam modeled as a perfect gas having an isentropic exponent of 1.1. For a specified mass flow, the perfect gas assumption because of its smaller specific mass flows yields conservative flow areas, which result was preliminarily reached in reference [1].

Conclusions

The analysis presented herein is consistent in that it uses the properties of real steam, initially saturated upstream of the safety valve inlet, throughout the calculation. The computer program, used to perform the calculations, is relatively straightforward if the equations described in the preceding sections are used. If a computer is unavailable, similar data can be easily calculated using the perfect gas approach described in reference [1].

References

1 Brandmaier, H. E., and Knebel, M. E., "Steam Flow Through Safety Valve Vent Pipes," *Journal of Fluids Engineering,* Vol. 98, June 1976, pp. 199–207.

2 Sale, J. W., "Safety Valve Vent Pipe Sizing for Open Discharge Systems" *Safety Relief Valves,* R. W. Haupt and R. A. Mayer 1979, pp. 79–95.

3 Sales, J. W., "Safety Valve Vent Pipe Sizing for Open Discharge Systems," *Safety Relief Valves,* edited by R. W. Haupt and R. A. Mayer 1979, pp. 79–95.

4 Meyer, C. A. et al, "Thermodynamic and Transport Properties of Steam," ASME, 1967.

5 Scarborough, J. B., *Numerical Mathematical Analysis,* The Johns Hopkins Press, Baltimore, 1962, pp. 160–163 and 194–199.

6 Owczarek, J. A., *Fundamentals of Gas Dynamics,* International Textbook Company, 1964, pp. 468–471.

7 Abbett, M., "The Mach Disk in Underexpanded Exhaust Plumes," *American Institute of Aeronautics and Astronautics Journal,* Paper No. 70–231.

8 Kochendorfer, F. D., and Rousso, M. D., "Performance Characteristics of Aircraft Cooling Ejectors Having Short Cylindrical Shrouds," NACA RM ES1E01, May, 1951.

9 Barakauskas, E. J., "Sudden Expansion of a Bounded Jet at a High Pressure," *AIAA Journal,* Vol. 2, No. 9, Sept. 1964, pp. 1644–1645.

10 Korst, H. H., Chow, W. L., and Zumwalt, "Research on Transonic and Supersonic Flow of a Real Fluid at Abrupt Increases in Cross-Section," University of Illinois ME Technical Report 392-5, Dec. 1959.

11 Wick, R. S., "The Effect of Boundary Layer on Sonic Flow Through an Abrupt Cross-Sectional Area Change," *Journal of the Aeronautical Sciences,* Vol. 20, No. 10, Oct. 1953, pp. 675–682.

12 Wick, R. S., Further Comments on "The Effect of Boundary Layer on Sonic Flow Through an Abrupt Cross-Sectional Area Change," *Journal of the Aeronautical Sciences,* Vol. 22, No. 2, Feb. 1955, pp. 136–137.

13 Korst, H. H., "A Theory for Base Pressures in Transonic and Supersonic Flows," *Journal of Applied Mechanics,* Vol. 23, Dec. 1956, pp. 593–599.

14 Charwat, A. F., "Boundary of Underexpanded Axisymmetric Jets Issuing into Still Air," *AIAA Journal,* Vol. 2, No. 1, Jan. 1964, pp. 161–163.

15 ASTM Standard for Metric Practice, E380-79, American Society for Testing and Materials.

16 Korst, H. H., Chow, W. L., and Zumwalt, G. W., "Research on Transonic and Supersonic Flow of a Real Fluid at Abrit Increases in Cross-Section," University of Illinois, ME Technical Report 392-5, December 1959.

Boundary Layer Transition and Separation on a Compressor Rotor Airfoil

R. P. Dring[1]

Nomenclature

B = airfoil chord
B_x = airfoil axial chord
C_x = axial flow speed
C_f = skin friction coefficient
P = pressure
P_1 = inlet static pressure
Q_1 = inlet relative dynamic pressure
R_e = Reynolds number based on B and V_1
S = surface arc length
T_u = free stream turbulence
U = wheel speed at midspan
V = relative flow speed
V_1 = inlet relative flow speed
X = axial distance

Introduction

Analytical design tools in the areas of the blade-to-blade potential flow and the boundary layer flow over the airfoils of axial compressors (and turbines) are in common use today. The substantiation of these tools is based primarily on cascade tests and relatively large scale wind tunnel tests. There is little in the way of actual rotating rig data and even less in the way of rotor data. Potential flow comparisons for flow over a compressor rotor airfoil have been presented by Dring et al. [1]. The current work presents boundary layer calculations based on these potential flow results and comparisons with surface flow visualization results indicating the locations of boundary layer transition and separation.

Experiment

The experiment was discussed in detail in reference [1]. It consisted of a 5-ft (1.52-m) dia isolated rotor (axial inlet) with a 0.8 hub/tip ratio and airfoils with a solicity of 1.0 and a 6 in. (0.152 m) true chord, i.e., an aspect ratio of 1.0. The airfolil (described in reference 1, table 1) and the velocity triangles were representative of a blade in the middle of a multistage compressor. The flow was incompressible ($M \approx 0.2$) but the Reynolds number was typical of an engine application ($Re \approx 0.5 \times 10^6$). A variety of measurements were made on the rotor including airfoil pressure distributions and surface flow visualization. The flow visualization technique employed ammonia, which was discharged from surface static pressure taps on the airfoil, and left a dark streak on Ozalid paper that had been attached smoothly to the airfoil surface.

Flow visualization results for the design flow coefficient

Gas Turbine Technology, United Technologies Research Center, East Hartford, Conn. 06108

Contributed by the Gas Turbine Division for publication in the JOURNAL OF ENGINEERING FOR POWER. Manuscript received at ASME Headquarters August 27, 1981.

Downloaded 01 Jun 2010 to 171.66.16.62. Redistribution subject to ASME license or copyright; see http://www.asme.org/terms/Terms_Use.cfm

for P_{SAT} = 1000 PSIA. Similar plots appear in reference [1]. At a specified A_1/A_0 and fL/D_1, the plot gives the minimum A_2/A_1 for no blowback. For each A_1/A_0, limiting values were taken to correspond to $P_2 = P_B$ and $S_1 = S_2$. However, at some fL/D_1, $P_4 = P_B$, which limit is also shown. The circled data points correspond to P_{SAT} = 250 psia. That they lie along the P_{SAT} = 1000 psia curve is further evidence that the perfect gas analysis is generally satisfactory.

For a given A_2/A_1, the curve gives the maximum value of fL/D_1 for no blowback. This corresponds to an 'equivalent' normal shock near section 2 followed by subsonic acceleration, due to fluid friction, to choked flow at section 4. The dotted curve for A_1/A_0 = 2.5 represents the maximum fL/D_1 for shockless supersonic flow in the vent pipe. Because of the oblique shock at section 2, this maximum will never be realized. Between the subsonic and supersonic limits, the shock system in the vent pipe adjusts to produce subsonic flow at section 4 which results in $P_4 = P_B$.

Presentation of the data in the form used in Fig. 5 provides convenient design curves. These can be prepared using a computer program with a steam property sub-routine. If steam is modeled as a perfect gas, a programmable calculator program is all that is required. However, to be more correct, the effect of diameter on f should be included when calculating fL/D_1.

Finally, Tables 2 and 3 compare data at sections 1 to 4 for real steam and steam modeled as a perfect gas having an isentropic exponent of 1.1. For a specified mass flow, the perfect gas assumption because of its smaller specific mass flows yields conservative flow areas, which result was preliminarily reached in reference [1].

Conclusions

The analysis presented herein is consistent in that it uses the properties of real steam, initially saturated upstream of the safety valve inlet, throughout the calculation. The computer program, used to perform the calculations, is relatively straightforward if the equations described in the preceding sections are used. If a computer is unavailable, similar data can be easily calculated using the perfect gas approach described in reference [1].

References

1 Brandmaier, H. E., and Knebel, M. E., "Steam Flow Through Safety Valve Vent Pipes," *Journal of Fluids Engineering,* Vol. 98, June 1976, pp. 199–207.

2 Sale, J. W., "Safety Valve Vent Pipe Sizing for Open Discharge Systems" *Safety Relief Valves,* R. W. Haupt and R. A. Mayer 1979, pp. 79–95.

3 Sales, J. W., "Safety Valve Vent Pipe Sizing for Open Discharge Systems," *Safety Relief Valves,* edited by R. W. Haupt and R. A. Mayer 1979, pp. 79–95.

4 Meyer, C. A. et al, "Thermodynamic and Transport Properties of Steam," ASME, 1967.

5 Scarborough, J. B., *Numerical Mathematical Analysis,* The Johns Hopkins Press, Baltimore, 1962, pp. 160–163 and 194–199.

6 Owczarek, J. A., *Fundamentals of Gas Dynamics,* International Textbook Company, 1964, pp. 468–471.

7 Abbett, M., "The Mach Disk in Underexpanded Exhaust Plumes," *American Institute of Aeronautics and Astronautics Journal,* Paper No. 70–231.

8 Kochendorfer, F. D., and Rousso, M. D., "Performance Characteristics of Aircraft Cooling Ejectors Having Short Cylindrical Shrouds," NACA RM ES1E01, May, 1951.

9 Barakauskas, E. J., "Sudden Expansion of a Bounded Jet at a High Pressure," *AIAA Journal,* Vol. 2, No. 9, Sept. 1964, pp. 1644–1645.

10 Korst, H. H., Chow, W. L., and Zumwalt, "Research on Transonic and Supersonic Flow of a Real Fluid at Abrupt Increases in Cross-Section," University of Illinois ME Technical Report 392-5, Dec. 1959.

11 Wick, R. S., "The Effect of Boundary Layer on Sonic Flow Through an Abrupt Cross-Sectional Area Change," *Journal of the Aeronautical Sciences,* Vol. 20, No. 10, Oct. 1953, pp. 675–682.

12 Wick, R. S., Further Comments on "The Effect of Boundary Layer on Sonic Flow Through an Abrupt Cross-Sectional Area Change," *Journal of the Aeronautical Sciences,* Vol. 22, No. 2, Feb. 1955, pp. 136–137.

13 Korst, H. H., "A Theory for Base Pressures in Transonic and Supersonic Flows," *Journal of Applied Mechanics,* Vol. 23, Dec. 1956, pp. 593–599.

14 Charwat, A. F., "Boundary of Underexpanded Axisymmetric Jets Issuing into Still Air," *AIAA Journal,* Vol. 2, No. 1, Jan. 1964, pp. 161–163.

15 ASTM Standard for Metric Practice, E380-79, American Society for Testing and Materials.

16 Korst, H. H., Chow, W. L., and Zumwalt, G. W., "Research on Transonic and Supersonic Flow of a Real Fluid at Abrit Increases in Cross-Section," University of Illinois, ME Technical Report 392-5, December 1959.

Boundary Layer Transition and Separation on a Compressor Rotor Airfoil

R. P. Dring[1]

Nomenclature

B = airfoil chord
B_x = airfoil axial chord
C_x = axial flow speed
C_f = skin friction coefficient
P = pressure
P_1 = inlet static pressure
Q_1 = inlet relative dynamic pressure
R_e = Reynolds number based on B and V_1
S = surface arc length
T_u = free stream turbulence
U = wheel speed at midspan
V = relative flow speed
V_1 = inlet relative flow speed
X = axial distance

Introduction

Analytical design tools in the areas of the blade-to-blade potential flow and the boundary layer flow over the airfoils of axial compressors (and turbines) are in common use today. The substantiation of these tools is based primarily on cascade tests and relatively large scale wind tunnel tests. There is little in the way of actual rotating rig data and even less in the way of rotor data. Potential flow comparisons for flow over a compressor rotor airfoil have been presented by Dring et al. [1]. The current work presents boundary layer calculations based on these potential flow results and comparisons with surface flow visualization results indicating the locations of boundary layer transition and separation.

Experiment

The experiment was discussed in detail in reference [1]. It consisted of a 5-ft (1.52-m) dia isolated rotor (axial inlet) with a 0.8 hub/tip ratio and airfoils with a solicity of 1.0 and a 6 in. (0.152 m) true chord, i.e., an aspect ratio of 1.0. The airfolil (described in reference 1, table 1) and the velocity triangles were representative of a blade in the middle of a multistage compressor. The flow was incompressible ($M \approx 0.2$) but the Reynolds number was typical of an engine application ($Re \approx 0.5 \times 10^6$). A variety of measurements were made on the rotor including airfoil pressure distributions and surface flow visualization. The flow visualization technique employed ammonia, which was discharged from surface static pressure taps on the airfoil, and left a dark streak on Ozalid paper that had been attached smoothly to the airfoil surface.

Flow visualization results for the design flow coefficient

Gas Turbine Technology, United Technologies Research Center, East Hartford, Conn. 06108

Contributed by the Gas Turbine Division for publication in the JOURNAL OF ENGINEERING FOR POWER. Manuscript received at ASME Headquarters August 27, 1981.

Copyright © 1982 by ASME

Downloaded 01 Jun 2010 to 171.66.16.62. Redistribution subject to ASME license or copyright; see http://www.asme.org/terms/Terms_Use.cfm

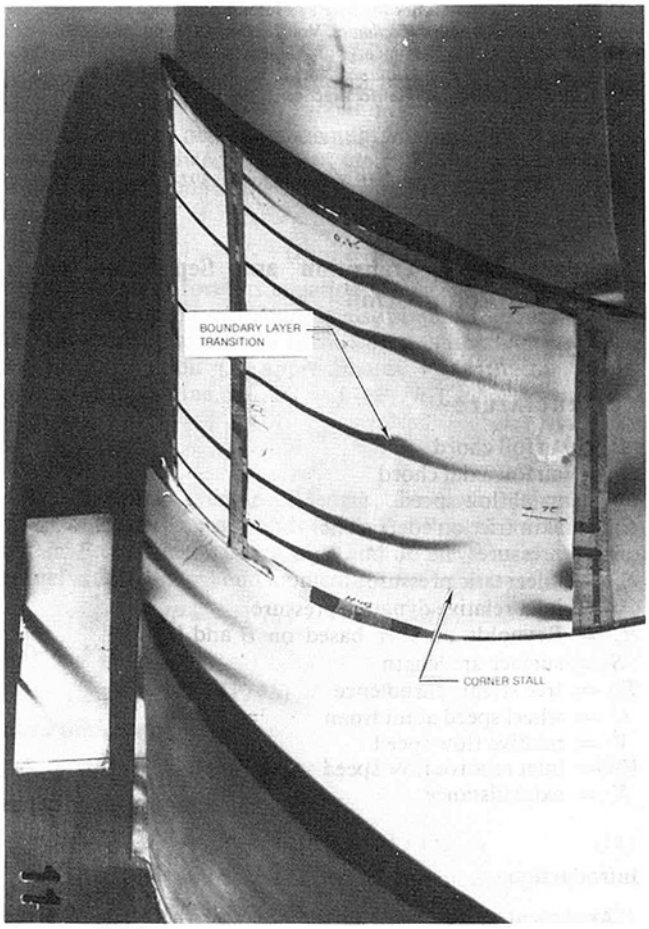


Fig. 1 Suction surface flow visualization at $C_x/U = 0.85$

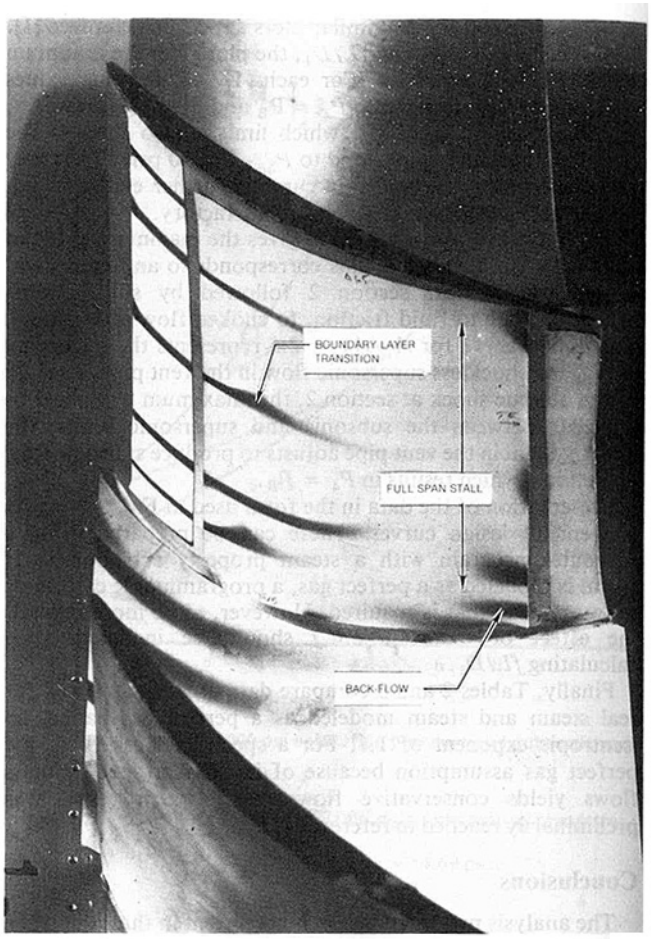


Fig. 2 Suction surface flow visualization at $C_x/U = 0.65$

(C_x/U) of 0.85 and for a lower value (0.65) are shown in Figs. 1 and 2, respectively. The cause and consequences of the hub corner stall at 0.85 were discussed in [1]. The present discussion is limited to the flows at midspan. At the design incidence ($C_x/U = 0.85$) there was a flaring in the streak line at midchord which appeared to be due to transition (as will be discussed below). The flow remained attached all the way to the trailing edge. In the more positive incidence case ($C_x/U = 0.65$) the flaring of the streak line (transition) had moved forward and there was back-flow at the trailing edge, i.e., the boundary layer had separated at about the 70 percent chord location.

Flow visualization had originally been carried out using a number of relatively short strips of Ozalid paper (as in reference [1], Figs. 3 and 4). When it was observed that a single streak extended over several strips it was decided to use fewer but longer strips (as in Figs. 1 and 2). Relatively short strips were used near the leading and trailing edges and a single long strip at midchord (extending from 15 to 90 percent chord). It was observed that the flaring of the streaks only occurred with the long midchord strip of Ozalid paper and that the location of the flaring was always slightly downstream of the minimum pressure, where transition would be expected. The location of the flaring is indicated by the "T" on the airfoil pressure distributions shown in Figs. 3 and 4. The added fact that the flaring occurred very close to the location of predicted laminar boundary layer separation (Figs. 5 and 6) lead to the conclusion that the flaring was evidence of boundary layer transition. The flaring did not occur with the short strips of Ozalid paper because the strip beginning downstream of the minimum pressure apparently tripped the boundary layer. The leading edge of the long midchord strip of Ozalid paper began at about 15 percent of

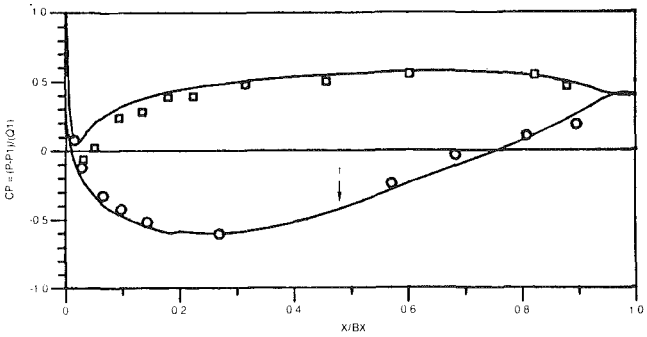


Fig. 3 Measured and computed midspan pressure distributions and measured transition (T) site at $C_x/U = 0.85$

axial chord which was at or slightly ahead of the minimum pressure. At this position it did not appear to trip the boundary layer. As the laminar flow passed the minimum pressure the skin friction dropped and the shape factor increased, making the boundary layer more prone to radial skewing due to centrifugal and Coriolis effects. Similar results were observed analytically by Thompkins and Usab [2]. Finally, from the flow visualization it was seen that the boundary layers were basically two-dimensional (i.e., collateral), except near the trailing edge at a (C_x/U) of 0.85 and downstream of the separation at 0.65.

Analysis

The measured and computed pressure distributions shown in Figs. 3 and 4 were discussed in detail in [1]. The computed distributions were based on the method of Caspar et al. [3] and on the experimentally determined values of inlet and exit

Downloaded 01 Jun 2010 to 171.66.16.62. Redistribution subject to ASME license or copyright; see http://www.asme.org/terms/Terms_Use.cfm

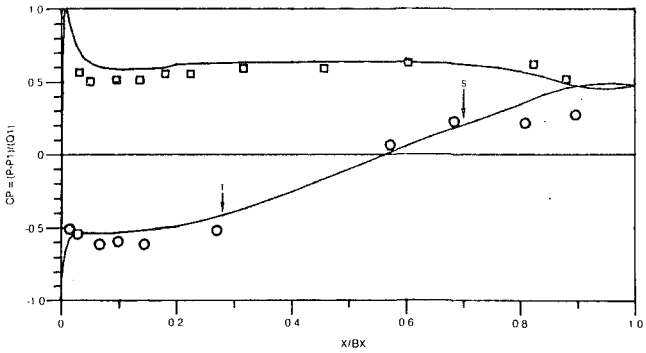


Fig. 4 Measured and computed midspan pressure distributions and measured transition (*T*) and separation (*S*) sites at $C_x/U = 0.65$

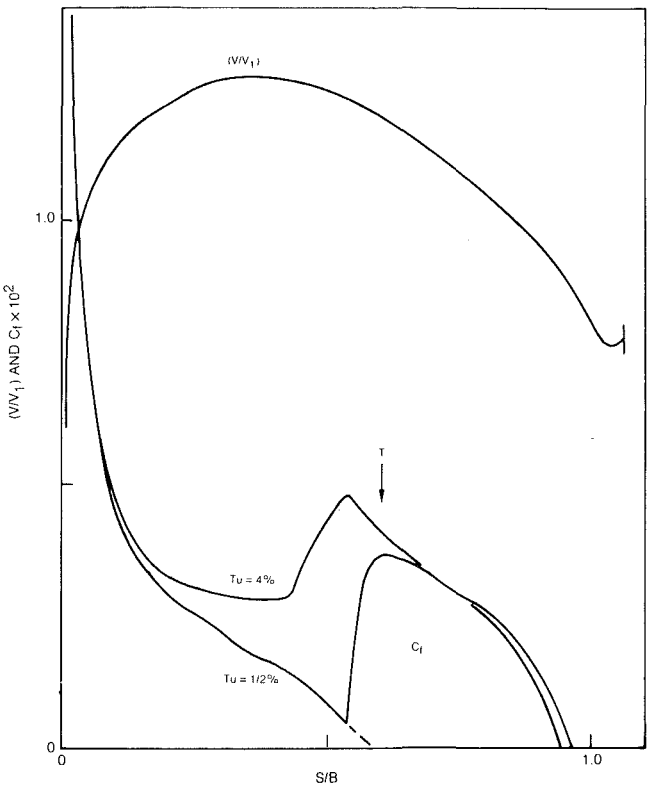


Fig. 5 Free-stream velocity and skin friction coefficient distributions at $C_x/U = 0.85$, Re = 0.51 × 10^6

flow angle, total pressure loss and stream tube contraction. At the (C_x/U) of 0.85 the agreement was excellent and at 0.65 it was good up to separation. The location of separation (*S*) was based on the flow visualization.

The computed velocity distributions were used to provide input to the transitional boundary layer analysis of McDonald and Fish [4]. For the case at (C_x/U) of 0.65 the leading edge overspeed was eliminated because its abruptness caused problems in the boundary layer calculation. Calculations were run at two freestream turbulence levels. The first (T_u = 1/2 percent) is typical of the rig environment and the second (T_u = 4 percent) is typical of a multistage rig or engine environment.

At T_u = 1/2 percent and a (C_x/U) of 0.85 (Fig. 5) the location of laminar separation (C_f = 0) closely matched the observed location of the flow visualization flaring. In this case natural transition was not predicted. It was modeled by restarting the calculation as a turbulent boundary layer at a location just upstream of the predicted location of laminar separation. The turbulent boundary layer calculation indicated separation close to the trailing edge. The fact that the

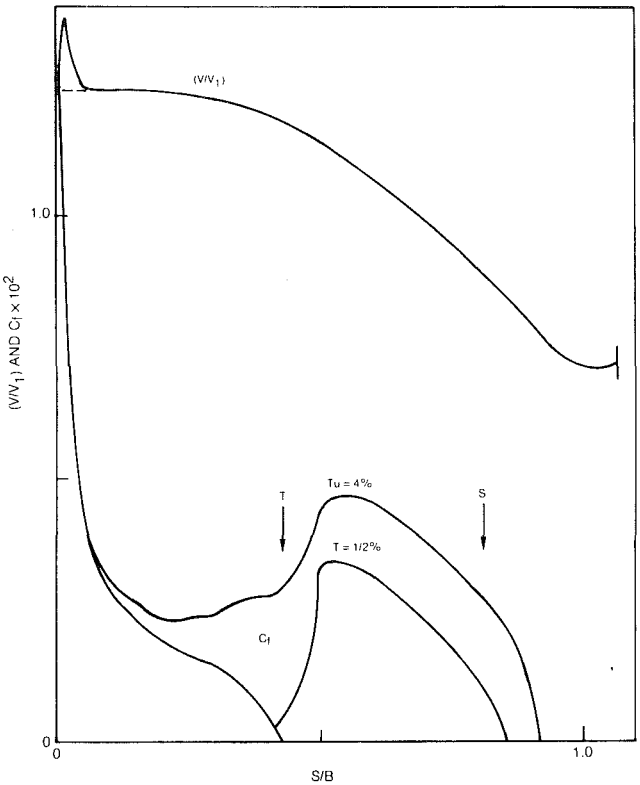


Fig. 6 Free-stream velocity and skin friction coefficient distributions at (C_x/U) = 0.65, Re = 0.45 × 10^6

actual boundary layer was attached at the trailing edge may be related to the three-dimensional effects there. At T_u = 4 percent natural transition and turbulent separation locations were very close to those at T_u = 1/2 percent.

At T_u = 1/2 and 4 percent and a (C_x/U) of 0.65 (Fig. 6), the results were similar to those at 0.85 in that the predicted transition location closely matched the measured location. In addition, however, the predicted location of turbulent trailing edge separation also matched the measured location. For this case strong three-dimensional effects were limited to the region downstream of separation.

Conclusions

The ammonia-Ozalid flow visualization technique was a good indicator of boundary layer transition on rotors where centrifugal and Coriolis forces were present to cause boundary layer skewing. A two-dimensional transitional boundary layer analysis has been shown to give an excellent prediction of the locations of transition and turbulent separation. High free-stream turbulence was predicted to have little effect on the locations of either transition or separation. Finally, the approach of using potential flow and boundary layer analysis for the design of compressor airfoils has been further substantiated for this case of flow over compressor rotor airfoils.

References

1 Dring, R. P., Joslyn, H. D., and Hardin, L. W., "An Investigation of Axial Compressor Rotor Aerodynamics," ASME paper No. 81-GT-56.

2 Thompkins, W. T., and Usab, W. J., "A Quasi-Three-Dimensional Blade Surface Boundary Layer Analysis for Rotating Blade Rows," ASME Paper No. 81-GT-126, ASME Gas Turbine Conference, Houston, Texas, March 1981.

3 Caspar, J. R., Hobbs, D. E., and Davis, R. L., "Calculation of Two-Dimensional Potential Cascade Flow Using Finite Area Methods," *AIAA Journal*, Vol. 18, No. 1, January 1980, pp. 103-109.

4 McDonald, H., and Fish, R. W., "Practical Calculation of Transitional Boundary Layer," *International Journal of Heat and Mass Transfer*, Vol. 16, No. 9, 1973.

Downloaded 01 Jun 2010 to 171.66.16.62. Redistribution subject to ASME license or copyright; see http://www.asme.org/terms/Terms_Use.cfm